

Middle Atmosphere Program

HANDBOOK FOR MAP VOLUME 18

Edited by
S. Kato

NASA-CR-179942

(MAP-HANDBOOK-18) MIDDLE ATMOSPHERE
PROGRAM. HANDBOOK FOR MAP. VOLUME 18:
EXTENDED ABSTRACTS (International Council of
Scientific Unions) 536 p HC A23/MF A01;
also available from SCOSTEP

N86-27719
THRU
N86-27832
Unclass
42926

CSSL 04A G3/46

No DAA needed

CAT. 46

(1+113)

536P

6011

↓

6124

ICSU

International Council of Scientific Unions

SCOSTEP

Scientific Committee on Solar-Terrestrial Physics

K. D. Cole, President
J. G. Roederer, Vice President
C. H. Liu, Scientific Secretary

MAP ORGANIZATION

MIDDLE ATMOSPHERE PROGRAM STEERING COMMITTEE

S. A. Bowhill, SCOSTEP, Chairman
K. Labitzke, COSPAR, Vice Chairman
C. H. Liu, SCOSTEP, Secretary

H. S. Ahluwalia, IUPAP
R. D. Bojkov, WMO
A. D. Danilov, COSPAR
J. C. Gille, COSPAR
I. Hirota, IUGG/IAMAP
A. H. Manson, SCOSTEP

L. R. Megill, IUGG/IAGA
T. Nagata, SCAR
R. G. Roper, IAMAP
P. C. Simon, IAU
J. Taubenheim, IUGG/IAGA
T. E. VanZandt, URSI

R. A. Vincent, URSI

MAP STANDING COMMITTEES

Data-Management -- G. Hartmann and I. Hirota, Co-Chairmen
Dynamics Calendar -- T. E. VanZandt, Chairman
Publications -- C. F. Sechrist, Jr., Chairman

MAP STUDY GROUPS

MSG-5 Ions and Aerosols, F. Arnold and M. P. McCormick, Co-Chairmen
MSG-8 Atmospheric Chemistry, G. Witt, Chairman
MSG-9 Measurement of Middle Atmosphere Parameters by Long Duration
Balloon Flights, J. E. Blamont, Chairman

APPROVED MAP PROJECTS

	Coordinator
AMA:	T. Hirasawa
ATMAP:	J. M. Forbes
CAMP:	G. Witt
CLIMAT:	J. M. Russell
DYNAMICS:	K. Labitzke
GLOBMET:	R. G. Roper
GLOBUS:	J. P. Pommereau
GOSSA:	M. P. McCormick
GRATMAP:	D. C. Fritts

	Coordinator
MAC-Epsilon:	E. V. Thrane
MAC-SINE:	E. V. Thrane
MAE:	R. A. Goldberg
MASH:	A. O'Neill
MSTRAC:	P. K. Rastogi
NIEO:	S. Kato
OZMAP:	D. F. Heath
SSIM:	P. C. Simon
WINE:	U. von Zahn

MAP REGIONAL CONSULTATIVE GROUP

Europe M. L. Chanin, Chairman

M I D D L E
A T M O S P H E R E
P R O G R A M

HANDBOOK FOR MAP

Volume 18

Extended Abstracts
of papers presented at the
MAP Symposium
November 26-30, 1984
Kyoto, Japan

Edited by

S. Kato

December 1985

Published for the ICSU Scientific Committee on Solar-
Terrestrial Physics (SCOSTEP) with financial assistance
from the National Aeronautics and Space Administration
under P.O. W-15,897 and Unesco Subvention 1984-1985

Copies available from SCOSTEP Secretariat, University of
Illinois, 1406 W. Green Street, Urbana, Illinois 61801

Table of Contents	iii
I: CLIMATOLOGY OF THE MIDDLE ATMOSPHERE.	1
1.1 On the interannual variability of the middle atmosphere during winter, K. Labitzke.	1
1.2 Middle atmosphere general circulation statistics, Marvin A. Geller.	10
1.3 Seasonal variation of the stratospheric circulation, I. Hirota and M. Shiotani	11
1.4 Aspects of the stratospheric circulation as derived from SSU data, V. Michaelis and A. O'Neill	14
1.5 The seasonal variation of the D region as inferred from propagation characteristics of LF radio waves, T. Ishimine, T. Ishii and Y. Echizenya	15
1.6 Mean winds of the upper middle atmosphere (60-110 km): A global distribution from radar systems (M.F., Meteor, VHF), A. H. Manson, C. E. Meek, M. Massebeuf, J. L. Fellous, W. G. Elford, R. A. Vincent, R. L. Craig, R. G. Roper, S. Avery, B. B. Balsley, G. J. Fraser, M. J. Smith, R. R. Clark, S. Kato and T. Tsuda.	19
1.7 Monthly mean values of the mesospheric wind field over Poker Flat, Alaska, B. B. Balsley and A. C. Riddle.	23
1.8 Trends in upper stratospheric temperatures as observed by rocketsondes (1965-1983), K. W. Johnson and M. E. Gelman.	24
1.9 Profiles of temperature and density based on extremes at 5, 10, 20, 30, and 40 km, Arthur J. Kantor, Paul Tattelman and Frank A. Marcos	28
1.10 Interannual variability of middle atmosphere during northern winter, B. K. Mukherjee, K. Indira and Bh. V. Ramana Murty.	32
1.11 Connection between mesopause temperature, circulation and noctilucent clouds, Volker Gartner and Michael Memmesheimer	35
1.12 Some studies of zonal and meridional wind characteristics at low latitude Indian stations, O. P. Nagpal and Somesh Kumar	42
1.13 Temporal variations of the tropical tropopause characteristics, B. V. Krishna Murthy, K. Parameswaran and K. O. Rose.	46
II: LARGE-SCALE WAVE DYNAMICS.	50
2.1 Middle atmosphere tides, Jeffery M. Forbes.	50
2.2 Diurnal nonmigrating tide due to land-sea distribution, Toshitaka Tsuda and Susumu Kato	57

2.3	Middle atmosphere (60 - 110 km) tidal oscillations at Saskatoon, Canada (52°N, 107°W) during 1983/84, A. H. Manson and C. E. Meek.	61
2.4	Mesospheric winds observed by the Kyoto meteor radar, Toshitaka Tsuda and Susumu Kato	66
2.5	Semidiurnal temperature oscillation and E-region absorption over Haringhata, N. N. Purkait.	69
2.6	Normal mode Rossby waves observed in the upper stratosphere, Toshihiko Hirooka and Isamu Hirota.	72
2.7	On the interaction between the quasi-2-day wave and the mean flow, R. L. Craig, R. A. Vincent and R. A. Plumb.	76
2.8	Planetary waves-mean flow interaction in the middle atmosphere: Lidar observations and modelisation, A. Hauchecorne	80
2.9	Discrimination of a major stratospheric warming event in February-March 1984 from earlier minor warmings, K. W. Johnson, R. S. Quiroz and M. E. Gelman	89
2.10	The 4-5 day mode oscillation in zonal winds of Indian middle atmosphere during MONEK-79, R. S. Reddy, B. K. Mukherjee, K. Indira and Bh. V. Ramana Murty	96
2.11	The evolution of Ertel's potential vorticity during stratospheric sudden warmings, T. D. A. Fairlie and A. O'Neill.	99
2.12	Seasonal changes in the structure of the stratospheric circulation, A. O'Neill and V. D. Pope	105
2.13	On the use of potential vorticity for the diagnosis of stratospheric synoptics, K. Rose, K. Labitzke and U. Kummel	109
2.14	The integrated enstrophy budget of the winter stratosphere diagnosed from LIMS data, Mark R. Schoeberl and Anne K. Smith	116
2.15	Planetary wave-mean flow interaction in the stratosphere: A comparison between the Northern and Southern Hemispheres, M. Shiotani and I. Hirota	117
2.16	Wave-mean flow interaction during the winter to summer transition in the Southern Hemisphere stratosphere, K. Yamazaki	121
2.17	A new model of resonance in the winter stratosphere, Peter H. Haynes.	126
2.18	Transient response to localized episodic heating in the tropics, Murry L. Salby and Rolando R. Garcia	132
2.19	Rossby wavetrains in the stratosphere forced by localised disturbances in the troposphere, C. J. Marks, A. O'Neill and V. D. Pope.	140

2.20	Low-frequency dynamics of quasi-geostrophic waves in a mid-latitude channel and the effects of tropical influence, K. K. Tung and A. J. Rosenthal.	145
2.21	Suppression of stationary planetary waves by internal gravity waves in the mesosphere, Saburo Miyahara.	154
2.22	Mean zonal winds and planetary waves induced by internal gravity wave packets, M. Takahashi and M. Uryu.	157
2.23	Wave-mean flow interaction in the NCAR stratospheric general circulation model, Byron A. Boville	161
2.24	Equatorial waves in the NCAR stratospheric general circulation model, Byron A. Boville	165
2.25	Vacillations induced by interference of stationary and traveling waves, Murry L. Salby and Rolando R. Garcia	169
2.26	Over-reflection of barotropic Rossby wave packet, K. Takano and M. Uryu	174
2.27	Effects of Rayleigh and Newtonian damping on wave-mean flow interaction, Yoshikazu Hayashi.	179
2.28	Variation of tidal winds in the ionosphere inferred from geomagnetic Sq field, M. Takeda and T. Araki.	182
2.29	Influence of geomagnetic disturbance on atmospheric circulation, Kunihiko Kodera	186
2.30	Behavior of neutral wind gradients at meteor heights over midlatitude stations, P. C. S. Devara, G. Chandrasekhar and M. I. Ahmed	190
III:	GRAVITY WAVES AND TURBULENCE.	196
3.1	Radar observations of mesospheric gravity waves and turbulence at Adelaide, R. A. Vincent.	196
3.2	The MU radar: Current status and first results, Susumu Kato, Shoichiro Fukao, Toshitaka Tsuda and Toru Sato.	201
3.3	A comparison of the spectrum of vertical wind velocities obtained by the MST radar technique at various seasons and locations, W. L. Ecklund, B. B. Balsley and D. A. Carter.	206
3.4	Power spectra of mesospheric velocities in polar regions, P. Czechowsky and R. Ruster	207
3.5	Gravity wave spectra observed by Doppler radar: Comparison of a model with mesospheric observations, T. E. VanZandt, S. A. Smith and D. C. Fritts.	212
3.6	Instabilities and turbulence at mesospheric heights as observed by VHF radar, R. Ruster and J. Klostermeyer.	216
3.7	Observation and analysis of thunderstorm-generated gravity waves in the lower stratosphere, Daren Lu, T. E. VanZandt and W. L. Clark, Jr.,	220

3.8	Gravity waves observed with GRAVNET: Saskatoon (52°N, 107°W), 1983/84, C. E. Meek, A. H. Manson and I. M. Reid.	226
3.9	Hierarchical structure of stratospheric wind fluctuations, M. D. Yamanaka and H. Tanaka.	232
3.10	Two classes of medium-scale traveling ionospheric disturbances observed with an array of HF-Doppler sounders, T. Shibata and T. Okuzawa.	237
3.11	Finite amplitude gravity waves: Harmonics, advective steepening, breaking and saturation, J. Weinstock	242
3.12	Gravity wave characteristics in the stratosphere and mesosphere at midlatitude, M. L. Chanin and A. Hauchecorne.	247
3.13	Gravity wave vertical energy flux at 95 km, P. G. Jacob and F. Jacka.	248
3.14	Wave motions in the upper atmospheric sodium layer observed with a lidar technique, Hiroshi Kamiyama and Fumihiko Tomita. .	253
3.15	Clear air turbulence and mesospheric gravity waves, R. S. Lindzen	259
3.16	Tropospheric gravity waves observed by three closely spaced ST radars, D. A. Carter, B. B. Balsley, W. L. Ecklund, M. Crochet, A. C. Riddle and R. Garello	260
3.17	The acoustic gravity wave induced by a point source in the middle atmosphere, Zhang Xun Jie and Xiong Nian Lu.	264
3.18	A numerical study of nonlinear interactions between mean flow and breaking internal gravity waves, Hideji Kida.	273
3.19	Effects of breaking gravity waves on the chemical composition of the mesosphere and lower thermosphere, S. Solomon and R. Garcia	281
3.20	Local effects of gravity wave propagation and saturation, David C. Fritts	282
3.21	The speed of wave-wave interactions in the atmosphere, K. C. Yeh and C. H. Liu	287
3.22	A ray tracing model of gravity wave propagation and breakdown in the middle atmosphere, Mark R. Schoeberl	292
3.23	A further study of gravity wave induced drag and diffusion in the mesosphere, J. R. Holton and Xun Zhu.	293
3.24	Gravity waves and turbulent diffusion coefficients for constituent and heat transport in the mesosphere and lower thermosphere, Darrell F. Strobel, John P. Apruzese and Mark R. Schoeberl	294
3.25	Gravity wave and tidal momentum fluxes at Poker Flat, Alaska, S. K. Avery, B. B. Balsley and T. Judasz.	295

3.26	A test of the validity of radar and scintillometer measurements and model estimates of C^2 , T. E. VanZandt, J. L. Green, W. L. Clark, J. M. Warnock and J. Vernin.	296
3.27	Comparisons of horizontal and vertical velocity spectra in the mesosphere, stratosphere and troposphere: Observations and theory, K. S. Gage, B. B. Balsley and R. Garelo.	297
3.28	Determination of the atmospheric kinetic energy density height profile over Poker Flat, Alaska, B. B. Balsley and R. Garelo	298
3.29	Gravity wave motions and momentum fluxes in the middle atmosphere at Adelaide, Australia, R. A. Vincent and D. C. Fritts.	299
3.30	Balloon observations of (inertio-) gravity waves and turbulence in the middle stratosphere, H. Tanaka and M. D. Yamanaka.	302
3.31	MAP-oriented research in the People's Republic of China, Daren Lu.	303
3.32	Quantitative study on dispersion relations of TIDs observed by an HF Doppler array, M. Tsutsui and T. Ogawa	306
3.33	HF Doppler observations of acoustic waves excited by the earthquake, T. Ichinose, K. Takagi, T. Tanaka, T. Okuzawa, T. Shibata, Y. Sato, C. Nagasawa and T. Ogawa	310
3.34	Estimation of neutral wind velocity in the ionospheric heights by HF-Doppler technique, T. Kitamura, M. Takefu and M. Hiroshige.	319
3.35	Observation of the ionospheric effect of typhoons by a network of HF-Doppler sounders in central Japan, T. Okuzawa, T. Shibata, T. Ichinose, C. Nagasawa, I. Nagano, M. Mambo, M. Tautsui and T. Ogawa	324
3.36	A correlation study of structures of sporadic E ionization clouds based on VHF radio propagation measurements, K. Marubashi, S. Kainuma, T. Ishimine and Y. Shimizu.	325
3.37	Satellite observations of 557.7 nm airglow as a diagnostic technique to study the dynamics of the lower thermosphere, L. L. Cogger, R. Elphinstone and J. S. Murphree	326
3.38	Local time distribution of the SSC-associated HF-Doppler frequency shifts, T. Kikuchi, H. Sugiuchi and T. Ishimine	327
3.39	Vertical Stokes drifts produced by vertically propagating internal gravity waves in a compressible atmosphere, L. Coy, J. Weinstock and D. Fritts.	328
IV:	TRANSPORT PROCESSES OF TRACE SPECIES AND AEROSOLS.	329
4.1	Transport processes as manifested in satellite and lidar aerosol measurements, M. P. McCormick	329
4.2	Ruby lidar observations and trajectory analysis of stratospheric aerosols injected by the volcanic eruptions of El Chichon, O. Uchino, T. Tabata, I. Akita, Y. Okada and K. Naito.	330

4.3	Lidar observations of the El Chichon cloud in the stratosphere over Fukuoka, M. Fujiwara, T. Shibata and M. Hirono	337
4.4	On the long term variation of stratospheric aerosol content after the eruption of volcano El Chichon: Laser radar measurements, S. Hayashida and Y. Iwasaka.	340
4.5	Behavior of decaying El Chichon cloud over Toyokawa, Japan (35°N) observed by 532-nm lidar, M. Takagi, A. Iwata and Y. Kondo.	343
4.6	Comparative study of aerosols observed by YAG lidar and airborne detectors, M. Hirono, M. Fujiwara and T. Shibata.	346
4.7	Optical properties of upper-tropospheric and stratospheric aerosols as estimated from solar aureole measurements, M. Tanaka, T. Nakajima and T. Hayasaka.	350
4.8	Excimer lidar measurements of ozone, T. Shibata, O. Uchino and M. Maeda.	351
4.9	Measurement of nitric oxide from 7 to 32 km and its diurnal variation in the stratosphere, Y. Kondo, W. A. Matthews, A. Iwata and M. Takagi.	354
4.10	Measurements of CCl_3F , CCl_2F_2 , CCl_4 , N_2O and SF_6 in the Northern Hemisphere stratosphere, Robert ⁶ Leifer and Russell Juzdan.	355
4.11	A dynamically based transport parameterization for one-dimensional photochemical models, J. R. Holton.	359
4.12	Transport of trace species deduced from LIMS observations, J. C. Gille, L. V. Lyjak, A. K. Smith, P. L. Bailey, S. T. Massie and C. M. Smythe	360
4.13	Limb-atmospheric infrared spectrum observed on the satellite "Ohzora", A. Matsuzaki, Y. Nakamura and T. Itoh	363
4.14	Atmospheric concentrations and behavior of halocarbons and methane, Y. Makide, A. Yokohata and T. Tominaga	364
4.15	Transport characteristics in the middle atmosphere and two-dimensional modeling, Hideji Kida	365
4.16	The zonally averaged transport characteristics of the atmosphere as determined by a general circulation model, R. Alan Plumb	373
4.17	Dynamical roles of planetary waves on the winter anomaly in the middle and lower latitudes, Kohji Kawahira.	375
4.18	Transport processes in the stratosphere: Model simulations and comparisons with satellite observations, W. L. Grose, R. E. Turner and J. E. Nealy.	381
4.19	Ozone during sudden stratospheric warming: A three-dimensional simulation, K. Rose and G. Brasseur	386

4.20	Instrusion process of stratospheric ozone into the troposphere over Japan, H. Muramatsu, Y. Makino, M. Hirota and T. Sasaki. .	391
4.21	An interpretation for the interannual variations of the global distribution of total ozone, Fumio Hasebe	395
4.22	Emission, absorption and group delay of microwaves in the atmosphere in relation to water vapour content over the Indian subcontinent, A. K. Sen, A. K. Dev Gupta, P. K. Karmakar, S. Dev Barman, A. B. Bhattacharya, N. Purkait, M. K. Das Gupta and J. S. Sehra	399
4.23	Aircraft observation of NO _x in the troposphere at mid-latitude, Y. Kondo, W. A. Matthews, A. Iwata, Y. Morita and M. Takagi	405
4.24	Numerical simulation of El Chichon volcanic cloud, T. Shibata, M. Fujiwara and M. Hirono	406
4.25	A negative ion model in the lower stratosphere, Hiroto Kawamoto and Toshio Ogawa.	408
4.26	Aircraft measurements of aerosols in the upper troposphere at midlatitudes, Y. Morita, M. Takagi and Y. Kondo	412
4.27	Lidar observations of the nighttime sodium layer at 33°N, Michihiro Uchiumi, Motokazu Hirono and Motowo Fujiwara.	417
4.28	Ion loss processes in the stratosphere, B. S. N. Prasad and S. Chandramma	421
4.29	Vertical distribution of acetonitrile in the atmosphere, J. Ingels, D. Nevejans and E. Arijs	426
4.30	Measurements of concentrations of chlorofluoromethanes (CFMs), carbon dioxide and carbon isotope ratio in stratospheric and tropospheric air by grab-sampling systems, T. Itoh, H. Kubo, H. Honda, T. Tominaga, Y. Makide, A. Yokohata and H. Sakai. . .	431
4.31	UV lidar measurements of the stratospheric aerosol layer and comparison with other optical data, O. Uchino	438
4.32	The recent improved ROCOZ (ROCOZ-A) ozone measurements, H. S. Lee	442
V:	MAP IN THE ANTARCTICA	443
5.1	Balloon-borne observations of stratospheric aerosol in Antarctica from 1972 to 1984, D. J. Hofmann	443
5.2	Laser radar observations of the polar stratospheric aerosol layer, Y. Iwasaka, T. Hirasawa, H. Fukunishi, M. Fujiwara, R. Fujii and H. Miyaoka	450
5.3	A special ozone observation at Syowa Station, Antarctica from February 1982 to January 1983, Shigeru Chubachi.	453
5.4	Observation of atmospheric minor constituents by FTIR at Syowa Station, Antarctica, Y. Makino, H. Muramatsu, S. Kawaguchi, T. Yamanouchi, M. Tanaka and T. Ogawa	458

5.5	Measurement of polar stratospheric NO ₂ from the 23rd and 24th Japanese Antarctic Research Expedition (JARE) balloon experiments, K. Shibasaki, N. Iwagami and T. Ogawa.	461
5.6	Decomposition of CO ₂ molecules due to auroral X-rays, K. Sekihara	466
5.7	VHF radar observation of the middle atmosphere at Syowa Station, Antarctica, K. Igarashi, T. Ogawa, T. Tanaka, Y. Kuratani, R. Fujii and T. Hirasawa	471
5.8	Winds in the lower thermosphere over Mawson, Antarctica, N. P. Jones and F. Jacka.	477
5.9	Balloon measurements of aerosol in the Antarctic stratosphere, Y. Morita, M. Takagi, Y. Iwasaka and A. Ono	482
5.10	Balloon-borne observation of Aitken nuclei in the Antarctic stratosphere and troposphere, Tomoyuki Ito, Miwako Ikegami, Izuo Kanazawa and Yasunobu Iwasaka.	486
5.11	Gas-chromatographic measurements of atmospheric CF ₂ Cl ₂ , CFCl ₃ and N ₂ O in Antarctica, M. Hirota, Y. Makino, S. Chubachi, H. Mufamatsu and M. Shiobara.	491
5.12	50-MHz meteor radar observation at Syowa Station, Antarctica, T. Tanaka, T. Ogawa, K. Igarashi and R. Fujii	495
5.13	Research activities on "Antarctic Middle Atmosphere" by JARE 25th Team, T. Hirasawa, H. Fukunishi, M. Ayukawa, M. Ejiri, R. Fujii, Y. Iwasaka and M. Tanaka.	498
5.14	Observation of total ozone fields in the Antarctic atmosphere from TOVS of TIROS-N/NOAA, T. Yamanouchi, Sadao Kawaguchi, I. Iwashina and K. Suzuki	502
5.15	Seasonal and diurnal variation of the atmospheric NO ₂ at Syowa Station, Antarctica, K. Shibasaki	506
5.16	The change of depolarization of backscattering light from the polar stratospheric aerosol layer, Y. Iwasaka	510
5.17	The stratospheric aerosol particle measurement by balloon at Syowa Station (69.00°S, 39.35°E): Outline of special sonde (rubber) campaign JARE 24-, Y. Iwasaka, T. Morita, T. Itoh, K. Shibasaki, Y. Makino, T. Tanaka, K. Tsukamura, T. Yano, K. Kondoh and G. Iwashita	513
5.18	Water vapor content in the polar atmosphere measured by Lyman-α/OH fluorescence method, Y. Iwasaka, T. Saitoh and A. Ono. . .	516
	Author Index.	519

1.1 ON THE INTERANNUAL VARIABILITY OF THE MIDDLE ATMOSPHERE DURING WINTER

K. Labitzke

Institut für Meteorologie, Freie Universität Berlin
Berlin, Federal Republic of Germany

Reference Atmospheres such as the new CIRA (COSPAR International Reference Atmosphere), which will be based on global satellite data form a very useful basis for climatological studies. When using such climatologies it is important to be aware of the interannual variability which in the middle atmosphere is particularly large during the northern winters and southern springs.

COMPARISON OF THE POLAR REGIONS

For a comparison of the two polar regions, the monthly mean temperature data for 90°N and 90°S are shown in Figure 1a (update of Figure 1 of NAUJOKAT, 1981) and 1b (Figure 1b, LABITZKE and NAUJOKAT, 1983) in the form of frequency distributions. The time scale is shifted by 6 months so that both polar regions can be compared easily. The main features to be noted and which have been pointed out previously (e.g., BARNETT, 1974; LABITZKE, 1974; KNITTEL, 1976) are:

- (1) In the middle stratosphere the variability during the northern mid-winters, Figure 1a, is much larger than during the southern mid-winters, Figure 1b, due to the major midwinter warmings which take place only during the northern winters; the largest variations over Antarctica are observed during late spring, i.e., October and November when very intense "Final Warmings" bring about the transition into summer.
- (2) The variability in the middle stratosphere is very small in summer when the planetary waves of the troposphere cannot propagate upwards into the stratosphere due to the prevailing easterly winds. This is true for both polar regions.
- (3) The annual temperature range is larger over the South Pole, because winters are colder and summers warmer than over the North Pole.

In the upper stratosphere the transition from winter to summer has already started over Antarctica in early July, while a late winter cooling in high northern latitudes, caused by dynamic processes in connection with stratospheric warmings and typical of the northern winter, delays the transition to a summer pattern for about 2 months. Figure 2 shows monthly mean 1-hPa temperatures for March (N.H.) and September (S.H.). These maps are based on data of the new CIRA. They show clearly that the transition to summer is well in progress in September over Antarctica while no indication of a transition is noticeable in March over the Arctic.

VARIABILITY OF NORTHERN WINTERS

In the following the discussion on the interannual variability will concentrate on the northern winters: The monthly mean 30-hPa temperatures over the North Pole are given in Figure 3 together with an indication of the winter events. Canadian Warmings (CW) are characterized by an intensification of the Aleutian anticyclone, i.e., an amplification of the planetary-scale height wave one (LABITZKE, 1977) and a reversal of the temperature gradient poleward of 60°N is possible. These warmings occur most often during early winter.

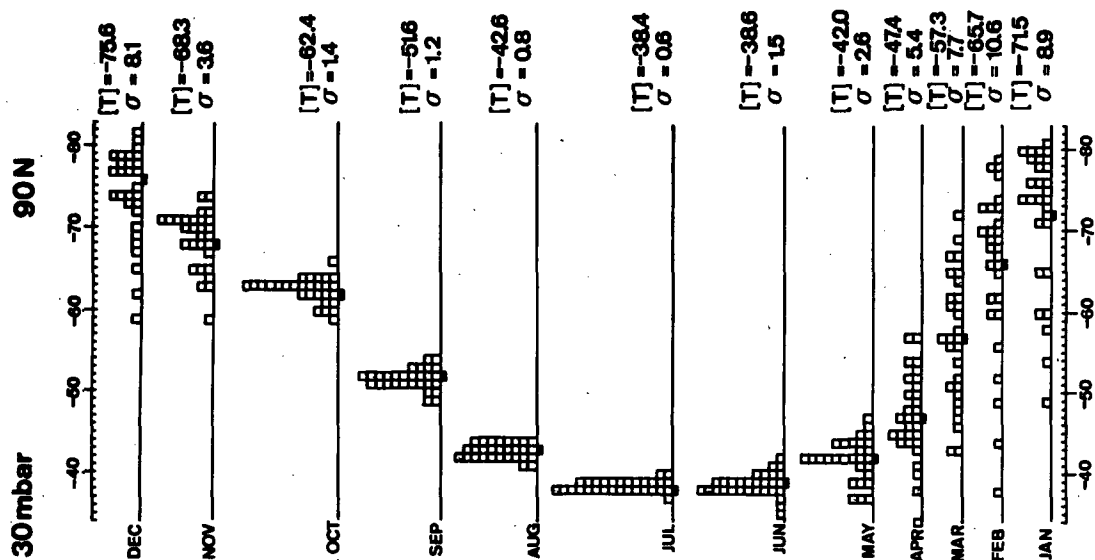


Figure 1a.

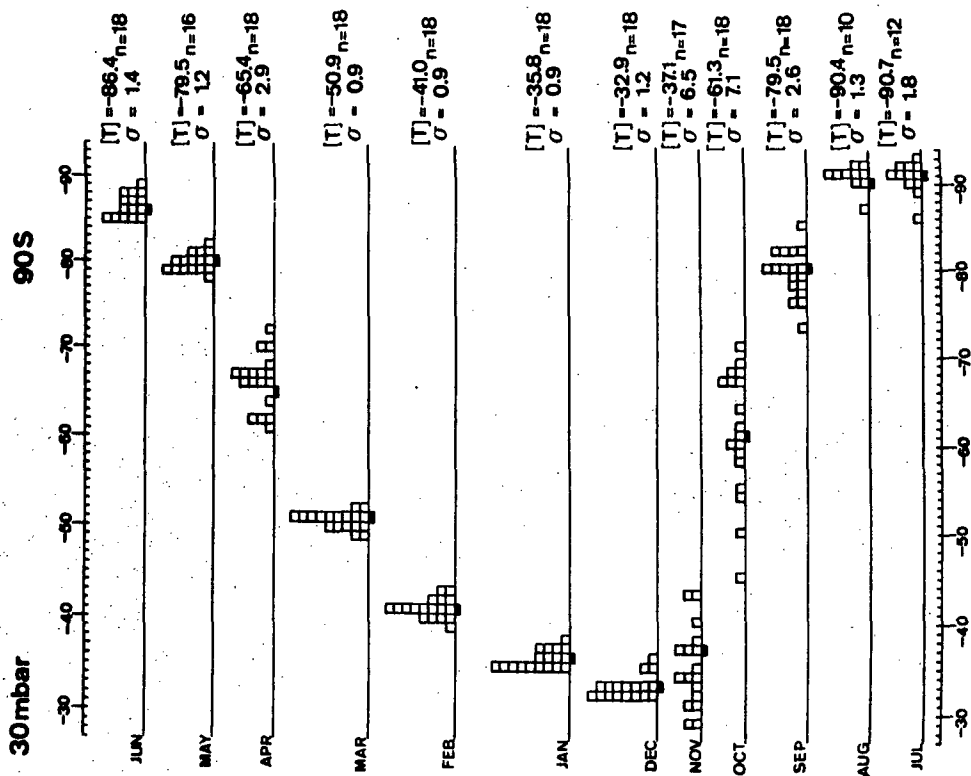
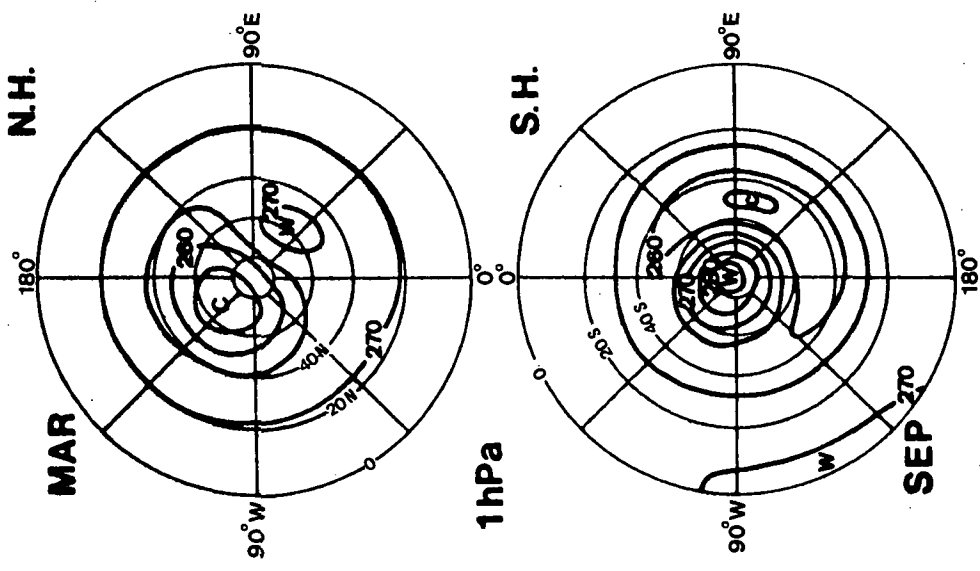


Figure 1b.

MONTHLY MEAN 30hPa NORTH POLE TEMPERATURES [°C]

Year	R _i	Nov	Dec	Jan	Feb	Mar	Apr	F.W.
1951/52	41	C.W.			*			[late] early
1952/53	27	C.W.						early
1953/54	0					* F.W.		early
1954/55	23		C.W.	*				[late]
1955/56	74	-68	-79 C	-76 C	-71 C	-61 C	-45	late
1956/57	185	-68	-73	-74	-38 *	-58	-53 C	[late]
1957/58	203	-70 C	-78 C	-71	-49 *	-61 C	-57 C	[late]
1958/59	217	-58 C.W.	-67 C.W.	-74	-73 C	-51 * F.W.	-43	early
1959/60	148	-71 C	-69 C.W.	-60	-70 C	-59 C	-41	early
1960/61	58	-54	-65 C.W.	-65	-72 C	-42 * F.W.	-47	early
1961/62	39	-67	-80 C	-79 C	-67	-65 C	-57 C	late
1962/63	20	-69 C.W.	-74	-74	-52 *	-61 C	-54 C	[late]
1963/64	15	-72 C	-81 C	-78 C	-77 C	-47 * F.W.	-44	early
1964/65	18	-70 C.W.	-77 C	-76 C	-73 C	-62 C	-45	late
1965/66	28	-69	-59 C.W.	-78 C	-60 *	-66	-48	[late]
1966/67	111	-65	-73 C.W.	-80 C	-78 C	-72 C	-48	late
1967/68	122	-71 C.W.	-75	-58 *	-68	-67 C	-52 C	[late]
1968/69	104	-63 C.W.	-62	-72	-74 C	-57	-47	late
1969/70	112	-71 C	-73	-49 *	-82	-67 C	-47	[late]
1970/71	91	-71 C	-78 C	-54 *	-66	-56	-51 C	[late]
1971/72	62	-72 C	-78 C	-79 C	-70 C	-56	-44	early
1972/73	43	-69 C.W.	-79 C	-73	-44 *	-66	-52 C	[late]
1973/74	28	-71 C	-78 C.W.	-78 C	-79 C	-50 * F.W.	-44	early
1974/75	19	-65 C.W.	-74	-65	-68	-48 * F.W.	-46	early
1975/76	8	-71 C	-77 C	-80 C	-78 C	-68 C	-34 * F.W.	early
1976/77	16	-63 C.W.	-68	-60 *	-69	-60 C	-40	early
1977/78	52	-68 C.W.	-77 C	-74	-66	-49	-44	early
1978/79	167	-74 C	-74 C.W.	-75 C	-60 * F.W.	-51	-49	early
1979/80	162	-64 C.W.	-72	-60 C	-70 C	-49 * F.W.	-45	early
1980/81	114	-68 C.W.	-82 C	-81 C	-56 *	-54	-54 C	[late]
1981/82	111	-71 C	-70 C.W.	-71	-69	-64 C	-38	early
1982/83	86	-74 C	-79 C.W.	-79 C	-62	-52	-46	late
1983/84	58	-70 C	-77 C	-80 C	-65	-43 * F.W.	-50	early
C (n)		-5.70 (N)	-5.77 (N)	-5.75 (N)	-5.70 (E)	-5.60 (E)	-5.61 (E)	
[T] _{n-29}		-68.5	-74.1	-72.1	-66.7	-64.9	-45.8	
δ		3.7	6.7	8.6	10.1	12.3	9.8	

Figure 3.



Monthly Mean Temperatures [K]
5-year Average (New CIRA)

Figure 2.

Major midwinter warmings (*) are defined as such events during which at the 10-hPa level or below the latitudinal mean temperature increases poleward from 60°N and an associated circulation reversal is observed. Final Warmings (FW) are the transition into summer conditions; a FW is called "early" if the monthly mean 30-hPa North Pole temperature is -51°C in March, or -44°C in April; late denotes a delayed FW due to the "late winter cooling," which follows a major midwinter warming. If the major warmings take place late in winter, they may turn directly in FW denoted here as *FW; in this instance the late winter cooling is less effective than the heating due to the returning sun. The 14 or 12 coldest months (for April only 8) are denoted with C. In Figure 4 the winters of Figure 3 are grouped into a "westerly" and an "easterly" category, (followup of LABITZKE, 1982). The grouping of the winters is based on the equatorial winds at the 50-hPa level in early winter. Only the winter 1977/78 was omitted because of a phase change of the equatorial 50-hPa wind in December 1977. Looking at Figure 4, two facts are obvious at once:

- (1) Most of the cold winter months denoted with C are to be found in the "westerly" category.
- (2) In the "easterly" category much more major warmings (*) are observed: major warmings took place during 8 out of 14 winters in contrast to 4 out of 18 winters in the "westerly" category.

As was discussed in LABITZKE (1982), the cold winter months are typically connected with the "cold wave two", which reflects an elongation of the polar vortex in troposphere and stratosphere, while the major warmings are usually connected with the amplification of height wave one. The different vertical

WESTERLY CATEGORY									30hPa		EASTERLY CATEGORY															
R _j	Year	Nov	Dec	Jan	Feb	Mar	Apr	FW	R _j	Year	Nov	Dec	Jan	Feb	Mar	Apr	FW									
27	1952/53	C.W.						early	41	1951/52	C.W.			*			[late]									
0	1953/54					*FW		early	23	1954/55		C.W.	*				[late]									
74	1955/56		C	C	C	C		late	165	1956/57				*		[C]	[late]									
203	1957/58	C	C		*	[C]	[C]	[late]	217	1958/59	C.W.	C.W.		C	*FW		early									
146	1959/60	C	C.W.		C	C		early	58	1960/61		C.W.		C	*FW		early									
39	1961/62		C	C		C	C	late	20	1962/63	C.W.			*	[C]	[C]	[late]									
15	1963/64	C	C	C	C	*FW		early	28	1965/66		C.W.	C	*			[late]									
18	1964/65	C/C.W.	C	C	C	C		late	104	1968/69	C.W.			C			late									
111	1966/67		C.W.	C	C	C		late	91	1970/71	C	C	*			[C]	[late]									
122	1967/68	C		*		[C]	[C]	[late]	43	1972/73	C.W.	C		*		[C]	[late]									
112	1969/70	C/C.W.		*		[C]		[late]	19	1974/75	C.W.				*FW		early									
62	1971/72	C	C	C	C			early	16	1976/77	C.W.		*		[C]		early									
28	1973/74	C	C/C.W.	C	C	*FW		early	162	1979/80	C.W.		C	C	*FW		early									
8	1975/76	C	C	C	C	C		early	111	1981/82	C	C.W.														
167	1978/79	C		C		*FW		early																		
114	1980/81	C.W.	C	C	*		[C]	[late]																		
86	1982/83	C	C/C.W.	C				late																		
58	1983/84	C	C	C		*FW		early																		
Σ C		12 ⁽¹⁴⁾	11 ⁽¹⁴⁾	12 ⁽¹⁴⁾	8 ⁽¹²⁾	9 ⁽¹²⁾	4 ⁽⁸⁾		Σ C		2 ⁽¹⁴⁾	2 ⁽¹⁴⁾	2 ⁽¹⁴⁾	4 ⁽¹²⁾	2 ⁽¹²⁾	4 ⁽⁸⁾										
Σ *				2	2				Σ *				3	5												
Σ *FW					1	4	1		Σ *FW						4											
n=42 Σ C _{N+D+J} = 35 = 83%									n=42 Σ C _{N+D+J} = 6 = 14%									n=14 Σ * = 8 = 57%								
Σ * = 4 = 22%																										

Figure 4.

structure of these waves is demonstrated in Figure 5, which shows the deviations of the monthly mean geopotential heights from the zonal mean at 60°N. Two distinctly different patterns evolve: During January 1970, a month with a major warming, the height wave one clearly dominates in the stratosphere, while during January 1974 the typical "cold wave two" pattern exists. This structure can be found during more than 90% of the C-months. Consistent with such different vertical structures also all derived quantities are different during the respective winters, on a daily as well as on a monthly time scale.

RECENT COOLING OF THE ARCTIC

It is of interest to note that during the last winters major midwinter warmings did not occur during January, (see Figure 3), and only one during February. The temperatures given in Figure 3 are plotted for January in Figure 6, together with a weighted (1-2-1) mean. Besides the very large variation between single years, a "cooling trend" is noticeable from approximately January 1970 until 1984.

This cooling is noticeable for December and January in all our data, from 100 to 10 hPa, as shown for January in Figure 7. The reason for such variations is not understood. One possible explanation could be the increase of aerosol in the stratospheric arctic after large volcanic eruptions, as observed recently by McCormick and others. The increased aerosol may be

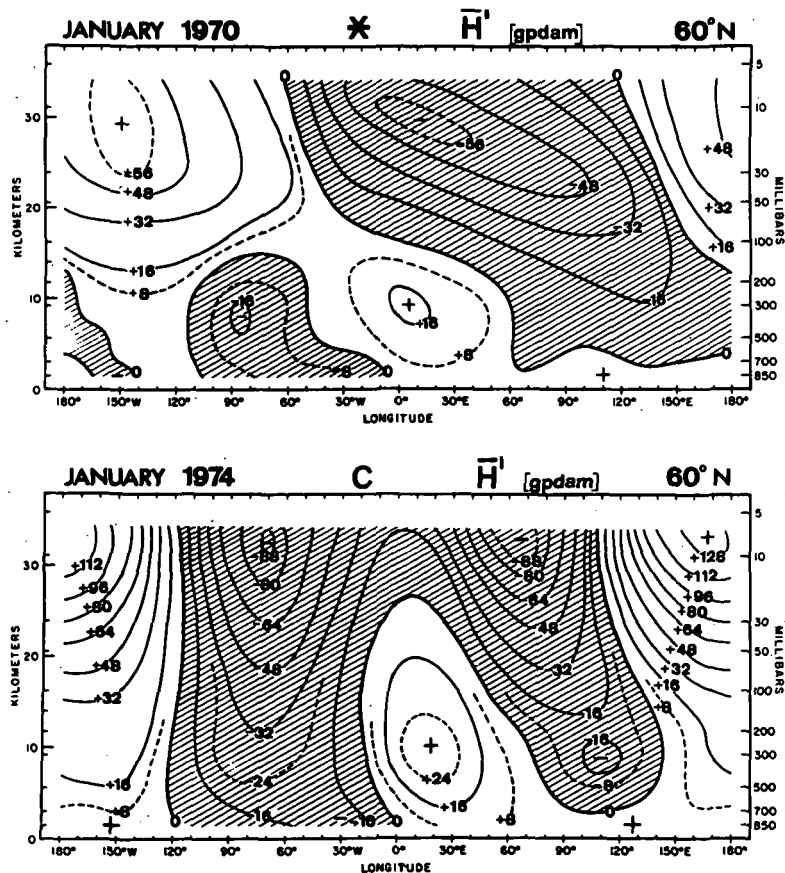


Figure 5.

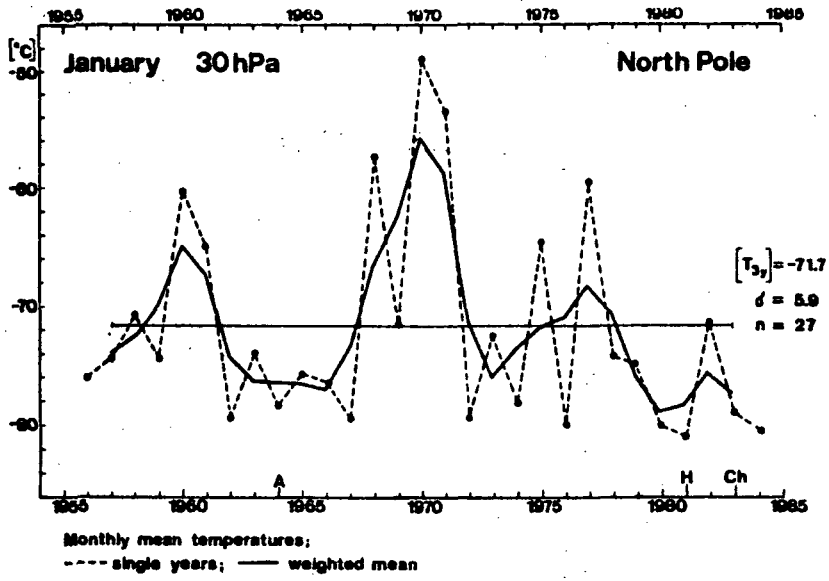


Figure 6.

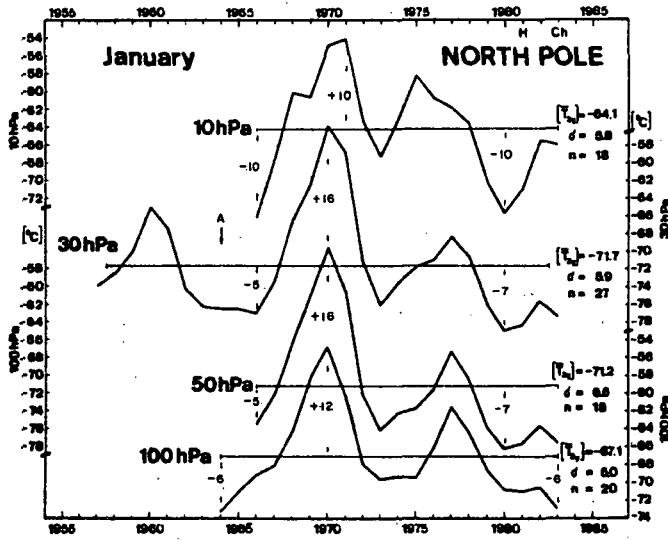


Figure 7.

responsible for the formation of polar stratospheric clouds, which may act as infrared radiators and cool the layer above the cloud, especially during the polar night. The Januarys which could have been affected by the recent strong eruptions are marked with A for Agung, H for St. Helens, and Ch for El Chichon, although several weaker eruptions took place since 1974. In contrast to the stratosphere, the troposphere does not show such a strong cooling. This is shown in Figure 8 with the weighted temperatures at 70°N and the data for 300 hPa included.

The cooling in winter is confined to high latitudes, as shown in Figure 9a, and we find the opposite temperature gradient results in an intensification of the polar night jet stream with especially strong winds observed during the last winters, (Figure 10). The anti-correlation of the polar temperatures and the mean zonal winds at 60°N is not surprising but still very important. The result of such cold midwinter conditions is that the warmings take place late during the winter. Therefore, we find the opposite situation in March, (Figure 9b), with a relatively warm arctic and colder tropics. The jet stream is, of course, weakened accordingly.

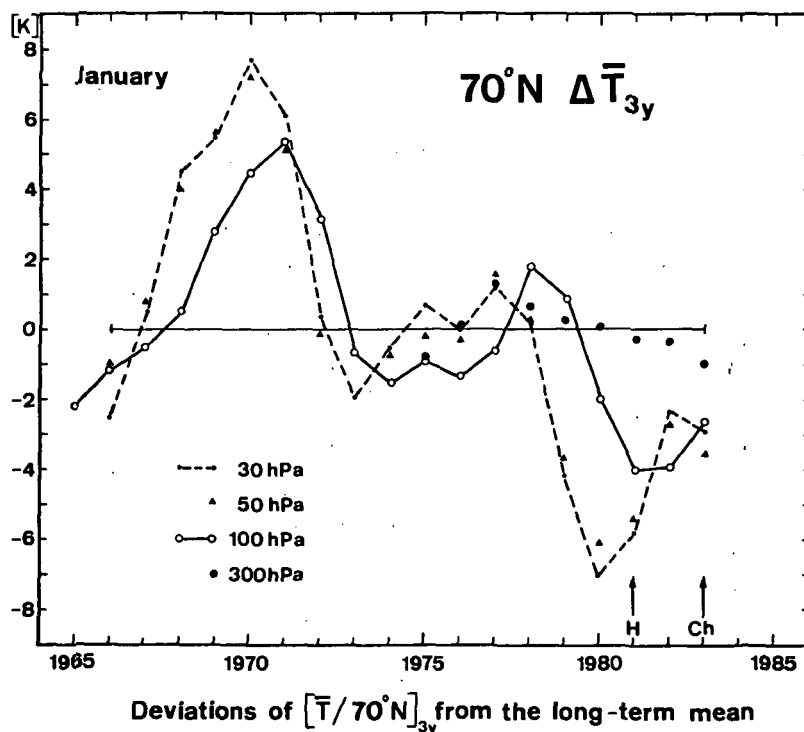


Figure 8.

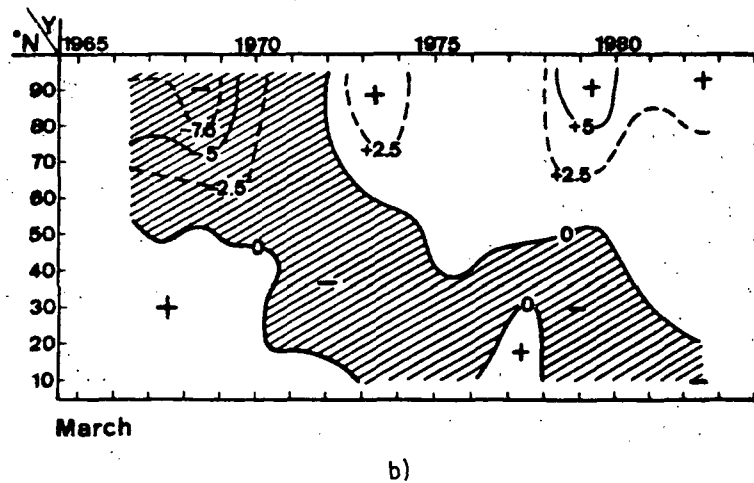
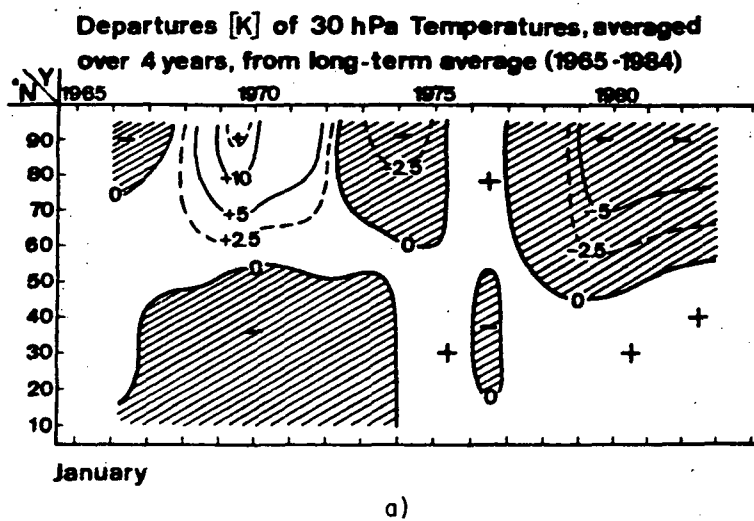


Figure 9.

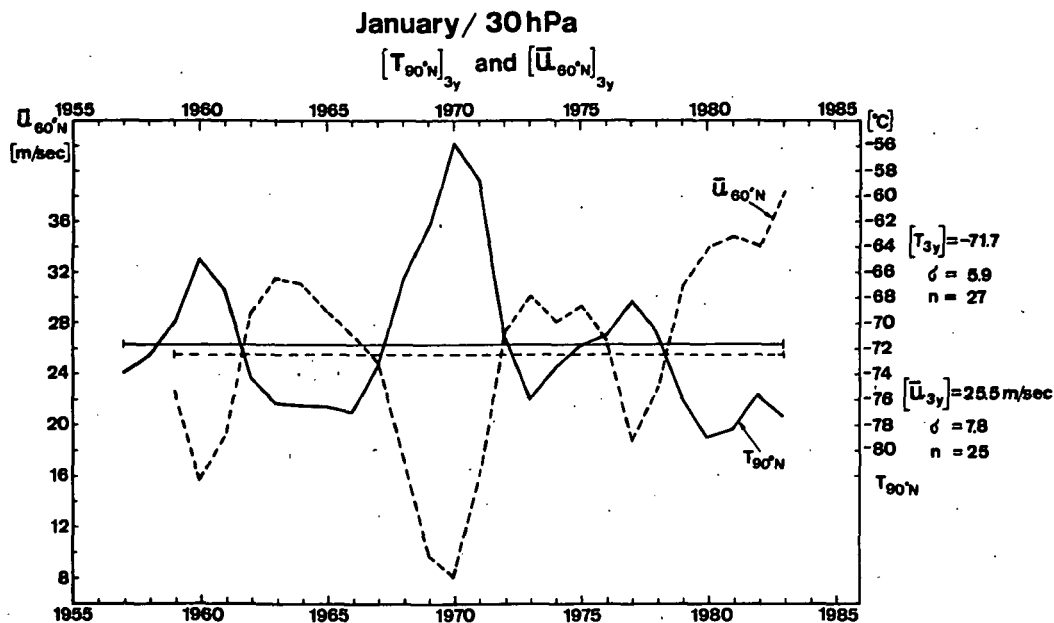


Figure 10.

REFERENCES

- Barnett, J. J. (1974). The mean meridional temperature behaviour of the stratosphere from November 1970 to November 1971 derived from measurements by the selective chopper radiometer on Nimbus IV., Quart. J. R. Met. Soc., **100**, 505-530.
- Knittel, J. (1976). Ein Beitrag zur Klimatologie der Stratosphäre der Sudhalbkugel, Meteor. Abh. der F. U. Berlin, **A2**, Nr. 1.
- Labitzke, K. (1974). The temperature in the upper stratosphere: Differences between hemispheres. J. Geophys. Res., **79**, 2171-2175.
- Labitzke, K. (1977). Interannual variability of the winter stratosphere in the northern hemisphere. Mon. Wea. Rev., **105**, 762-770.
- Labitzke, K. (1982). On the interannual variability of the middle stratosphere during northern winters. J. Met. Soc. Japan, **60**, 124-139.
- Labitzke, K. and B. Naujokat (1983). On the variability and on trends of the temperature in the middle stratosphere. Contributions to Atmos. Phys., **56**, 495-507.
- Naujokat, B. (1981). Long-term variations in the stratosphere of the northern hemisphere during the last two sunspot cycles. J. Geophys. Res., **86**, 9811-9816.

1.2 MIDDLE ATMOSPHERE GENERAL CIRCULATION STATISTICS

Marvin A. Geller

NASA Goddard Space Flight Center
Greenbelt, Maryland 20771 USA

With the increased availability of remote sensing data for the middle atmosphere from satellites, more analyses of the middle atmosphere circulation are being published. Some of these are process studies for limited periods, and some are statistical analyses of middle atmosphere general circulation statistics. Results from the latter class of studies will be reviewed. These include analysis of the zonally averaged middle atmosphere structure-temperature, and zonal winds; analysis of planetary wave structures; analysis of heat and momentum fluxes; and analysis of Eliassen-and-Palm flux vectors and flux divergences. Emphasis will be put on the annual march of these quantities; Northern and Southern Hemisphere asymmetries; and interannual variability in these statistics. Statistics involving the global ozone distribution and transports of ozone will also be discussed.

1.3 SEASONAL VARIATION OF THE STRATOSPHERIC CIRCULATION

I. Hirota and M. Shiotani

Geophysical Institute, Kyoto University
Kyoto 606, Japan

During the last decade, global observations of the middle atmosphere became available by means of satellite measurements of infrared radiation. By using these satellite data, in our previous study (HIROTA et al., 1983), we have made a preliminary analysis of the upper stratospheric circulation and shown some characteristic features such as the zonal mean field, planetary waves and their interrelations.

In the present study, an extensive analysis is made of the extratropical stratospheric circulation in terms of the seasonal variation of large-scale motion fields, with the aid of height and temperature data obtained from the TIROS satellite. Special attention is paid to a comparison of climatological aspects between the Northern Hemisphere (NH) and the Southern Hemisphere (SH).

ANNUAL MARCH

In order to see the general picture of the annual march of the upper stratosphere, the zonal mean values of geopotential height of the 1 mb level at 70°N and 70°S are plotted on the daily basis throughout a year (Figure 1). Note that the abscissa has a log of 6 months between the two hemispheres.

It is easily observed that, during the winter, the zonal mean 1 mb height in the NH is much more variable than that in the SH.

It is also notable that the SH height is rather oscillatory throughout the longer period from midwinter to early summer. Since the zonal mean height in the polar latitude is a rough measure of the mean zonal flow in extratropical latitudes, the difference of the seasonal variation between the two hemispheres mentioned above is considered to be due mainly to the planetary wave-mean flow interaction in the middle atmosphere. In fact, the planetary wave activity, measured by the height variance around the zonal mean at the 1 mb level for 40° - 60° latitudes (Figure 2), shows a notable difference in their seasonal march between the NH and the SH, especially during the winter and spring.

PLANETARY WAVE-MEAN FLOW INTERACTION

The wave activity in the middle atmosphere is represented more rigorously by the Eliassen-Palm flux associated with vertically propagating planetary waves forced from below.

The day-to-day variation of the EP flux in the upper stratosphere shows that the wave activity varies intermittently with a characteristic time scale of about two weeks. Moreover, it is shown that the magnitude of the EP flux is significantly correlated with the zonal mean wind acceleration. For the detailed cross-section analysis of the EP flux and the zonal wind variation, see our subsequent paper (Shiotani and Hirota) in this volume.

This result reconfirms the earlier study of the NH winter circulation by HIROTA and SATO (1969) and extends to both hemispheres for a wider time span to present observational evidence for the planetary wave-mean flow interaction in the middle atmosphere.

Note: A full version of this paper (SHIOTANI and HIROTA, 1985) is to appear soon.

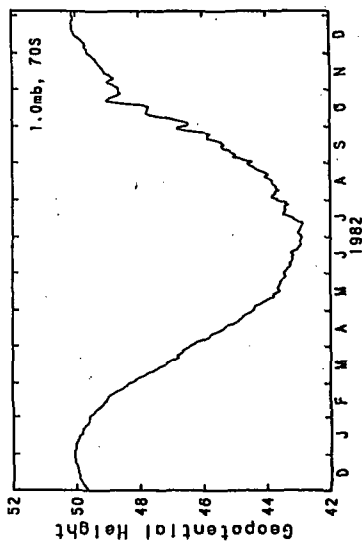
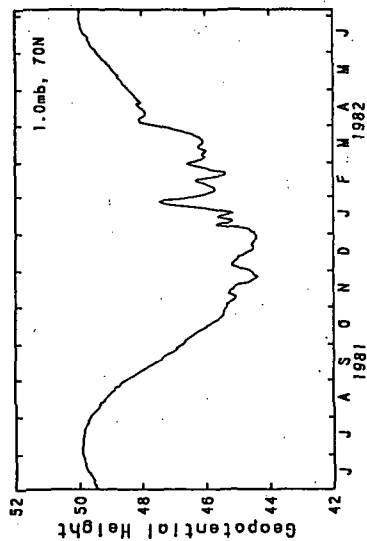


Figure 1. Annual march of the zonal mean geopotential height at 1 mb for 70°N (above) and 70°S (below). Units are km.

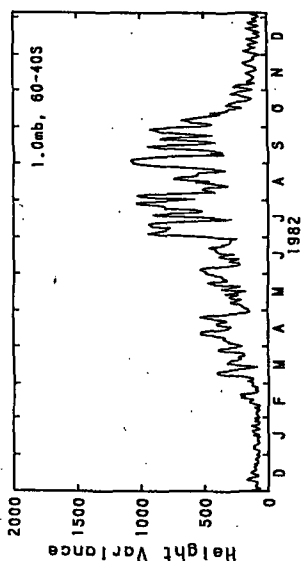
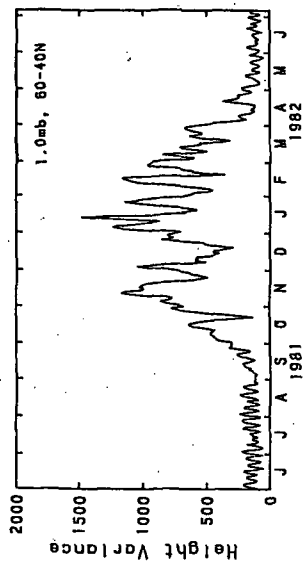


Figure 2. Annual march of the height variance around the zonal mean, at 1 mb for 70°-40°N (above) and 60°-40°S (below). Units are m.

REFERENCES

- Hirota, I. and Y. Sato (1969), J. Met. Soc. Japan, 47, 390-402.
Hirota, I., T. Hirooka and M. Shiotani (1983), Quart. J. Roy. Met. Soc.,
109, 443-454.
Shiotani, M. and I. Hirota (1985), Quart. J. Roy. Met. Soc., 111,
(in press).

1.4 ASPECTS OF THE STRATOSPHERIC CIRCULATION
AS DERIVED FROM SSU DATA

V. Michaelis and A. O'Neill

Meteorological Office
Bracknell, Berkshire, U. K.

Five years of global data are available for the stratosphere up to 1 mb from Stratospheric Sounding Units (SSUs) on board NOAA satellites. These data form the basis for a climatological study which concentrates on the seasonal and inter-annual variability of the stratosphere and the connection between the stratospheric circulation and that of the troposphere. There will be particular emphasis on the structure of the Southern Hemisphere and how it compares with that of the Northern Hemisphere.

While time averaging of a range of diagnostic quantities is used to condense the available information for a climatology, frequent reference is made to daily synoptic charts to provide dynamical interpretations of monthly mean fields. In particular, isentropic maps of Ertel potential vorticity at various levels in the stratosphere are used to follow the movement of air during disturbed periods. They show the importance of quasi-horizontal non-linear advection associated with "wave-breaking". The advection is greater at higher levels where winds are stronger, and this can account for some aspects of long-wave structure in the stratosphere, which cannot be understood using a linear theory of wave propagation. The behaviour of diagnostics related to zonal averaging is interpreted in the light of local changes to the distribution of potential vorticity.

The characteristic difference in the vertical structure and propagation of disturbances in the two hemispheres will be related to differences in the tropospheric flow and the long-term variation of the basic state of the stratosphere. Disturbances in both hemispheres occur in preferred geographical locations. The final warming, marking the transition from westerly to easterly winds, is an example. These occur asymmetrically with respect to the pole as warm air moves over the pole, usually from the same region.

1.5 THE SEASONAL VARIATION OF THE D REGION AS INFERRED FROM PROPAGATION CHARACTERISTICS OF LF RADIO WAVES

T. Ishimine and T. Ishii

Hiraiso Branch, Radio Research Labs.

Ministry of Posts and Telecommunications, Ibaraki 311-12, Japan

Y. Echizenya

Akita Radio Wave Observatory, Radio Research Labs.

Ministry of Posts and Telecommunications, Akita 010, Japan

The propagation data of JG2AS 40 kHz (Japanese Standard Frequency), Loran C 100 kHz radio waves, and the meteorological data were analyzed to study the association of propagation characteristics of LF radio waves with the atmospheric circulation in the mesosphere.

The JG2AS kHz radio wave was received at Akita ($39^{\circ}42'N$, $140^{\circ}87'E$), 395 km distance from Nazaki ($36^{\circ}17'N$, $139^{\circ}51'E$), transmitting station, during the period from Sept. 1978 to Aug. 1979. The Loran C 100 kHz radio wave was measured at Hiraiso ($36^{\circ}22'N$, $140^{\circ}38'E$), 1285 km distance from Iwojima transmitting station during the period from Jan. to Dec. 1983.

The data of the atmospheric circulation in the mesosphere were obtained from meteorological rocket observations made once a week at Ryori ($39^{\circ}2'N$, $141^{\circ}50'E$).

In Figure 1, depicted are the monthly averaged electric fields on the complex plane for typical summer and winter months, June and November. The attached number represents local time, and the triangle indicates sunrise or sunset.

Noting that the LF radio waves propagated over short distances (less than 1000 km) consist of ground waves and sky waves reflected from the ionosphere and variation of the sky wave vector is entirely responsible for that of the received electric field vector, as the ground wave vector is expected to be constant, the following points are made clear from this Figure:

- (1) The locus traced out by the electric field vector during daytime is nearly circular. This is because during daytime the amplitude of the sky wave remains nearly constant while its phase changes in accord with the height change of the reflection layer, and thus the electric field vector traces out a circular locus with its center at the tip of the supposed ground wave vector.
- (2) The locus has a loop during the sunrise or sunset period, which seems to arise from interference of two waves reflected by two different layers. In comparison of June locus with the November one, we notice a remarkable difference between summer-type interference pattern and winter-type one; the loop of summer locus is smaller and elongated compared with the nearly circular loop in winter.
- (3) In June the amplitude of the sky wave decreases rapidly before the dawn or increases after the dusk. In November such rapid change is not observed.

22778-088

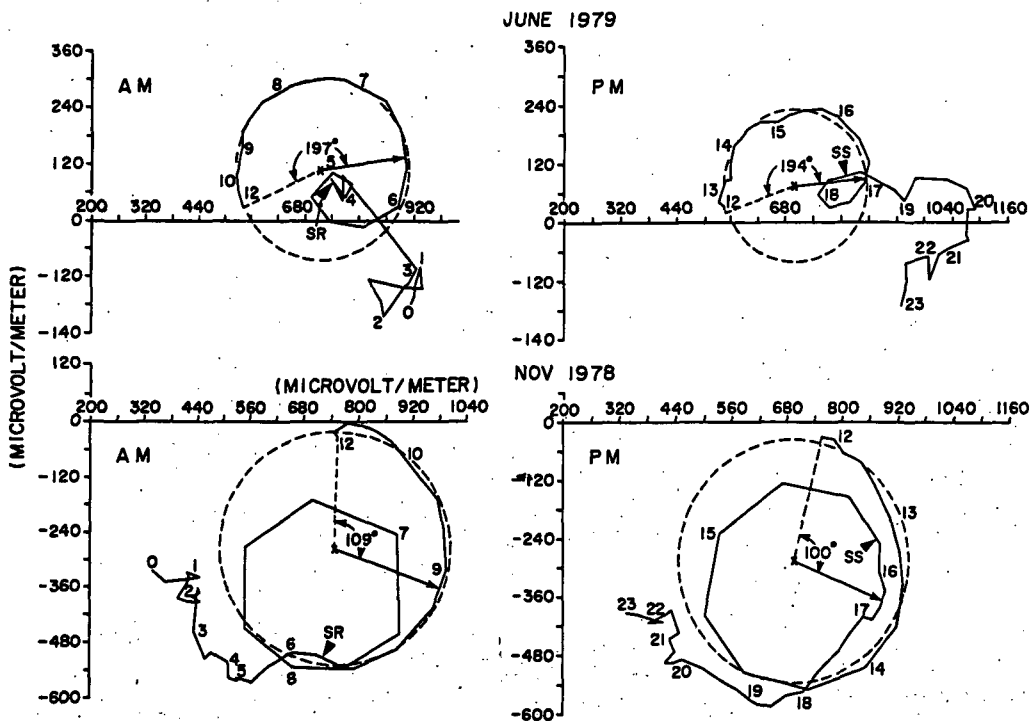


Figure 1.

- (4) During nighttime, the sky wave phase changes in such a way as to suggest that the reflection height moves upwards with time before midnight or lowers after midnight in November. In June it changes similarly before midnight, but after midnight it varies erratically.
- (5) Phase difference between sky wave vector at noon and ground wave vector given by the angle between broken line and line with the arrow head in the figure is larger in June than in November, which suggests that the reflection height at noon is lower in summer than in winter.

The above-mentioned characteristics are, needless to say, closely related to the structure of the D region, which is clearly shown by simulating the loci traced out by electric fields.

In Figure 2 depicted are loci traced out by composite electric fields of two waves reflected at different heights (in km) specified in columns headed LAYER 1 and LAYER 2 with amplitudes given in columns headed by AMP 1 and AMP 2. The upper locus simulates the summer-type one and the lower the winter-type one. From this figure it is inferred that during the sunset or sunrise period two layers are formed in the D region and in summer the reflection by the lower layer is stronger than that by the upper layer, but in winter the latter gradually surpasses the former.

To see seasonal variation of propagation characteristics, the sky wave field was separated from the ground wave by determining the locus circle of daytime by means of the least square method.

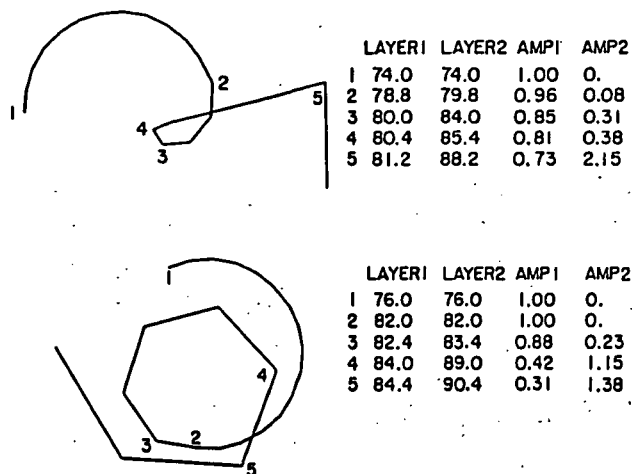


Figure 2.

The deduced sky wave field strength is shown in Figure 3 together with the wind direction (in meteorological sense) at altitude of 55 km over Ryori. As seen from this figure, the larger field strength in winter time from November to May is associated with the eastward circulation conditions and the smaller field strength in summer time from June to October with reverse conditions with about one month delay of onset of D-region summer.

In the light of results obtained by PIGGOTT et al. (1965) and DEEKS (1966) we can attribute the increase of the amplitude to the enhancement of dN/dh , the vertical gradient of the electron density near the level where $X=Z$, that is, $e^2 N/m\epsilon_0 = \omega v$ (in the usual ionospheric nomenclature) (RATCLIFFE, 1959). So it is inferred that during daytime the vertical gradient of the electron density in the main part of D region responsible for reflection of LF radio waves is steeper in winter than in summer.

Another example of association of the propagation characteristics of LF radio waves with the mesospheric circulation is given in Figure 4. Here shown are differences between daytime phase and nighttime phase of Loran C radio waves and again wind direction at an altitude of 55 km. Vertical arrows indicate launchings of meteorological rockets.

As clearly seen, a smaller phase difference is associated with westward wind direction while a larger difference is associated with reverse wind direction with one month earlier onset of the mesospheric winter than the D-region winter.

LF radio waves are reflected at the height where $e^2 N/m\epsilon_0 = \omega v$ holds as mentioned above, this correspondence between seasonal variation of the sky wave phase of Loran C and that of the mesospheric wind direction suggests that the electron density structure depends on the atmospheric motion in the D region.

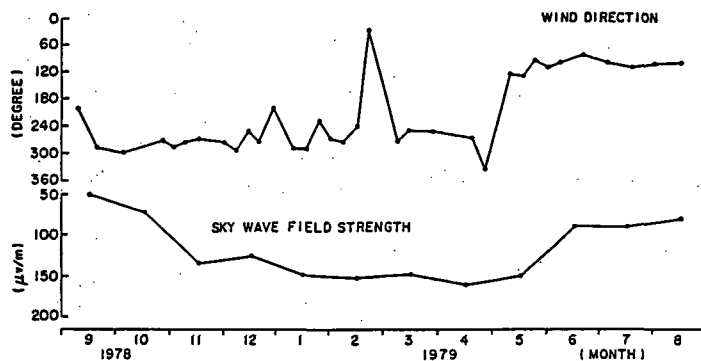


Figure 3.

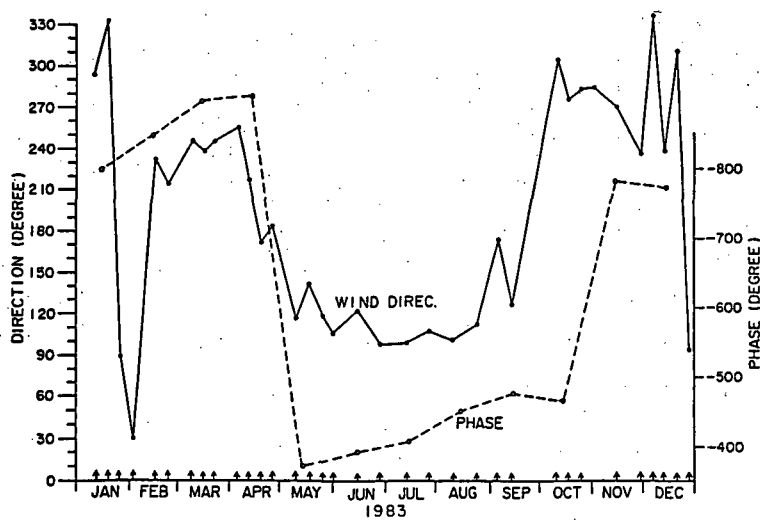


Figure 4.

REFERENCES

- Piggott, W. R., M. L. V. Pitteway, and E. V. Thrane (1965), Phil. Trans. A, **257**, 243-271.
- Deeks, D. C. (1966), Proc. Roy. Soc., **291A**, 413-437.
- Ratcliffe, J. A. (1959), The Magneto-Ionic Theory and its Applications to the Ionosphere, 81-91, Cambridge University Press, Cambridge.

1.6 MEAN WINDS OF THE UPPER MIDDLE ATMOSPHERE (60-110 km): A GLOBAL DISTRIBUTION FROM RADAR SYSTEMS (M. F., METEOR, VHF)

A. H. Manson and C. E. Meek¹, M. Massebeyf and J. L. Fellous²,
W. G. Elford, R. A. Vincent and R. L. Craig³, R. G. Roper⁴, S. Avery
and B. B. Balsley⁵, G. J. Fraser and M. J. Smith⁶,
R. R. Clark⁷, S. Kato and T. Tsuda⁸

¹I.S.A.S., University of Saskatchewan, Canada, ²CNRS/CRPE and CNES,
France, ³University of Adelaide, Australia, ⁴Georgia Institute of
Technology, USA, ⁵CIRES and NOAA, Boulder, USA, ⁶University of Canter-
bury, New Zealand, ⁷University of New Hampshire, USA,
⁸Kyoto University, Japan

INTRODUCTION

Since the development of the last CIRA in 1972, the number of radars providing winds in the upper middle atmosphere has increased significantly. These systems fill the data gap between 60 km and 110 km. The radars include medium frequency (MF) radars or partial reflection systems giving data from 60/70 - 100/110 km; meteor radars, 80 - 110 km, and M.S.T. radars operating as meteor radars. We show here data from 12 locations, which represent a good Northern Hemispheric (NH) North American chain (18 - 65°N, ~90°W), an Oceanian chain (44°S - 35°N, 140°E) which is mainly in the Southern Hemisphere (SH), and some Western Europe data (44 - 68°N, ~0°E). The methods of data analyses are discussed in detail elsewhere. Generally, however, tidal oscillations have been removed from days or groups of days, and the remaining mean winds and longer period oscillations plotted as height-time contours. Composite cross sections from the years 1978-1982 were formed where possible so that only the major temporal features remain.

ZONAL WINDS

Generally, for latitudes as low as 35°, there are westerly/easterly flows during winter/summer-centred months below 95-85 km, and the reverse above. There is room here only to show Saskatoon at 52°N (Figure 1) as an example; other cross sections are shown in MANSON et al. (1984), MEEK and MANSON (1984). High latitude data, such as Kiruna and Poker Flat, which were not available for CIRA-72, are reasonable extrapolations of midlatitude data. At midlatitudes (~45°) the reversals in the mesopause region are less clear in winter months, and are at a greater altitude. There is also more systematic mesospheric variability during the seven winter-like months. The causes of this are planetary waves, stratospheric warmings, and annual and semiannual oscillations (MANSON et al., 1981). This is a major difference from CIRA-72, which shows an unrealistically smooth winter vortex with a maximum in December/January. The seasonal differences in circulations and the strength of lower thermospheric circulations have important implications for gravity wave momentum deposition processes.

The comparison between CIRA-72 and the radar winds is well illustrated in height-latitude cross sections, and we show here December (clear of NH stratospheric warmings) and July for ~90°W in the NH, and ~140°E in the SH. From CIRA, July (June 15 - July 15) and January (December 15 - January 15) are shown in Figure 2. The time rates of change are small in midseason, so that conclusions drawn here are usually typical of the entire solstitial seasons. The lack of hemispheric symmetry is immediately obvious: the winters are most alike and even then the NH zero line is 10 - 15 km higher, reflecting smaller poleward temperature gradients there. Comparing with CIRA-72: the upper zero

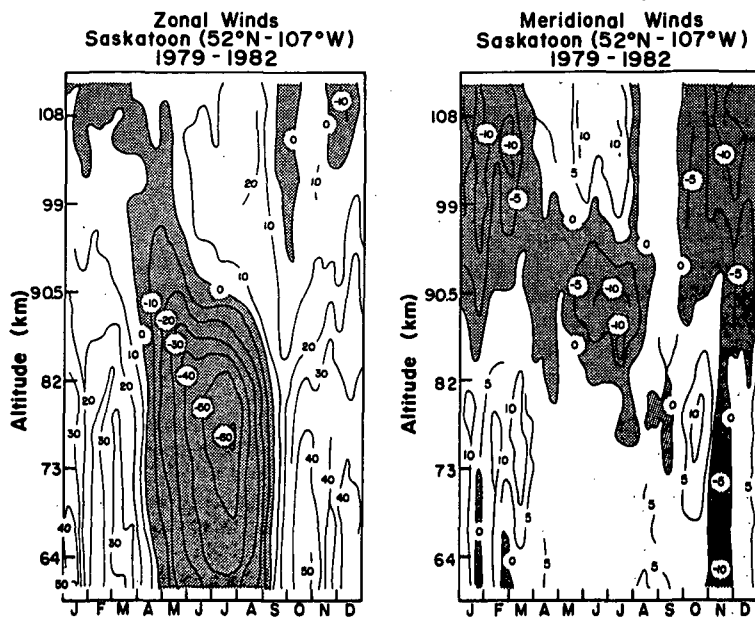


Figure 1. Saskatoon, 52°N, 107°W: 10d means used; s.d. typically 4 ms⁻¹ for EW, 4 ms⁻¹ for NS at 90 km.

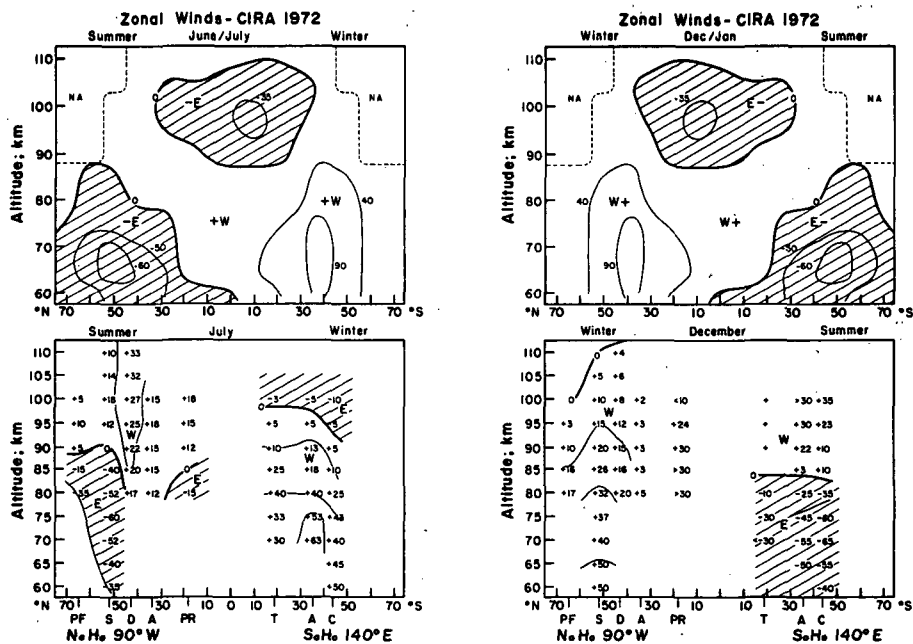


Figure 2. Zonal winds; radar network in lower sections.

lines were not available for that model; but it shows an easterly tropical cell above 87 km which is not evident at our four low latitude stations. For the summers, these stations again do not have the easterly flow above 87 km. The main differences between the SH and NH at these longitudes are due to the consistent westerly flow at and above 80 km revealed at Durham (43°N) and Atlanta (35°N) and the high reversal heights in Oceania. The systematic reduction in the height of the zero line with decreasing latitude which is shown by CIRA-72, is not in evidence.

Some of the differences evident in Figure 2 and existing between Durham and Monpazier (MANSON et al., 1984) will be due to planetary waves ($n=1,2$), especially in the NH. Satellite data will be useful in quantifying this effect.

MERIDIONAL WINDS

The tabulations of GROVES (1969) show strong summer-centred equatorward flow (NASTROM et al., 1982) which dominates the year. Although our data generally show this feature, the flow is weaker and more variable. As well as the summer flow (which is consistent with cooling at high latitudes, and hence the zonal winds through the thermal wind equation) Poker Flat (65°N), Saskatoon (52°N) and Christchurch (44°S) also have poleward flow in the winter mesosphere, and equatorward and above (Figure 1).

Finally we show meridional height-latitude cross sections and compare with Groves' data (Figure 3). For July, the general agreement is quite good, but the NH summer equatorward flow is weaker and more restricted in height than Groves. December illustrates hemispheric asymmetry, as the SH summer flow is more like Groves. However, the NH winter flow is then quite different from Groves, although overall there is poleward flow within the mesosphere in both cross sections.

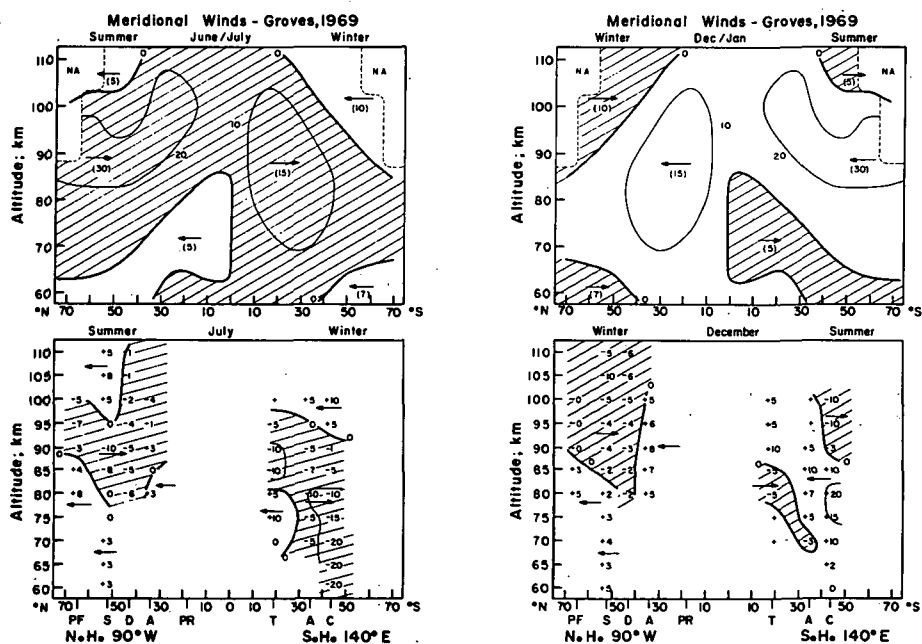


Figure 3. Meridional winds; radar network in lower sections.

CONCLUSION

The radar zonal wind cross sections differ considerably from CIRA-72, especially regarding winter variability and heights of reversals. There is good evidence (MANSON et al., 1984) that winds from 43° - 52° in the Northern Hemisphere vary quite significantly with latitude and longitude, being near CIRA's 45° - 50° in some cases and CIRA's 35° in others; and that winds $\sim 35^{\circ}$ N may demonstrate midlatitude or tropical characteristics (20° CIRA-72). In the Southern Hemisphere 35° is similar to CIRA-72 at 35° or even 45° and is more midlatitude in behaviour. The winds from near 20° show a mixture of midlatitude and tropical characteristics. The meridional cross sections evidence considerable seasonal and latitudinal variability, the main feature being a summer equatorward ($\sim 10 \text{ ms}^{-1}$) mesospheric flow. However, this does not dominate the year as in Groves' compilation. In other months at midlatitudes there is considerable poleward flow in the mesosphere. It is possible that the elimination of tidal components, which is crucial for these weak winds, was not complete in the earlier data.

REFERENCES

- Groves, G. V. (1969), Wind models from 60 to 130 km altitude for different months and latitudes, J. Brit. Interplanet. Soc., **22**, 285.
- Manson, A. H., C. E. Meek and J. B. Gregory (1981), Long period oscillations in the mesospheric and lower thermospheric winds (60 - 110 km) at Saskatoon (52° N, 107° W, $L=4.3$), J. Geomag. & Geoelectr., **33**, 613.
- Manson, A. H., C. E. Meek, M. Massebeuf, J. L. Fellous, W. G. Elford, R. A. Vincent, R. L. Craig, R. G. Roper, S. Avery, B. B. Balsley, G. J. Fraser, M. J. Smith, R. R. Clark, S. Kato, T. Tsuda and A. Ebel (1984), Mean winds of the upper middle atmosphere (60-110 km): a global model from radar systems (M. F., meteor, VHF), Advances in Space Research.
- Meek, C. E. and A. H. Manson (1984), Comparisons between Primrose Lake (54° N, 110° W) Rocob winds (20-60 km) and Saskatoon (52° N, 17° W) MF radar winds (60-110 km): 1978-1983, Report #1, Dynamics Group, Institute of Space and Atmospheric Studies, University of Saskatchewan, Saskatoon, Canada S7N 0W0.
- Nastrom, G. D., B. B. Balsley and D. A. Carter (1982), Mean meridional winds in the mid and high latitude summer mesosphere, Geophys. Res. Lett., **9**, 139.

1.7 MONTHLY MEAN VALUES OF THE MESOSPHERIC WIND FIELD OVER POKER FLAT, ALASKA

B. B. Balsley and A. C. Riddle *

Aeronomy Laboratory
National Oceanic and Atmospheric Administration
Boulder, Colorado 80303 USA

We present monthly-averaged values of the mesospheric wind field for the 15 month period May 1980 - July 1981 obtained by the Poker Flat MST Radar in Alaska (65°N). In addition to both zonal and meridional results, we present measurements of the vertical wind during the same period. This latter data set is unique, since no other technique has the requisite accuracy to measure the relatively small (\approx cm/sec) values of the mean vertical wind in the presence of much larger (\approx tens of m/s) horizontal wind.

* CIRES Research Associate, University of Colorado, Boulder, CO 80309

1.8 TRENDS IN UPPER STRATOSPHERIC TEMPERATURES AS OBSERVED BY ROCKETSONDES (1965-1983)

K. W. Johnson and M. E. Gelman

NOAA, NWS, NMC, Climate Analysis Center
Washington, DC 20233

Recent interest in possible anthropogenically induced changes in stratospheric ozone has led to a number of modeling studies. These studies indicate that stratospheric temperature changes would be related to stratospheric ozone changes (cf. WUEBBLES, 1983). Therefore, this study was motivated by a concern to find out whether or not any significant trend in upper stratospheric temperatures could be ascertained from available observational data.

Recent studies of upper stratospheric temperature trends have been carried out by ANGELL and KORSHOVER (1978, 1983) and by QUIROZ (1979). ANGELL and KORSHOVER (1983) found a 3 to 5 deg C decrease in mean annual temperatures in the middle and upper stratosphere (26-55 km) between 1970 and 1976. This cooling was found at Western Hemisphere rocketsonde stations at all latitudes.

QUIROZ (1979) restricted his study to summer (June, July, and August) seasonal mean temperatures at 35 and 50 km from 1965 to 1977 at seven Western Hemisphere rocketsonde stations. This study used summer data because of the well-known reduced daily temperature variability during that season. In addition to many careful quality control procedures, Quiroz applied adjustments for solar radiation of as much as 3.0 deg C where necessary. This study showed a decline in temperature of 3 to 6 deg C between 1970 and 1976.

In the current study the Western Hemisphere rocketsonde network reports will again be the primary data base. The period of record will be extended to include 1965 to 1983 and additional quality control procedures to the data will be used.

Ideally, a study of global temperature trends would be carried out with a uniform global distribution of data. However, no fully satisfactory long-term global data set is yet available for the upper stratosphere. Changes from one instrument system to another in experimental and operational satellite observing systems, as well as uncompensated drifts in the operating parameters of these systems would make it difficult if not impossible to develop a consistent temperature time series over a period of a decade or more. Hence, the current study will make use of in situ observations, i.e., rocketsonde observational data.

Initially, it was decided to study mean temperatures for June, since June is a meteorologically quiescent month in the upper stratosphere of the Northern Hemisphere. (Although July would also qualify, a preliminary analysis showed little difference in trend results if bi-monthly mean temperatures for June and July were used in the analysis.) Annual mean temperature values are difficult to interpret due to the varying effects of sudden stratospheric warmings which occur at varying intervals during the late winter. Other upper stratospheric perturbations may also be superimposed upon wintertime temperature patterns.

QUIROZ (1979) has discussed some of the problems involved in using rocketsonde data as published by World Data Center A for Meteorology Asheville, N.C (in print through 1976 and extended on microfilm through 1983). Quiroz points out that the published monthly averages may include data from falling sphere soundings, and may also need to have an appropriate adjustment ("correction") applied, based on the work of BALLARD (1967), KRUMINS (1972), or STAFFENSEN, et

al. (1972). In addition, some observations are reported to have abnormally high or abnormally low fall velocities, which render the observational data from these soundings suspect.

June monthly mean values for 40-45 km layer were calculated for all Western Hemisphere rocketsonde stations for which data was available. The quality control scheme was as follows: (1) All falling sphere or experimental sensor soundings were rejected. (QUIROZ and GELMAN 1976, discuss the problems in using the data from sphere soundings). (2) Any soundings flagged in the data books as having doubtful or missing temperatures in the 40 to 45 km region were rejected. (3) All soundings with a 43 km fall velocity more than two standard deviations from the mean June 43 km fall velocity for the station were rejected. (4) Adjustments for radiation were applied in a similar manner to that used by QUIROZ (1979). (5) If fewer than three soundings were available for a station for the month, or if the soundings were all at the beginning or end of the month, the mean was not included.

Mean temperatures for each June were then used to calculate linear least-squares regression coefficients with latitude of the stations as the independent variable. The resulting coefficients were used to calculate area-weighted mean temperatures for 25°N to 55°N. Results are displayed in Figure 1. A two-to-three degree temperature drop in the early 1970s is indicated in this diagram similar to the findings by QUIROZ (1979) and ANGELL and KORSHOVER (1978). We note, however, that this temperature decline coincides with a change in the principal observing system from the Arcasonde system to the Data-sonde system.

In order to study this temperature decrease more closely, similar mean temperatures were calculated for the 25-30 km layer using both rocketsondes and support radiosondes.

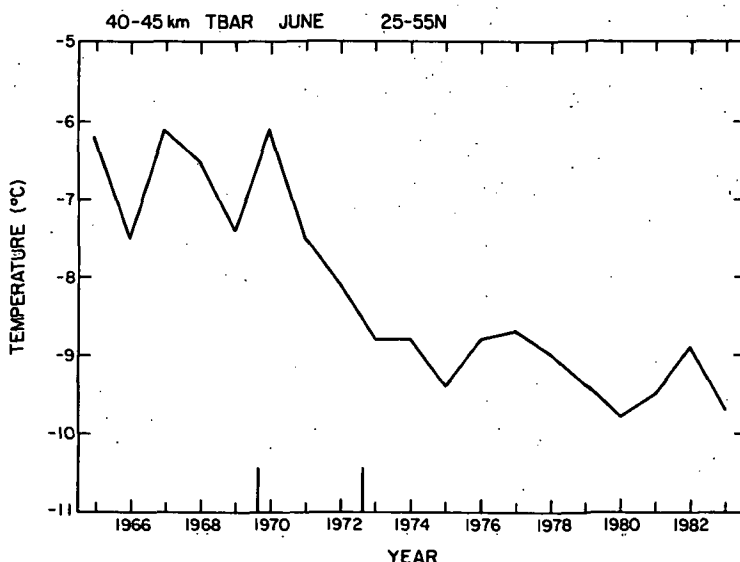


Figure 1. 40-45 km layer mean rocketsonde temperatures averaged over North America (25-55 north latitude) for June in years 1965 to 1983. Heavy ticks indicate beginning and end of transition from Arcasonde to Data-sonde observing systems.

Results are displayed in Figure 2. There is no discernable long-term trend in radiosonde temperatures; however, in the 1965-1971 time period the rocketsonde temperatures averaged 1.11 C higher than the radiosonde means while in the 1972-1978 time period the rocketsondes averaged 1.06 C lower than the radiosonde temperatures. This approximately 2 C decrease in rocketsonde mean temperatures again corresponds to the change in observing systems.

QUIROZ (1979) suggested a possible explanation for the decline in temperature in the early 1970s could be the reduced solar activity (see Figure 3 for sunspot numbers -- a commonly used measure of solar activity). However, the increase in solar activity after 1976 is not reflected in a discernible increase in temperature. We believe that the change in reported temperatures in the early 1970s simply reflects a previously uncompensated change in the rocketsonde temperature measurement system.

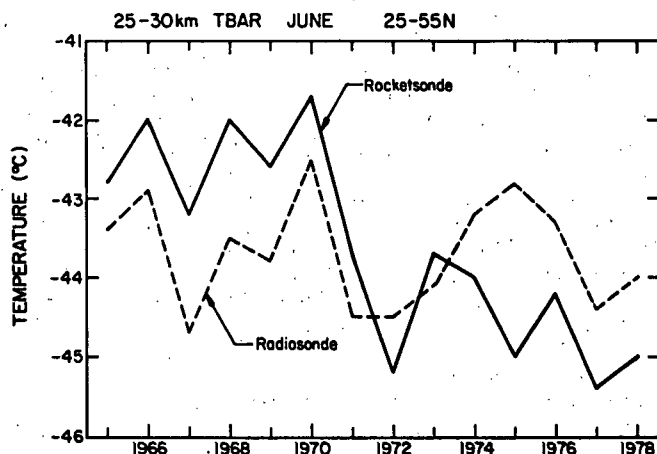


Figure 2. As in Figure 1, except for 25-30 km; dashed line indicates mean temperatures derived from support radiosondes; solid line for corresponding rocketsondes.

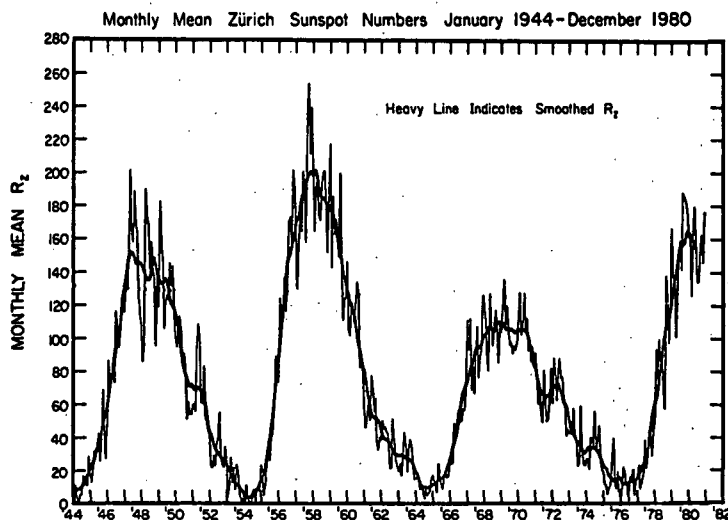


Figure 3. Monthly mean Zurich sunspot numbers (from World Data Center A for Solar-Terrestrial Physics; courtesy of R. M. Nagatani).

ACKNOWLEDGEMENTS

Cooperation of Mr. Francis Schmidlin of NOAA, Wallops Station, in obtaining computer tapes of rocketsonde data is gratefully acknowledged. The authors also appreciated many helpful discussions with Mr. Schmidlin, Mr. Roderick S. Quiroz, and Mr. Alvin J. Miller on the subject of rocketsonde observational systems.

REFERENCES

- Angell, J. K., and J. Korshaver (1978), Recent rocketsonde-derived temperature variations in the Western Hemisphere, J. Atmos. Sci., 35, 1758-1764.
- Angell, J. K., and J. Korshaver (1983), Global temperature variations in the troposphere and stratosphere, Monthly Wea. Rev., 111, 901-921.
- Ballard, H. N. (1967), A review of seven papers concerning the measurement of temperature in the stratosphere and mesosphere, Tech. Rep. ECOM-5125, 67 pp., U.S. Atmos. Sci. Lab., White Sands Missile Range, NM.
- Krumins, M. V. (1972), Corrections for the upper atmosphere temperatures using a thin-film loop mount, Tech. Rep. NOLTR, 72-152, U.S. Navy Ord. Lab., Silver Springs, MD.
- Quiroz, R. S. (1979), Stratospheric temperatures during solar cycle 20, J. Geophys. Res., 84, 2415-2420.
- Quiroz, R. S. and M. E. Gelman (1976), An evaluation of temperature profiles from falling sphere soundings, J. Geophys. Res., 81, 406-412.
- Staffensen, F. L., S. Kikkawa, and R. G. Phibbs (1972), Meteorological data processor and results from the solar eclipse of March 7, 1970, J. Appl. Meteorol., 11, 722-730.
- Wuebbles, D. J. (1983), A theoretical analyses of the past variations in global atmospheric composition and temperatures structure, UCRL-53423, Lawrence Livermore Laboratory, Livermore, CA.

1.9 PROFILES OF TEMPERATURE AND DENSITY BASED ON EXTREMES AT 5, 10, 20, 30, AND 40 KM

Arthur J. Kantor, Paul Tattelman and Frank A. Marcos

Air Force Geophysics Laboratory
Hanscom AFB, Massachusetts

INTRODUCTION

Information on the vertical distribution of expected extremes of temperature and density are required for the design and operation of systems traversing the atmosphere. Such data are particularly important at altitudes from the surface to approximately 80 km for developing all types of airborne vehicles ranging from helicopters and airplanes to sophisticated aerospace systems.

Several temperature models of regional extremes have been developed for a few selected locations. They provide temperature profiles based on estimated 1-percent hot and cold temperatures at pressure levels between 850 mb (1.5 km) and 100 mb (16 km). NASA (1982) also presents temperature and density envelopes and extreme profiles up to 90 km, but only at several missile ranges.

The Air Force Reference Atmospheres present monthly mean temperatures, densities and pressures at 15-deg intervals of latitude from the equator to the pole, including estimated day-to-day variability around the monthly averages. Also available are several reports containing information on the time and space variations of density in the upper stratosphere and lower mesosphere for time periods up to 72 hours and horizontal distances out to nearly 400 km (200 n mi). Unfortunately, these do not directly address low probabilities of occurrence. MIL-STD-210B (DEPARTMENT OF DEFENSE, 1973) contains vertical envelopes of global extremes (excluding Antarctica) of hot and cold temperatures and high and low densities. However, these envelopes are unrealistically severe for many engineering and design problems. Low density or high density, for example, cannot occur simultaneously at any given location through a vertical thickness more than a few kilometers.

To fill this void, vertical profiles of temperature and density have been developed based on 1- and 10-percent hot and cold temperatures and 1- and 10-percent high and low densities occurring during the most severe month at the worst locations for which reliable upper-air data are available. The model profiles, from the surface to 80 km, are based on extremes that occur at 5, 10, 20, 30, and 40 km. There are 20 profiles for extreme temperatures (5 levels by 4 percentiles) that include associated densities, and 20 analogous profiles for extreme densities including associated temperatures. Consequently, a set of realistic profiles (rather than envelopes) of temperature and density, associated with extremes at each of 5 specified levels in the troposphere and stratosphere, are now available for altitudes up to 80 km.

The atmospheric profiles are defined by temperature-altitude segments in which vertical gradients of temperature are linear with respect to geopotential altitude. For simplicity, gradient changes occur at "breakpoints" of whole and half km of altitude and the "breakpoint" temperatures are in whole and half degrees Kelvin. It is assumed that the air is dry, is in hydrostatic equilibrium, and behaves as a perfect gas. The molecular weight of air at sea level is considered to be constant to 80 km. Greater detail on the basic assumptions and computational equations will be available in a report being published by AFGL (KANTOR and TATTELMAN, 1984).

DATA

The data used consist primarily of two types of observations:

- (1) Rawinsonde observations from the surface to approximately 25 km, and
- (2) Meteorological Rocket Network (MRN) observations for altitudes roughly 25 km to 55 km. The total period of record spans 14 years from 1969 through 1982. About 130 locations from the U.S., Central and South America, and Oceania, and some 40 Canadian controlled high-latitude stations make up the input of rawinsonde observations. MRN data were available for 18 MRN stations that lie mostly in the Western Hemisphere and are located between latitudes 77°N and 38°S.

DATA PROCESSING AND ANALYSIS

Analysis of available rawinsonde data entailed assimilation of as many as 9000 soundings per station (two per day for 13 years). Computer techniques and analyses produced threshold values of 1-, 10-, 90- and 99-percent temperatures and densities at 5, 10 and 20 km for the most severe month and location. A procedure analogous to that used for rawinsondes was used to analyze MRN temperatures and densities at 30 and 40 km. MRN data from 18 stations were used to produce the desired threshold temperatures and densities. Although the period of record, 1969-1982, is approximately the same as that available for the rawinsonde analysis, MRN observations are limited to locations mostly in the Western Hemisphere, and both the number of stations and the number of soundings are an order of magnitude smaller than that for the rawinsondes.

All soundings that met or exceeded the 40 criteria established for temperature and density were carefully analyzed for development of model vertical profiles typical of each of the indicated atmospheric conditions. For threshold values at 5, 10, and 20 km (rawinsonde altitudes), MRN stations used to complement the rawinsonde stations were chosen from the 18 usable MRN sites considering proximity, climate and specific synoptic situation for the dates that threshold values were equalled or exceeded. MRN observations at the selected locations were matched with the corresponding rawinsonde dates ± 1 day. For threshold values at 30 and 40 km (MRN altitudes), observations at the same time/location were used to determine the model profiles because rawinsonde observations are made at MRN sites. Since MRN data can be used only up to about 50-55 km, model profiles were extended to 80 km, based on the 50 km value, using either interlevel temperature correlations from a previous study (KANTOR and COLE, 1977), or the AF Reference Atmospheres. Figure 1 shows the model profile subjectively fitted to coincide with the 1X-10 km threshold temperature.

RESULTS

Tables defining the model profiles are in the process of being published in an AFGL report (KANTOR and TATTELMAN, 1984). Results are presented at 2 km intervals of geometric altitude, from sea level to 80 km, and also in the form of temperature-altitude profiles with lapse-rate breakpoints in geopotential km.

Four of the 40 temperature-altitude profiles, based on the 1- and 99-percent temperatures at 10 km (Figure 2) and 1- and 99-percent temperatures at 30 km (Figure 3), are compared with the 1973 MIL-STD-210B envelopes. In a similar manner, the 1-percent temperature profiles at 10 and 30 km (Figure 4) and the 99-percent profiles at 10 and 30 km (Figure 5), are compared to the MIL-STD envelopes. In all 4 examples, it is obvious that the profiles gener-

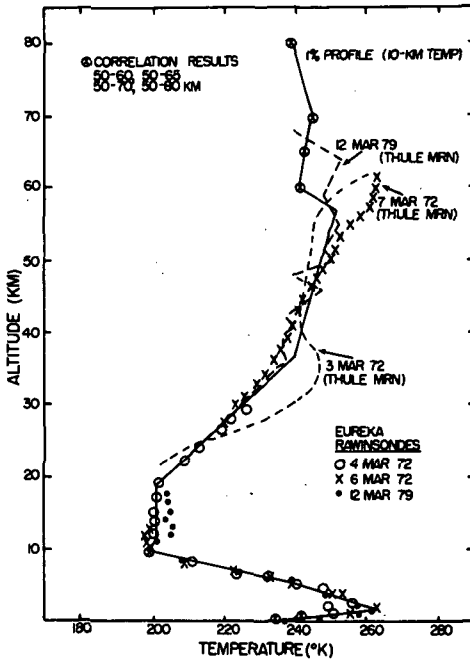


Figure 1. Profiles based on 1-percent 10-km threshold temperature at Eureka and concomitant Thule MRN data.

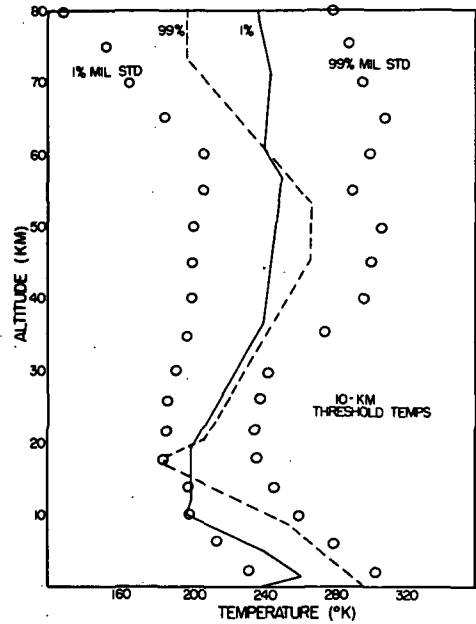


Figure 2. Model profiles for 10-km threshold temperatures versus MIL-STD-210B envelopes.

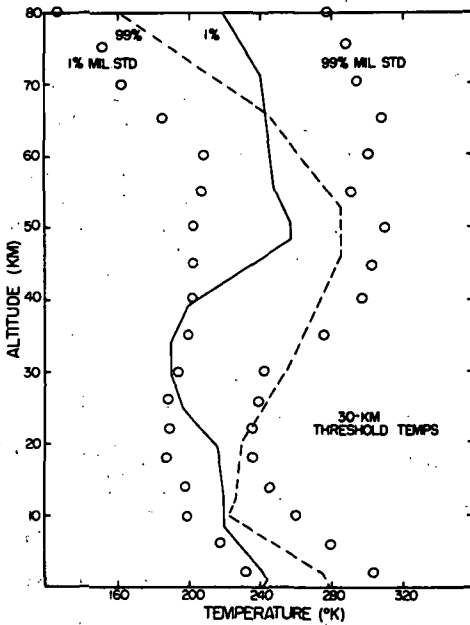


Figure 3. Model profiles for 30-km threshold temperatures versus MIL-STD-210B envelopes.

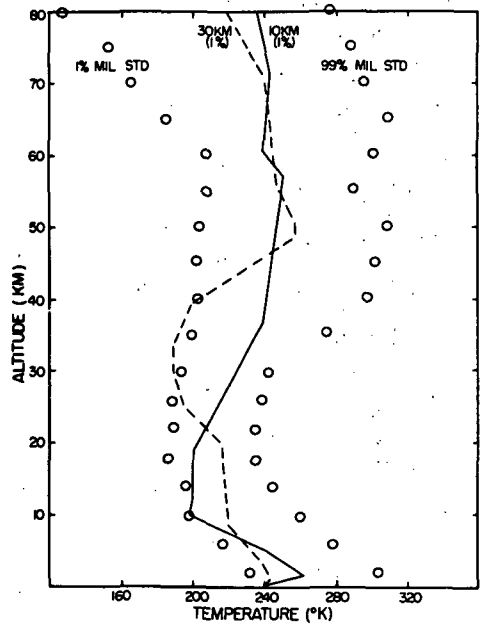


Figure 4. Model profiles for 1-percent threshold temperatures at 10 and 30 km, and MIL-STD-210B envelopes.

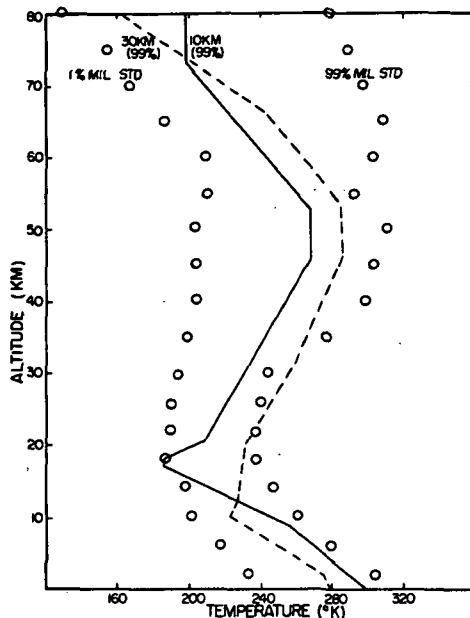


Figure 5. Model profiles for 99-percent threshold temperatures at 10 and 30 km, and MIL-STD-210B envelopes.

ally are much less extreme than the MIL-STD envelopes at all but the threshold altitudes.

The results clearly point out the difference between profiles that are consistent in time and space and envelopes which indicate extremes at each altitude that are unrelated in time and space to those at other altitudes. Each of the presentations of upper air data have their applications. The envelopes can be used to determine low probability conditions at a specific altitude of concern. These would most commonly be applied to design considerations involving constant level flight. The model profiles are more appropriate for the design of vehicles traversing the atmosphere, or other considerations for which the total influence of the atmosphere is needed.

REFERENCES

- Department of Defense (1973), Military standard, climatic extremes for military equipment, MIL-STD-210B, December 15, 1973, Office of the Under Secretary of Defense, Research and Engineering, Washington, D.C.
- Kantor, A. J., and A. E. Cole (1977), Monthly 90 N atmospheres and high-latitude warm and cold winter stratosphere/mesosphere, AFGL-TR-77-0289.
- Kantor, A. J., and P. Tattelman (1984), Profiles of temperature and density Based on 1- and 10-percent extremes in the stratosphere and troposphere, AFGL-TR-84-0336.
- NASA (1982), Terrestrial environment (climatic) criteria guidelines for use in aerospace vehicle development, 1982 Revision, NASA Tech. Memo, 82473, Marshall Space Flight Center, Alabama.

1.10 INTERANNUAL VARIABILITY OF MIDDLE ATMOSPHERE DURING NORTHERN WINTER

B. K. Mukherjee, K. Indira and Bh. V. Ramana Murty

Indian Institute of Tropical Meteorology,
Pune-411005, India

INTRODUCTION

Recent investigation has shown the presence of interannual variability in the middle atmosphere over high latitude during the northern winter (e.g., LABITZKE 1982). It is suggested that the varying activity of planetary waves 1 and 2 is the prime factor responsible for the interannual variability of the high latitude middle atmosphere. The dynamical features occurring over the high latitude middle atmosphere during winter affect the middle atmosphere over low latitudes LABITZKE 1972, 1984; MUKHERJEE and RAMANA MURTY 1972). Nowadays, it is also believed that the disturbances in the middle atmosphere influence the tropospheric circulation and vice versa. With this end in view, the present study was undertaken to examine the characteristics of the interannual variability of the zonal wind and the temperature of the middle atmosphere of the Northern Hemisphere during winter and to search for a relationship of the variability of the middle atmosphere with the activity of the following Indian summer monsoon. For this purpose, the rocketsonde temperature and wind data for 8 stations, namely, Thule ((76.6°N, 80.0°W), Poker Flat (65.1°N, 147.5°W), Fort Churchill (58.7°N, 93.8°W), Wallops Island (37.8°N, 75.5°W), Cape Kennedy (28.5°N, 80.5°W), Fort Sherman (9.3°N, 80.0°W), Kwajalein (8.7°N, 167.7°E) and Ascension Island (80.0°S, 14.4°W)), for the 6-year period 1970-1972 and 1974-1976 for the month of January have been collected. These data were readily available from Data Report-High Altitude Meteorological Data (World Data Center A, USA) in the authors' institute. The mean zonal wind (ms⁻¹) and the mean temperature (°C) for January at an interval of 5 km from 25-55 km are plotted and analysed. Since the data for January 1973 was not available, it could not be included in the present study.

RESULTS AND DISCUSSION

The analysis of mean zonal wind has pointed out marked interannual variation north of 35-50°N. During the group of years comprising of 1970, 1971 and 1975, the westerly zonal wind in the stratosphere (25-45 km) reached its peak near 35-50°N. But during the group of years comprised of 1972, 1974 and 1976 it reached its peak near 60°N, where the polar night jet is normally located. Such variability was noticed to decrease above 45 km. The maximum westerly wind at 50 and 55 km was located near 35-40°N only during all the 6 years. For brevity, a plot of latitudinal distribution of the zonal wind at 40 km only for different years is given (Figure 1).

Major warmings occurred in December during the winters of 1969-1970 and 1970-1971 (McINTURFF, 1978). Although the major warming during 1974-1975 occurred in the late February 1975, the stability of the zonal flow in this winter was weakened by frequent interruption of height-wave 1 and 2 during December 1974 and January 1975. These features led to distortion or weakening of the polar night jet in the high latitude middle atmosphere in January during 1970, 1971, and 1975. No major warming occurred during 1971-1972 and 1975-1976. During 1973-1974, major warming occurred as late as in February 1974 (McINTURFF, 1978). Such features strengthened the polar night jet in January during 1972, 1974 and 1976. It is, therefore, clear from the above study that the interannual variability noticed in the zonal wind of the high latitude middle atmosphere during two groups of years was caused by the differential

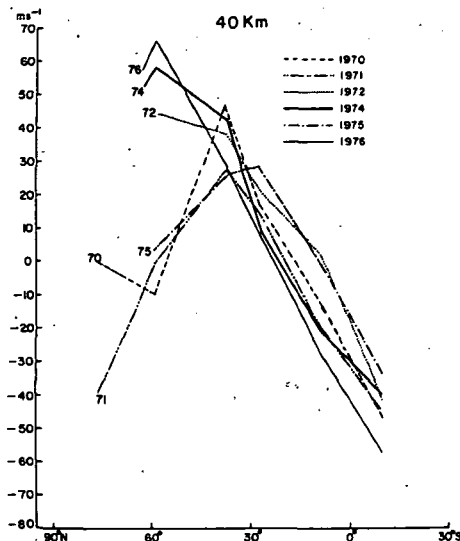


Figure 1. Mean zonal wind for January at 40 km for eight stations during 1970-1972 and 1974-1976.

activity of the long-period planetary waves.

At low latitudes, interannual variability was noticed below 40 km only and could not be identified distinctly due to its interaction with other prominent low latitude oscillations such as the semiannual and the quasi-biennial. Also, the planetary wave activity, which causes interannual variability, is weak or absent over low latitudes during winter.

The stratopause (50 km) temperature at 60°N in January was cold during 1970, 1971 and 1975, and warm during 1972, 1974 and 1976, showing interannual variability in the temperature field at the stratopause. As a result, the equator-to-pole temperature gradient strengthened during 1970, 1971 and 1975, and weakened during 1972, 1974 and 1976 (Figure 2).

In order to examine whether the stability of the polar night jet in the high latitude middle atmosphere has any influence on the spectacular tropospheric weather phenomenon such as Indian summer monsoon, the rainfall activity (June-Sept.) for India for 1970-1972 and 1974-1976 has been studied concurrently. The percentage departures of rainfall from the 32-year (1951-1982) normal for the entire country were -17.8, -1.8 and +0.1 during 1972, 1974 and 1976, and were +10.6, +2.7 and +18.9 during 1970, 1971 and 1975. The study revealed that:

- (1) Strong and stable polar night jet with weak equator to pole temperature gradient at the stratopause in January was linked with the forthcoming weak monsoon activity and,
- (2) Weak and distorted polar night jet with strong equator-to-pole temperature gradient at the stratopause in January was linked with the forthcoming strong monsoon activity. Further study is, however, necessary to arrive at a firm conclusion.

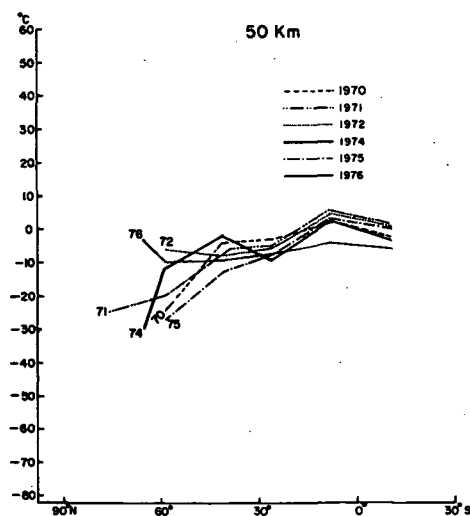


Figure 2. Mean temperature for January at 50 km for eight stations during 1970-1972 and 1974-1976.

ACKNOWLEDGEMENT

The authors are grateful to Dr. A. S. R. Murty for his helpful suggestions.

REFERENCES

- Labitzke, K. (1972), Temperature changes in the mesosphere and stratosphere connected with circulation changes in winter, J. Atmos. Sci., **29**, 756-766.
- Labitzke, K. (1982), On the interannual variability of the middle stratosphere during the northern winters, J. Met. Soc. Japan, **60**, 124-139.
- Labitzke, K. (1984), On the interannual variability of the middle atmosphere during winter, Program and Abstracts, International MAP Symposium (Kyoto, Japan), **1**.
- McInturff, R. M. (1978), Stratospheric Warmings: Synoptic, dynamic and general circulation aspects, NASA Reference Publication, **1017**, 19-30.
- Mukherjee, B. K. and Bh. V. Ramana Murty (1972), High-level warmings over a tropical station, Mon. Wea. Rev., **100**, 674-681.

1.11 CONNECTION BETWEEN MESOPAUSE TEMPERATURE, CIRCULATION AND NOCTILUCENT CLOUDS

Volker Gartner and Michael Memmesheimer

Institut für Astrophysik und Extraterrestrische Forschung
Auf dem Hugel 71, D-5300 Bonn 1
Federal Republic of Germany

To investigate the connection between mesopause temperature in summer and the induced circulation upon possible formation of the observed polar mesospheric (noctilucent) cloud layer (PMC), a two-dimensional semiempirical model is used to calculate the zonally averaged diabatic circulation. In that model the vertical-meridional circulation is derived by an iterative solution of the zonally averaged continuity and energy equation:

$$\frac{1}{\cos\theta} \frac{\partial}{\partial y}(v \cos\theta) + \frac{1}{\rho_0} \frac{\partial}{\partial z}(\rho_0 w) = 0 \quad (1)$$

$$w \Gamma = Q - v \frac{\partial T}{\partial y}$$

where v and w are the meridional and vertical velocities. T is temperature, θ is the latitude and ρ_0 is a reference density profile. The diabatic heating rate Q is given by the sum of solar and infrared heating. For the solar heating rates we used the algorithm of STROBEL (1978), and for the infrared part of the spectrum the so-called Newtonian cooling approximation is used with the coefficients of DICKINSON (1973) for the stratosphere and those of WEHRBEIN/LEOVY (1982) for the mesosphere. The static stability parameter is given by:

$$\Gamma = \frac{\partial T}{\partial z} + \frac{R}{c_p} \frac{T}{H} \quad (2)$$

where H is a (constant) scale height, R is the gas constant for dry air and c_p the specific heat at constant pressure. In Figure 1 a schematic diagram of the semiempirical model is shown.

For calculation of the solar heating rates, an ozone distribution for January derived from observations of the SME and NIMBUS satellites is used (Figure 2). To study the sensitivity of the circulation upon temperature variations in the mesopause region, different model runs have been made. In the basic state case we used the temperature distribution based on the Air Force reference atmosphere for January, which is shown in Figure 3.

The inferred vertical-meridional circulation is shown in Figures 4 and 5. A strong meridional flow from the summer to the winter hemisphere is found in the vicinity of the mesopause region (Figure 4). The maximum is located near 60° on the summer hemisphere with a value of 11.3 m/s. This is in good agreement with observations of NASTROM et al. (1982), who reported about zonally averaged meridional winds of up to 20 m/s in that location.

Connected with those large meridional winds also large vertical velocities (up to 46 mm/s) are found near the summer polar mesopause. Another interesting feature is the area of subsident motion, which can be seen in Figure 5 reaching from the equator until 50° S in the summer hemisphere. It is caused by the nonlinear temperature transport which contributes in the energy

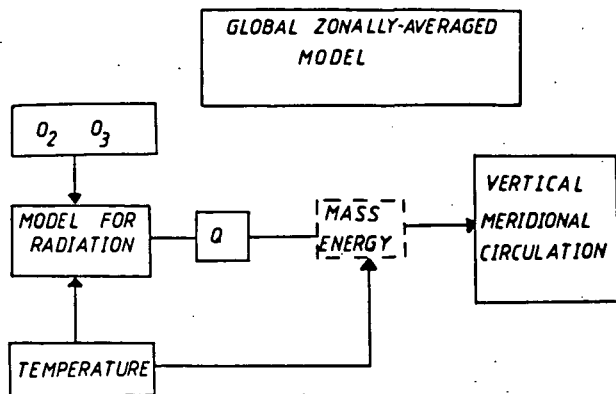


Figure 1. Schematic diagram of the semiempirical model.

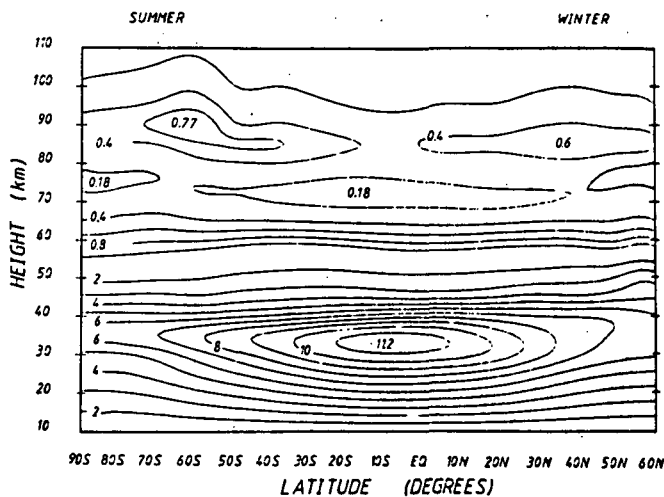


Figure 2. Observed ozone mixing ratios (ppmv) for January.

equation to the heating rates by a cooling of about 10 to 15 K/day in the midlatitude mesopause region.

To study the effect of temperature variations in the summer polar mesopause region we artificially changed the temperature distribution of Figure 3 by subtracting, for example, the following function of altitude z and latitude :

$$f(z, \theta) = 20. \times \exp\left[\left|\frac{90.-z}{6.7}\right|\right] \times \sin^2(\theta + 10.) \quad (3)$$

where z has to be specified in kilometers and θ in degrees. By the choice of this specific function a maximum cooling of 20 K is achieved at 90 km altitude

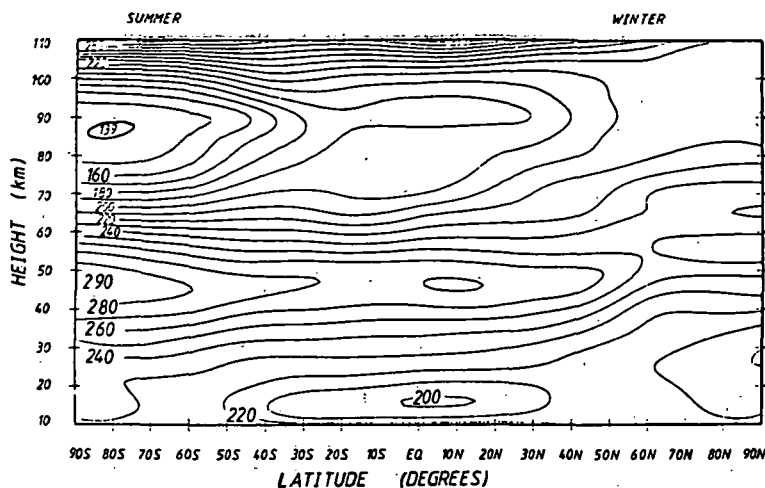


Figure 3. Zonally averaged temperatures (K) for January.

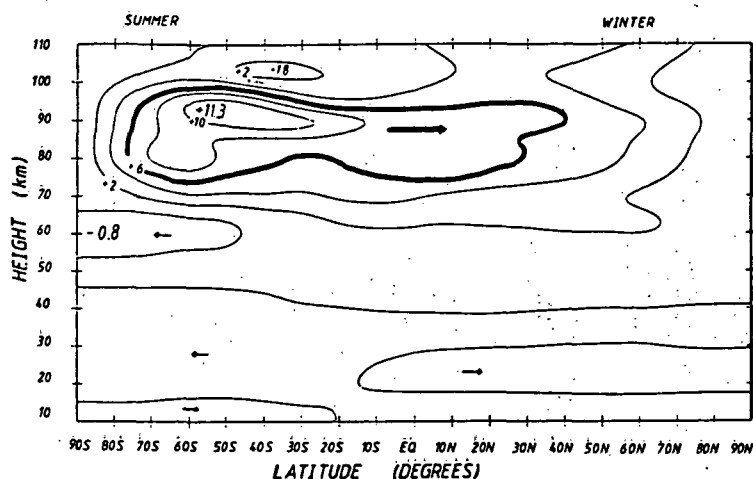


Figure 4. Meridional wind (m/s) calculated with temperatures of Figure 3.

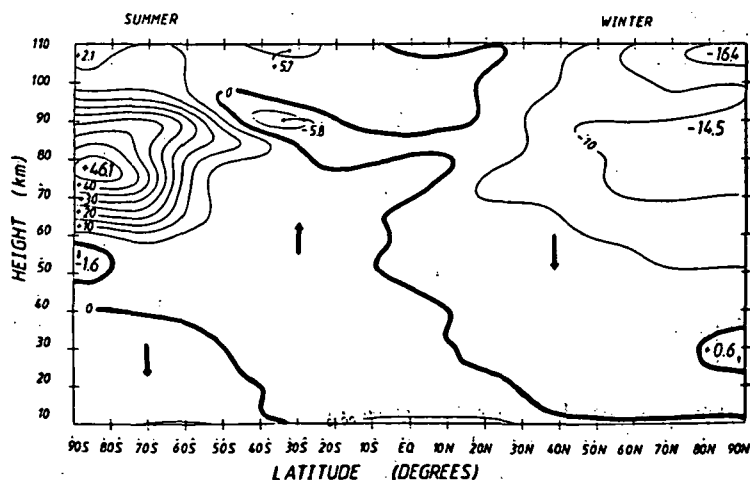


Figure 5. Vertical wind (mm/s) calculated with temperatures of Figure 3.

and 80°S . These new temperatures are shown in Figure 6. The summer polar mesopause is now very cold (121 K), but even colder temperatures have been observed during summer solstice (BALSLEY, personal communication).

With these cold temperatures, the calculated circulation is found to be much more vigorous (Figures 7 and 8). The maximum of the meridional winds is very close to the observed values of NASTROM et al. as well in location as absolute value. The area of subsidence (Figure 8) in the summer hemisphere has now the same strength as the subsident motion at the winter pole. Also its latitudinal extent now reaches up to 55°S .

This area of subsidence can also contribute to the limitation of the cap of polar mesospheric clouds, which have been observed first by DONAHUE et al. (1972) and more recently by the SME satellite (THOMAS, 1984), because it coincides with the observed equatorward boundary of this cloud layer. The necessary but not sufficient condition for polar mesospheric (noctilucent) cloud formation is that the temperatures are below about 145 K . This condition is

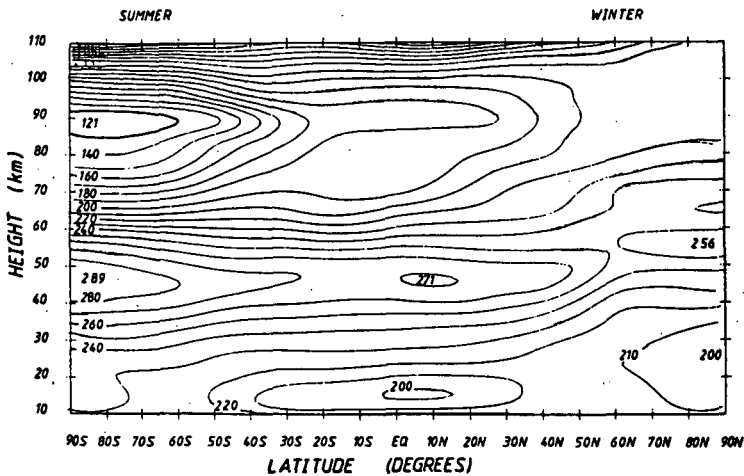


Figure 6. Modified temperatures (K) of Figure 3.

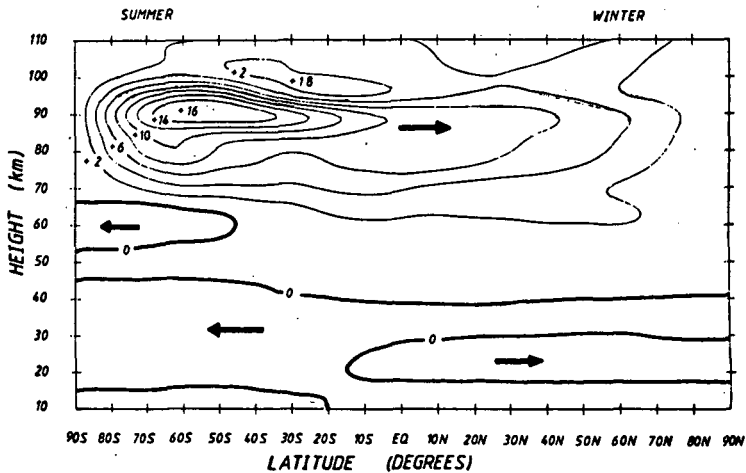


Figure 7. Meridional wind (m/s) calculated with T of Figure 6.

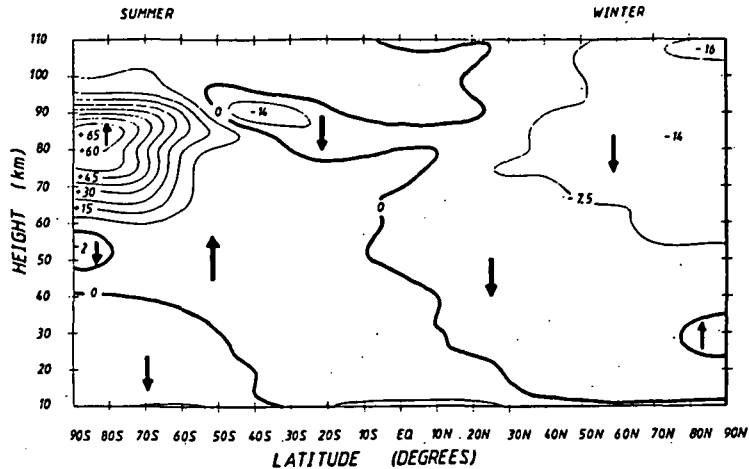


Figure 8. Vertical wind (mm/s) calculated with temperatures of Figure 6.

met for the calculations of our latter case in the region between 50°S and 90°S. In Figure 9 the ratios between observations with clouds and the total number of observations of the SME satellite (THOMAS, 1984) for the northern summer of 1982 are shown.

The commonly known noctilucent clouds (observable from ground) may be interpreted as the equatorial fringe of the observed (from space) "polar hood" of polar mesospheric clouds. In Figure 10 the average percentage of PMC observations versus latitude for the recent 6 summer seasons (northern and southern) are shown (THOMAS, 1984, personal communication). Also shown are the vertical velocities at 85 km for the cases shown in Figures 5 and 8. It can be seen that in the colder temperature case the region of summertime rising motions at mesopause heights is much closer related to the area of the cloud observations.

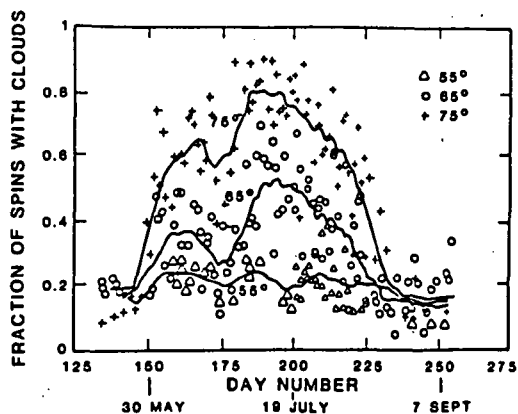


Figure 9. Percentage of PMC-observations for 10°-latitude bins. (THOMAS, 1984) solid curves are eleven-day running averages.

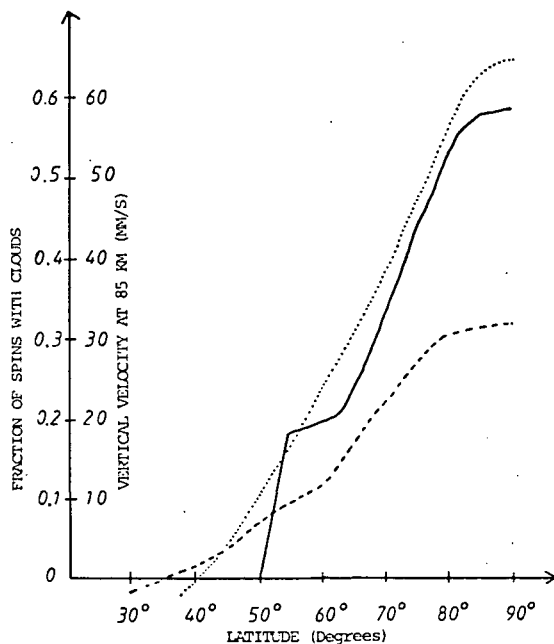


Figure 10. Percentage of PMC-observations (—) and the vertical velocities at 85 km of Figure 5 (---) and Figure 8 (.....).

On the basis of the above calculations, one may draw the following conclusions:

- (1) If the large departures from radiative equilibrium which occur at the summer mesopause at high latitudes should be balanced by adiabatic processes of the mean circulation alone, a vigorous circulation is needed. There is some evidence that such a vigorous circulation has been observed.
- (2) The vertical velocities of some cm/s at the polar summertime mesopause will support the formation of polar mesospheric clouds, because those large wind speeds support larger ice particles against gravitational sedimentation.
- (3) A region of mild subsidence in the summertime midlatitude mesosphere due to the effect of nonlinear temperature advection would tend to limit the occurrence of ice particles to latitudes poleward of about 55°. This is the approximate boundary of the very dense layers observed by DONAHUE et al. (1972) and THOMAS (1984).

REFERENCE

- Dickinson, R. E. (1972), Method of parameterization for infrared cooling between altitudes of 30 and 70 kilometers, *J. Geophys. Res.*, **78**, 4451-4457.
- Donahue, T. M., B. Guenther and J. E. Blamont (1972), Noctilucent clouds in daytime: Circumpolar particulate layers near the summer mesopause, *J. Atmos. Sci.*, **29**, 1205-1209.

- Nastrom, G. D., B. B. Balsley and D. A. Carter (1982), Mean meridional winds in the mid and high-latitude summer mesosphere, Geophys. Res. Lett., 9, 139-142.
- Strobel, D. F. (1978), Parameterization of the atmospheric heating rate from 15 to 120 km due to O_2 and O_3 absorption of solar radiation, J. Geophys. Res., 83, 6225-6330.
- Thomas, G. E. (1984), Solar mesosphere explorer measurements of polar mesospheric clouds (noctilucent clouds), J. Atmos. Terr. Phys., 46, 819-824.
- Wehrbein, W. M. and C. B. Leovy (1982), An accurate radiative heating and cooling algorithm for use in a dynamical model of the middle atmosphere, J. Atmos. Sci., 39, 1532-1543.

1.12 SOME STUDIES OF ZONAL AND MERIDIONAL WIND CHARACTERISTICS AT LOW LATITUDE INDIAN STATIONS

O. P. Nagpal and Somesh Kumar

Department of Physics,
University of Delhi
Delhi-110007, India

At the beginning of the Indian Middle Atmosphere Programme (IMAP), we considered it to be useful to prepare consolidation reports of already available parameters for the middle atmosphere. Atmospheric wind data obtained by rockets and balloons constituted one such parameter which had to be consolidated. The present paper summarises the results of this consolidation study. Both zonal and meridional components of winds at four low latitude Indian stations namely Thumba (8.5°N, 77°E), Shar (13.4°N, 80°E), Hyderabad (17.2°N, 78.3°E) and Balasore (21.5°N, 87°E), have been analysed to yield reference wind profiles for each month (NAGPAL and DHAR, 1983; KUMAR and NAGPAL, 1984). The monthly mean values have been used to bring out the amplitudes and phases of the annual, semianual and quasi-biennial oscillations.

The steady component of the zonal winds show that barring the monsoon months (i.e., June to September), they are westerlies up to about 18 km altitude with their magnitude increasing with latitude. Above this height, they turn into easterlies for all months, and a reversal to westerlies takes place again between 50-60 km altitude. Figure 1 (a and b) shows the latitude-height section of the "raw" mean zonal winds for months of January and July of two years, i.e., 1979 and 1980. The wind data at Hyderabad station is obtained by balloons only and hence the maximum altitude up to which the data are available is 35 km. Although, above about 20 km, the winds remain easterlies for all months, their magnitude increases by a factor of two or more during monsoon months as compared to winter months.

Figure 2 shows the altitude variations of the amplitude and phase of the semianual and annual oscillations in the zonal winds. The semianual oscillation (marked SA in Figure 2) shows a maxima between 40-50 km at all stations, with its amplitude decreasing with increasing latitude. Another small maxima is seen around tropopause heights at all the stations. The phase (time of maxima) of this oscillation remains constant in the entire stratosphere. The upper tropospheric region (around 15 km) and lower mesospheric region (around 60 km) show strong annual oscillations (marked A in Figure 2) in the zonal winds. The amplitude of this oscillation is minimum at Thumba and increases as we move away from the equator towards higher latitudes. These results are in general agreement with results for other low latitude stations (CIRA, 1972; BELMONT et al., 1974).

Figure 3a depicts time-height section of the zonal wind for Hyderabad station where wind data from 1977 to 1983 were available. Quasi-biennial oscillation (QBO) is clearly visible in this figure for the data plotted after 1980. There are large data gaps during 1977, 1978 and 1979 and hence, QBO is not discernible before 1980. Figure 3b shows the amplitude and phase of the QBO. The amplitude is maximum at 28 km ($\approx 23 \text{ msec}^{-1}$) and decreases rapidly to about 4 msec at 15 km. The phase occurs at a higher level (32 km) earlier and propagates downward at a speed of about 1 month or little less per kilometer as described by HOLTON (1979) and PLUMB (1984).

Since the theories for the generation of the QBO, the annual and semianual variations currently accepted depend on the existence and modula-

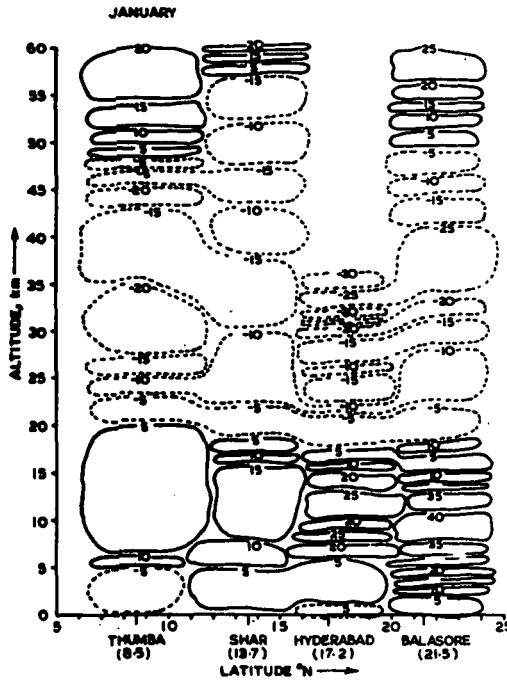


Figure 1a. January mean winds.

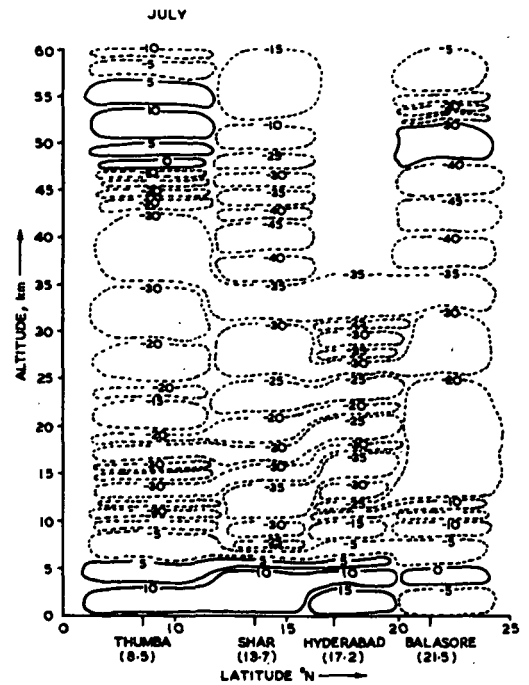


Figure 1b. July mean winds.

Figure 1a,b. Latitude-height section of the mean zonal wind. The mean is taken for two years 1979-1980.

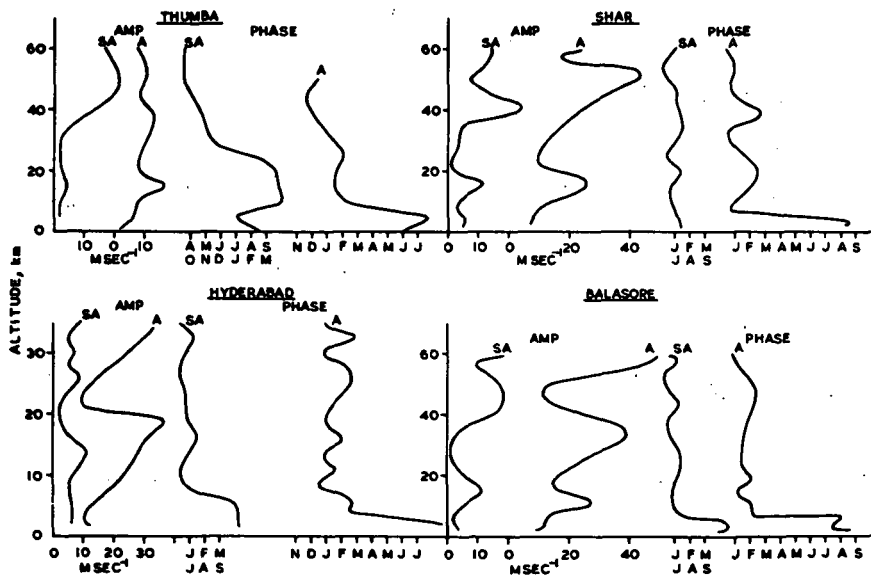


Figure 2. Semianual and annual oscillations in the zonal winds. Amplitudes and phases are shown for all four stations.

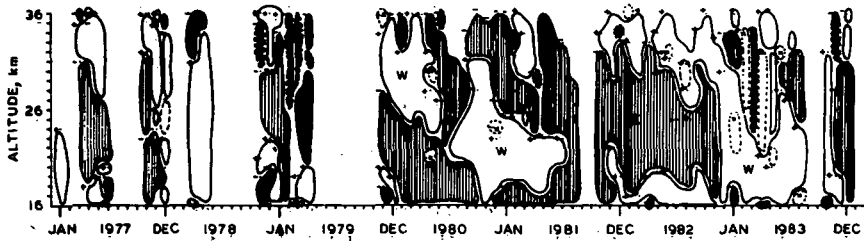


Figure 3a. Time-height section of the zonal wind shear at 17.2 N (Hyderabad 1977-1983). The 7-year average of monthly means were subtracted to remove the annual and semiannual cycles. Isotachs are drawn at intervals of 10 ms^{-1} . Easterlies are shaded.

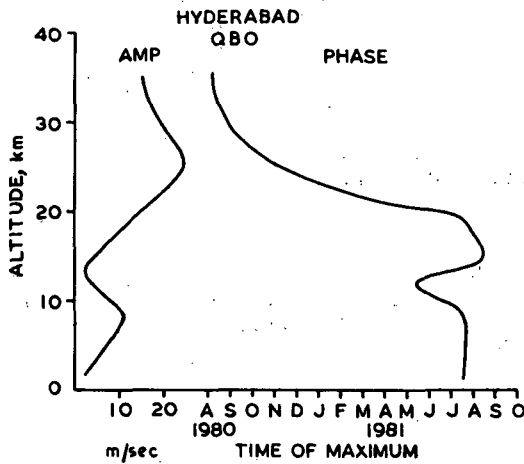


Figure 3b. Amplitude and phase of QBO at Hyderabad station.

tion of planetary scale motion (e.g. equatorial waves) which provides the forcing mechanism (HOLTON, 1979), it is scientifically important to have observational data on various equatorial wave modes. With this in view, we have analysed high altitude balloon wind data at three stations, namely, Thumba, Madras (13.4°N , 80°E) and Bhubneshwar (21.5°N , 87°E) for the presence of equatorial waves. Thrice a week measurements of winds from January to September 1984 have been analysed by the Method of Natural Orthogonal Component (MNOC) for obtaining the presence of predominant wave characteristics, e.g., periods, amplitudes and vertical wavelengths.

Figure 4 shows the third eigenvector which depicts wave-like patterns. The vertical wavelength of the wave is determined by calculating the distance between two maxima. Accordingly, the eigenvector represents a wavy pattern with two characteristic wavelengths of about 5-6 km and 8-14 km. The lower wavelength is associated with wave periods between 5-6 days (determined from the coefficients associated with eigenvector), and the larger wavelength with larger period wave (10-20 days). These characteristics are indicative of the fact that wave disturbances are mixed-Rossby waves and Kelvin waves

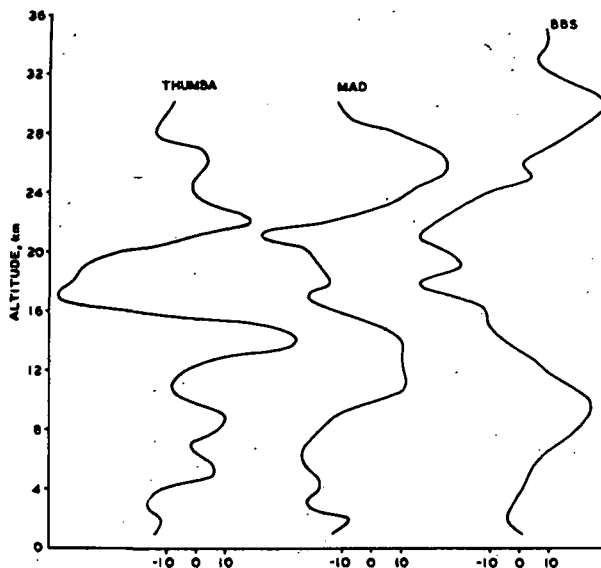


Figure 4. Height profiles of third eigenvector for zonal winds at three stations: Thumba, Madras and Bhubneshwar indicating wavy pattern.

respectively. Further analysis to establish these wave modes rigorously is in progress. Efforts are also underway to acquire rocket data for detection of waves at higher heights (> 30 km).

REFERENCES

- Belmont, A. D., D. G. Dartt and G. D. Nastrom (1974), Q. J. Roy. Met. Soc., **100**, 203-211.
- CIRA 1972 (1972), COSPAR International Reference Atmosphere, Academic-Verlag, Berlin.
- Hirota, I. (1978), J. Atmos. Sci., **35**, 714-722.
- Holton, J. R. (1979), An Introduction to Dynamic Meteorology, Academic Press, New York.
- Kumar, S. and O. P. Nagpal (1984), ISRO-IMAP-SR-18-84, May 1984.
- Nagpal, O. P. and J. Dhar (1983), ISRO-IMAP-SR-14-83, ISRO Off., Bangalore, June 1983.
- Plumb, R. A (1984), Dynamics of the Middle Atmosphere, edited by J. R. Holton and T. Matsuno, Terra Pub. Company, Tokyo Japan, **217**.

1.13 TEMPORAL VARIATIONS OF THE TROPICAL TROPOPAUSE CHARACTERISTICS

B. V. Krishna Murthy, K. Parameswaran and K. O. Rose

Space Physics Laboratory, Vikram Sarabhai Space Centre,
Trivandrum - 695022, India

In this communication, results of a detailed study of tropopause characteristics at eleven Indian stations spread over a latitude range of 8.4°N to 28.6°N , using the data obtained during the period 1969-1978, are presented and discussed.

The general features of tropopause height (H), temperature (T) and pressure (P) are illustrated in Figures 1a, 1b and 1c, respectively for Trivandrum (18.4°N), Madras (13.1°N), Visakhapatnam (17.7°N) and Delhi (28.6°N) covering the latitude range. At Trivandrum H shows maximum in April and minimum in August. This pattern changes to summer maximum and winter minimum at the extratropical station Delhi. At Visakhapatnam the variations are small. As expected, P shows just the opposite pattern to the altitude. Tropopause at Delhi is warmer than that at the equator-ward stations throughout the year. Trivandrum T shows prominent broad maximum during June-September with secondary peak in February-March, whereas Delhi shows winter maximum and summer minimum.

In order to examine the latitudinal profile of tropopause altitude, in Figure 1d, the average tropopause altitude is shown as a function of latitude for the four seasons. H increases with latitude in the zone 8.4°N to 28.6°N except in winter, when it shows a decrease. A noteworthy feature in Figure 1d is the fluctuation over and above the general trend in H at latitudes south of Visakhapatnam. North of Visakhapatnam, H shows relatively smooth variation with latitude. Though the stations Hyderabad and Visakhapatnam are situated at the same latitude, the tropopause at Visakhapatnam is lower than that at Hyderabad except in autumnal equinox. Hyderabad is located on the deccan plateau, far from coast and relatively free from vegetation, leading to higher tropopause. But in autumnal equinox, a rainy season, Hyderabad area is generally cloudy, and this may lead to lower tropopause in contrast to other seasons. Bangalore and Madras constitute a similar pair. In autumnal equinox, also tropopause at Madras is lower than at Bangalore, unlike the other pair of stations. This could be due to the northeast monsoon being quite intense at Madras.

The parameters that can contribute to the tropopause are incoming solar radiation, earth-atmospheric albedo and their thermal radiation, water vapour, ozone and wind field. An increase in thermal radiation from earth would lead to an increase in tropopause altitude. The summer maximum of tropopause altitude at stations situated on land interior, like Delhi and Lucknow, is due to the increased convection in troposphere. Water vapour and cloud cover essentially would decrease the solar insulation, at the same time increasing the "green-house" effect. This would reduce the tropopause altitude. REID and GAGE (1981) proposed that tropical tropopause responds to the annual variation in average tropical solar insulation, causing corresponding change in sea surface temperature (SST). The maximum potential temperature attainable by an ascending air parcel would be the same as the equivalent potential temperature of the same parcel at the surface, say TP(S). The variation of TP(S) represents the surface contributed component of tropopause potential temperature TP(T). The lower stratospheric (18 km) potential temperature TP(18) represents the stratospheric contributed component of TP(T). The variation of TP(S), TP(T) and TP(18) are shown in Figure 2a, b and c for Trivandrum,

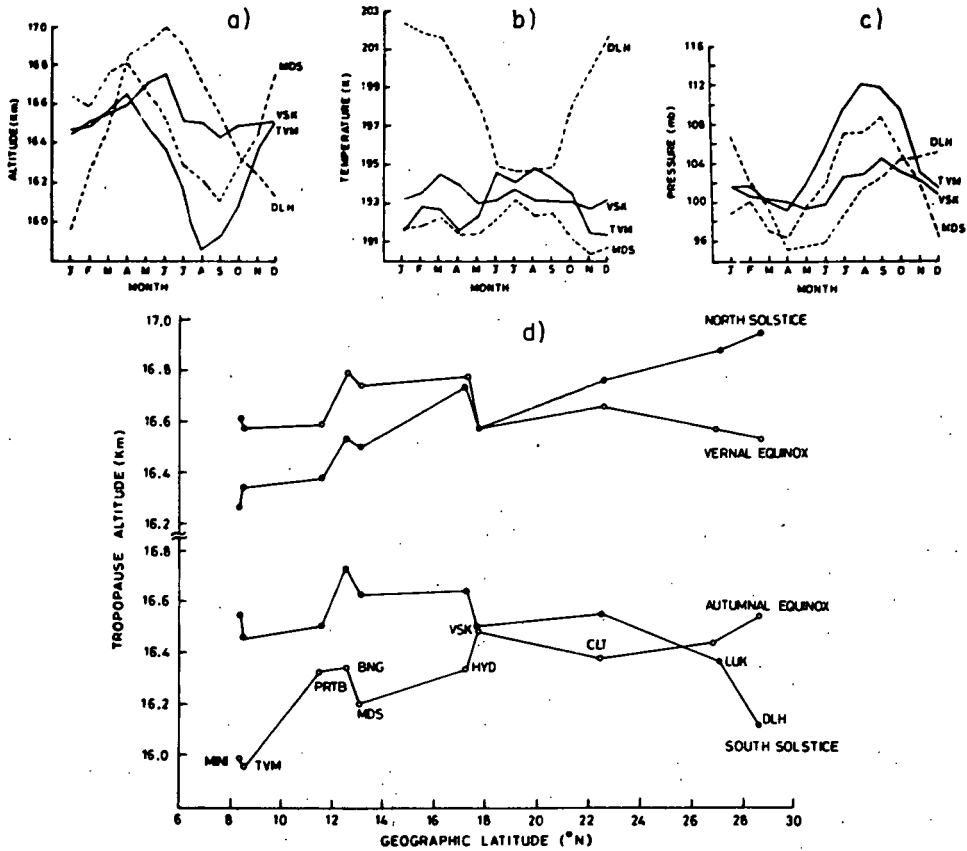


Figure 1. Temporal and latitudinal variations of tropopause characteristics.

Madras and Delhi, respectively. TP(T) and TP(18) show opposite variations to each other for Trivandrum and Madras as in the case of pacific stations (REID and GAGE, 1981), but at Delhi TP(18) minimum shows a lag of about 3 months with respect to TP(T) maximum. TP(T) and TP(S) show generally similarity at Trivandrum, but corresponding to the deep minimum in TP(T) during July-December, TP(S) shows only a shallow trough. At Madras and Delhi, TP(S) and TP(T) variations are not similar. The dissimilarities appear to be more during monsoon months, especially at Trivandrum and Madras.

The annual and semiannual components of TP(T) TP(S) and TP(18), along with tropopause altitude for the three stations, are presented in Table 1. The annual components are stronger than the semiannual components. The annual component of H shows maximum in January-February for stations south of Visakhapatnam, while it shifts to April-May for Visakhapatnam and north of it, for stations north of Visakhapatnam the amplitude of semiannual component in H shows an increase with increase in latitude. The maximum of the semiannual component occurs in equinoxes for all stations irrespective of latitude. An interesting feature is the near constancy of phase of annual and semiannual components of TP(T) and TP(S) with latitude. On the other hand, the time of maximum of annual component of TP(18) shows a shift to later months with latitude while semiannual phase remains almost constant with latitude. The behaviour of TP(T) is in contrast to the behaviour of tropopause temperature and pressure. This indicates that factors influencing the convective heat

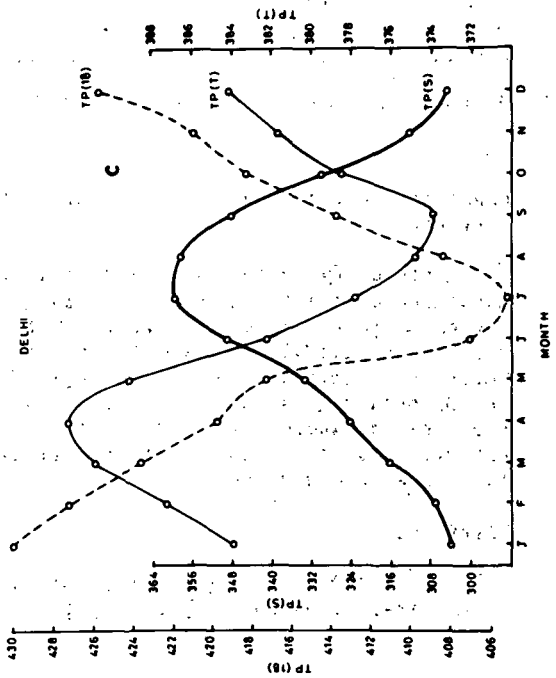
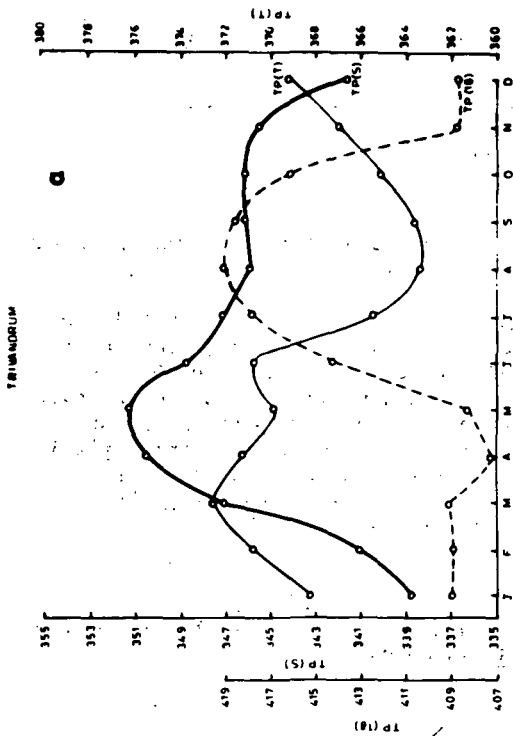
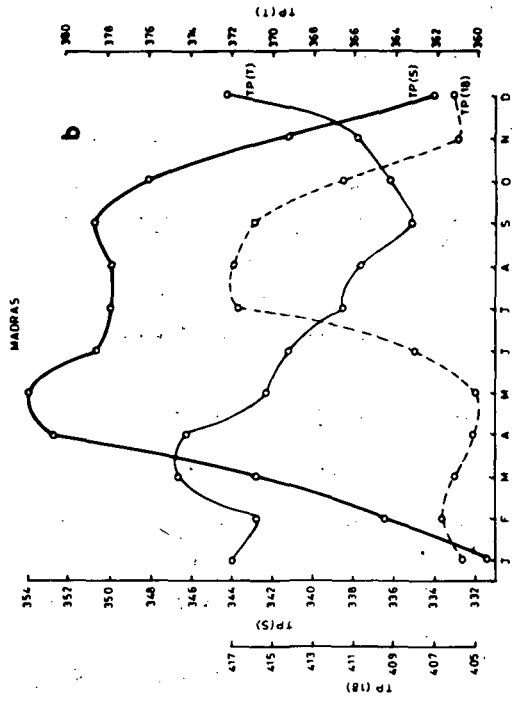


Figure 2. Temporal variations TP(1), TP(5) and TP(18) for Trivandrum, Madras, and Delhi.

Table 1.
Annual and Semiannual Components.

Parameter	Periodicity	Trivandrum		Visakhapatnam		Delhi	
		Amplitude	Phase*	Amplitude	Phase*	Amplitude	Phase*
H (km)	Annual	0.29	1.70	0.09	4.10	0.47	0.10
	Semi-annual	0.14	4.30	0.07	4.30	5.20	3.60
TP(T) (K)	Annual	3.48	2.15	2.91	2.57	7.46	1.40
	Semi-annual	1.04	4.39	0.47	4.27	2.71	3.60
TP(S) (K)	Annual	3.63	5.00	14.03	5.47	27.78	6.19
	Semi-annual	3.10	3.29	4.30	2.75	5.21	1.02
TP (18) (K)	Annual	5.31	7.21	1.92	9.50	11.04	0.10
	Semi-annual	2.75	0.99	1.79	1.40	1.08	2.15

* Phase in months reckoned from 1st January.

transport in the troposphere in this latitude zone show similar variation with latitude.

This study reveals that the semiannual component in TP(T) can mainly be accounted by the corresponding variation on the solar insolation, whereas the annual component is greatly affected by the monsoon phenomenon, which is a large-scale annual one. During this period, the large-scale cloud cover would reduce the convective activity. Again, the annual components of TP(T) and TP(18) show a phase difference of about 6 months, except at the extratropical stations and about 2 to 3 months in the case of semiannual component. At extratropical stations the phase difference is much less, indicating the influence of convective process in the lower stratosphere.

REFERENCE

Reid G. C. and K. S. Gage (1981), On the annual variation in the height of the tropical tropopause, J. Atmos. Sci., **38**, 1928-1938.

2.1 MIDDLE ATMOSPHERE TIDES

Jeffery M. Forbes

Department of Electrical, Computer, and Systems Engineering
Boston University, Boston, MA. 02215

INTRODUCTION

The recent direction of theoretical and observational research in middle atmosphere tides is reviewed. The diurnal tide has received considerable emphasis, including observations of evanescent components at high latitudes, numerical simulations of nonmigrating propagating components due to longitudinally varying water vapor insolation absorption in the troposphere, and implications and origins of "unsteadiness" in tidal oscillations over periods of days. Recent analyses of LIMS temperatures and partial reflection drift measurements of neutral winds in the tropical mesosphere have also emphasized the diurnal propagating tide. A description of the Atmospheric Tides Middle Atmosphere Program (ATMAP) and an overview of ATMAP campaign results are also presented.

OBSERVATIONS

The installation in recent years of radars at the high latitude sites of Poker Flat (65°N, 147°W), Scott Base (78°S, 168°E) and Mawson (68°S, 63°E), offer a different view of tidal motions from those available at middle and low latitudes. At high latitudes, diurnal evanescent modes dominate over propagating components, and shorter vertical wavelength semidiurnal modes become more apparent. MACLEOD and VINCENT (1984) make comparisons with theory and Poker Flat measurements which summarize the existing status of high latitude tidal studies. Figure 1 illustrates their results for the diurnal and semidiurnal wind components. The Poker Flat data delineate significantly greater summer winds for both diurnal and semidiurnal components. However, the Mawson summer winds are small compared to those observed at Poker, suggesting either hemispheric or interannual differences. The phases exhibit remarkable consistency in all cases. The FORBES (1982) theoretical model for summer conditions nicely fits the Poker semidiurnal amplitudes but underestimates the diurnal winds. The difference may be accounted for by trapped mode contributions due to a nonsymmetric heat source of unknown origin, or high-latitude broadening of the (1,1) wind structure due to the distorting effects of mean wind interaction of turbulent dissipation above 85 km.

Additional observations of interest include diurnal tidal variations of temperature between 20 and 65 km and 0° and 50° latitude inferred from day-night differences of Nimbus 7 LIMS temperatures (HITCHMAN and LEOVY, 1985). The derived temperature structures are consistent with what one would expect from the (1,1) propagating tide. In addition, time variations in the tidal intensity and height of amplitude minimum appear to be modulated by basic state oscillations on a quasi-biennial time scale. Other observations of diurnal propagating tidal winds by the partial reflection drifts technique at Townsville, Australia (19°S, 147°E, R. A. VINCENT, unpublished data) are discussed in the next section in the context of "variability".

TEMPORAL VARIABILITY

Observations of tides are often characterized as being temporally "variable" over time scales of a few days or more. MF-radar observations at Townsville, Australia (19°S, 147°E, R. A. VINCENT, unpublished data) as depicted in Figure 2, aptly illustrate this feature. The diurnal oscillations depicted

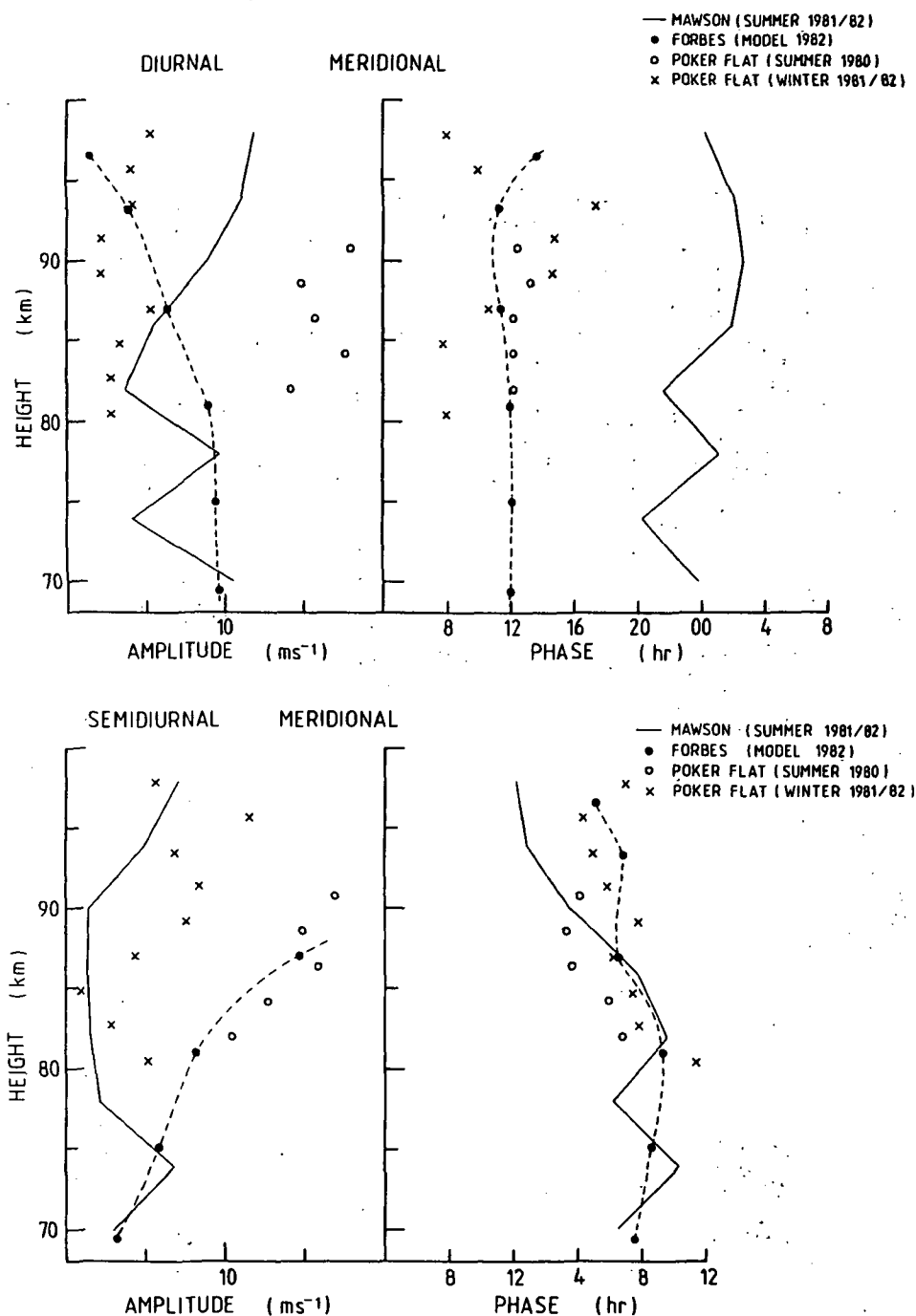


Figure 1. Diurnal and semidiurnal meridional winds observed at Mawson, Antarctica (MACLEOD and VINCENT, 1984) and Poker Flat, Alaska (CARTER and BALSLEY, 1982) compared with the model of FORBES (1982).

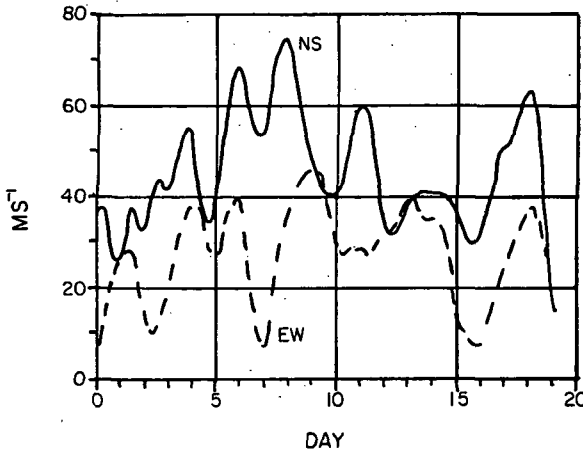


Figure 2. Band-pass filtered winds near the diurnal frequency at 88 km at Townsville, Australia, during July/August, 1980 (R. A. VINCENT, unpublished data, used with permission).

here are very likely associated with the (1,1) propagating diurnal tide, which attains its maximum wind amplitudes near 18° latitude. A similar degree of variability is reflected in the semidiurnal component at Townsville, as well as at midlatitudes (GLASS et al., 1978).

It is not known to what extent such variability may be associated with global changes in tidal forcing and background propagation conditions or with the introduction of energy near tidal frequencies by local or synoptic-scale disturbances. Let us define here an atmospheric tide to be a global-scale oscillation at a frequency corresponding to a subharmonic of a solar or lunar day which is in steady-state equilibrium with existing forcing and background propagation conditions. Now if one assumes that a tidal oscillation bears an intrinsic adjustment time with respect to changing, forcing or background propagation conditions, and if the time scale of these changes is long compared with the tidal adjustment time, then one could still say that steady-state equilibrium exists. One consequence of nonequilibrium is that the latitude structures of meteorological fields at tidal periods would be "distortions" of these corresponding to the steady-state equilibrium situation. The practical relevance of possible nonequilibrium distortion occurs when attempting to interpret data from different latitudes. BERNARD (1982) has suggested that the characteristic adjustment time for a particular tidal mode might reasonably be approximated by its propagation-time (τ_p) around the earth. He estimates values of τ_p from horizontal group velocities (V_{gh} , a function of latitude) determined by an "equivalent gravity wave approximation" wherein the value of V_{gh} is evaluated at the latitude (θ_0) where the vertical group velocities of the tidal mode and EGW are equal. The propagation times range between 2.5 days for the (2,2) mode and 11.9 days for the (1,1) mode. These values may be some indication of time scales over which one might expect equilibrium conditions and hence global coherence to exist for these modes.

The above discussion pertains to steady-state equilibrium criteria for global-scale oscillations. Presumably, averaging over periods of order τ_p will also remove local "noise" at tidal frequencies. The correlation between simultaneous tidal determinations around the globe would be expected to saturate and thus approach global coherence as the fit span for determining the tidal components is increased towards τ_p .

Although it is necessary that observational and theoretical studies be performed to clarify the above speculations, the tentative conclusion that might be drawn is that it is meaningful to refer to variations in most tides over periods of order 6-10 days, whereas variations over shorter time scales may reflect nonglobal effects. To achieve the highest degree of consistency between data sets and provide a meaningful comparison with theoretical models, it can be recommended that tidal measurements are best represented as vector averages of no less than 6 days' observation.

LONGITUDINAL VARIABILITY

KATO et al. (1982) and TSUDA and KATO (1984) investigate the generation and propagation characteristics of diurnal nonmigrating tides due to geographically localized sources of excitation. Simulations of the southward wind velocity at 20° latitude associated with the differential heating between land and sea are illustrated in Figure 3. The simulations reveal short vertical wavelength (< 10 km) oscillations similar to observations of stratospheric tides observed at Jicamarca, Peru (12°S).

The penetration of larger-scale diurnal nonmigrating tides above 80 km are investigated by FORBES and GROVES (1985). They show that longitudinal variations in diurnal insolation absorption by tropospheric H_2O can account for longitudinal variations of at least ± 12 -15% about zonal mean values in the diurnal wind amplitude at low latitudes (0°-20°) between 80 and 100 km, by virtue of the nonmigrating propagating tidal nodes which are excited. Phase variations of ± 7.5 hours also occur. The height-longitude variations of the northward diurnal wind speed at 18° latitude, as calculated by these authors, is depicted in Figure 4.

THE ATMOSPHERIC TIDES MIDDLE ATMOSPHERE PROGRAM

The nature of atmospheric tides requires investigations and coordination on a global, and hence international, scale. ATMAP is one of several projects comprising the international Middle Atmosphere Program (MAP). The purpose of ATMAP is to create an interaction among observationalists, data analysts, theoreticians and modellers working towards the following goals:

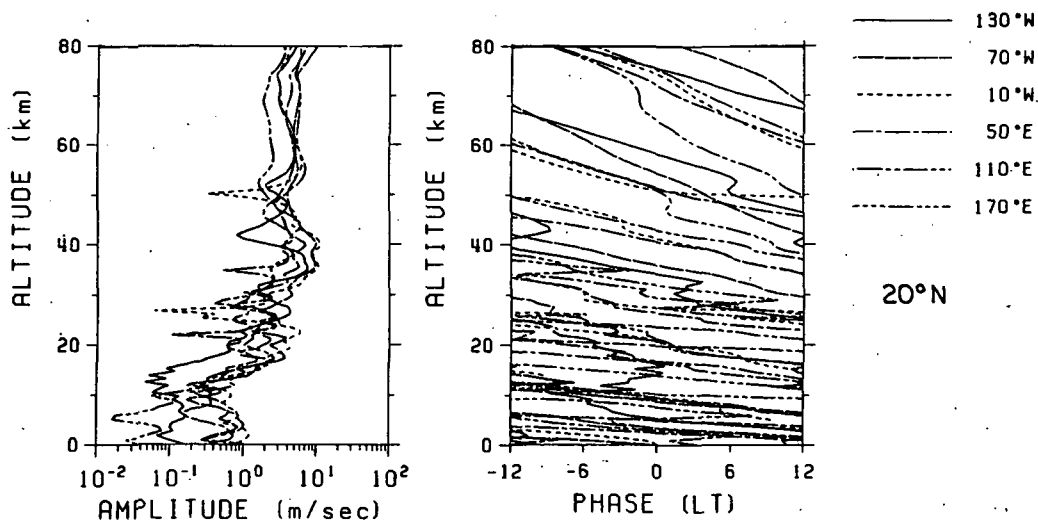


Figure 3. Southward diurnal winds at 20°N for various longitudes excited by the heat source localized on land (TSUDA and KATO, 1984).

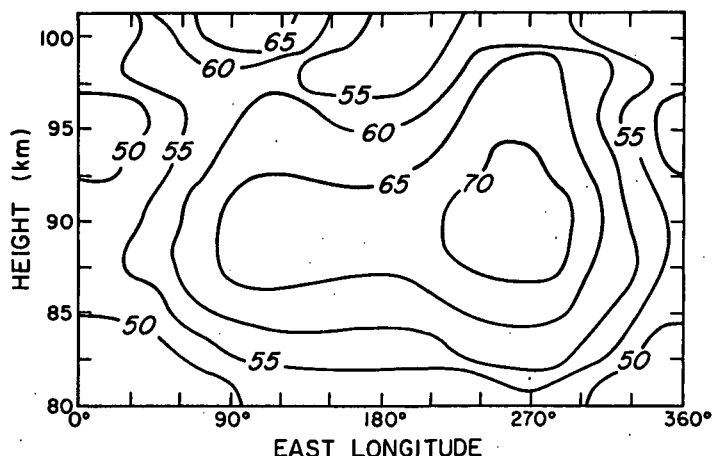


Figure 4. Height-longitude contours of northward diurnal wind speed at 18° latitude. (FORBES and GROVES, 1984).

- 1) To delineate the global morphology of tides in the middle atmosphere, including temporal and spatial variability on various scales;
- 2) To elucidate the role of tides in affecting mean winds and temperatures in the middle atmosphere;
- 3) To elucidate the role of tides in giving rise to gravity waves and turbulence through nonlinear cascade and instability processes; and
- 4) To examine the influence of mean wind and temperature fields on tidal wave propagation.

The focus for this interaction is a series of global observational campaigns involving meteor, partial reflection drift, and incoherent scatter radars, lidars, and optical instruments. The main mechanism for interchange is workshops dealing specifically with the interpretation of the campaign measurements. A 1-day workshop was held in conjunction with IAMAP General Assembly, Hamburg, Federal Republic of Germany, August 1983, and a 2-day workshop is scheduled with the International MAP Symposium, Kyoto, Japan, November 1984.

The Hamburg workshop concentrated on observations during the core period 19-22 November, 1981, of Campaign #1. Results were reported from the partial reflection drift, meteor, and incoherent scatter radars listed in Table 1. In one scheme of data presentation, the tidal amplitudes and phases measured at each station at a mean height of 90 km were plotted as a function of latitude and compared with theoretical curves which summarized the predictions of tidal models due to ASO et al. (1982), FORBES (1982), and WALTERSCHEID et al. (1980). An example of this depiction of tidal winds measured during the 4-day core periods for campaign #1 (19-22 November 81) and #2 (3-6 May 82) for the semi-diurnal eastward velocity is given in Figure 5. A panel discussion on the interpretation of the campaign #1 results in Hamburg concentrated first on the consistency of the observations. There was general consensus that the core period was essentially undisturbed and that the mean circulation was representative of early solstitial conditions. There was general agreement that the tidal observations were remarkably consistent as a function of latitude, but

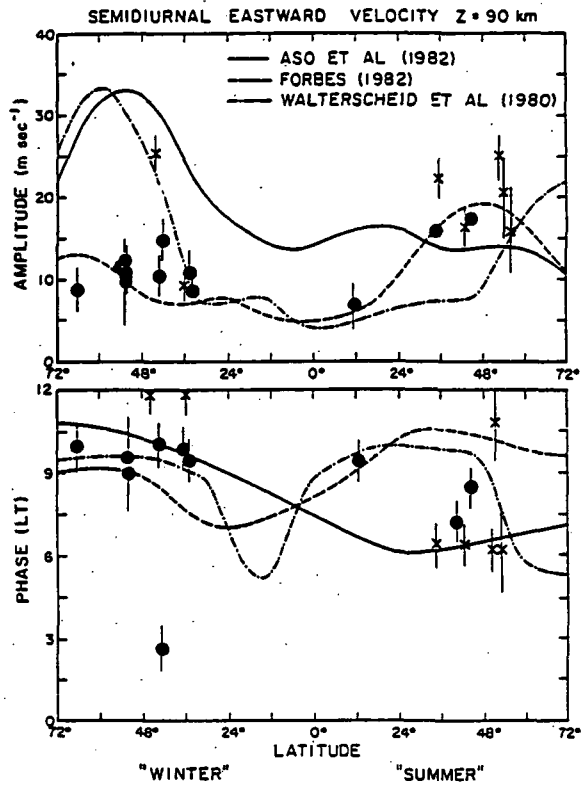


Figure 5. Semidiurnal amplitudes (top) and phases (bottom) of westerly velocity at 90 km as observed by participating radar facilities (see Table I) during the November 19-22, 1981, and May 3-6, 1982, ATMAP campaigns, and compared with the theoretical models of ASO et al. (1982), FORBES (1982), and WALTERSCHEID et al. (1980).

there were a number of significant deviations from theory. At high winter latitudes the theoretical amplitudes for the semidiurnal tide were significantly in excess of the observed amplitudes (cf. Figure 5). The predicted variations in phase as a function of latitude were, however, in better agreement with the experimental results. Possible reasons for these discrepancies were discussed, and it was felt that the models may underestimate the role of damping. Intercomparison of observations made at the same latitude but different longitudes showed that tidal phases could differ by several hours. In addition, the diurnal tide exhibited significant differences in tidal structures between Northern and Southern Hemispheres not explicable in terms of current models. Similar features and discrepancies can be recognized in the May 3-6 1982 data.

Examination of vertical structures at the Hamburg workshop for individual stations also proved illusory. It was suggested that a theoretical problem that should be addressed is the relative importance of reflection of tides and the interaction of tidal modes. This is motivated by several observations at all latitudes that show amplitude modes and associated 180° phase shifts. Arguments were presented that suggested that the reflection mechanism was more important than mode interaction in describing these observations. Other areas recommended for further theoretical research included studies of nonmigrating

TABLE I

Facilities and Investigators Contributing
Data to the November, 1981, ATMAP Campaign Analyzed
at the 1983 Workshop in Hamburg

Facility	Latitude (deg)	Longitude (deg)	Key Investigators
Poker Flat	65 N	147 W	S. Avery, D. Carter, B. Balsley (USA)
Kuhlungsborn	54 N	12 E	K. Greisiger (GDR)
Collm	52 N	15 E	R. Schminder (GDR)
Badary	52 N	104 E	E. Kazimirovsky (USSR)
Saskatoon	52 N	107 W	A. Manson (Canada)
Durham	43 N	71 W	R. Clark (USA)
Urbana	40 N	88 W	S. Avery, S. Bowhill (USA)
Atlanta	34 N	84 W	R. Roper (USA)
Kyoto	35 N	136 E	T. Aso, T. Tsuda, S. Kato (Japan)
Arecibo	18 N	67 W	J. Rottger (FRG)
Jicamarca	12 S	77 W	T. Aso (Japan)
Adelaide	35 S	138 E	R. Vincent, G. Elford (Australia)
Christchurch	44 S	173 E	G. Fraser (New Zealand)

Theory and Modeling: T. Aso (Japan), J. Forbes (USA), H. Teitelbaum (France),
F. Vial (France), R. Walterscheid (USA).

tides, the breaking of tides in the mesosphere, longitudinal asymmetries in
ozone and water vapor heating, the interaction of tides with gravity waves and
planetary waves, and mechanisms for dissipating tides above 85 km.

ACKNOWLEDGEMENTS:

J. M. Forbes received support for this work under Grant ATM-8319487.

REFERENCES

- Aso, T., T. Naoyama and S. Kato (1982), J. Geophys. Res., **86**, 388.
 Bernard, R. (1981), J. Atmos. Terr. Phys., **43**, 663.
 Carter, D. A. and B. B. Balsley (1982), J. Atmos. Sci., **39**, 2905.
 Forbes, J. M. (1982), J. Geophys. Res., **87**, 5222.
 Forbes, J. M. and G. V. Groves (1984), submitted to J. Atmos. Terr. Phys.
 Glass, M., R. Bernard, J. L. Fellous and M. Massebeuf (1978), J. Atmos. Terr.
 Terr. Phys., **40**, 923.
 Hitchman, M. H. and C. B. Leovy (1984), submitted to J. Atmos. Sci.
 Kato, S., T. Tsuda and F. Watanabe (1982), J. Atmos. Terr. Phys., **44**, 131.
 MacLeod, R. and R. A. Vincent (1984), submitted to J. Atmos. Sci.
 Tsuda, T. and S. Kato (1984), submitted to J. Atmos. Sci.
 Walterscheid, R. L., J. G. De Vore and S. V. Venkateswaran (1980), J. Atmos.
 Sci., **37**, 455.

2.2 DIURNAL NONMIGRATING TIDES DUE TO LAND-SEA DISTRIBUTION

Toshitaka Tsuda and Susumu Kato

Radio Atmospheric Science Center,
Kyoto University, Uji 611, Japan

This paper is concerned with thermal excitation of diurnal nonmigrating tides by differential heating between land and sea. The nonmigrating tide is defined as a wave with a period corresponding to a subharmonic of a solar day. It is excited when heat sources of atmospheric tides have zonal asymmetries, and does not necessarily propagate westward with the sun.

Observationally, the existence of nonmigrating tides have been known for more than half a century as reviewed by CHAPMAN and LINDZEN (1970). For example, HAURWITZ (1965) detected nonmigrating tides in diurnal surface pressure oscillation. WALLACE and TADD (1974) investigated global tidal motions by using rawinsonde measurements. Recently, the vertical structure of tidal winds has been observed by using MST radars (FUKAO et al., 1978, 1980). Amplitudes of the diurnal tidal wind in the lower stratosphere observed at Arecibo and Jicamarca ranged from 1 to 5 m/sec with maximum occurring at around 20 km altitude. And their vertical wavelengths were fairly short.

By using classical tidal theory, MCKENZIE (1968) examined the excitation of diurnal tides due to longitudinally dependent heat source. His numerical model successfully explained fundamental features of diurnal tides detected by rocket measurements such as large wind velocity below 30 km at 20°N. and rapid decrease in strength with latitude. KATO et al. (1982) discussed non-migrating tides which are excited by certain localized heat source near the equator. They found the excited tides have short vertical wavelengths consistent with the Arecibo and Jicamarca results (FUKAO et al., 1978, 1980).

The present study took the same treatment as used by KATO et al. (1982), and assumed similar heat source model used by McKenzie, although fine structure of land-sea distribution was taken into account.

We assumed that the diurnal component of the upward heat flux in the boundary layer excites the nonmigrating tide. Furthermore, the heat source is assumed to be restricted only over land. We have expanded the longitudinal distribution into Fourier series, and used up to twentieth component of both westward and eastward traveling waves. Each wave is further expressed by 20 positive and 20 negative Hough modes. The amplitude of the heat input is assumed to decrease exponentially with altitude at a decay distance of 1 km. The amplitude of the corresponding temperature variation at ground at the equator is set equal to 3 K.

Figure 1 shows our numerical result of the amplitude of the sine component of the diurnal surface pressure oscillation in comparison with observations by HAURWITZ (1965). The observations showed that the diurnal surface pressure oscillation was largely affected by the land-sea distribution such that its amplitude was large over continents around the equator. The numerical result shown in the lower panel approximately reproduced the observed characteristics. However, an additional heat source for the migrating tide seems to be necessary to explain the zonally uniform component of the surface pressure oscillation. According to our numerical results at other altitudes, as the altitude increased the enhanced area of the nonmigrating tide converges into the region equatorward of 30 degrees, and spreads longitudinally.

Vertical structure of the zonal wind of the diurnal tide is shown in

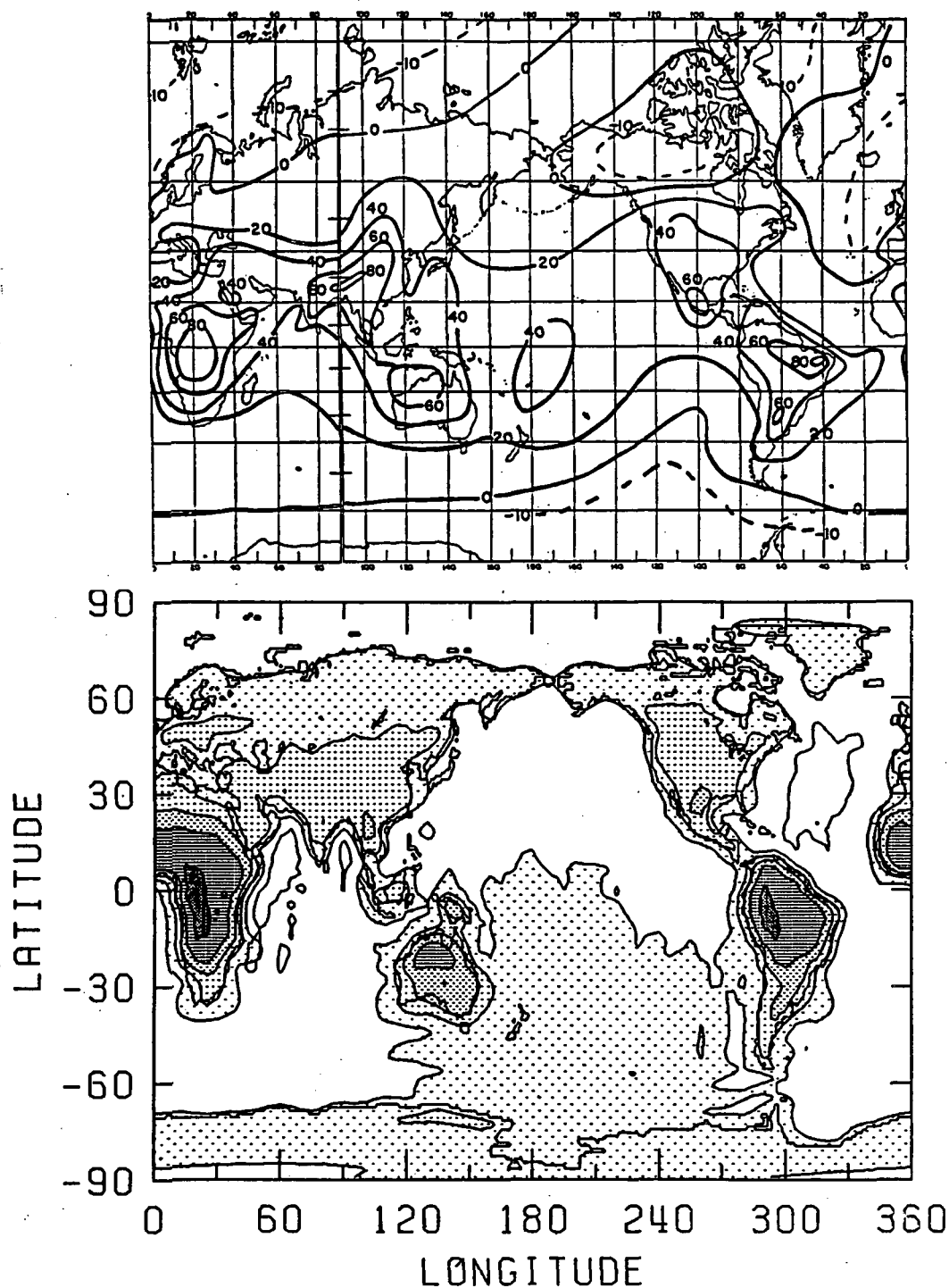


Figure 1. Amplitude of the sine component of the diurnal surface pressure oscillation. Top panel: observations by HAURWITZ (1965). Bottom panel: our numerical result. Contour lines are drawn at intervals of 0.2 mmHg.

EASTWARD WIND VELOCITY

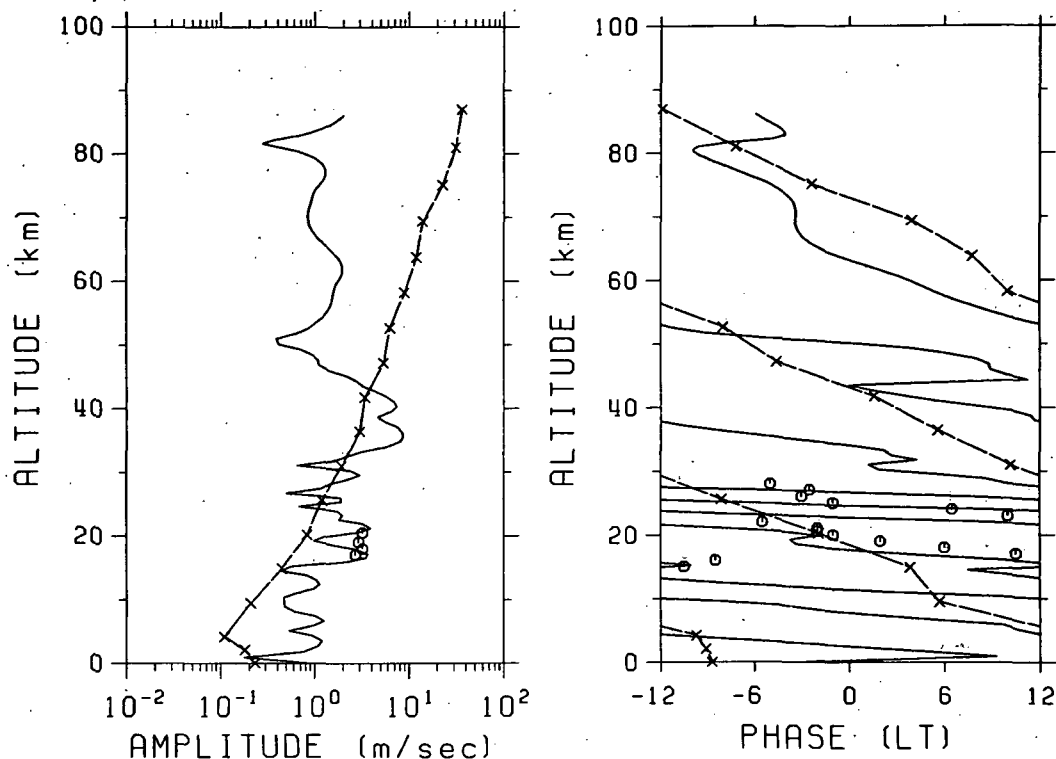


Figure 2. Vertical profile of the diurnal tidal wind. A solid line: the present result at 70°W and 20°N . A broken line with a cross symbol: numerical model of the migrating diurnal tide at 18°N (from FORBES, 1982). A circular symbol: observations at Arecibo (after FUKAO et al., 1980).

Figure 2, where phase is defined as local time of the eastward maximum wind velocity. The nonmigrating tide had larger amplitude than the migrating one, and its vertical wavelength was fairly short below 30 km. In upper stratosphere and mesosphere, the migrating tide becomes dominant.

Circular symbols in Figure 2 correspond to the observation at Arecibo (FUKAO et al., 1980). The amplitude exceeded the migrating tide at around 20 km altitude, and agrees well with our model. The observed short vertical wavelength could be reproduced by our model, although the absolute value of phase differs slightly.

As a conclusion, if our assumption of the heat source model is acceptable, we could explain behavior of diurnal surface pressure oscillation and tidal wind in the lower stratosphere over Arecibo. The nonmigrating component seems to be dominant in the diurnal tidal winds below 30 km altitude in the low latitude region.

REFERENCES

- Chapman, S. and R. S. Lindzen (1970), Atmospheric Tides, D. Reidel Publ. Co., Dordrecht, Holland.
- Forbes, J. M. (1982), Atmospheric tides 1. Model description and results for the solar diurnal component. J. Geophys. Res., 87, 5222-5240.
- Fukao, S., S. Kato, S. Yokoi, R. M. Harper, R. F. Woodman and W. E. Gordon (1978), One full-day radar measurement of lower stratospheric winds over Jicamarca, J. Atmos. Terr. Phys., 40, 1331-1337.
- Fukao S, T. Sato, N. Yamasaki, R. M. Harper and S. Kato, (1980), Radar measurement of tidal winds at stratospheric heights over Arecibo, J. Atmos. Sci., 37, 2540-2544.
- Haurwitz, B. (1965), The diurnal surface-pressure oscillation, Arch. Meteorol. Geophys. Bioklimatol., A. Met. Geophys., 14, 361-379.
- Kato, S., T. Tsuda and F. Watanabe (1982), Thermal excitation of non-migrating tides, J. Atmos. Terr. Phys., 44, 131-146.
- McKenzie, D. (1968), The diurnal atmospheric tide with Newtonian cooling and longitudinally dependent drive, Ph. D. thesis, University of Washington, Seattle.
- Wallace, J. M. and R. F. Tad (1974), Some further results concerning the vertical structure of atmospheric tidal motions within the lower 30 kilometers, Monthly Wea. Rev., 102, 795-803.

2.3 MIDDLE ATMOSPHERE (60-110 KM) TIDAL OSCILLATIONS AT SASKATOON, CANADA (52°N, 107°W) DURING 1983/84

A. H. Manson and C. E. Meek

Institute of Space and Atmospheric Studies,
University of Saskatchewan, Saskatoon, Canada S7N 0W0

INTRODUCTION

Since mid-1978, the medium frequency (2.2 MHz; M.F.) radar at Saskatoon has run continuously, measuring winds by the spaced antenna method in the upper middle atmosphere (60-110 km) (MANSON et al., 1981, 1982, 1983). As there is so much dynamics activity during the years of MAP it seems very important to establish the features of the tidal field at Saskatoon during 1983/84, and compare these with the climatology from the four years 1978/79 - 1981/82.

MEAN WINDS

Wind profiles with 60-110 km (80-110 km at night) with 3 km resolution are obtained every 5 minutes by means of a full-correlation analysis. Hourly means are formed and harmonic analysis applied to sets of data to obtain the mean winds and tidal oscillation amplitudes and phases. From Figure 1, the zonal wind field at Saskatoon is structurally similar to CIRA-72; however, the wind eastward cell is weaker and much more structured, and the summer eastward cell above 85 km is also weaker. Overall this cross section differs substantially from wind models used in the tidal modeling which is discussed later. The meridional cross section is for considerations of zonal momentum, but not important for tidal modeling.

SEMI-DIURNAL AND DIURNAL OSCILLATIONS (MONTHLY MEAN)

For the semidiurnal tide, a strong seasonal change exists, with larger amplitudes and shorter wavelengths in winter-like months (November-March) and the reverse in summer-like months (May-August). A summary of the tidal parameters at 90 km is given in Figure 2, where mean values from 1978-82 are also shown. This seasonal variation of tides is a midlatitude climatology, as comparisons with Monpezier, France (44°N) and Christchurch, New Zealand (44°S) show very similar behaviour, as does Durham (43°N); and requires antisymmetric tidal modes such as 2,3 and 2,5. FORBES (1982a,b) and WALTERSCHEID et al., (1980) use an early empirical wind field but revised heating rates in their models: however after trying these (ASO et al., 1981), ASO and KATO (1984) used the preferred (although still not ideal) CIRA-72 wind model and "conventional" forcing, which gives best agreement with midlatitude measured tidal data. (Figure 2).

Considering the diurnal tide, for most months centred on summer there are long wavelength modes, or superposition of several modes. However, some winter months show a short wavelength mode. A summary of the 90 km characteristics is shown in Figure 3; it is similar at Christchurch (44°S), Garchy, France (47°N), and Durham (43°N). FORBES (1982a) model, in which the symmetric (1,1) mode dominates, agrees best in winter months; however, increased presence of the antisymmetric (1,-1) mode will be required to give the observed seasonal variation, and probably the trapped (1,-2) mode to provide the observed complex phase structures.

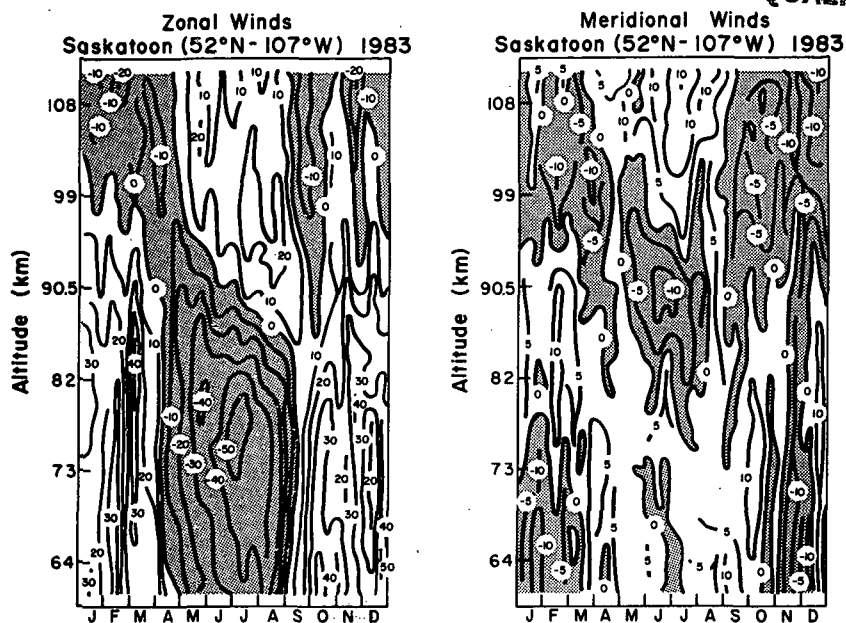


Figure 1. Mean winds with tidal corrections, 10 d means.

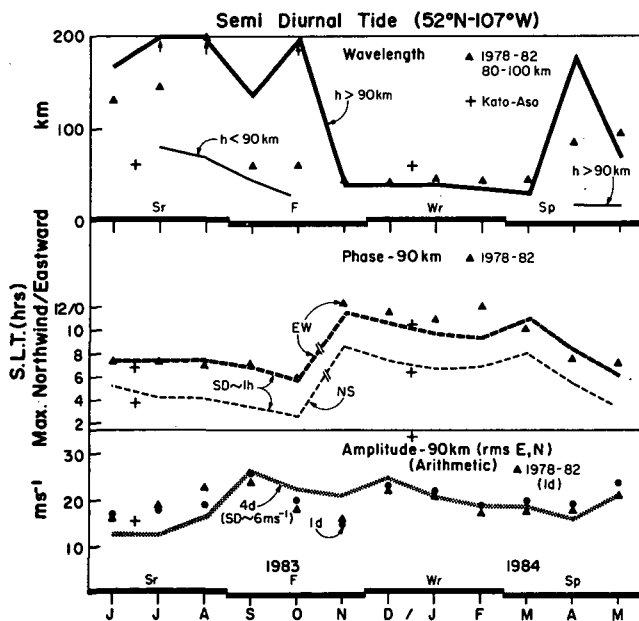


Figure 2. Semidiurnal 90 km tidal characteristics. Values from ASO and KATO (1984) are shown.

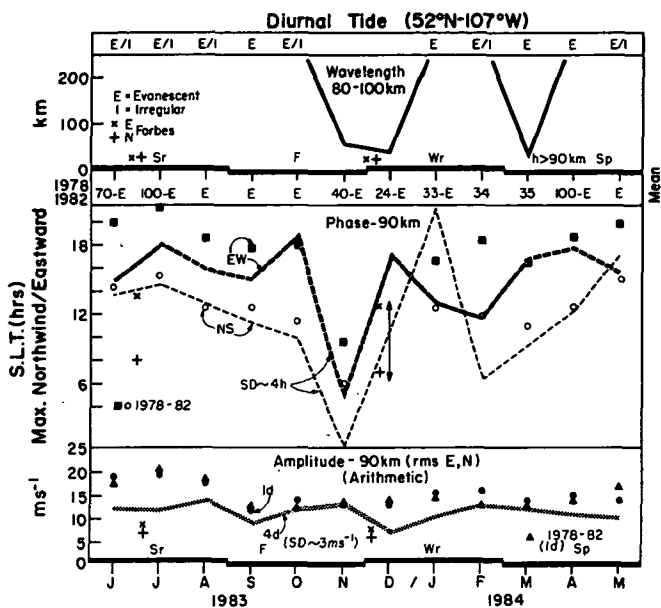


Figure 3. Diurnal 90 km tidal characteristics. Values from FORBES (1982a) are shown.

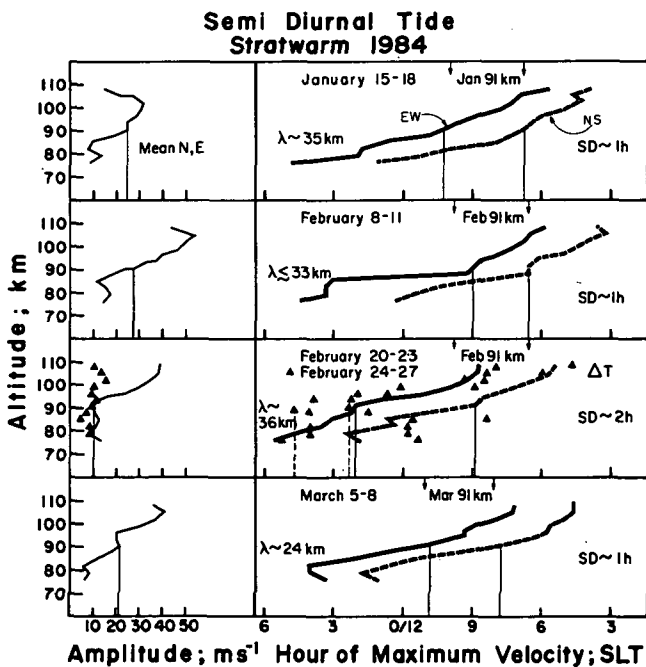


Figure 4. Tidal profiles during the 1984 stratwarm.

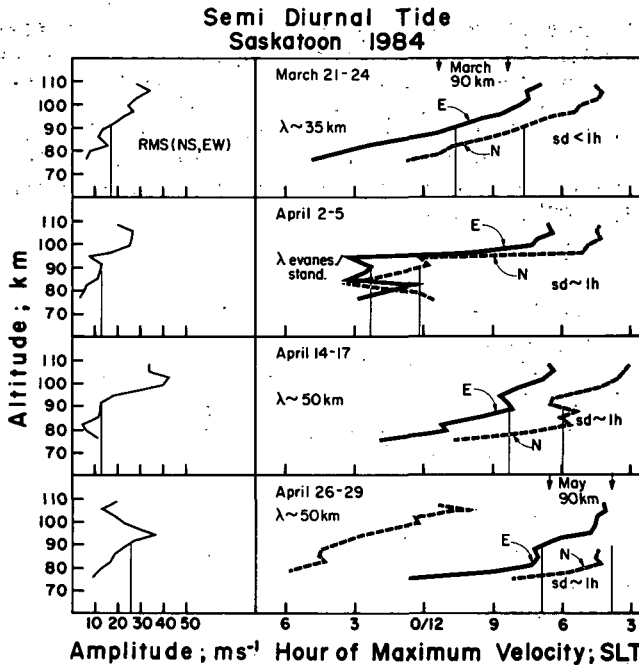


Figure 5. Tidal profiles during the 1984 spring transition.

TRANSITIONS AND DISTURBANCES IN 1984

The STRATALERT messages from the Free University of Berlin described the maximum warming over N. Europe on 23 February 1984 with breakdown of the stratospheric polar vortex. The Saskatoon radar winds show closely related westward perturbations. The 12-h tidal phases responded strongly to the warming, with phase lags of up to ~6h (Figure 4). The spring transition began at the beginning of April (Figure 5): there was an ATMAP campaign centred on March 30. The phases by the end of April are typical of summer at 90 km but the wavelength is still a transitional equinoctial value.

REFERENCES

- Aso, T., and S. Kato (1984), Linearized steady calculations of semidiurnal tides in the middle atmosphere, Dynamics of the Middle Atmosphere, edited by J. R. Holton and T. Matsuno pp. 173-180.
- Aso, T., T. Nonoyama, and S. Kato (1981), Numerical simulation of semidiurnal atmospheric tides, J. Geophys. Res., **86**, 11,388-11,400.
- Forbes, J. M. (1982a), Atmospheric Tides 1. Model description and results for the solar diurnal component, J. Geophys. Res., **87**, 5222-5240.
- Forbes, J. M., (1982b), Atmospheric Tides 2. The solar and lunar semidiurnal component, J. Geophys. Res., **87**, 5241-5252.
- Manson, A. H., C. E. Meek, and J. B. Gregory (1981). Winds and waves (10 min-30 days) in the mesosphere and lower thermosphere at Saskatoon (52°N, 107°W, L=4.3) during the year, October 1979 - July 1980, J. Geophys. Res., **86**, 9615-9625.
- Manson, A. H., C. E. Meek, and J. B. Gregory (1983), The semidiurnal tide at the equinoxes: M. F. radar observations for 1978-1982 at Saskatoon (52°N, 107°W), J. Atmos. Sci., **40**, 969-976.

- Manson, A. H., C. E. Meek, J. B. Gregory, and D. K. Chakrabarty (1982). Fluctuations in tidal (24-, 12-h) characteristics and oscillations (8-h - 5-d) in the mesosphere and lower thermosphere (70-110 km): Saskatoon (52°N, 107°W), 1979-1981, Planet. and Space Sci., 10, 1283-1294.
- Walterscheid, R. L., J. G. DeVore, and S. V. Venkateswaran (1980), Influence of mean zonal motion and meridional temperature gradients on the solar semidiurnal atmospheric tide: A revised spectral study with improved heating rates, J. Atmos. Sci., 37, 455-470.

2.4 MESOSPHERIC WINDS OBSERVED BY THE KYOTO METEOR RADAR

Toshitaka Tsuda and Susumu Kato

Radio Atmospheric Science Center,
Kyoto University, Uji 611, Japan

The Kyoto meteor radar described elsewhere (e.g., ASO et al., 1979, 1980) has been operated almost continuously from May 1983. By using a large amount of radar data, seasonal variations of mean winds, planetary waves and atmospheric tides can be delineated. For these observations, an antenna main beam was fixed in the eastward direction. Because the antenna beam is fairly wide, an arrival angle of each meteor echo might not be right eastward, thus, the wind measurement usually contains both zonal and meridional components. Elevation and azimuth angles of each meteor echo can be determined by an interferometer, so that a fitting analysis can give both zonal and meridional wind components, although the zonal one is more reliable than the other. We have taken a time-height bin of 2 hrs x 4 km for this unlike other than the tidal analysis which utilizes a least square fitting of sinusoidal functions with periods of 24 hrs and 12 hrs.

Seasonal and latitudinal variation of tidally corrected mean winds including Kyoto observations have been examined in comparison with CIRA 1972 model (MANSON et al., 1984).

A power spectral density of the zonal wind field for 60 days of data is formed from an autocorrelation function with a maximum time lag of 30 days. The seasonal variation of power spectral density is plotted in Figure 1. Note that a linear trend in 60 days is removed before the ACF calculation so that the intensity of the mean wind cannot be estimated from Figure 1.

A quasi-2-day oscillation was evident in the period from June to September, and seems to be repeated in 1983 and 1984. It had large amplitudes in June and July and became weak in August; then it was again amplified in September. In summer months, the period of the wave was indicated as 2.2 days, and it became shorter in September.

A wave with a period of approximately 3 days was conspicuously enhanced in summer in 1984. Long-period oscillations with periods of 6.8 and 15 days sometimes became dominant, although a clear seasonal variation was not recognized from Figure 1. Because Figure 1 is based on the analysis of 60 days of data, a short-term variation of the behavior of these waves would be smoothed. By investigating the variation of wind field, the amplification of long-period oscillations such as 6- and 8-day wave in 1983, or 15-day wave in 1984, coincided with the decrease of the mean eastward wind in August.

At Kyoto (35°N), diurnal tide is the main component of atmospheric tides whose seasonal variations in 1979-1980 has been reported by TSUDA et al., (1982). The monthly mean amplitude of the eastward component of diurnal tide is plotted for the period from May 1983 to September 1984. It was clearly amplified in summer months at around 92-96 altitudes. This feature was repeated in two successive years except for the maximum amplitude which exceeded 40 m/sec and 30 m/sec in 1983 and 1984, respectively.

Figure 3 shows the local time of the eastward maximum of diurnal tide at 94 km. In summer months, the phase was stable at 9 to 10 a.m. (0900 to 1000 hrs). However, it became 2200 to 0200 hrs (10 p.m. to 2 a.m.) in October, November and December. The diurnal tide seems to be evanescent in summer, and contains propagating waves with short vertical wavelengths in winter. This

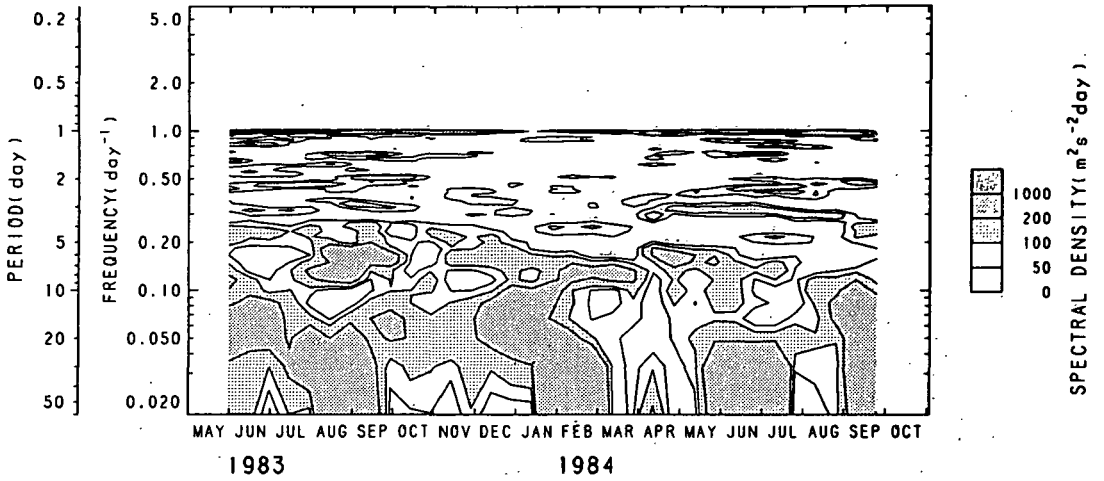


Figure 1. Seasonal variation of power spectral density for long-period oscillations.

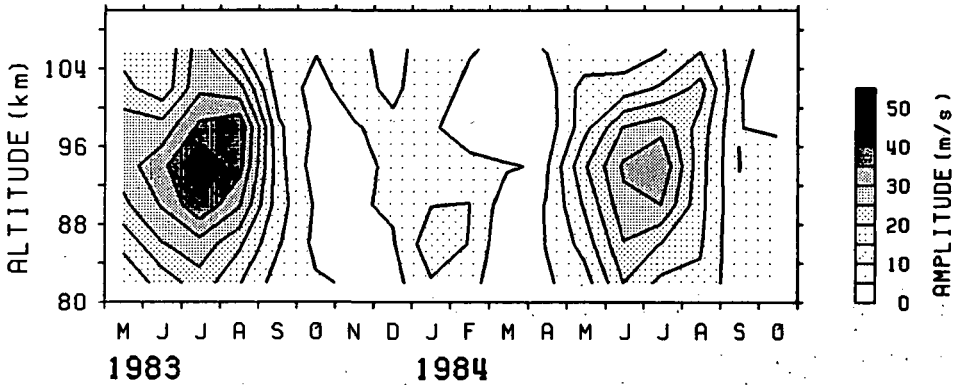


Figure 2. Monthly mean amplitude of the eastward component of diurnal tide.

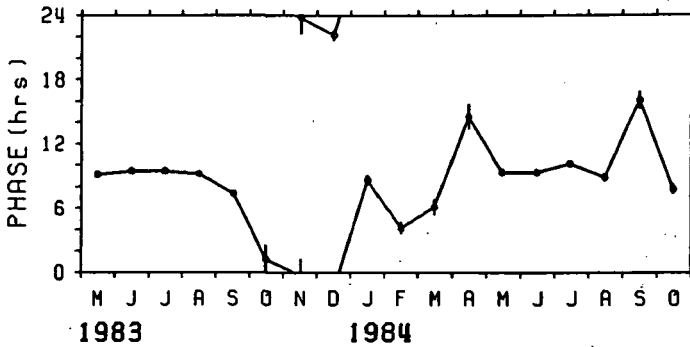


Figure 3. Monthly mean value of the local time of maximum eastward wind velocity of diurnal tide at 94 km.

behavior was also recognized in the 1979-1980 observations at Kyoto. This work would suggest that a meteor radar observation of long duration can provide a climatology of mean winds, planetary waves and atmospheric tides in the 80-110 km region.

REFERENCES

- Aso, T., T. Tsuda and S. Kato (1979), Meteor radar observations at Kyoto University, J. Atmos. Terr. Phys., **41**, 517-525.
- Aso, T., T. Tsuda, Y. Takashima, R. Ito and S. Kato (1980), Observations of lower ionospheric wind by the Kyoto meteor radar, J. Geophys. Res., **85**, 177-184.
- Manson, A. H., C. E. Meek, M. Massebeuf, J. L. Fellous, W. G. Elford, R. A. Vincent, R. L. Craig, R. G. Roper, S. Avery, B. B. Balsley, G. J. Fraser, M. J. Smith, R. R. Clark, T. Aso and A. Ebel (1984), Mean winds of the upper middle atmosphere (60-110 km): A comparison of radar data (M. F. meteor VHF) from 1973-1983 with CIRA 1972 and other models, Paper 1.6, MAP Symposium, Kyoto.
- Tsuda, T., T. Aso and S. Kato (1983), Seasonal variation of solar atmospheric tides at meteor heights, J. Geomag. Geoelectr., **35**, 65-86.

2.5 SEMIDIURNAL TEMPERATURE OSCILLATION AND E-REGION ABSORPTION OVER HARINGHATA

N. N. Purkait

Institute of Radio Physics & Electronics
92 Acharya Prafulla Chandra Road
Calcutta, India 700009

ABSTRACT

An attempt has been made to explain the observed asymmetry in the diurnal curves on absorption for the E region at 2.2 MHz for our Field Station at Haringhata (22°56'N, 88°36'E). A comparison between the computed and observed diurnal curves on absorption revealed that a part of the asymmetry was a manifestation of the effect of semidiurnal temperature oscillation present in the E layer. It was further noted that the degree of the asymmetry of the observed diurnal curves depends profoundly on the rate of downwards phase progression of the temperature oscillation.

INTRODUCTION

The asymmetry in the diurnal curves on total absorption for low latitude station was observed by several workers including SHARMA (1967), GANGULY and KHASTGIR (1972) and also by PURKAIT (1976). The diurnal asymmetry was also found to be present for midlatitude stations. (BEYNON and DAVIES, 1955; THRANE, 1972). This asymmetry in the diurnal curves caused the values of the exponent n (characterizing the diurnal variation of absorption, L in the relation $L\alpha(\cos \chi)^n$) to differ considerably for the forenoon and postnoon periods (GANGULY and KHASTGIR, 1972; PURKAIT, 1976). The diurnal curves on absorption pertaining to the E region only, indeed exhibited the aforesaid asymmetry.

The purpose of this paper is to explain the asymmetry of a monthly mean diurnal curve on E-layer absorption at 2.2 MHz derived from the data collected from Haringhata (22°56'E) in terms of the semidiurnal temperature oscillation present in the E layer.

RESULTS AND DISCUSSION

The mean diurnal curve on total absorption at 2.2 MHz for the month of June, 1981 is shown in Figure 1. The contributions of the regions above and below 97 km are also shown separately in the same figure. The method of separating the contribution is similar to that outlined by PURKAIT and DUTTA (1972). It is to be mentioned that the observed E-region diurnal curve actually represents the absorption value corresponding to the height range of 97 km up to reflection height. This experimental diurnal curve is found to be asymmetric with respect to local noon and is compared with a theoretical absorption curve computed for the same height range. The theoretical absorption curve is computed through the following steps:

(1) The variation of E-layer temperature with height and local time is obtained from the following analytical expression derived by SALAH et al. (1975):

$$T(h, t) = T_0(h) + T_1 \cos \frac{2\pi}{P} (t - t_{\max})$$

where $T(h)$ is the mean temperature at any height, h , and is given in CIRA (1972), the value of T_1 , P and t_{\max} as obtained from Arecibo results are

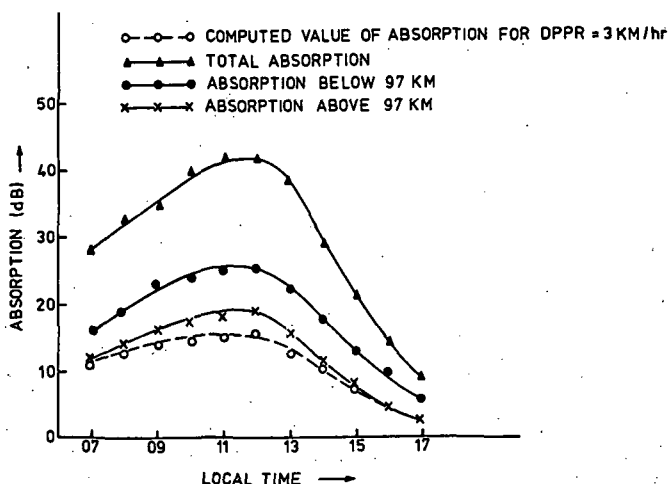


Figure 1. Diurnal variation of absorption at 2.2 MHz for the month of June 1981; the solid lines through triangles, circles and crosses represent respectively the value of total absorption, the absorption below and above 97 km. The dotted line through open circles represents the computed diurnal absorption curve for the region extending from 97 km up to the reflection height.

given respectively by 43 K, 12 hr and 1.00 hr at 120 km. These values are used in the present study. The value of t_{\max} at any other height below 120 km is determined from the knowledge of the downwards phase progression rate (hereafter will be abbreviated as DPPR) of the temperature oscillation using the relation:

$$t_{\max}(h) = t_{\max}(120) + (120-h)/\text{DPPR}.$$

In the present study the value of DPPR is treated as a variable and is changed in a step of 1 km/hr in the range 2-5 km/hr. The temperature measurement for the E layer over Arecibo, however, exhibits this range of variability for DPPR.

(2) The temperature distribution, thus obtained, is used to depict the height and local time variations of the effective recombination coefficient, α_{eff} for the E layer assuming that the electrons are lost mostly through dissociative recombination process with NO^+ and O_2^+ ions. For such a loss process the expression for α_{eff} is given by CHAKRABARTY, 1973; RATNASIRI, 1977):

$$\alpha_{\text{eff}} = \frac{\alpha_0(\text{O}_2^+)(T_0/T) + \alpha_0(\text{NO}^+)(T_0/T)^{1.4}}{1 + [\text{NO}^+]/[\text{O}_2^+]}$$

where $\alpha_0(\text{O}_2^+) = 2 \times 10^{-7} \text{ cm}^3 \text{ sec}^{-1}$, $\alpha_0(\text{NO}^+) = 4 \times 10^{-7} \text{ cm}^3 \text{ sec}^{-1}$, $T_0 = 300 \text{ K}$, T = electron temperature which for the E layer is equal to the neutral temperature. The variation of the ratio $[\text{NO}^+]/[\text{O}_2^+]$ with height and local time is obtained from the works of GOLDBERG (1972), DANILOV (1972) and GOLSHAN and SECHRIST (1975).

(3) The resulting $\alpha_{\text{eff}}-h$ profiles for different local time is then incorporated with the production function for appropriate height range and local time to produce the height distribution of electron density ($N-h$ profile) for different local time for each specified value for DPPR.

(4) The N-h profiles together with a realistic model for the collisional frequency are used to compute the diurnal curve on E-region absorption at an exploration frequency of 2.2 MHz. For each prescribed value of DPPR a diurnal absorption curve appropriate for the month of June over Haringhata is obtained.

The resulting computed curves are then fitted with the experimental curve for the same height range. It is found that for DPPR = 3 km/hr the agreement is best. The computed curve for DPPR = 3 km/hr, which shows best agreement with the experimental diurnal curve, is also shown by dotted line in Figure 1. For other values of DPPR the magnitude of the values of absorption as well as the degree of the asymmetry are found to depart significantly from those for the experimental curve. It may also be mentioned that asymmetry of opposite nature (afternoon values of absorption exceeding the morning values) as observed in some occasions (not presented here) can also be explained by shifting the time of occurrence of maximum temperature at the reference level. Thus, it can be concluded that the semidiurnal temperature oscillation (produced by the absorption of solar ultraviolet radiation by ozone and the absorption of infrared by CO₂ and H₂O of the atmosphere) plays a vital role in causing the diurnal absorption curves to be asymmetric about the local noon. The disagreement between the theoretical and the experimental curves during the central part of the day signifies the role of some other agency/agencies which will be examined in a future communication. It is to be mentioned that in deriving the theoretical diurnal curve on absorption, the change in optical depth and local neutral density caused by the semidiurnal temperature oscillation is assumed to cancel each other (FORBES, 1981).

ACKNOWLEDGEMENT

The author is grateful to Prof. B. R. Nag for his interest. The financial support from the UGG, India and the computational help from the Computer Centre, C. U., are also thankfully acknowledged.

REFERENCES

- Beynon, W. J. G. and K. Davies (1955), Proc. Int. Conf. on the Physics of the Ionosphere, Physical Soc. Lond., 40.
 Chakraborty, D. K. (1973), Ph.D. Thesis, University of Delhi, 99.
 CIRA (1972), Cospas International Reference Atmosphere.
 Danilov, A. D. (1972), University of Illinois, Aeronomy Report 48, 195.
 Forbes, J. M. (1981), J. Geophys. Res., 86, NoA3, 1551.
 Ganguly S. and S. R. Khastgir (1972), J. Atmos. Terr. Phys., 34, 1261.
 Goldberg, R. A. (1972), University of Illinois, Aeronomy Report 48, 160.
 Golshan, N. and C. F. Sechrist, Jr. (1975), Radio Science, 10, No. 3, 305.
 Purkait, N. N. (1976), Ph. D. Thesis, University of Calcutta, 69.
 Purkait, N. N. and S. K. Dutta (1972), J. Geophys. Res., 77, 2371.
 Ratnasiri, P. A. J., (1977), J. Atmos. Terr. Phys., 39, 999.
 Salah, J. E., J. V. Evans and R. H. Wand (1975), J. Atmos. Terr. Phys., 37, 461.
 Sharma, M. C. (1967), J. Inst. Tel. Engrs., 13, No. 8, 316.
 Thrane, E. V. (1972), Magnetosphere Ionosphere Interactions, edited by K. Folkestad, Oslo Univ. Press, 29.

2.6 NORMAL MODE ROSSBY WAVES OBSERVED IN THE UPPER STRATOSPHERE

Toshihiko Hirooka and Isamu Hirota

Geophysical Institute, Kyoto University
Kyoto 606, Japan

INTRODUCTION

In recent years, the observational evidence has been obtained for westward traveling planetary waves in the middle atmosphere, with the aid of global data from satellites. There is no doubt that the fair portion of the observed traveling waves can be understood as the manifestation of the normal mode Rossby waves which are theoretically derived from the tidal theory. In this paper, we will report some observational aspects of the structure and behavior of the normal mode Rossby waves in the upper stratosphere.

The used data are the global stratospheric geopotential thickness and height analyses which are derived mainly from the Stratospheric Sounding Units (SSUs) on board TIROS-N and NOAA satellites. These data were obtained through the British Meteorological Office. The analysis period is November 1979 - April 1982.

In this study, a normal mode Rossby wave will be expressed by the ordered pair (s, ℓ) , where s is the zonal wave number and ℓ is the number of nodes in the meridional velocity field between the poles. As for the geopotential height field, $|\ell - 1|$ is the number of nodes between the poles, $(1,1)$, $(1,2)$, $(1,3)$ and $(2,1)$ modes are often called 5-day, 10-day, 16-day and 4-day waves from each observed average period, respectively.

SUMMARY OF THE OBSERVED NORMAL MODE ROSSBY WAVES

Characteristic features of the observed normal mode Rossby waves in the stratosphere are summarized as follows, after HIROTA and HIROOKA (1984) and HIROOKA and HIROTA (1985). We investigated six kinds of the modes, i.e., $(1,1)$, $(1,2)$, $(1,3)$, $(2,1)$, and $(2,3)$ modes. These modes have some common features:

(1) The modes are irregularly predominant throughout the year. In most cases, they will persist for 1-2 months.

(2) In general, the amplitude is larger in the Northern Hemisphere than in the Southern Hemisphere, in association with the asymmetric meridional distribution of the mean zonal flow.

(3) The vertical structure is similar to that of the simple Lamb mode, although little westward phase tilt is seen, probably owing to damping effect and background shear.

With increasing s and ℓ , the Rossby normal modes become more sensitive to the background fields, and their period ranges become wider. The $(1,1)$ and $(2,1)$ modes are insensitive to background nonuniformities, at least up to the upper stratosphere. These results are consistent with those of the theoretical study by SALBY (1981).

The $(1,1)$ and $(2,1)$ modes are not observed at the same time, while the higher degree modes often appear simultaneously. In particular, it attracts our attention that some different modes appear simultaneously just before the occurrence of stratospheric sudden warmings, and the amplitudes of the modes

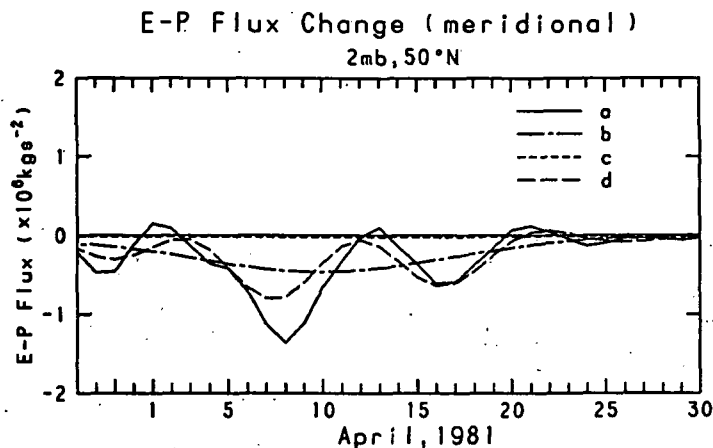


Figure 1. Time change of the meridional component of E-P flux calculated from various Fourier components for April 1981: (a) total contribution of $s=1$. (b) quasi-stationary wave component of $s=1$. (c) 10-day wave component. (d) superposition of quasi-stationary and 10-day waves.

are of the same order of magnitude as those of the quasi-stationary waves. It is also noteworthy that the $s=2$ modes are largely amplified less frequently than the $s=1$ modes.

INTERFERENCE BETWEEN THE TRAVELING AND QUASI-STATIONARY WAVES

In this section, we will report a clear example of the influence of the normal mode Rossby wave on the mean flow. The mechanism considered here is interference between the normal mode Rossby wave and the quasi-stationary wave. This mechanism was suggested by MADDEN (1975) and later reexamined observationally (FADDEN, 1983) and theoretically (SALBY, 1984).

The quasi-stationary wave, which is a forced wave with westward tilting phase with height, has nearly constant E-P flux in time. On the other hand, the normal mode Rossby wave, which is a free wave and travels westward, has nearly zero E-P flux. If superposition of the two occurs, E-P flux will oscillate in time, following the constructive and destructive phases.

Figure 1 shows the time change of the meridional component of E-P flux at 2 mb and 50°N for April 1981, when the 10-day wave ((1,2) mode) was predominant (HIROOKA and HIROTA, 1985). The E-P flux of the 10-day and quasi-stationary wave components are calculated from the Fourier components of periods between westward traveling 8 and 12 days and longer than 30 days, respectively. The E-P flux calculated from the superposition of the two almost elucidates the total change. Namely, the time change of the total $s=1$ E-P flux is considered to be mainly due to the interference phenomenon. The similar result is obtained for the vertical component of E-P flux (not shown).

Figure 2 shows the relation between the mean zonal wind and the divergence of E-P flux at the 2 mb level for April 1981 in the Northern Hemisphere. It is revealed from these figures that the periodic change of the mean zonal wind observed in this month was caused by the interference.

The fact that the acceleration occurs earlier at higher latitudes can be elucidated by the horizontal structure of the quasi-stationary wave, i.e., the

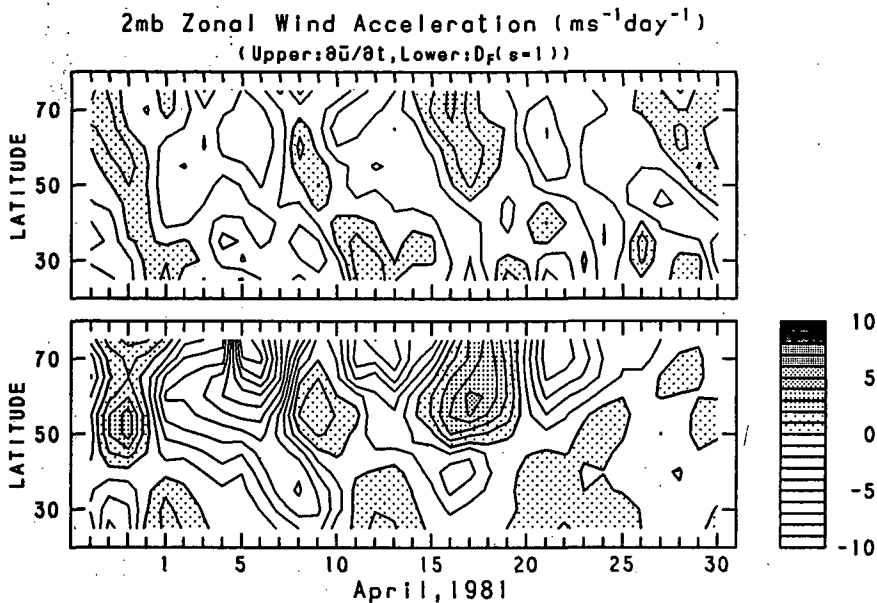


Figure 2. Latitude time sections of the acceleration rate at the 2 mb level for April 1981 in the Northern Hemisphere. Upper: zonal mean wind acceleration rate calculated geostrophically. Lower: divergence of the $s=1$ E-P flux. The contour interval is $1 \text{ ms}^{-1} \text{ day}^{-1}$. The shading denotes the acceleration of westerlies.

westward phase tilt towards the equator. This phase tilt results in the earlier occurrence of the interference at higher latitudes.

This example is for the equinoctial season. As for the solstitial season, MADDEN (1983) suggested that the interference between free Rossby waves and forced stationary waves plays a fundamental role in the sudden warming event. As mentioned in Section 2, our analysis also suggests a possibility of the interference among these large scale waves. Therefore, further studies are needed for physical properties of the normal mode Rossby waves to understand the dynamics of stratospheric circulations.

REFERENCES

- Hirooka, T. and I. Hirota (1985), Normal mode Rossby waves observed in the upper stratosphere. Part II: Second anti-symmetric and symmetric modes of zonal wave numbers 1 and 2, *J. Atmos. Sci.*, 42 (in press).
- Hirota, I. and T. Hirooka (1984), Normal mode Rossby waves observed in the upper stratosphere. Part I: First symmetric modes of zonal wave numbers 1 and 2, *J. Atmos. Sci.*, 41, 1253-1267.
- Madden, R. A. (1975), Oscillations in the winter stratosphere. Part 2: The role of horizontal eddy transport and the interaction of transient and stationary planetary-scale waves, *Monthly Wea. Rev.*, 103, 717-729.
- Madden, R. A. (1983), The effect of the interference of traveling and stationary waves on time variations of the large scale circulation, *J. Atmos. Sci.*, 40, 1110-1125.

Salby, M. L. (1981), Rossby normal modes in nonuniform background configurations. Part II: Equinox and solstice conditions, J. Atmos. Sci., 38, 1827-1840.

Salby, M. L. (1984), Vacillations in the circumpolar vortex induced by interference between stationary and traveling waves, Submitted to J. Atmos. Sci..

2.7 ON THE INTERACTION BETWEEN THE QUASI-2-DAY WAVE AND THE MEAN FLOW

R. L. Craig and R. A. Vincent

Department of Physics, University of Adelaide
Adelaide, SA 5001, Australia

R. A. Plumb

CSIRO Division of Atmospheric Research, PMB#1
Mordialloc, Vic 3195, Australia

Studies of the quasi-2-day wave show that it is a summertime phenomenon. Long-term measurement of the winds in the 60-100 km height range at Adelaide (35°S, 138°E) show that the wave appears in late December but that the peak amplitudes are not reached until mid-January. In the summer of 1983-84 the main phase of the wave appeared as a "pulse" in mid-January which lasted about 7 cycles (14 days), as shown in Figure 1. Little or no amplification with height was observed; peak amplitudes were about 60ms⁻¹ for the meridional and 20ms⁻¹ for the zonal component. These maximum amplitudes are typical of those observed at Adelaide in other years (CRAIG and ELFORD 1981).

Coincident with the onset of the pulse, a temporary but substantial change occurred throughout a deep layer of the upper mesosphere over a period of about 3 days. This effect is illustrated for 86 km in Figure 2. A change of more than 10ms⁻¹ occurred in the northward flow while the change in the zonal flow (about 30ms⁻¹ westward) actually caused a reversal of the prevailing zonal circulation. In view of the magnitudes of these changes and of the coincidence with the two-day wave pulse, it is tempting to associate the two.

Observations in other years (CRAIG et al., 1980; RODGERS and PRATA, 1981) have identified the quasi-2-day wave as an upward and zonally propagating wave number 3 disturbance. While there is no direct evidence to confirm the longitudinal structure during the present event, we interpret the data of Figure 1 on the same basis. Similarly, we further assume that the prevailing winds observed at Adelaide are representative of all longitudes, so that they may be interpreted as zonal mean quantities.

The zonal mean, quasigeostrophic momentum budget may be written

$$\frac{\partial \bar{u}}{\partial t} - f\bar{v} = -\frac{\partial}{\partial y} (\overline{u'v'}) + \bar{X} \quad (1)$$

where x is the frictional force per unit mass and other symbols have their usual meaning. Estimates of the eddy flux term show it to be small compared with $f\bar{v}$. However, since $\bar{v} \approx 10\text{ms}^{-1}$, the Coriolis term in (1) would, alone, generate zonal accelerations of about 70ms⁻²/day, far in excess of what is observed. Writing \bar{X} in the form of a Rayleigh friction, $\bar{X} = -\lambda\bar{u}$, satisfaction of the momentum budget requires $\lambda = (3\text{d})^{-1}$, a value in line with theoretical estimates (e.g., MIYAHARA 1984).

The impact of the wave on the mean state is best assessed using the transformed Eulerian-mean form of the quasigeostrophic momentum budget (EDMON et al., 1980).

$$\frac{\partial \bar{u}}{\partial t} - f\bar{v}_* = \overline{v'q'} - \lambda\bar{u} \quad (2)$$

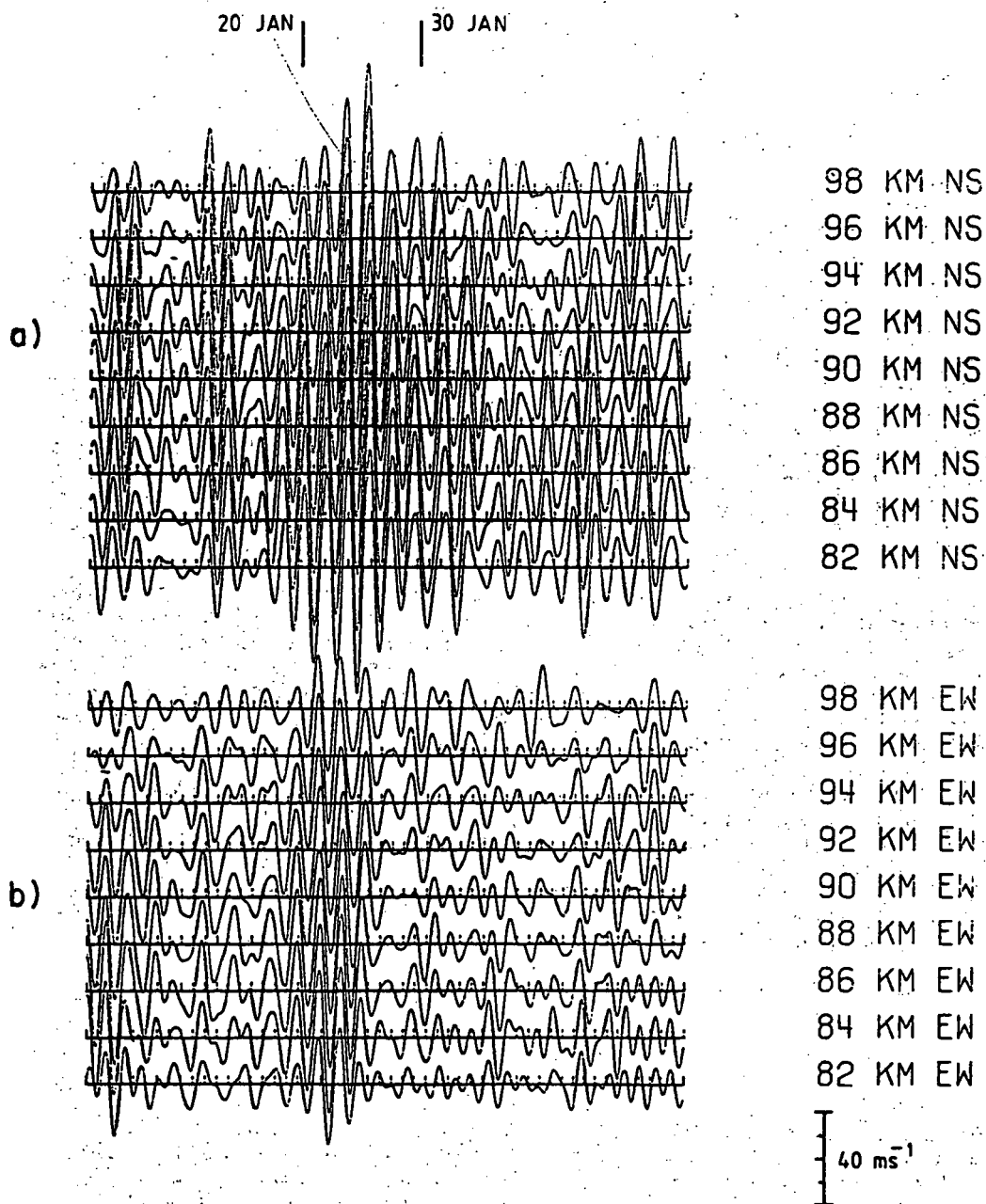


Figure 1. a) Northward and b) Eastward components of the winds between 82 and 98 km during January and early February 1984. Data have been band-pass filtered to retain only periods between 30 hr. and 80 hr. Scale at lower right. Tick marks on axes denote daily intervals.

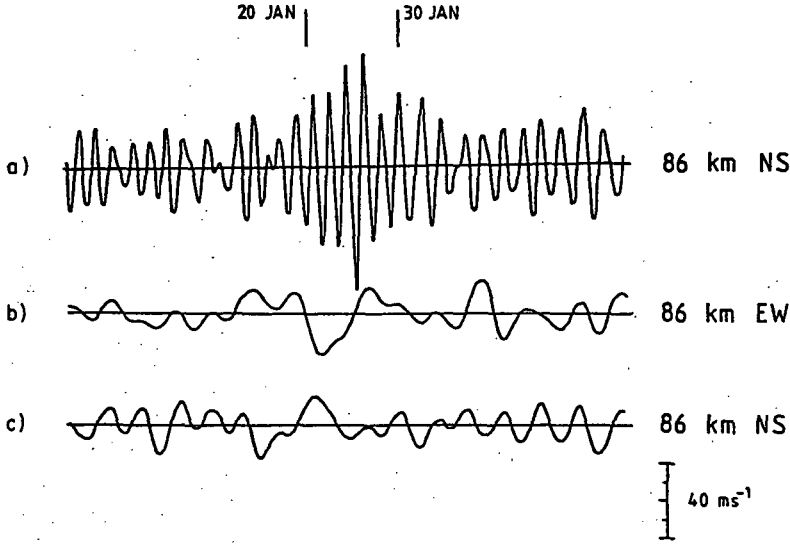


Figure 2. Winds at 86 km. a) Northward component, band-passed as in Figure 1. b) Eastward and c) Northward components, low-passed to retain periods longer than 80 hrs (with mean and trend removed). Scale at lower right.

where \bar{v}_* is the "residual" northward flow and q the potential vorticity. For a deep system such as we are considering (cf. Figure 1) the Coriolis term is usually small so that

$$\frac{\partial \bar{u}}{\partial t} \approx \bar{v}' q' - \lambda \bar{u} \quad (3)$$

We write the N-S parcel displacement η in the wave pulse (on the assumption that the eddy transport is reversible) as

$$\eta = \text{Re } Y e^{ik(x-ct)} e^{-t^2/2T^2} \quad (4)$$

where, on the basis of the observed wave pulse, we take $T = 7.5d$ and estimate $|Y| \approx 3000$ km in the region around 86 km. (This enormous north-south displacement of about 60° latitude peak-to-peak serves to illustrate the magnitude of the wave at these levels). Then it can be shown that

$$\bar{v}' q' = - \frac{\partial}{\partial t} (A e^{-t^2/2T^2}) \quad (5)$$

where $A \approx 90 \text{ ms}^{-1}$. Then solution of (3) gives the results shown in Figure 3a. For $\lambda^{-1} = 3d$, the calculated response in the zonal and meridional wind components agree well during the growth phase of the pulse ($t < 0$) but the predicted reversal of the response during the decay phase is not observed. However, if the wave transport is irreversible, so that there is no eddy forcing of the mean state during the decay phase, then the predicted response for

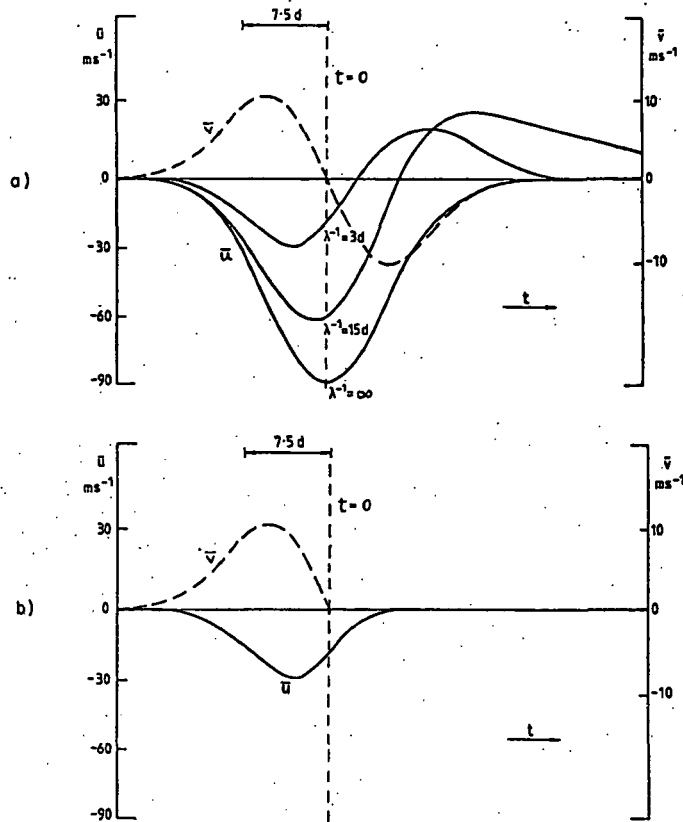


Figure 3. Predicted response of mean flow (\bar{u} , \bar{v}) to a wave pulse, calculated from (3). a) reversible wave transport, b) irreversible transport.

$\lambda^{-1} = 3d$ is as shown in Figure 3b. Both in amplitude and phase, these results agree well with the observed behaviour.

We conclude that such pulses of quasi-2-day wave activity are dramatic events which have major, if temporary, impact on the prevailing mesospheric circulation.

REFERENCES

- Craig, R. L. and W. G. Elford (1981), Observations of the quasi 2-day wave near 90 km altitude at Adelaide (35°S), *J. Atmos. Terr. Phys.*, **43**, 1051-1056.
 Craig, R. L., R. A. Vincent, G. J. Fraser and M. J. Smith (1980), The quasi 2-day wave in the Southern Hemisphere mesosphere, *Nature*, **287**, 319.
 Edmon, H. J., Jr., B. J. Hoskins and M. E. McIntyre (1980), Eliassen-Palm cross-sections for the troposphere, *J. Atmos. Sci.*, **37**, 2640-2616.
 Miyahara, S. (1984), Suppression of stationary planetary waves by internal gravity waves in the mesosphere, *J. Atmos. Sci.*, (to appear).
 Rodgers, C. D. and A. J. Prata (1981), Evidence for a travelling 2-day wave in the middle atmosphere, *J. Geophys. Res.*, **86**, 9661-9664.

2.8 PLANETARY WAVES-MEAN FLOW INTERACTION IN THE MIDDLE ATMOSPHERE; LIDAR OBSERVATIONS AND MODELISATION

A. Hauchecorne

Service d'Aeronomie du CNRS
BP 3 - Verrieres-le-Buisson, France

ABSTRACT

Lidar observations of the temperature from 30 to 80 km have been made at the Observatory of Haute-Provence on an operational basis since 1981. Data obtained during the four last winters indicate the quasi-systematic presence of traveling Rossby waves with periods ranging from 5 to 20 days and a vacillation of the zonal mean circulation leading to a succession of upper stratospheric warmings and associated mesospheric coolings spaced by 25 to 50 days. A semi-spectral model of the wave-one-mean flow interaction has been used to interpret these results. When a stationary wave forcing is imposed at the lower boundary of the model, a vacillation of the zonal flow is obtained as soon as the amplitude of this wave reaches a critical value of about 140 m. When an 18-day westward traveling wave is imposed in supplement to this forcing, the date of occurrence of the upper stratospheric warmings is imposed by the coincidence of the phases of the two waves that enhanced the forcing.

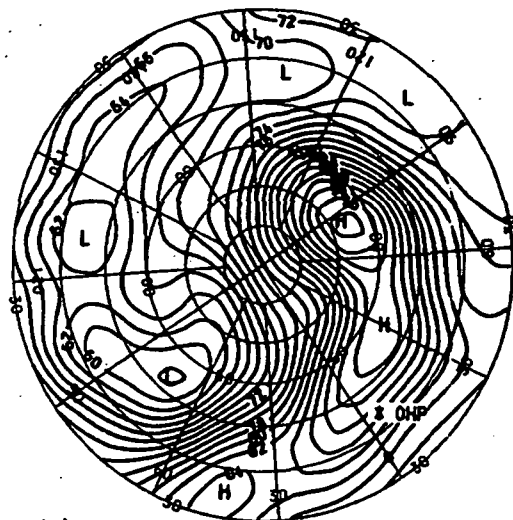
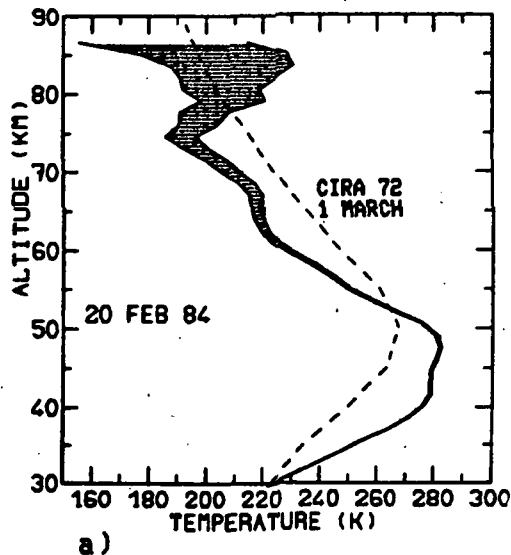
INTRODUCTION

Since the discovery of the sudden stratospheric warmings (SCHERHAG, 1952), numerous studies of such events have been made. These studies indicate that the so-called "major warmings" (LABITZKE, 1981), which produce a very intense warming in the whole stratosphere north of 60°N and lead to the breakdown of the winter polar vortex, occur, at the most, one time during each winter. On the contrary, "minor warmings", which may produce very high temperatures in the middle and upper stratosphere, but do not lead to the breakdown of the polar vortex, may occur several times during each winter.

LIDAR OBSERVATIONS

Lidar observations of the middle atmospheric temperature made at the Observatory of Haute Provence (OHP, 44°N , 6°E) have been used since 1981 to study the propagation of planetary waves and the occurrence of such minor warmings during the period of prevailing westerly winds in the stratosphere from October to March (HAUCHECORNE and CHANIN, 1982, 1983). In spite of the relatively low latitude of the lidar station, the polar stratospheric warmings are in general clearly seen in the temperature profiles obtained at OHP. Figure 1 shows a good example of a temperature profile during a strong upper stratospheric warming which extends from the pole to 35°N at the longitude of the lidar station, as seen by the radiance map in the channel 27 of the Stratospheric Sounding Unit (SSU). At the same time the lidar profile presents a strong warming in the altitude range 40-50 km and an associated mesospheric cooling with a minimum of temperature near 75 km.

The temporal evolution of the temperature perturbations during all the winter 1981-82 is shown on Figure 2. Lidar data have been extended below 30 km using the radiosonde data of the two nearby stations at Nimes (44°N , 4°E) and Lyon (46°N , 5°E). During all the period from October to March, corresponding to westerly winds in the lower stratosphere, the planetary waves may propagate from the troposphere to the middle atmosphere and a succession of warm and cold perturbations is observed. The maximum of wave activity occurs in January, just before the "strong minor warming" observed on a global scale in the lower



b)
CHANNEL 27 RADIANCE
DATE = 20 FEB 84 TIME = 12Z

Figure 1. a) Lidar temperature profile (the standard deviation $\pm \sigma$ is indicated) and b) radiance of the SSU channel 27 on February 20, 1984.

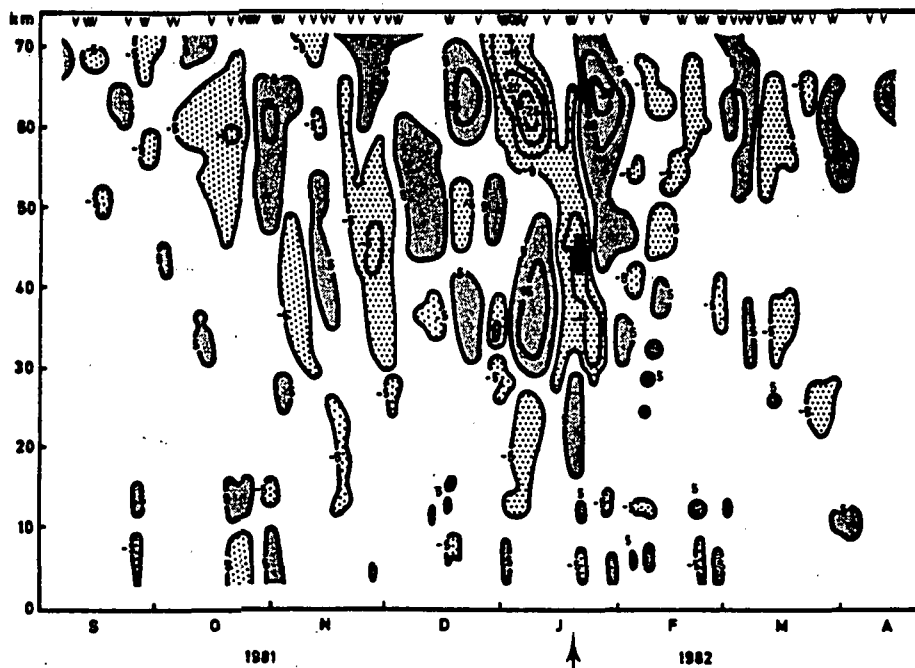


Figure 2. Time-height section of the temperature deviation from a 45-days running average in 1981-1982. The days of lidar data are indicated by arrows. Contour lines are plotted in step of 10 K (from HAUCHECORNE and CHANIN, 1983).

stratosphere (NAUJOKAT et al., 1982). The structure of these temperature variations does not seem to be due to the propagation of a single planetary wave but to a superposition of different waves.

In order to explain these structures, a special analysis of the data has been made. The results obtained on the pressure data are presented in Figure 3. A well-defined maximum is observed at all altitudes above 30 km corresponding to a period of 18 days. Broader maxima are also present near 25 and 40 days. The pressure variations have been filtered in order to separate the shorter periods (shorter than 20 days) and longer periods (longer than 20 days). The results obtained during the winter 1982-83 are compared on Figure 4 with the radiance in the SSU channel 27. The SSU data above OHP show the short periods oscillations observed on lidar data, especially the 11-day wave clearly developed in December 1982, but only the longer periods' variations are visible in the zonal mean of SSU data, as for instance the two maxima at the end of December and the end of January corresponding to two minor warmings in the upper stratosphere. From such a study (HAUCHECORNE, 1983) we conclude that the perturbations with periods shorter than 20 days, not visible on the zonal mean, are due to propagating planetary waves. The prevailing period observed in winter 1981-82 is 18 days and may be related to the well known 16 days' symmetric Rossby wave (MADDEN, 1979), while in 1982-83, the prevailing period is close to 11 days and may correspond to the 10 days' antisymmetric Rossby wave (HIROOKA and HIROTA, 1984). On the contrary, perturbations with periods longer than 20 days, visible in the zonal mean of atmospheric warmings, are associated with the succession of upper stratospheric warmings and may be called "vacillations" of the stratospheric circulation (HOLTON and MASS, 1976).

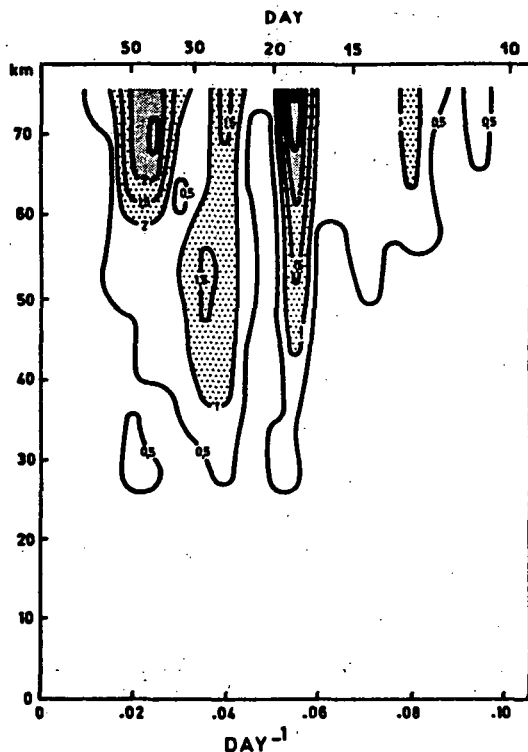


Figure 3. Frequency-height section of the pressure oscillation in $\%/0.005$ day $^{-1}$ (from HAUCHECORNE and CHANIN, 1983).

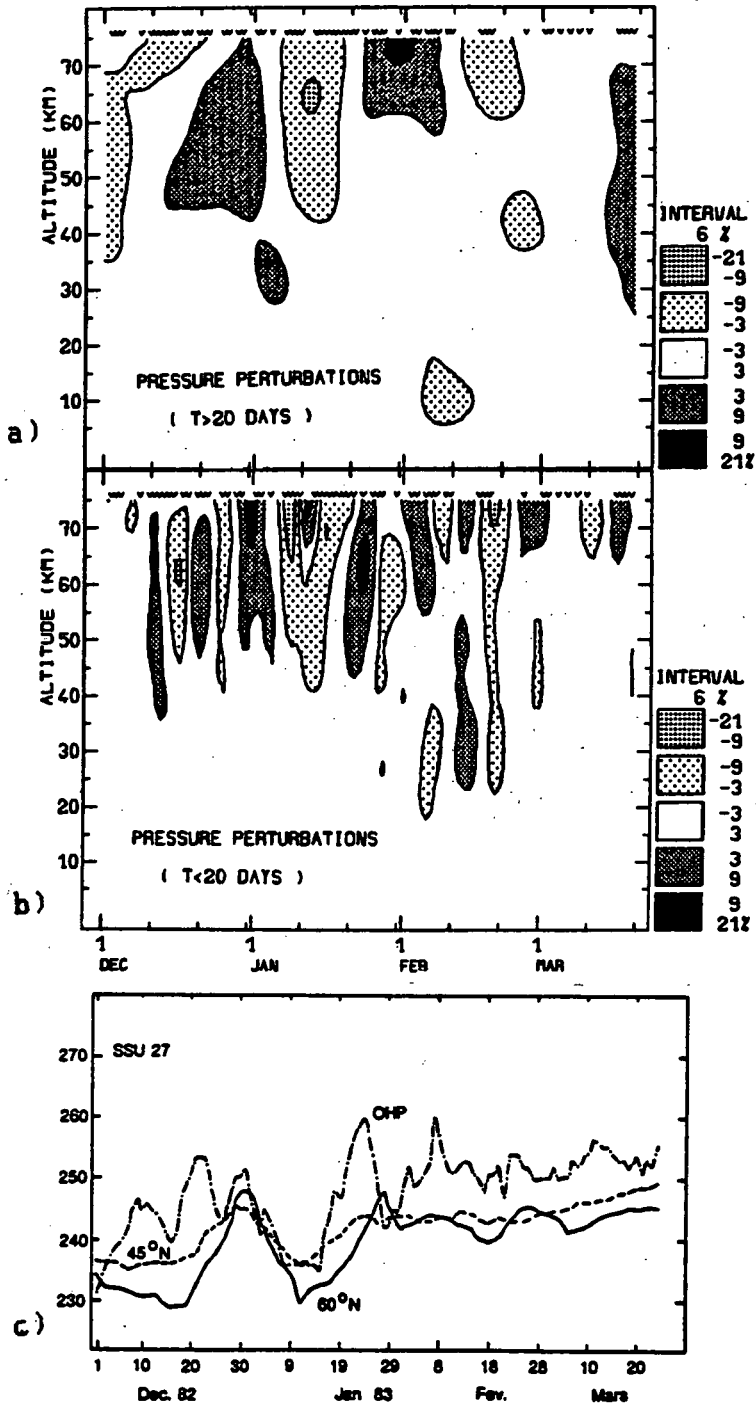


Figure 4. Pressure variations a) with periods shorter than 20 days and b) longer than 20 days. c) Radiance of the SSU channel 27 above OHP and in zonal mean at 45°N and 60°N.

MODELISATION

A semispectral model of the wave 1 — zonal flow interaction based on the primitive equation has been developed to interpret these results. The basic equations are those formulated in HOLTON (1976) (see HAUCHECORNE (1983) for a complete description of this model). The simulation domain extends from 10 to 110 km with a 5 km step in altitude and from 0° to 90° north with a 10° step in latitude. Each variable V is split into its zonal mean \bar{V} and its first Fourier component V'

$$V(\lambda, \theta, z) = \bar{V}(\theta, z) + V'(\theta, z) \exp\left(\frac{2i\pi\lambda}{360}\right)$$

where λ is the longitude in degrees, θ the latitude and z the altitude. The independent variables are the zonal and meridional components of the wind U and V and the geopotential Φ . The seasonal variation of the zonal circulation is simulated by a radiative equilibrium geopotential with a sinusoidal variation giving a maximum of easterly winds at the summer solstice and a maximum of westerly winds at the winter solstice. The radiative damping is simulated by Newtonian cooling and the dissipation of gravity waves by Rayleigh friction. The forcing of the circulation is made by introducing a planetary wave at the lower boundary of the model at 10 km. The assumed forcing is either a stationary wave with a maximum at 90° W, as observed in the climatological data at 100 mb, or the sum of this stationary wave plus an 18-day westward traveling wave, as observed in winter 1981-82. In each run of the model, the computation begins at the summer solstice (day 0) and is performed during 300 days. For simplification, the duration of the year is assumed to be 360 days. The zonal wind at 60°N for different runs is presented on Figure 5. In the first run, performed without planetary wave forcing, the east to west inversion of the wind is observed near the day 80; the maximum of the westerly jet occurs a few days after the winter solstice (day 180) with a speed of about 70 ms^{-1} at 60 km and the west to east inversion is observed near the day 290. In the second run, for which a 130 m stationary wave is imposed at 10 km, the evolution of the zonal wind is quite similar to that observed without planetary wave. The maximum of westerly wind is a little weaker (65 ms^{-1} at 55 km) and the west to east inversion occurs earlier, from the day 240 at 75 km to the day 260 at 30 km. In the third run, for which a 150 m stationary wave is imposed, the zonal wind evolution is quite similar to that of the second run till the day 140, but after this date a succession of decreases and increases of the zonal wind is observed. The maxima of westerly winds are reached near the days 145, 177 and 212. After the two last maxima, a strong deceleration of the wind is observed, leading to a temporary inversion of the mesospheric wind and corresponding to a warming in the upper stratosphere. The simulated vacillation of the zonal wind is similar to that observed on lidar data, and the periods are in good agreement, about 35 days for the model and from 25 to 50 days for the data. In the fourth run the amplitude of the stationary wave is again 150 m but a 30 m - 18-days traveling wave is also applied at 10 km. The 35-day vacillation is again visible, but it is modulated by the 18-day wave. The period of the vacillation is about twice the one of the traveling wave, and the interference of the two oscillations gives a succession of strong and weak maxima of the westerly wind. The time-height section of the temperature deviation obtained above the North pole in the fourth run (Figure 6) shows a succession of upper stratospheric warmings and associated mesospheric coolings, the stronger one taking place at the end of the winter near the day 238 in the upper stratosphere and goes down into the lower stratosphere near the day 250. The interference of the 35-day and 18-day oscillations also modulates the intensity of these warmings. The 4 first warmings take place 2 to 3 days after the correlation of phase between the stationary and the traveling waves at 10 km, but this is not true for the last and stronger one. It seems that, as long as the warmings are localized into the upper stratosphere, their data of

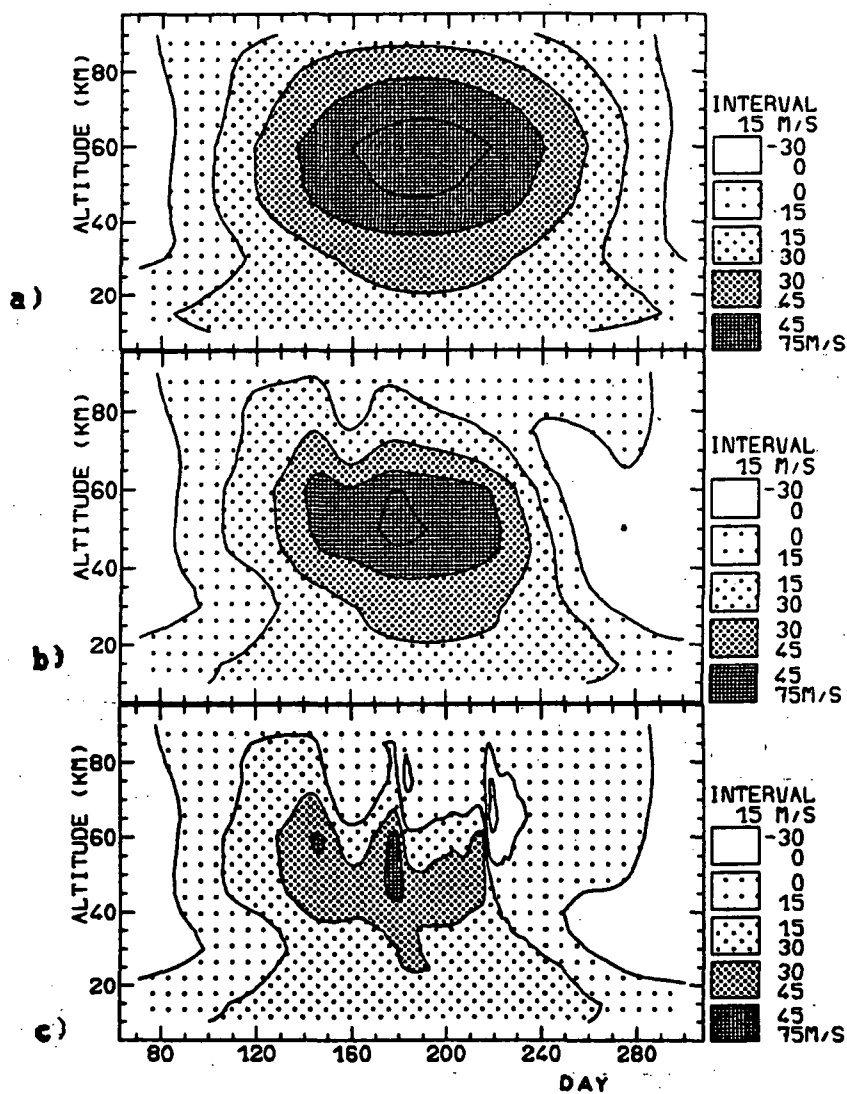


Figure 5. Time-height section of the zonal wind at 60°N, a) in the run 1 without planetary wave, b) in the run 2 with a 130 m stationary wave and c) in the run with a 150 m stationary wave (westerly winds are >0).

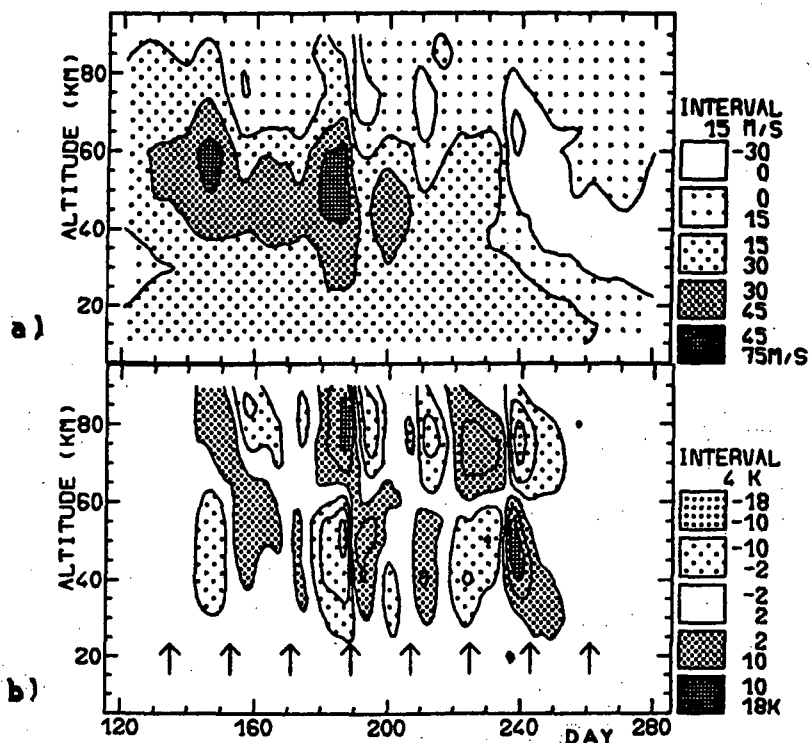


Figure 6. Time-height section a) of the zonal wind at 60°N and b) of the temperature perturbation at 90°N in the run 4 with a 150 m stationary wave plus a 30 m - 18 days westward traveling wave.

occurrence is imposed by the conjunction of the phases of the stationary and traveling waves that enhanced the forcing.

The evolution of the temperature deviation above some fixed location in the fourth run is presented in Figure 7. At 45°N the perturbations are more developed at 0°E (near the OHP) than at other longitudes, for instance at 90°W. This is due to the mean position of the center of the warmings, which is in general located over Northern Europe in the upper stratosphere, and explains why the stratospheric warmings are in general clearly visible above the OHP and not on the zonal mean at 45°N. The evolution at 45°N, 0°E is qualitatively similar to that observed in the lidar data (Figure 2), with the same downward displacement of warm pulses from the upper mesosphere to the stratosphere. However, the amplitude of the perturbations is greater in the lidar data than in the model and is more similar to the amplitude computed at 60°N, 0°E.

CONCLUSION

Lidar data obtained at OHP since 1981 have shown that the upper stratospheric and mesospheric temperature is continuously perturbed from October to March, due to the propagation of planetary waves through the westerly stratospheric winds. These perturbations may be divided in two categories:

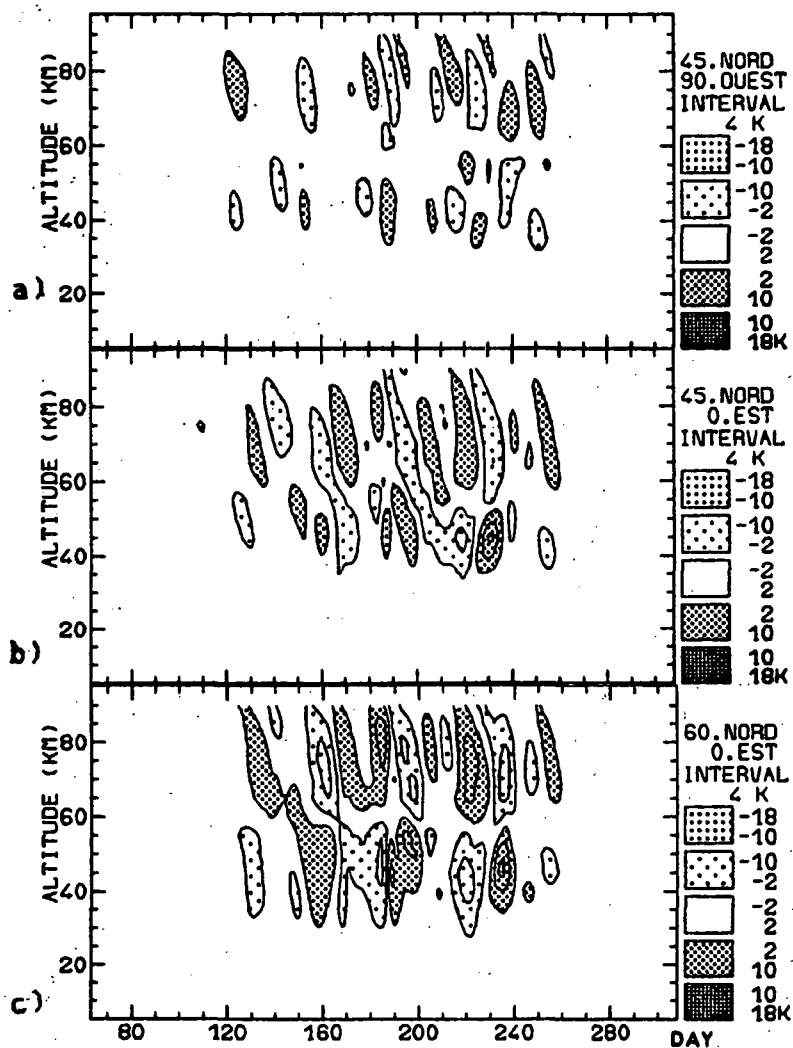


Figure 7. Time-height section of the temperature perturbation in the run 4, a) at $45^{\circ}\text{N} - 90^{\circ}\text{W}$, b) at $45^{\circ}\text{N} : 0^{\circ}\text{E}$ and c) at $60^{\circ}\text{N} - 0^{\circ}\text{E}$.

(1) Westward propagating Rossby waves with periods ranging from 5 to 20 days.

(2) Vacillations of the zonal circulation, with periods ranging from 25 to 50 days, and associated with the succession of upper stratospheric warmings observed in the polar region.

A primitive equation model of the wave one-zonal flow interaction has been developed to interpret these results. This model is able to simulate the vacillations observed by lidar in the presence of a constant forcing by a stationary planetary wave as soon as its amplitude is above a critical value of about 140 m at 10 km. When a westward traveling wave is imposed in addition to this forcing, the time of occurrence of the upper stratospheric warmings is determined by the coincidence of phase between the two waves that enhanced the forcing.

REFERENCES

- Hauchecorne, A. (1983), Observation par lidar et modelisation des echauffements brusques et des ondes planetaires dans l'atmosphere moyenne, These de Doctorat d'Etat, Universite de Paris VI.
- Hauchecorne, A. and M. L. Chanin (1982), A mid-latitude ground-based lidar study of stratospheric warmings and planetary waves propagation, J. Atmos. Terr. Phys., **44**, 577-589.
- Hauchecorne, A. and M. L. Chanin (1983), Mid-latitude lidar observations of planetary waves in the middle atmosphere during the winter of 1981-1982, J. Geophys. Res., **88**, 3843-3849.
- Holton, J. R. (1976), A semi-spectral numerical model for wave-mean flow interactions in the stratosphere: Application to sudden stratospheric warmings, J. Atmos. Sci., **33**, 1639-1649.
- Holton, J. R. and C. Mass (1976), Stratospheric vacillation cycles, J. Atmos. Sci., **33**, 2218-2225.
- Labitzke, K. (1981), Stratospheric-mesospheric mid-winter disturbances: A summary of observed characteristics, J. Geophys. Res., **86**, 9665-9678.
- Madden, R. A. (1979), Observations of large-scale traveling Rossby-waves, Rev. Geophys. Space Phys., **17**, 1935-1949.
- Naujokat, B., K. Petzoldt, K. Labitzke and R. Lenschow (1982), The fourth winter of PMP-1 1981-1982: A winter with several interesting features, Beilage zur Berliner Wetterharte 56-82.
- Scherhag, R. (1952), Die explosionsartige Stratospharenmerwarming des Spatwinters 1951-1952, Ber. Det. Wetterdienstes, **38**, 51-63.

2.9 DISCRIMINATION OF A MAJOR STRATOSPHERIC WARMING EVENT IN FEBRUARY-MARCH 1984 FROM EARLIER MINOR WARMINGS

K. W. Johnson, R. S. Quiroz, and M. E. Gelman

NOAA, NWS, NMC Climate Analysis Center
Washington, DC 20233

As part of its responsibility for stratospheric monitoring, the Climate Analysis Center derives time trends of various dynamic parameters from the NMC stratospheric analyses. Selected figures from this stratospheric monitoring data base are published in Climate Diagnostics Bulletin in March and October, after each hemispheric winter.

During the Northern Hemisphere winter of December 1983-February 1984 several warming events may be seen in the plot of 60°N zonal mean temperatures for 10 mb (Figure 1). Minor warmings may be noted in early December, late December, mid January and early February. A major warming with the 60°N zonal mean temperatures reaching -40°C is observed in late February, associated with a circulation reversal (Figure 2). In all of the minor warming episodes, there is a polarward movement of the Aleutian anticyclone; however, at 10 mb the North Pole remains in the cyclonic circulation of the stratospheric vortex which is not displaced far from its usual position (Figure 3a,b,c). In the case of the late February major warming, the 10 mb circulation pattern over the North Pole is anticyclonic, and the cyclonic circulation has moved to the south and east with a considerable elongation (Figure 3d). Cross sections of heat transport (Figure 4,a,b,c,d) and momentum transport (Figure 5,a,b,c,d) are not dramatically different for the minor and major warming episodes.

Although Figure 6 shows that the minor warming episodes and the major warming episodes have similar maximum upward values of eddy geopotential flux ($\overline{\omega'\phi'}$) through the 100 mb surface (-600 to $-700 \text{ J m}^{-2} \text{ s}^{-1} \times 10^{-3}$) a significant difference is that strong upward flux ($< -300 \text{ J m}^{-2} \text{ s}^{-1}$) lasts for only 3-4 days in the case of the minor warming episodes, while upward flux of a similar magnitude lasts for over 10 days in connection with the major warming (cf. QUIROZ et al., 1975). This amplification in upward eddy geopotential flux was associated with strong tropospheric blocking activity in the Atlantic Ocean-European sector (QUIROZ, 1984).

Although the full dynamical picture cannot be discussed in this brief paper, the major discriminator between the minor warming events of the early winter 1983-84 and the major warming of mid-February 1984 was the duration of the large-amplitude upward eddy geopotential flux.

REFERENCES

- Quiroz, R. S. (1984), The climate of the 1983-84 winter - a season of strong blocking and severe cold in North America, Monthly Wea. Rev., **112**, 1894-1912.
- Quiroz, R. S., A. J. Miller and R. Nagatani (1975), A comparison of observed and simulated properties of sudden stratospheric warmings, J. Atmos. Sci., **32**, 1723-1736.

01778-227

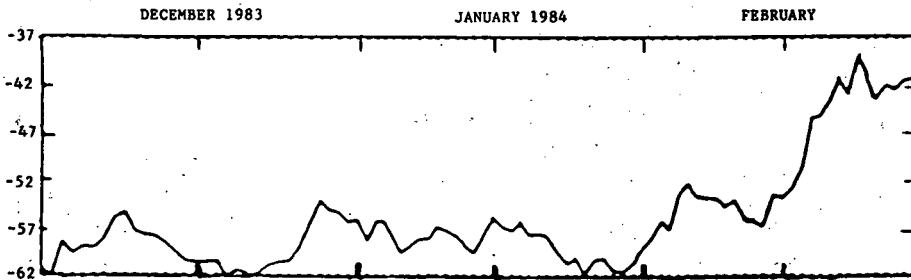


Figure 1. 10 mb daily temperature values ($^{\circ}\text{C}$) averaged around 60°N from NMC operational analyses. Period: Dec. 1, 1983 - March 15, 1984.

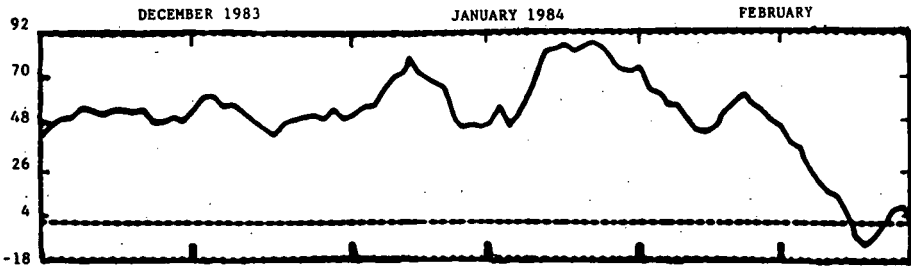


Figure 2. 10 mb daily zonal geostrophic winds (m/sec; positive from the west) averaged around 60°N from NMC operational height analyses.

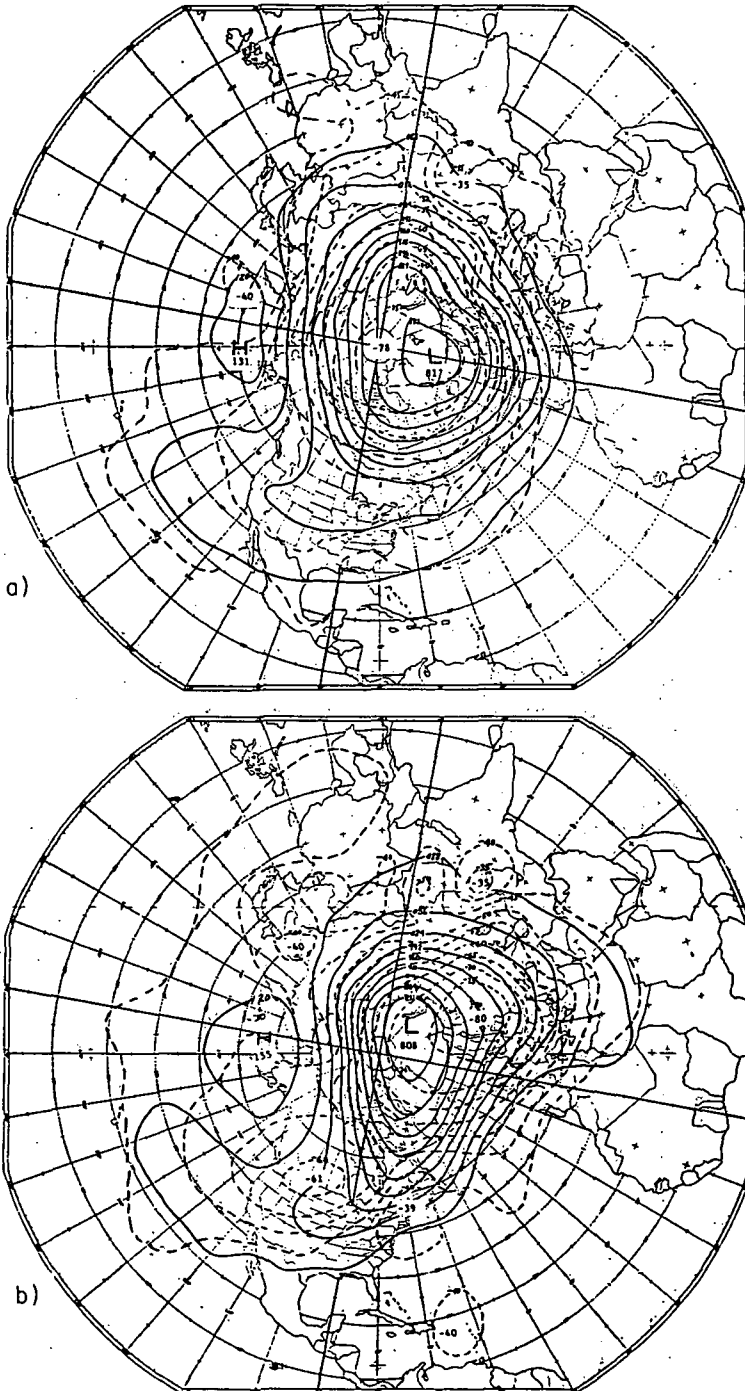


Figure 3. 10 mb NMC Operational analyses. Solid lines are contours in decameters (initial digit suppressed) with a contour interval of 16 decameters. Dashed lines are isotherms ($^{\circ}\text{C}$ -contour interval 5°C). a) Analyses for 1200 GMT, Dec. 17, 1983; b) Analyses for 1200 GMT, Dec. 26, 1983; c) Analyses for 1200 GMT, Feb. 12, 1984; d) Analyses for 1200 GMT, Feb. 23, 1984.

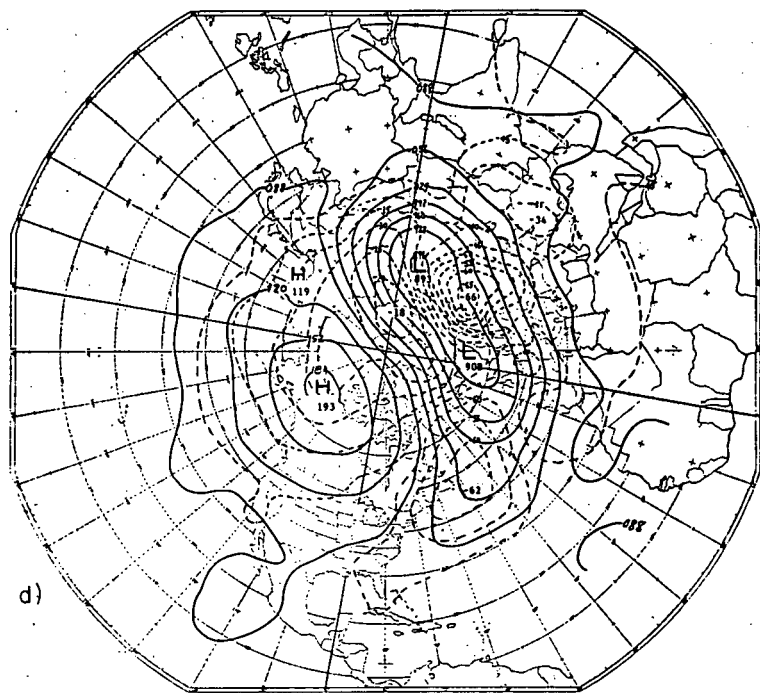
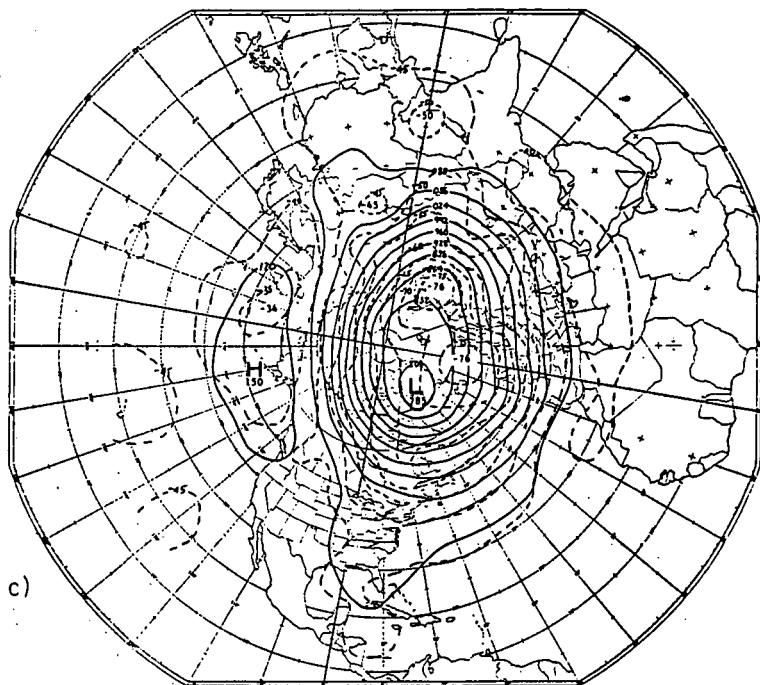


Figure 3 continued.

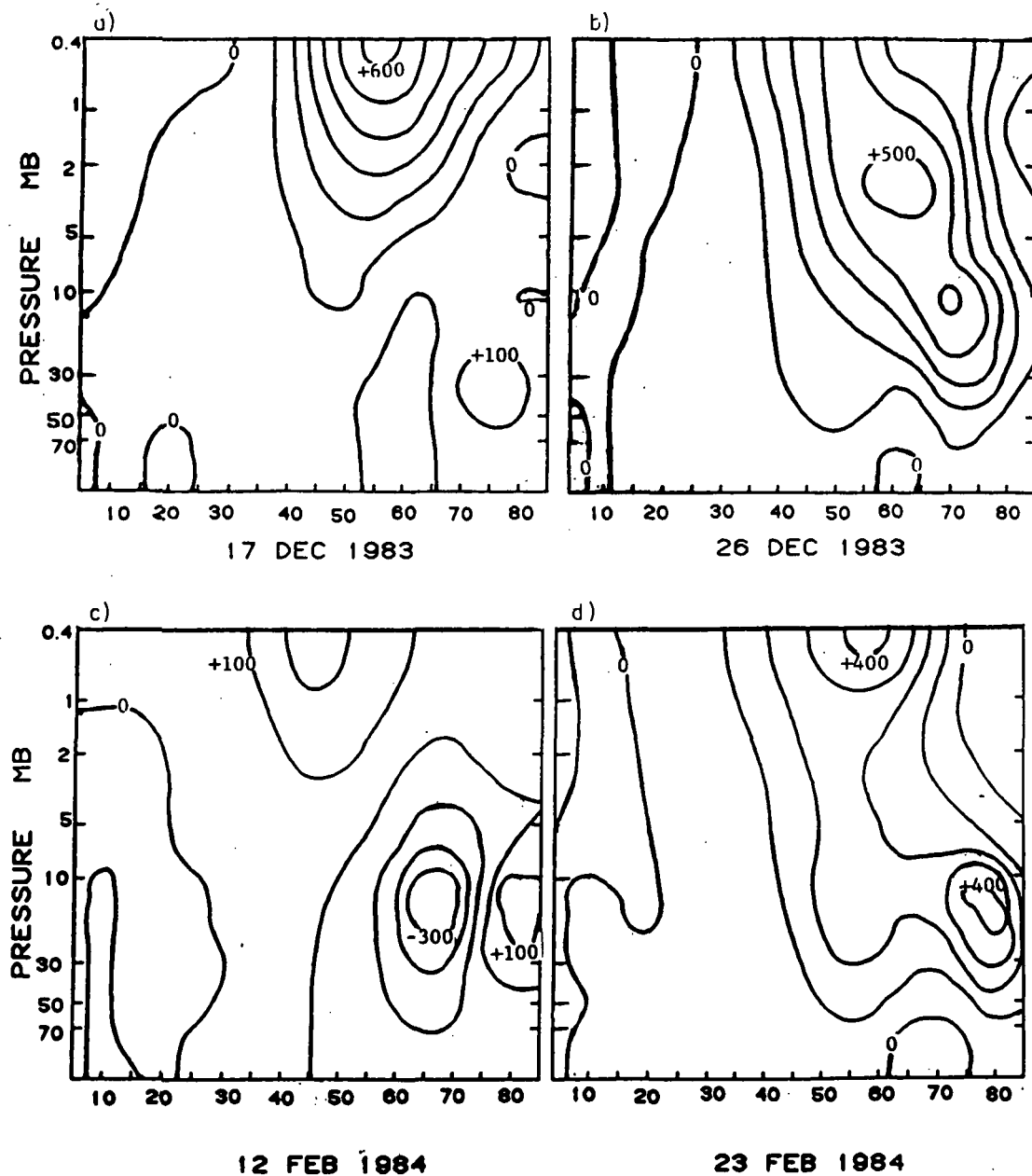


Figure 4. Cross sections of eddy transport of momentum ($U'V'$) units $m^2 \text{ sec}^{-2}$. Range 5° - 85°N and 70-0.4 mb contour interval: $100 m^2 \text{ sec}^{-2}$. a) From Dec. 17, 1983 analyses; b) From Dec 26, 1983 analyses; c) From Feb. 12, 1983 analyses; d) From Feb. 23, 1983 analyses.

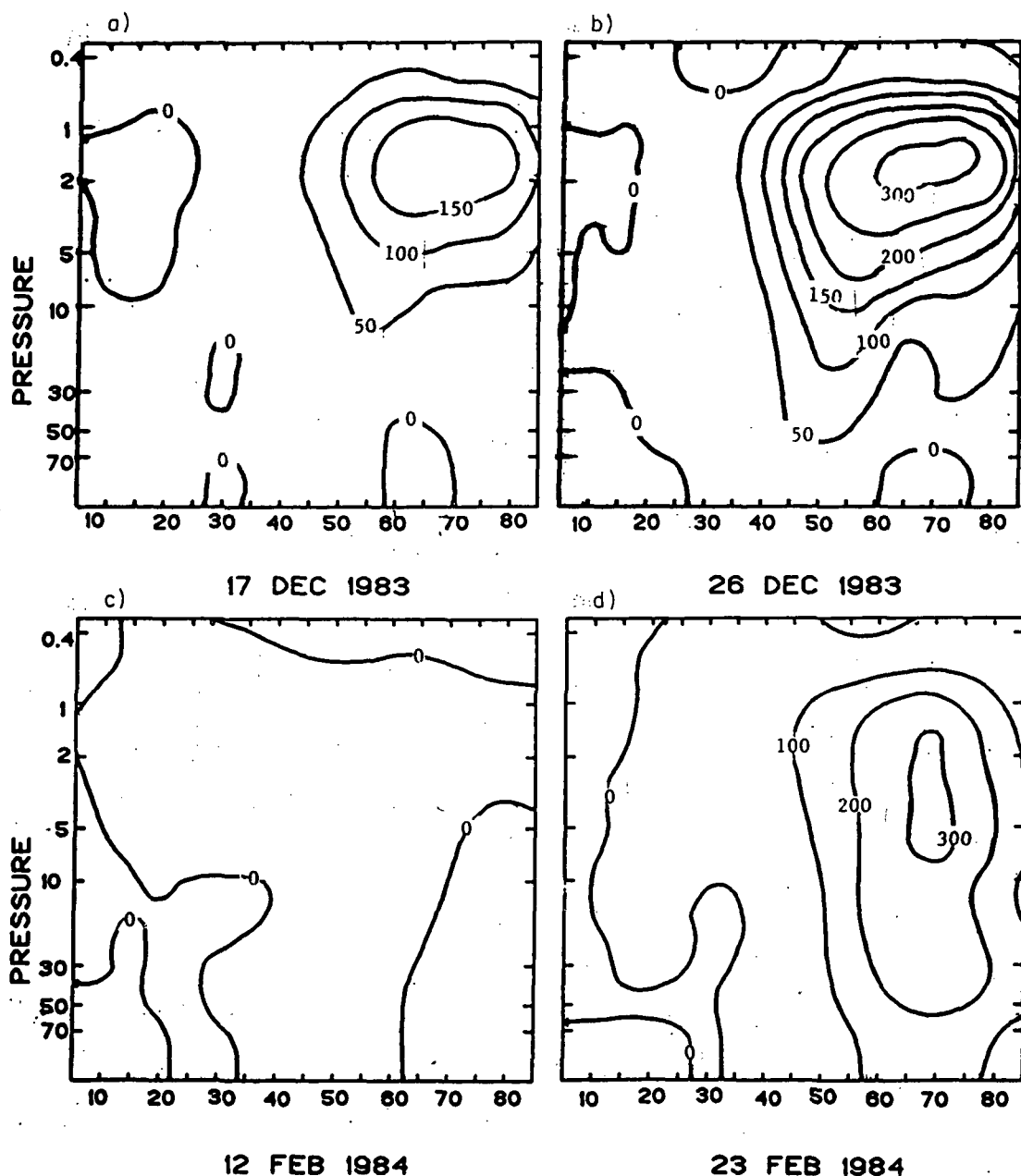


Figure 5. Cross sections of eddy transport of heat ($V'T'$) units $m K sec^{-1}$. Range $5^{\circ}-85^{\circ}N$ and $70-0.4$ mb. a) From Dec. 17, 1983 analyses contour interval of $50 m K sec^{-1}$; b) From Dec. 26, 1983 analyses with contour interval at $50 m K sec^{-1}$. c) From Feb. 12, 1984 analyses with contour interval of $100 m K sec^{-1}$; d) From Feb. 23, 1984 analyses with contour interval of $100 m K sec^{-1}$.

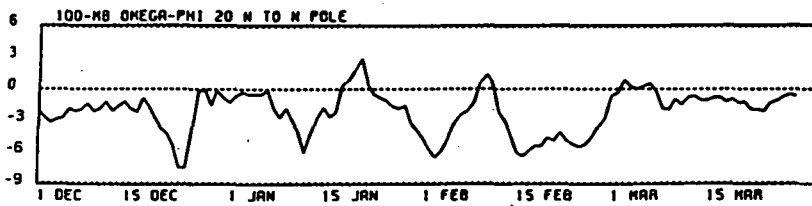


Figure 6. Eddy flux of eddy geopotential ($\overline{\omega' \phi'}$) through the 100 mb surface (units - $\text{J m}^{-2} \text{s}^{-1} \times 10^{-1}$). Period Dec. 1, 1983 - Mar. 15, 1984.

2.10 THE 4-5 DAY MODE OSCILLATION IN ZONAL WINDS OF INDIAN MIDDLE ATMOSPHERE DURING MONEX-79

R. S. Reddy, B. K. Mukherjee, K. Indira
and

Bh. V. Ramana Murty

Indian Institute of Tropical Meteorology,
Pune-411005, India

INTRODUCTION

In the early studies based on time series of balloon observations, the existence of 4-5 day period waves and 10-20 day wind fluctuations were found in the tropical lower stratosphere, and they are identified theoretically as the mixed Rossby-gravity wave and the Kelvin wave, respectively (YANAI and MURUYAMA, 1966). On the basis of these studies, HOLTON and LINDZEN (1972) have established that the vertically propagating equatorial waves play an important role in producing the QBO (quasi-biennial oscillation) in the mean zonal wind through the mechanism of wave-zonal flow interaction. These studies are mainly concentrated over the equatorial Pacific and Atlantic Oceans. APPARAO and RAMANA MURTY (1976) have observed similar prominent wave disturbances over the region east of the Indian Ocean during a quasi-biennial oscillation. Zonal winds in upper troposphere and lower stratosphere (10-20) km of the middle atmosphere over the Indian subcontinent may bear association with the activity of summer monsoon (June-September). Monsoon Experiment (MONEX-79) has provided upper air observations at Balasore (21°30'N; 85°56' E), during the peak of monsoon months July and August, using Metox equipment. A unique opportunity has, therefore, been provided to study the normal mode oscillations present in the zonal winds of lower middle atmosphere over India, which may have implication on large scale wave dynamics. This aspect has been examined in the present study.

DATA

The data considered are the maximum zonal winds over Balasore observed between 10-20 km and obtained from First GARP. Global experiment, MONEX Data Set, published by International MONEX Management Centre, India Meteorological Department. The observations were taken four times a day (00, 06, 12 and 18 GMT) during July and two times a day (00 and 12 GMT) during August, 1979.

ANALYSIS

The daily values of the maximum wind have been smoothed by two-point moving average method. The values so obtained have been subjected to power spectrum analysis following the method of BLACKMAN and TUKEY (WMO; 1966). To achieve satisfactory resolution in the spectrum and for examining the period oscillations of 4-5 days, a maximum lag of 10 has been used. The period corresponding to any spectral estimate is obtained from the relation $P = 2m/L$, where m is the maximum lag (10) and L is lag in days of the spectral estimate in question.

RESULTS AND DISCUSSION

Figure 1 gives the smoothed daily values of zonal wind for the months July and August. Day-to-day fluctuation in the intensity of zonal winds is noticeable with maximum (15-30 mps) in the region 12-14 km. A 4-5 day mode oscillation is identified in these zonal winds. Such oscillation appears to be inherent in the nature of northern summer. Also the analysed wind field is

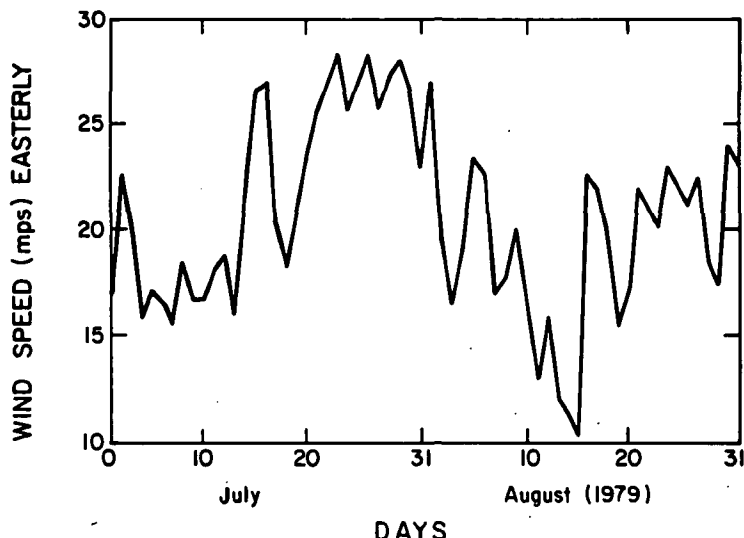


Figure 1. Daily smoothed values of maximum zonal winds observed between 10-20 km over Balasore for the months of July and August during MONEX-79.

subjected to power spectrum analysis to confirm this feature. The values obtained by spectral estimate are shown in Figure 2. The associated 99.95 and 90 per cent confidence limits have been calculated. The spectral peak at lag in days, = 4 in Figure 2 corresponds to a period of 5 days. It is significant at 99% level. We conclude from the present study that there is a 5-day oscillation in zonal winds (easterly) of upper troposphere and lower stratosphere during summer monsoon period.

CADET (1981) identified different waves propagating in the lower stratosphere over eastern Atlantic Ocean during summer 1984. These are westward moving waves with a period around 4-5 days and eastward moving waves with a similar or slightly greater period. In recent years, observational studies have shown some evidence of wave motions and theoretical studies have stressed the dynamical significance of waves in the general circulation of the tropical middle atmosphere (HIROTA, 1981).

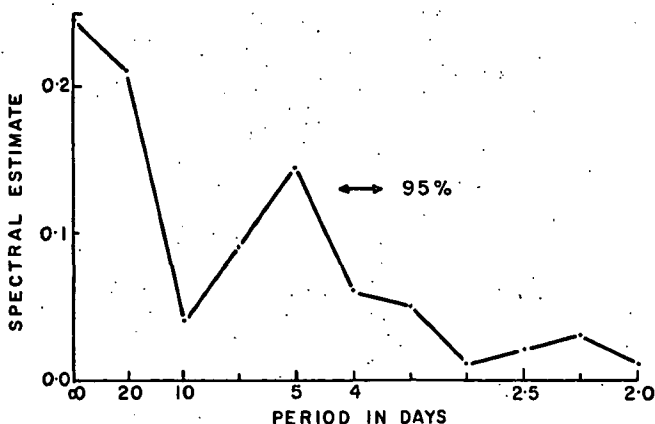


Figure 2. Power spectrum of daily values of maximum zonal winds observed between 10-20 km over Balasore for the months July and August during MONEX-79.

ACKNOWLEDGEMENT

The authors express their sincere thanks to Dr. A. S. R. Murty for the help received while preparing the paper.

REFERENCES

- Appa Rao, G., Bh. V. Rāmāna Murty (1976), Pageoph, 114, 365-377.
Cadet, D. (1981), MAP Handbook, 2, 218-236.
Hirota, I. (1981), MAP Handbook, 2, 214-217.
Holton, J. R., R. S. Lindzen (1972), J. Atmos. Sci., 29, 1076-1080.
WNO Technical Note No. 79 (1966), Geneva, Switzerland, 33.
Yanai, M., T. Muruyama (1966), J. Meteor. Soc. Japan, 44, 291-294.

2.11 THE EVOLUTION OF ERTEL'S POTENTIAL VORTICITY DURING STRATOSPHERIC SUDDEN WARMINGS

T. D. A. Fairlie and A. O'Neill

Meteorological Office,
Bracknell, U. K.

INTRODUCTION

In the winter stratosphere of the Northern Hemisphere, the disruption of the westerly vortex and associated warming of polar latitudes is a well known phenomenon. It has become apparent that some important dynamical processes in the stratosphere are highly nonlinear and are best thought of locally rather than in terms of the interaction between the zonal-mean flow and harmonic waves around latitude circles.

The importance of nonlinear processes was suggested by McINTYRE and PALMER (1983, 1984) who used isentropic maps of Ertel's Potential Vorticity, to show that during disturbed episodes material lines may become strongly and irreversibly deformed in certain places. They adopted the term "planetary wave breaking" to describe this process.

In this paper we use isentropic maps of Q to follow the evolution of a Canadian warming in November - December 1981 and a particularly strong warming in January 1982. The advection of Q over large distances on isentropic surfaces was a striking feature of the flow during each event. This could be identified because of our ability to follow the movement of material lines due to the approximate conservation of Q over several days. The advection of Q was a nonlinear process because its changing distribution affected the advecting wind field.

We describe how the Canadian warming did not lead to a permanent change in the structure of the westerly vortex, as defined by the coarse-grain field of Q , whereas the January event was accompanied by a substantial loss of resolved Q which was never fully recovered.

DATA

The stratospheric data used in this study are taken from the daily analysis of data from a stratospheric sounding unit (SSU) on board the satellite NOAA-6. Details of the instrument and of the method of analysis are given by CLOUGH et al. (1985) who also describe the way in which we calculate isentropic maps of Q . Following CLOUGH et al., we have assessed the reliability of the maps used in this study by comparing them with maps based on data from another SSU on board the satellite NOAA-7, in independent orbit. The features to which we draw attention are closely reproduced in both analyses.

THE EVOLUTION OF Q DURING STRATOSPHERIC WARMINGS IN WINTER 1981/82

During November - December 1981, a strong "Canadian warming" occurred in the stratosphere of the Northern Hemisphere in which the warmest air was drawn north-eastwards over Canada. The disturbance extended through the lower and middle atmosphere exhibiting little tilt with height. The vertical averaging inherent in our analysis was therefore not a serious limitation of our derived maps of Q .

Figure 1 shows the distribution of Q on the 850 K surface of potential temperature for November 25, 1981. The 850 K surface lies near 10 mb in the middle stratosphere. Near 180°E there was an incursion of air with low Q into the edge of the westerly vortex. To the north, a tight gradient of Q was established, associated with a jet stream over the polar cap. By December 7, Figure 2 shows that the area of low Q had been drawn right across polar regions. The tongue of high Q in low latitudes was eventually pinched off the main vortex near 0°E . Discrete maxima within the tongue of high Q were shown to be realistic by CLOUGH et al. The detached region of high Q continued to be resolved and eventually recombined with the main body of high Q in the westerly vortex. The vortex itself had a very similar overall distribution of Q before and after the disturbance. Thus, any irreversible mixing of Q to unresolved scales was clearly limited during this event, or was offset radiatively.

In January 1982, a strong warming took place in the course of which the polar vortex was split into two distinct cyclonic vortices. Soon after, values of Q in the centre of one of these vortices were sharply reduced in our derived fields.

The most rapid changes in the circulation of the stratosphere occurred from about January 18th. Figure 3 shows a map of Q on that day. A striking feature of the flow was a southward extending tongue of high Q to the east of an incursion of low Q over the North Atlantic. This pattern is characteristic of a type of blocking that occurs in the troposphere (see, for example, NAMIAS and CLAPP, 1951, Figure 11 and associated discussion). Indeed, the stratospheric feature lay directly above a blocking system in the troposphere, whose associated pattern of Q extended right up to 10 mb with little tilt with height. This suggests an intimate connection between stratospheric

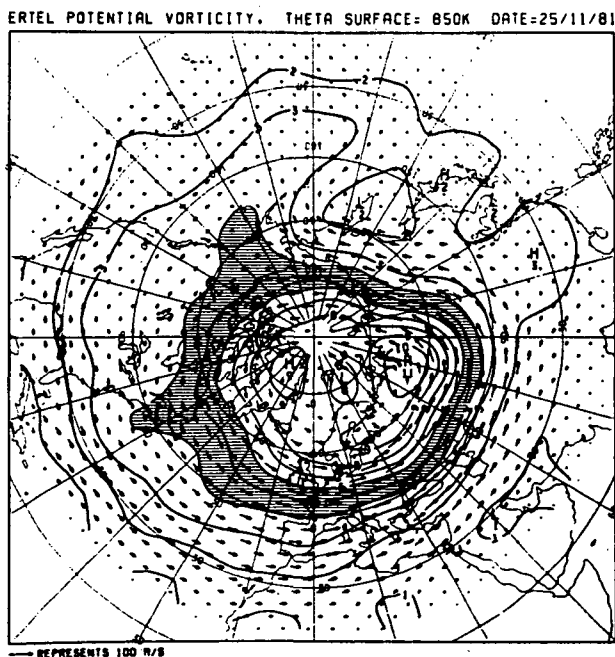


Figure 1. Ertel's potential vorticity, Q , and geostrophic winds evaluated on the 850 K isentropic surface for November 25, 1981. Units: $\text{K m}^2 \text{ kg}^{-1} \text{ s}^{-1} \times 10^{-4}$. In these units, areas with values of Q between 4 and 6 are shaded.

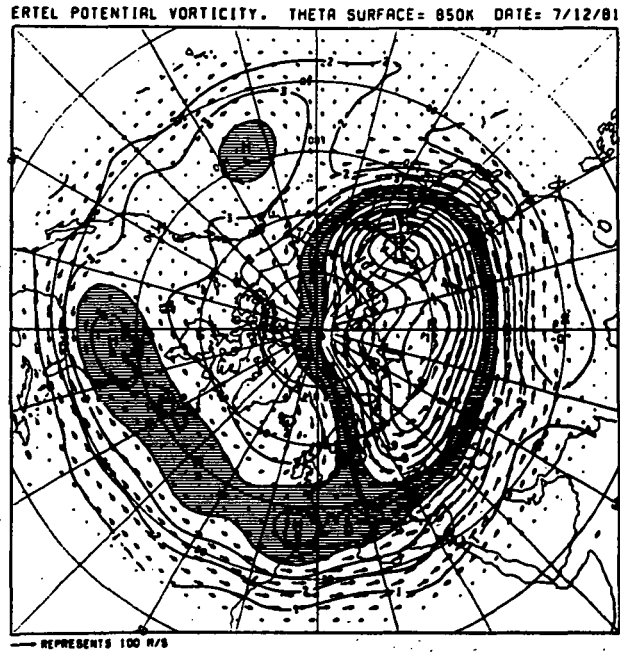


Figure 2. As for Figure 1 but for December 7, 1981.

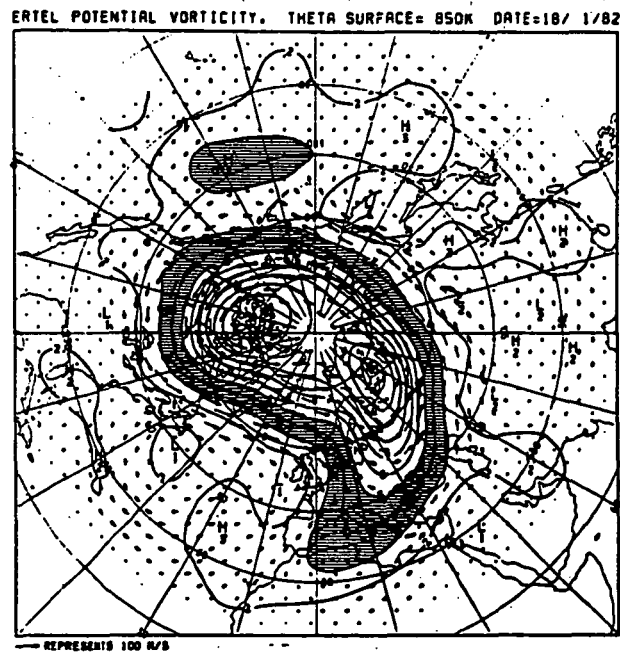


Figure 3. As for Figure 1 but for January 18, 1982. Areas with values of Q between 3 and 5 are shaded.

disturbances and blocking in the troposphere which should be viewed locally, rather than in terms of propagating planetary waves 1 or 2.

After January 18, the westerly vortex became increasingly elongated as the anti-cyclone associated with the intrusion of low Q over the North Atlantic continued to intensify. Air or low Q was drawn around the southern side of the westerly vortex towards the Northern Pacific where another large anti-cyclone developed, above a northward extending ridge in the troposphere. By January 24, the vortex was split into two distinct centers of high Q , as shown in Figure 4. Shortly after, values of Q within the centre, over North America, were sharply reduced in our maps. Figure 5 shows that by January 27, only a long tongue of relatively high Q remained. This feature largely disappeared from our maps during the following week, leaving a singly westerly vortex in polar latitudes, substantially reduced in area, and a region of relatively weak gradient of Q over the Northern Pacific.

The locally poor conservation of Q associated with the rapid weakening of the North American vortex was at least partly due to the limited resolution of the satellite data, particularly in the vertical. In an independent 10 mb analysis on January 27 of radiosonde and rocket data by NAUJOKAT et al. (1982), the vortex was retained.

Extreme values of Q may be lost in the analysis of SSU data when vertical or horizontal structure is generated on scales below those which can adequately be resolved. Strong vertical wind and temperature shears could be produced by the advection of Q at different rates on different isentropic surfaces (differential advection). A warm air mass may, for example, be advected over a cold air mass. Radiosonde data clearly shows such structure in the vicinity of the North American vortex. Colocated temperature profiles derived from both radiosonde and SSU data confirm that the temperature stratification was not

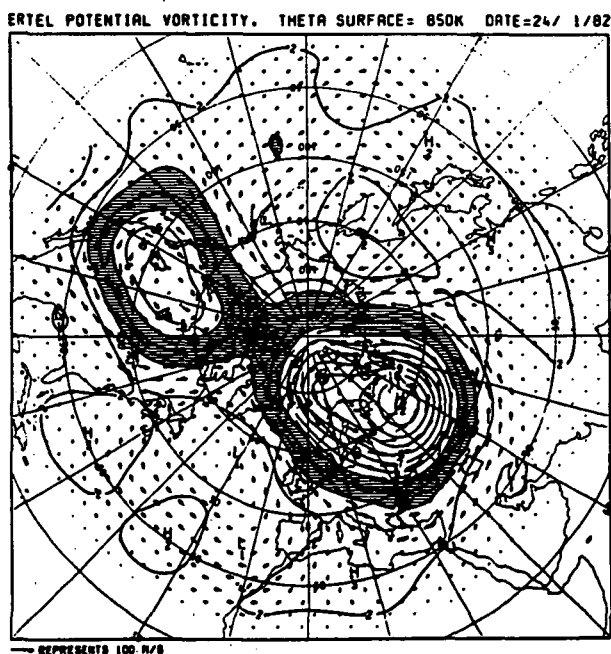


Figure 4. As for Figure 3 but for January 24, 1982.

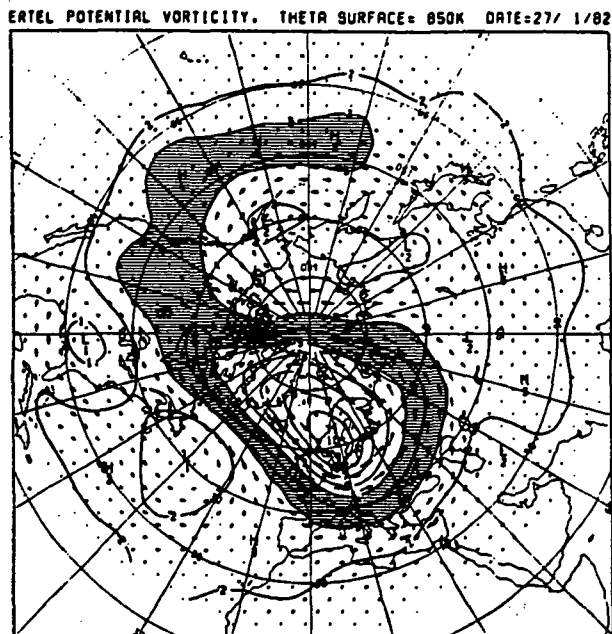


Figure 5. As for Figure 3 but for January 27, 1982.

fully resolved by the SSU. The static stability, and hence Q , was seriously underestimated.

The introduction of strong vertical shears to the stratosphere may lead to a permanent reduction in Q . Non-conservative changes to Q due to radiation occur on much shorter time scales in regions where strong vertical temperature gradients exist (FELS 1982).

CONCLUSION

During stratospheric warmings, Q is advected over large distances on isentropic surfaces as material contours are strongly and irreversibly deformed. This is a non-linear process because the changing distribution of Q affects the advecting wind field. Air of low Q is drawn from low latitudes to high latitudes, displacing high values of Q associated with the westerly vortex. This is consistent with a general increase in geopotential height over the polar cap and a weakening of zonal-mean westerly winds.

During the Canadian warming of November - December 1981, a region of high Q was temporarily separated from the main vortex. When regions of high Q recombined, the vortex recovered its previous structure to a large degree, showing that any apparent non-conservation of Q by irreversible mixing to small scales was limited.

Conservation of Q was locally poor, however, during the strong warming of January 1982. We propose that the apparent loss of Q was due to the introduction of vertical structure to the stratosphere associated with differential advection of Q . Such structure, confirmed by independent radiosonde measure-

ments, was inadequately resolved by the SSU. Radiative processes which tend to wipe out strong vertical structure could account for the fact that values of Q, apparently lost during the warming, never recovered.

The warming of January 1982 was apparently initiated by the vertical extension of a blocking disturbance in the troposphere into the middle of the stratosphere. A possible mechanism for this and its implications for the dynamics of stratospheric warmings will be given in a forthcoming paper by Fairlie and O'Neill.

REFERENCES

- Clough, S., N. Grahame and A. O'Neill (1985), Potential vorticity in the stratosphere derived from satellite data. To appear in the April edition of the Q. J. Roy. Meteor. Soc.
- Fels, S. (1982), A parametrisation of scale-dependent radiative damping rates in the middle atmosphere, J. Atmos. Sci., **39**, 1141-1152.
- McIntyre, M. and T. Palmer (1983), Breaking planetary waves in the stratosphere, Nature, **305**, 593-600.
- McIntyre, M. and T. Palmer (1984), The surf zone in the stratosphere, J. Atmos. Terr. Phys., **46**, 825-849.
- Namias, J. and P. Clapp (1951), Observational studies of general circulation patterns. Compendium of Meteorology, Amer. Meteor. Soc., 551-567.
- Naujokat, B., K. Petzoldt, K. Labitzke and R. Lenschow (1982), The fourth winter of PMP-1, 1981/82: A winter with several interesting features, Beilage zur Berliner Wetterkarte, Free University, Berlin.

2.12 SEASONAL CHANGES IN THE STRUCTURE OF THE STRATOSPHERIC CIRCULATION

A. O'Neill and V. D. Pope

Meteorological Office,
Bracknell, U. K.

INTRODUCTION

Our aim is to study the seasonal evolution of the stratospheric circulation in both hemispheres using a coordinate independent diagnostic tied to the vortex, wherever it lies, rather than to latitude circles.

Zonally averaged quantities are highly variable in the winter stratosphere, as the vortex moves on and off the pole, masking systematic changes in the structure of the vortex. The quantities we show here are the areas $A(Q)$, where Ertel's potential vorticity is greater than a specified value Q , for various Q . In these calculations, Q is evaluated on the 850 K isentropic surface which lies near 10 mb in the middle of the stratosphere. The advantage of using contours of Q (rather than contours of geopotential height, say) is that area enclosed by such contours is approximately constant for quasi non-divergent, adiabatic, inviscid motion. Changes in area will occur if any of the above restrictions on the motion are invalid, and also if scales of motions are generated below those that can be adequately resolved.

The evolution of area shows the systematic change in the average structure of the vortex. At a given time, the rate of change of Q with $A(Q)$ gives a measure of the average gradient of Q . The gradient of Q is relevant for the propagation of large-scale disturbances into the stratosphere. Experience has also shown that winds tend to be strong (weak) when the gradient of Q is strong (weak).

DATA

The data used in this study were obtained primarily from stratospheric sounding units (SSUs) on board the satellites TIROS-N and NOAA-6. Details of the retrieval and analysis are given by CLOUGH et al. (1985) who also describe the calculation of isentropic fields of Q .

RESULTS AND CONCLUSIONS

Figure 1 shows curves of $A(Q)$ for the Northern Hemisphere from July 1979 to June 1980. Figure 2 is for the Southern Hemisphere from January to December 1981. Figures 3 and 4 (discussed later) are isentropic maps of Q which include the contours corresponding to the area curves, $A(Q)$.

The seasonal march of solar heating has a dominant effect on the areas shown in Figures 1 and 2. There are low values and weak gradients of Q in summer and high values with strong gradients of Q with respect to area in winter. Seasonal changes in Q are much greater at high latitudes corresponding to the stronger cycle in solar heating. Superimposed on this seasonal cycle are changes which are related to dynamical disturbances, e.g., the rise in $A(3)$ in Figure 1, and $A(2)$ in Figure 2 during spring.

The increasing separation between the curves $A(3)$ and $A(4)$ in Figure 1 corresponds to a weakening of gradients of Q around a shrinking westerly vortex. McIntyre and Palmer (op. cit.) suggested that mixing by an irreversi-

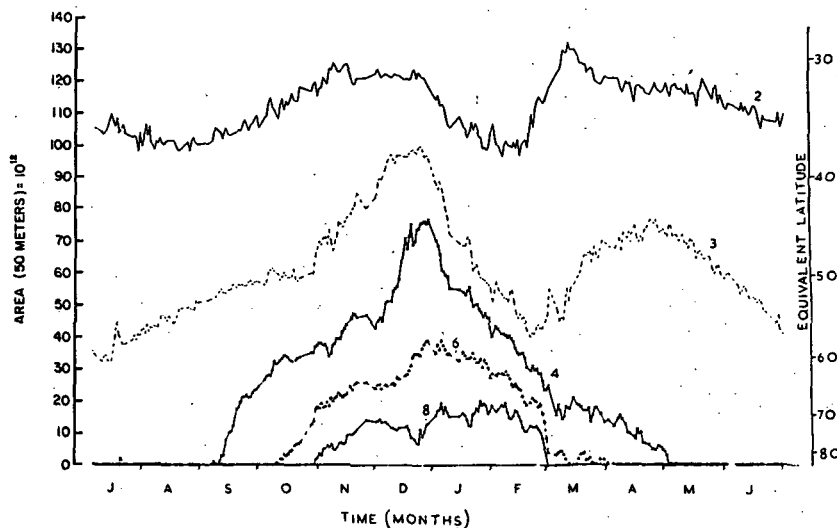


Figure 1. Graphs of areas $A(Q)$ ($\text{km}^2 \times 10^6$) as described in the text. Each curve is labeled with the corresponding value of Q in units of $\text{km}^2 \text{ kg s}^{-1} \times 10^{-4}$. The period covered is July 1, 1979 to June 30, 1980 for the Northern Hemisphere. The equivalent latitude, marked on the right hand axis, is calculated as the latitude circle that encloses the area marked on the left hand axis.

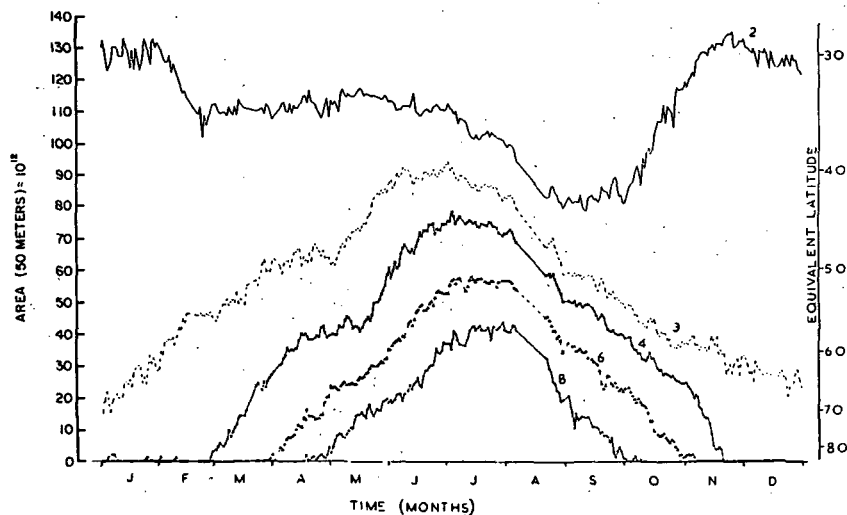


Figure 2. As Figure 1 but for the Southern Hemisphere for the period of January 2 to December 31, 1981. Curves are labeled with the value of $-Q$.

ble cascade to small scales on an isentropic surface could produce such a behaviour. The importance of this process remains to be quantified. Another contender is nonconservation of Q due to departures from radiative equilibrium induced by disturbances. To see how this could affect the curves $A(Q)$ in Figure 1, we refer to Figure 3 which is an isentropic map of Q for February 21, 1980. There is a band of low Q stretching across high latitudes associated with a strong and persistent Aleutian High in geopotential height and high temperatures.

In much of this region, the air is comparatively stagnant. Radiative cooling would cause air to descend through the isentropic surface bringing down higher Q , and thus act to destroy the minimum in Q . Subsequent isentropic maps show that the increase in $A(3)$ is mainly associated with a shrinking of the band of low Q over the Pacific.

Brevity precludes a comparable description of the figures for the Southern Hemisphere, which we offer mainly for completeness. Figure 4 shows the isentropic map for October 21, 1981 when $A(2)$ in Figure 3 starts to increase. Noting the similarity in structure to that shown in Figure 3 and examining subsequent behaviour suggests that if the radiative mechanism is relevant then it is relevant for both hemispheres.

A priority for future work is to quantify the role of radiation and of the generation of unresolved scales of motion in governing the coarse-grain distribution of Q in the stratosphere.

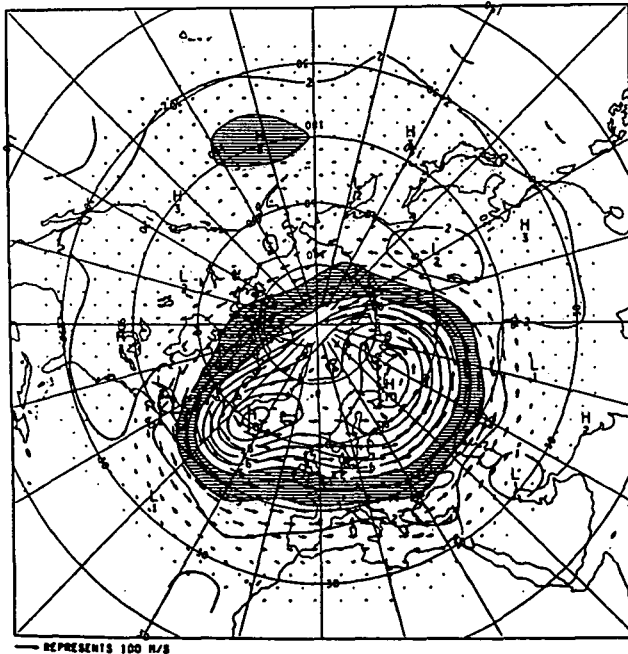


Figure 3. Ertel's potential vorticity, Q , and geostrophic winds evaluated on the 850 K isentropic surfaces for February 21, 1980. Units: $\text{km}^2 \text{kg}^{-1} \text{s}^{-1} \times 10^4$. In these units, areas with values of Q between 3 and 5 are shaded.

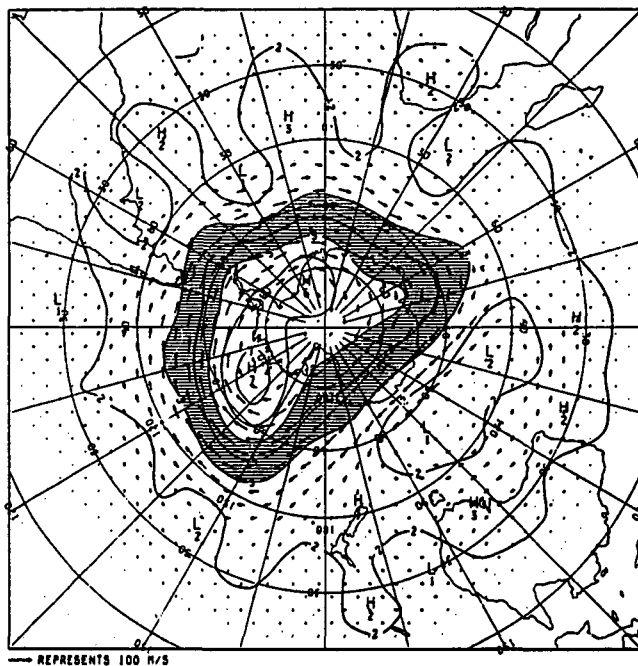


Figure 4. As Figure 3 but for the Southern Hemisphere for October 21, 1981. The quantity plotted here is $-Q$.

REFERENCES

- Clough, S., N. Grahame and A. O'Neill (1985), Potential vorticity in the stratosphere derived using data from satellites, To appear in the April 1985 issue of J. Roy. Meteorol. Soc.
- McIntyre, M. E. and T. N. Palmer (1983), Breaking planetary waves in the stratosphere, Nature, **305**, 593-600.
- McIntyre, M. E. and T. N. Palemer (1984), The "surf zone" in the stratosphere, J. Atmos. Terr. Phys., **9**, 825-849.

2.13 ON THE USE OF POTENTIAL VORTICITY FOR THE DIAGNOSIS OF STRATOSPHERIC SYNOPTICS

G. Rose, K. Labitzke, and U. Kummel

Institut für Meteorologie,
Freie Universität, Berlin
Federal Republic of Germany

INTRODUCTION

According to quasi-geostrophic approximation, regions of strong cross flow gradient of geopotential vorticity support Rossby wave propagation. Using potential vorticity as a dynamical tracer, the polar vortex can be considered as a material entity. In addition to synoptic charts of geopotential heights and temperatures, maps of potential vorticity are used to describe some distinct features of the circulation of the winter stratosphere.

DATA

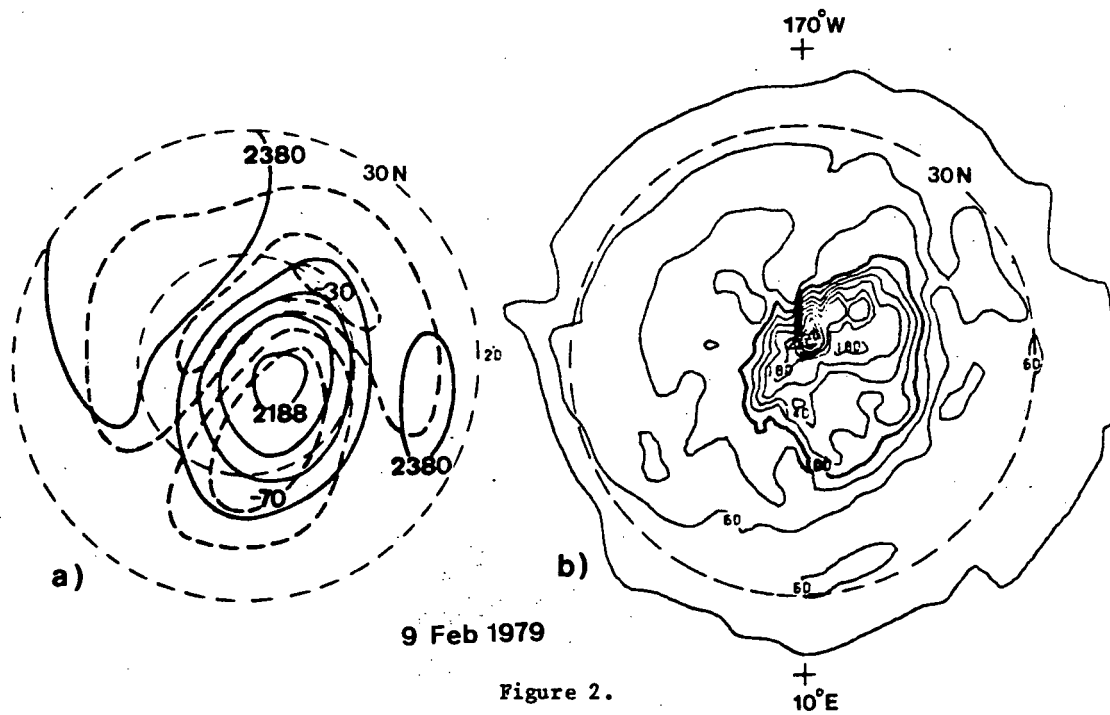
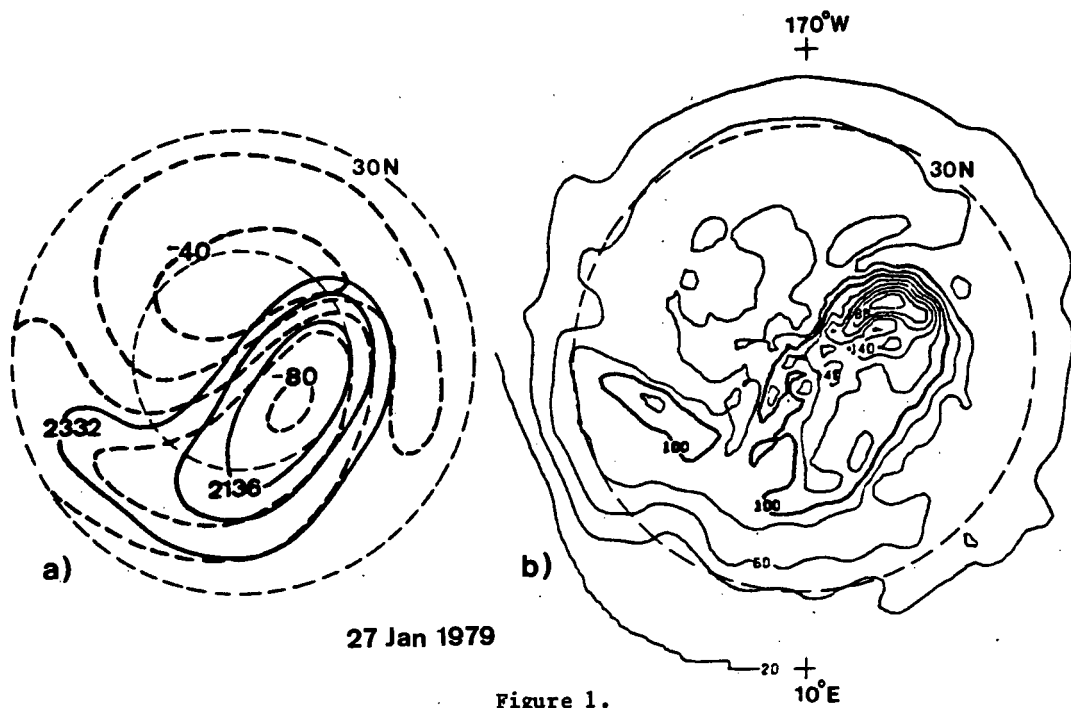
The maps of potential vorticity are derived from daily analyses of geopotential heights and temperatures at the 50, 30, and 10 mbar levels, analyzed by the Stratospheric Research Group, Free University, Berlin.

SELECTED SYNOPTIC FEATURES DURING WINTER

Figures 1 to 4 show the main characteristic features of the major stratospheric warming during January/February 1979: On January 27, Figure 1, the vortex is diminished materially, as air with high potential vorticity is cut off over USA. A relatively undisturbed vortex is found on February 9, Figure 2. This quiet period ends by mid-February, when the polar vortex becomes elongated and low potential vorticity is advected polewards above Asia, Figure 3, February 20. At this time the gradients of potential vorticity are steep around the vortex, favouring Rossby wave propagation which may cause interaction with the mean flow. Within 2 days, on February 22, the vortex is split, as noticeable in the height field, Figure 4a, as well as in the distribution of the potential vorticity, Figure 4b.

Also in January 1977, an elongated vortex with two distinct centers in the height field as well as in the distribution of the potential vorticity, Figure 5a,b, January 7, leads to a breakdown of the polar vortex, Figure 6, January 14.

In December 1965 a "Canadian warming" (LABITZKE, 1977) develops, resulting in a displacement of the cold polar vortex, Figure 7a, December 21. This coincides with the displacement of the maximum of potential vorticity, Figure 7b. Although there is cross polar flow and high potential vorticity is pulled away from the vortex, Figure 7b, this time no breakdown occurs and the vortex moves back to the pole, Figure 8, December 25. On January 11, 1966 the synoptic pattern shows again an elongated polar vortex, Figure 9a, and the distribution of potential vorticity shows two distinct centers, Figure 9b. However, a week later the circulation returns to normal winter conditions, Figure 10, January 18.



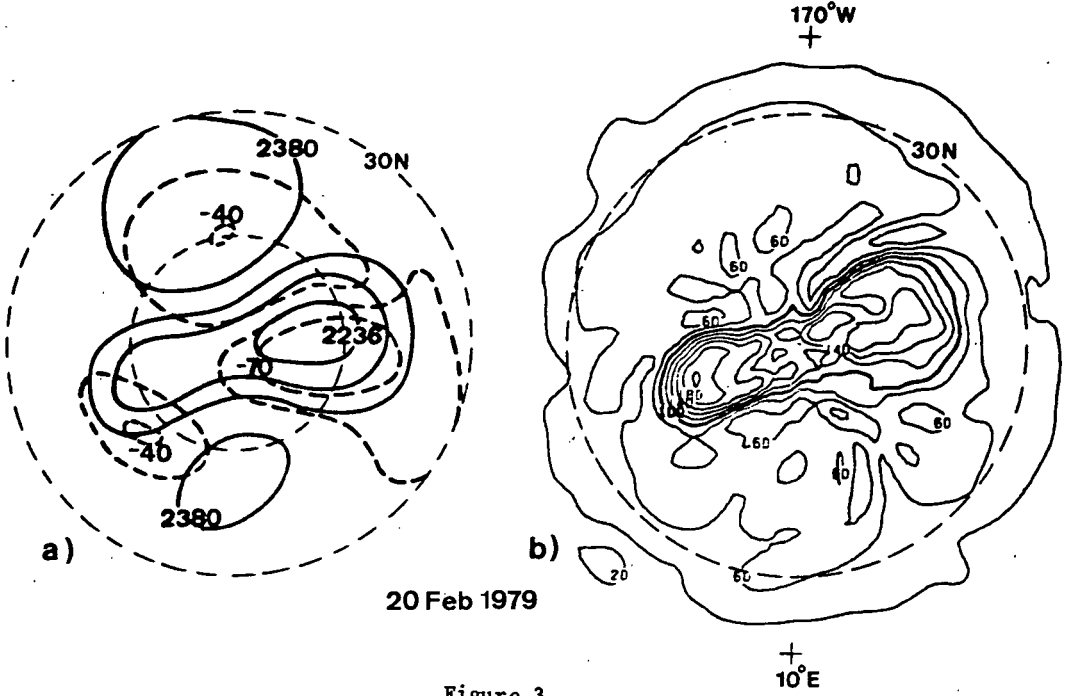


Figure 3.

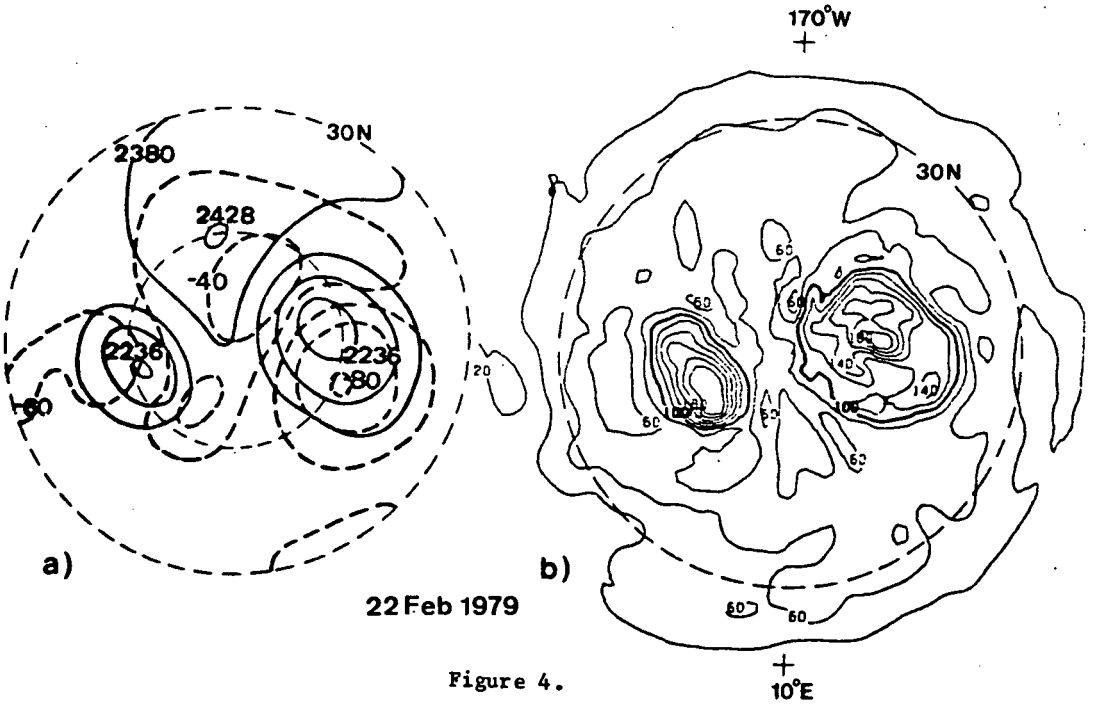


Figure 4.

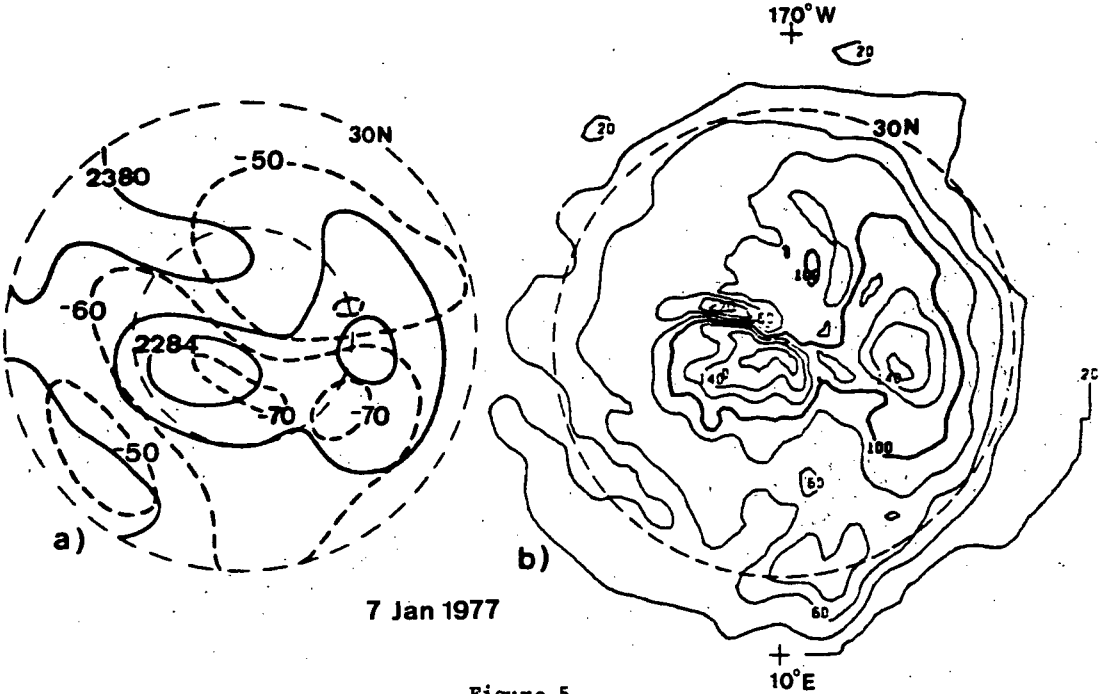


Figure 5.

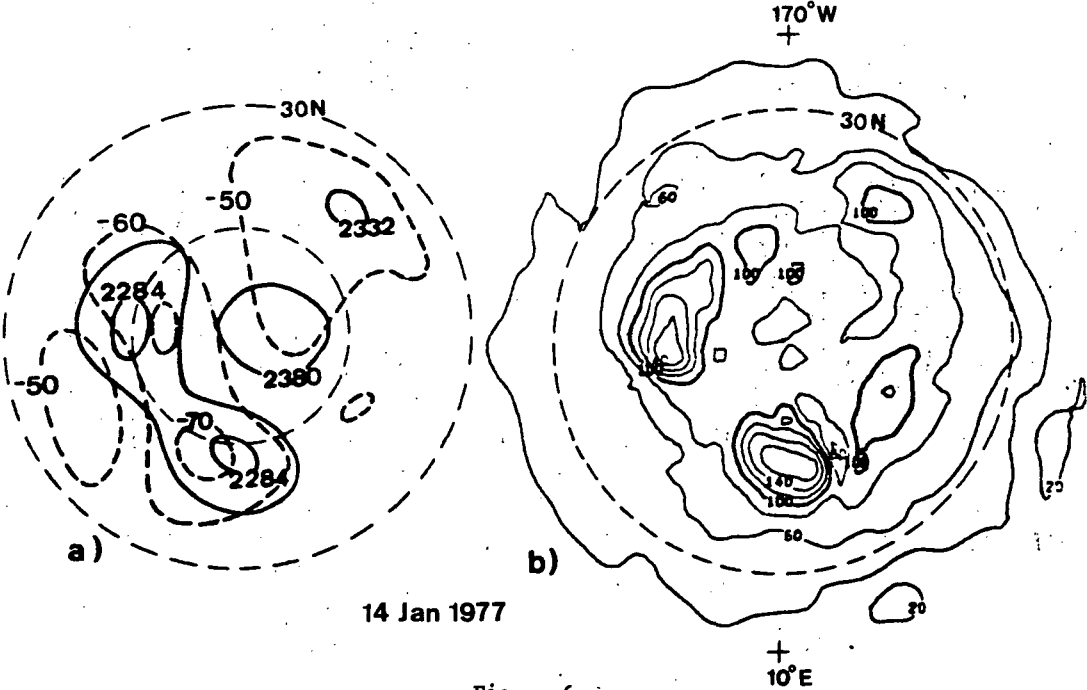


Figure 6.

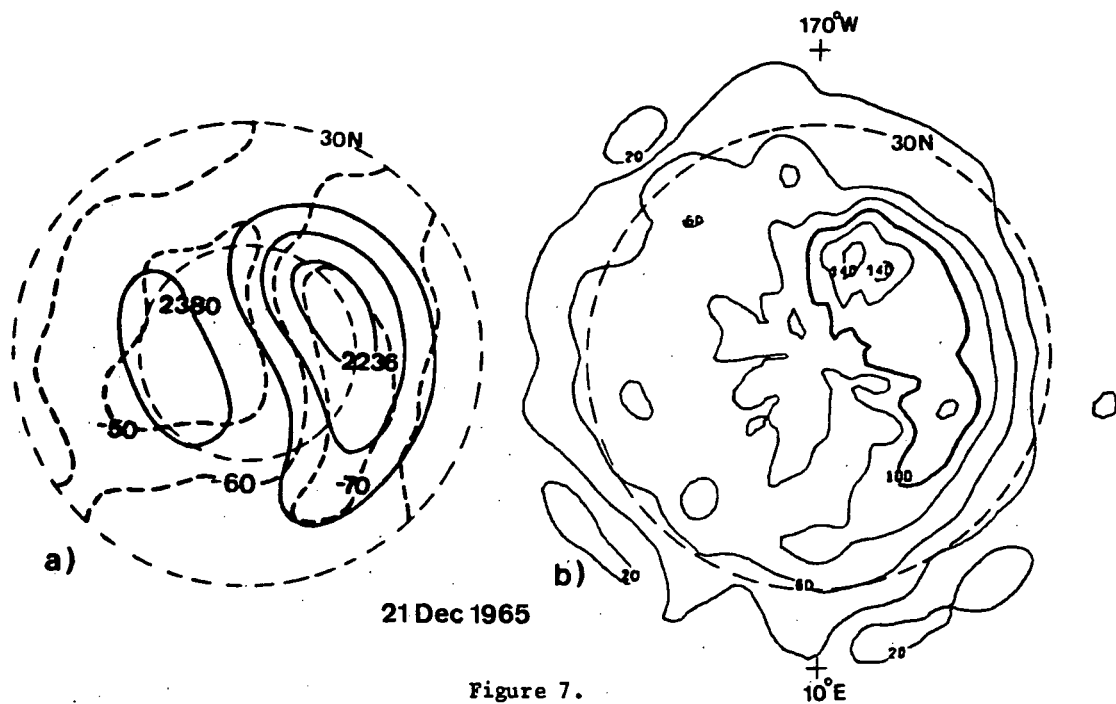


Figure 7.

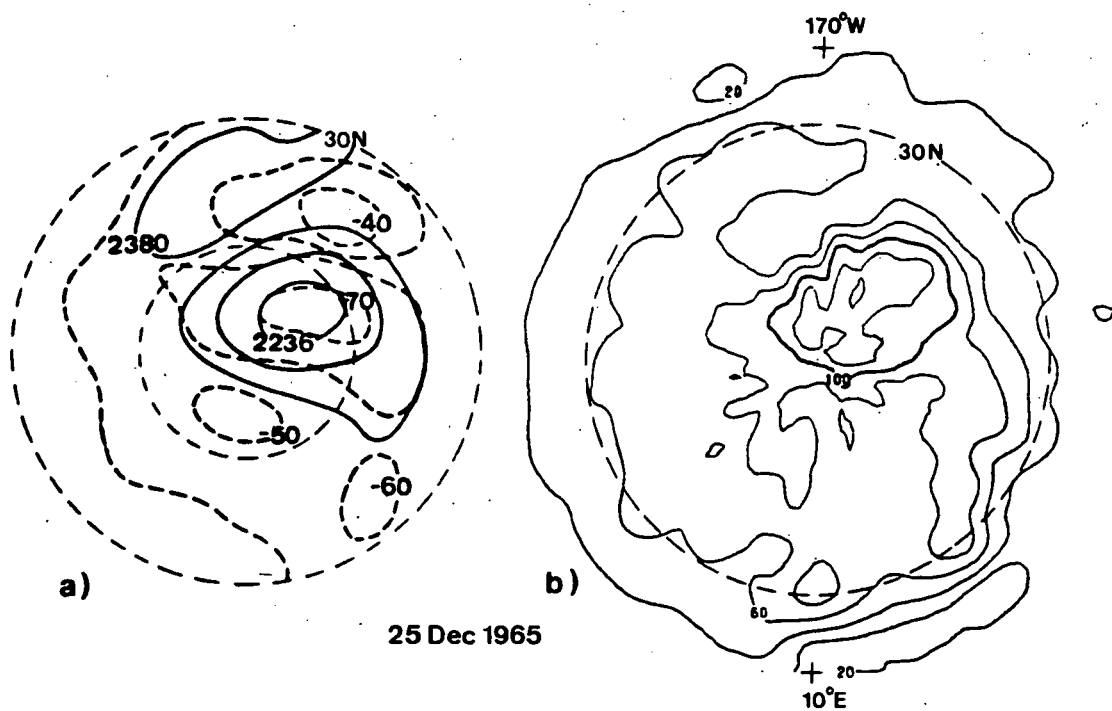


Figure 8.

CONCLUSION

The synoptic patterns of the lower stratosphere, i.e., temperature and height fields as well as maps of potential vorticity have been used to describe the developments of the stratospheric circulation. Rather similar patterns lead to distinctly different developments. This indicates that a discussion in terms of causes and effects is impossible solely by the use of those maps. Even for a complete descriptive study, a fully three-dimensional treatment is inevitable. Moreover, to gain a better insight into the mechanisms of stratospheric warmings, a combination of three-dimensional theoretical and synoptic investigations is desired.

REFERENCES

- Kummel, U. (1985), Die Ertel'sche potentielle Vorticity als dynamischer Tracer während verschiedener winterlicher Stratosphärenwärmungen, Diplomarbeit, Fb 24, F. U. Berlin.
- Labitzke, K. (1977), Interannual variability of the winter stratosphere in the Northern Hemisphere, Month. Wea. Rev., 105, 762-770.

2.14 THE INTEGRATED ENSTROPY BUDGET OF THE
WINTER STRATOSPHERE DIAGNOSED FROM LIMS DATA

Mark R. Schoeberl

Laboratory for Atmospheres
NASA/Goddard Space Flight Center
Greenbelt, MD 20771

and

Anne K. Smith

National Center for Atmospheric Research
P.O. Box 3000
Boulder, CO 80307

ABSTRACT

The quasi-geostrophic integrated enstrophy budget for the 78/79 winter has been analyzed from 10-0.1 mb using LIMS data. During January and late February periods a significant imbalance in the budget appear at 10 mb. We attribute this imbalance to Rossby wave breaking. It is produced by the irreversible transfer of enstrophy to smaller scales not resolved by LIMS. The imbalance episodes correspond well to the appearance of Ertel vorticity filaments shown by McINTYRE and PALMER (1984).

From a seasonal viewpoint, the integrated enstrophy shows an average (although irregular) transfer from a zonal mean reservoir to waves which are then dissipated. On a shorter time scale the integrated enstrophy sloshes back and forth between the waves and mean flow in early winter; then, beginning with the January sudden warming, the total enstrophy is reduced more rapidly. Between 10 mb and 1 mb this reduction is more or less continuous until the end of February. However, in the mesosphere the total enstrophy decrease is very short lived, being quickly restored after the January warming.

Even though the zonal mean integrated enstrophy is large, only about 10% can be utilized by the waves. We therefore introduce the available integrated potential enstrophy, which is a better measure of how close the flow is to saturation by Rossby waves. The largest amount of available potential enstrophy in early January is at 1 mb with decreasing amounts above and below. Saturation of the flow by Rossby waves occurs below 1 mb only coincident with sudden warmings; however, at mesospheric heights the flow appears to be nearly saturated throughout the winter.

REFERENCE

McIntyre, M. E. and T. N. Palmer (1984), J. Atmos. Terr. Phys., **46**, 825-849.

2.15 PLANETARY WAVE-MEAN FLOW INTERACTION IN THE STRATOSPHERE: A COMPARISON BETWEEN THE NORTHERN AND SOUTHERN HEMISPHERES

M. Shiotani and I. Hirota

Geophysical Institute, Kyoto University,
Kyoto 606, Japan

By the use of satellite-derived data supplied by National Meteorological Center (NMC), dynamical interaction between planetary waves and mean zonal winds in the stratosphere is investigated. Special attention is paid to the differences between the Northern Hemisphere (NH) and the Southern Hemisphere (SH). An analysis is made by using Eliassen-Palm (E-P) flux diagnostics for the period from June 1981 to May 1982.

In a climatological sense, HIROTA et al. (1983) and HIROTA and SHIOTANI (1.3, in this volume) showed different seasonal evolutions of large-scale motions between the NH and the SH in the stratosphere. In this study, we present vertical cross-section analysis to see the day-to-day variation in the mean zonal wind and wave activity, in particular, noticing the following phenomena: (a) the poleward shifting of the westerly jet, and (b) episodes after the shifting of the westerly jet.

SHIFTING OF THE WESTERLY JET

In the NH (Figure 1), the stratospheric westerly jet in the midlatitude upper stratosphere is weakened due to a minor warming. On January 9 the E-P flux in the middle stratosphere points nearly equatorward, while the upward E-P flux exists in the lower stratosphere. The distribution of D_F (E-P flux divergence expressed as the zonal force per unit mass) shows a dipole pattern, which was first mentioned by HARTMANN et al. (1984) on the basis of their observations in the SH. After a few days, on January 12, the stratospheric westerlies are established at high latitudes, in association with the redistributing process of potential vorticity.

In the SH, the poleward and downward shifting of the stratospheric westerly jet in late winter is a well-known feature (e.g., LEOVY and WEBSTER, 1976; HARTMANN, 1976; HARTMANN et al., 1984). Figure 2 shows the shifting of the stratospheric westerly jet occurred in mid-August 1981, due to a minor warming which leads the negative D_F at mid-latitudes and the positive D_F at high latitudes. Again, we are interested in the distribution of the D_F on August 15, a dipole pattern similar as seen in the NH.

A complementary (but compatible) idea of the physical cause of the shifting of the westerly jet has been presented by McINTYRE (1982) and McINTYRE and PALMER (1983, 1984), in terms of erosion of the potential vorticity distribution in the polar vortex.

EPISODES AFTER THE SHIFTING OF THE WESTERLY JET

With regard to the shifting of the westerly jet, the seasonal march of the mean zonal wind in the two hemispheres is similar; however, episodes after the shifting are quite different between the two hemispheres.

In the NH (Figure 3) the stratospheric westerly jet situated in the high latitude upper stratosphere leads to the focusing of the E-P flux (January 21). The E-P vectors point strongly upward and, at high latitudes, poleward. A

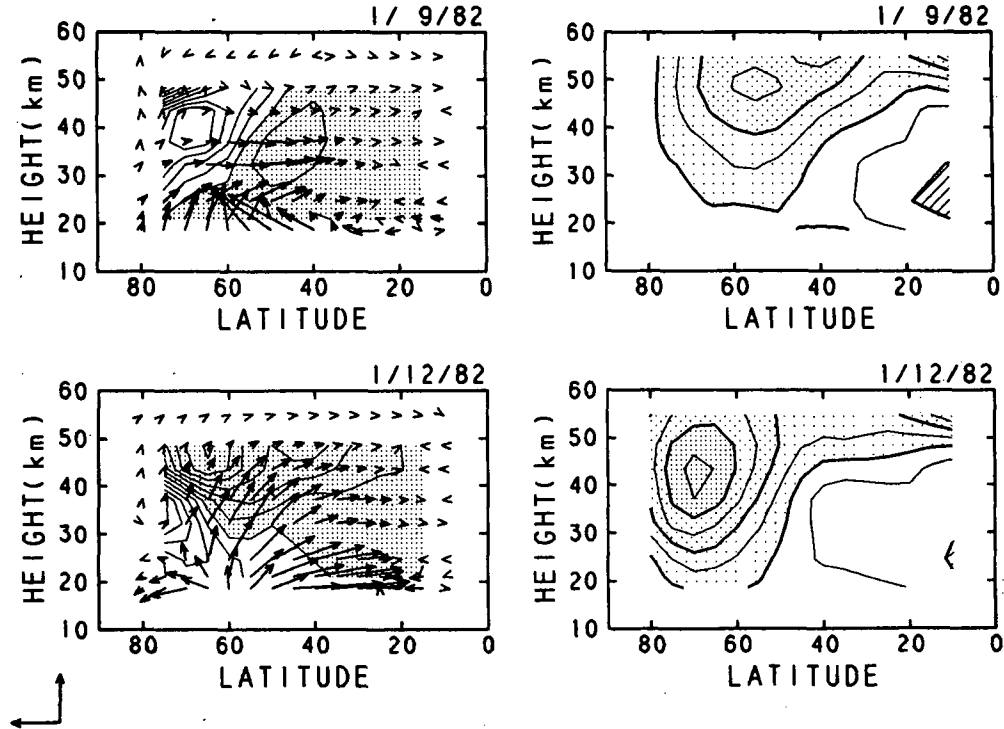


Figure 1. Latitude-height sections of the total E-P flux (waves 1-6) and its divergence expressed as the zonal force per unit mass D_F (left) and the mean zonal wind (right) for the NH on January 9 and 12. The horizontal arrow scale is 10^7 kgs^{-2} and the vertical arrow scale is 10^7 kgs^{-2} divided by the scaling factor 125. The contour interval of D_F is 10^{-4} ms^{-2} ; negative values are shaded. The contour interval of the wind speed is 10 ms^{-1} ; easterlies are over oblique lines.

convergence zone is observed in the high latitude upper stratosphere. Then the westerlies are dramatically broken to the easterlies (January 27), i.e., a major warming.

On the other hand, in the SH, even after the shifting, the stratospheric westerly jet continues to be stably situated in the high latitude middle stratosphere. The E-P flux occasionally focuses into high latitudes, but the westerlies are not broken to the easterlies. Figure 4 is the only one example in 1981 that shows the focusing of the E-P flux into high latitudes.

In conclusion, we emphasize that the poleward shifting of the westerly jet is essential for the two hemispheres in the seasonal march of the stratospheric circulations, although the evolution of the mean zonal wind after the shifting is different between the two hemispheres. To have a deeper understanding of the stratospheric dynamics, it is interesting to make more extensive analyses of the seasonal evolution of the stratospheric circulation, such as those of the development and erosion of the polar vortex.

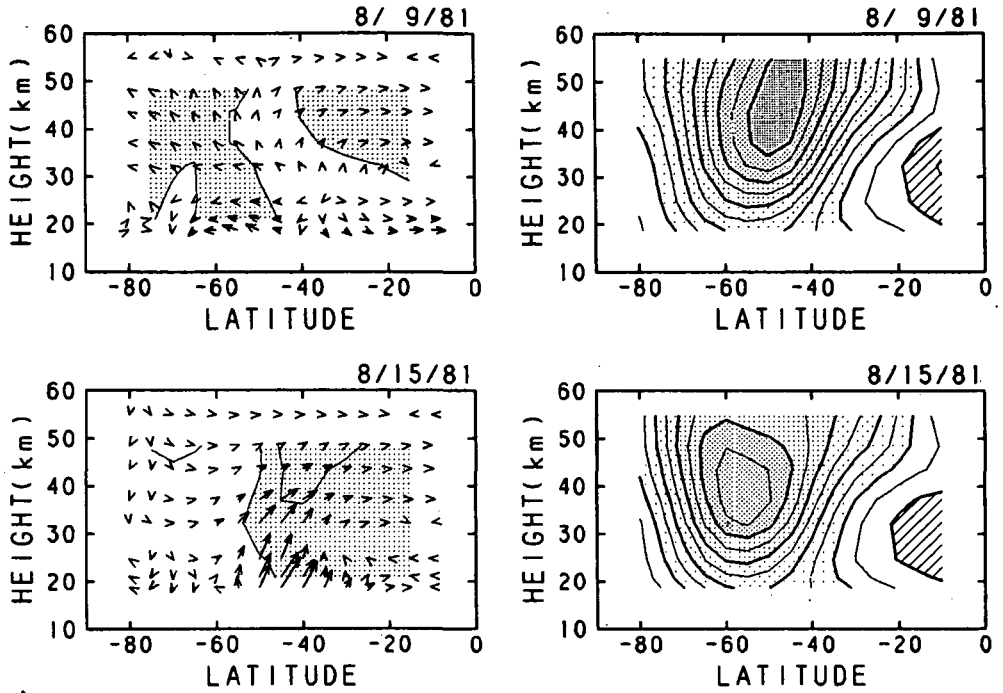


Figure 2. As Figure 1 but for the SH on August 8 and 15, 1981.

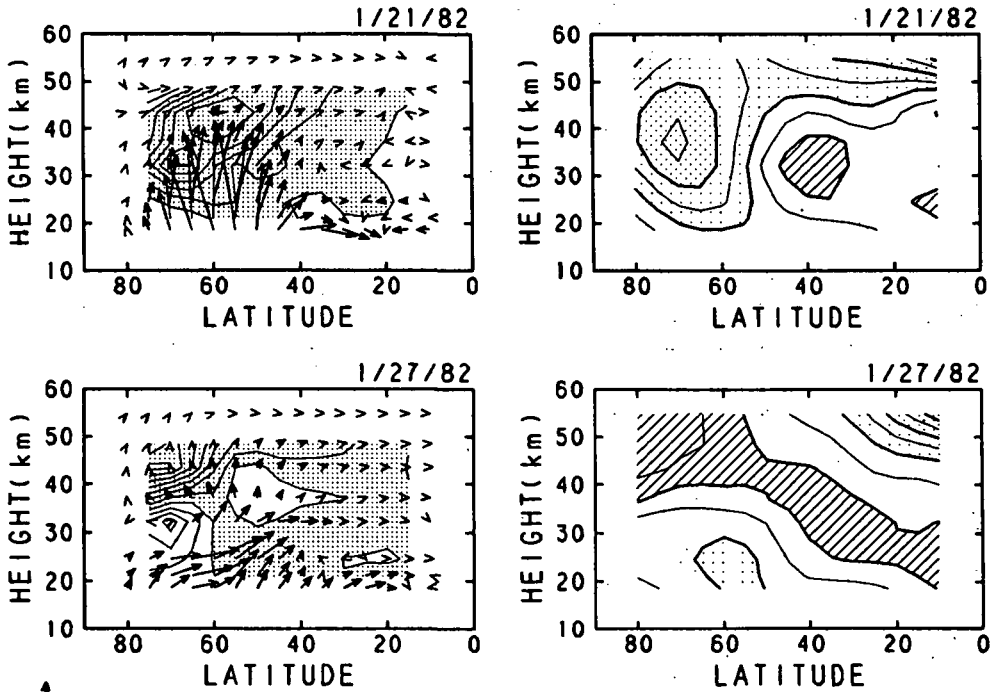


Figure 3. As Figure 1 but for the NH on January 21 and 27, 1982.

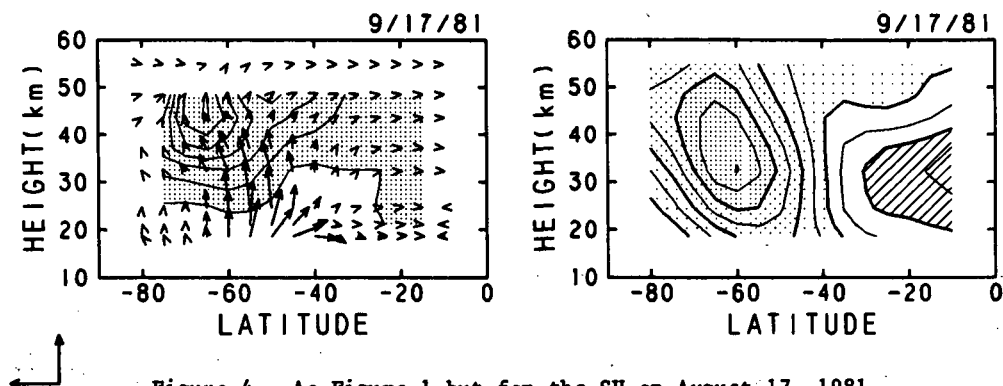


Figure 4. As Figure 1 but for the SH on August 17, 1981.

For details, the reader may refer to the full paper of this work (SHIOTANI and HIROTA, 1985).

Note: We have made a 6-minute, 16 mm color movie to show the seasonal evolution of the mean zonal wind and wave activity in the zonal cross section for the two hemispheres. A copy of this film is available at cost (about \$200) from the authors.

REFERENCE

- Hartmann, D. L. (1976), J. Atmos. Sci., **33**, 1141-1154.
 Hartmann, D. L., C. R. Mechoso and K. Yamazaki (1984), J. Atmos. Sci., **41**, 351-362.
 Hirota, I., T. Hirooka and M. Shiotani (1983), Quart. J. R. Meteo. Soc., **109**, 443-454.
 Hirota, I. and M. Shiotani (1985), Paper No 1.3, in this volume.
 Leovy, C. B. and P. J. Webster (1976), J. Atmos. Sci., **33**, 1624-1638.
 McIntyre, M. E. (1982) J. Meteo. Soc. Japan, **60**, 37-65.
 McIntyre, M. E. and T. N. Palmer (1983), Nature, **305**, 593-600.
 McIntyre, M. E. and T. N. Palmer (1984), J. Atmos. Terr. Phys., **46**, 825-849.
 Shiotani, M. and I. Hirota (1985), Quart. J. R. Meteo. Soc., in press.

2.16 WAVE-MEAN FLOW INTERACTION DURING THE WINTER TO SUMMER TRANSITION IN THE SOUTHERN HEMISPHERE STRATOSPHERE

K. Yamazaki

Forecast Research Division, Meteorological Research Institute,
Tsukuba, Ibaraki, 305, Japan

This paper describes the evolution of the flow and wave-mean flow interactions in the Southern Hemisphere during the period when the final stratospheric warming and the associated reversal of the flow in the upper stratosphere occurred. The spring is the most interesting season as far as the wave-mean flow interaction in the Southern Hemisphere is concerned. The data for this study are NMC analysis of temperature and geopotential fields between 1000 and 0.45 mb for the period August 31 to November 10, 1979. The analysis for the winter season of the same year was reported by HARTMANN et al. (1984).

The time evolution of zonal-mean geostrophic wind at 2 mb and 10 mb is shown in Figure 1. During the early part of the period the stratospheric jet at both levels was centered at about 60°S, and was decelerating. The jet was stronger at 10 mb than at 2 mb. Consistently, at 2 mb, the temperature in the polar region was higher than in middle latitudes.

Rapid changes in the stratospheric circulation occurred during mid-October. There was an acceleration of the flow followed by a rapid deceleration in high latitudes, and a simultaneous warming of the polar region. After the event easterlies appeared at 2 mb south of about 30°S, and the temperature in the polar region became higher than in midlatitudes at 10 mb, at 10 mb and below, westerlies appeared in late November over the polar region.

The zonal mean northward eddy heat flux at 2 mb, 50 mb and 850 mb is shown in Figure 2. The relative maxima in poleward flux at 2 mb seem to be correlated with others that occurred a few days earlier at lower levels. Dotted lines in the figure show the zero-wind line. The eddy activity at 2 mb decreased considerably a few days after the easterlies were established.

Figure 3 shows latitude-height cross sections of zonal-mean wind and E-P diagrams during the mid-October warming event. On October 6 the stratospheric jet core was at about 60°S, 30 mb, and there were easterlies in the lower-subtropical and upper-polar stratosphere. The phase of QBO was easterly in 1979. E-P fluxes in the stratosphere north of 60°S were nearly equatorward and largest in middle latitudes. These large fluxes had relatively strong divergence around 60-70°S and convergence around 40°S. This dipole pattern of wave forcing prevailed during winter (HARTMANN et al., 1984). The convergence was associated with the extension of the easterlies at that time. The divergence brought about the intensification and poleward and upward shift of the jet. These poleward movements of the critical line and jet led to focus planetary wave activities toward the polar stratosphere.

On October 10, E-P fluxes in the stratosphere were more vertical. In particular, they were upward and large in the lower stratosphere about 60°S. In the upper troposphere, E-P fluxes were poleward south of about 40°S. From October 10 to 14, the region of easterlies extended further upward and poleward from the lower-subtropical stratosphere. On October 14, E-P fluxes at middle latitudes were large and upward throughout the atmosphere. A broad region with the strongest E-P flux convergence was apparent in the middle and upper stratosphere. The strong convergence was associated with the large decelerations. From October 14 to 18, the easterlies in the upper stratosphere increased in intensity and extended further down. The summer circulation replaced the

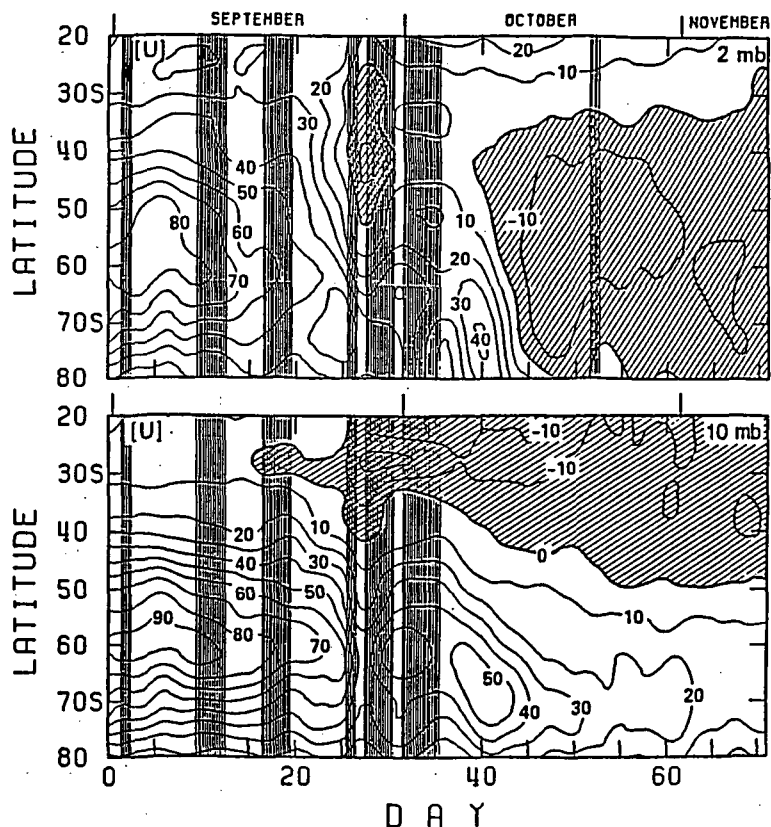


Figure 1. Zonal mean geostrophic wind (m s^{-1}) at 2 mb and 10 mb during the period August 31 - November 10, 1979. Vertical lines indicate times data are missing from the record. Shadings denote easterly regions.

winter circulation above 5 mb at that time. E-P flux on October 18 in the mid-latitude stratosphere were again equatorward, and their divergence was weak. Moreover, E-P flux in the troposphere at middle-latitudes turned equatorward. After the event, the critical line did not move downward until late November.

The E-P diagnosis revealed the intense upward propagating planetary wave activities forced in the troposphere was the main ingredient of this event. The quasi-stationary wave number 1 wave played the major role in this event, while the eastward traveling wave number 2 was secondary (Figures are not shown here). The behavior of the warming event is similar to the stratospheric sudden warming in the Northern Hemisphere in many respects. However, there are interesting differences between this event and a typical N. H. SSW. One is the important role of the equatorial critical line observed in this case, and the other is the shallow vertical extent of the wind reversal.

The equatorial easterlies seem to have played a crucial role in this event. Therefore, let us check the relationship between QBO and the final warming in the Southern Hemisphere. Figure 4 shows the first date when temperature at 30 mb became higher than -3°C or -30°C at Showa station (40°E ,

ORIGINAL PAGE IS
OF POOR QUALITY

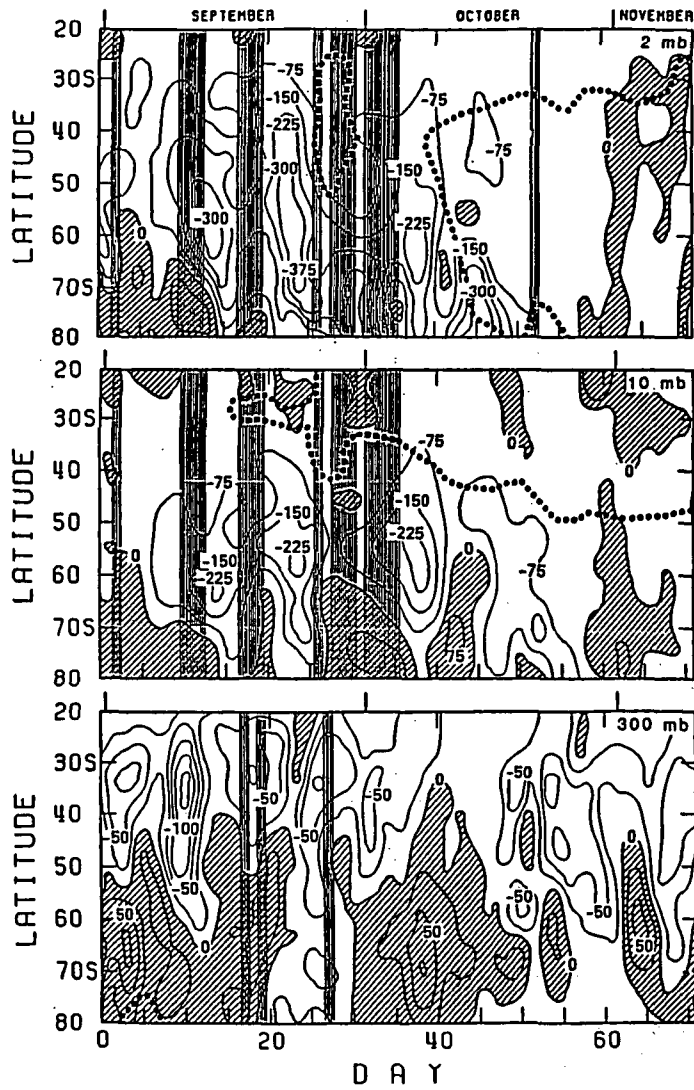


Figure 2. As in Figure 1, except for northward eddy heat flux at 2 mb, 50 mb and 850 mb. The thick dotted lines indicate zero zonal-mean wind.

ORIGINAL PAGE IS
OF POOR QUALITY

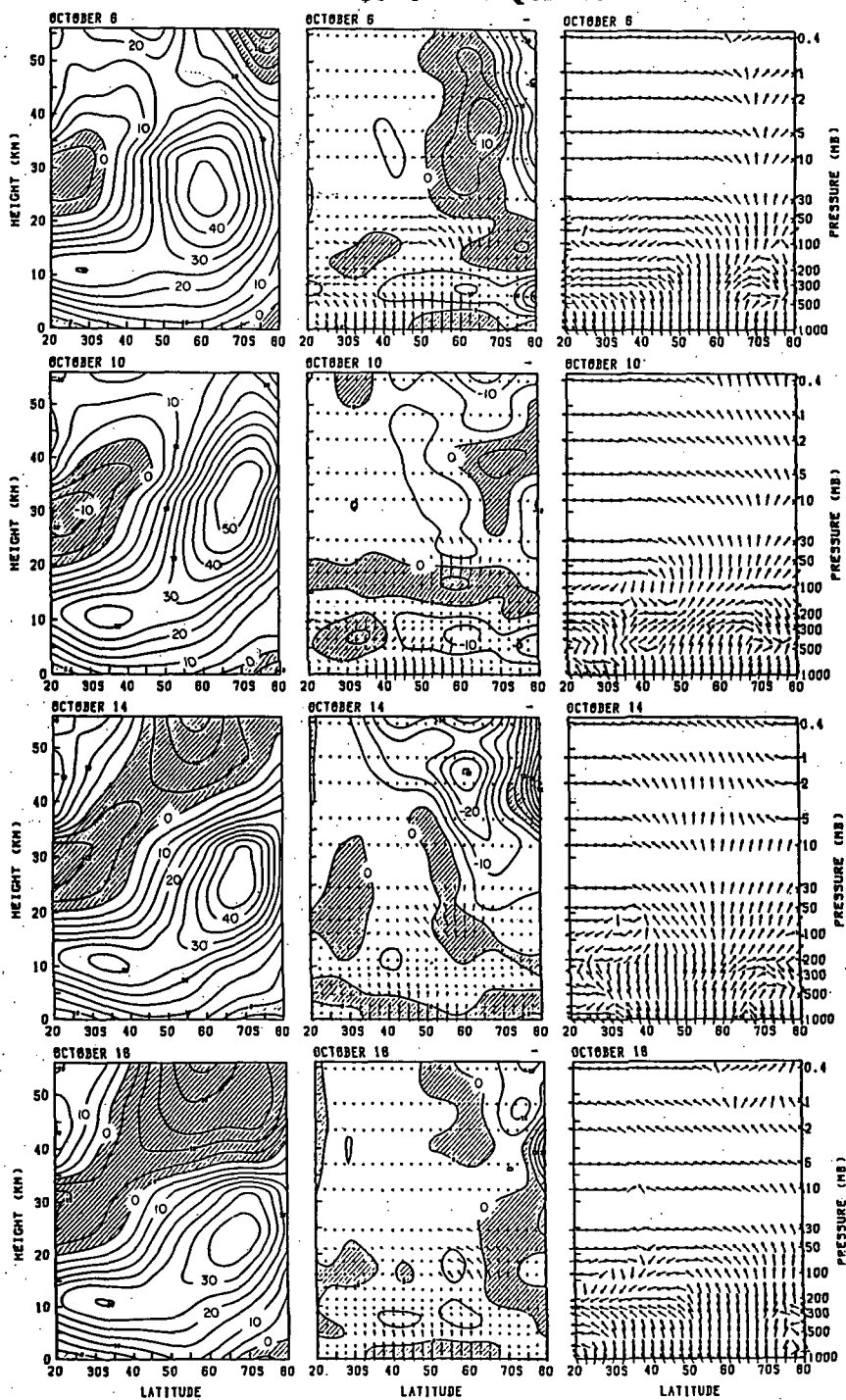


Figure 3. left: Zonal-mean wind. Contour interval is 5 m s^{-1} . middle: E-P diagnosis maps. Arrows are E-P vectors. The lengths of arrows are multiplied by 10 at 100 mb and above so that the arrows in the stratosphere may more easily be seen. The reference arrow (top right of each panel) is $10^{15} \text{ kg m s}^{-1}$. Contours are wave forcing. The interval is $5 \text{ m s}^{-1} \text{ day}^{-1}$. right: E-P flux vectors. The length of arrows is normalized.

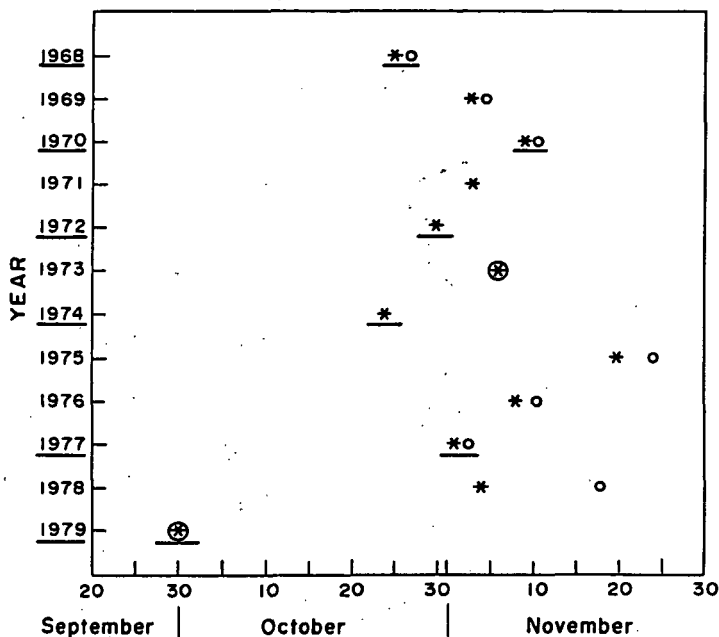


Figure 4. Observed dates of "final warming" at Showa station (40°E, 69°S). "*" denotes the first date when temperature exceeded -35°C at 30 mb at 12Z. An open circle is the same as "*" but for -30 C. The underline indicates the year when the phase of the equatorial QBO (50mb) on October was easterly.

69°S). The figure was plotted from data by MESHIDA et al. (1983). We can see that when the phase of QBO is easterly (underlined year), winter to summer transition tends to take place earlier. Since this figure is based solely on the local observation, further study is needed to confirm this relationship.

REFERENCES

- Hartmann, D. L., C. R. Mechoso, and K. Yamazaki (1984), Observations of wave-mean flow interactions in the Southern Hemisphere, *J. Atmos. Sci.*, **41**, 351-362.
- Meshida, S., K. Tsukamura, Y. Yamamoto, and M. Kosha (1983), Meteorological observation at Syowa Station in 1979 by the 20th Japanese Antarctic Research Expedition, *Antarctic Report*, **78**, 83-116 (in Japanese).

2.17 A NEW MODEL OF RESONANCE IN THE WINTER STRATOSPHERE

Peter H. Haynes

J.I.S.A.O
University of Washington
Seattle, WA 98195

INTRODUCTION

It is generally accepted that the planetary waves observed in the winter stratosphere are primarily a response to dynamical forcing from the troposphere. Nevertheless, the mechanism by which wave amplitudes sometimes become large remains uncertain. It is possible that anomalously large waves in the stratosphere might simply be the result of anomalously large tropospheric forcing. However, it has also been suggested, by TUNG and LINDZEN (1979), that they are a response to a stratospheric-tropospheric cavity being in a near-resonant configuration. This idea has been further developed by PLUMB (1981), who demonstrated that nonlinear self-tuning effects could play an important role in the behavior of such a cavity. Self-tuning may occur when a system starts to one side of resonance, such that the mean-state change induced by growing waves brings the system closer to resonance. Here a new model of the stratospheric cavity is introduced and is then used to re-examine the possibility of wave growth in the real atmosphere and in atmospheric models due to self-tuning effects.

The new model is based on the picture of the winter-time stratosphere which has been revealed by the observations of Ertel's potential vorticity, Q , presented by McINTYRE and PALMER (1983), (1984). Isentropic maps of Q show two rather distinct regions, the first containing the circumpolar vortex, where gradients of Q are large and Rossby waves may propagate easily. Surrounding this is a second, low-latitude region where the gradients are generally weak and where, because the Eulerian-mean flow is comparable with their phase speed, Rossby waves must be continually breaking. McIntyre and Palmer refer to this wave-breaking region as the stratospheric "surf zone". As the waves are observed to grow the relative sizes of these two regions change in time. This leads to the interesting possibility (McINTYRE and PALMER, 1983) that self-tuning, mainly due to irreversible changes in the size of the polar vortex, is taking place.

An essential requirement would be that wave activity is sufficiently confined to the polar vortex region, as it changes in size, by a certain amount of reflection from the surrounding wave-breaking regions. It has been proved that, in the circumstances of interest here, the time-integrated amount of absorption that a wave-breaking region can do is strictly limited (KILLWORTH and McINTYRE, 1985). However, temporary absorption can be expected while the wave-breaking region is entraining new potential contours, which occurs when the wave amplitude grows. In other words, the cavity might be most "leaky" just when the most rapid wave growth is taking place. Whether or not the absorption is sufficient to inhibit wave growth is a question which can only be answered by modeling the phenomenon quantitatively.

MODEL FORMULATION AND MOTIVATION

The prime aim in formulating the model is to allow, somehow, for the effects of large-amplitude transient and breaking Rossby waves. One approach would be to attempt a full-blown numerical simulation in which the complicated small-scale motion, which would almost inevitably arise, was resolved explicitly. However, the demands made on the model used for the simulation, were the results to be accepted unequivocally, would be considerable and would not

doubt require large computational expense. Instead, the simplest possible semianalytical model is formulated so as to include, at least in a qualitatively reasonable way, those processes which appear to be important.

Here, only an outline of the formulation will be given. For details the reader is referred to HAYNES (1983). The key step is to incorporate the fact that the large amplitude of the waves has very different effects in the two regions identified by McINTYRE and PALMER (1983). In the breaking region the deformation of material lines is irreversible and not at all wave-like, so there is no possibility that linear-wave theory can describe this process, even qualitatively. On the other hand, in the jet region, the motion appears to be much more nearly reversible, but nonetheless of large amplitude, manifested by the fact that the whole vortex is, at times, shifted completely off the pole.

The proposed model contains these two regions, separated by a moving interface; in other respects the model is made as simple as possible. Vertical structure is ignored, absolute vorticity replaces potential vorticity, and further, the beta-plane is used, described by Cartesian coordinates x and y . The configuration chosen for the model and shown in Figure 1 is the half-plane $y < 0$, with a rigid corrugated wall at $y=0$ which acts as wave-source. The first region, representing the polar vortex, lies between the wall and the moving interface whose position $y = -\lambda(t)$ is a function of time. In this region wave propagation according to the linearized barotropic vorticity equation is allowed on a basic state where the velocity u_0 and absolute vorticity gradient $\partial q_0 / \partial y$ are taken to be constant in time, corresponding to intuition about the vortex being reversibly displaced, and, for simplicity, constant in space. On the other hand, irreversible changes in the basic state are represented by allowing the width of this region, $\lambda(t)$ to decrease as the wave amplitude increases.

One way of modeling the wave-breaking region would be to assume that the vorticity was constant, so that as the interface moved through the fluid the vorticity in the entire region behind would be mixed instantaneously. Of course, in a real fluid such mixing could not be instantaneous and seems likely to be far from perfect. Nevertheless, the assumption of constant basic-state vorticity will be used in this model, although, as discussed later, a non-zero disturbance part of the vorticity will be allowed so that the wave-breaking region may act as an absorber of wave activity.

The wave-breaking region is assumed to be bounded on its equatorward side by another interface whose position is fixed, at $y = \lambda_0$ and in $y < -\lambda_0$ linear wave dynamics is again assumed to apply. In the counterpart of this equator-most region in the real atmosphere, one might expect there to be easterly winds, which prevent propagation of quasi-stationary Rossby waves. The artificial modeling device adopted to give this effect is to pose the basic-state absolute vorticity constant, leaving the motion in this region irrotational and then imposing that the disturbances must decay as $y \rightarrow -\infty$.

As may be seen in Figure 1, the model assumptions lead to sharp delta-function vorticity gradients at the two interfaces at $y = -\lambda$ and $y = -\lambda_0$. Any displacement of the interfaces therefore induces across them a finite discontinuity in the tangential velocity which must be taken into account when solving the boundary-value problem for the stream function. The model equations therefore have to include the linearized equations describing the interface displacements.

We now return to the problem of specifying the vorticity in the wave-breaking region. In order to allow the model to represent absorption of wave activity, a distribution of disturbance vorticity (with the same harmonic x -dependence as the waves in the jet region) is imagined to be superimposed on

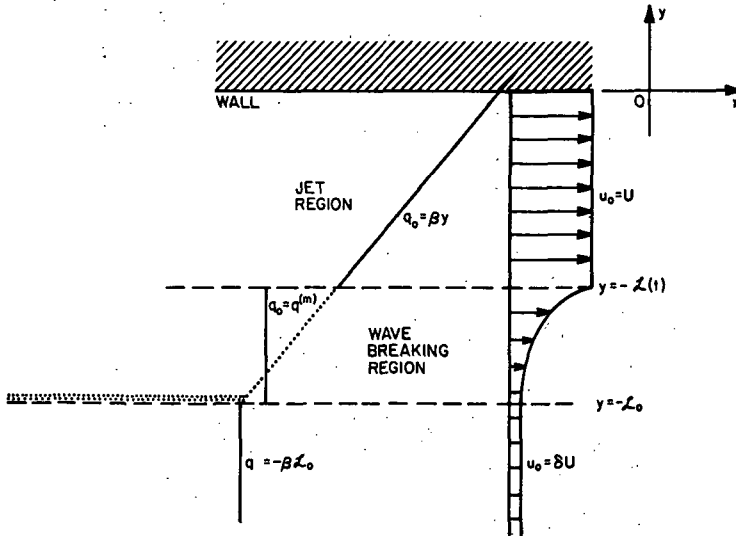


Figure 1. Model configuration, showing basic state velocity (u_0) and absolute vorticity (q_0) fields. The dotted line indicates the absolute vorticity field when $\lambda = \lambda_0$, including a δ -function of strength $-u(1-\delta)$ at $y = -\lambda_0$.

the constant basic state vorticity. This disturbance vorticity is not required to satisfy any dynamical equation, but is linked to the meridional velocity at the edge of the wave-breaking region. This assumption may be qualitatively correct for present purposes if we regard this vorticity as being "injected" into the wave-breaking region, as is seen in the observations of Q, and recall from nonlinear critical layer theory that it is the correlation between meridional velocity and vorticity which allows absorption. This modeling device also allows the effective absorptivity to be varied, perhaps choosing it to conform to the estimate given by KILLWORTH and MCINTYRE (1985), hereafter referred to as "normal" absorptivity, or to be higher or lower than this.

To complete the model formulation it remains to link the width of the wave-breaking region to the size of the waves in the jet region. It is plausible from kinematical arguments that the width is the order of the rms particle displacement at the interface, at $y = -\lambda(t)$. However, if the wave-breaking region is of zero thickness then the system is barotropically unstable. Rather arbitrarily then, the increase in the width of the wave-breaking region from that which corresponds to marginal stability, $\lambda_0 - \lambda_c$, say, is set equal to the rms particle displacement at the interface. This is sufficient to close the model and allow solution of the governing equations.

MODEL RESULTS AND CONCLUSIONS

The nonlinearity of the model equations, even though it only enters through the relation between the displacement and the width of the wave-breaking region, makes it impossible to find a general time-dependent solution. However, it is straightforward to find steady-state solutions, on the assumption that they were reached via monotonic growth. For given values of the external parameters, each steady state may be characterized by the value of the forcing, or of the width of the jet region. Plotted on a graph where each of these two quantities is a coordinate, the possible steady states of the system lie on a particular curve, a typical example of which is shown in Figure 2.

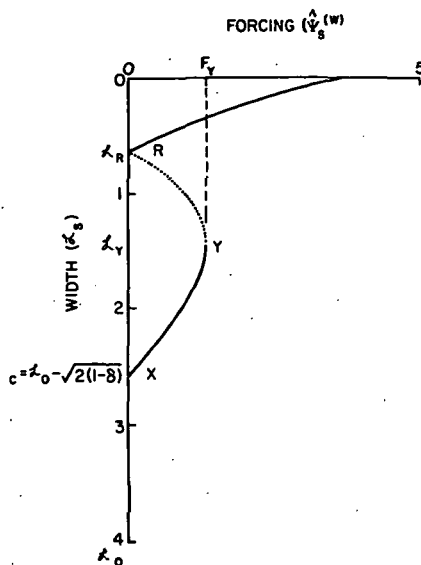


Figure 2. Graph of forcing amplitude against width, both nondimensionalised, in a steady-state configuration. The length-scale used for nondimensionalisation was equal to model parameters were chosen to correspond very roughly with a jet centered at 60°N and a wave number 1 disturbance.

The curve always takes this form providing that there is some width of the jet region, less than λ_c , for which the system is resonant. Then zero forcing is required to maintain this steady state and also that when the width of the jet region is equal to λ_c , so it follows that there is a range of values of the forcing for which there are multiple steady states. In fact it may be shown that the states on the arc YR in Figure 2 are unstable, and those on the rest of the curve are stable. This instability is a consequence of the self-tuning behavior.

It appears from the configuration of the steady states that a drastic change must take place in the system if the forcing is slowly increased past the value F_Y . This was confirmed by performing a number of numerical integrations of the governing equations. The results from two typical experiments where the forcing was increased to a value greater than F_Y are shown in Figures 3(a) and 3(b). As may be seen, soon after the forcing has passed this threshold value, there is a rapid increase in the wave amplitude, and a consequent decrease in the width of the jet region. The sudden change also generates a substantial free wave, which propagates eastward as the jet region is then narrower than in the resonant configuration. The difference between the two experiments (a) and (b) is that in (a) the absorptivity of the wave-breaking region is set to the normal value, while in (b) it is set to twice that value. However, even in case (b) the time for the wave to double in size is still only about a week.

This experiment and many others that were performed, some with earlier versions of the model in which details of the formulation differed, all suggest

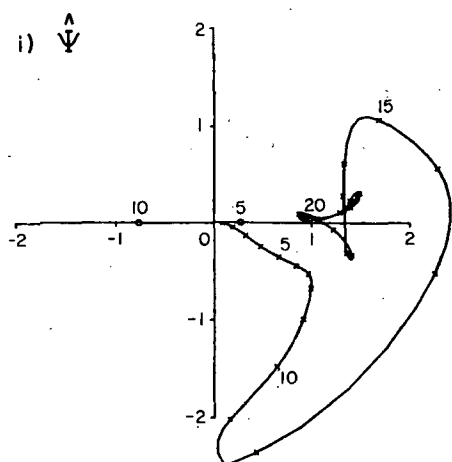


Figure 3(a) "normal" absorptivity

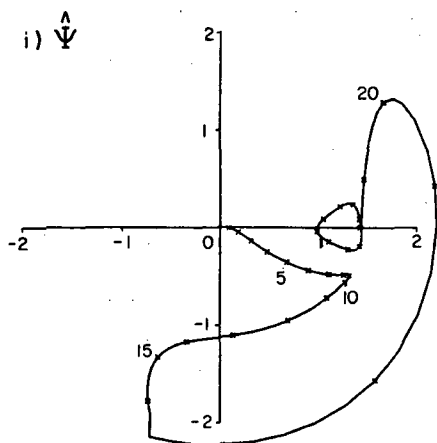
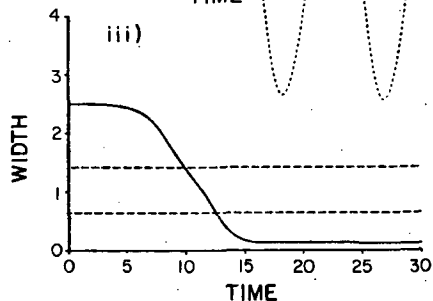
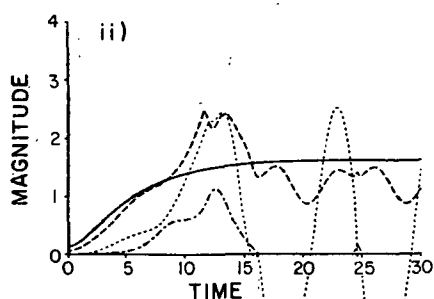


Figure 3(b) twice "normal" absorptivity

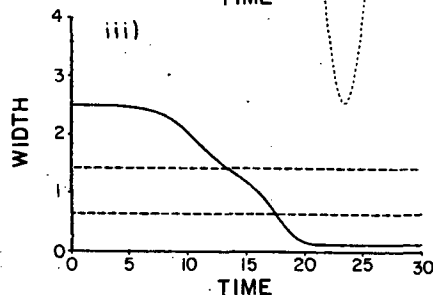
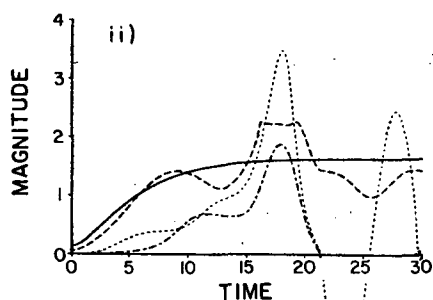


Figure 3(a) and 3(b)

Each of Figures 3(a) and 3(b) shows the time evolution of various nondimensional model variables, in the following manner:

i) polar plot of the stream function, i.e., the longitude and amplitude of the high pressure ridge at a particular latitude. Crosses are marked at intervals of one time unit, with every fifth one labelled. In 3(a) the circles denote the steady-state value for the appropriate instantaneous width and forcing.

ii) the following quantities against time:
solid line - amplitude of forcing; dashed line - amplitude of stream function; dotted line - EP flux into system at wall; dash-dot line - rate of irreversible loss of wave activity from system through wave breaking.

iii) nondimensional width, χ_s , of the jet region, against time. Dashed lines indicate the values of χ_R and χ_L , as shown in Figure 2. One nondimensional time unit corresponds to about one day.

that the wave-growth in the model is quite robust to increasing the absorptivity of the wave-breaking region to two or three times the "normal" value. This is at least a first indication that wave-breaking regions in the real atmosphere may be sufficiently reflective to sustain self-tuning or other resonance-associated effects.

REFERENCES

- Haynes, P. H. (1983), Nonlinear Rossby wave critical layers in the stratosphere, Ph.D. Thesis, University of Cambridge.
- Killworth, P. D., and M. E. McIntyre (1985), Do Rossby-wave critical layers absorb, reflect, or over-reflect? To be submitted to J. Fluid Mech.
- McIntyre, M. E., and T. N. Palmer (1983), Breaking planetary waves in the stratosphere, Nature, **305**, 593-600.
- McIntyre, M. E., and T. N. Palmer (1984), The "surf zone" in the stratosphere, J. Atmos. Terr. Phys., **46**, 825-850.
- Plumb, R. A. (1981), Instability of the distorted polar night vortex: a theory of sudden stratospheric warmings, J. Atmos. Sci., **38**, 2514-2531.
- Tung, K. K., and R. S. Lindzen (1979), A theory of stationary long waves. Part I: A simple theory of blocking, Monthly Weather Rev., **107**, 714-734.

2.18 TRANSIENT RESPONSE TO LOCALIZED EPISODIC HEATING IN THE TROPICS

Murry L. Salby

Department of Astrophysical, Planetary and Atmospheric Sciences
University of Colorado, Campus Box 391
Boulder, CO 80309

Rolando R. Garcia

National Center for Atmospheric Research
P.O. Box 3000
Boulder, CO 80307

It is generally recognized that equatorial disturbances in the lower stratosphere are excited by convective latent heat release associated with the Inter Tropical Convergence Zone (ITCZ). Recently, attention has also focused on tropical convection with regard to extratropical teleconnection patterns (WALLACE and GUTZLER, 1981; HOSKINS and KAROLY, 1981). Unlike equatorial waves which are trapped about the equator but propagate vertically, the latter extend well out of the tropics but are barotropic. They have been most widely discussed in connection with long-term climatological features. Both types of disturbances have been examined largely from the standpoint of steady "monochromatic" forcing, in the latter case zero frequency or time-mean heating. However, tropical convection as revealed by recent geostationary satellite imagery is anything but regular, surely not steady. Much of the heating variance is concentrated spatially within three localized convective centers: Indonesia, the Amazon, and the Congo. Convective activity within these regions undergoes an irregular evolution over the span of a couple of days. It involves a rather broad spectrum of spatial and temporal scales. ORLANSKI and POLINSKY's (1977) analysis of cloud brightness over the Eastern Atlantic and Africa suggests a characteristic time scale of 3-4 days and correlations scales in latitude and longitude of approximately 30° .

We explore here the large-scale dynamical response to such convective activity. Since the latter cannot be described by any simple heating signature, we relax the conventional problem whereby the forcing is presumed known. Instead we consider heating which evolves randomly in space and time. In particular we consider a second-order stationary stochastic process whose variance is localized in a region such as Indonesia. The dynamical problem is solved in a spherical, generally baroclinic atmosphere using the linearized Primitive Equations. Solutions emerge as a stochastic process, involving Hough harmonics, whose covariance statistics depend upon those of the applied random heating. We consider the problem in two elements: (1) short-time near-field behavior, controlled largely by excitation and (2) far-field response, involving the modification of initial disturbances by refractive and absorptive influences.

The short-time near-field behavior may be described in terms of a Hough space-time spectrum, determined by the projection of the random heating onto 3-dimensional Hough harmonics. These range continuously over frequency and vertical wave number. The vertical projection coefficient over vertical wave number (Figure 1) exhibits two principal components of response: (1) a projection response peaked about vertical wavelengths twice the depths of the heating and (2) a discrete barotropic response associated with an equivalent depth of 10 km and atmospheric normal modes. These features are robust; they appear virtually unchanged for rather different heating profiles (Figure 1). The projection response corresponds to large values of Lamb's parameter, and hence, modes which are trapped about the equator but radiate vertically away from the

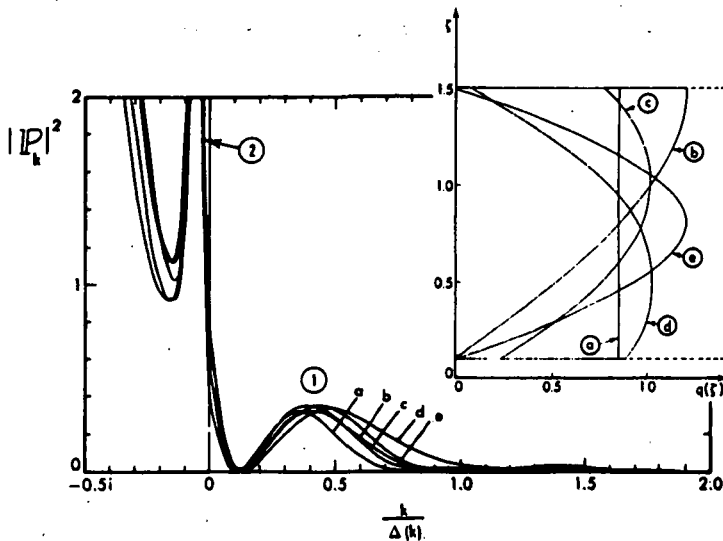


Figure 1.

source (Figure 2). The barotropic response, on the other hand, corresponds to small values of Lamb's parameter, and thus modes which extend well out of the tropics but are vertically trapped. From the synoptic viewpoint, modes corresponding to these two ingredients of the response synthesize into disturbances (Figure 3) which (1) are confined to the tropics but radiate vertically out of the source region and (2) disperse energy laterally out of the tropics but displace the entire atmospheric column in phase.

Corresponding to the vertical scale selection of the projection response is a discrimination in frequency for individual modes according to their dispersion relationships (i.e., between vertical wavelength and frequency). Likewise, for a particular mode, propagation of wave activity in the zonal-height plane is confined to a limited range of angles. Variance for the wave number 1 Kelvin and gravest symmetric Rossby modes are plotted in Figure 4 in polar form against group velocities and periods. While response in both components is restricted to fairly narrow lobes, dispersion is evidenced by the divergence of rays. The dispersive character of the combined disturbance is even more strongly indicated by other wave numbers which propagate at entirely different angles.

In the far-field the initial disturbance is modified by refraction and absorption. Of these effects the latter, through radiative damping in the stratosphere, exerts an important and particularly robust influence. Because it acts differentially on frequencies in the projection continuum (1), which are also of shorter vertical scale, radiative damping has the effect of absorbing in slow components relative to faster species. As a consequence, the projection continuum shifts to progressively higher frequencies with altitude above the source. Such behavior emerges in a variety of wind configurations just as conspicuously as in a resting atmosphere. It explains the striking correspondence between HAYASHI et al. (1984) analysis of a GCM integration under "annual-mean" conditions with satellite observations (SALBY et al., 1984) during radically different solstitial conditions. An example, calculated in solstice conditions with an easterly phase of the QBO, is shown in Figure 5. Eastward variance over the equator emerges above the heating (1.5 scale

MODAL STRUCTURE

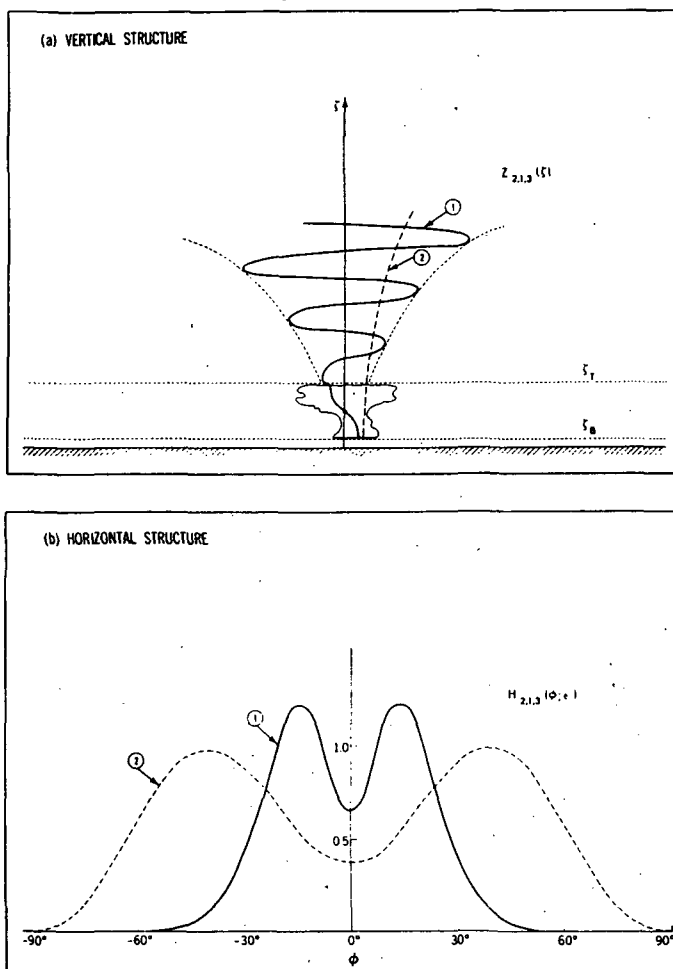


Figure 2.

heights) centered at a period of 12 days and corresponds to WALLACE and KOUSSKY's (1968) Kelvin wave involved in the QBO (LINDZEN and HOLTON 1968; HOLTON and LINDZEN, 1972). By the middle and upper stratosphere the eastward variance, although still localized in frequency, is shifted to HIROTA's (1978, 1979) 5-8 day Kelvin wave. By stratopause and the mesosphere, Kelvin wave variance has moved out to periods of 4 days and shorter corresponding to the ultra-fast Kelvin wave reported in satellite observations (SALBY et al., 1984). Just how quickly the slow components, dominant at lower levels, are absorbed depends upon the nature of the winds, e.g., QBO in the lower stratosphere. At westward frequencies the barotropic component corresponding to the 5-day wave (MADDEN and JULIAN, 1972a; HIROTA and HIROOKA, 1984) is evident at all heights.

Amplitude and phase behavior for these components are in agreement with theoretically expected Kelvin and Rossby wave structures. The wave number 1 5-day eastward component of the response (Figure 6) is symmetric about the equator, nearly Gaussian in latitude, and penetrates to at least the mesopause.

Dispersion of Tropically Excited Disturbances

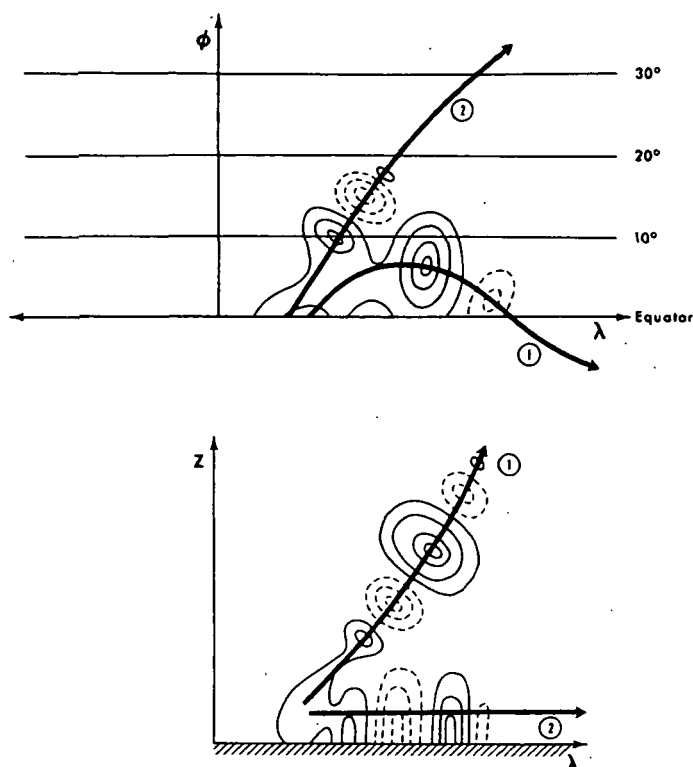


Figure 3.

Phase structure tilts eastward monotonically, corresponding to roughly a 30 km vertical wavelength which propagates downward. The EP flux is also centered on the equator and is directed downward, indicating an upward flux of westerly momentum.

Although these covariance statistics, e.g., variance, coherence, relative phase, probably afford the greatest fidelity in describing the complex response to tropical convection, it is nevertheless desirable to construct a time-varying description of a particular episode. Such behavior may be regarded as a "cardinal realization" of the stochastic response. It is defined by choosing a simple heating transient whose power spectrum is identical to that of the random heating, in which case the stochastic forcing may be constructed by random superposition of the simple transient. For a simple localized heat pulse, the response emerges in the form of a wave packet which disperses away from the source. The cardinal realization corresponding to the Kelvin variance shown in Figure 4 is presented in Figure 7. Heating used to define this episode is localized in longitude and latitude by 40 and 20°, respectively, and consists of a Gaussian pulse from $t = -3.0$ to $+3.0$ days. At $t = 0$ a wave packet is emanating from atop the heating to the east. Yet faster, larger vertical wavelength components have already reached the mesosphere at this stage. As the heating scenario evolves, the wave packet propagates dispersively to the east and vertically out of the source region. Longer vertical wavelength components, propagating at higher phase speeds, leave slower, shorter vertical

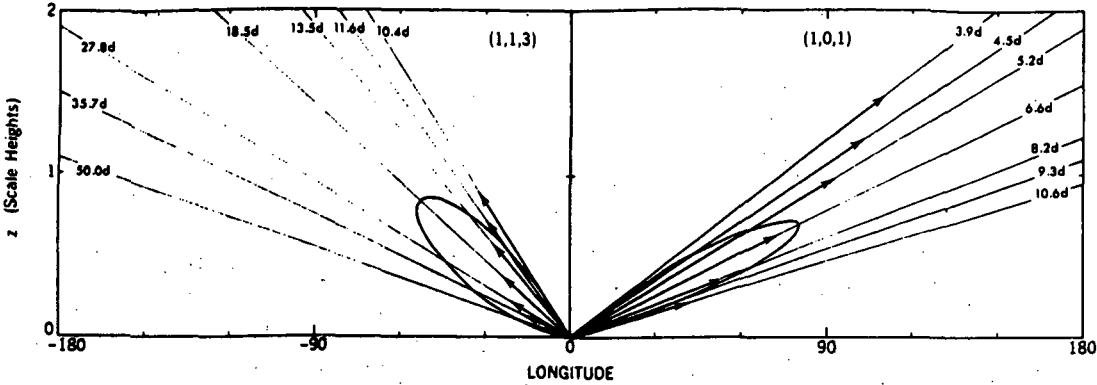


Figure 4.

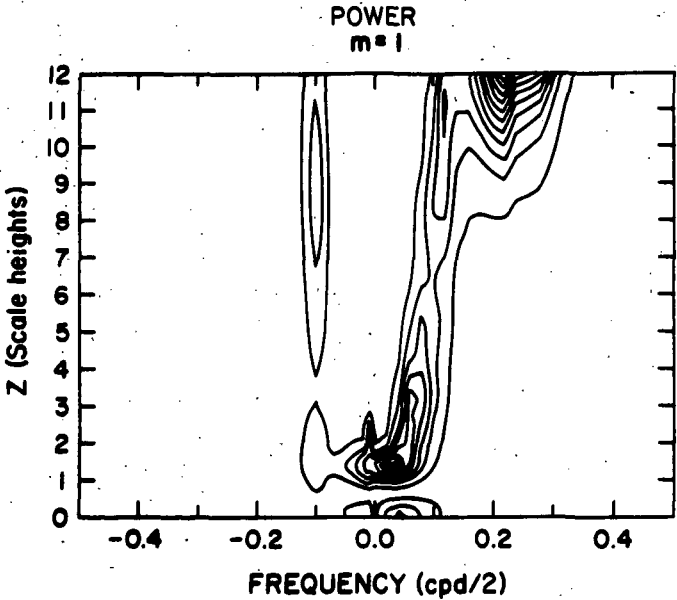


Figure 5.

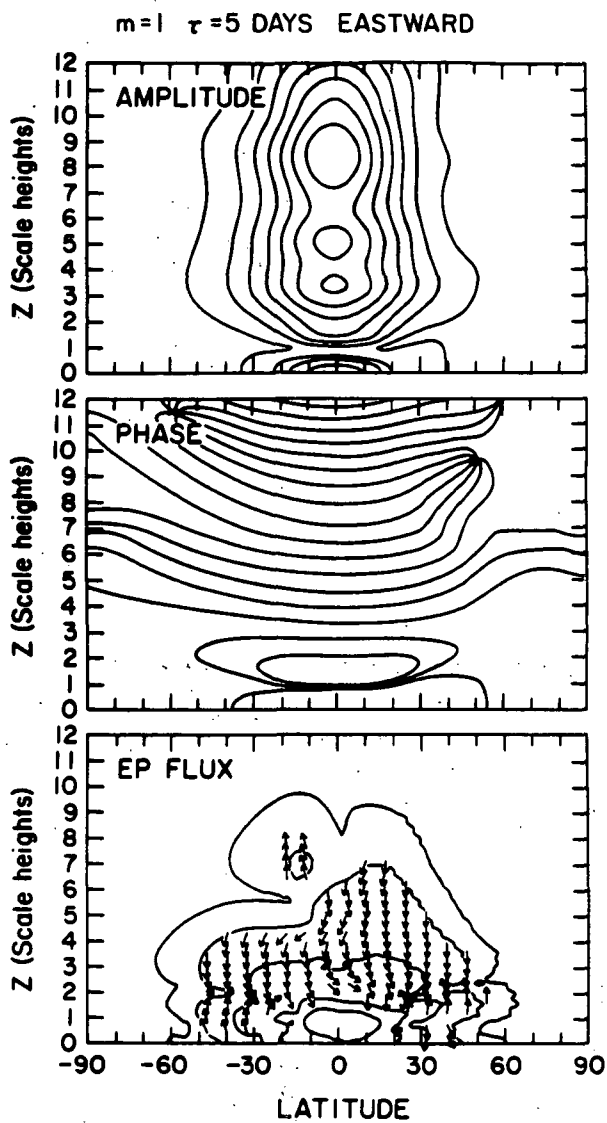


Figure 6.

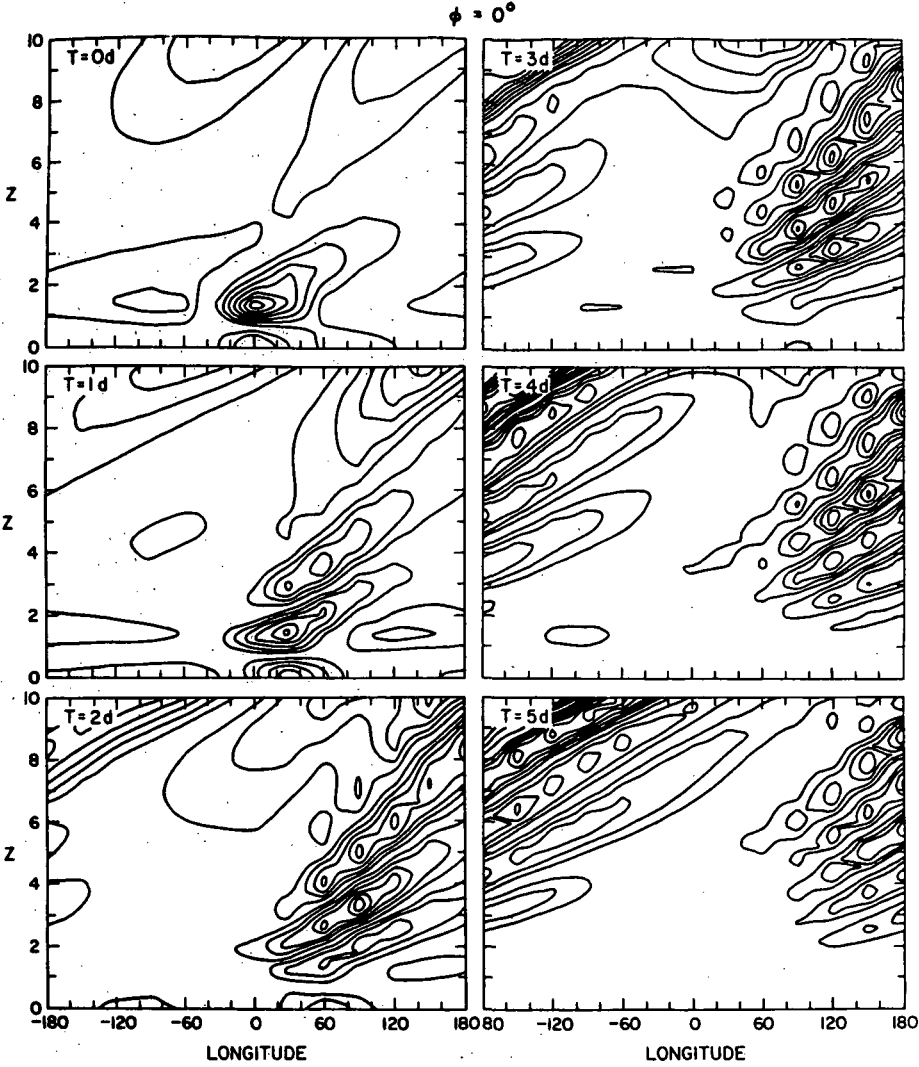


Figure 7.

wavelength disturbances behind. The latter eventually reach the uppermost altitudes as is indicated by a gradual rotation of phase surfaces at these levels.

Although we have focused here expressly on fast tropical forcing, indicative of convection within the ITCZ, there is another more gradual element of tropical heating, associated with the seasonal translation of monsoon and convective activity between the hemispheres. The fast heating variability is presumably superimposed upon this more gradual component of global convection. When such slow heating is prescribed, the response still emerges in the form of two components: a projection response and the barotropic response. However, in this case, the equatorial response is confined to the troposphere because of damping. The Kelvin mode assumes the form of a damped transient Walker circulation which migrates eastward out of Indonesia, traverses the Pacific, and eventually collapses. It captures the salient features of MADDEN and JULIAN's (1972b) 40-50 day tropical disturbance. The barotropic response has the form of a Rossby wavetrain, which propagates into one or both hemispheres, dependent upon details of the heating and mean wind, along great circle routes as in HOSKINS AND KAROLY's (1981) barotropic calculations. At higher levels this wavetrain is dispersed by the strong circumpolar flow into zonally broad disturbances involving only wave numbers 1 and 2 in the stratosphere.

* The National Center for Atmospheric Research is sponsored by the National Science Foundation.

REFERENCES

- Hayashi, Y., D. Golder, and J. Mahlman (1984), Stratospheric and mesospheric Kelvin waves simulated by the GFDL "SkyHI" general circulation model, J. Atmos. Sci., **41**, 1971-1984.
- Hirota, I. (1978), Equatorial waves in the upper stratosphere and mesosphere in relation to the semianual oscillation of the zonal wind, J. Atmos. Sci., **35**, 714-722.
- Hirota, I. (1979), Kelvin waves in the equatorial middle atmosphere observed by Nimbus-5 SCR, J. Atmos. Sci., **36**, 217-222.
- Hirota, I. and T. Hirooka (1984), Normal mode Rossby waves observed in the upper stratosphere, Part I: First symmetric modes of wavenumbers 1 and 2, J. Atmos. Sci., **41**, 1253-1267.
- Holton, J., and R. Lindzen (1972), An updated theory of the quasi-biennial cycle of the tropical stratosphere, J. Atmos. Sci., **27**, 1076-1080.
- Hoskins, B. and D. Karoly (1981), The steady linear response of a spherical atmosphere to thermal and orographic forcing, J. Atmos. Sci., **38**, 1179-1196.
- Lindzen, R. and J. Holton (1968), A theory of the quasi-biennial oscillation, J. Atmos. Sci., **25**, 1095-1107.
- Madden, R. and P. Julian (1972a), Further evidence of global-scale 5-day pressure waves, J. Atmos. Sci., **29**, 1464-1469.
- Madden, R. and P. Julian (1972b), Description of global-scale cells in the tropics with a 40-50 day period, J. Atmos. Sci., **29**, 1109-1123.
- Orlanski, I. and L. Polinsky (1977), Spectral distribution of cloud cover over Africa, J. Atmos. Soc. Japan, **55**, 483-493.
- Salby, M., D. Hartmann, P. Bailey, and J. Gille (1984), Evidence for equatorial Kelvin modes in Nimbus-7 LIMS, J. Atmos. Sci., **41**, 220-235.
- Wallace, J. and V. Kousky (1968), Observational evidence of Kelvin waves in the tropical stratosphere, J. Atmos. Sci., **25**, 900-907.
- Wallace, J. and P. Gutzler (1981), Teleconnections in the geopotential height field during the Northern Hemisphere winter, Monthly Wea. Rev., **109**, 785-812.

2.19 ROSSBY WAVETRAINS IN THE STRATOSPHERE FORCED BY LOCALISED DISTURBANCES IN THE TROPOSPHERE

C. J. Marks

Department of Atmospheric Physics
University of Oxford, U. K.

A. O'Neill and V. D. Pope

Meteorological Office, Bracknell, U. K.

INTRODUCTION

There have been a number of studies which have linked elements of the stratospheric circulation with particular localised features in the tropospheric circulation (e. g., HAYASHI, 1981; O'NEILL and TAYLOR, 1979). This suggests a study of the response of the stratosphere to forcing by localised disturbances in the troposphere.

We use a multilevel, primitive equation model of the stratosphere and mesosphere (described by BUTCHART et al., 1982) the height of whose lower boundary at 300 mb can be prescribed. Localised height disturbances which grow to steady amplitude are applied at this lower boundary, and the response of the initially axially symmetric stratosphere is studied. The perturbation, centered at 45°N , has a Gaussian distribution with a half width of 15° , corresponding roughly to the size of persistent troughs and blocking ridges in the troposphere. The forcing is nearly at full amplitude 10 days after being switched on, and thereafter remains steady. Two types of experiments are conducted: in one the forcing is of small amplitude (100 gpm) and in the other it is of large amplitude (600 gpm). These pairs of experiments are compared to determine how nonlinear processes affect the perturbation fields. This is done locally by defining the perturbation response to the forcing as an anomaly, i.e., as a departure from the response in a controlled experiment in which no asymmetric forcing was applied at the lower boundary of the model. Experiments have been conducted for a number of atmospheric states obtained as zonal means of observations made by a stratospheric sounding unit (SSU). In this summary, we outline results for the zonal mean flow on January 19, 1982.

The zonal mean winds for the Northern Hemisphere are shown in Figure 1. Figure 2 shows the associated distribution of Ertel's potential vorticity, Q , on the 850 K isentropic surface (near 10 mb, about 30 km) along with the wind vectors on the same surface. For this case, Q decreases monotonically from the pole to middle latitudes where there is a band where the meridional gradient is weakly reversed (shaded in the figure). The zero-wind contour, marked by the dashed line, is embedded in this region of reversed gradient, a point which should be noted for the interpretation of results. Where winds are westerly, linear theory predicts that stationary Rossby waves can only propagate in regions where Q increases towards the pole.

RESULTS AND CONCLUSIONS

Localised disturbances in the troposphere generate Rossby wavetrains which propagate upwards and downstream in the stratosphere. This is shown for a small-amplitude perturbation in Figure 3.

The meridional distribution of potential vorticity, Q , in the basic state influences the propagation of Rossby wavetrains of small amplitude. In particular, a region where the meridional gradient of Q is negative at midlatitudes

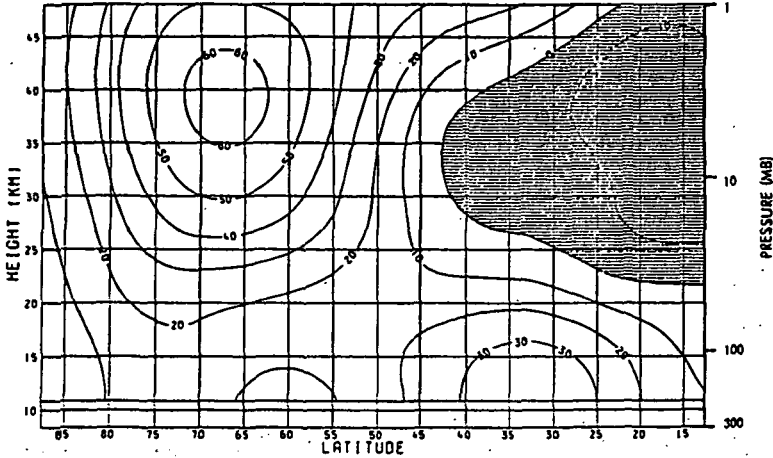


Figure 1. Cross section of zonal mean wind (ms^{-1} with easterlies shaded) for the Northern Hemisphere on January 19, 1982. On this and other vertical sections, the height coordinate, Z , is given by $Z = H \ln(1000/P)$ where P is the pressure in mb and $H = 6.95 \text{ km}$.

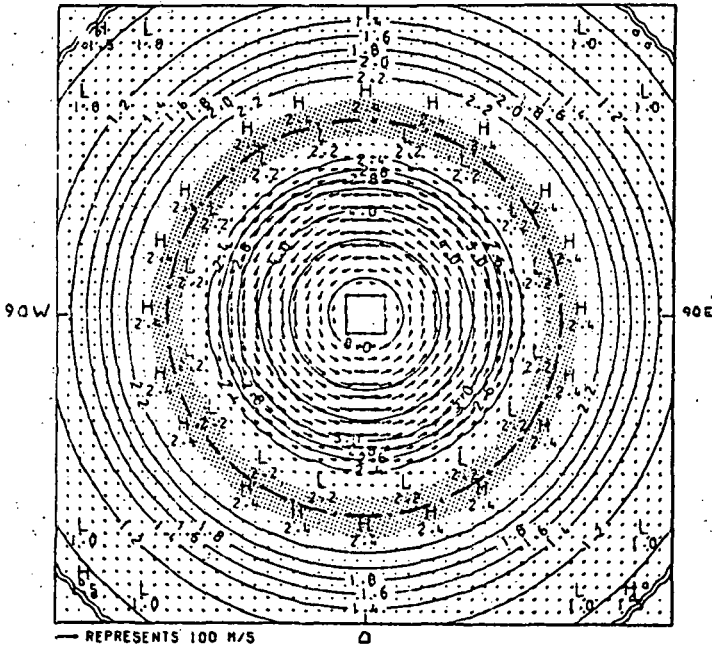


Figure 2. Polar-stereographic map of Ertel's potential vorticity, Q , and winds on the 850 K isentropic surface of the initial state shown in Figure 1. The units are $10^{-4} \text{ km}^2 \text{ kg}^{-1} \text{ s}^{-1}$. The region where the poleward gradient of Q is negative is finely dotted, and dashed and dotted curve gives the location of the zero-wind line. In the above units, the contour interval is 0.2 between values 1 and 3, while the interval is 1 for values greater than 3. The frame surrounding the figure is tangential to latitude 20°N .

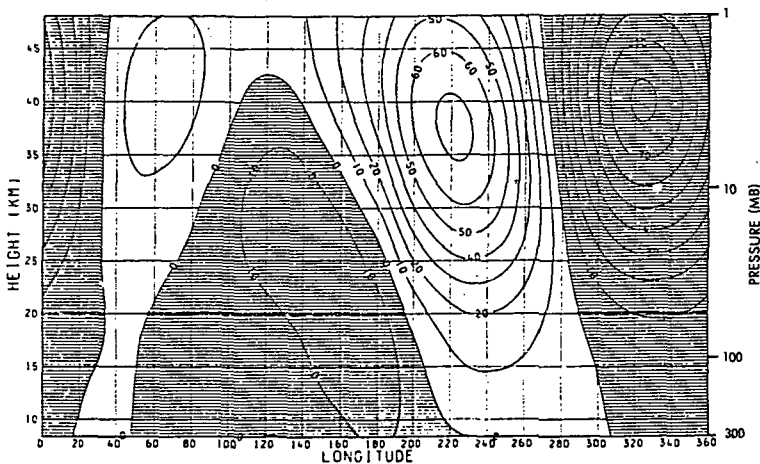


Figure 3. Longitude height section at 62.5°N of the perturbation field in geopotential height for day 11 of the experiment with a "low" of amplitude 100 gpm at the lower boundary. The perturbation field is scaled by a factor of 6 for comparison with the experiment where the forcing has amplitude 600 gpm (not included here). The units are geopotential dekametres and negative values are shaded.

in the stratosphere acts as an "over-reflecting" barrier, confining the wave-train to higher latitudes as though the perturbation was propagating downstream in a channel. This interpretation is made by observing that the Eliassen-Palm fluxes point polewards and diverge from the region where the gradient of Q is reversed.

The use of linear arguments is justified by noting that the perturbation response changes sign over most of the domain studied when the sign of the forcing is altered.

Nonlinearities in the vicinity of the zero-wind line are confined meridionally owing to the smallness of the perturbation amplitudes.

The properties of the large-amplitude wavetrain cannot be explained beyond a certain time using linear theory. Rather, the contours of Q on isentropic surfaces exhibit extreme and irreversible buckling, as shown in Figure 4 for an experiment with large-amplitude forcing. McINTYRE and PALMER (1983, 1984) refer to this phenomenon as "wave breaking". Wave breaking occurs near the initial location of the zero-wind line, and is an inherently nonlinear phenomenon.

For the basic state shown in Figures 1 and 2, the evolution of wave breaking is determined by the fact that the zero-wind line is initially embedded in a region where the meridional gradient of Q is negative. The evolution begins with an "over-reflecting" stage (when EP fluxes diverge and point polewards near the region where the gradient of Q is reversed) followed by an "absorbing" stage (when EP fluxes converge and point equatorwards). It appears that the associated strong deformation of Q contours inhibits the downstream propagation of the disturbance.

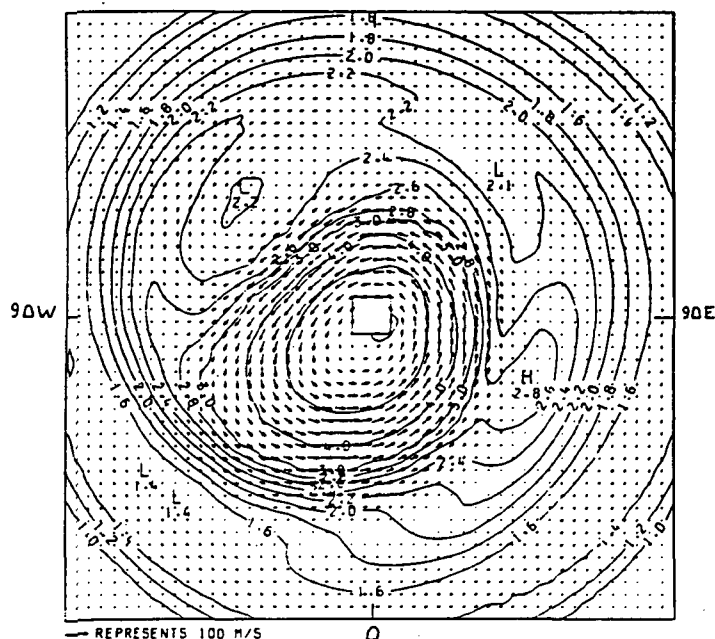


Figure 4. Polar-stereographic map of Ertel's potential vorticity, Q , and winds on the 850 K isentropic surface on day 16 for the experiment with a "low" of 600 gpm at the lower boundary. Units and contour intervals as in Figure 2.

When the zero-wind line is embedded in a region where (the modulus of) Q decreases monotonically towards the equator, the EP fluxes converge and initially point equatorwards near the zero-wind line. This initial absorbing stage is not followed by a reflecting or over-reflecting stage in our experiments. For more details see Marks et al. (to be submitted).

A feature of the breaking regions revealed by our maps of Q is that they widen considerably with time. This is in accord with a key prediction of theories of critical regions which take their full nonlinear nature into account (KILLWORTH and McINTYRE, 1985). These broad regions of nonlinearity mean that we must treat with caution conclusions made using diagnostics taken from linear theory. An examination of isentropic maps of Ertel's potential vorticity is therefore recommended before interferences about wave propagation are made.

REFERENCES

- Butchart, N., S. Clough, T. Palmer and P. Trevelyan (1982), Simulations of an observed stratospheric warming with quasi-geostrophic refractive index as a model diagnostic, *Quart. J. Roy. Met. Soc.*, **108**, 475-502.
- Hayashi, Y. (1981), Vertical-zonal propagation of a stationary planetary wave packet, *J. Atmos. Sci.*, **38**, 1197-1205.
- Killworth, P. and M. McIntyre (1985), Do Rossby wave critical layers absorb, reflect or over-reflect? To be submitted to *J. Fluid. Mech.*
- Marks, C. J., A. O'Neill and V. D. Pope, Rossby wavetrains in the stratosphere forced by localised disturbances in the troposphere, to be submitted.

McIntyre, M. and T. Palmer (1983), Breaking planetary waves in the stratosphere, Nature, 305, 593-600.

McIntyre M. and T. Palmer (1984), The surf zone in the stratosphere, J. Atmos. Terr. Phys., 2, 825-849.

O'Neill, A. and B. Taylor (1979), A study of the major stratospheric warming of 1976-77, Quart. J. Roy. Met. Soc., 105, 71-92.

2.20 LOW-FREQUENCY DYNAMICS OF QUASI-GEOSTROPHIC WAVES IN A MIDLATITUDE CHANNEL AND THE EFFECTS OF TROPICAL INFLUENCE

K. K. Tung and A. J. Rosenthal

M.I.T., Mathematics Department
Cambridge, MA 02139

It is known that both the zonal mean flow and stationary waves in the stratosphere have large variabilities from month to month and from year to year (see GELLER et al., 1984). One plausible mechanism that can account for these variabilities is the interaction between the forced stationary waves and the mean zonal flow. Given the large energy source contained in the stationary waves which are forced in the lower atmosphere, they are probably responsible for inducing the bulk of the variability in the mean flow in the stratosphere. Variability in the mean flow can in turn produce variability in the stationary wave amplitudes due to the possible sensitivity of wave response in the stratosphere to the configuration of the wave guide determined by the mean flow (see TUNG and LINDZEN, 1979; for a counterpoint see JACQMIN and LINDZEN, 1985).

A major aim of the present work is to assess the likely causes for the low-frequency variability of the stationary waves-mean flow system in extra-tropical latitudes. (By concentrating only on the low-frequency portion of the variability, we will not be able to model the more rapid changes, such as sudden warming, in adequate detail.) We divide, in an admittedly artificial fashion, the causes of variability into "internal" and "external" ones. Internal mechanisms include transition between equilibria and vacillation cycles, while mechanisms external to the midlatitude system include eddy heat and momentum fluxes from the tropics and the Hadley circulation forced in the tropics.

We consider quasi-geostrophic flows in a midlatitude channel governed by the following pseudo-potential vorticity equations:

$$\frac{\partial}{\partial t} P\psi + J[\psi, P\psi + f] = f_0 \left(\frac{\partial}{\partial z} - \frac{1}{H_0} \right) (Q/\Gamma) \quad (1)$$

$$\text{where } P \equiv \nabla^2 + \frac{H_0 f_0^2}{R} \left(\frac{\partial}{\partial z} - \frac{1}{H_0} \right) \frac{\partial}{\partial z} \frac{1}{\Gamma}, \quad z \equiv H_0 \ln \frac{p^\infty}{p}$$

ψ : stream function, Q : diabatic heating, Γ : static stability

To isolate the low-frequency portion of the flow, TUNG and ROSENTHAL (1985a) applied a running-time mean to (1). For simplicity in the present short presentation (and also because we have not made an adequate assessment of the effect of the transient eddy-flux terms for the stratosphere), we shall omit such an operation here. In any case, if one is interested only in the low-frequency evolution of the stationary waves, it seems justified to drop the first term, $\frac{\partial}{\partial t} P\psi$, compared to a part of the second term involving the advection or the wave potential vorticity by the mean zonal flow, $U \frac{\partial}{\partial z} P\psi$. The same approximation cannot be adopted for the zonal mean equation, because the advection or the zonal mean potential vorticity by the mean zonal flow is zero. So the idea is to treat the variability of the stationary waves as arising from quasi-steady adjustments to the time varying mean flow and ignore the higher frequency transients generated from initial value problems.

The lateral channel boundary conditions are that the normal velocity due to the stationary geostrophic waves vanish, i.e.,

$$\frac{\partial \psi}{\partial x} = 0 \text{ at } y = y_1 \text{ and } y_2 \quad (2)$$

Transient eddy fluxes of momentum and heat as well as the ageostrophic mean Hadley circulation are allowed to cross the southern boundary. Condition (2) translates into the statement that ψ is a function of only z and t at the lateral boundaries, but does not specify that function. Physically, we know that since $u = -\frac{\partial \psi}{\partial y}$, the difference of the two boundary values of ψ measures the total mass flow rate inside the channel. We define

$$U(t) = \frac{1}{y_2 - y_1} [\psi|_{y_1} - \psi|_{y_2}] \quad (3)$$

(The dependence of U on z is not displayed) and use (3) instead of (2) as the lateral boundary condition. That is, for each specified value of $U(t)$ a solution $\psi(U(t))$ is found from solving

$$J[\psi, P\psi + f] = f_0 \left(\frac{\partial}{\partial z} - \frac{1}{H_0} \right) (Q/\Gamma) \quad (4)$$

and (3). Of course $U(t)$ cannot really be independently specified in a non-linear system like the one we are studying; it evolves in response to wave-mean interaction. The evolution equation can be derived by considering the angular momentum balance in the channel and shown to have the form:

$$\frac{\partial}{\partial t} U = \frac{1}{\tau_E} (U^* - U) + T(U) \quad (5)$$

Equation 5 states that the rate of change of angular momentum inside the channel is due to:

1. Lateral flux of angular momentum through the channel boundaries, written in the form $\frac{1}{\tau_E} U^*$. For the atmosphere only the flux of eddy momentum through the southern boundary ($\sim 30^\circ N$) is important. Taking an Ekman damping time τ_E of 6 days, we find that $U^* \sim 3$ m/s. The parameter U^* is externally specified in our model.
2. Deceleration due to the frictional stress at the surface, which takes the form of $-\frac{1}{\tau_E} U$, when the Ekman boundary layer formulation is adopted.
3. Deceleration by mountain torque T generated by pressure differences on the east and west sides of topography. In our model this term is calculated interactively using the stationary wave solutions of (4). Mountain torques generated by gravity waves are not explicitly calculated, but these can presumably be lumped together into the "external" parameter U^* in the present model for the stationary waves.

Equation 5 is evaluated at the top of the Ekman layer, z_1 . The vertical variation of U is determined from the thermal wind relation according to

$$\frac{\partial}{\partial z} U = \frac{R}{(y_2 - y_1) H_0 f_0} \Delta \bar{T} \quad (6)$$

where $\Delta \bar{T} = \bar{T}|_{y_1} - \bar{T}|_{y_2}$ is an externally imposed temperature gradient in our model.

The lower boundary condition used for the stationary wave is (TUNG, 1983)

$$J[\psi, \frac{f_0 H_0}{RT} \psi_z + h] + \frac{H_0}{f_0} \frac{1}{\tau_E} \nabla^2 \psi = 0 \text{ at } z = z_1 \quad (7)$$

This includes forcing due to nonlinear flow over and around a realistic topography $h(x,y)$, but no diabatic forcing is included. Ekman pumping with a time scale of $\tau_E \sim 6$ days is incorporated. This is the only form of damping in the present form of our model.

The upper boundary condition is either boundedness of energy density or upward wave radiation. The numerical domain spans from the surface to 100 km. However, the neglect of radiative and momentum dampings in the interior of our model should make our results not too applicable in the mesosphere and upper stratosphere. The numerical method used to solve the "steady" nonlinear wave equation is Newton's method with arc-length continuation. It is spectral in the horizontal and high resolution with 50 or more levels in the vertical. Resolutions are increased until convergence is obtained.

Flow in the channel is forced by the two external parameters U^* and $\Delta \bar{T}$ mentioned above. Both are related to the flux of momentum and heat into the midlatitude channel from the tropics. Thus when we discuss the sensitivity of model response to tropical influence, we specifically mean the sensitivity to changes in the parameters U^* and $\Delta \bar{T}$ in a realistic range. In the absence of eddy momentum flux across our southern boundary at $30^\circ N$, $U^* = 0$ and the equilibrium solution in our channel has no net surface flow and no forced stationary wave. This situation is common in channel models with rigid lateral wall boundaries. The zonally symmetric flow (with zero surface velocity and a westerly upper level flow forced by the temperature gradient) is referred to by some authors as the "Hadley regime". When a positive momentum flux consistent with observations (with $U^* \sim 3m/s$) is imposed, a westerly surface flow (above the Ekman layer) is forced in the midlatitudes. Stationary waves are produced by this flow over the topography. Therefore, in some sense the observed zonally asymmetric westerly flow in the wintertime midlatitude region can be regarded as largely maintained by tropical momentum sources.

By the thermal wind relation, it can be seen that the vertical shear of the net zonal flow in the channel is maintained by the gross horizontal temperature difference across the meridional channel (see equation 6). If we examine the thermodynamics equation evaluated at, say, the southern boundary

$$\frac{\partial \bar{T}}{\partial t} = \bar{Q} - \bar{r}w - \frac{\partial}{\partial y} \overline{v'T'} \quad (8)$$

we see that eddy heat flux convergence and mean Hadley circulation from the tropics can play an important role in affecting changes in $\Delta \bar{T}$. (In the present model the eddy heat flux convergence due to the stationary waves in the mid-latitudes vanish at the lateral boundaries because of condition (2)).

Let us first assume that the terms on the right-hand side of (8) balance each other so that $\Delta \bar{T}$ is independent of time and can be specified by the initial condition. In the first calculation, we specify $\Delta \bar{T}(z)$ to be such that it produces the "climatological" meridionally averaged vertical shear \bar{U}_z taken from the analytic formula in TUNG and LINDZEN (1979) (evaluated at $45^\circ N$). This together with the surface value determined from (5) then yields $\bar{U}(z)$. It should be noted that the actual zonal flow $\bar{U}(y,z)$ is in general not the same as $\bar{U}(z)$, the latter being the channel average of the former. The meridional variation of \bar{U} is to be determined as part of the nonlinear solution. In the set of calculations presented here, it is assumed that the meridional shear of \bar{U} is induced entirely by the stationary waves. Specifically, we assume that in the absence of topography (and hence zonal asymmetry in the present model) $\bar{U} = \bar{U}(z)$ and so $\bar{U} = U(z)$.

In the presence of realistic topography, the calculated zonal mean flow $\bar{u}(y,z)$ is depicted in Figure 1. Whatever prior notions we may have concerning the processes which maintain the tropospheric and stratospheric jets, Figure 1 convincingly demonstrates that the stationary waves alone are capable of maintaining the horizontal jet structures. Both the location and strength of the two jets are quite realistic, except that perhaps the easterlies over the high latitudes may be too strong. The wave amplitudes in the channel are shown in Figure 2 for the zonal wave number 1 component and in Figure 3 for zonal wave-number 2 component. Compared with the "climatology" of van LOON et al. (1973) (Due to the large variability of the stratospheric stationary wave amplitudes that has been observed (GELLER et al., 1984) and calculated here, comparisons with the so-called "climatology" should only be taken as a reference for discussion.) with data available only below 30 km, we find that the wave number 1 amplitude in the lower stratosphere is slightly under-predicted by the model (400 meters vs 600 meters observed) and the calculated wave number 2 amplitude is less than half the observed (100 meters vs 250 meters observed). We will show in a moment that there is no difficulty in reproducing van LOON et al., amplitudes in the stratosphere with a slight change of the external parameters. Our purpose here is to show the range of variability in the wave amplitudes and to point out that one should not demand each model simulation to produce the "observed climatology," because the latter is only a composite of many monthly means with large interannual variance.

However, this variability does not extend into the troposphere, where we always obtain underestimates for the stationary wave amplitudes (by a factor of about 2). It has often been suggested that diabatic heating has to be included in order to get the stationary wave amplitudes right for the troposphere. Perhaps this is so, but JACQMIN and LINDZEN (1985) seem to disagree. Their calculation based on the linear primitive equations over the globe appears to have the right amplitudes in the troposphere, even when topography is the only

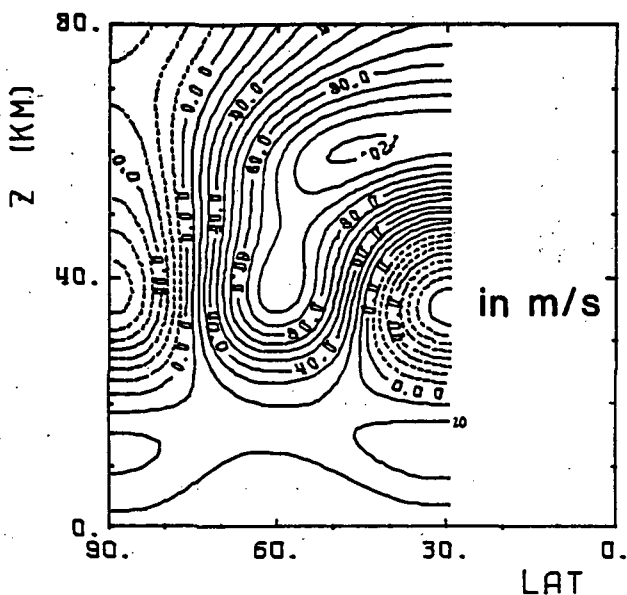


Figure 1. Mean zonal wind. Solid line: westerly; dashed line: easterly. Surface zonal index: 3 m/s.

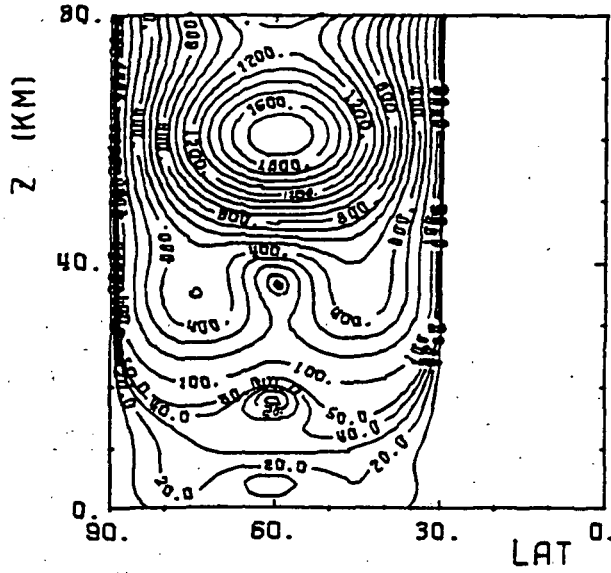


Figure 2. Wave number 1. Geopotential height in meters.

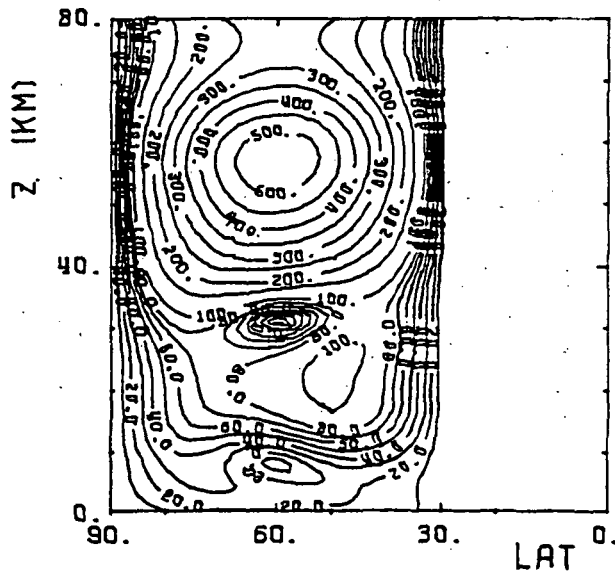


Figure 3. Wave number 2. Geopotential height in meters.

form of forcing for their stationary waves. Our experience based on our model has been that amplitudes calculated using the fully nonlinear version are always lower than the linear calculations; the magnitude of the difference varies depending on the meridional structure of the zonal mean wind used in the linear calculation, but in some cases can be as large as to account for the factor of 2 mentioned earlier. The problem of simulating the tropospheric stationary wave amplitudes is a difficult one and debates on topographic vs diabatic forcing are likely to continue for some time.

Given the large variability of the stratospheric wave amplitudes, it is not difficult to come up with a case that yields the so-called "correct climatological" wave amplitudes if that is what one desires. One such case is presented here. This is obtained by decreasing the temperature gradient, $\Delta\bar{T}(z)$ at the stratospheric jet level by about 20% (specifically, the parameter U_2 , in the analytic formula in Tung and Lindzen for the stratospheric jet strength is decreased from 150 m/s to 120 m/s), and the momentum flux from the tropics and hence the equilibrium U at the surface is increased by 30%, (from 3 to 3.9 m/s). The amplitudes for stationary wave numbers 1 and 2 are presented in Figures 4 and 5, respectively. It is seen that the wave number 1 amplitude now reaches 600 meters and wave number 2 reaches 250 meters near the 30 km level as observed (although the maximum occurs nearer the equator than in the climatology of van Loon et al.). The mean zonal flow induced is depicted in Figure 6. The tropospheric jet is now located closer to the midlatitudes, and the stratospheric jet is moved equatorward. The easterlies over the pole now largely disappear. The important point here is not how well we have simulated the climatology, but that by varying the momentum and heat fluxes ("tropical influence") by amounts reasonably within the observed range, we have produced a substantial change in the wave-mean flow system in midlatitudes.

The phase diagrams that describe the time variation of U are calculated according to Equation 5 and shown in Figure 7 for the $\Delta\bar{T}$ used in Figure 1. The corresponding phase diagram (not shown) for the second case (with a 20% smaller $\Delta\bar{T}$ at the stratospheric jet level) has an almost identical shape ex-

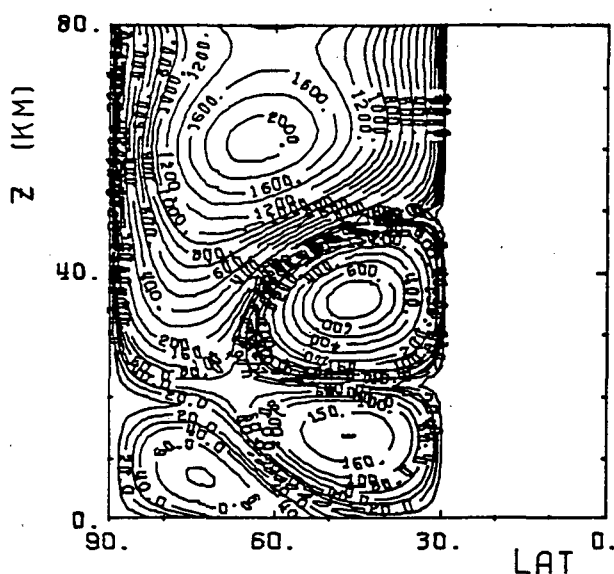


Figure 4. Wave number 1. Geopotential height in meters.

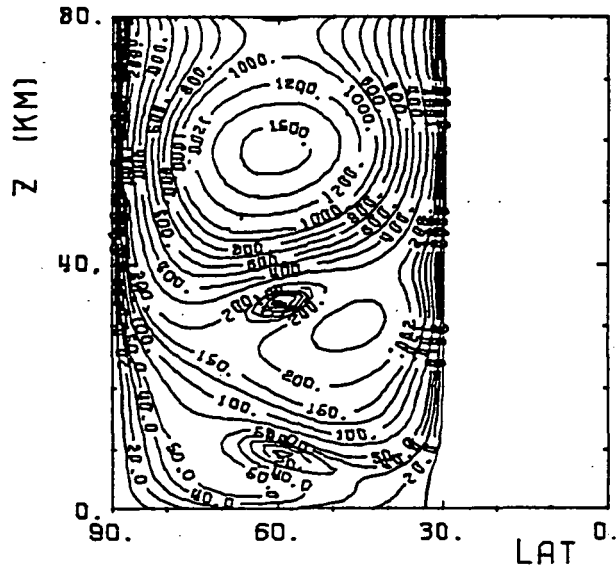


Figure 5. Wave number 2. Geopotential height in meters.

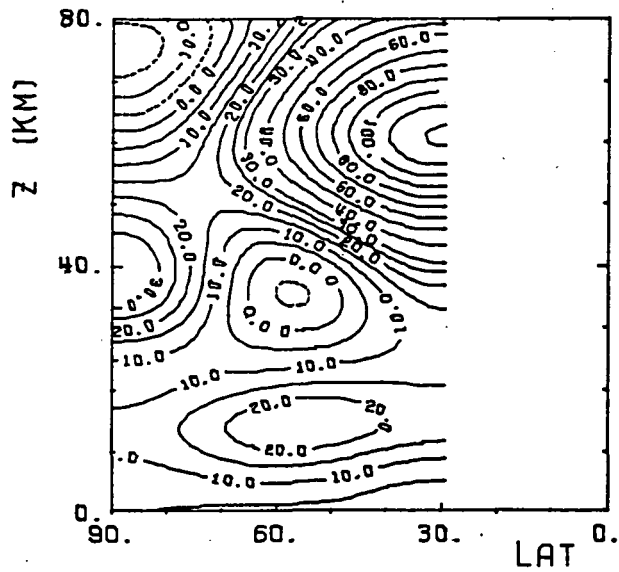


Figure 6. Mean zonal wind. Surface zonal index: 3.9 m/s.

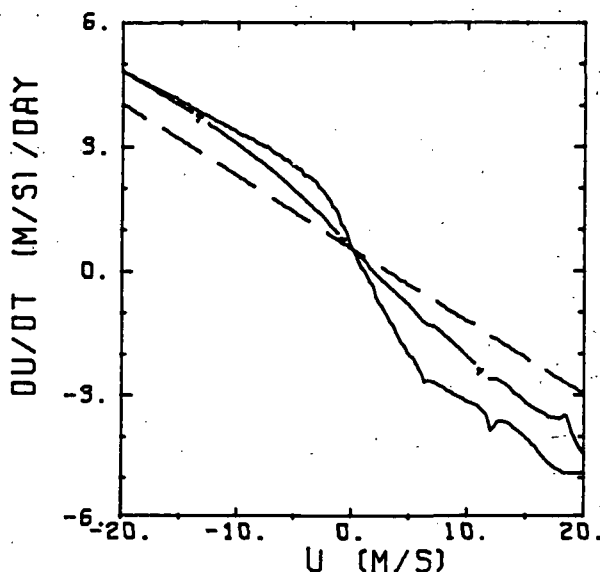


Figure 7. Phase diagram. Dashed line: no mountain; solid line: linear case; line with crosses: nonlinear.

cept for the location of some of the small glitches. A different choice for U^* would move the horizontal axis (i.e., the location where $\frac{d}{dt} U = 0$) up or down without affecting the shape of the curve, but the location of the equilibrium would change. An important point is that there is only one equilibrium now. We are aware that many authors have argued for the existence of multiple equilibria based on simpler (barotropic or 2-layer) models. We have reexamined many of the earlier model results (see TUNG and ROSENTHAL, 1985b) and found that problems exist when these simple model results are applied to the atmosphere. For our model with only one equilibrium, stationary wave-mean flow systems whose net mass flow rate, U , is not the same as that equilibrium value will relax to the equilibrium value in an Ekman damping time scale. When the equilibrium is reached, the system will remain at the equilibrium until external parameters (U^* or $\Delta \bar{T}$) are changed. We have found that it is mainly the tropical momentum flux (U^*) that is responsible for changing the location of the equilibrium net mass flow rate for the midlatitude system.

In conclusion, we have shown that our nonlinear model of stationary waves possesses substantial variability in both the stratospheric stationary wave amplitudes and the zonal mean wind, and more importantly, that such variabilities can be caused by changes in eddy momentum and heat fluxes from the tropics into the midlatitudes with magnitudes that lie within the observable ranges.

REFERENCES

- Geller, M. A., M-F Wu, and M. E. Gelman (1984), Troposphere-stratosphere (surface-55 km) monthly winter general circulation statistics for the Northern Hemisphere - interannual variations, *J. Atmos. Sci.*, **41**, 1726-1744.

- Jacqmin, D., and R. S. Lindzen (1985), The causation and sensitivity of the northern winter planetary waves, (submitted)
- Tung, K. K. (1983), On the nonlinear vs. linearized lower boundary conditions for topographically forced stationary long waves, Monthly Wea. Rev., 111, 60-66.
- Tung, K. K. and A. J. Rosenthal (1985a), On the extended-range predictability of large-scale quasi-stationary patterns in the atmosphere, Tellus, submitted.
- Tung, K. K., and A. J. Rosenthal (1985b), Multiple equilibria, a critical reexamination, J. Atmos. Sci., submitted.
- Tung, K. K., and R. S. Lindzen (1979), A theory of stationary long waves, Part II: Resonant Rossby waves in the presence of realistic vertical shears, Monthly Wea. Rev., 107, 735-750.
- van Loon, H., R. L. Jenne, and K. Labitzke (1973), Zonal harmonic standing waves, J. Geophys. Res., 78, 4463-4471.

2.21 SUPPRESSION OF STATIONARY PLANETARY WAVES BY INTERNAL GRAVITY WAVES IN THE MESOSPHERE

Saburo Miyahara

Geophysical Fluid Dynamics Program
Princeton University
Princeton, NJ 08542

Department of Physics, Kyushu University
Fukuoka, 812 Japan

The suppression of stationary planetary waves by internal gravity waves in the mesosphere is treated using a quasi-geostrophic model on a midlatitude beta-plane. The drag forces due to internal gravity waves are parameterized based on the wave-breaking assumption proposed by LINDZEN (1981). In the present model the vertical propagation of internal gravity waves is affected not only by mean zonal wind distribution but also by eastward and northward velocity perturbations associated with stationary planetary waves, viz. the total local velocity.

In the present model, we consider only two stationary upward propagating internal gravity waves with the same horizontal wavelength 57 km, but whose wave number vectors are different. One component has a wave number vector which is directed towards northeast, and the other is directed southeast. Planetary waves with zonal wave number 1 are considered, and the amplitudes of the geopotential height at the bottom ($z=20\text{km}$) are specified to be 50 m.

Figure 1 shows the vertical variations of amplitude of calculated stationary planetary wave geopotential height. When effects of drag forces due to internal gravity waves are neglected, the amplitude grows gradually with height up to 78 km due to the effect of density stratification. The maximum amplitude is 1130 m at 78 km height. If the effects of internal gravity waves are taken into account, the amplitude of the stationary planetary wave in the stratosphere is almost unchanged. However, the amplitude in the mesosphere is greatly reduced, and the maximum amplitude achieved is 610 m at 74 km height.

Figure 1 also shows the vertical profiles of the amplitudes of the drag forces due to gravity waves and the profile of zonally averaged drag force due to gravity waves.

In order to elucidate the mechanism of suppression, the longitudinal distributions of zonal wind, meridional wind associated with the mean zonal winds, and the stationary planetary wave, zonal drag force F_x and meridional drag force F_y due to gravity waves at 70 km height are shown in Figure 2. F_x and F_y have obvious negative correlations with the perturbations of zonal wind and the meridional wind associated with the planetary wave. Thus, the effects of the drag forces of the internal gravity waves act like Rayleigh friction as pointed out by SCHOEERL and STROBEL (1984). Coefficients of equivalent Rayleigh friction at 70 km height are about $9 \times 10^{-6} \text{s}^{-1}$.

The equivalent Rayleigh friction coefficients depend on the mean zonal wind profile and the planetary wave amplitudes (which needless to say, greatly depend on the gravity wave activities), so that the coefficient cannot be independently prescribed, even though the gravity wave activities are given.

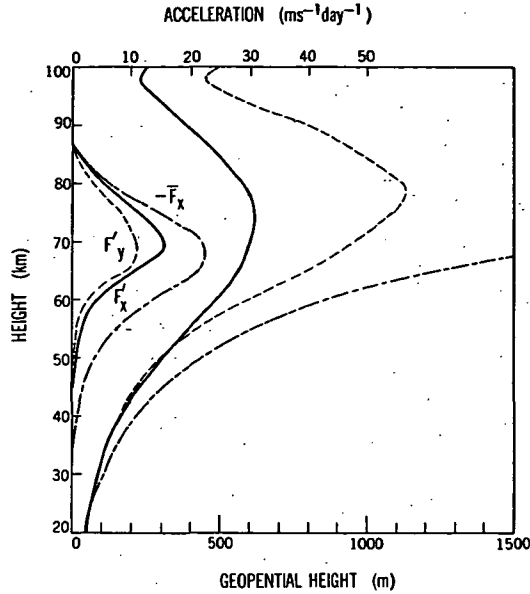


Figure 1. Height variations of amplitudes of stationary planetary wave geopotential height with (solid line) and without (dashed line) effects of internal gravity waves, and height variations of mean zonal drag force and $e^{ik_x x} \cos l_y y$ and $e^{ik_x x} \sin l_y y$ components of the zonal and the meridional drag forces, respectively. Dash-dotted lines shows $5 \times 10^6 z/2H_m$ for reference.

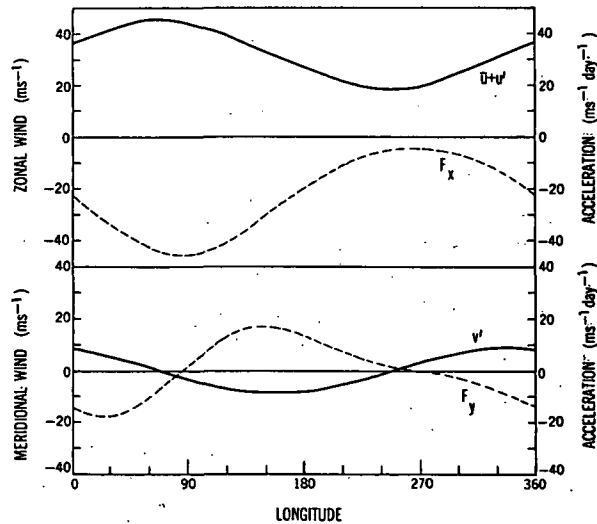


Figure 2. Longitudinal distributions of the zonal wind, meridional wind, zonal drag force and meridional drag force at 70 km height.

REFERENCES

- Lindzen, R. S. (1981), Turbulence and stress due to gravity wave and tidal breakdown, J. Geophys. Res., 86, 9707-9714.
- Schoeberl, M. R. and D. F. Strobel (1984), Nonzonal gravity wave breaking in the winter mesosphere, Dynamics of the Middle Atmosphere, edited by J. R. Holton and T. Matsuno, 45-64, Terra Sci. Pub. Co.

2.22 MEAN ZONAL WINDS AND PLANETARY WAVES INDUCED BY INTERNAL GRAVITY WAVE PACKETS

M. Takahashi and M. Uryu

Department of Physics, Faculty of Science
Kyushu University, Fukuoka 812 Japan

The generation of mean zonal winds and planetary waves induced by internal gravity wave packets are investigated by numerical experiments. The numerical model is a 3-dimensional primitive equation model on the equatorial β -plane with boundaries at the equator and North Pole. Because of equatorial boundary conditions, equatorial symmetric modes only are included in the model. Internal gravity wave packets are produced by thermal heating at the bottom boundary. Because of restriction of grid size, convective instability is parameterized by time-independent vertical and horizontal eddy viscosity (cf. LINDZEN, 1981). Other dissipation mechanisms (e.g., Newtonian cooling, ion drag, molecular viscosity etc.) are also included in the model.

The functional form of bottom forcing is as follows.

$$\phi_z = F(t) \cdot \exp\left[-\frac{(\chi - ct)^2}{(500 \text{ km})^2}\right] \cdot \sin[k(\chi - ct)] \text{ at } z = 60 \text{ km}$$

Dominant horizontal wavelength $2\pi/k = 1250 \text{ km}$. Horizontal phase velocity $c = \pm 25 \text{ m s}^{-1}$, respectively. Maximum amplitude of temperature perturbation is 26.4 K. Figure 1 shows time variation of $F(t)$.

Case 1 is a westward propagating case ($c = -25 \text{ m s}^{-1}$).

Figures 2(a,b) show the longitude-height sections of zonal wind near the equator at 2 days. Dotted regions show easterly wind. Figure 2(a) corresponds to the linear case, and Figure 2(b) to the nonlinear case. Figure 2(a) shows vertical propagation of a gravity wave packet explicitly. On the other hand, the eastward propagating wave is also intensified the same as the westward propagating wave in Figure 2(b). Spectral analysis shows white noise spectra.

Figures 3(a,b) show the longitude-height sections of the zonal wind at 6 days. Dominant zonal wave number is 5, and the amplitude is 1 m s^{-1} at most in the linear case (Figure 3a). On the other hand, in the nonlinear case, dominant zonal wave number is 1, and the maximum amplitude is 14 m s^{-1} , due to wave-wave interaction and dissipation.

Figure 4 shows the longitude-latitude section of velocity and geopotential of wave number 1 component at $z=100 \text{ km}$, and at 6 days. The wave pattern clearly shows Rossby wave motion.

Figure 5 shows the latitude-height section of the mean zonal wind at 6 days. Easterly winds with the maximum amplitude -8 m s^{-1} blow in low latitudes and westerly winds with maximum amplitude 6 m s^{-1} blow in high latitudes.

Case 2 is an eastward propagating case ($c=25 \text{ m s}^{-1}$).

Figure 6 shows the longitude-latitude section of the zonal wave number 1 velocity and geopotential at 6 days. Near the equator, Kelvin wave-like motion is identified. On the other hand, Rossby wave-like motion is shown in high latitude regions.

Figure 7 shows the latitude-height section of the mean zonal wind at 6 days. Near the equator, easterly wind blows in the upper layers and westerly wind blows in the lower layers.

We have discussed the generation of planetary scale waves due to internal gravity wave packets using a simple 3-dimensional numerical model. Then, the large amplitude planetary scale waves have been obtained in the model. Very fast Kelvin waves ($c \sim 120 \text{ m s}^{-1}$), which has been discovered by SALBY et al. (1984), may be partly produced by these wave-wave interactions of the internal gravity waves.

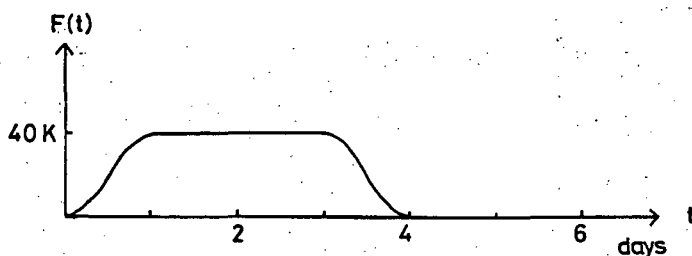


Figure 1. Time variation of boundary forcing.

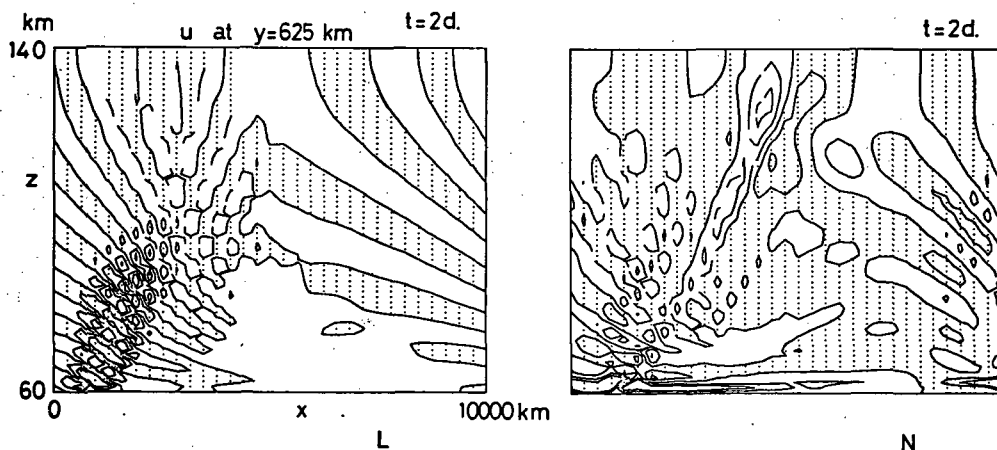


Figure 2. Longitude-height section of zonal wind at $y=625 \text{ km}$, $t=2 \text{ days}$.
(a) linear case (b) nonlinear case.

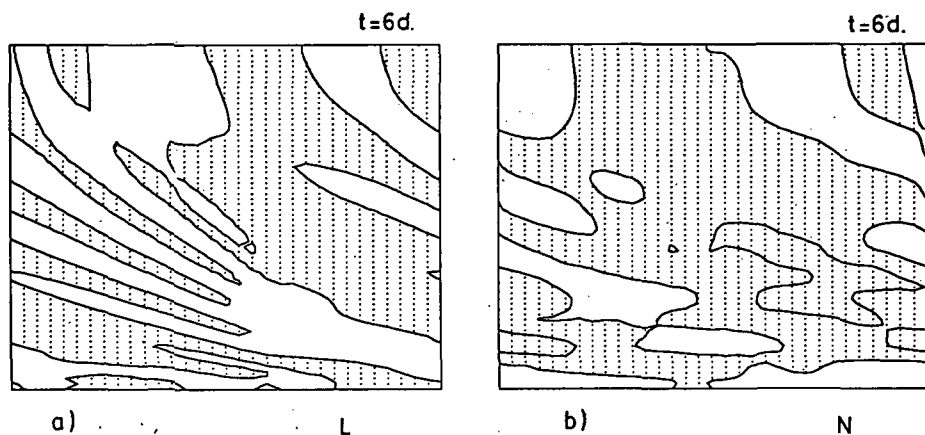


Figure 3. Same as Figure 2 but for $t=6$ days.

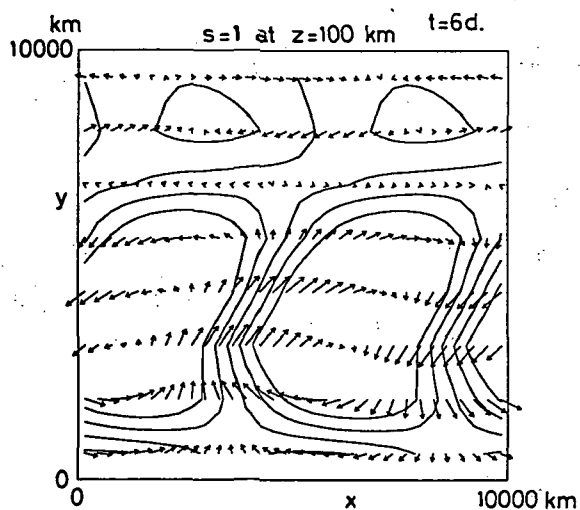


Figure 4. Longitude-latitude section of velocity and geopotential of wave number 1 component at $z=100$ km, $t=6$ days.

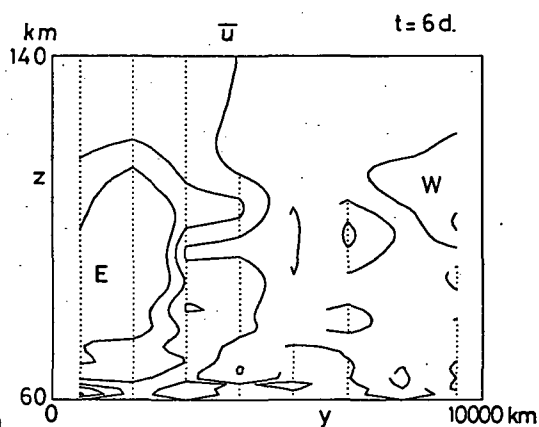


Figure 5. Latitude-height section of the mean zonal wind at $t=6$ days.

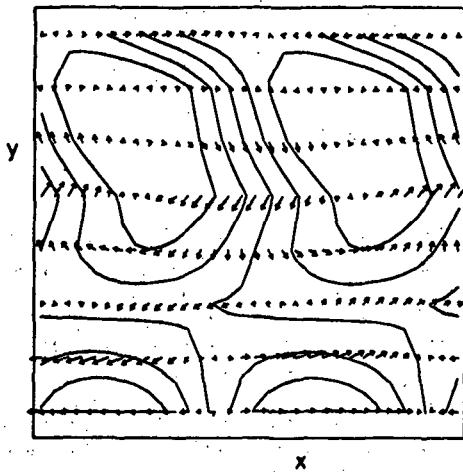


Figure 6. Same as Figure 4
but for Case 2.

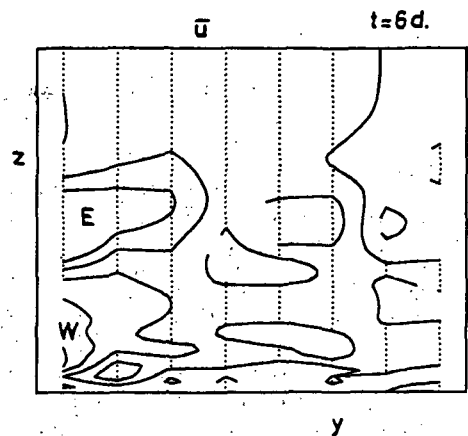


Figure 7. Same as Figure 5
but for Case 2.

REFERENCES

- Lindzen, R. S. (1981), Turbulence and stress owing to gravity wave and tidal breakdown, J. Geophys. Res., **86**, 9707-9714.
- Salby, M. L., D. L. Hartmann, P. L. Bailey and J. C. Gille (1984), Evidence for equatorial Kelvin modes in Nimbus-7 LIMS, J. Atmos. Sci., **40**, 220-235.

2.23 WAVE-MEAN FLOW INTERACTION IN THE NCAR STRATOSPHERIC GENERAL CIRCULATION MODEL

Byron A. Boville

National Center for Atmospheric Research*
Boulder, CO 80307

A version of the NCAR General Circulation Model has been developed which extends from the surface into the mesosphere. The model was forced by climatological January sea surface temperatures and insolation and gives a fairly reasonable simulation of the troposphere and stratosphere. The transformed Eulerian formation (ANDREWS and MCINTYRE, 1976) is used to examine the interaction of the eddies with the mean flow in the winter hemisphere.

The numerical algorithms are the same as in the standard NCAR Community Climate Model used for tropospheric simulation. The number of levels has been increased from 9 to 33 with the top level at 0.1 mb (about 65 km) and a vertical resolution of about 2.1 km ($\Delta \ln p = 0.3$) above 500 mb. The ∇^2 horizontal diffusion operator of the original model was replaced with a ∇^4 operator which leaves the large-scale waves essentially undamped. The ozone distribution was obtained from DUTSCH (1978) and is zonally symmetric.

A Rayleigh friction term was added to the zonal momentum equation in the mesosphere. The time constant follows a hyperbolic tangent profile and is infinite below 40 km, 50 days at 50 km, and 3 days at 65 km.

Since the Rayleigh friction term is an extremely crude parameterization of mesospheric gravity drag, we will confine our attention to the troposphere and stratosphere in the model. No results are presented for the 6 levels above 0.7 mb.

Figure 1 shows the zonally averaged temperatures and zonal winds for the whole globe averaged over the last 90 days of a 300-day run. Both the temperature and the wind structures are quite reasonable, although far from perfect, when compared to observations (e.g., GELLER et al., 1983, 1984). The winter polar stratosphere is about the right temperature although the minimum extends too high. In conjunction, the subtropical jet and the polar night jet are well separated and of reasonable magnitudes. The polar night jet does not tilt southward with height as is usual in the observations.

The essence of the transformed Eulerian formation is an attempt to distinguish between the mean meridional circulation driven by diabatic heating and that driven by eddies. The net effect of eddies can then be determined, and is given by the Eliassen-Palm (EP) flux divergence. In practice, this method works reasonably well but is far from perfect. For instance, in the absence of eddy forcing, the winter stratosphere would go to radiative equilibrium and there would be no diabatic heating to drive a mean meridional circulation.

The conventional Eulerian zonal mean momentum equation (quasi-geostrophic on a β -plane) is,

$$\frac{\partial \bar{u}}{\partial t} - f \bar{v} = - \frac{\partial}{\partial y} \overline{u'v'} + D \quad (1)$$

*The National Center for Atmospheric Research is sponsored by the National Science Foundation.

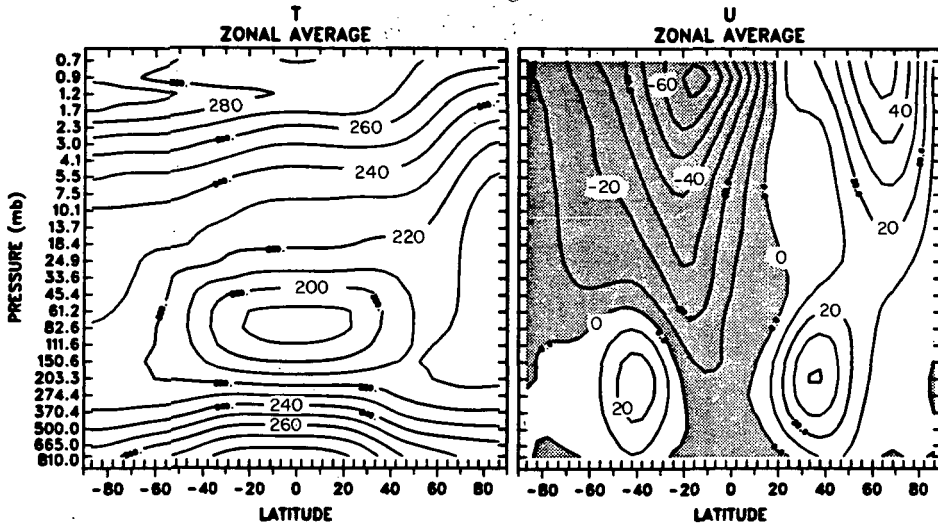


Figure 1. Zonally averaged temperature (left) and zonal wind (right) averaged over 90 days. Contour intervals are 10 K and 10 ms^{-1} .

In the time mean, the Coriolis torque associated with the mean meridional wind is balanced by the eddy momentum flux and any zonal mean drag and diffusion terms. The transformed Eulerian momentum equation is:

$$\frac{\partial \bar{u}}{\partial t} - f \bar{v}^* = \bar{\nabla} \cdot \mathbf{F} + D \quad (2)$$

In the time mean the Coriolis torque associated with the residual mean meridional wind is balanced by the divergence of the EP flux and the drag. Note that all quantities appearing in the figures are calculated using the full primitive equation forms on a sphere (see DUNKERTON et al., 1983) not the quasi-geostrophic β -plane forms shown above for simplicity.

The conventional Eulerian meridional circulation components are shown in Figure 2 and the transformed Eulerian components in Figure 3. The conventional Eulerian circulation shows a strong, thermally indirect cell around the polar night jet with rising motion to the north and subsidence to the south of the jet core. The southward motion through the jet results in large Coriolis torques (Figure 4) decelerating the jet, which must then be balanced by large eddy momentum flux convergence. The transformed Eulerian circulation is very different, showing poleward and downward motion through almost the entire Northern Hemisphere from the surface to the stratosphere. The polar night jet does not appear as an obvious feature of the mean meridional circulation, which tends to accelerate the zonal flow throughout the Northern Hemisphere (Figure 4). Since the drag terms are small, the EP flux divergence is nearly equal to the mean flow acceleration. As found by ANDREWS et al. (1983) the conventional and transformed Eulerian views of the stratospheric circulation give opposing results as to the effects of the eddies and of the mean circulation.

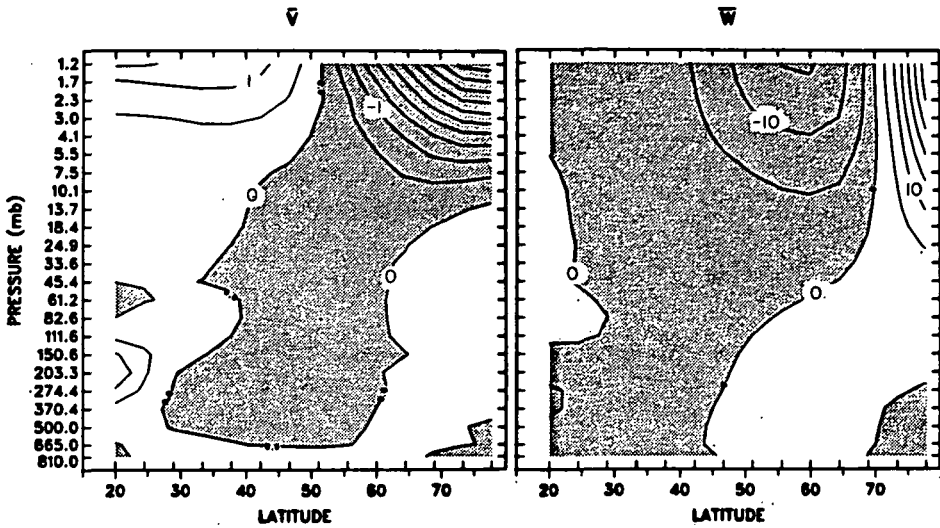


Figure 2. Eulerian mean meridional and vertical wind components averaged over 90 days for the Northern Hemisphere. Contour intervals are 0.5 ms^{-1} and 5 mm s^{-1} , respectively.

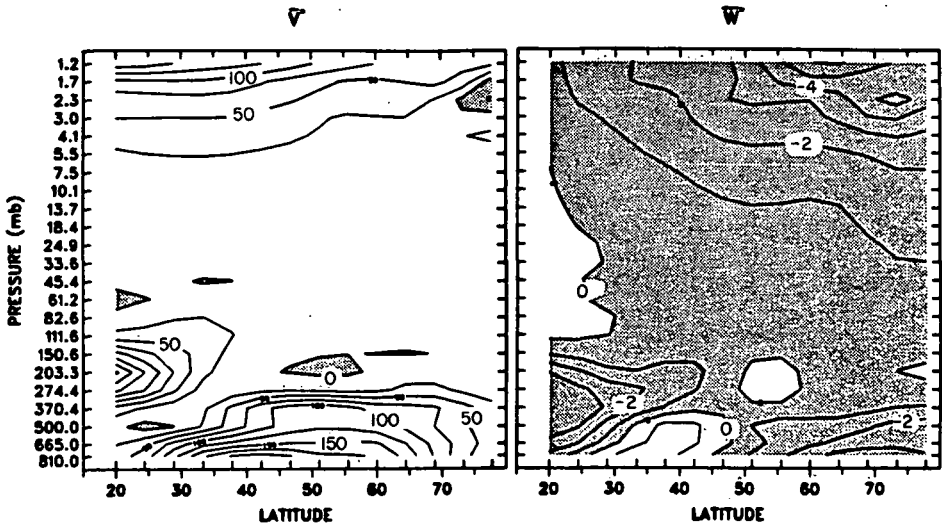


Figure 3. Transformed Eulerian mean meridional and vertical wind components averaged over 90 days. Contour intervals are 25 cm s^{-1} and 1 mm s^{-1} , respectively.

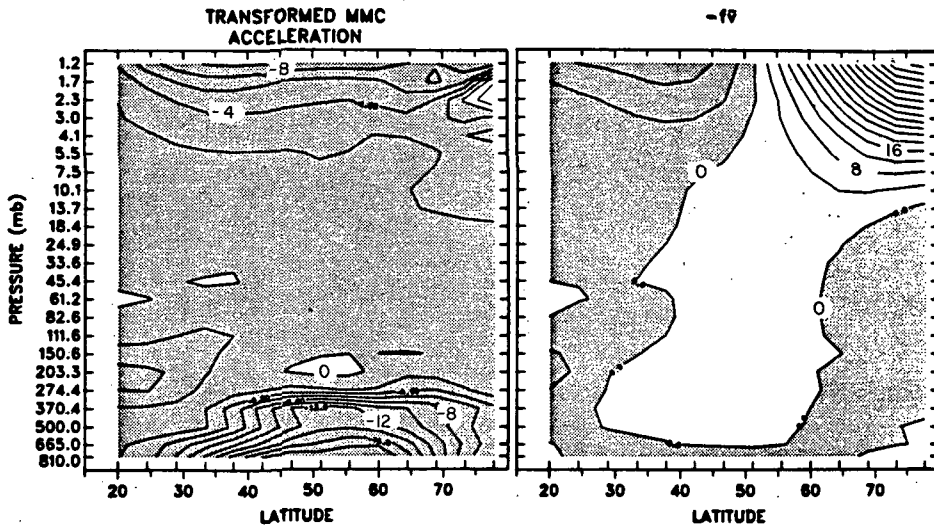


Figure 4. Deceleration of the mean zonal wind by the transformed Eulerian meridional circulation (left) and conventional Eulerian meridional circulation (right). Contour intervals are 2 and 4 $\text{ms}^{-1} \text{ day}^{-1}$, respectively.

REFERENCES

- Andrews, D. G., and M. E. McIntyre (1976), Planetary waves in horizontal and vertical shear: The generalized Eliassen-Palm relation and the mean zonal acceleration, *J. Atmos. Sci.*, **33**, 2031-2048.
- Dunkerton, T. J., C. P. F. Hsu, and M. E. McIntyre (1981), Some Eulerian and Lagrangian diagnostics for a model stratospheric warming, *J. Atmos. Sci.*, **38**, 819-843.
- Geller, M. A., M. F. Wu, and M. E. Gelman (1983), Troposphere-stratosphere (surface - 55 km) monthly winter general circulation statistics for the Northern Hemisphere - Four year averages, *J. Atmos. Sci.*, **40**, 1334-1352.
- Geller, M. A., M. F. Wu, and M. E. Gelman (1984), Troposphere-stratosphere (surface - 55 km) monthly winter general circulation statistics for the Northern Hemisphere - Interannual variations, *J. Atmos. Sci.*, **41**, 1726-1744.

2.24 EQUATORIAL WAVES IN THE NCAR STRATOSPHERIC GENERAL CIRCULATION MODEL

Byron A. Boville

National Center for Atmospheric Research*
Boulder, CO 80307

Equatorially trapped wave modes are very important in the tropical stratospheric momentum balance. Kelvin waves and mixed Rossby-gravity waves are believed to be responsible for the quasi-biennial oscillation of the zonal winds in the equatorial lower stratosphere (e.g., HOLTON and LINDZEN, 1972). Both Kelvin and mixed Rossby-gravity waves have been identified in observations and in numerical models (e.g., WALLACE and KOUSKY, 1968; SALBY et al., 1984; HAYASHI et al., 1984). This study identifies Kelvin and mixed Rossby-gravity waves in a general circulation model extending from the surface into the mesosphere and looks at the effect on the waves of lowering the top of the model.

The formal top boundary condition of most general circulation models is on the vertical velocity: $dp/dt=0$ at $p=0$. Because of the finite differencing in the vertical, this condition appears to have the practical effect of reflecting waves which propagate up to the top level of the model (e.g., KIRKWOOD and DEROME, 1977). Experiments with modified versions of the NCAR Community Climate Model indicate that the tropical stratospheric easterlies are reasonably well simulated if the vertical resolution is extremely coarse or if the top model level is in the mesosphere. If the model has sufficient vertical resolution to resolve the equatorial waves (vertical scales ~ 10 km) but has the top level at 10 mb as is usual, then the tropical easterlies accelerate dramatically. This indicates a possible problem with the reflection of vertically propagating equatorial waves and a resulting alteration of the momentum balance.

Substances with tropospheric sources (such as water vapor) are thought to enter the stratosphere primarily through the tropical tropopause. The transport properties of the lower tropical stratosphere and, consequently, the momentum balance there are of great importance in determining the distribution of such substances in the middle atmosphere. To study the entry of tropospherically generated substances into the stratosphere it would be desirable, if only because of cost, to use the usual type of tropospheric general circulation model with a top level in the middle stratosphere but with sufficient vertical resolution to be useful in transport studies. If the lower stratospheric momentum balance in such model is incorrect, it will not be usable for this problem.

Kelvin waves propagate eastward, decay away from the equator, are symmetric across the equator in the temperature and zonal wind, and have no meridional wind component. Mixed Rossby-gravity waves propagate westward, decay from the equator, are antisymmetric in the temperature and zonal wind and symmetric in the meridional wind.

Figure 1 shows a frequency-latitude cross section of the power in the temperature at 10.1 mb in zonal wave 1 from two general circulation model experiments. The experiments are identical except that the first (case 1)

*The National Center for Atmospheric Research is sponsored by the National Science Foundation.

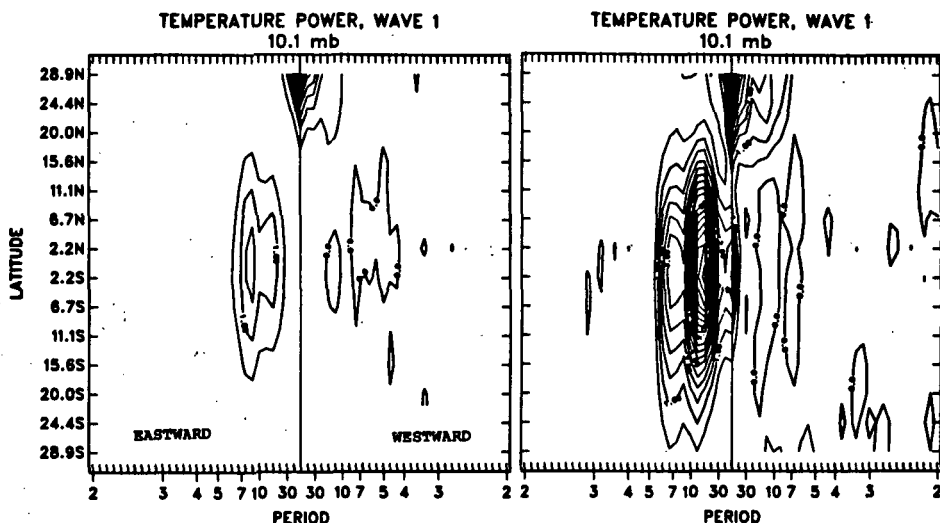


Figure 1. Power in the wave 1 temperature for case I (left) and II (right) at 10.1 mb. The contours on both panels of this and subsequent plots are the same.

contains 33 levels from the surface to 0.1 mb while the second (case II) has every level above 10 mb removed. Both cases are dominated by eastward propagating tropically trapped waves (two of the Kelvin wave properties) of two distinct frequencies but the amplitudes of these waves are radically larger in case II and the largest amplitude shifts to the longer period wave.

Figures 2 and 3 show frequency-height plots of the power in wave 1 of the temperature and zonal wind averaged across the equator to isolate the symmetric component corresponding to Kelvin waves. In case I the stratosphere is dominated by a Kelvin wave with a period of about eight days and maximum amplitude (in T) near the stratopause. This corresponds fairly well with the observations of SALBY et al. (1983). In the lower stratosphere a Kelvin wave with a period near 15 days is larger. In case II both Kelvin waves have amplified dramatically, with the longer period wave now clearly dominating. The zonal wind amplitude maximum is between the temperature maxima giving the impression of a vertically standing wave. This wave may in fact be resonant between the forcing region in the troposphere and the reflecting top in the middle stratosphere.

Figure 4 shows frequency-height plots of the power in wave 1 of the meridional wind averaged across the equator to isolate the mixed Rossby-gravity waves. The mixed Rossby-gravity waves in case I appear as a maximum in the westward power with a period of three days in the lower stratosphere approaching two days at the stratopause. In case II there is a large maximum in the middle stratosphere but no coherent vertical structure. The same features are seen in the antisymmetric T field (not shown) but is much more difficult to identify in the zonal wind.

The above discussion shows that the model produces equatorial waves which compare reasonably well to the observations when the waves are allowed to propagate into the mesosphere where they are dissipated. When the waves are trapped in the lower stratosphere their characteristics change dramatically, and it is likely that the momentum balance is also changed. Such a model would

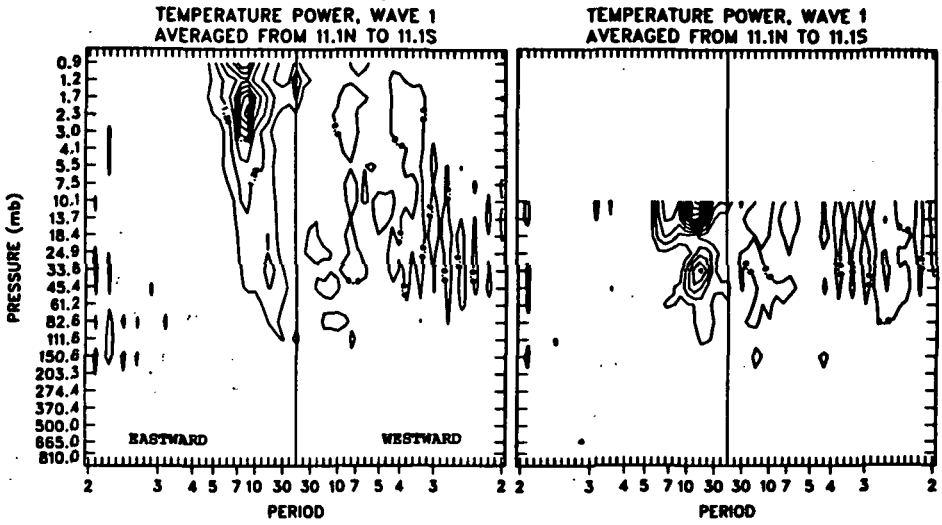


Figure 2. Power in the wave 1 temperature averaged across the equator.

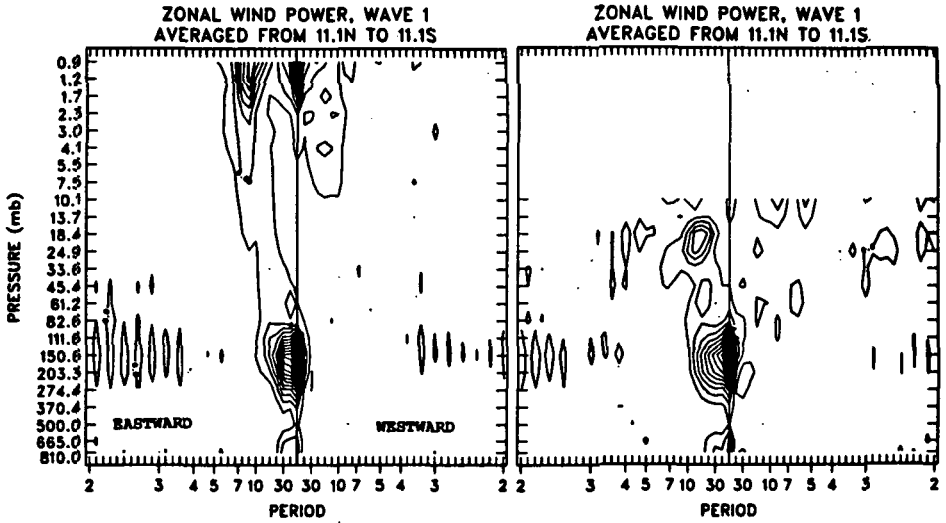


Figure 3. Power in the wave 1 zonal wind averaged across the equator.

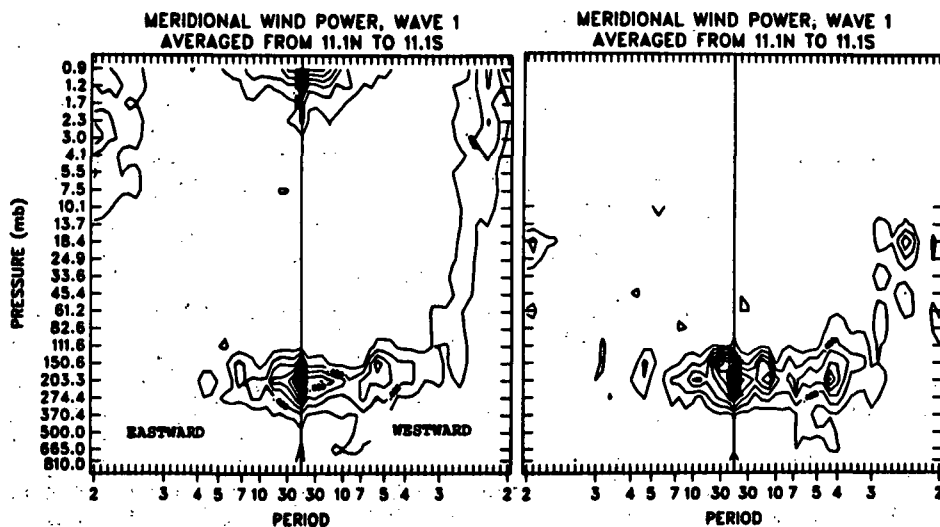


Figure 4. Power in the wave 1 meridional wind averaged across the equator.

be unsuitable for use in lower stratospheric transport studies although an absorbing upper boundary condition might improve the situation.

REFERENCES

- Hayashi, Y., D. G. Golder, and J. D. Mahlman (1984), Stratospheric and mesospheric Kelvin waves simulated by the GFDL "SKYHI" general circulation model, *J. Atmos. Sci.*, **41**, 1971-1984.
- Holton, J. R., and R. S. Lindzen (1972), An updated theory for the quasi-biennial cycle of the tropical stratosphere, *J. Atmos. Sci.*, **32**, 712-719.
- Kirkwood, E., and J. Derome (1977), Some effects of the upper boundary condition and vertical resolution on modeling forces stationary planetary waves, *Monthly Wea. Rev.*, **105**, 1239-1251.
- Salby, M. L., D. L. Harman, P. L. Bailey, and J. C. Gille (1984), Evidence for equatorial Kelvin modes in Nimbus-7 LIMS, *J. Atmos. Sci.*, **41**, 220-235.
- Wallace, J. M., and V. Kousky (1968), Observational evidence of Kelvin waves in the tropical stratosphere, *J. Atmos. Sci.*, **25**, 900-907.

2.25 VACILLATIONS INDUCED BY INTERFERENCE OF STATIONARY AND TRAVELING WAVES

Murry L. Salby

Department of Astrophysical, Planetary, and Atmospheric Sciences
University of Colorado, Campus Box 391,
Boulder, CO 80309

Rolando R. Garcia

National Center for Atmospheric Research
P.O. Box 3000, Boulder, CO 80307

INTRODUCTION

MADDEN (1983) has shown that there exists a correspondence between interference of the 16-day wave with the stationary planetary wave and vacillations in eddy heat and momentum fluxes. He has speculated upon the role such interference may play in stratospheric warmings. HIROOKA and HIROTA (1985) has also noted the appearance of higher-order normal modes, e.g., the 16-day wave, prior to disturbances in the stratospheric vortex. Since amplitudes of the 16-day wave are comparable to those of the stationary component, it can significantly alter the instantaneous total wave field. Figure 1 shows the behavior of the wave number 1 height field at 60°N during January 1979 when a large amplitude disturbance retrogressed barotropically around the globe over much of the troposphere and stratosphere. MADDEN and LABITZKE (1981) have identified this transient disturbance with the 16-day wave. More generally, the presence of fluctuating planetary wave activity can, through combined interference, alter the instantaneous planetary wave field as well as the transports it produces. We explore the implications of such interference in a quasi-geostrophic framework, using the Eliassen-Palm (EP) flux as a diagnostic.

FORMULATION

Consider an arbitrary, unsteady streamfield ψ represented as

$$\psi(\lambda, \phi, z, t) = \frac{1}{2\pi} \int_{-\infty}^{\infty} d\sigma e^{i\sigma t} \sum_{m=-\infty}^{\infty} e^{im\lambda} \psi_m^{\sigma}(\phi, z) \quad (1)$$

where

$$\psi_m^{\sigma} = \frac{1}{2\pi} \int_{-\infty}^{\infty} dt e^{-i\sigma t} \int_{-\pi}^{\pi} d\lambda e^{-im\lambda} \psi(\lambda, \phi, z, t) \quad (2)$$

The quasi-geostrophic EP flux \vec{F} is given by

$$\vec{F} = (F_{\phi}, F_z) = \left(-\frac{\bar{\rho}}{a} \overline{\psi_{\phi} \psi_{\lambda}}, \quad \bar{\rho} \left(\frac{f}{N^2} \right) \overline{\psi_{\lambda} \psi_z} \right) \quad (3)$$

Substitution of (1) into (3) yields

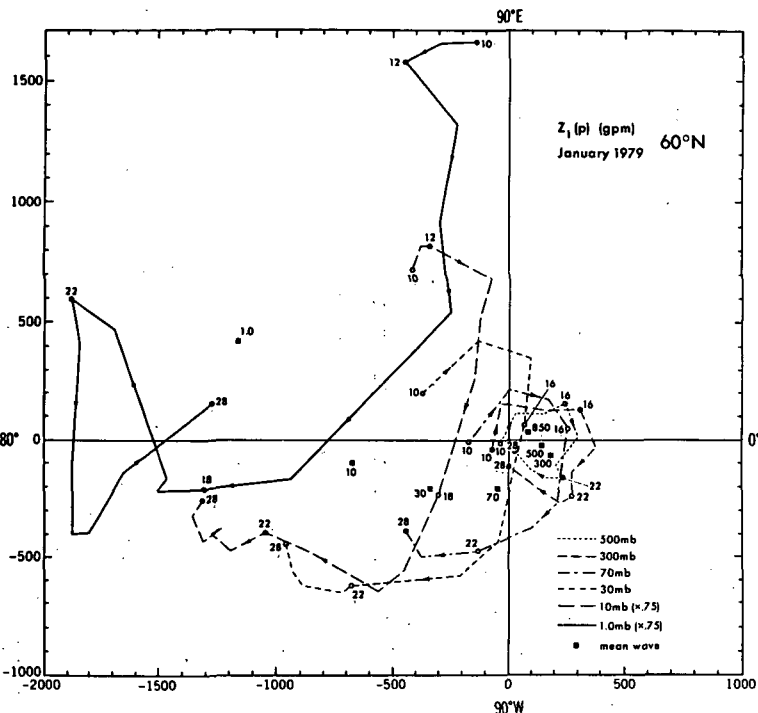


Figure 1.

$$\vec{F}(\phi, z, t) = \sum_{m=0}^{\infty} \frac{1}{(2\pi)^2} \int_{-\infty}^{\infty} d\sigma \int_{-\infty}^{\infty} d\sigma' \vec{F}_m^{\sigma\sigma'}(\phi, z, t) \quad (4)$$

where

$$\vec{F}_m^{\sigma\sigma'}(\phi, z, t) = \begin{pmatrix} -\frac{2\bar{\rho}}{a} \operatorname{Im}\left\{m \frac{\partial \psi_m^{\sigma}}{\partial \phi} \psi_m^{\sigma'*} e^{-i(\sigma-\sigma')t}\right\} \\ 2\bar{\rho}\left(\frac{f^2}{N}\right) \operatorname{Im}\left\{m \frac{\partial \psi_m^{\sigma}}{\partial z} \psi_m^{\sigma'*} e^{-i(\sigma-\sigma')t}\right\} \end{pmatrix} \quad (5)$$

The instantaneous EP-flux vector is thus seen to be a convolution of frequency components of the same wave number. $\vec{F}_m^{\sigma\sigma'}$ represents the contribution from wave number m at frequencies σ and σ' and oscillates as $e^{-i(\sigma-\sigma')t}$.

SIMPLE LAMB MODE AND STATIONARY WAVE

Consider the case of a two-component wave field made up of a stationary plane wave $\psi_m^0 = A_m^0 \exp[z/2H + i(\ell\phi + kz/H)]$ and a barotropic Lamb mode $\psi_m^{\sigma} = A_m^{\sigma} \exp[\kappa z/H] H_m^{\sigma}(\phi)/f$. Then, the EP flux (4) reduces to the sum of a steady and a fluctuating component, i.e., $\vec{F} = \vec{F}_0 + \vec{F}_{\sigma}$, where

$$\vec{F}_0 = \left(-\frac{\rho_0 m}{a} |A_m^0|^2, \rho_0 m \left(\frac{f^2}{N^2}\right) \frac{k}{H} |A_m^0|^2 \right) \quad (6.1)$$

$$\vec{F}_\sigma = (A_\phi \cos(\sigma t - \delta), A_z \cos(\sigma t - \delta)) \quad (6.2)$$

and $A_\phi(\phi, z)$, $A_z(\phi, z)$ and $\delta(\phi, z)$ involve the amplitudes and phases of the two waves. In particular,

$$\delta \approx -(L\phi + kz/H). \quad (7)$$

From (6.2) and (7), it can be seen that the fluctuating component of the EP flux describes a vacillation that propagates upward, and equatorward or poleward depending on the sign of L . Locally, the EP flux vector describes an ellipse about the time mean component \vec{F}_0 (Figure 2). For traveling wave amplitudes comparable to that of the stationary wave, the instantaneous EP-flux vector may completely change direction: equatorward switching to poleward, upward flux varying from zero to double its time mean value.

We investigate the structure of these vacillations for the case $m=1$, $\sigma = 0.06$ cpd, and $A_m^\sigma/A_m^0 = 3$ consistent with the behavior observed in January 1979 (Figure 1). Vacillations in wave amplitude due to the superposition of the stationary and traveling components are shown in Figure 3 for $\phi = 50^\circ$. The magnitude and the direction of the EP flux \vec{F} (Figure 4) also undergo a substan-

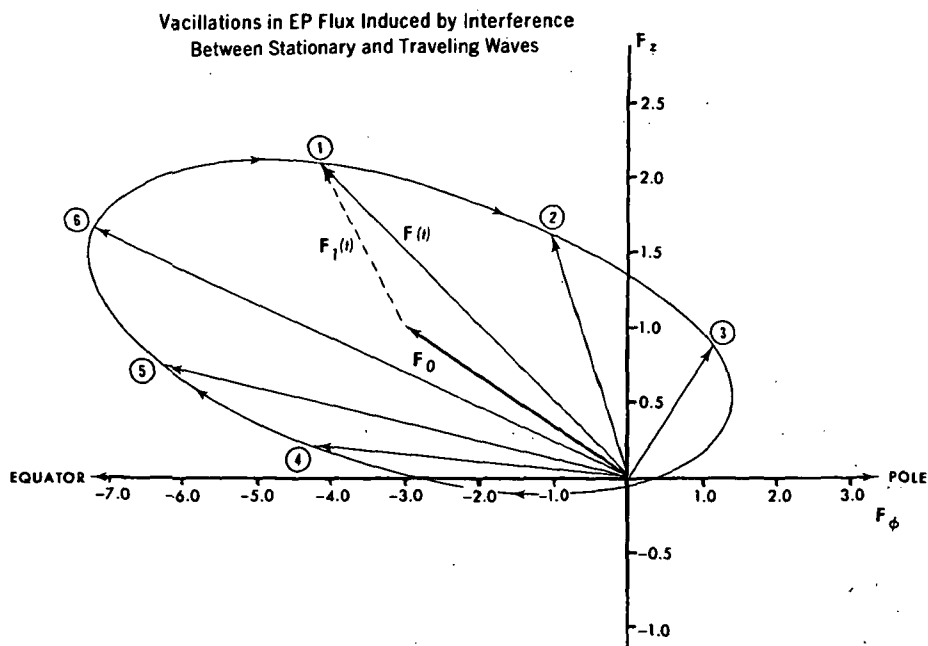


Figure 2.

INSTANTANEOUS WAVE 1 HEIGHT AMPLITUDE

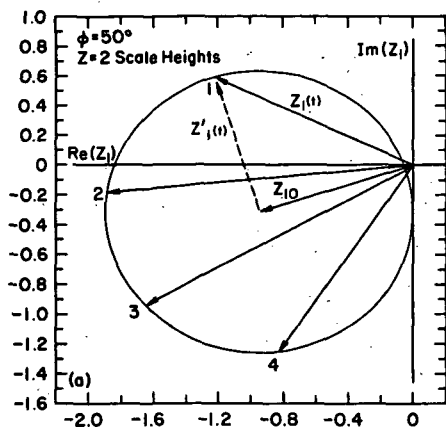


Figure 3 (a).

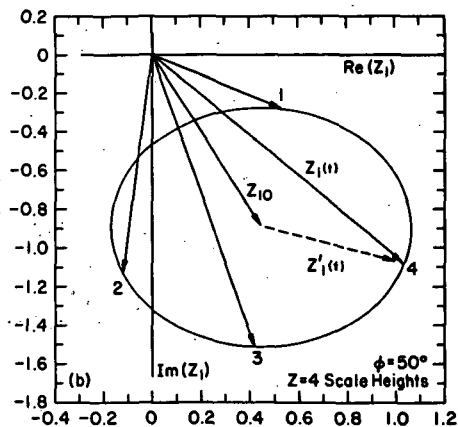


Figure 3 (b).

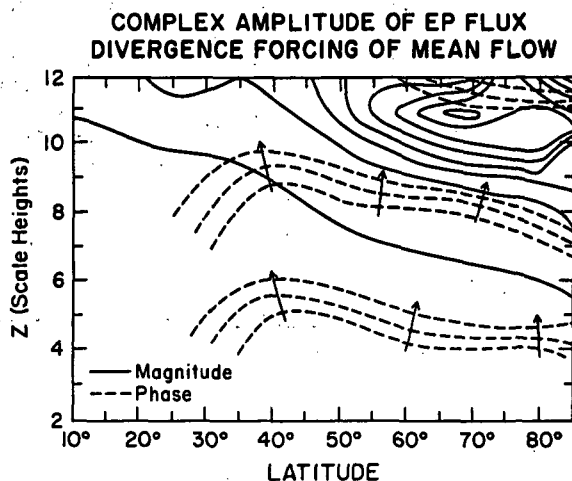


Figure 4.

tial vacillation in the lower and middle stratosphere. Poleward veering of \vec{F} due to the transient component can be seen as high as 6 scale heights.

The forcing of the mean flow at $\phi=50^\circ$ is shown in complex form in Figure 5. Largest values occur at the uppermost levels (both components in this simple picture grow unabated in the vertical) and near the pole due to convergent geometry when F is directed poleward. The vacillation in EP flux divergence propagates upward and poleward.

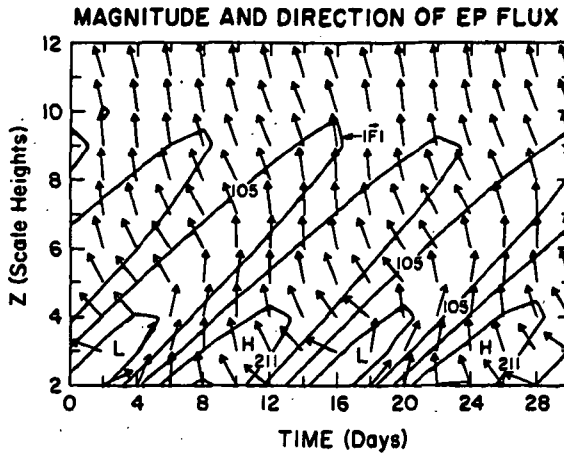


Figure 5.

CONCLUSIONS

Interference of stationary and traveling waves of sufficiently large amplitude can cause vacillations in the instantaneous EP-flux and its divergence. Such fluctuations may provide an explanation for some of the vacillations in transport and in the mean flow observed in the stratosphere. Whereas we have focused upon a simple two-component system, in reality several spectral components are likely to be present. For sufficiently large mean flow deceleration, the local wave field and the quasi-linear description developed here would presumably break down.

REFERENCE

- Hirooka, T., and I. Hirota (1985), J. Atmos. Sci., in press.
 Madden, R. A., and K. Labitzke (1981), J. Geophys. Res., **86**, 1247.
 Madden, R. A. (1983), J. Atmos. Sci., **40**, 1110.

2.26 OVER-REFLECTION OF BAROTROPIC ROSSBY WAVE PACKET

K. Takano and M. Uryu

Department of Physics, Kyusyu University
Hakozaki, Fukuoka 812, Japan

In winter, the gradient of the zonal mean potential vorticity in the stratosphere sometimes becomes negative. For example, in the preconditioning stage of stratospheric sudden warmings in 1973, there existed the negative gradient of the mean potential vorticity region for two weeks (KANZAWA, 1980).

It is well known that such a situation is a necessary condition of barotropic or baroclinic instability. One method to analyze it is to solve the eigenvalue problem. But if e-folding time of instability and the time that an unstable Rossby wave arrives the boundary is in the same order, it is a problem that how the unstable mode is formed in time. Furthermore, vertically propagating Rossby waves from the troposphere may be incident to these negative gradients of potential vorticity regions. So, we discuss this problem as the incidence of Rossby wave packet to the negative gradient of the mean vorticity region. For simplicity, we use the geostrophic linear barotropic equation of the beta plane. The basic state is shown in Figure 1.

If the Rossby wave has a critical level at the negative gradient of the mean vorticity region, wave over-reflection occurs. The reflection coefficient (the ratio of reflected wave amplitude to incident wave amplitude) can be calculated numerically by solving the boundary value problem (LINDZEN et al., 1980). According to the theory of Lindzen, wave over-reflection may be the mechanism of barotropic instability (LINDZEN and TUNG, 1978).

To examine how over-reflection occurs and how a normal mode is formed in time, we solve the initial value problem numerically. At $t=0$, we put the wave packet, which has a critical level in the negative gradient of the mean vorticity region, at the center of the domain (Figure 2). The center of the wave packet is incident to the negative gradient of the mean vorticity region after 14 days, which is estimated by group velocity of Rossby wave. Figures 3 and 4 show the time evolution of the wave packet. At day 14 the wave packet is incident to the negative gradient of the mean vorticity region. At day 31, we can see that the first half of the reflected wave packet is amplified and remains the same shape and same velocity (0 m/s) as incident wave packet, but wave-train, whose CR (real part of phase velocity) is 11 m/s and CI (imaginary part of phase velocity) is 2 m/s, follows after the reflected wave packet. (The phase velocity is estimated at a fixed point which is located at the center of right-hand half in the domain.)

The reflection coefficient estimated by the initial value problem is 1.7, and that calculated by boundary value problem is 1.5. These tend to agree with each other. When CR=11.7 m/s and CI=2.1 m/s, the reflection coefficient calculated by the boundary value problem becomes infinity (Figure 5). The solution of the boundary value problem on the condition that CR=11.7 m/s, CI=2.1 m/s, "stream function" = 1 m/s at the right boundary, and "stream function" = 0 m/s at the left boundary is shown in Figure 6. This is also the unstable solution of the eigen value problem when the left boundary is located at infinity. (The following wave-train after the reflected wave packet in the initial value problem corresponds to this solution). In other calculations, we find that when the dominant phase velocity of the initial wave packet is 11 m/s, the reflection coefficient estimated by the initial value problem does not agree with that calculated by the boundary value problem.

MEAN ZONAL WIND

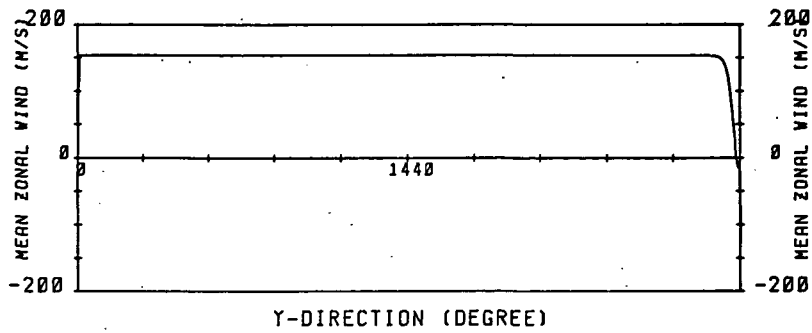


Figure 1a. Mean zonal wind profile.

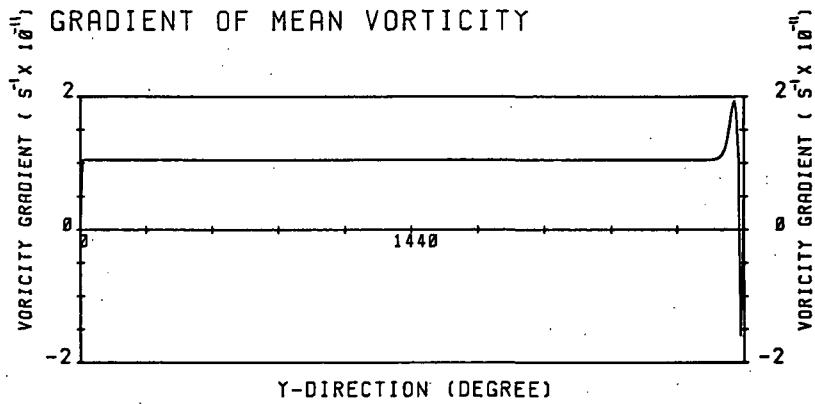


Figure 1b. Profile of gradient of mean vorticity.

MEAN ZONAL WIND NEAR TURNING POINT

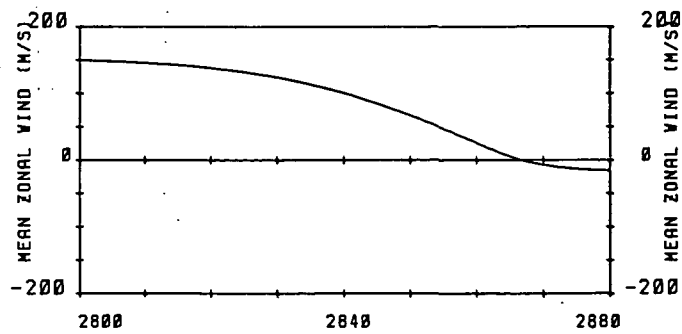


Figure 1c. Expanded mean zonal wind profile near right boundary.

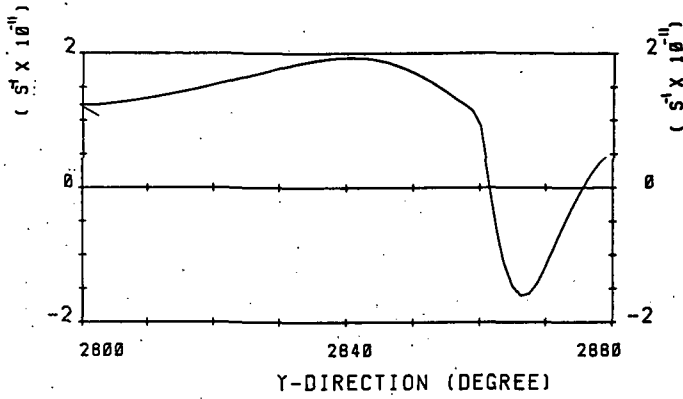


Figure 1d. Same as Figure 1c except gradient of mean vorticity.

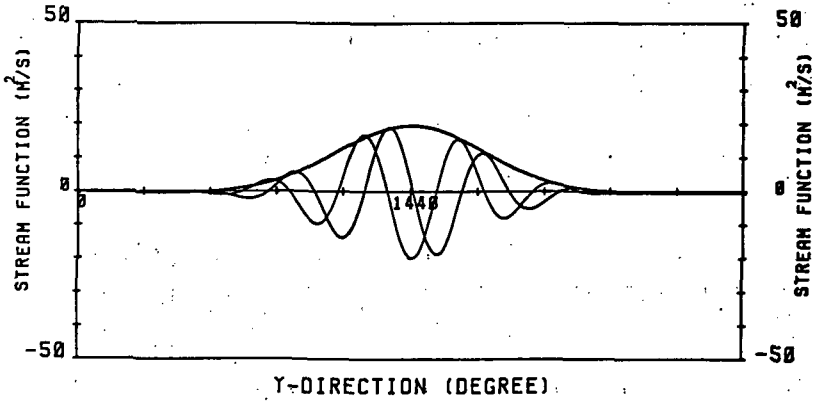


Figure 2. Initial condition.

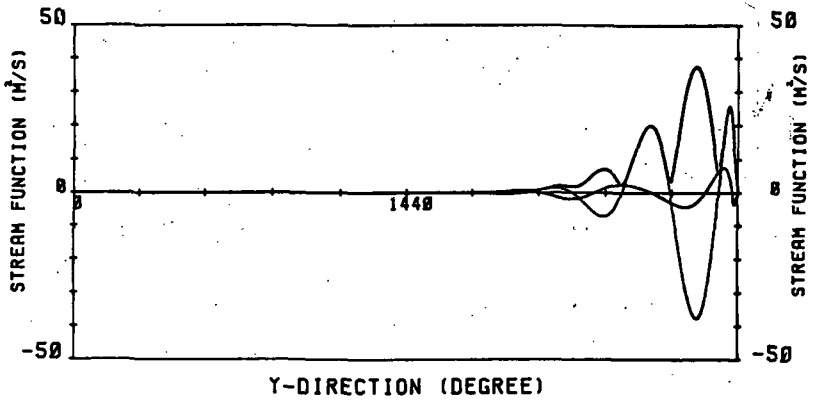


Figure 3. $t=14$ day

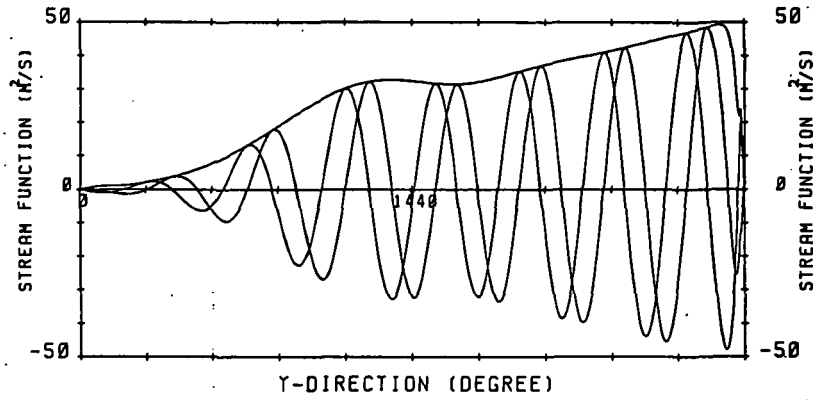


Figure 4. $t=31$ day

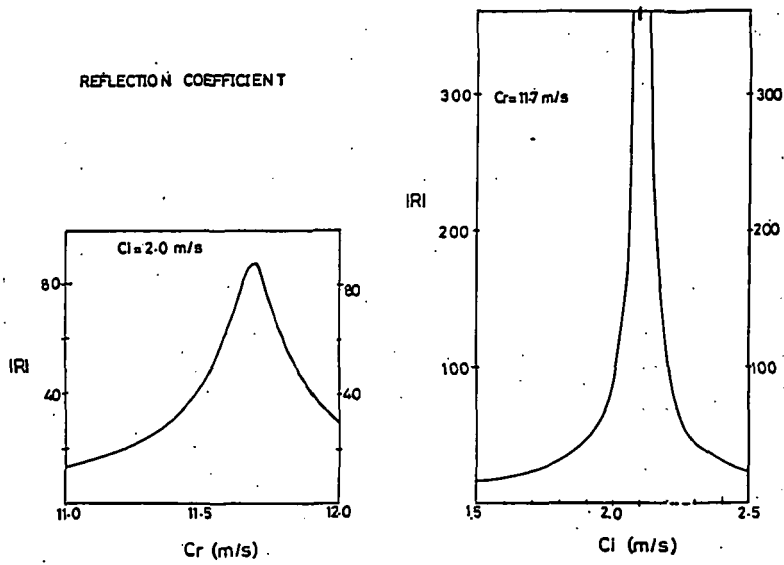


Figure 5. Reflection coefficient.

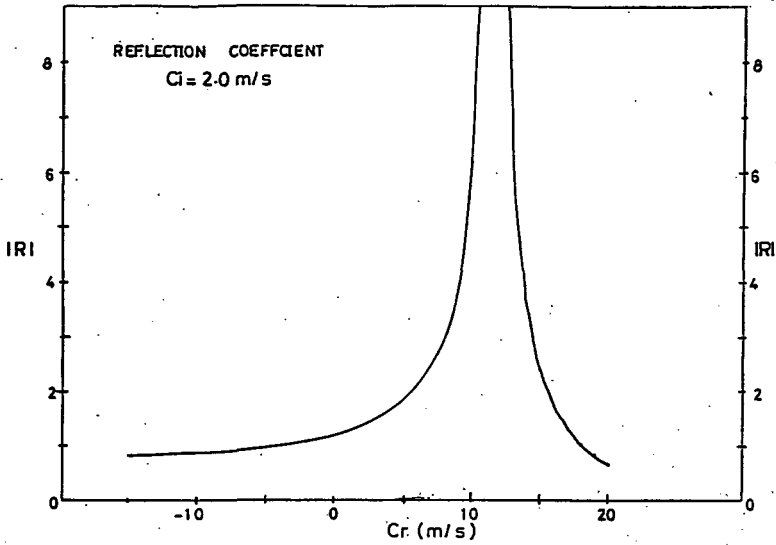
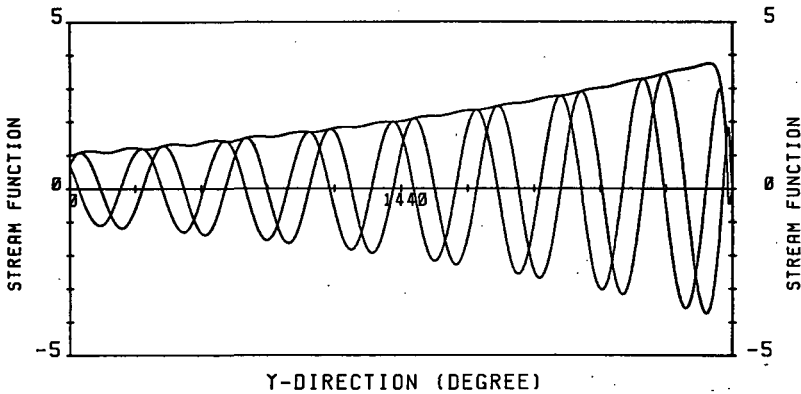


Figure 5 continued.

Figure 6. Solution of boundary value problem. $CR=11.7$ m/s, $CI=2.1$ m/s.

REFERENCES

- Kanzawa, H. (1980), The behavior of mean zonal wind and planetary scale disturbance in the troposphere and stratosphere during the 1973 sudden warming, *J. Meteorol. Soc. Japan*, **54**, 329-356.
- Lindzen, R. S., B. Farrell, and K. K. Tung (1980), The concept of wave over-reflection and its application to baroclinic instability, *J. Atmos. Sci.*, **37**, 44-63.
- Lindzen, R. S., and K. K. Tung (1978), Wave over-reflection and shear instability, *J. Atmos. Sci.*, **35**, 1626-1632.

2.27 EFFECTS OF RAYLEIGH AND NEWTONIAN DAMPING ON WAVE-MEAN FLOW INTERACTION

Yoshikazu Hayashi

Geophysical Fluid Dynamics Laboratory/NOAA
Princeton University, P.O. Box 308
Princeton, NJ 08542

A theoretical study is made of the effects of mean damping on wave-mean flow interactions (HAYASHI, 1985). A condition is derived (Appendix) for the Eliassen-Palm flux divergence to balance the steady-state residual circulations induced by eddies in the presence of mean damping. It is shown (Table 1) by a simple analytical model that this balance holds for stratospheric planetary waves when the Rayleigh friction coefficient is one order smaller than the Newtonian cooling coefficient, although the "tall mean flow condition" (ANDREWS and MCINTYRE, 1976) is not violated. In this case, the Eliassen-Palm flux divergence can be interpreted as approximating the steady residual circulation (\approx Lagrangian-mean circulations) induced by eddies as well as the net mean acceleration in the absence of mean damping. This balance is consistent with the stratospheric circulations of a dynamical model (ANDREWS et al., 1983).

It is also shown (Table 2) that, unlike the residual circulations, the steady-state Eulerian-mean circulations in the nonaccelerating condition are rather insensitive to the mean damping, since these circulations are nearly balanced with both eddy heat and momentum flux convergences. When the Rayleigh coefficient is sufficiently smaller than the Newtonian coefficient, these circulations are mostly due to the eddy momentum convergence, although they are nearly balanced by the eddy heat flux convergence. The present study is helpful for interpreting the results of dynamical models with and without eddies.

APPENDIX

Conditions for Eliassen-Palm Diagnostics

Steady-state mean momentum and heat balances are written in the conventional and transformed representations as

$$\epsilon \Delta \bar{u} = - (\overline{u'v'})_y + f \Delta \bar{v} \quad (1.a)$$

$$= \nabla \cdot \mathbf{F} + f \Delta \bar{v}^* \quad (1.b)$$

$$\gamma \Delta \bar{T} = - (\overline{T'v'})_y - R^{-1} N^2 \Delta \bar{w} \quad (2.a)$$

$$= - R^{-1} N^2 \Delta \bar{w}^* \quad (2.b)$$

Here, ϵ and γ denote the Rayleigh friction and Newtonian cooling coefficients. The overbar and prime denote the zonal mean and deviation. Δ denotes the difference between the zonal means with and without mean wave interactions. $\nabla \cdot \mathbf{F}$ denotes the Eliassen-Palm flux divergence, while the asterisk denotes the residual mean circulations.

TABLE 1. Conventional and transformed mean momentum (Table 1a) and heat (Table 1b) balances at 50 km of an analytical isothermal and f-plane model of mean flows forced by imposed planetary $\nabla \cdot \mathbf{F}$ for two ratios ($\epsilon/\gamma=1$ and $\epsilon/\gamma=0.1$) of mean damping coefficients.

Table 1a			Table 1b		
MOMENTUM BALANCE			HEAT BALANCE		
	$\epsilon/\gamma=1$	$\epsilon/\gamma=0.1$		$\epsilon/\gamma=1$	$\epsilon/\gamma=0.1$
$\epsilon \Delta \bar{u}$	-0.76	-0.26	$\gamma \Delta \bar{T}$	0.12	0.38
$-(\bar{u}'\bar{v}')_y$	1	1	$-(\bar{T}'\bar{v}')_y$	1	1
$f \Delta \bar{v}$	-1.76	-1.26	$-R^{-1} N^2 \Delta \bar{w}$	-0.88	-0.62
$\nabla \cdot \mathbf{F}$	-1	-1	$-R^{-1} N^2 \Delta \bar{w}^*$	0.12	0.38
$f \bar{v}^*$	0.24	0.74			

TABLE 2. $\Delta \bar{v}$ and $\Delta \bar{v}^*$ at 50 km for various values of ϵ/γ for $-(\bar{u}'\bar{v}')_y = 1$ and $\nabla \cdot \mathbf{F} = -0.11$.

ϵ/γ	$\Delta \bar{v}$	$\Delta \bar{v}^*$
10^{-3}	-1.01	0.10
10^{-2}	-1.01	0.10
10^{-1}	-1.03	0.08
1	-1.08	0.03
10^1	-1.11	0.00
10^2	-1.11	0.00
10^3	-1.11	0.00

Elimination of variables from the governing mean equations gives the elliptic equation as

$$\epsilon \frac{\partial^2 \Delta \bar{u}}{\partial y^2} + \gamma f^2 N^{-2} (\rho_0^{-1} \frac{\partial}{\partial z} \rho_0 \frac{\partial \Delta \bar{u}}{\partial z}) = \frac{\partial^2 \nabla \cdot \mathbf{F}}{\partial y^2} \quad (3)$$

This yields the following conditions:

$$\frac{\epsilon}{\gamma} \frac{L_z^2}{L_y^2} \gg \frac{f^2}{N^2}, \text{ then } \nabla \cdot \mathbf{F} \approx \epsilon \Delta \bar{u} \quad (4.a)$$

$$\ll \frac{f^2}{N^2}, \text{ then } \nabla \cdot \mathbf{F} \approx -f \Delta \bar{v}^* \quad (4.b)$$

where L_z and L_y are the representative vertical and meridional scales of $\Delta \bar{u}$, while f and N are the Coriolis and Brunt-Vaisala frequencies.

When $\epsilon = \gamma$, the condition (4.a) is analogous to the following "tall mean flow condition" of ANDREWS and MCINTYRE (1976) for $\frac{\partial \bar{u}}{\partial t}$ in the absence of mean damping:

$$\frac{L_z^2}{L_y^2} \gg \frac{f^2}{N^2}, \text{ then } \nabla \cdot \mathbf{F} \approx \frac{\partial \bar{u}}{\partial t} \quad (5)$$

It should be noted that for $\epsilon \gg \gamma$, the condition (4.b) can be satisfied even if the condition (5) is not violated.

REFERENCES

- Andrews, D. G., and M. E. McIntyre (1976), Planetary waves in horizontal and vertical shear: The generalized Eliassen-Palm relation and the mean zonal acceleration, J. Atmos. Sci., **33**, 2031-2048.
- Andrews, D. G., J. D. Mahlman, and R. W. Sinclair (1983), Eliassen-Palm diagnostics of wave-mean flow interaction in the GFDL "SKYHI" general circulation model, J. Atmos. Sci., **40**, 2768-2784.
- Hayashi, Y. (1985), Theoretical interpretations of the Eliassen-Palm diagnostics of wave-mean flow interaction. Part I: Effects of the lower boundary, Part II: Effects of mean damping, Submitted to J. Meteor. Soc., Japan.
- Holton, J. R., and W. M. Wehrbein (1980), A numerical model of the zonal mean circulation of the middle atmosphere, Pure Appl. Geophys., **118**, 284-306.
- Holton, J. R. and W. M. Wehrbein (1980,b), The role of forced planetary waves in the annual cycle of the zonal mean circulation of the middle atmosphere, J. Atmos. Sci., **37**, 1968-1983.

2.28 VARIATION OF TIDAL WINDS IN THE IONOSPHERE INFERRED FROM
GEOMAGNETIC SQ FIELD

M. Takeda and T. Araki

Data Analysis Center for Geomagnetism and Spacemagnetism,
Faculty of Science, Kyoto University, Kyoto 606, Japan

Geomagnetic Sq field is mainly generated by the dynamo action of tidal winds in the ionosphere, and therefore we can get some information from the variation of the Sq field. We have analyzed the geomagnetic Sq field during March 1-18, 1980, when the geomagnetic activity was exceptionally low, and calculated the equivalent Sq currents every 2 hours by using the spherical harmonics method. Then we extracted additional Sq currents by subtracting the currents averaged through all days in the period from the original currents at each UT. We discuss the change of the instantaneous Sq current system by the above-mentioned method. The details of the method are given in TAKEDA and ARAKI (1984).

There are several typical patterns in the additional Sq current system, as shown in Figure 1. Among them (P+), (P-) and (a) have the center of current vortex in high latitudes, and therefore are related to the effect of the interplanetary magnetic field ((P+) and (P-)) or geomagnetic substorms ((A)) and are not necessarily caused by the currents in the ionosphere. On the other hand, (+) < (-) and (2) have the centers in middle or low latitudes, and seem to reflect the variation of the dynamo action in the ionosphere. The patterns are similar to those expected by the dynamo action by diurnal ((+) and (-)) or semidiurnal ((2)) tidal winds. Therefore, the variation of these tidal winds is suspected to generate the additional currents. Table 1 gives the UT and day when these patterns appear. This table shows that duration of the patterns is typically several hours, but in some cases over ten hours, and therefore tidal winds in the ionosphere are expected to fluctuate in the above time constant. Figures 2 and 3 show the examples of the days when (+) or (-) continues for relatively long time. Each of these figures represents a typical transition of a pattern.

REFERENCE

Takeda and Araki (1984), Time variation of instantaneous equivalent Sq current system, J. Atmos. Terr. Phys., **46**, 911-915.

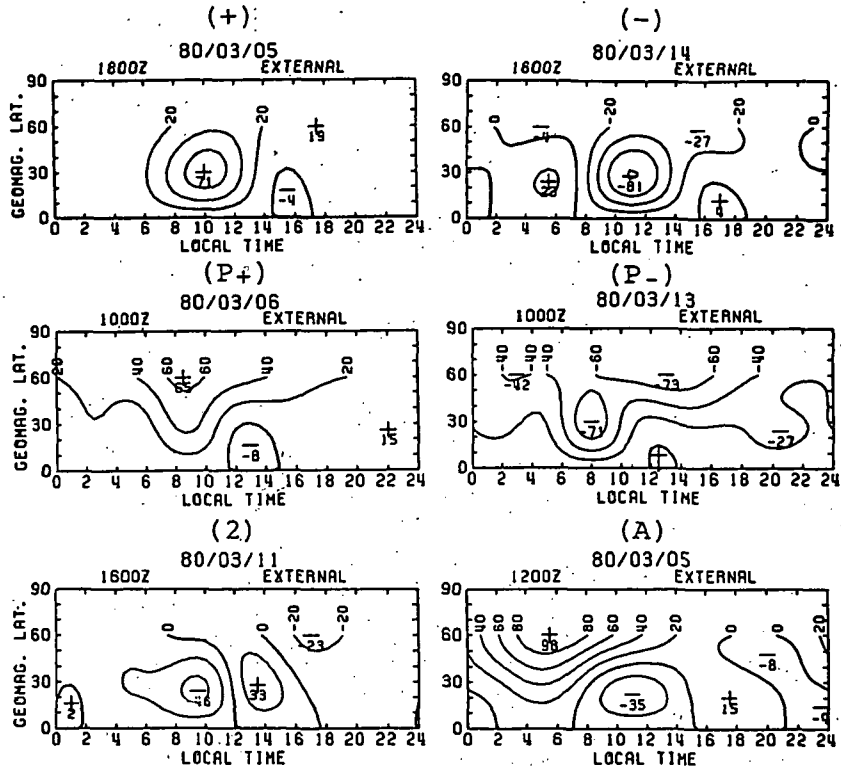


Figure 1. Six typical patterns ((+), (-), (P+), (P-), and (A)) of the additional current systems. Contours are drawn at every 20 kA.

Table 1. Distribution of the six patterns shown in Figure 1. with day and UT.

		UNIVERSAL TIME											
		2	4	6	8	10	12	14	16	18	20	22	24
D A Y	1	P.				+	+		-	-	+	+	+
	2					P.	P.	-	-	-	-	-	-
	3			-	-		+	+	+	A	-	-	-
	4			-	-	A	A	-	2	2	-	-	-
	5	A	A	A	-	A	A	-	2	+	+	-	-
	6	-	-		P.	P.	A	+	+	+	+	+	2
	7	2	2	2			P.	+	+	+	+	2	2
	8	+			-			+	+	+	+	+	+
	9	+	+	+	+	-	-	-		+	+	+	+
	10	+	+	+			-	-	-		+	+	+
	11			P.	P.	P.			2	2	2		+
	12				P.	P.	P.	2	2	-	-	2	
	13	-	-		P.	P.			-	-	-		+
	14				P.	-	-	-	-	-	-	-	+
	15	+	+	+	+	+	+	+					2
	16			+	+	+	+	+	+	2	2		
	17		2	P.	P.				+		2	2	
	18	+	+	+	+	+	+	+	+		2	2	2

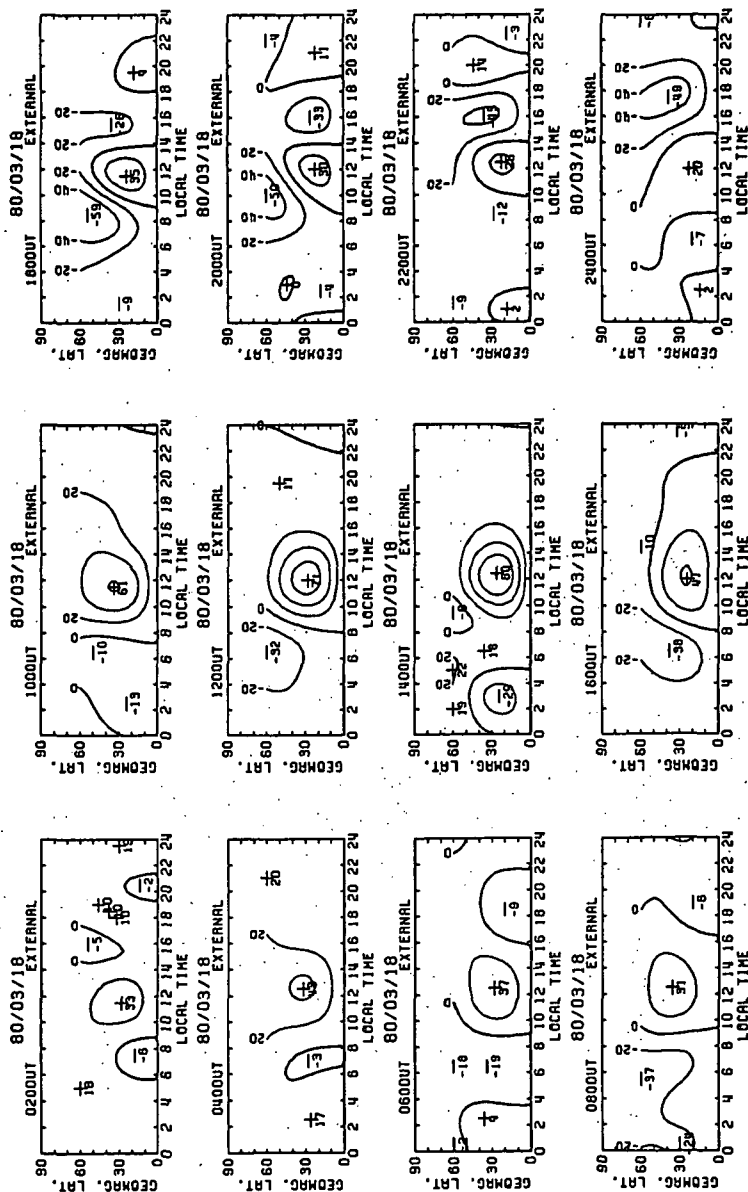


Figure 3. The additional currents on March 18. The pattern (+) succeeds during 02-16 UT on this day.

2.29 INFLUENCE OF GEOMAGNETIC DISTURBANCE ON ATMOSPHERIC CIRCULATION

Kunihiko Koderu

Meteorological Research Institute
Nagamine, Yatabe, Ibaraki, 305 Japan

The influence of geomagnetic disturbance or passage of the solar sector boundary on the atmospheric circulation has been reported by many authors. Unfortunately, we know little about the general morphology of Sun weather relationships. In order to know the general characteristics, we have analyzed pressure height variations on an isobaric surface over the Northern Hemisphere. Although it may be suitable to use some index, or some integrated value for statistical purposes, we have used weather prediction data to verify whether the obtained tropospheric response is caused externally or not.

DATA ANALYSIS

The superposed epoch method was employed to investigate the possible relationship between the geomagnetic disturbance and the tropospheric circulation. The dates of large geomagnetic disturbances were selected using the criterion by ROBERT and OLSON (1973); the daily Ap index must be greater than or equal to 15, and also greater than the previous day's Ap, at least the monthly mean. Thirty-two geomagnetic disturbed days were selected as key days for 5 winter seasons from November 1976 to February 1981. We studied only the Northern Hemispheric winter period, from November to February, because the troposphere seems to be especially influenced during winter (WILCOX et al., 1975).

Tropospheric meteorological data were taken from the daily grid point of data of 12Z, compiled by the Japan Meteorological Agency.

SURFACE PRESSURE AND PRESSURE HEIGHT VARIATIONS AFTER GEOMAGNETIC DISTURBANCE

Figure 1 shows the surface pressure difference between the key day and 2 days after the key day. Contour interval is every 2 mb with negative values shaded. Hatched area denotes the region less than -2 mb.

It can be clearly seen that the pressure decrease takes place in the northern part of Canada and off the coast of Alaska. This result confirms the remark, "a noticeable pressure drop at the places of the main winter depressions of the meteorology" by MUSTEL et al. (1981).

To investigate the vertical structure of this perturbation, we also calculated the pressure height difference between the key day and 2 days after the key day for 700 mb, 500 mb, 300 mb and 100 mb pressure levels.

Figure 2 shows the 500 mb height variation after a geomagnetic disturbance. Contour interval is 20 m with negative values shaded. Hatched area denotes the region less than -20 m. The pattern of pressure height change at 500 mb is quite similar to that of surface pressure. Note that the 500 mb pattern is shifted westward. From the results of other pressure levels, it is found that the pattern shifts westward as the pressure level becomes higher. These pressure height changes, after a geomagnetic disturbance are closely related to the positions of trough and ridge of stationary waves. The variation may be attributed to the change of activities of planetary waves.

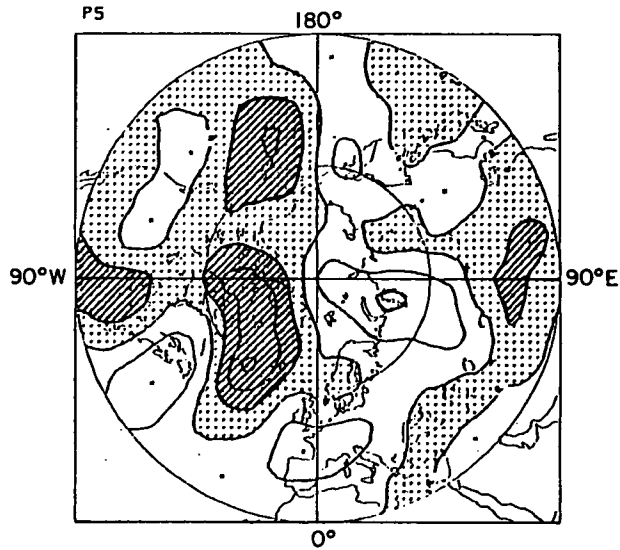


Figure 1. Surface pressure difference between the key day and 2 days after the key day. Contour interval is 2 mb with negative values shaded. Hatched area denotes the region less than -2 mb.

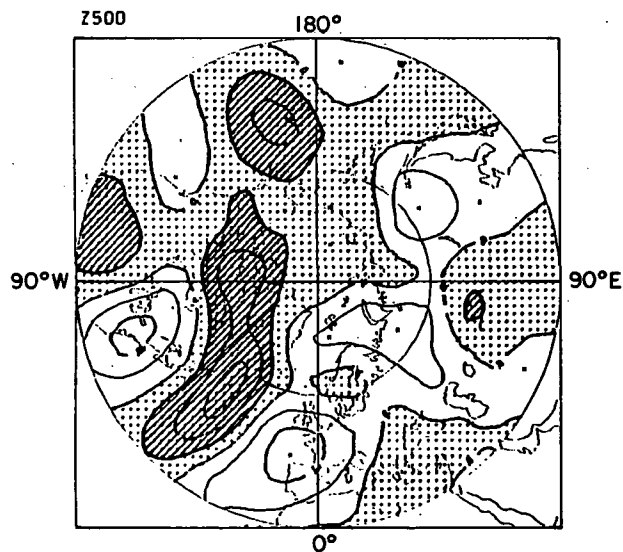


Figure 2. 500 mb pressure height difference between the key day and 2 days after the key day. Contour interval is 20 m with negative values shaded. Hatched area denotes the region less than -20 m.

EFFECT ON THE WEATHER PREDICTION

Further analysis is made using the weather prediction data to examine whether or not the troposphere responds to the geomagnetic disturbance. If it is true, weather prediction becomes poor after the geomagnetic disturbance.

We have used 500 mb Northern Hemispheric 24 h and 48 h predicted data calculated routinely by the Japan Meteorological Agency. The data are available for two winter seasons from November 1979 to February 1981, and 14 key days are used to calculate the superposed average.

As we are interested in the prediction of the variation of pressure, we calculated pressure height tendency, Δz , and its predicted value, Δz^* , as follows:

$$\begin{aligned}\Delta z(n) &= z^{00h}(n) - z^{00h}(n-1) \\ \Delta z^*(n) &= z^{48h}(n-2) - z^{24h}(n-2)\end{aligned}\quad (1)$$

where $z(n)$ indicates the 500 mb pressure height on n day from key day, and the superscript indicates the prediction time. Then the correlation between Δz and Δz^* is calculated over the Northern Hemisphere higher than 30 deg north (Figure 3).

Prior to the geomagnetic disturbance, correlation coefficients are around 0.5. It becomes suddenly less than 0.2 after the key day. This decrease of the correlation means that the pressure height variations after the geomagnetic disturbance cannot be predicted by the tropospheric weather forecasting model. It may be said that the variations may be triggered by the geomagnetic disturbance.

DISCUSSION

The results of the present analysis on the surface pressure change after geomagnetic disturbances reproduce the main characteristics obtained by MUSTEL et al. (1980), which are based on the data covering the different periods from 1880 to 1974. We find that the tropospheric weather forecasting model cannot predict the pressure change; therefore, we consider that the tropospheric pressure change after a geomagnetic disturbance really exists.

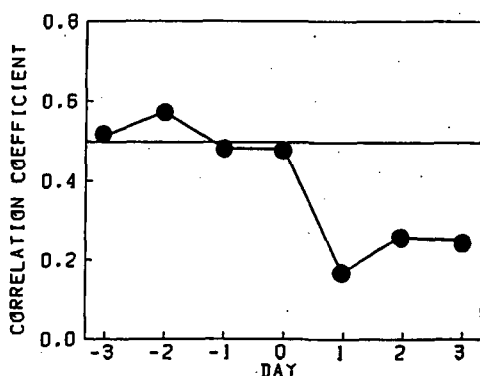


Figure 3. Correlation between the observed pressure height tendency and its predicted value.

We do not know how the geomagnetic storms can influence the troposphere. Present results indicate that the tropospheric response appears as the (planetary wave activities) change. The coupling between disturbances caused by geomagnetic activities and planetary waves (HINES, 1974) is a possible mechanism.

REFERENCES

- Hines, C.O. (1974), A possible mechanism for the production of the Sun-weather correlations, J. Atmos. Sci., 31, 581-591.
- Mustel, E. R., V. E. Chertoprud and N. B. Moulukova (1980), The reality of solar-weather relations and the changes of atmospheric circulation of solar origin, Proceedings in Sun and Climate, Toulouse, C.N.E.S., 151-161.
- Roberts, W. O. and R. H. Olson (1973), Geomagnetic storms and wintertime 300 mb trough development, J. Atmos. Sci., 30, 135-140.
- Wilcox, J. M., L. Svalgaard, and P. H. Scherrer (1975), Seasonal variation and magnitude of the solar sector structure-atmospheric vorticity effect, Nature, 255, 539-540.

2.30 BEHAVIOR OF NEUTRAL WIND GRADIENTS AT METEOR HEIGHTS OVER MIDLATITUDE STATIONS

P. C. S. Devara

Indian Institute of Tropical Meteorology
Pune- 411 005, India

and

G. Chandrasekhar and M. I. Ahmed

Space Research Laboratories, Department of Physics
Andhra University, Waltair - 530 003, India

INTRODUCTION

The region 80-100 km of the earth's atmosphere has been explored by means of meteor technique at mid- and high latitudes, and recently this technique has been made more powerful and sophisticated in order to achieve maximum height resolution of order 1 km to study the height variation of neutral wind parameters in detail. The variability in wind gradients with height has been extensively studied by ELFORD and ROBERTSON (1953) and GREENHOW and NEUFELD (1956). They report that these gradients in amplitude and phase vary, respectively, as high as 4m/sec/km and $12^\circ/\text{km}$ within the height band 85-95 km. In a comparison experiment between meteor winds and ionospheric drifts, MULLER (1968) observed the height gradients in amplitude and phase of 1.06 m/sec/km and $4.7^\circ/\text{km}$, respectively. By analysing the meteor wind data recorded over Adelaide, AHMED and DEVARA (1979) found that the gradients in amplitude and phase of semidiurnal wind components varied markedly between 80-90 km and 90-100 km height intervals.

An attempt has been made in this paper to study the variation of wind gradients in the altitude range of 80-100 km, which contributes information on propagational characteristics of wave phenomena prevailing at those altitudes. For this purpose, diurnal and semidiurnal components of the zonal (EW) and meridional (NS) neutral wind data collected over Atlanta (34°N , 84°W) using the Georgia Tech Meteor Wind Radar Facility during the period August 1974 - March 1978 over the height range 80-100 km are analysed in detail to obtain information on height gradients in amplitude and phase of neutral wind components over the height intervals of 80-90 km and 90-100 km. The details of analysis of data, major results achieved and conclusions are presented below.

DATA AND ANALYSIS

Monthly values of both the EW and NS wind components are taken as the data base. The data on diurnal and semidiurnal components of meteor winds at 80, 90, 100 km for the Atlanta station during the period August 1974 - March 1978 are used in the analysis. These values are averaged to obtain monthly and seasonal mean values over the 44-month period, and they are used for a detailed study of the behavior of gradients in amplitude and phase of both the EW and NS wind components in the height intervals of 80-90 km and 90-100 km.

RESULTS

Variation of height gradients in amplitude of diurnal and semidiurnal components over different months

Figure 1 (a,b,c,d) shows the monthly values of the height gradients in

amplitude of diurnal component of EW and NS wind. It is clear from Figure 1a that the zonal wind gradient is positive in the height interval of 90-100 km for all months of the year, and it exhibits a near semiannual oscillation. For the same component in the height interval between 80-90 km (Figure 1b) the gradient is negative throughout the year and also exhibits a near semiannual oscillation. These results indicate that in general the diurnal oscillation is damped at lower heights and amplified at higher heights. Maximum growth of amplitude occurred in winter months, and maximum damping occurred in summer months. The monthly variation of the gradient of the NS diurnal component between 90-100 km is positive; it is negative in the height interval of 80-90 km, and it is found to exhibit fluctuations with a period of 4 months in both cases (Figures 1c, 1d).

Figure 2 (a,b,c,d) depicts monthly variation of the gradients in amplitude of semidiurnal components of EW and NS wind. Figures 2a & 2b clearly show that the gradient of semidiurnal component of EW wind in the height interval of 90-100 km is positive throughout the year except during March and September, whereas in the height interval of 80-90 km the same gradient is negative in all the months except during September. It is clear from Figures 2c and 2d that the gradient of the semidiurnal component of NS wind is positive throughout the year and the same gradient in the interval 90-100 km is negative throughout the year. This component in the height interval of 80-90 km (Figure 2d) exhibits an oscillation with a period of 4 months.

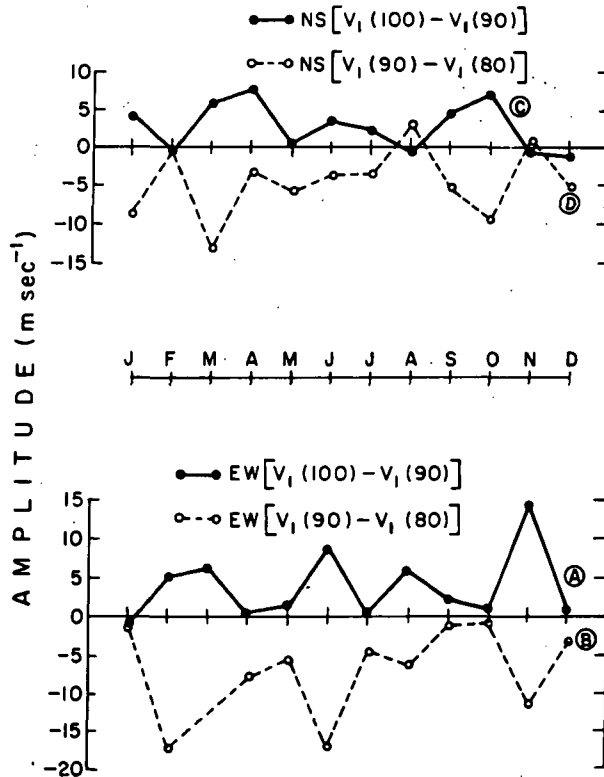


Figure 1. Monthly variation of gradients in amplitude of diurnal component of EW and NS wind.

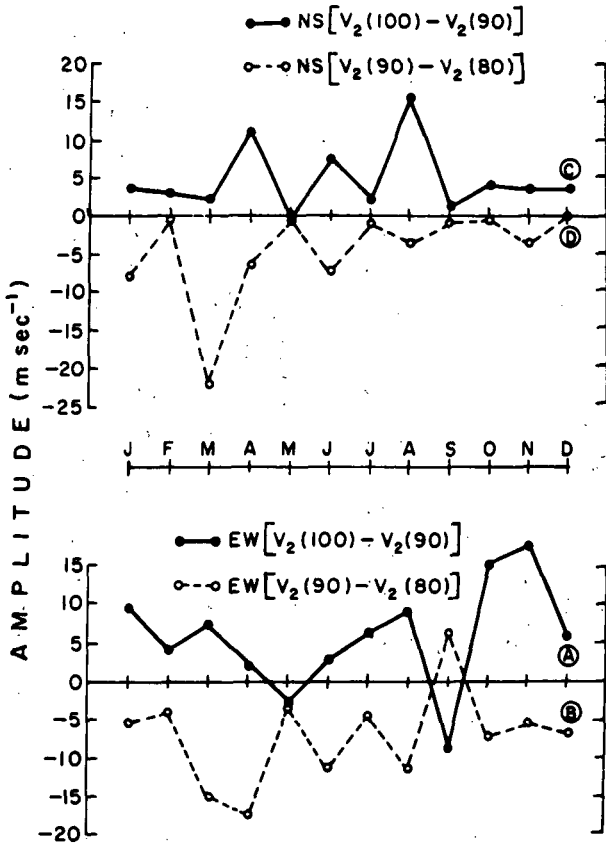


Figure 2. Same as Figure 1 but for semidiurnal component.

Variations of height gradients in the phase of diurnal and semidiurnal components over different months

The month-to-month variations of the height gradients in the phase of the diurnal component of EW and NS wind in the height intervals of 90-100 km and 80-90 km are shown in Figure 3a,b,c,d. Figures 3a and b show that monthly variations of the height gradients in the phase of the diurnal component of EW winds are quite erratic in both the height intervals. Also, it is evident from Figures 3c and d that almost throughout the year the nature of variations of gradient in the height interval of 80-90 km appears to be 180 out of phase with that in the 90-100 km height interval. This feature indicates that the variations in two successive height intervals of 10 km each of the phases of the diurnal component of EW and NS wind differ appreciably over a height change of 10 km.

The monthly variations of the gradients in phases of semidiurnal components of EW and NS wind in the height intervals of 90-100 km and 80-90 km are displayed in Figures 4a,b,c,d. It appears that there is an appreciable change in phase with height for the semidiurnal component of EW and NS wind, particularly during June, July and August, which represent summer months for the Atlanta station.

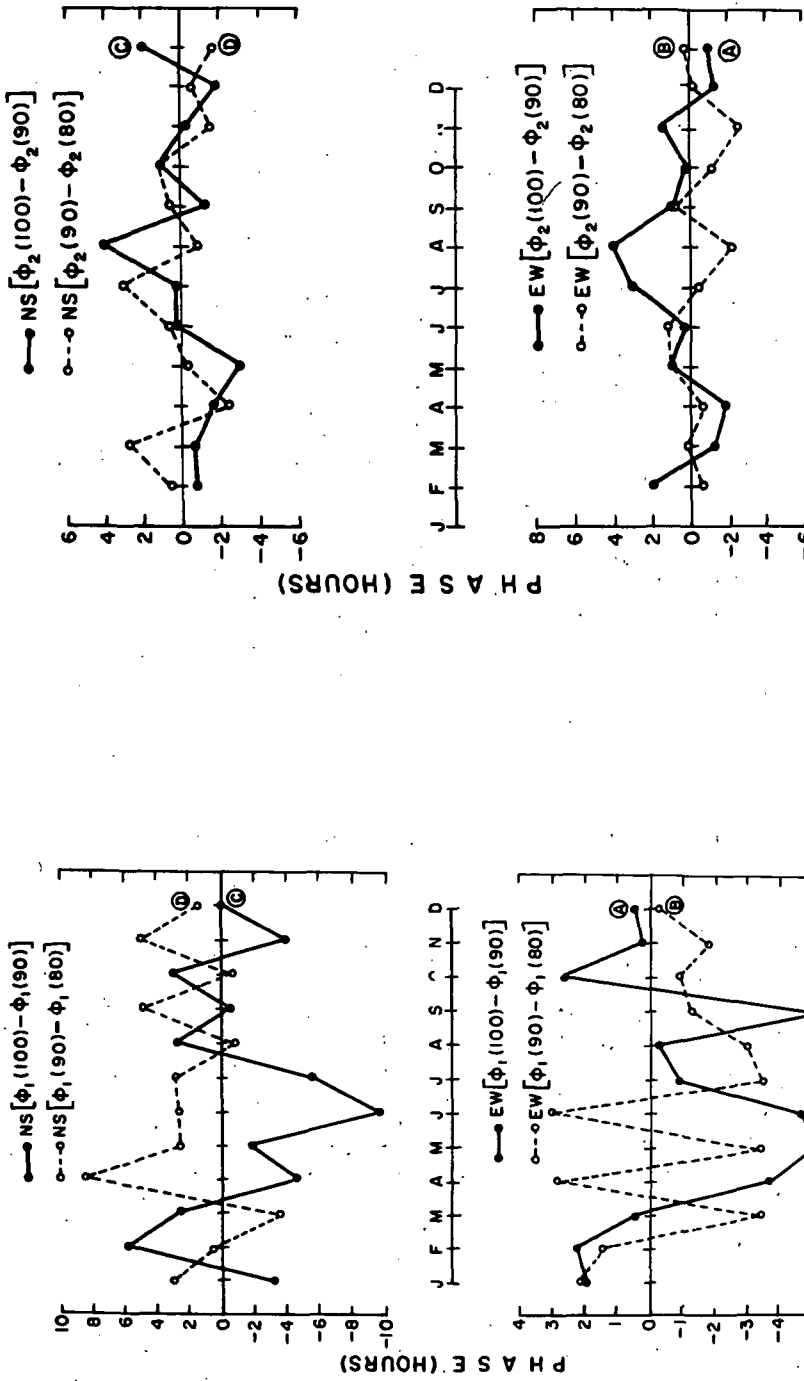


Figure 3. Monthly variation of gradients in phase of diurnal component of EW and NS wind. Figure 4. Same as Figure 3 but for semidiurnal component.

Seasonal and annual variation of height gradients in amplitude and phases of diurnal and semidiurnal components

The seasonal and annual mean gradients in amplitude and phase of diurnal and semidiurnal components of EW and NS wind for the height intervals of 90-100 km and 80-90 km are presented in Table 1. For comparison purposes, results of Adelaide (35°S, 139°E) data are indicated in this table with parentheses. The most striking event which can be seen from this table is that, at Atlanta, except for the height gradient in the phase of the diurnal component of EW wind, the seasonal mean height gradients in amplitude and phase of both diurnal and semidiurnal components of EW and NS wind are opposite to each other. This aspect clearly points out that the amplitude and phase of diurnal and semidiurnal components of EW and NS neutral wind changes appreciably over a height difference of 10 km.

DISCUSSION

The observed variations of height gradients in amplitude and phase of the neutral wind components over the height intervals of 80-90 km and 90-100 km are discussed in relation to the atmospheric oscillations. In general, the height variations in amplitude and phase of the diurnal and semidiurnal wind components at meteor heights can be described by means of the propagational aspects

Table 1. Seasonal and annual mean variation in gradients in amplitude and phase of diurnal (V_1, ϕ_1) and semidiurnal (V_2, ϕ_2) components of EW and NS wind for the height intervals 100-90 km and 90-80 km.

Gradient	Spring	Summer	Autumn	Winter	Annual
EW $V_1(100)-V_1(90)$	3.92	3.54	3.15	4.88	3.87
(6.97)	(-2.77)	(-10.44)	(1.27)	(-1.24)	
EW $V_1(90)-V_1(80)$	-12.87	-8.98	-6.23	-5.37	-8.36
(5.9)	(3.7)	(-1.34)	(-7.24)	(-2.69)	
NS $V_1(100)-V_1(90)$	4.43	2.17	3.80	0.89	2.82
(-5.2)	(7.57)	(-5.0)	(5.0)	(0.59)	
NS $V_1(90)-V_1(80)$	-5.66	-4.44	-4.04	-4.15	-4.57
(0.94)	(4.0)	(2.87)	(-4.43)	(0.84)	
EW $V_2(100)-V_2(90)$	4.90	2.22	5.32	11.59	6.00
(0.56)	(0.64)	(0.99)	(0.34)	(0.64)	
EW $V_2(90)-V_2(80)$	-12.36	-6.67	-3.96	-5.87	-7.22
(0.05)	(0.72)	(-0.50)	(0.82)	(-0.11)	
NS $V_2(100)-V_2(90)$	5.47	3.25	7.11	3.91	4.94
(-0.18)	(0.86)	(0.36)	(0.57)	(0.49)	
NS $V_2(90)-V_2(80)$	-9.61	-3.28	-1.47	-3.72	-4.52
(0.39)	(0.23)	(0.80)	(-0.20)	(0.31)	
EW $\phi_1(100)-\phi_1(90)$	-4.95	-54.35	-14.70	13.20	-5.20
(-38.00)	(-81.40)	(8.34)	(-64.34)	(-43.83)	
EW $\phi_1(90)-\phi_1(80)$	4.65	-19.65	-26.81	0.19	-10.40
(-48.00)	(-82.70)	(-33.00)	(-66.67)	(-47.58)	
NS $\phi_1(100)-\phi_1(90)$	19.35	-86.70	26.85	35.85	-1.16
(-12.67)	(1.67)	(-50.66)	(-23.67)	(-21.34)	
NS $\phi_1(90)-\phi_1(80)$	26.55	40.65	15.95	48.45	32.90
(-34.70)	(-11.67)	(6.67)	(-39.67)	(-19.84)	
EW $\phi_2(100)-\phi_2(90)$	-21.18	75.60	26.40	-2.25	-2.25
(3.99)	(-1.40)	(9.10)	(-1.9)	(2.44)	
EW $\phi_2(90)-\phi_2(80)$	5.88	-11.40	29.70	-3.60	5.15
(-9.22)	(10.40)	(0.20)	(-3.40)	(1.75)	
NS $\phi_2(100)-\phi_2(90)$	-5.49	-43.08	-3.75	-5.10	-14.35
(14.30)	(-1.83)	(11.40)	(0.40)	(6.02)	
NS $\phi_2(90)-\phi_2(80)$	0.81	27.51	-4.11	-16.02	-2.05
(-4.20)	(-6.8)	(-0.01)	(1.50)	(-2.38)	

of tidal energy from troposphere to upper atmosphere. The variations found in the present analysis of Atlanta data can be explained on the basis of the recent investigations made by AHMED and ROPER (1983). The seasonal variation of the height gradients in amplitude and phase of wind components noted in the present study may be interpreted in terms of the variations in vertical wavelengths of diurnal and semidiurnal tides over Atlanta.

The semiannual oscillation observed in the variations of height gradients in amplitude of the diurnal component of EW wind of the present study is in good agreement with the similar variation reported for the semidiurnal component by AHMED and DEVARA (1979) for the data recorded at Adelaide. This aspect reveals the similar nature of the variation of height gradient in amplitude of diurnal and semidiurnal components of EW wind at two midlatitude stations located in opposite hemispheres. It may be possible to explain this feature by extrapolating the rocketsonde observations of BELMONT and DARTT (1973). Also, analysis of the data at possible closer height intervals may provide further understanding of the problem.

CONCLUSION

Analysis of meteor wind data at Atlanta, a northern midlatitude station, showed considerable variations in the gradients in amplitude and phase of diurnal and semidiurnal components of EW and NS wind in the height intervals of 80-90 km and 90-100 km. Both the components of EW and NS wind showed almost positive gradients in the height interval of 80-90 km and negative gradients in the 90-100 km interval. The variations in height gradient in amplitude of the diurnal component of EW wind showed a semiannual oscillatory nature and comparison of these variations with those observed at Adelaide, a southern midlatitude station, suggested a similar type of behavior. Diurnal and semidiurnal components of NS wind exhibited oscillations with a period of about 4 months. The seasonal mean gradients in amplitude and phase of both the components of NS and EW wind are found to vary in an opposite manner between the height intervals of 80-90 km and 90-100 km. This suggests that the formation of amplitude node at 90 km is a regular feature for Atlanta. This could be explained in terms of reflection of energy associated with a phase reversal at 90 km. This feature is observed for both the diurnal and semidiurnal components. Similar features were observed for Adelaide, in the Southern Hemisphere, with nearly the same latitude as that of Atlanta.

ACKNOWLEDGEMENT

The authors wish to thank Dr. R. G. Roper, Georgia Institute of Technology, Atlanta, for making available the meteor wind data for Atlanta used in the present analysis.

REFERENCES

- Ahmed, M. I., and P. C. S. Devara (1979), Curr. Sci., **21**, 925.
- Ahmed, M. I., and R. G. Roper (1983), J. Atmos. Terr. Phys., **45**, 181.
- Belmont, A. D., and D. G. Dartt (1973), J. Geophys. Res., **78**, 6373.
- Elford, W. G., and D. S. Robertson (1953), J. Atmos. Terr. Phys., **4**, 271.
- Greenhow, J. S., and E. L. Neufeld (1956), Phil. Mag., **1**, 1157.
- Muller, H. G. (1968), J. Atmos. Terr. Phys., **38**, 701.

3.1 RADAR OBSERVATIONS OF MESOSPHERIC GRAVITY WAVES AND TURBULENCE AT ADELAIDE

R. A. Vincent

Physics Department, The University of Adelaide,
Adelaide, Australia, 5001

INTRODUCTION

Recent studies made at Adelaide (35°S , 138°E), of gravity waves and turbulence in the 60-100 km altitude range are reviewed. The observations were made with a radar operating at 2 MHz and both the spaced antenna (SA) and Doppler techniques were used. The SA observations were made on a continuous real-time basis from November 1983 to December 1984 with a time resolution of 10 min and a 2 km height resolution. More details may be found in VINCENT (1984). The Doppler observations were made on a campaign basis and were used to study gravity wave momentum fluxes with the dual-beam technique of VINCENT and REID (1983) and also turbulence dissipation rates (HOCKING, 1983, a,b).

SEASONAL VARIATIONS OF GRAVITY WAVE ENERGY

The SA winds data were used to investigate the morphology of gravity waves in the mesosphere. Time series of the EW (u) and NS (v) wind components for each height were produced by forming 30-min averages. These time series were then filtered to remove fluctuations due to long period planetary waves and atmospheric tides. The quantities $\overline{u'^2}$, $\overline{v'^2}$ and $\overline{u'v'}$ were then computed for the 1-8 hr and 8-24 hr period bands, where u and v are the EW and NS perturbation velocities, respectively. Figure 1 shows contours constructed from 10-day averages of the total mean square amplitudes, $\overline{v'^2} = (\overline{u'^2} + \overline{v'^2})$ in the 1-8 hr range. Above 80 km the wave energy remains fairly constant as a function of time; it is only below 80 km that there is a significant seasonal variation. The variation is mainly semiannual in character, with the minimum amplitudes occurring at the equinoxes when the mean zonal circulation in the middle atmosphere is changing. The dashed lines in Figure 1 show the contours of zero \overline{u} . A similar but less pronounced pattern is also evident for waves in the 8-24 hr period range. This seasonal pattern is different from that found by HIROTA (1984) for gravity waves at low to midlatitudes in the Northern Hemisphere stratosphere where gravity wave activity shows a semiannual variation with a maximum at the equinoxes.

Height profiles of $\overline{v'^2}$ averaged for 12-week periods centred around the solstices are shown in Figure 2. Also shown for comparison are the mean square amplitudes for wind fluctuations due to planetary waves in the 2-30 day period range. Two things are apparent. Firstly, the wave amplitudes grow only slowly with height or not at all, which indicates that the waves are saturated or are being heavily damped. Secondly, the gravity wave amplitudes are larger than the planetary wave amplitudes at all heights except below 80 km in winter. It is believed that gravity waves and planetary waves play important roles in determining the mean temperature and wind structures of the middle atmosphere (e.g., LINDZEN, 1981). The observations presented here suggest that gravity waves play the dominant role except, perhaps, the lower mesosphere in winter.

Figure 3 shows seasonally averaged height profiles of $\overline{u'v'}$. The fluxes for the two period bands are mainly negative in summer but have opposite signs in winter. For comparison, the $\overline{u'v'}$ fluxes for planetary waves were found to be small in summer but quite large in magnitude in late winter, achieving values as large as $-140 \text{ m}^{-2} \text{ s}^{-2}$ near 70 km altitude.

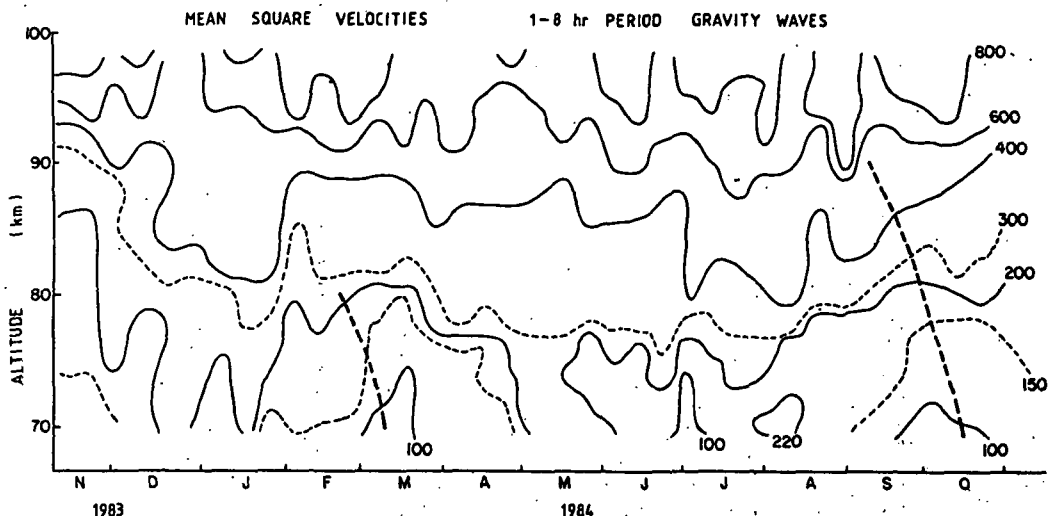


Figure 1. Contours of mean square energy density (m^2s^{-2}) for gravity waves in the 1-8 hr period range. The heavy dashed lines indicate the zero mean zonal velocity contour.

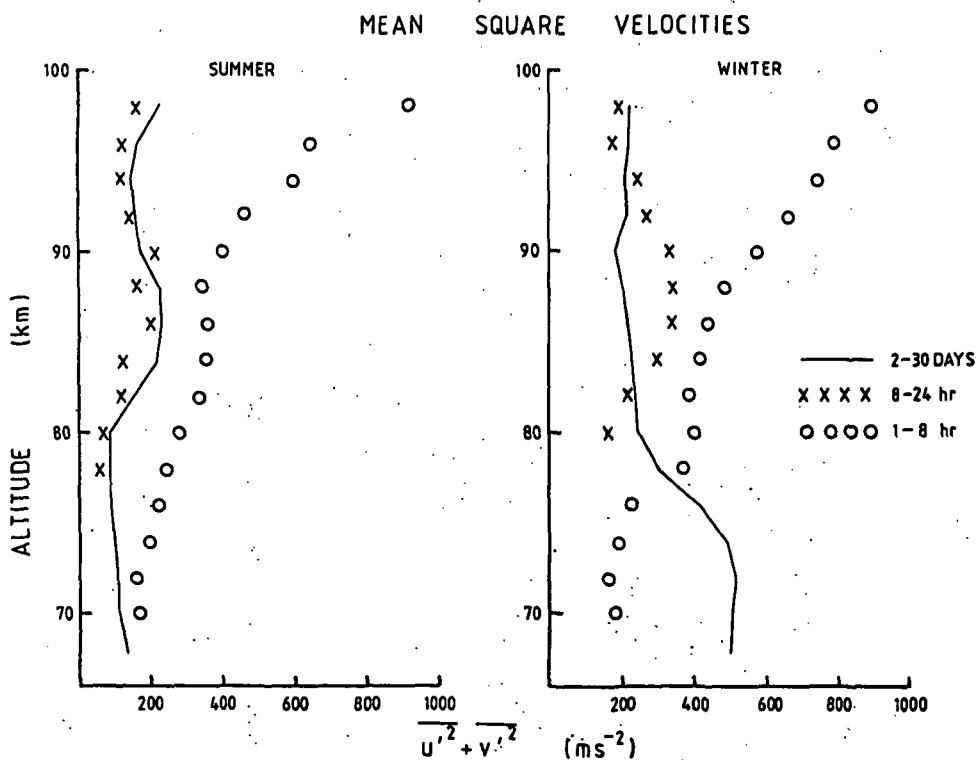


Figure 2. Height profiles of the seasonally averaged energy densities for 1-8 hr and 8-24 hr period gravity waves and planetary waves with periods between 2 and 30 days.

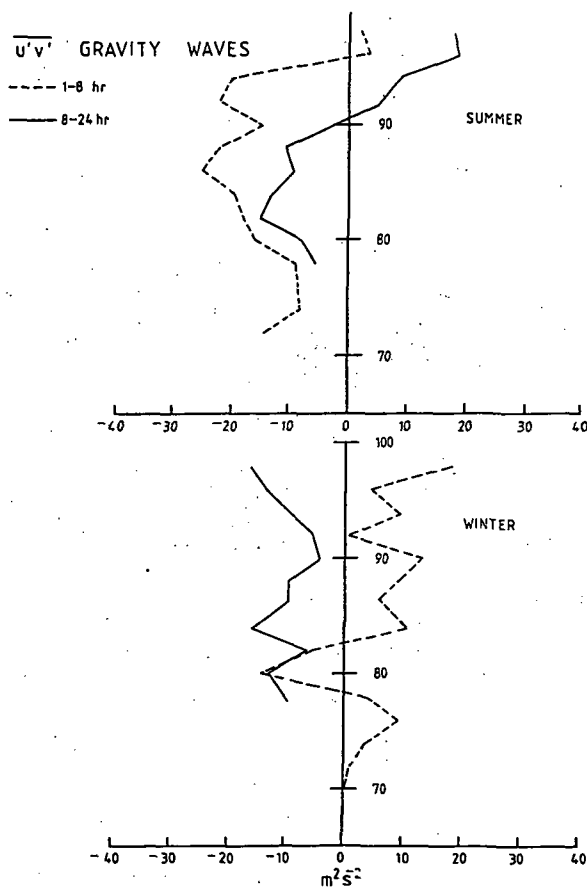


Figure 3. Height profiles of $\overline{u'v'}$ for gravity waves in the 1-8 hr and 8-24 hr period ranges.

One interesting feature of the observations is that the ratio $\overline{(v'^2/u'^2)}$ is almost always greater than unity. In summer the mean ratio is about 1.2 but in winter the average ratio is 1.8 for the 1-8 hr waves. Since the $\overline{u'v'}$ fluxes are nonnegligible this indicates that the wave field is partially polarized. By treating the quantities $(\overline{u'^2} + \overline{v'^2})$, $(\overline{v'^2}/\overline{u'^2})$ and $\overline{u'v'}$ as if they were "Stokes parameters", in analogy to a partially polarized electromagnetic wave-field, it has been possible to estimate the degree of polarization. Calculations suggest that the wave field at the mesopause is on the average 15% polarized in summer and 30% polarized in winter. If it is further assumed that the waves are propagating up from below then, from the sign of $\overline{u'v'}$, it can be inferred that the polarized waves are propagating towards the SE in summer and towards the SW in winter. In a given season, the zonal component of propagation is in the opposite direction to that of the prevailing zonal wind in the middle atmosphere. This indicates that the polarization is due to filtering effects as the waves propagate up through the stratosphere.

Although the above discussion pertains to waves with periods longer than 1 hr, some high-time resolution wind observations made in June 1984 show that

waves with periods less than 1 hr are also partially polarized. In this case the short period waves had a preferred direction of propagation towards the NW rather than the southwestward direction of the 1-8 hr components.

GRAVITY WAVE $\overline{u'w'}$ FLUXES

The first observations of $\overline{u'w'}$ fluxes in the mesosphere were reported by VINCENT and REID, (1982) and subsequent observations at Adelaide were discussed by REID (1984). Usually, the average magnitudes of $\overline{u'w'}$ over several days are in the range $1-3 \text{ ms}^{-1}$ but can be as large as 5 ms^{-1} . In general, the momentum flux ($\rho_0 \overline{u'w'}$) decreases exponentially with increasing height indicating momentum deposition. The induced wave drag is

$$\overline{F}_u = - \frac{1}{\rho_0} d(\rho_0 \overline{u'w'})/dz \approx \overline{u'w'}/H$$

where H is the scale height. Hence \overline{F}_u is of the order of $\approx 20-80 \text{ m s}^{-1} \text{ day}^{-1}$ and is in general in the right sense to balance the Coriolis torques induced by the mean meridional velocity, \bar{v} . Typically, \bar{v} is 5 to 10 ms^{-1} in magnitude and equatorward in summer and poleward in winter.

It is important to note, however, that there can be significant temporal variations in $\overline{u'w'}$ on time scales ranging from hours to days. Some of this variability may be due to changes in the wave sources, but some appear to be due to interactions with tides and planetary waves (see also VINCENT and FRITTS, this volume). It is important, therefore, to take longer term observations of the wave fluxes in order to understand better the role played by gravity waves in the mesosphere.

The relative contributions to the vertical momentum fluxes by low and high frequency waves have been investigated by filtering the radar data. It is found that a large fraction ($> 50\%$) of the momentum flux is carried by the waves with periods of less than 1 hr. Similar finding for the vertical energy fluxes were contained by VINCENT (1984). When studying the effects of gravity waves it is therefore desirable to use as good a time resolution as possible.

TURBULENCE DISSIPATION RATES

HOCKING (1983 a,b) has carried out some studies of turbulence at the mesopause by using vertical and off-vertical beams to measure the spectral broadening due to the random motions. Some care is required to account for the effects of shear and beam-broadening caused by the large scale winds. Hocking has also shown that it is important to account for the effects of gravity wave motions. Figure 4 shows observations of the inferred eddy dissipation rates made on one day in July 1984 (HOCKING, private communication). The average rate is about 0.08 W kg^{-1} and there is a hint of a diurnal variation with the rates being slightly larger near noon.

FUTURE WORK

It is obviously important to make further studies of gravity waves and turbulence in the mesosphere. To this end it is planned to integrate the spaced antenna and Doppler wind measurements so that simultaneous observations of winds, waves and turbulence can be made in real time.

ENERGY DISSIPATION RATES 20-21 JULY 1984
ADELAIDE, AUSTRALIA (35°S, 142.5°E)
80-88 km

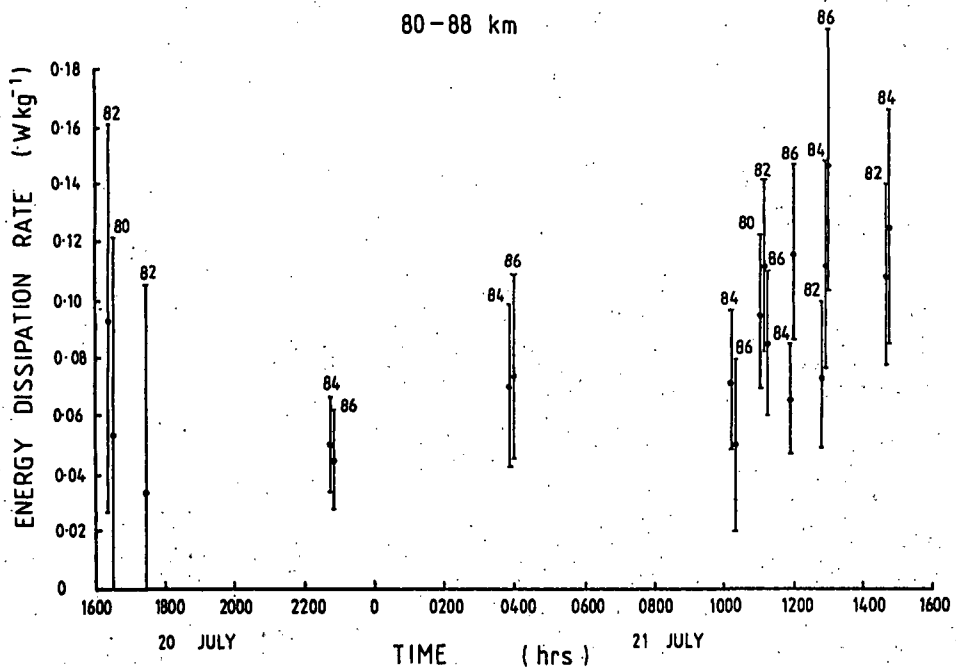


Figure 4. Turbulence energy dissipation rates measured between 80 and 88 km altitude on 20-21 July 1984.

REFERENCES

- Hirota, I. (1984), Climatology of gravity waves in the middle atmosphere, *J. Atmos. Terr. Phys.*, **46**, 767-773.
- Hocking, W. K. (1983a), On the extraction of atmospheric turbulence parameters from radar backscatter Doppler spectra - I Theory, *J. Atmos. Terr. Phys.*, **45**, 89-102.
- Hocking, W. K. (1983b), Mesospheric turbulence intensities measured with a HF radar at 35 S - II, *J. Atmos. Terr. Phys.*, **45**, 103-114.
- Lindzen, R. S. (1981), Turbulence and stress owing to gravity wave and tidal breakdown, *J. Geophys. Res.*, **86**, 9707-9714.
- Reid, I. M. (1984), Radar studies of atmospheric gravity waves, Ph.D. thesis, University of Adelaide.
- Vincent, R. A. (1984), Gravity-wave motions in the mesosphere, *J. Atmos. Terr. Phys.*, **46**, 119-128.
- Vincent, R. A. and I. M. Reid (1983), H. F. Doppler measurements of mesospheric gravity wave momentum fluxes, *J. Atmos. Sci.*, **40**, 1321-1333.

3.2 THE MU RADAR: CURRENT STATUS AND FIRST RESULTS

Susumu Kato¹, Shoichiro Fukao², Toshitaka Tsuda¹, and Toru Sato¹

¹Radio Atmospheric Science Center, Kyoto University
Uji, Kyoto 611, Japan

²Department of Electrical Engineering, Kyoto University
Yoshida, Kyoto 606, Japan

ABSTRACT

The MU radar (Middle- and Upper-atmosphere radar) is a 46.5-MHz pulse-modulated monostatic Doppler radar with an active phased array system. The nominal beam width is 3.6° , and the peak radiation power is 1 MW with maximum average power of 50 kW. A brief description of the system and initial observational results are presented herein.

INTRODUCTION

An MST (Mesosphere-Stratosphere-Troposphere) radar operating in the VHF-band was completed in November, 1984 at Shigaraki, Shiga, Japan (34.85°N , 136.10°E), by the Radio Atmospheric Science Center of Kyoto University (KATO et al., 1984). This radar has been named "MU radar" in reference to the middle and upper atmosphere, which are the system's principal objects of investigation. Here we first outline the MU radar system and then present a few preliminary results of upper-tropospheric, lower-stratospheric and mesospheric observations carried out in June 1984.

SYSTEM OUTLINE

The most outstanding feature of the MU radar is an active phased array system (FUKAO et al., 1980). In conventional radar systems a high-power transmitter feeds all array elements via an appropriate cascading feeding network. The MU radar system, on the other hand, does not incorporate such a passive array connected to a high-power transmitter. Instead, each element of the phased array is provided with a low-power amplifier, and all the amplifiers are coherently driven by low-level pulses in order to produce the desired peak output power.

This system configuration enables very fast and continuous beam steering as well as various flexible operations made possible by dividing the antenna array into independent subarrays. With these capabilities we can expect various sophisticated observations of the fast changing dynamical behavior of the atmosphere, such as gravity waves with fairly short periods.

The operational frequency is 46.5 MHz and the peak and average radiation powers are 1 MW and 50 kW, respectively. The antenna is a circular array with an aperture of 8330 m^2 . The nominal beam width is 3.6° . The shortest 1- μs pulse width or a 150-m height resolution is available. The basic parameters of the MU radar are given in Table 1.

OBSERVATIONAL RESULTS

Wind

In order to demonstrate that the MU radar functions properly, the radar-deduced winds are compared with the results of conventional meteorological observations. These observations are conducted using a partial system of 19

Table 1. Basic parameters of the MU radar.

Operational frequency	46.5 MHz
Antenna	Circular array of 475 crossed Yagi's
Aperture	8330 m ² (103 m in diameter)
Beam width	3.6° (one-way; half power for full array)
Steerability	Steering is completed in each IPP
Beam directions	1657; 0-30° zenith angle
Polarizations	Linear and circular
Transmitter	475 solid-state amplifiers (each with output power of 2.4 kW peak and 120 W average)
Peak power	1 MW
Average power	50 kW (duty ratio 5%)
Bandwidth	1.65 MHz (max) (pulse width: 1-512 μ s variable)
IPP	400 μ s-65 ms (variable)
Receiver	
Dynamic range	70 dB
Bandwidth	1.65 MHz (max)
Pulse compression	Binary phase-coding up to 32 elements

out of 25 subarrays (KATO et al., 1984). The antenna beam is switched every IPP sequentially in three or four different directions.

Figure 1(a) compares a MU radar wind profile in a height range of 5.4 - 24.5 km with that of a routine rawinsonde detected by the Japan Meteorological Agency (JMA) at Shionomisaki, approximately 150 km south of Shigaraki. The general agreement seems to be excellent between the two, considering the distance between the two observational sites. In Figure 1(b), the meridional and zonal wind velocities obtained in a height range of 67-90 km are compared with the meteorological rocket sounding obtained by the JMA at Ryori, about 700 km to the northeast. Although the two data patterns do not overlap, the two profiles are likely to be continuous from 60 to 70 km.

Tropospheric and stratospheric echoes

Figure 2 shows a time-height section of echo power at the upper-tropospheric and lower-stratospheric heights obtained by the vertically pointing beam. A few fundamental scattering properties which have been found by other radars (e.g., BALSLEY and GAGE, 1980) are reconfirmed: strong scattering layers of 1-2 km thickness exhibit large time-height variability in the troposphere, often showing clear downward motion. On the contrary, much thinner and more stable isolated layers are typical in the stratosphere. Their thickness seems to be comparable to, or even smaller than, the height resolution of 150 m.

Mean echo power profiles are compared between vertical and off-vertical beam directions. It is clearly observed in the stratosphere that the echo power received in the vertical direction is about 10 dB stronger than that in other directions. Stronger aspect sensitivity seems to be related to thinner and more stable layer. Large aspect sensitivity is not seen in most of the tropospheric region.

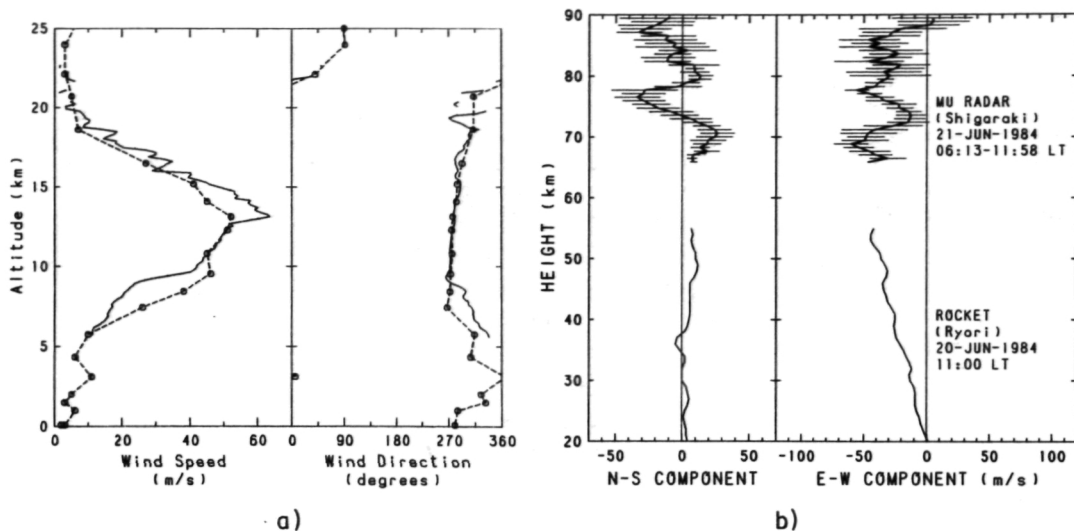


Figure 1. (a) Comparison of winds between the MU radar (solid line) and the rawinsonde launched at Shionomisaki (dotted line with circles) on June 1, 1984. (b) Comparison of winds between the MU radar (thick line with horizontal bars) and a routine rocket sounding at Ryori (thin line). The horizontal bars show wind variation around an average value over 0613-1158 LT on June 21, 1984.

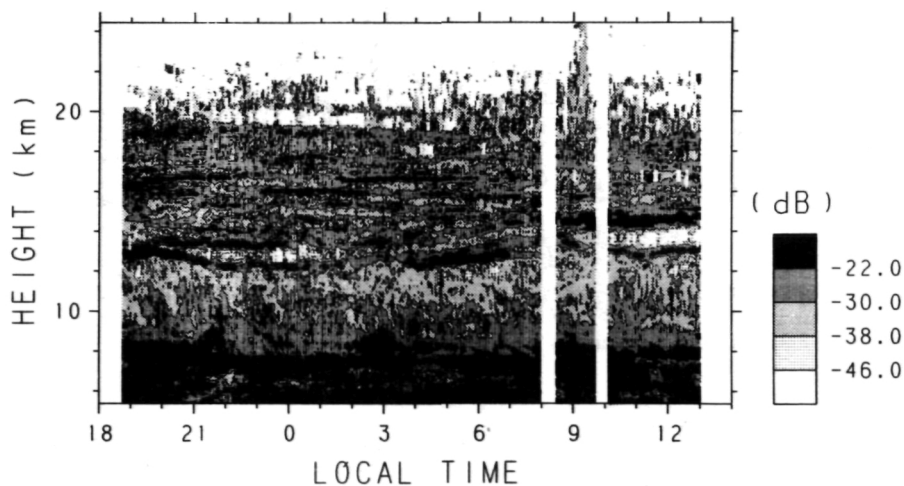


Figure 2. Time-height section of the tropospheric and stratospheric echo power in the vertical direction on June 1-2, 1984. The echo power is in an arbitrary unit, and contours are drawn at 8 dB intervals.

Mesospheric echoes

The MU radar detects turbulent echoes in the 60-90 km height range, and intermittent meteor echoes above 80 km. Figure 3 shows a time-height section of the mesospheric echo power in the vertical direction. The discrete intense echo superimposed on the generally weak background above 80 km are generated by meteors. There seem to be two different kinds of turbulent layers in 70-75 km region. One is the layer at 70 km which is very stable in height, and the other is the stronger layer around 74 km which shows a clear fluctuating motion.

These two layers, although located close to each other, can also be distinguished by the aspect sensitivity shown in Figure 4. This figure contains mean echo power profiles in three beam directions for the same period as in Figure 3. The vertical echo power is about 5 dB stronger than the other two directions for the layer at 70 km, while no clear aspect sensitivity can be seen for the echo in 72-76 km. The relationship between echo power is quite similar to that in the troposphere and stratosphere.

CONCLUDING REMARKS

The final detailed examination of the functioning of the system is currently in progress, and the system will begin nearly continuous operations in the near future. Short-term observations including the one presented here show that the MU radar is living up to the high standards of performance specified by the design.

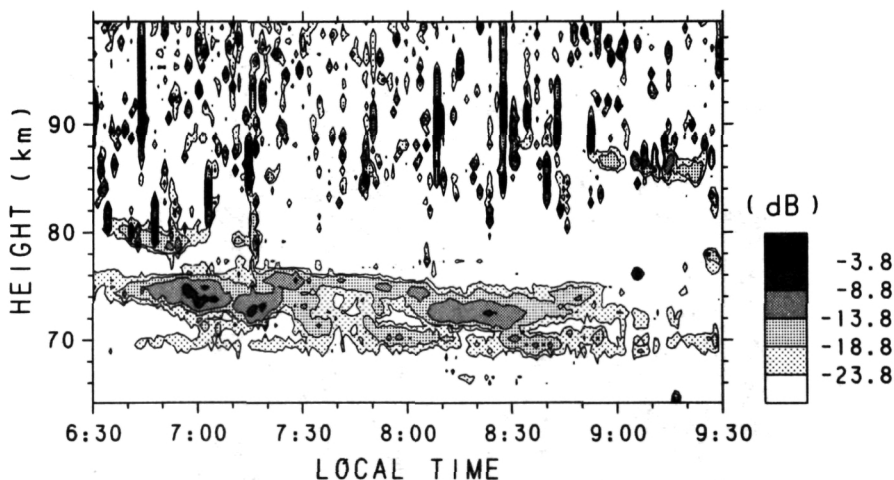


Figure 3. Time-height section of the mesospheric echo in the vertical beam direction on June 21, 1984. The echo power is in an arbitrary unit, and contours are drawn at 5 dB intervals.

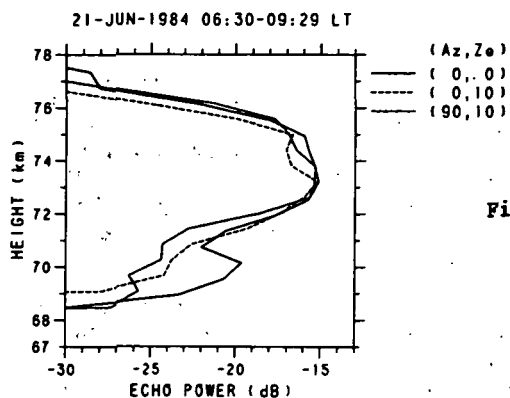


Figure 4. Average echo power profile of three different beam directions. Az: azimuth angle; Ze: zenith angle. Azimuth angle is measured clockwise from the north.

REFERENCES

- Balsley, B. B. and K. S. Gage (1980), Pure Appl. Geophys., **118**.
 Fukao, S., S. Kato, T. Aso, M. Sasada and T. Makihiro (1980), Radio Sci., **15**.
 Kato, S., T. Ogawa, T. Tsuda, T. Sato, I. Kimura and S. Fukao (1984), Radio Sci., **19**.

3.3 A COMPARISON OF THE SPECTRUM OF VERTICAL WIND VELOCITIES OBTAINED BY THE MST RADAR TECHNIQUE AT VARIOUS SEASONS AND LOCATIONS

W. L. Ecklund, B. B. Balsley, and D. A. Carter

Aeronomy Laboratory
National Oceanic and Atmospheric Administration
Boulder, CO 80303

Studies of the vertical wind variability in the atmosphere have been greatly facilitated by the MST radar technique, which enables almost continuous observations of the vertical wind field over extended periods. Power spectral studies of the vertical wind show a number of interesting characteristics, many of which are strongly dependent on the mesoscale wind pattern in the vicinity of the radar.

In the present study we report on general features of these spectra obtained under a variety of local wind conditions and at a number of locations.

3.4 POWER SPECTRA OF MESOSPHERIC VELOCITIES IN POLAR REGIONS

P. Czechowsky and R. Ruster

Max-Planck-Institut für Aeronomie,
3411 Katlenburg-Lindau,
Federal Republic of Germany

INTRODUCTION

The mobile SOUSY radar was operated on Andoya in Northern Norway (69°17'N, 16°01'E) during the MAP/WINE campaign from November 1983 to February 1984 and for about two weeks in June 1984 to study the seasonal dependence of mesospheric for about two weeks in June 1984 to study the seasonal dependence of mesospheric structures and dynamics at polar latitudes.

During the winter period, measurements were carried out on 57 days, primarily in coordination with the schedule of the rocket experiments. Echoes were detected in the troposphere and stratosphere up to 30 km and at mesospheric heights from about 50 to 90 km with a distinct maximum around noon. In summer, the radar system was operated continuously from 19 to 28 June 1984. Echoes occur almost for 24 hours in the height range from 70 to 95 km showing no recognizable diurnal variation. Similar observations in polar latitudes have been carried out for several years with the Poker Flat Radar in Alaska (BALSLEY, 1983; BALSLEY et al., 1983).

INSTRUMENTAL SETUP

The technique of the mobile radar is mainly based on the concept of the stationary radar, which has operated for several years in the Harz mountains in Germany (CZECHOWSKY et al., 1984). Therefore only the most relevant technical parameters are presented. The radar frequency was 53.5 MHz, the transmitter peak pulse power was 150 kW with a duty cycle of 4%. Based on scientific requirements a pulse length of 2 μ s and 4 μ s was used, corresponding to a height resolution of 300 m and 600 m, respectively. The antenna systems consist of 576 four-element Yagis located on an area of 8880 m². The antenna gain is 35.5 dB and the one-way-beam width 3°. The main beam is steerable in 4 directions.

RESULTS

The general picture of mesospheric structures detected during winter is summarized in Figure 1, which presents a contour plot of the mean diurnal variation of the frequency of echo occurrence. The contour lines are plotted in steps of 5%; the shaded area in the center represents the 50% probability. The height extension and the number of echoes were greatest around noon, ranging from 50 to 90 km, whereas at night echoes were only observed at altitudes between 70 and 90 km. During the entire observational period in winter, the occurrence of mesospheric echoes clearly coincides with radio-wave absorption events measured with a 32.5 MHz riometer. During daytime the onset, the intensity, and the variation of absorption were almost completely correlated with all characteristics of the scattering regions such as thickness and lifetime of the layers as well as signal-to-noise ratio of the radar returns. In the evening hours, strong absorption events were not always accompanied by the occurrence of mesospheric structures. During the absence of riometer activity, no echoes were detected at any time (CZECHOWSKY et al., 1985). Contrary to this, summertime echoes were detected almost continuously for 24 hours, showing no recognizable diurnal variation (Figure 2) in the height range from 70 to 95 km. The maximum probability of echo occurrence of 100% is indicated by shaded

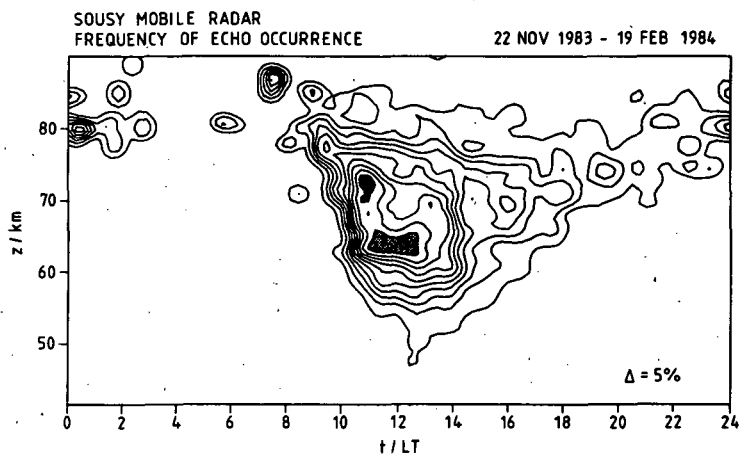


Figure 1. Frequency of echo occurrence observed in winter.

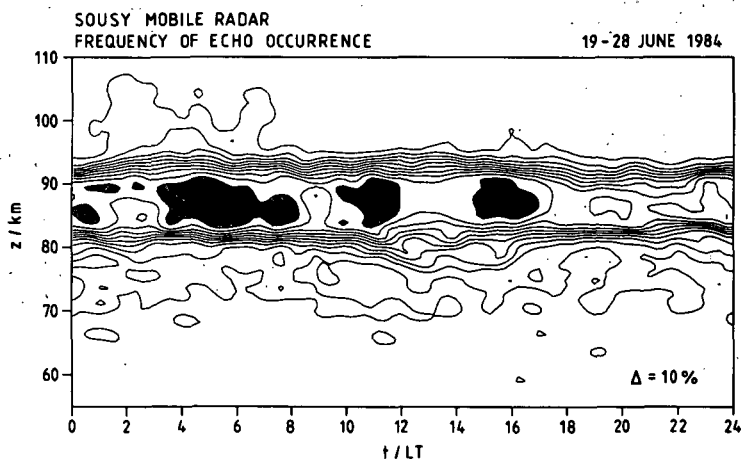


Figure 2. Frequency of echo occurrence observed in summer.

areas. Only a few structures were detected below 70 km, although the activity of radio-wave absorption was comparable to that in the winter season.

The analysis of individual structures indicates that in summer peaks of the echo power are statistically distributed only within the height range from 82 to 87 km with signal-to-noise ratios from about 30 to 50 dB lasting for several days. In winter the echoes appear in general as thin laminated layers separated by 3 to 4 km with a signal-to-noise ratio of only 5 to 25 dB. The mean lifetime varies between one and four hours (RUSTER and KLOSTERMEYER, 1985).

These different characteristic features between summer and winter observations indicate that the generation mechanism for irregularities with 3 m-scales changes with season. The corresponding velocity power spectra, there-

fore, may contain further information about the generation and the dynamics of structures in summer and winter.

In general, the velocity power spectra and the spectral density of the zonal and meridional component were calculated from data received from the vertical and two oblique directions. A typical time resolution was approximately 50 s, resulting in a maximum detectable frequency $f_{\max} = 1/(2 \cdot \Delta t) = 10^{-2}$ Hz. Due to averaging processes, this value was sometimes reduced by a factor of 2 or 4, enabling the investigation of periods above 4 min, which includes the Brunt-Vaisala period for that height range. Series of spectra were calculated from data sets of different time intervals to prevent the weighting or suppression of individual spectral components. To reduce windowing effects, Tukey-filters with various slopes were applied. By averaging sections of data, short term fluctuations were smoothed out. To minimize nonrelevant components, the spectra were height integrated, reducing the resolution from 300 and 600 m to 1.8 km. Since mesospheric wind systems at polar latitudes are predominantly orientated in the east-west direction, only the zonal component is presented.

Figure 3 shows a summary of results of winter data from layers lasting for more than 3 hours. All calculated components, symbolized by more than 1000 dots, were plotted (instead of mean values) in order to accentuate the variability of the power spectral density which exceeds one order of magnitude per period. The solid line represents the $-5/3$ slope, which seems to be somewhat steeper than the cloud of dots. Since only very few layers were continuously present for about 6 hours, the significance of periods above 3 hours was small and, therefore, neglected.

The summer results are based on continuous observations for nine days. The short- and long-term analyses were carried out separately, causing two maxima in the distribution of dots in Figure 4. It is evident that the variability of the power spectral density is approximately half of that derived for the winter season, and that the rather uniform slope of the dotted area is clearly less than $-5/3$. The value based on these measurements is -1.2 . Mean values were calculated at the low frequency range resulting in five pronounced spectral peaks at about 54, 24, 16, 12 and 8 hours as demonstrated by the thick solid line.

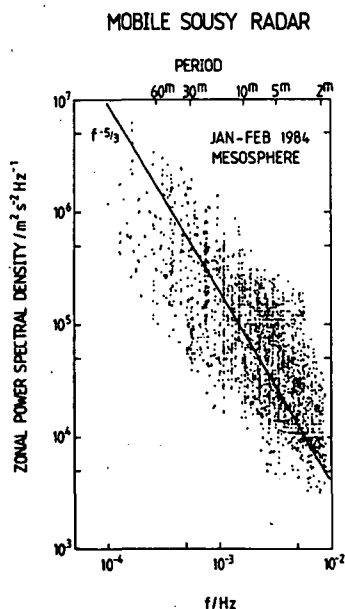


Figure 3. Power spectrum of zonal wind fluctuations for winter.

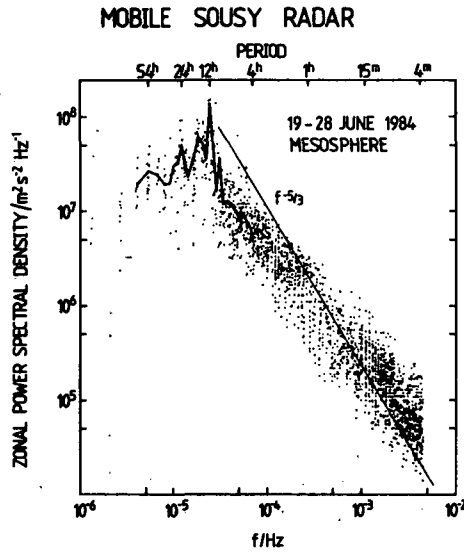


Figure 4. Power spectrum of zonal wind fluctuations for summer.

In addition, profiles of the echo power, the velocity components, the power spectra and the temperature were analysed to investigate the seasonal dependence of the generation mechanism. The following table summarizes all results:

	Winter	Summer
Height interval of echo occurrence	50 - 90 km	70 - 95 km
Signal-to-noise ratio	5 - 25 dB	30 - 50 dB
Time interval of echo occurrence	1 - 4 h	several days
Type of structure	up to five thin laminated layers	one dominating layer
Height of echo power maximum	variable between 50 - 90 km	82 - 87 km
Height dependence of zonal wind power spectrum	decreasing with increasing height	height independent
Variability of zonal wind power spectral density	$< 50 \text{ m}^2 \text{ s}^{-2} \text{ Hz}^{-1}$	$< 10 \text{ m}^2 \text{ s}^{-2} \text{ Hz}^{-1}$
Temperature variation at height intervals of echo occurrence	no height gradient	strong height gradient
Wind variation at height intervals of echo occurrence	shears occurring intermittently in height and time	long lasting shear

Concluding all observations, mesospheric radar echoes may be caused by breaking of upward propagating gravity waves in winter and by strong height gradients of temperature with local wind shears in summer.

ACKNOWLEDGEMENTS

Measurements using the mobile SOUSY VHF radar have been carried out on Andoya in Northern Norway. The authors would like to thank the staff of the Andoya Rocket Range for efficient cooperation. The measurement campaign in Norway and the antenna system of this radar were funded by the Deutsche Forschungsgemeinschaft.

REFERENCES

- Balsley, B. B. (1983), Radio Sci., 18, 1011.
Balsley, B. B., W. L. Ecklund and D. C. Fritts (1983), Radio Sci., 18, 1053.
Czechowsky, P., G. Schmidt and R. Ruster (1983), Radio Sci., 19, 441.
Czechowsky, P., R. Ruster and G. Schmidt, (1984), Adv. Space Res., 4, 47.
Ruster, R. and J. Klostermeyer (1985), this issue.

3.5 GRAVITY WAVE SPECTRA OBSERVED BY DOPPLER RADAR: COMPARISON OF A MODEL WITH MESOSPHERIC OBSERVATIONS

T. E. VanZandt

Aeronomy Laboratory
National Oceanic and Atmospheric Administration
Boulder, CO 80303

S. A. Smith and D. C. Fritts

Geophysical Institute
University of Alaska
Fairbanks, Alaska 99701

It has been proposed that mesoscale fluctuations of wind and temperature in the free atmosphere are due to gravity waves (DEWAN, 1979; VANZANDT, 1982). Critical tests of this hypothesis must involve the comparison of models based on the theory of buoyancy waves with suitable measurements. The MST radar technique is particularly attractive for this purpose, because it can measure several independent power spectra simultaneously.

The model used here is a further development by VANZANDT (1985) of the model developed by PINKEL (1981) to interpret spectra from Doppler sonar in the ocean. The input gravity wave spectrum is the GARRETT AND MUNK (1975) (GM75) model for oceanic internal waves, which has been shown to be a good approximation to observed atmospheric mesoscale spectra (VANZANDT, 1982).

In Figure 1 numerically calculated scale energy-content spectra (McCOMAS and MULLER, 1981) $F_V^*(\kappa) = F_V(\kappa)/E m_*^{t-1}$ are plotted versus the radial wave number κ , parametric in the zenith angle of the radar beam χ and m_* . The shape of these curves is approximately the shape of the assumed wave number spectrum in GM75, which is $(1 + (m/m_*)^t)^{-1}$, where m and m_* are the vertical wave number and the wave number bandwidth, respectively. t is observed to lie in the range $2 < t < 3$. E is the energy per unit mass. The dependence of the spectrum on the parameters is discussed in VANZANDT (1985).

The observed spectra are derived from mesospheric data taken by the Poker Flat MST radar in support of the STATE experiment during June 1983. The data were taken at zenith angles of 0 and 15°, with a time resolution of three minutes and an altitude resolution of 300 m. The echoing region lay between 82 and 90 km, but because of fluctuations in the echo amplitude, the actual altitude range varied with time. The wave number spectra were derived from spatial series 4500 m long. The method of editing and analyzing the data is described in detail in SMITH et al. (1985).

In Figures 2-4 such spectra are compared with the model spectra for three days when suitable data were available. In fitting the model spectra to the observed spectra, the spectral slope t was chosen to give the best straight-line fit to the largest oblique spectrum in each figure. The values of t were 2.3, 3.0, and 2.8 for the three days. Then the model ratio between the oblique and vertical spectra was used to set the amplitude of the model vertical spectra. It can be seen that the agreement is quite good in Figures 2 and 4 and at large wave numbers in Figure 3. The agreement is by no means perfect, however, because of day-to-day variability and anisotropy. Indeed, in Figure 4, the N and V curves are essentially identical. This implies that there was almost no horizontal wave energy in the N spectrum; that is, that almost all of the wave energy was propagating in the east-west plane.

Nevertheless, the agreement between the model and observed spectra is good enough to support the hypothesis that the mesoscale fluctuations were dominated by gravity waves. Although this conclusion holds strictly only for the mesosphere at the time and place of these observations, the fact that mesoscale spectra are observed to have about the same shape at all altitudes, times, and places (VINCENT, 1984; BALSLEY and GARELLO, 1985; SCHEFFLER and LIU, 1985) suggests that gravity waves are dominant under most, if not all, conditions. A great deal more theoretical and experimental work needs to be done before the importance of gravity waves can be fully assessed, however. In particular, the effect of the background wind (Doppler shifting) needs to be included in the model, and the present kind of study must be extended to a wide range of conditions, including the lower atmosphere.

These spectra also show that during these periods of observation two-dimensional turbulence (2DT) could not have been dominant, as GAGE (1979) has suggested. First, since the vertical component of motion in 2DT is quite small, the vertical spectra must be dominated by gravity waves in any case. Then the portion of the oblique spectrum that matches the model ratio can be attributed to gravity waves. Any contribution from 2DT would increase the oblique to vertical ratio, and it would very probably also distort the shape. It is clear from inspection of Figures 3-4 that little if any of the oblique energy can be attributed to 2DT. Second, 2DT should lead to isotropic horizontal motions, while the horizontal motions are appreciably anisotropic on all three days shown here.

We conclude that in this study the mesoscale fluctuations were dominated by gravity waves, and the contribution of 2DT was small.

REFERENCES

- Balsley, B. B. and R. Garello (1985), The kinetic energy density in the troposphere, stratosphere and mesosphere: A preliminary study using the Poker Flat MST radar in Alaska, to appear in Radio Sci..
- Dewan, E. M. (1979), Stratospheric wave spectra resembling turbulence, Science, **204**, 832-835.
- Gage, K. S. (1979), Evidence for a $k^{-5/3}$ law inertial range in mesoscale two-dimensional turbulence, J. Atmos. Sci., **36**, 1950-1954.
- Garrett, C. and W. Munk (1975), Space-time scales of internal waves: A progress report, J. Geophys. Res., **80**, 291-297.
- McComas and Muller (1981), The dynamic balance of internal waves, J. Phys. Ocean., **11**, 970-986.
- Pinkel, R. (1981), On the use of the Doppler sonar for internal wave measurements, Deep-Sea Res., **28A**, 269-289.
- Scheffler, A. O. and C. H. Liu, (1985), On observation of gravity wave spectra in the atmosphere using MST radars, to appear in Radio Sci..
- Smith, S. A., D. C. Fritts and T. E. VanZandt (1985), Use of a gravity wave model for classifying atmosphere wind fluctuations, Radio Sci..
- VanZandt, T. E. (1982), A universal spectrum of buoyancy waves in the atmosphere, Geophys. Res. Lett., **9**, 575-578.
- VanZandt, T. E. (1985), A model for buoyancy wave spectra observed by Doppler sounding systems, Radio Sci., submitted 1985.
- Vincent, R. A. (1984), Gravity-wave motions in the mesosphere, J. Atmos. Terr. Phys., **46**, 119-128.

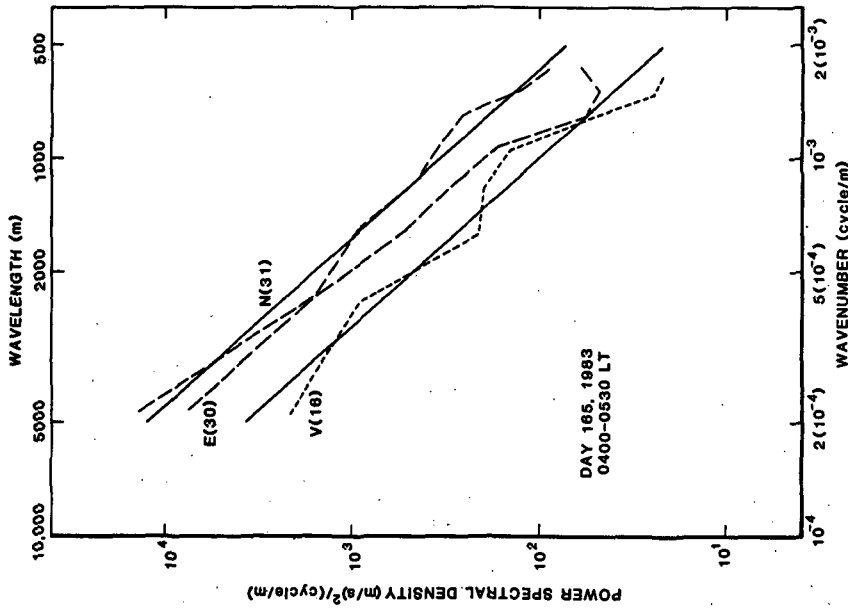


Figure 2. Vertical wave number spectra for Day 165, 1983. Dashed lines are spectra computed from observations along the east (E), north (N), and vertical (V) beams. Each plotted spectrum is the average of the number of spectra given in parentheses obtained between 0400 and 0530 local time. Solid lines are model curves.

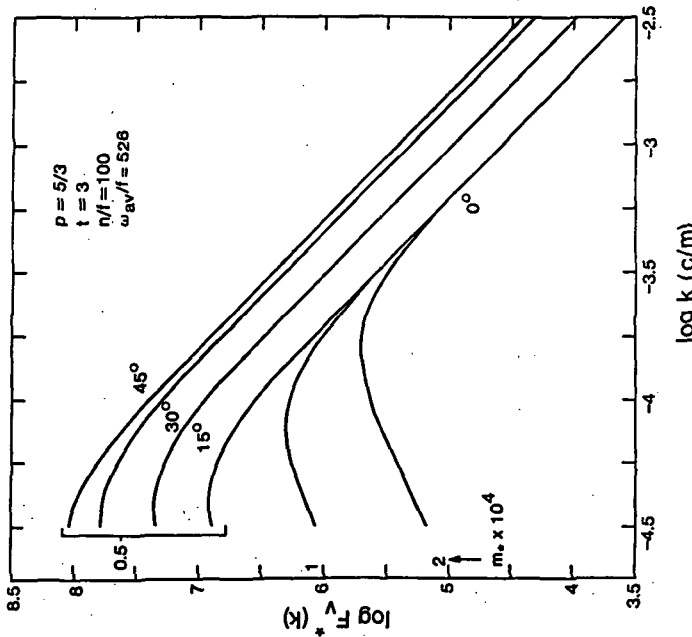


Figure 1. The scaled energy-content spectrum $F_v^*(k) = \kappa F_v(k)/Em_*^*$, versus radial wave number k , parametric in χ and m_*^* . For $\chi = 0^\circ$, curves for $m_*^* = 0.5, 1$, and 2×10^{-4} (c/m) are given, but for other χ , only $m_*^* = 0.5 \times 10^{-4}$ is given.

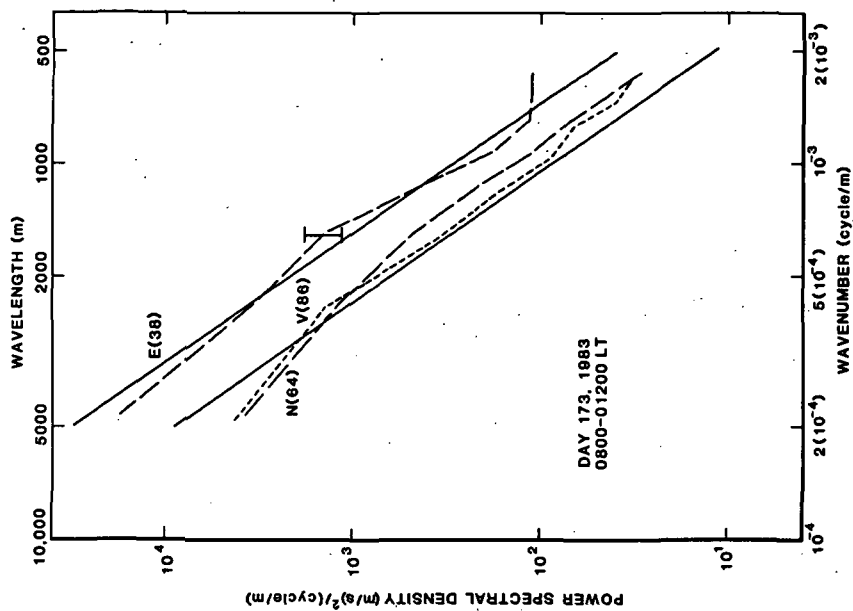


Figure 4. Same as Figure 1 but for day 173, 1983.

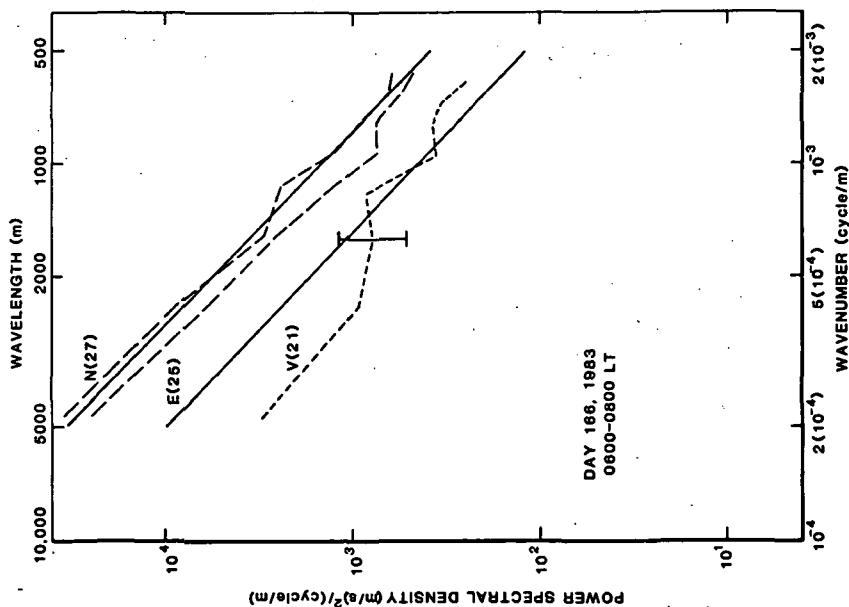


Figure 3. Same as Figure 1 but for day 166, 1983.

3.6 INSTABILITIES AND TURBULENCE AT MESOSPHERIC HEIGHTS AS OBSERVED BY VHF RADAR

R. Ruster and J. Klostermeyer

Max-Planck-Institut für Aeronomie
3411 Katlenburg-Lindau
Federal Republic of Germany

INTRODUCTION

VHF radars operating at frequencies near 50 MHz can simultaneously measure mean winds, waves and turbulence at scales equal to half the radar wavelength (≈ 3 m). HARPER and WOODMAN (1977) pointed out that short-period evanescent gravity waves act as a direct energy source for turbulence at mesospheric heights. It is the purpose of this paper to present a few examples of observational results of strong mesospheric turbulence bursts and to compare them with recently observed turbulence bursts in a tropospheric jet stream to gain insight into the generation mechanism.

EXPERIMENT

Radar observations of the mesosphere have been carried out using the stationary SOUSY VHF Radar in Germany as well as the mobile one in Northern Norway (KLOSTERMEYER and RUSTER, 1985; RUSTER, 1985). The height resolution was 1.5 and 0.6 km, respectively. The antenna beam was sequentially directed vertically upwards and 7 or 4 degrees off-vertically at two azimuth directions. The resulting time resolution is about 30 s.

OBSERVATIONAL RESULTS

Occasionally the radar signal power was characterized by strong bursts appearing almost simultaneously in all antenna beam directions at one or two adjacent height intervals. Figure 1 shows a particularly clear example. It presents the radar signal-to-noise ratios (linear scale) at a height of 77 km as a function of time for three different beam positions (vertically, off-vertically towards the east and towards the south). At 1310 LT, the power rises by a factor of approximately 150 (22 dB) in the vertical beam, a few minutes later also in the off-vertical beams indicating that the burst propagates horizontally with a speed of several ten meters per second. Figure 1 further shows that two or more bursts can occur successively with a quasi-period of about 10 min.

Figure 2 shows a comparison between the temporal variation of the signal-to-noise ratio and the air velocity observed in the vertical beam direction. The gaps in the velocity time series are due to weak signals. Between 1310 and 1340 LT, the velocity oscillates with an amplitude of 1.5 m/s and a dominant period of about 10 min which is identical with the quasi-period of the power bursts. The bursts coincide essentially with the minima and the subsequently increasing parts of the velocity curve.

Hourly wind profiles have been calculated from incoherently added power spectra. Figure 3 shows the zonal and meridional wind components from 1045 to 1345 LT. The profiles have a wave-like structure with a vertical wavelength near 11 km and a downward phase speed of 0.3 m/s. These values yield a period of about 10 h, indicating that the wave structure is due to a long-period internal gravity wave which, within the accuracy of the results, could be a semi- or terdiurnal tide. The amplitude of the meridional component increases by a factor of 2 from 1245 to 1345 LT yielding a strong vertical shear between

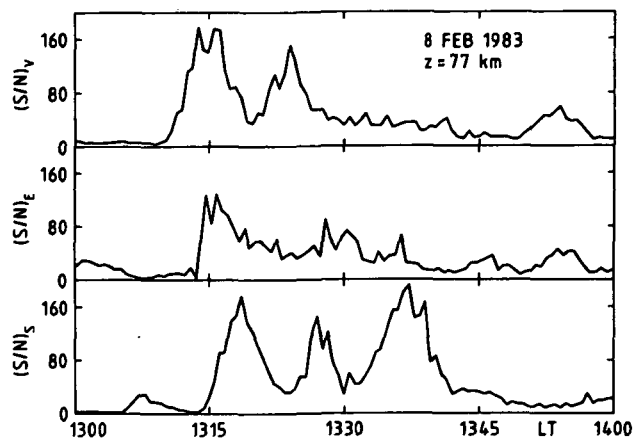


Figure 1. Time series of the signal-to-noise ratios measured in the vertical $((S/N)_V)$, eastward $((S/N)_E)$ and southward $((S/N)_S)$ antenna beam directions.

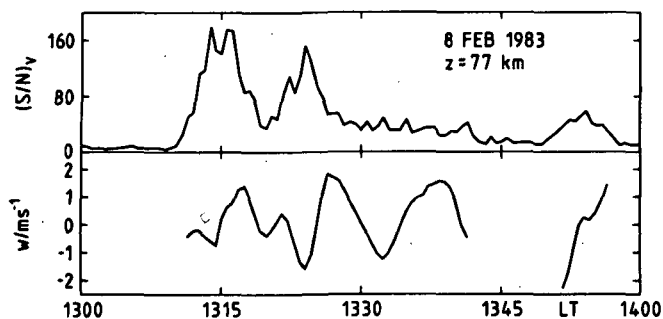


Figure 2. Time series of signal-to-noise ratio (upper part) and the low pass-filtered velocity (lower part), measured with the vertical antenna beam.

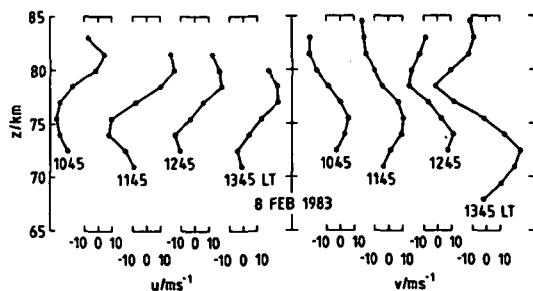




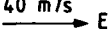


Figure 3. Hourly height profiles of the zonal (u , positive eastward) and meridional (v , positive northward) wind components.

75 and 77 km. These are just the time and height intervals in which the strong signal power bursts were observed.

The horizontal propagation velocities \underline{c} of the signal power bursts have been calculated by cross correlating the signal-to-noise series of different antenna beams in pairs, yielding three velocity vectors shown in Table 1. Table 1 also contains the wind vector of \underline{u} at 1345 LT. A comparison shows that, within the accuracy of the results, \underline{c} and \underline{u} are identical. A second example observed on February 1, 1985 reveals exactly the same characteristic features (KLOSTERMEYER and RUSTER, 1985).

Table 1. Horizontal propagation velocity of signal power burst, \underline{c} , resulting from three different cross-correlations, and wind vector \underline{u} .

DATE	z/km	\underline{c}	\underline{u}
1 FEB '83	82		
8 FEB '83	77		
			

INTERPRETATION

The power bursts at mesospheric heights are very similar to bursts observed by KLOSTERMEYER and RUSTER (1981) in a tropospheric jet stream. VHF radar measurements showed radial velocity oscillations with a period near the Brunt-Vaisala period associated with a Kelvin-Helmholtz (KH) instability in the region of strongest wind shear. At the same time, the radar signal was characterized by a sequence of strong power bursts. Model computations showed that the bursts were produced by static instabilities at the 3-m scale which were due to KH-induced superadiabatic lapse rates around the critical level. The mesospheric observations can be explained in the same way except that a long-period internal gravity wave plays the role of the tropospheric jet stream in generating a strong wind shear. Detailed studies allow us to interpret the 10-min velocity oscillation as a KH instability. The power bursts, having also a quasi-period of 10 min and a horizontal propagation velocity equal to the wind velocity, are due to strong turbulence at the 3-m scale which is generated whenever the KH instability produces superadiabatic lapse rates. Since the phase velocity of the KH instability is equal to the wind velocity at the critical level, also the power bursts must propagate with the wind velocity.

A further quite instructive result supporting these conclusions has been derived from measurements carried out in January/February 1984 on Andoya/Norway (69°N, 16°E) during the MAP/WINE campaign using the mobile SOUSY VHF Radar RUSTER, 1985). The observed height profiles of the zonal and meridional wind components are presented in Figure 4 on the left-hand side. Superimposed on the mean background profile are wave-like patterns with an apparent vertical

wavelength of about 4 km. On the right-hand side, the height-time contour plot of the received radar echo power is shown. Several parallel echo structures are observed -- revealing a downward motion of about 1 km/h (0.3 m/s) and a vertical separation of about half the apparent vertical wavelength of the periodic wind pattern. These preliminary results also indicate that the echo power maxima are associated with instabilities generated in the region of maximum wind shear produced by internal gravity waves with downward phase propagation.

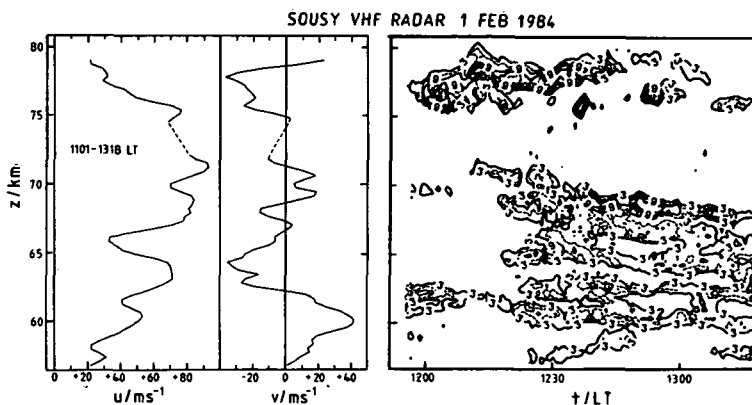


Figure 4. Left: Height profiles of zonal (u , positive eastward) and meridional (v , positive northward) wind components observed on Andoya/Norway. Right: Height-time contours of echo power received in the vertical beam position.

CONCLUSION

Within limited height regions in the mesosphere, gravity waves and tides with downward phase propagation can cause strong vertical shears with Richardson numbers less than $1/4$. Kelvin-Helmholtz instabilities, therefore, may be generated and produce the observed velocity oscillations with periods of the order of ten minutes. These primary instabilities, in turn, can produce superadiabatic lapse rates, finally resulting in secondary static instabilities at the 3-m scale which are responsible for the observed quasi-periodic power bursts.

REFERENCES

- Harper, R. M. and R. F. Woodman (1977), J. Atmos. Terr. Phys., **39**, 959.
 Klostermeyer, J. and R. Ruster (1981), J. Geophys. Res., **86**, 6631.
 Klostermeyer, J. and R. Ruster (1985), Adv. Space Res., in press.
 Ruster, R. (1985), Adv. Space Res., in press.

3.7 OBSERVATION AND ANALYSIS OF THUNDERSTORM-GENERATED GRAVITY WAVES IN THE LOWER STRATOSPHERE

Daren Lu

Institute of Atmospheric Physics
Academia Sinica
Beijing, China

T. E. VanZandt and W. L. Clark, Jr.

NOAA/ERL/Aeronomy Laboratory
Boulder, CO 80303

INTRODUCTION

It has been recognized that the relation between internal gravity waves and thunderstorms may be important in at least two respects: first, some thunderstorm cells could be excited or initiated by propagating gravity waves in the troposphere; second, thunderstorms may contribute to the energy of the atmospheric gravity wave field. In the latter respect, there have been a lot of case studies which show good correlations between thermospheric waves and thunderstorm activities. But there were only very few observations about thunderstorm-generated gravity waves in the middle atmosphere.

This paper reports further observations of gravity waves associated with thunderstorms. The analysis will emphasize the differences of thunderstorm-generated gravity waves (TS-GW) in the troposphere and lower stratosphere. TS-GW in the troposphere have been analyzed in a companion paper (LU et al., 1984).

OBSERVATIONS

Field observations were made from late July to early August 1981, during the period of maximum thunderstorm frequency in northeastern Colorado. The principal instrument used was the Platteville VHF Doppler radar located on the Colorado piedmont near Platteville, Colorado (see Figure 1). The radar made observations both in the zenith and at a slant, from which both the vertical and horizontal wind components can be inferred. But in this paper only the vertical observations are used. The radar system parameters are given in Table 1.

This radar system gathered data almost continuously for 12 days. In order to identify thunderstorms and periods of thunderstorm activity, we used the PPI maps from the conventional 10 cm weather radar operated by the National Weather Service at Limon, Colorado, (about 135 km southeast of the Platteville radar) and visible and infrared images taken by the GOES West satellite and recorded by the Atmospheric Sciences Department of the Colorado State University. Routine NWS radiosonde ascents from Denver were used to determine the height of the tropopause.

ANALYSIS

The time series of vertical velocities measured by the Platteville radar of the entire 12-day period are shown for each range gate in Figure 2. Each point is a 15-min average of the Doppler spectra. The vertical velocities fluctuate about a mean value that is approximately zero. The background level of fluctuation in the troposphere up to 12.9 km was of the order 0.5 m/s peak to peak. But there existed time periods that lasted from several to more than

Table 1.
Platteville radar system parameters.

Latitude	40°11'N
Longitude	104°44'W
Elevation	1536 m
Frequency	49.920 MHz
Peak pulse power	~15 kW
Average power	133 W
Pulse width	16 μ s
Range resolution	2.4 km
Antenna area	100 x 100 m ²
Beamwidth (two-way)	~ 2°

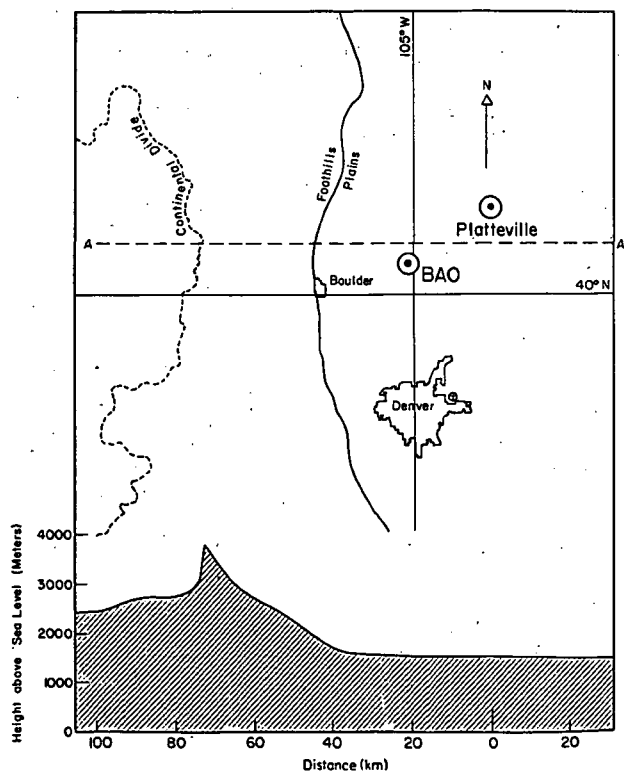


Figure 1. Map showing the location of the Platteville VHF Doppler radar, with a cross section of the terrain along line A shown at the bottom.

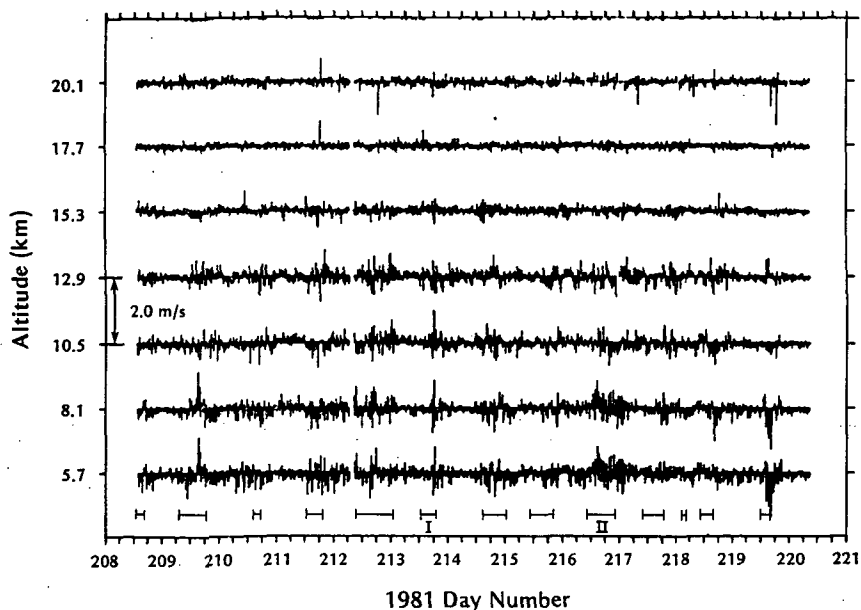


Figure 2. Time series of vertical velocity during the 12 day period of observations for seven separate altitudes above sea level. Each point is the average velocity for 15 minutes. Thunderstorm active periods are bracketed just above the abscissa.

10 hours when the level of fluctuation increased greatly. These enhanced fluctuations are typically quasi-sinusoidal.

In order to study the relation between the periods of large fluctuations and periods of local thunderstorm activity, we use the Limon radar PPI maps to divide the 12-day period into "thunderstorm-active" and "thunderstorm-quiet" periods. The thunderstorm-active periods are indicated on Figure 2 just above the abscissal axis.

It can be seen that the periods of enhanced fluctuations usually correspond to thunderstorm-active periods, but with a lag of one to several hours. It seems very likely, therefore, that the coherent wave trains are associated with thunderstorms.

Detailed analyses have been given in LU et al. (1984). In this paper, some statistical differences of TS-GW in the troposphere and stratosphere are analyzed.

Enhancement of TS-GW as a function of frequency

Figure 3 shows the average enhancement of TS-GW as a function of wave period for three active periods versus three nearby quiet periods. The variance in each frequency interval is the integral of the power spectrum over that interval. The variance is significantly enhanced at all frequencies at all tropospheric heights. But there is almost no enhancement at the 17.7 km lower stratospheric range gate.

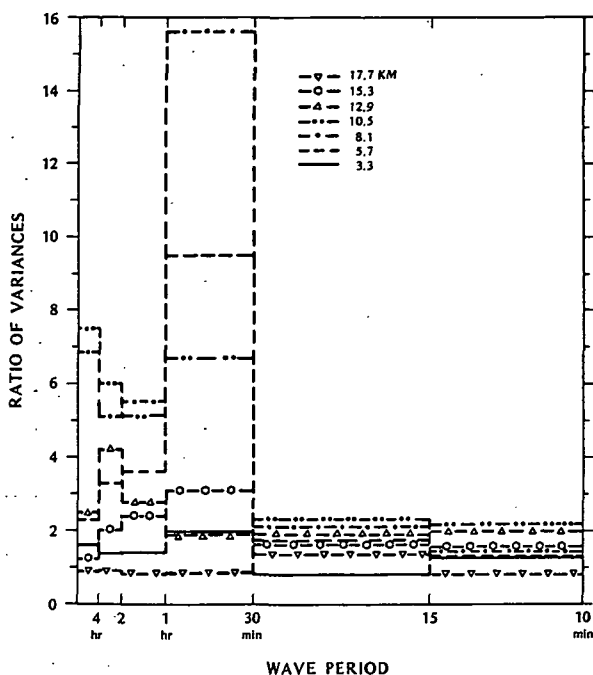


Figure 3. The enhancement due to thunderstorm activity as a function of wave period and observation altitude. The measure of enhancement plotted is the ratio of the power, or velocity variance, observed in each interval of wave period for three wave-active periods to the variance observed during three quiet periods.

Enhancement of TS-GW as a function of altitude

The enhancement as a function of altitude is shown in Figure 4 as the ratio of active to quiet variance for six active and four quiet periods. Here the variance is the integral over the entire spectrum. The enhancement is largest in midtroposphere, from the 5.7 to 12.9 km range gates.

Over the entire 12-day period the average height of the tropopause was 15.3 km, and it ranged from 14.2 to 16.2 km, as indicated in Figure 4. There was no enhancement in the purely stratospheric 17.7 range gate.

Comparison of GW spectra for different local time periods

For obtaining further statistical results about the difference of TS-GW in the troposphere and stratosphere, averaged power spectra of the vertical velocities at each range gate were made for two different local time periods. Local time 00-06 h is typically the thunderstorm-quiet period and 12-18 h the thunderstorm-active period. Figure 5 shows the comparison of the spectra on the tropospheric (8.1 km) and stratospheric (17.7 km) altitudes. It is very clear that in the troposphere the spectra for active periods are much stronger than that for quiet periods in whole wave periods. In the lower stratosphere, there is statistically no difference between the spectra of active and quiet periods.

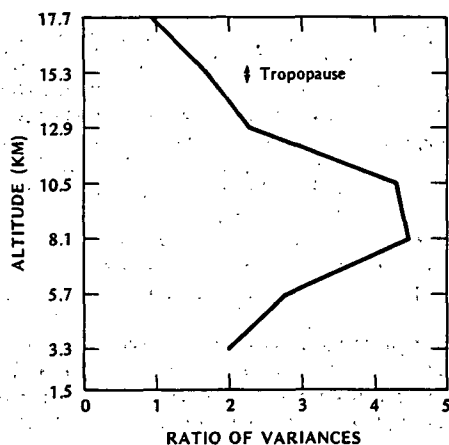


Figure 4. The enhancement due to thunderstorm activity as a function of altitude. The ratio of the mean velocity variance at each altitude during six wave-active periods to the mean variance during four quiet-periods is plotted versus altitude above sea level. The range of tropopause heights determined from radiosonde data over the 12 day period is also indicated.

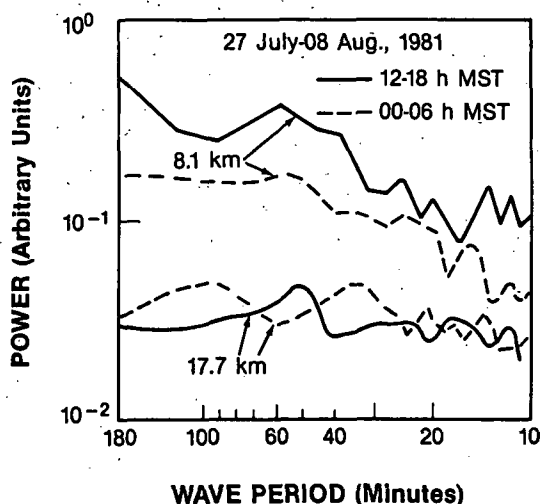


Figure 5. Comparison of spectral enhancement in the troposphere to that in the stratosphere.

SUMMARY

The present observations show that in the lower stratosphere, no significant influence of TS-GW is existed. On the contrary, there are strong TS-GW existed in the middle and upper troposphere during the thunderstorm-activity periods. It seems that the ducting effect is very important for GW propagation near the tropopause. Comparing the present observations and other observations of the stratospheric GW induced by the overhead penetrating thunderstorm cells (ROTTGER, 1980; LARSEN et al., 1982), we can conclude that only the strong overshooting cells can contribute to the TS-GW in the stratosphere. As during the observation period there were no overshooting cells passing over the Platteville radar, it was expected that no significant stratospheric GW would exist in Platteville radar observations.

Further observations and theoretical work are needed. If the above conclusion is true, we can make the GW parameterization scheme and statistics in the stratosphere and upper atmosphere with the overshooting thunderstorm cell statistics which can be obtained by using geostationary satellite IR images and ST radar observations.

REFERENCES

- Larsen, M. F., W. E. Swartz and R. F. Woodman (1982), Geophys. Res. Lett., **9**, 571-574.
Lu, D-R., T. E. VanZandt and W. L. Clark (1984), J. Atmos. Sci., **41**, 272-282.
Ruttger, J. (1980), Pure Appl. Geophys., **118**, 484-527.

3.8 GRAVITY WAVES OBSERVED WITH GRAVNET: SASKATOON (52°N, 107°W), 1983/84

C. E. Meek, A. H. Manson and I. M. Reid

ISAS, University of Saskatchewan,
Saskatoon, Canada

INTRODUCTION

The GRAVNET system is based on an MF radar (2.22 MHz) with one site consisting of transmitting and spaced receiving antennas; and two remote receiving sites (~40 km distant, forming an approximately equilateral triangle) also with spaced receiving antennas. The winds of the upper middle atmosphere (60-110 km) are measured at each of the three sites in real time, using the Spaced Antenna method: up to 12 profiles per hour are obtained. The operating schedule is 6h about noon.

Spectral analysis is performed separately on northward and eastward velocity components for each site at the same heights. Cross spectra are then found between sites. Data selection criteria include the Normalized Phase Discrepancy (NPD), defined as $|\Sigma \Delta \phi| / \Sigma |\Delta \phi|$, where the sum of the phase differences ($\Delta \phi$) are done around the site pairs. This parameter is zero for wave-like motions. An additional measure of significance used is the coherence. The directions of horizontal motion, and the wavelengths (λ_h) are then available for particular observed periods (T); and thence the horizontal phase speeds (c). Since these can be calculated for northward and eastward components, in many cases a further consistency check is available. Limitations on wave parameters set by the system and analysis are; 10 min < T < 100 min, c < 120 m/s, $\lambda_h > 40$ km.

OBSERVED WAVE PARAMETERS

The relative occurrence of the observed horizontal wavelengths and phase speeds are shown in Figure 1. The majority of wavelengths are less than 80 km while the mean value is 110 km. Observed phase speeds are centered roughly about 50 m/s. Agreement with other estimates is good (Figures 2, 3), and the observed wavelength shows a clear tendency to increase with increasing observed period, from a value of ~45 km at T=10 min to ~210 km at T=100 min. Observed phase speeds tend to decrease with increasing observed period, from a value of ~70 m/s at T=10 min to ~35 m/s at T=100 min. Typical rms values of horizontal perturbation velocity are ~5 m/s.

INTRINSIC WAVE PARAMETERS

The horizontal wavelength, phase velocity and period are constant for waves whose source is stationary with respect to the observer. Since most wave sources are believed to be tropospheric, it is reasonable to assume that this is true for a ground-based observer. However, the wave period and phase velocity as seen by an observer at rest with respect to a background wind (the intrinsic period and phase velocity, respectively) are doppler shifted so that they are related by $T_* = \lambda_h / (c - \bar{u})$, where T_* , $(c - \bar{u})$ and \bar{u} are the intrinsic period, phase velocity and component of the background wind in the direction of the wave vector, respectively. The observed wavelength is the same as the intrinsic wavelength. Since it is the intrinsic quantities which determine wave behavior, they are rather more important than observed quantities. The arithmetic mean of the hourly mean winds for each height in each 6-hour observing period in which waves were detected, the observed wavelength, and the phase velocity have been used to evaluate T_* and $(c - \bar{u})$, and the intrinsic wave parameters are shown in Figures 4 and 5. Intrinsic phase speed shows a clear tend-

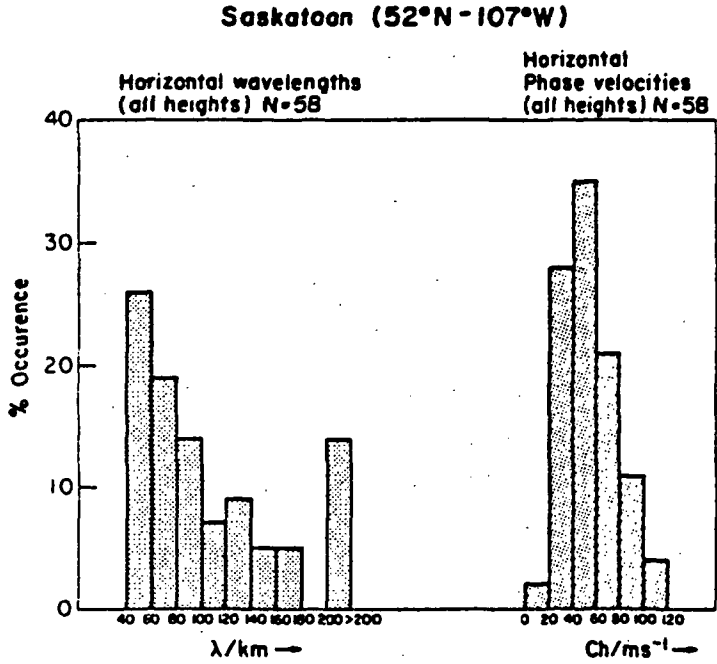


Figure 1. Relative occurrence of horizontal wavelength and observed phase speeds.

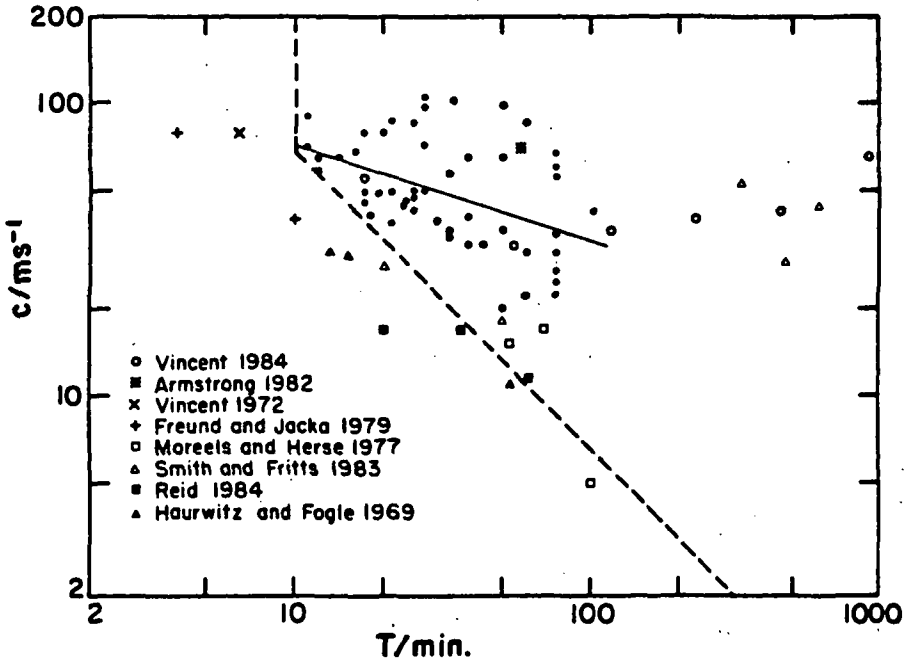


Figure 2. Observed phase speed vs observed period.

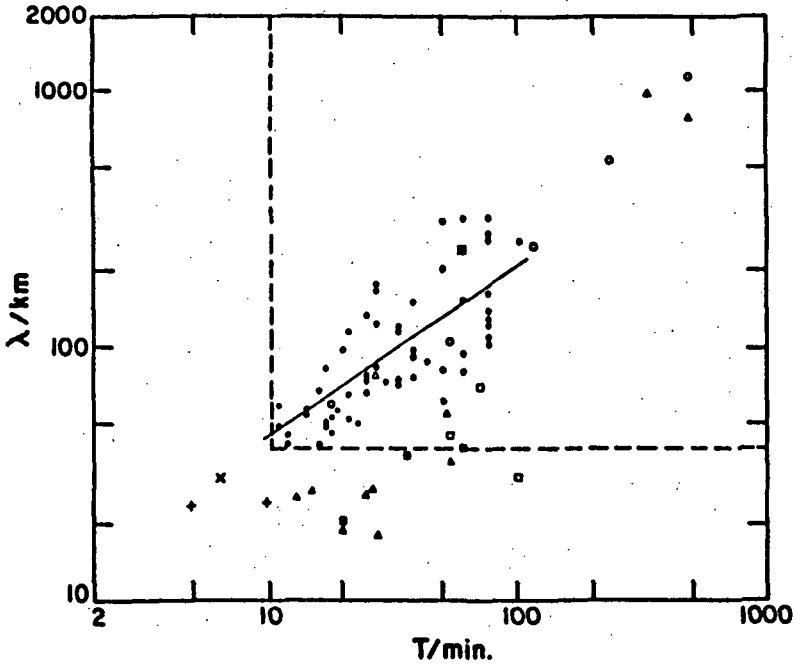


Figure 3. Horizontal wavelength vs observed period.

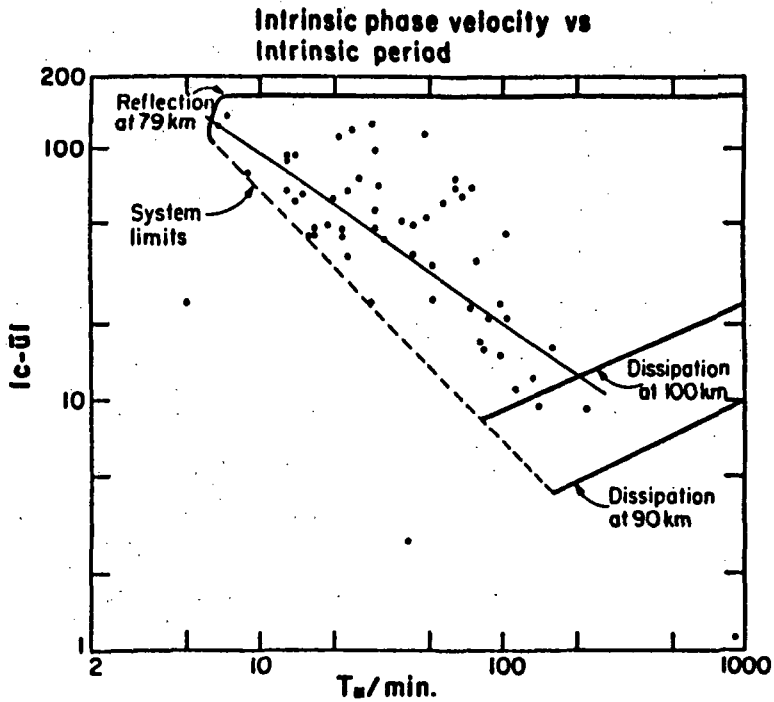


Figure 4. Intrinsic phase speed vs intrinsic period. Values of kinematic viscosity used are $4 \text{ m}^2/\text{s}$ at 90 km, and $36 \text{ m}^2/\text{s}$ at 100 km.

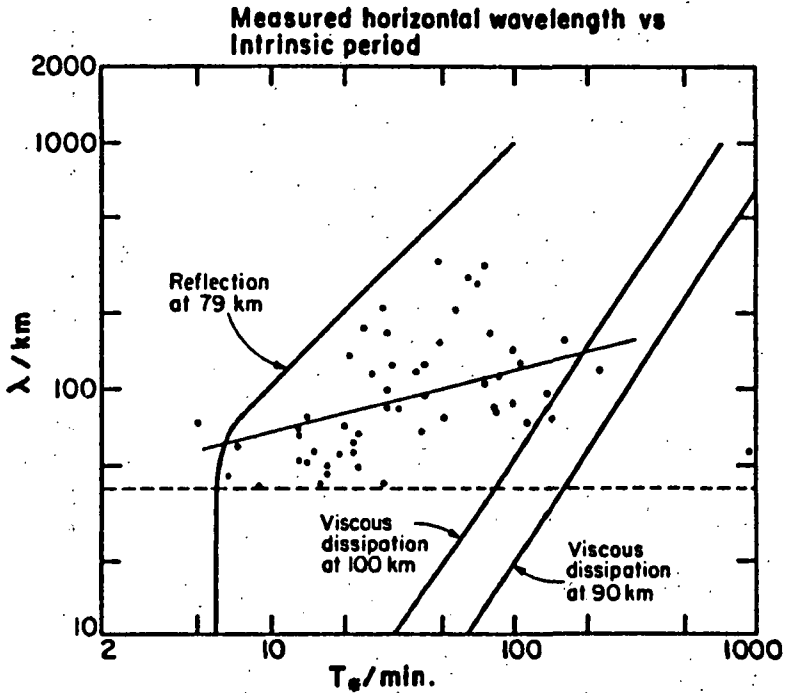


Figure 5. Horizontal wavelength vs intrinsic period.

ency to decrease with increasing intrinsic period from ~ 95 m/s at $T_*=10$ min to ~ 20 m/s at $T_*=100$ min. The observed horizontal wavelength shows a tendency to increase with increasing intrinsic period, but this is less well defined than for that with the observed periods. Values are ~ 70 km at $T_*=10$ min and ~ 120 km at $T_*=100$ min. The general form of the wavelength results when presented in this form may be explained by references to the limits determined by reflection at levels below the height of observation, and by viscous dissipation. These are indicated on Figure 5 for reflection at the 79 km level, and for viscous dissipation at the 90 and 100 km levels (HINES, 1960).

Evaluation of the vertical wavelength is possible by applying the dispersion relation (HINES, 1960), which relates horizontal wavelength, vertical wavelength and intrinsic frequency. Vertical wavelength is shown as a function of intrinsic period in Figure 6. Values are ~ 30 km at $T_*=10$ min and ~ 6 km at $T_*=100$ min. The median value is ~ 10 –15 km. These results are in good agreement with previously obtained directly measured values (see e.g. FRITTS, 1984).

Two very short vertical wavelengths (<1 km) are evident. One of these ($T_*=935$ min, altitude=76 km) exceeds the expected limits determined by viscous dissipation similar to those indicated in Figure 5 but for 70 km (HINES, 1960), and is evidently in the process of being dissipated. The other ($T_*=41$ min, altitude=97 km) meets the condition $|c-\bar{u}| \sim 0$ and consequently appears to be within a critical level. It is also noteworthy that both these waves meet the condition for convective instability $\bar{u}' > |c-\bar{u}|$, where \bar{u}' is the horizontal perturbation velocity (FRITTS, 1984), and are the only waves in the sample for which this is true.

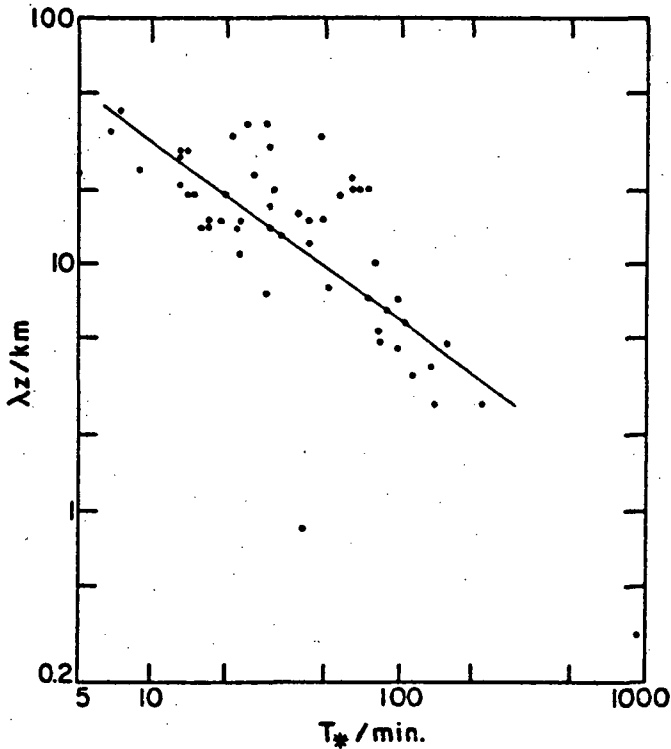


Figure 6. Vertical wavelength vs intrinsic period.

CONCLUSION

Preliminary analysis of spaced wind measurements to determine upper middle atmospheric gravity wave parameters λ_h , c , yields results in good agreement with previous studies. In the (observed) period range 10–100 min, horizontal wavelengths are typically less than 80 km, and observed phase velocities ~ 50 m/s. Calculation of the intrinsic period and application of the dispersion relation to determine the vertical wavelength indicates typical values of 10–15 km, in good agreement with direct measurements. Two waves which appear to be subject to dissipation through viscous drag, and to absorption within a critical layer, respectively, have been identified.

REFERENCES

- Armstrong, E. B. (1982), The association of visible airglow features with a gravity wave, *J. Atmos. Terr. Phys.*, **44**, 325.
 Freund, J. T. and F. Jacka (1979), Structure in the 557.7 nm OI airglow, *J. Atmos. Terr. Phys.*, **41**, 25.
 Fritts, D. C. (1984), Gravity wave saturation in the Middle Atmosphere. A review of theory and observations, *Rev. Plan. Space Sci.*, **22**, 275.
 Haurwitz, B. and B. Fogle (1969), Waveforms in noctilucent clouds, *Deep Sea Res.*, **16**, 85.
 Hines, C. O. (1960), Internal gravity waves at ionospheric heights, *Can J. Phys.*, **38**, 1441.

- Moreels, G. and H. Herse (1977), Photographic evidence of waves around the 85 km level, Planet. Space Sci., 25, 265.
- Reid, I. M. (1984), Radar Studies of Atmospheric Gravity Waves, Ph.D. Thesis, University of Adelaide, Adelaide, Australia.
- Smith, S. A. and D. C. Fritts (1984), Estimation of gravity wave motions, momentum fluxes and induced mean flow accelerations in the winter mesosphere over Poker Flat, Alaska, Proc. 21st Conf. Radar Meteorol., Edmonton, Canada, 104.
- Vincent, R. A. (1972), Ionospheric irregularities in the E-region, J. Atmos. Terr. Phys., 34, 1881.
- Vincent, R. A. (1984), Gravity wave motions in the mesosphere, J. Atmos. Terr. Phys., 46, 119.

3.9 HIERARCHICAL STRUCTURE OF STRATOSPHERIC WIND FLUCTUATIONS

M. D. Yamanaka and H. Tanaka

Water Research Institute, Nagoya University,
Nagoya 464, Japan

INTRODUCTION

In order to verify the gravity-wave-breaking theories, high resolution observations of middle-stratospheric winds have been carried out by the balloon-borne anemometers (YAMANAKA and TANAKA, 1984a,c; YAMANAKA et al., 1985c). Here we shall summarize the observed features, estimate the parameters of waves generating the turbulence and discuss their effect on the general circulation and the transport process.

OBSERVATIONS

We developed and used anemometers of propeller type (sensitivity: 0.9 m/s) and of ionic type (0.005 m/s). Four zero-pressure balloons mounting these anemometers have been launched during 1982-84 from Sanriku, Japan (39°N, 142°E). Detailed description on the instrumentation has been published in YAMANAKA et al. (1985a,b).

There is a "hierarchical structure" in the observed stratospheric turbulence (Table 1 and Figure 1). The fluctuations listed in the class (i) may be detected also by rawin-sondes and radars, whereas (iv) and (v) can be detected only by the ionic anemometer (cf. BARAT, 1982).

BREAKING WAVES

We can estimate the input of gravity waves at the bottom of the middle atmosphere by the following two techniques:

(1) The distance between the critical and breaking levels (TANAKA, 1983; YAMANAKA and TANAKA, 1984a, b) can explain the vertical scales of the class (i). However, the maximum magnitude of the internal structure (i.e., one wavelength and unstable zones) corresponding to (ii) and (iii) is limited due to the viscosity and Newtonian cooling. These two classes can be generated by inertio-gravity waves of about 50 km in zonal wavelength (YAMANAKA and TANAKA, 1985).

(2) The Lagrangian power spectrum of the gravity waves can be obtained by level-flight balloon tracking (Figure 2). Detailed inspection leads that it obeys a -2 (rather than -5/3) power law of the intrinsic frequency (YAMANAKA and Tanaka, 1985).

LOCALIZATION OF WAVEBREAKING TURBULENCE

It can be speculated from Figure 2 that most of the gravity waves are saturated in the lower stratosphere, since the total power is not so amplified between the upper troposphere and the middle stratosphere. The wave saturation is also recognized in the classes (ii) and (iii); the power spectrum (Figure 3) almost satisfies a -3 power law of the vertical wave number (YAMANAKA and TANAKA, 1985).

These are evidences for the fact that the gravity waves interact with the stratospheric general circulation. However, the theoretical prediction (TANAKA and YAMANAKA, 1985) suggested that the wave-breaking effect parameterized after

LINDZEN (1981) might be too strong. This quantitative coincidence may be explained by the localization effect of the wave-breaking turbulence (YAMANAKA and TANAKA, 1985).

Table 1. The "hierarchical structure" detected by vertical scanning of balloon-borne anemometers.

Class	Vertical Scale	Wind Speed Amplitude	Propeller Anemometer Data Record	Ionic Anemometer Data Record	Theoretical Interpretation
i	Some Hundreds Meters	1-3 m/s	Envelope of Multiple Gust Layers	Concentration of Thin Turbulence Layers	Distance between Critical and Breakdown Levels
ii	50-100 m	>1 m/s	Isolated Gust Layer	Thick Turbulence Layer	Marginal Vertical Wavelength
iii	Some Ten Meters	1 m/s	Sheet of Multiple Gust Layers	Thin Turbulence Layer	Local Unstable Zone within one Wavelength
iv	Some Meters	0.5 m/s	(undetected)	Spiky Strong Fluctuation	KH-Billow
v	1 m	0.1 m/s	(undetected)	Noisy Weak Fluctuation	Random Eddy

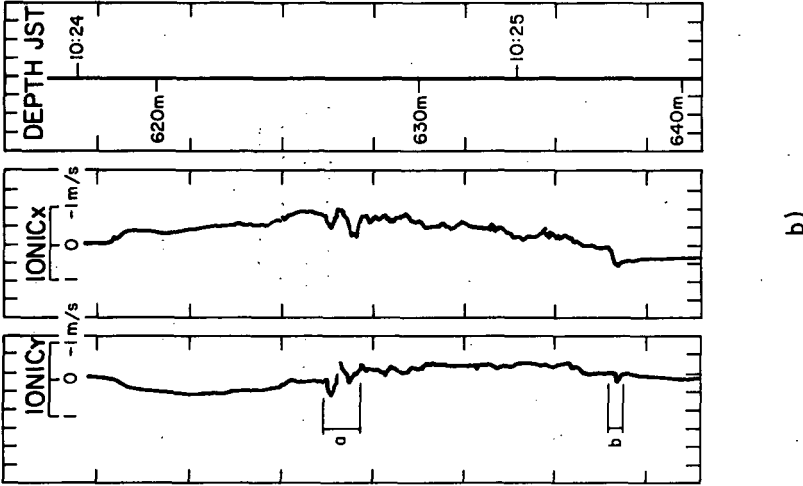
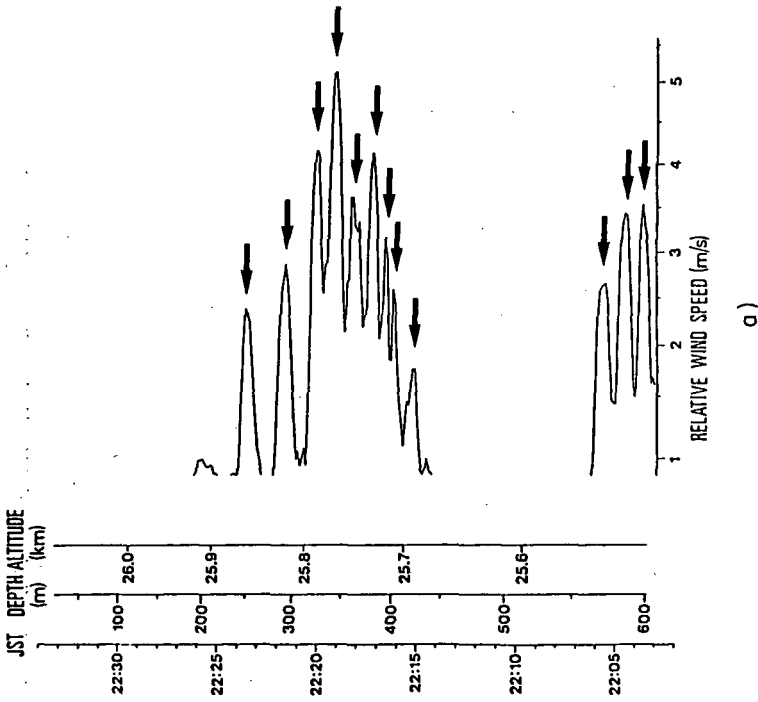


Figure 1. Observed stratospheric turbulence. (A) Gusts (arrows) obtained by a propeller anemometer; (B) Billows ("a" and "b") detected by an ionic anemometer. "Depth" means the distance between the anemometer and the balloon-gondola.

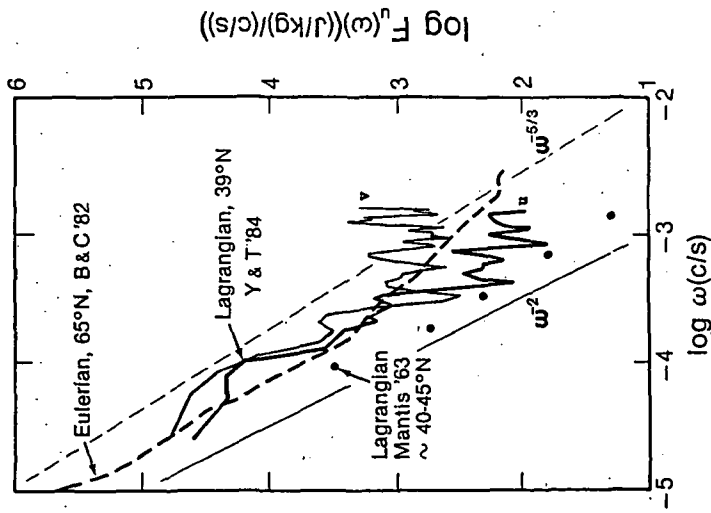


Figure 2. Lagrangian power spectrum (v_y & T) for zonal (u) and meridional (v) component winds obtained from a balloon tracking. Spectra obtained by other authors (MANTIS, 1963; BALSLEY and CARTER 1982) and the ideal $-5/3$ and -2 power laws are also indicated. Reproduced and modified from VANZANDT (1984, private communication).

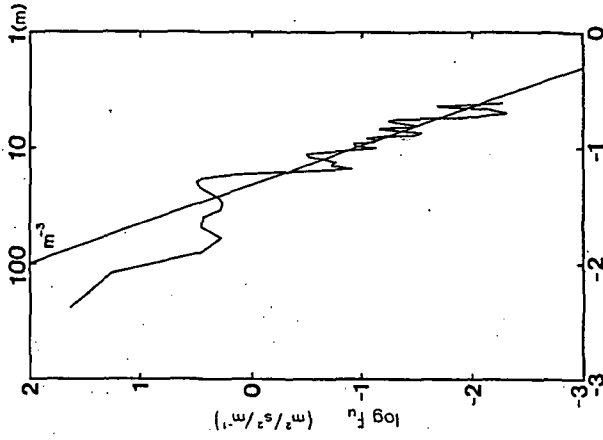


Figure 3. Power spectrum of vertical micro-structure of horizontal winds, based on a series of propeller anemometer data.

REFERENCES

- Balsley, B. B. and D. A. Carter (1982), Geophys. Res. Lett., **9**, 465-468.
- Barat, J. (1982), J. Atmos. Sci., **39**, 2553-2564.
- Lindzen, R. S. (1981), J. Geophys. Res., **86**, 9707-9714.
- Mantis, H. T. (1963), J. Appl. Meteor., **2**, 427-424.
- Tanaka, H. (1983), J. Meteor. Soc. Japan, **60**, 1034-1040.
- Tanaka, H. and M. D. Yamanaka (1985), J. Meteor. Soc. Japan, **63**, in press.
- Yamanaka, M. D. et al. (1985a), Rev. Sci. Instrum., **61**, in press.
- Yamanaka, M. et al. (1985b), J. Atmos. Ocean. Tech., **2**, in press.
- Yamanaka, M. et al. (1985c), J. Meteor. Soc. Japan, **63**, in press.
- Yamanaka, M. and H. Tanaka (1984a), Dynamics of the Middle Atmosphere, edited by J. R. Holton and T. Matsumo, TERRAPUB/D. Reidel, 117-140.
- Yamanaka, M. and H. Tanaka (1984b), J. Meteor. Soc. Japan, **62**, 1-17.
- Yamanaka, M. and H. Tanaka (1984c), J. Meteor. Soc. Japan, **62**, 177-182.
- Yamanaka, M. and H. Tanaka (1985), To be submitted to J. Meteor. Soc. Japan.

3.10 TWO CLASSES OF MEDIUM-SCALE TRAVELING IONOSPHERIC DISTURBANCES OBSERVED WITH AN ARRAY ON HF-DOPPLER SOUNDERS

T. Shibata and T. Okuzawa

Department of Applied Electronic Engineering,
University of Electro-Communications,
Chofu-shi, Tokyo 182, Japan

INTRODUCTION

The importance of the quasi-evanescent mode of acoustic-gravity waves (AGW) has recently been stressed by SHIBATA and OKUZAWA (1983) to elaborate on the daytime dispersion characteristics of horizontal velocity of medium-scale traveling ionospheric disturbances (MS-TID) which were observed by an HF-Doppler (HFD) sounder array in central Japan. A further study on this subject is described in this paper, with emphasis on possible classification of the observed MS-TID into two categories: the internal mode and the quasi-evanescent mode as regards physical implication. Nonlinear wave-wave interaction is proposed in an attempt to explain salient features of the latter-class TID.

OBSERVATION AND DATA ANALYSIS

Observations of MS-TID by an array of HFD sounders were carried out from September 17 to October 11, 1982, during MAP period. The JJY-8 MHz standard radio signals transmitted on a continuous basis from Nazaki (36.18°N, 139.85°E), Ibaraki, were received simultaneously at Onahama (36.94°N, 140.93°E), Sugadaira (36.52°N, 138.32°E), and Fuji (35.42°N, 138.62°E), giving an array of reflection points in the ionospheric F region with horizontal separations of 63-134 km. The true reflection heights for the 8-MHz waves were estimated to range from 240 to 280 km in daytime.

The cross-spectrum analyses were made dynamically on sample data with 0.5-min sampling interval for each pair among three sites. The data window of 200-min length has been shifted by every 3-min increment in the whole data set. The method of BLACKMAN-TUKEY (1958) with the maximum lag of 10% length of the data window has been adopted here. Then, the horizontal trace velocity (in both magnitude and direction) has been calculated as a function of the wave period (T) through the obtained cross-spectral lags and the array dimension. For further details of the analysis, the reader may refer to our previous paper (SHIBATA and OKUZAWA, 1983).

RESULTS

Scatter plot of the horizontal trace velocity vs the azimuthal angle (measured clockwise from the north) for the wave component of a 40-min period is shown in Figure 1. (The hatched portion in the figure indicates a forbidden region in which the estimate of the velocity vector becomes unreliable when the calculated time lags are smaller than the sampling time interval.) Taking a glance at this figure, we like to propose that the waves can be grouped into two classes with a border line of the horizontal velocity $V_h = 300 \sim 400 \text{ ms}^{-1}$. The waves of $V_h < 300 \text{ ms}^{-1}$ are found to be distributed mostly in the restricted angles of $\pm 40^\circ$ around the southeast direction, whereas the waves of $V_h > 400 \text{ ms}^{-1}$ are seen to be rather omnidirectional. This statement will be better elucidated from Figures 2(a) and (b) that show the occurrence histograms against the propagation azimuth. We tentatively call the former class "Type-1" and the latter "Type-2" in this paper.

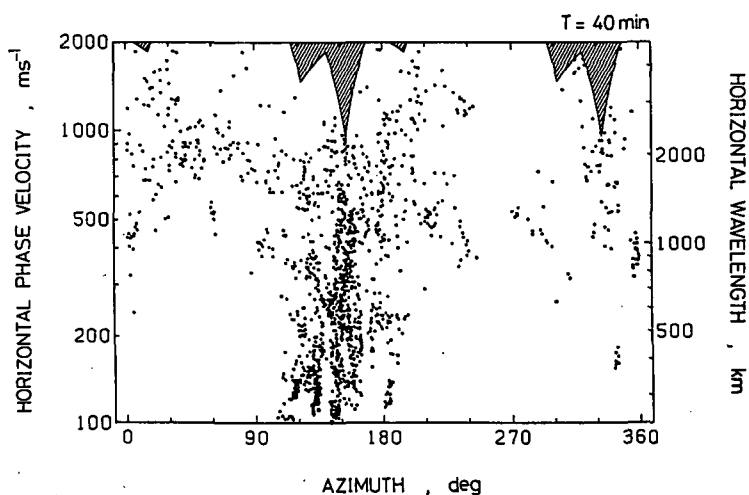


Figure 1. Scatter plot of the horizontal phase velocity vs azimuthal angle for $T = 40$ -min wave component.

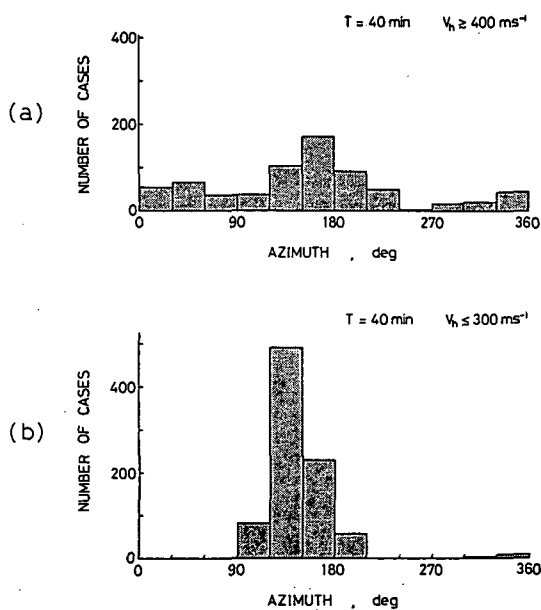


Figure 2. Occurrence histograms of $T = 40$ -min wave component. (a) for $V_h > 400 \text{ ms}^{-1}$; (b) for $V_h < 300 \text{ ms}^{-1}$.

In order to examine what AGW mode corresponds to the observed TID, we carried out a full-wave calculation with a model thermosphere assumed. Details of the calculation are given elsewhere (SHIBATA, 1983), and only a part of the results will be quoted here. Figure 3 indicates one of such results that shows a clear distinction among the associated wave modes for upgoing waves; parameter space is composed of the horizontal velocity and the wave period at the height of $z=250$ km. The shaded portion of the figure stands for the region where the waves fall under the category of quasi-evanescent (abbreviated hereafter to QE) mode in the sense that the magnitude of the real part of vertical wave number becomes smaller than that of its imaginary part; i.e., $|k_z^r| < |k_z^i|$. The internal mode occupies the remaining area in which the relationship, $|k_z^r| > |k_z^i|$, holds. It is evident from this figure that the waves in the period range of 20 to 100 min, with horizontal velocities greater than about 400–500 ms^{-1} , are the QE modes at the height of 250 km. It will, therefore, be safe to identify the majority of the Type 2 TID with an ionospheric manifestation of the QE mode, and the most part of the Type-1 with that of the internal-gravity mode.

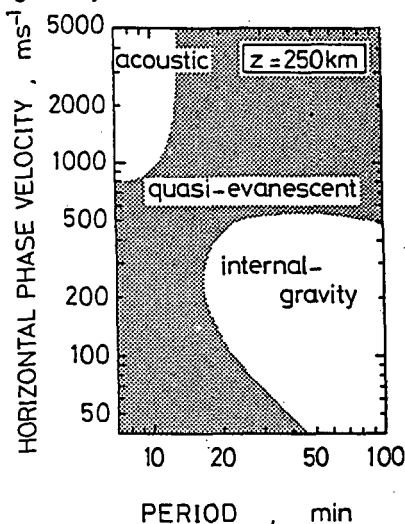


Figure 3. Calculation result of horizontal phase velocity vs wave period for the acoustic-gravity waves in a windless, dissipative thermosphere.

DISCUSSION

Considering the Type-2 waves are to be omnidirectional, we like to assume that possible sources of these waves are distributed widely in every direction from our observation array. Then, our guess is that these waves may be the secondary waves produced by a nonlinear, wave-wave interaction which operates probably in the ionospheric F region.

Let the secondary wave be assumed such that it has the frequency (ω_s) and wave number vector (K_s) which are equal to either the sum or the differences of the frequencies (ω_1, ω_2) and wave number vectors (K_1, K_2) of the two seed waves, respectively (YEH and LIU, 1970; BEER, 1974); i.e.,

$$\omega_s = \omega_1 \pm \omega_2 \quad (1)$$

$$K_s = K_1 \pm K_2 \quad (2)$$

It should be noted that any three waves may not necessarily satisfy the above resonance conditions since some other restriction should be imposed on the values of ω and K through the dispersion relation. The choice of K is somewhat complicated (HINES et al., 1974) by the fact that AGW in the thermosphere is by nature subjected to the exponential growth of the amplitude with height, with a rate of $1/2H$ (H being the locally defined scale height of the neutral atmosphere).

The vertical component, K_z , of the wave number vector of AGW is, in general, complex and can be cast in the form,

$$K_z = k_z^r + i(k_z^i - 1/2H). \quad (3)$$

The first term, k_z^i , in the parenthesis represents the dissipative attenuation rate, and the second one, $1/2H$, is the growth rate. In Figure 4, we present typical calculated example of k_z^r and k_z^i vs horizontal phase velocity V_h for the upgoing gravity wave in a dissipative thermosphere. The solid part of the curves in the figure corresponds to the QE mode, and the remaining part is for the internal mode. The dotted line in the figure represents the marginal condition, $k_z^i = 1/2H$, at a specified altitude; e.g., $H \approx 40$ km at $z = 250$ km in the present model.

If we take Equation 3, the imaginary part of Equation 2 will be

$$k_{zs}^i - 1/2H = k_{z1}^i - k_{z2}^i \quad (4)$$

We have chosen here the minus sign by reason of long wavelength of the observed Type-2 waves. It will be reasonably assumed that for a given wave period the waves of the smallest attenuation predominate initially at an assumed height. The attenuation coefficient, k_z^i , decreases down to the minimum which is of one order of magnitude below the $1/2H$ level (see Figure 4). If the two seed waves are assumed to be such waves, the rhs of Equation 4 becomes so small that it may be negligible in comparison with the term of $1/2H$ on lhs. This means that the vertical attenuation rate of the generated (secondary) wave tends to meet the quasi-marginal condition, $k_z^i \approx 1/2H$. Satisfaction of the quasi-marginal condition can be observed at Figure 4 in two regions; i.e., one

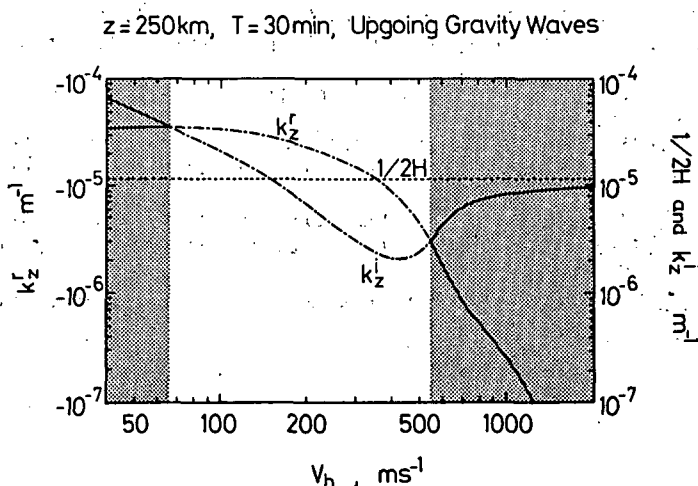


Figure 4. Calculation result of vertical wave number vs horizontal phase velocity for upgoing gravity waves.

is that in the vicinity of the crossing point of k_z^i and $1/2H$ curves where the waves are identified with the internal mode, and the other is located at high- V_h region where the waves are the QE mode. For the secondary waves being assumed here, the waves of the latter region are expected more plausibly to occur, because the vertical phase constant, k_z^r , of the QE wave in the high- V_h region is so small as to satisfy Equation 2 with a minus sign.

We will, of course, not disregard for any other possible explanations of the Type-2 disturbances. Nevertheless, we are inclined to advocate that the generation of the QE wave may for the most part owe to the resonant interaction operating in the thermosphere, and therefore the Type-2 disturbances may be identified with the secondary waves produced through such a nonlinear process.

Thorough test of the resonance conditions (especially Equation 1) must be beyond the scope of this paper, because our present study concerns the apparent horizontal phase velocities for the specified wave periods of 40, 20 and 13.3 min only. Needless to say, nonlinear theory which involves the gravity waves in dissipative medium is needed in order to seek the sources of the Type-2 waves in a more sophisticated manner.

CONCLUSION

The horizontal trace velocities of MS-TID in the period range of 13.3-40 min have been investigated through a cross-correlation analysis on the HFD array data of 12 days (daytime of about 151 hours). It has been deduced that the waves with the 40-min period are grouped into two classes according to the horizontal velocity in magnitude, $V_h \leq 300 \text{ ms}^{-1}$ and $V_h \geq 400 \text{ ms}^{-1}$.

The former class, which takes the propagation azimuth in a confined range of about $\pm 40^\circ$ around the southeast direction, can be identified with the ionospheric internal gravity waves. The other class defined with $V_h \geq 400 \text{ ms}^{-1}$, whose propagation is omnidirectional, may be explicable in terms of the QE mode inherent to the dissipative thermosphere. A qualitative discussion has led to the suggestion that the generation of the second-class waves might owe for the most part to a nonlinear (wave-wave) process.

REFERENCES

- Beer, T. (1974), Atmospheric Waves, Adam Hilger, London, 277.
 Blackman, R. B. and J. W. Tukey (1958), The Measurement of Power Spectra, Dover, New York.
 Hines, C. O. et al. (1974), The upper atmosphere in motion, Geophys. Monogr., 18, AGU, Washington, D. C., 312.
 Shibata, T. (1983), A numerical calculation of the ionospheric response to atmospheric gravity waves in the F-region, J. Atmos. Terr. Phys., 45, 797-809.
 Shibata, T. and T. Okuzawa (1983), Horizontal velocity dispersion of medium-scale travelling ionospheric disturbances in the F-region, J. Atmos. Terr. Phys., 45, 149-159.
 Yeh, K. C. and C. H. Liu (1970), On resonant interactions of acoustic gravity waves, Radio Sci., 5, 39-48.

3.11 FINITE AMPLITUDE GRAVITY WAVES: HARMONICS, ADVECTIVE STEEPENING, BREAKING AND SATURATION

J. Weinstock

Aeronomy Laboratory
National Oceanic & Atmospheric Administration,
Boulder, CO 80303

PURPOSE AND THEORETICAL APPROACH

Our purpose is to present a simple theory that determines details of the breaking and saturation of a gravity wave as it propagates upward in the atmosphere. Breaking and saturation are here due to nonlinear advection (e.g., the $\mathbf{v}' \cdot \nabla \mathbf{v}'$ term of the Navier-Stokes equation) analogous to the beaching of a surface wave and to the breaking of a planetary wave analyzed by MCINTYRE and PALMER (1983). Much simplification is obtained by the assumption that in a wave packet consisting of a primary wave and its harmonics, the primary wave remains dominant. This assumption, referred to as a "quasi-monochromatic" approximation, is suggested by observations (e.g., FRITTS et al., 1984; CHANIN and HAUCHECORNE, 1981). Determined by this approximate theory are: a detailed picture of the waveform as it steepens and breaks; harmonics of the wave; the saturation value of the wave amplitude; convective and dynamic instabilities; turbulence generation; and an underlying relationship between superadiabatic lapse rate and saturation by wave-wave interactions.

DISPERSION RELATION FOR FINITE AMPLITUDE WAVES

To solve the standard hydrodynamic equations for large amplitude gravity waves we assume, for simplicity, that in a wave packet consisting of a primary wave and its harmonics, the primary wave is dominant. This assumption is expressed by $\partial \rho' / \partial t \approx i \omega \rho'$ and $\partial \rho' / \partial x \approx i k_x \rho'$, $\partial \rho' / \partial z \approx (i k_z + \beta) \rho'$ where ρ' is the density fluctuation of the wave packet, ω , k_x , and k_z are the frequency, horizontal wave number, and vertical wave number of the primary wave, and β is the rate of amplitude growth with height. Harmonics are not neglected by this approximation, but, rather, the primary wave is assumed dominant. With this approximation, the nonlinear dispersion relation for gravity waves is obtained from the linear dispersion relation by simply replacing ω with $\omega + \mathbf{k} \cdot \mathbf{v}'$, where \mathbf{k} is the wave vector of the primary wave and \mathbf{v}' is the velocity fluctuation of the entire wave packet.

The nonlinear dispersion relation, with compressibility fully accounted for, is straightforwardly derived to be

$$(i k_z + \beta)^2 + \frac{\partial \rho_0}{\rho_0 \partial z} (i k_z + \beta) + \left[\frac{N^2}{(\omega_0 + \mathbf{k} \cdot \mathbf{v}')^2} - 1 \right] k_x^2 = 0 \quad (1)$$

$$\mathbf{k} \cdot \mathbf{v}' = \frac{\omega_0 R_k \cos \phi}{1 + (\gamma k_z H) R_k \sin \phi} \quad (2)$$

where $\phi \equiv (\omega t + k_x x + k_z z)$ is the wave phase, $\omega_0 \equiv \omega + k \cdot v_0$ is the intrinsic frequency, $N \equiv (g\theta_0^{-1} \partial \theta_0 / \partial z)^{1/2}$ is the Brunt-Vaisala frequency, θ_0 is the mean potential temperature, $R_k = (\gamma H \theta_0^{-1} \partial \theta_0 / \partial z)^{-1} \rho_k / \rho_0$ is proportional to the density amplitude ρ_k , and H is the pressure scale height.

WAVE STEEPENING, BREAKING AND SATURATION

Let us first consider infinite amplitude effects from a heuristic, but physical point of view provided by the expression for $k \cdot v'$. This expression is itself of interest. It provides information about wave steepening and breaking, unstable lapse rate, shear instability and harmonic generation. To begin with, it is seen that the linearized form of (2) is simply $k \cdot v' = \omega_0 R_k \cos \phi = (\gamma H \theta_0^{-1} \partial \theta_0 / \partial z)^{-1} \rho_k / \rho_0 \approx (\gamma - 1)^{-1} \omega_0 \rho_k / \rho_0$, and the nonlinear correction is

$$\frac{1}{1 + \gamma k_z H R_k \sin \phi} \quad \text{to } k \cdot v' \quad (3)$$

which is a resonance form. It gives all harmonics of the primary wave. This nonlinear correction can be very large even at small amplitudes because of the large factor $\gamma k_z H$ in the denominator.

When the amplitude satisfies $\gamma k_z H R_k \approx 1$, the wave can no longer propagate as a linear wave since, then, $|k \cdot v'| / \omega_0 \gg 1$ at $\phi = \pi/2$, and consequently, $N^2(\omega_0 + k \cdot v')^{-2} \sim 0$ in (1). The wave can be said to have been broken

(saturated) by nonlinear wave interaction. More precisely, the wave velocity fluctuation steepens along ϕ owing to harmonics. This steepening of wave velocity is shown in Figures 1 and 2, wherein are calculated $k \cdot v' / \omega_0$ and $k_x u' / \omega_0$ versus ϕ , for progressively increasing values of R_k . The steepening

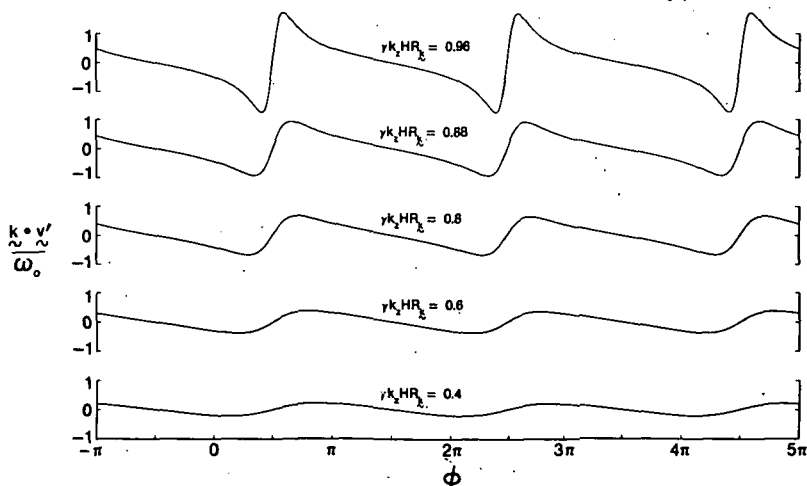


Figure 1. Theoretical $k \cdot v' / \omega_0$ versus ϕ for increasing wave amplitudes: $\gamma k_z H R_k = 0.4, 0.6, 0.8, 0.88, 0.96$. This graph also determines w' since $w'(\phi + \pi/2) = -\gamma H k_z v'(\phi)$. This figure extends for 3 cycles (3 periods) of wave oscillation ($-\pi < \phi < 5\pi$).

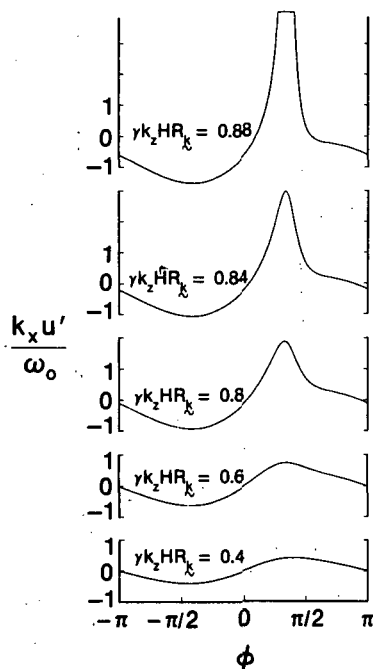


Figure 2. Theoretical $k_x u' / \omega_0$ versus ϕ for increasing density amplitudes: $\gamma k_z H R_k = 0.4, 0.6, 0.8, 0.84, 0.88$. Only one oscillation cycle is shown.

increases as $\gamma k_z H R_k$ increases until, finally, at $\gamma k_z H R_k \approx 1$ the wave

velocity becomes too steep to grow further. It is saturated. At that point, energy flows sufficiently fast from the primary wave into higher harmonics and the mean flow to balance linear growth. The cascading energy is dissipated by turbulence. We add a note of caution that $k \cdot \bar{v}'$ in (3) does not become infinite at $\gamma k_z H R_k = 1$ because the wave saturates slightly before.

The density amplitudes at saturation is obtained by substitution of the definition of R_k into $\gamma k_z H R_k = 1$

$$\frac{\rho_k}{\rho_0} = \frac{\gamma H d \ln \theta_0 / dz}{\gamma k_z H} \approx \frac{\gamma - 1}{\gamma k_z H} \quad (\text{saturation}) \quad (4)$$

which yields $\rho_k / \rho_0 \approx 0.1$ when $2\pi k_z^{-1}$ is about 12 km (consistent with lidar variations by CHANIN and HAUCHECORNE, 1981).

A very interesting result is found if one examines how the breakup condition, given by $\gamma k_z H R_k \approx 1$ (velocity steepening) relates to the superadiabatic condition (HODGES, 1967; LINDZEN, 1967; ORLANDSKI and BRYAN, 1969). To do so we substitute the approximate relation $\rho_k / \rho_0 \approx |\theta_k / \theta_0|$, where θ_k is the amplitude of the potential temperature fluctuation θ' , into R_k and so obtain

$$\left(\frac{\partial \theta'}{\partial z} \right)_{\max} \approx \frac{\partial \theta_0}{\partial z} \quad (\text{at } \gamma k_z H R_k \approx 1) \quad (5)$$

This is recognized to be the condition of marginal stability at which the potential temperature gradient is just about to become negative. Therefore, the wave velocity $k \cdot \bar{v}'$ begins to strongly steepen because of nonlinear, wave-

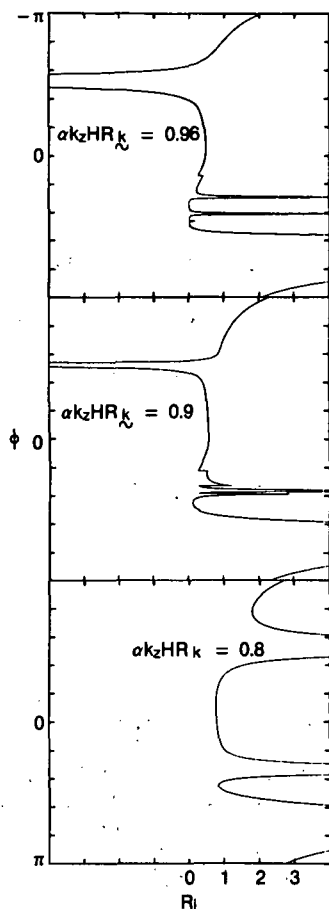


Figure 3. Theoretical $Ri = N_T (\partial u / \partial z)^{-2}$ versus ϕ for increasing wave amplitudes: $\gamma_k^{H R_k} = 0.8, 0.9, 0.96$.

wave interaction at the same time that the potential temperature gradient passes through zero. One phenomenon does not cause the other. Rather they are simultaneous consequences of a large wave amplitude.

INSTABILITY, STEEP GRADIENTS AND TURBULENCE

The presence of harmonics may cause dynamic or static instabilities to occur on very short length scales -- the length scale of high harmonics. To find short scale instabilities, we calculate the gradient Richardson number Ri , where $Ri \equiv N_T^2 (\partial u' / \partial z)^{-2}$ and $N_T \equiv [g \partial \ln(\theta_0 + \theta') / \partial z]^{1/2}$ is the local Brunt-Vaisala frequency. The fluctuations u' and θ' are obtained from the theory.

A graph of calculated Ri versus ϕ is given in Figure 3. A region of static instability $Ri < 0$ occurs near the phase $\phi = 4.7$ radians, and regions of dynamic instability $0 < Ri < 1/4$ occur near the phases $\phi = 1.9$ and 2.5 radians. The static instability is close to what is expected from linear theory. The two regions of dynamic instability are not expected from linear theory. These dynamical instabilities are due to nonlinear steepening (harmonics) of the perturbation velocity u' . Consequently, three narrow layers of turbulence can occur. In the atmosphere, the three layers of turbulence may be too close together to be individually discerned, although WAND et al. (1983) have observed multiple layers. A note of caution we hasten to add is that Ri is approximate, since θ' and u' are approximate, and should be taken with a grain of salt.

SOLUTION OF DISPERSION RELATION AND SATURATION

The nonlinear dispersion relation (1) and (2) can be self-consistently solved for the precise, saturation condition. It is thereby found that saturation occurs when $\gamma k_z H R_k \approx [1 + (\gamma k_z H)^{-2}]^{-1/2}$, which corresponds to

$|k_z \theta_k| \approx \partial \theta_0 / \partial z$. This formal result confirms the more heuristic arguments given in the preceding sections.

SUMMARY AND CONCLUSION

The propagation of a finite amplitude gravity wave is investigated by a new and straightforward method for calculating nonlinear wave interactions. The method employed requires little more than the mathematics of linearized theory.

A principal consequence of the theory is that the velocity wave form (velocity fluctuation \tilde{v}) steepens as the amplitude increases and the wave steepening increases to the point of breaking and saturation when the density amplitude ρ reaches the value $|k_z \theta_0 (\partial \theta_0 / \partial z)^{-1} \rho_k / \rho_0| \approx 1$ (equiva-

lently given by $\gamma k_z H R_k \approx 1$). This steepening resembles the beaching of an

ocean wave. In both cases, steepening of the velocity wave form is caused by the nonlinear advection term $\tilde{v} \cdot \nabla \tilde{v}$ in the Navier-Stokes equation. Energy flows from the primary wave into harmonics down to turbulence. Of special interest is that the lapse rate becomes unstable, $|k_z \theta_k| \approx \partial \theta_0 / \partial z$, at about the same time as wave-wave interactions cause the steepened wave velocity to break. This conforms to observations that saturation of wave velocity amplitude is accompanied by near adiabatic lapse rate and turbulence. However, the unstable lapse rate does not cause saturation in the idealized case considered here although it does contribute. Turbulence is produced -- by a steepened velocity gradient as well as by unstable lapse rate -- but eddy diffusion is not invoked. The importance of the adiabatic lapse rate is that it identifies where saturation is taking place -- a "signature" of wave breaking.

REFERENCES

- Chanin, M. L. and A. Hauchecorne (1981), J. Geophys. Res., **86**, 9715.
 Fritts, D. C., B. B. Balsley and W. L. Ecklund (1984), Dynamics of the Middle Atmosphere, edited by J. R. Holton and T. Matsumo (Terra Publ. Co.).
 Hodges, R. R., Jr. (1967), J. Geophys. Res., **74**, 4087.
 Lindzen, R. S. (1967), J. Roy. Meteorol. Soc., **93**, 18.
 McIntyre, M. E. and T. N. Palmer (1983), Nature, **305**, 593-600.

3.12 GRAVITY WAVE CHARACTERISTICS IN THE STRATOSPHERE AND MESOSPHERE AT MIDLATITUDE

M. L. Chanin and A. Hauchecorne

Service d'Aeronomie du CNRS
BP 3 - Verrieres le Buisson, France

A more complete description of the characteristics of gravity waves in the middle atmosphere is required in order to evaluate their effects on the general circulation. A new approach is now available to describe these waves in terms of density and temperature fluctuations by using Rayleigh back-scattering of a laser beam. The so-called Rayleigh Lidar is able to provide continuous information from 30 to 90 km with high spatial and temporal resolutions. Several years of data have been used to study the characteristics of these waves at mid-latitude from the Observatory of Haute-Provence in France (44°N, 6°E), and to relate their presence with specific meteorological situations. Furthermore the behaviour of the wave as a function of altitude provides an insight on the dissipation and the saturation mechanisms.

3.13 GRAVITY WAVE VERTICAL ENERGY FLUX AT 95 KM

P. G. Jacob and F. Jacka

Mawson Institute for Antarctic Research
University of Adelaide
G.P.O. Box 498,
Adelaide, South Australia 5001.

INTRODUCTION

A three-field photometer (3FP), located at Mt. Torrens near Adelaide, is capable of monitoring different airglow emissions from three spaced fields in the sky. A wheel containing up to six different narrow bandpass interference filters can be rotated, allowing each of the filters to be sequentially placed into each of the three fields. The airglow emission of interest here is the 557.7 nm line which has an intensity maximum at 95 km. The background continuum is also monitored at 500 nm and 530 nm. Each circular field of view is located at the apexes of an equilateral triangle centred on zenith with diameters of 5 km and field separations of 13 km when projected to the 95-km level. The sampling period was 30 seconds and typical data lengths were between 7 and 8 hours. The analysis and results from the interaction of gravity waves on the 57.7 nm emission layer are derived using a model atmosphere similar to that proposed by HINES (1960) where the atmosphere is assumed isothermal and perturbations caused by gravity waves are small and adiabatic, therefore resulting in linearised equations of motion. In the absence of waves, the atmosphere is also considered stationary; however this criterion can be relaxed if a suitable reference frame is chosen. Thirteen nights of quality data from January 1983 to October 1984, covering all seasons, are used in this analysis.

HORIZONTAL PHASE VELOCITIES

To investigate the propagation of gravity waves the data were spectrally analysed. Each pair of fields was taken in turn and estimates of the amplitude, phase and coherence spectra were computed and averaged for each frequency interval (JENKINS and WATT 1969). This analysis was carried out using data windows of one to several hours and stepping the windows at 15-minute intervals along the entire data length. Each data window was treated with a cosine taper to reduce spectral leakage and the mean and any linear trend removed before computing the spectra (BRAUNT and WHITE 1971). Periodicities showing a peak in the mean cross power in all three fields and a mean coherence corresponding to a 90% or greater significance over two or more successive windows were considered as real manifestations of gravity waves. The waves are assumed to exhibit plane wave fronts which do not significantly change in structure as they pass over the fields of view. These assumptions, considering the separation of the fields, seem valid for the case of medium scale gravity waves and make for the simplest calculation of horizontal phase velocity.

From the phase shifts an apparent velocity can be assigned to selected periodicities whereby a true phase velocity can be realised from the method discussed by FREUND and JACK (1979). Estimates in the error of the velocity calculated in this was are typically up to 20%.

DISPERSION EQUATION

The dispersion equation for gravity waves of small perturbation in an isothermal, stationary atmosphere is given by (GOSSARD and HOOKE, 1975):

$$k_z^2 = \left[\frac{N^2 - \omega^2}{\omega^2 - f^2} \right] k_x^2 + \left[\frac{\omega^2 - N^2}{C^2} \right] - \Gamma^2 \quad (1)$$

Here k_x and k_z are the horizontal and vertical wave numbers, respectively, N the Vaisala-Brunt frequency and C the velocity of sound. The rotational effects of the earth have been included with f the inertial frequency. For an isothermal atmosphere the parameter $\Gamma = (g/2C^2)(2-\gamma)$, γ being the ratio of specific heats. The dispersion equation (1) is shown graphically in Figure 1 with selected constant period contours plotted using atmospheric parameters suitable for the 95-km level. Points plotted are detected gravity waves using (1) and the observed period and horizontal wave number ($k_x = \omega/v_x$). Note that the wave frequency observed is doppler shifted due to the mean wind. Estimated values of the mean flow at 95 km were used to infer an intrinsic frequency since $\omega = \omega_{\text{obs}} - (\mathbf{k} \cdot \mathbf{U})$, \mathbf{U} being the mean flow, assumed to have negligible vertical components (GROVES 1969). Since photometer observations are limited to nighttime, with data lengths of around 8 hours, then measurements of periods greater than about 4 hours become unreliable so detected waves with periods greater than this are rare.

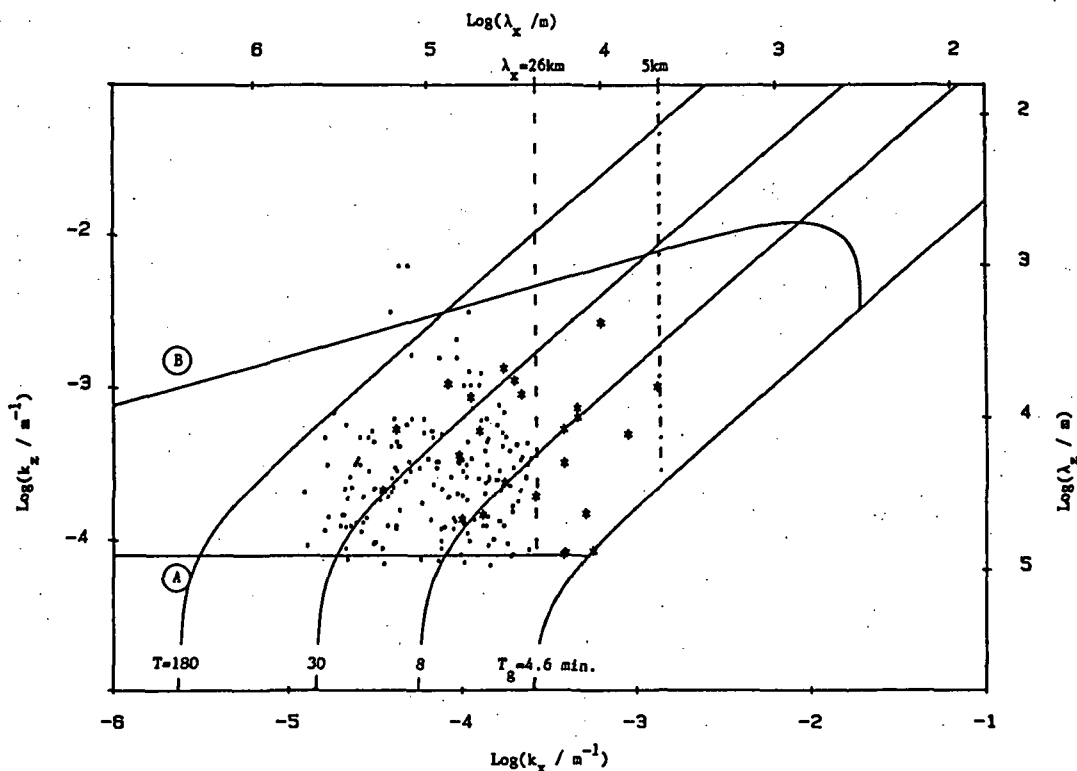


Figure 1. Gravity waves detected at 95 km. Boundary A - indicates a lower limit to the vertical wave number below which waves propagating from lower in the atmosphere will be reflected. Determined from the condition $k_z^2 < 0$. Boundary B - viscous dissipation limit. Waves above this limit are severely attenuated through viscous damping (HINES 1960). The vertical line at $\lambda_x = 25$ km indicates an instrumental limitation of the photometer. Since field spacings are 13 km then wavelengths less than twice this spacing become ambiguous. Some data were recorded with each 5 km diameter field divided into 3 subfields with separations of 2.5 km. The $\lambda_x = 5$ km line shows the cutoff of these data which are represented by asterisks.

VERTICAL GROUP VELOCITY

The vertical group velocity for gravity waves can be derived from (1)

$$v_{gz} = \left| \frac{\partial \omega}{\partial k_z} \right| = \frac{C^2 \left(\frac{\omega^2 - f^2}{\omega} \right) k_z}{C^2 (k_x^2 + k_z^2) - 2\omega^2 + f^2 + N^2 + C^2 \Gamma^2} \quad (2)$$

Using the above equation, vertical group velocities for each wave were calculated and are shown in Figure 2. As indicated, the boundaries which confine the observations in Figure 1 also restrict the range of velocities. Although the data are limited, particularly those waves indicated by asterisks, it is reasonable to suggest that the vertical group velocities are uniformly distributed within the allowed boundaries. As a result, a mean velocity was taken and extrapolated to periods beyond the observations to the inertial period. Gravity waves cannot propagate with periods larger than the inertial period or less than the Väisälä Brunt; therefore, the velocity must approach zero at these limits.

ENERGY DENSITY

The mean energy per unit volume or the energy density of a stationary, isothermal atmosphere of mean density ρ_0 due to a gravity-wave perturbation is given by (GOSSARD and HOOKE, 1975):

$$\bar{E} = \frac{1}{2} \rho_0 (\overline{V^2} + N^2 \overline{\zeta^2}) \quad (3)$$

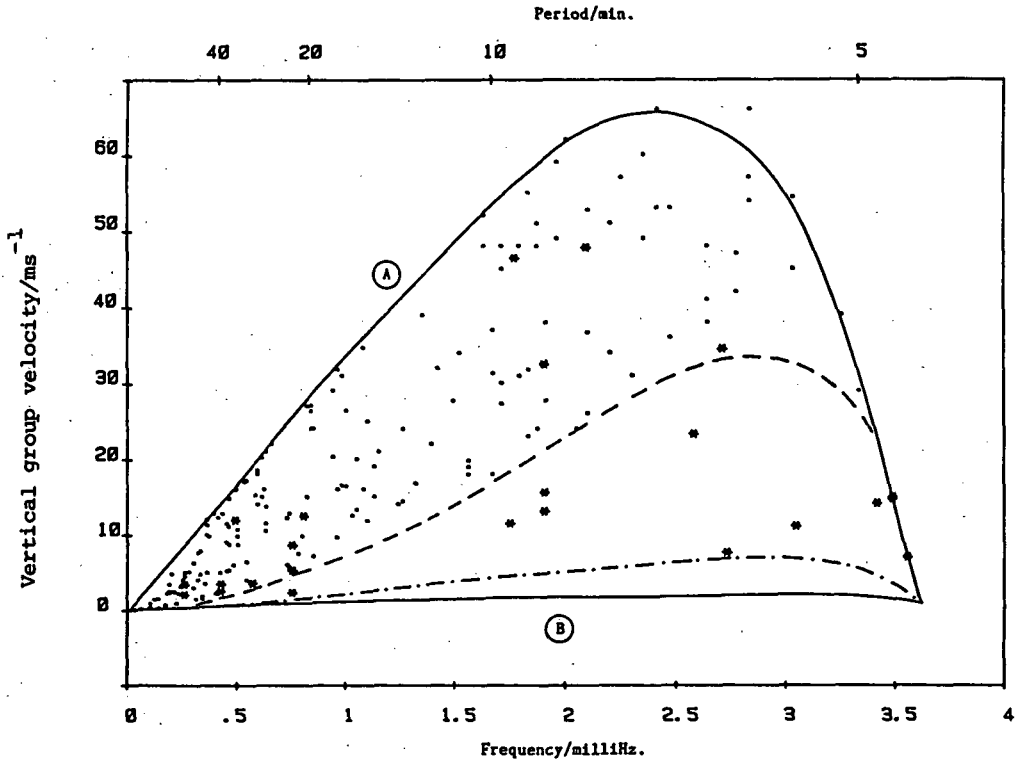


Figure 2. Vertical group velocities of detected waves contained by the boundaries of Figure 1.

where V is the amplitude of the horizontal velocity perturbation and ζ the vertical displacement of the atmosphere due to the passage of a gravity wave. This expression is effectively the sum of the kinetic and potential energies and can be rewritten as

$$\overline{V^2} = \frac{g^2}{N^2} \left(\frac{\omega^2 + f^2}{\omega^2 - f^2} \right) \left(\frac{\rho}{\rho_0} \right)^2 \quad (4)$$

Using the polarization equations of GOSSARD and HOOKE (1975) the mean square velocity perturbation, $\overline{V^2}$ can be expressed as a function of the mean square fractional density perturbation

$$\overline{E} = \frac{1}{2} \rho_0 \overline{V^2} \left(1 + \frac{k_x^2 N^2}{k_z^2 (\omega^2 + f^2)} \right) \quad (5)$$

Following BATTENER and MOLINA (1980), fluctuations in the atmospheric density can be related to fluctuations in the 557.7 nm intensity by $\Delta\rho/\rho_0 \approx \beta \Delta Q/Q_0$. Here β is taken to be 0.9 which assumes the maximum in the airglow emission is slightly displaced from the peak in the atomic oxygen profile. Assuming sinusoidal oscillations, then the mean square fractional density perturbation can be found from the airglow intensity power spectra since the area under the spectrum is the variance, Q^2 of the oscillation over that interval.

The mean airglow intensity, Q_0 is inferred from the background emissions measured at 530 nm and 500 nm. Scaling is necessary to allow for different filter transmission characteristics and photomultiplier spectral responses. The background intensities were taken to be equal at all three wavelengths (BROADFOOT and KENDALL 1968). Data from all nights showed that the energy spectra are related by a power law for the frequency range of the observations, i.e., $E \propto \omega^{-k}$ where the spectral index k lies between 1 and 2. Similar indices are found from the spectra of mesospheric wind fluctuations caused by gravity waves which also suggest the power law holds over the entire gravity-wave spectrum (CARTER and BALSLEY, 1982; VINCENT, 1984).

VERTICAL ENERGY FLUX

The average energy crossing unit area per second or the mean vertical energy flux is given by $\overline{F_z} = \rho_0 \overline{E V_{gz}}$. Although the main contributor to the excess energy of the atmosphere due to gravity waves is the large amplitude, long period waves, their near horizontal motions make the upward transport of this energy quite small. Figure 3 shows the energy flux of the gravity-wave spectrum based on the product of the mean vertical group velocity and the mean energy density from photometer measurements. The majority of the flux is contained in the shorter periods with between 85% and 90% contributed from waves with periods less than four hours, periods directly measurable using the 3FP.

Assuming that gravity waves are incident at 95 km from below, and the data used represents a seasonal average, then from this analysis the total upward going energy flux is $\approx 15 \text{ mW/m}^2$. VINCENT (1984) measures vertical energy flux at 85 km to be $\approx 10 \text{ mW/m}^2$ using partial reflection measurements of horizontal winds near Adelaide averaged over a full year.

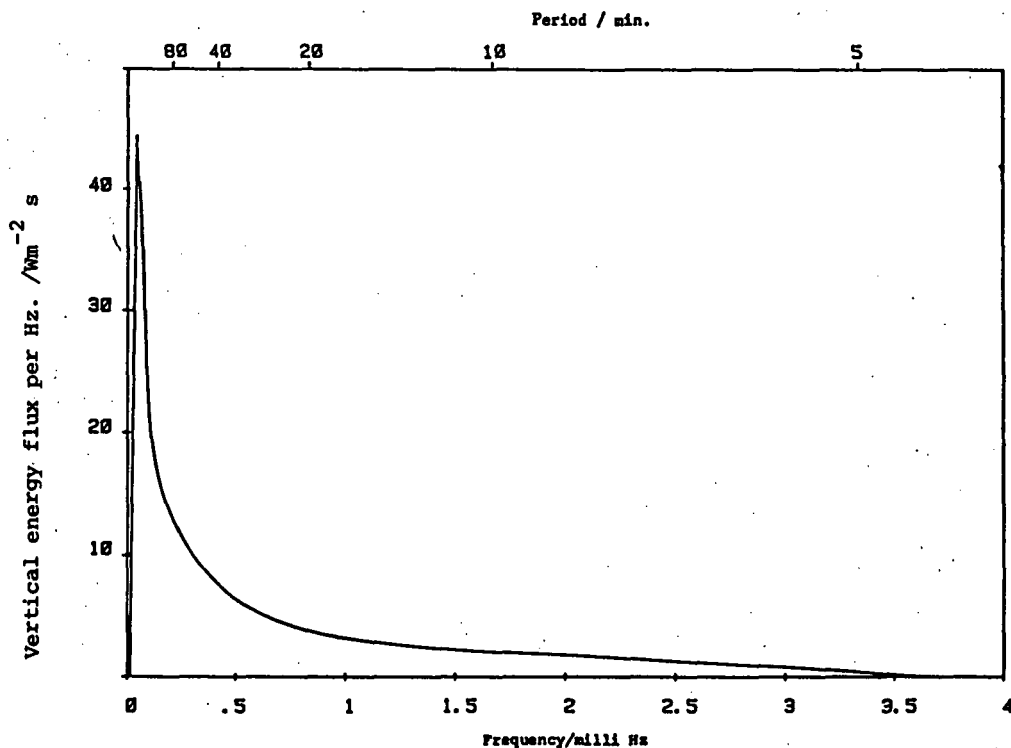


Figure 3. Mean vertical energy flux spectrum. The area under the curve is the total energy flux at the 95 km level extrapolated from 3FP measurements.

REFERENCES

- Battaner, E. and A. Molina (1980), J. Geophys. Res., **85**, 6803.
 Brault, J. W. and O. R. White (1971), Astronomy and Astrophys., **13**, 169.
 Carter, D. A. and B. B. Balsley (1982), J. Atmos. Sci., **39**, 2905.
 Freund, J. T. and F. Jacka (1979), J. Atmos. Terr. Phys., **41**, 25.
 Gossard, E. E. and W. M. Hooke (1975), Waves in the atmosphere, (Elseviers Scientific Publishing, Amsterdam.)
 Groves, G. V. (1969), J. Brit. Interplan. Soc., **22**, 285.
 Hines, C. O. (1960), Can. J. Phys., **38**, 1441.
 Jenkins, G. M. and D. G. Watts (1969), Spectral analysis and its applications (Holden Day, San Francisco).
 Vincent, R. A. (1984), J. Atmos. Terr. Phys., **46**, 119.

3.14 WAVE MOTIONS IN THE UPPER ATMOSPHERIC SODIUM LAYER OBSERVED WITH A LIDAR TECHNIQUE

Hiroshi Kamiyama and * Fumihiko Tomita

Upper Atmosphere and Space Research Laboratory
Tohoku University, Sendai 980, Japan

*Radio Research Laboratories,
Ministry of Posts and Telecommunications, Tokyo 184, Japan

INTRODUCTION

Since the middle of 1980, the vertical profile of the atmospheric sodium layer has been observed with a tunable laser radar at Mt. Zao Observatory (38.1°N, 140.6°E) in northern Japan. The instrumentation of the lidar system employed was described in detail in the previous paper (KAMIYAMA et al., 1981). Principal characteristics of the system are summarized in Table 1. The output wavelength is continuously monitored by using a sodium resonance cell, a spectrometer, and a Fabry-Perot interferometer provided with the reference spectrum of the sodium lamp. Owing to the strict temperature control of the filters, the tuning is sufficiently stable throughout a night.

The calibration of the absolute sodium density has been carried out by adopting the method established by previous works (e.g., MEGIE and BLAMONT, 1977; CERNY and SECHRIST, 1980; SIMONICH and CLEMSHA, 1983).

NOCTURNAL AND SHORT PERIOD VARIATIONS

Various types of nocturnal variations in the sodium layer have so far been observed. One of the most characteristic features is the wave-like structure showing a downward progression of the phase throughout the night, and is suggested to be associated with the propagation of gravity waves or atmospheric tides. Some examples showing characteristic variations in the vertical profile of the sodium density are given in Figures 1 and 2. Each of the profiles is obtained on the basis of hourly integrated data and is shown by the solid line. The profile averaged over the night concerned is shown by the dotted lines for reference, and the regions where the density exceeds the averaged profile are marked with hatching. Also shown in the upper panel is the trend of hourly values of the column content. It is seen that the pronounced feature common in these examples is the decrease, with time, in the altitude of the density enhancement. In the case shown in Figure 1 (March 11-12, 1981) the height of the density enhancement descends at the rate of about 1.5 km/hr on an average accompanying the increase in the column content. It is also pointed out that the variation in the sodium density is much more pronounced in the lower part of the layer than in the higher part. These characteristics are shown more clearly by contour maps. In Figure 3(a), the differences between each profile and the profile averaged over the night are shown in terms of the sodium density, while in Figure 3(b), they are given in the percentage deviation from the average. The areas for large deviations in both the figures are distinguished by two sorts of shading according to their signs, respectively. One can see clearly the much more pronounced variation of the sodium density in the lower part of the layer in Figure 3(a), and the downward phase progression of the percentage deviation in Figure 3(b). In the latter figure, the wave-like structure reveals a vertical wavelength of 14 - 22 km and a period of about 12 hr. This wave motion seems to be of the same semidiurnal oscillation as reported by CLEMSHA et al. (1982). Another example given in Figure 2 (April 7-8, 1981) shows such a feature more clearly as illustrated in Figures 4(a, b). In Figure 4(b), the vertical wavelength is estimated to be 16-22 km, and the

Transmitter		Receiver	
Wavelength	589.0 nm	Effective area	0.2 m ²
Divergence	3 mrad	Field of view	5 mrad
Transmitted bandwidth	16 pm	Bandwidth	2 nm
Repetition rate	0.25 Hz	Height resolution	1.5 km
Output energy	80 mJ/pulse		
Pulse duration	2.2 μs FWHM		

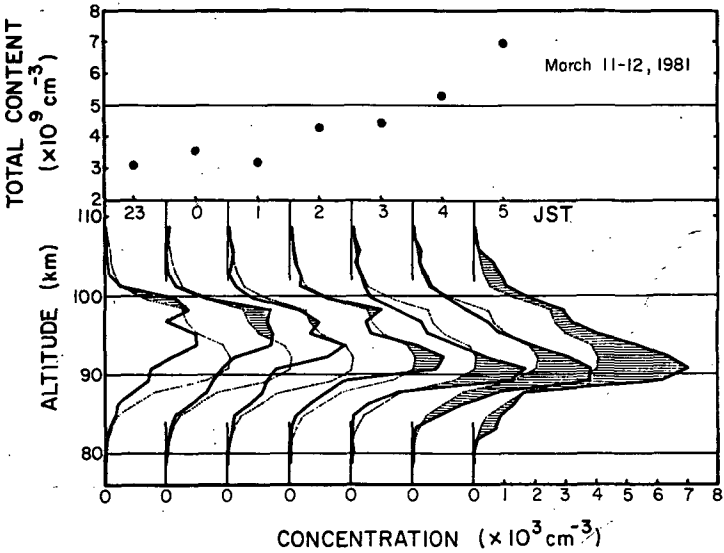


Figure 1.

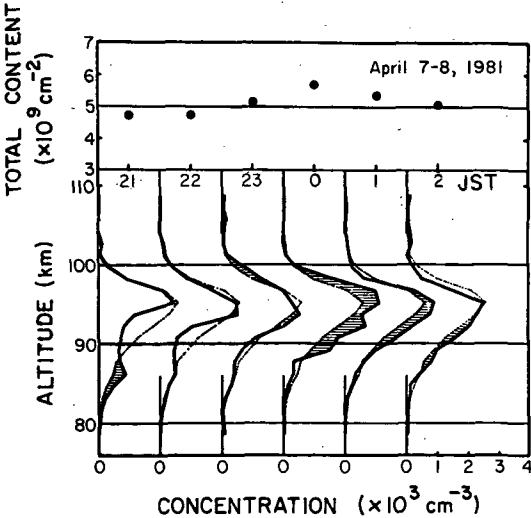


Figure 2.

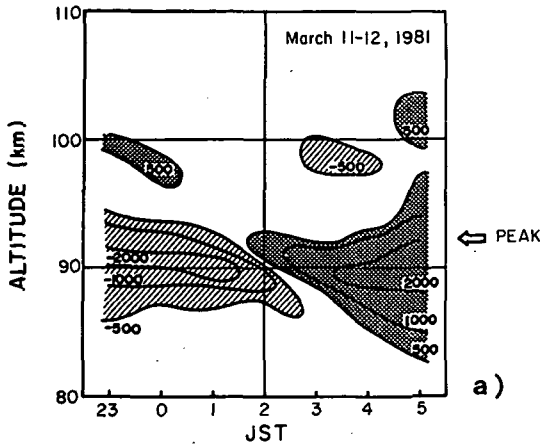
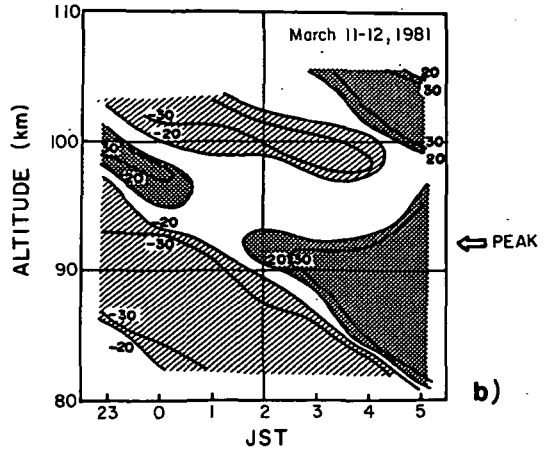


Figure 3(a).



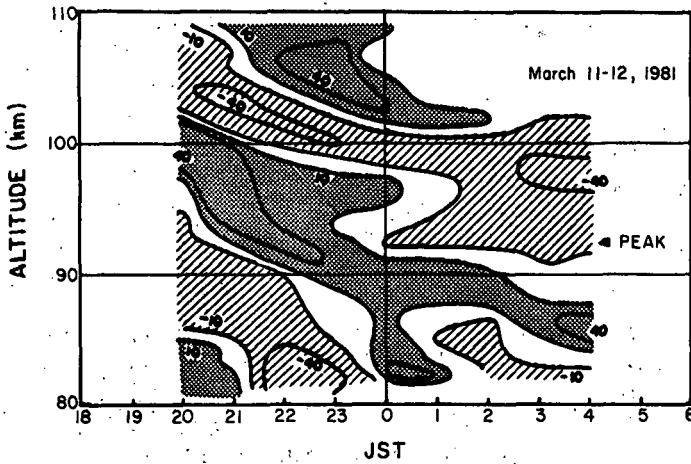


Figure 5.

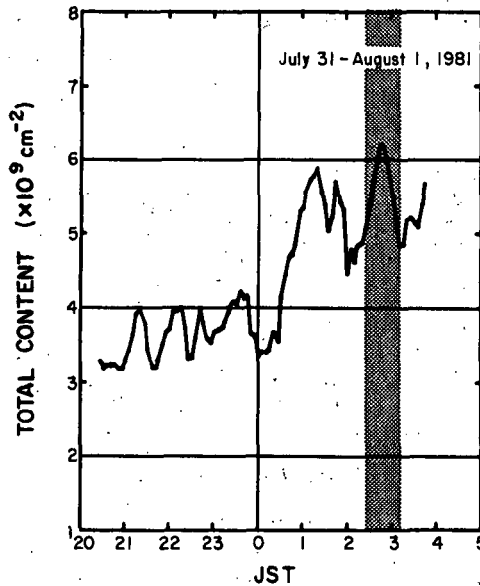


Figure 6.

dotted lines for reference, and column contents are plotted in the upper panel of the figure. One can see a downward shift of the wave-like structure, the density variations at altitude of 83 km and 95 km being inphase, but their phases being opposite to those at 89 km and 98 km. From these characteristics, it is obvious that there are short period oscillations having a vertical wavelength of 9-12 km and a period of about 60 min. In another example (May 17, 1982, 23^h25^m 24^h00^m JST) shown in Figure 8, the variations at the altitudes of 87 km and 98 km, respectively, seem to be in-phase, whereas the phase of the variation at 92 km is quite different from those of the above pair. In this event, the vertical wavelength is found to be about 11 km and the period is estimated to be 30-50 min. These short period fluctuations are considered to be the same sort of oscillations as those reported by SHELTON et al. (1980).

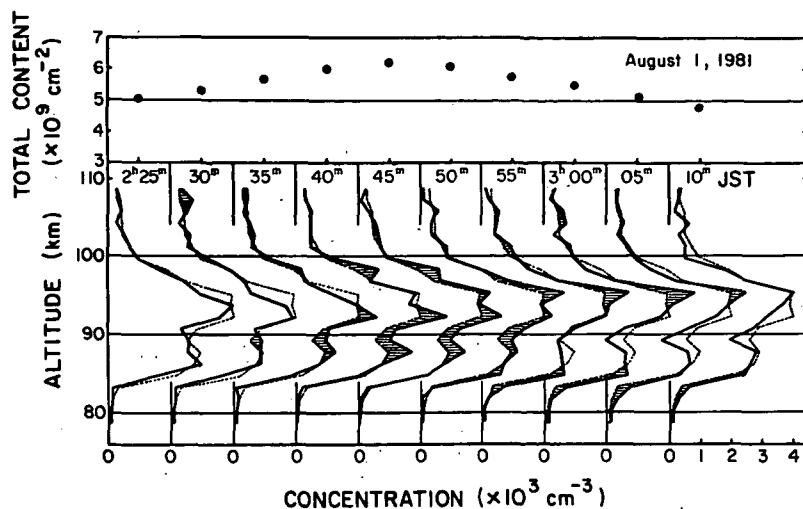


Figure 7.

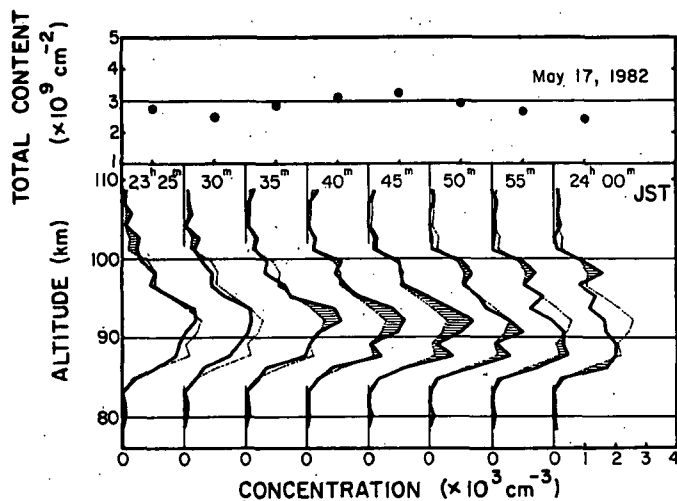


Figure 8..

There is, however, another kind of event in which the sodium density is enhanced simultaneously at almost the entire height range accompanying the enhancement of the column content. Most of these events were observed during the periods of high meteoric activity, suggesting the meteoric origin of the sodium layer.

CONCLUDING REMARKS

The nocturnal sodium layer shows a large variety of variations, reflecting not only possible changes in the source of atmospheric sodium but also a combined effect of the dynamics and chemistry of the sodium layer. Our observational results show the wave-like structure with a vertical wavelength of 14-22 km and the downward phase progression ranging from 0.4 to 7 km/hr.

The short period fluctuations having periods of about 1 hour or so are frequently superposed on a nocturnal variation. Most of them are accompanied by the descending wave-like structures in which the vertical wavelength is estimated to be 9-12 km.

Some of the results showing the wave-like structure of the sodium layer observed with the lidar technique in northern Japan (38°N) are presented in this paper. The structural variations of the sodium layer with various time-scales suggests that the stratification of the sodium layer is related not only to the change in the composition of the atmosphere in the height range concerned, but to a large extent, to atmospheric tides or wave propagations.

ACKNOWLEDGEMENTS

Our thanks are due to Dr. M. Jumonji of Hachinohe Institute of Technology for his effectual co-operation in developing the high-power dye laser for our lidar system, and also to Messrs. T. Ohnuma, S. Okano, and K. Ide for their co-operation in carrying out observations.

REFERENCES

- Cerny, T. and C. F. Sechrist, Jr., (1980), Aeronomy Report, 94, University of Illinois, Urbana.
- Clemsha, B. R., D. M. Simonich, P. P. Batista, and V. W. J. H. Kirchhoff (1982), J. Geophys. Res., 87, 181.
- Kamiyama, H., F. Tomita, T. Ohnuma, S. Okano, and M. Jumonji (1981), Tohoku Geophys. Journ., 28, 105.
- Megie, G. and J. E. Blamont (1977), Planet. Space Sci., 25, 1093.
- Simonich, D. M. and B. R. Clemsha (1983), Appl. Opt., 22, 1387.
- Shelton, J. D., C. S. Gardner, and C. F. Sechrist, Jr. (1980), Geophys. Res. Lett., 7b, 1069.

3.15 CLEAR AIR TURBULENCE AND MESOSPHERIC GRAVITY WAVES

R. S. Lindzen

Department of Earth, Atmospheric, and Planetary Sciences
Massachusetts Institute of Technology,
Cambridge, MA 02139

It has long been known (NEWTON 1971), that orography exerts a significant torque on the atmosphere. These torques are associated with orographically generated mountain waves whose momentum is deposited in the upper troposphere/lower stratosphere (LILLY, 1972). The momentum deposition appears to be associated with wave breaking which occurs at levels where \bar{u} , the zonally averaged zonal wind, has a minimum -- and the wave momentum flux may, in fact, contribute to the minimum.

Of importance to the middle atmosphere is the fact that such wave breaking will cease above the minimum in \bar{u} . The reason for this is that increasing \bar{u} (assuming phase speed, c , equals zero) causes wave amplitudes to decrease (LINDZEN, 1981), and above the minimum in \bar{u} , this effect more than balances the tendency of decreasing mean density to amplify waves. Eventually, this situation reverses, and simple calculations show that gravity waves which break at the minimum of \bar{u} will again break above 60 km -- where in fact breaking is observed.

In both the troposphere and the mesosphere, the absorption of these gravity waves plays a major role in maintaining the momentum budget and the meridional temperature gradient.

REFERENCES

- Lilly, D. K. (1972), Wave-momentum flux - A GARP problem, Bull. Amer. Meteorol. Soc., **53**, 17-23.
Lindzen, R. S. (1981), Turbulence and stress due to gravity wave and tidal breakdown, J. Geophys. Res., **86**, 9707-9714.
Newton, C. W. (1971), Mountain torques in the global angular momentum balance, J. Atmos. Sci., **28**, 623-628.

3.16 TROPOSPHERIC GRAVITY WAVES OBSERVED BY THREE CLOSELY-SPACED ST RADARS

D. A. Carter, B. B. Balsley, W. L. Ecklund

Aeronomy Laboratory
National Oceanic and Atmospheric Administration
Boulder, Colorado 80303

M. Crochet

LSEET, ERA/CNRS 668
Universite de Toulon, France

A. C. Riddle and R. Garellio

CIRES
University of Colorado
Boulder, CO 80309

During a 6-week period in 1982, 3 ST (Stratosphere-Troposphere) radars measured horizontal and vertical wavelengths of small-scale ($\lambda_x < 50$ km) tropospheric gravity waves. These 50 MHz, vertically-directed radars were located in a triangular network with approximately 5 km spacing on the southern coast of France at the mouth of the Rhone River during the ALPEX (Alpine Experiment) program.

Aside from occasional Brunt-Vaisala period oscillations, there were very few instances of definite monochromatic fluctuations in the vertical velocity. In order to detect those additional gravity waves which may have been masked by the continuous background of uncorrelated velocity fluctuations, a coherence analysis was performed on the vertical velocities observed at the 3 radar sites. Complex cross-spectra were computed for each pair of stations, averaged over 6-24 hours in time and over 5 or 6 independent (750m) range gates, and then converted to coherence spectra. A stringent significance test was applied which required that the computed coherence exceed the 99% confidence level for at least 3 contiguous frequency points on all 3 coherence spectra. For those significantly coherent frequencies, a horizontal wavelength and phase velocity were computed from the phase differences between stations and a vertical wavelength was derived from cross-spectra between heights.

Seven events met the acceptance criteria. The coherent wave periods ranged from 20 to 90 minutes and the deduced horizontal wavelengths were between 10 and 40 km. The background winds (measured 60 km away at Nimes) were generally moderate, averaging about 10-15 m/s in the 3-7 km observational height range. Figure 1 shows the computed directions of the waves along with the background wind directions. The striking point to notice is that in most cases the waves were propagating into the mean wind. On May 10 and 14, the waves were propagating perpendicular to the background wind, but during the May 10 event, the wind just above the observed wave also had a strong component opposite the wave direction.

Using the observed wave frequency, f_o , and the horizontal wind component in the direction of wave propagation, u_k , the intrinsic wave frequency, f can be computed from

$$f = f_o - \frac{u_k}{\lambda_x} \quad (1)$$

Figure 2 shows the computed intrinsic period ($T = 1/f$) as a function of height for all the wave events. The observed period is shown at the bottom of each

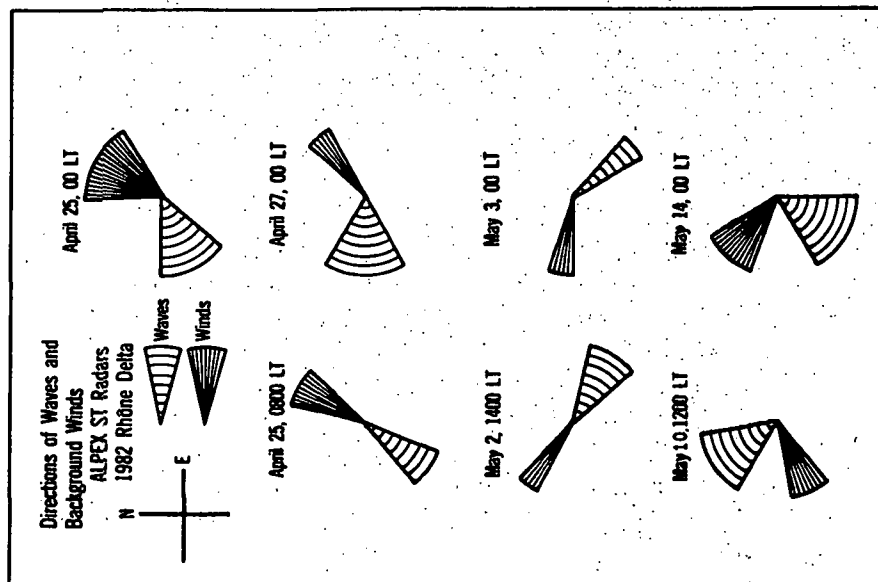


Figure 1. Directions of waves observed by radar and winds measured by rawinsonde. Sectors indicate the directions from which waves and winds were coming averaged over 6-24 hours and over approximately 3-6 km height range.

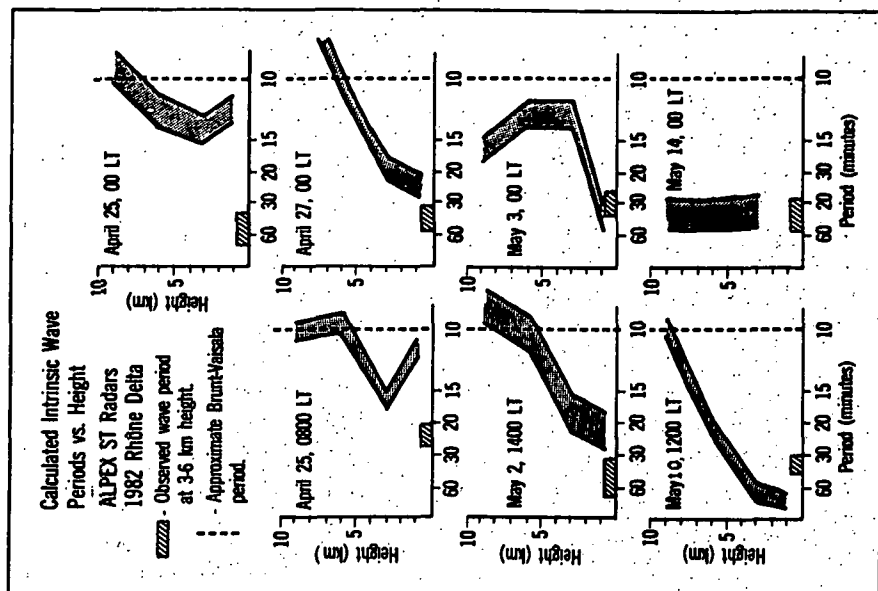


Figure 2. Intrinsic wave periods for the same events as in Figure 1. The hatched bar along the abscissa indicates the wave period observed by the radar. A typical tropospheric Brunt-Vaisala period of 10 minutes is indicated by the vertical dashed line.

graph and a typical Brunt-Vaisala period of 10 minutes is also indicated. It can be seen that in almost every case, the intrinsic frequency has been Doppler shifted to higher frequencies by the opposing background wind. In fact, at some height in the upper troposphere, the intrinsic frequency often reaches the Brunt-Vaisala frequency. At that point, further upward propagation is not permitted, and the wave is reflected and trapped in the troposphere. On May 14, when the wind and wave propagation were at right angles, no Doppler shifting took place.

Although the coherence between radar sites was very good during the periods shown here, the coherence between heights separated by more than 2 km was generally quite poor. Even when those coherences were significant, the phase differences between heights often appeared quite scattered and did not permit a reasonable calculation of vertical wavelengths. This result would be expected for trapped waves, where there is both upward and downward wave propagation.

On May 2, 1400-2400 LT, however, there was significant and approximately linear phase progression with height, which was consistent with an untrapped wave with upward energy (downward phase) propagation. From the observed phase differences, vertical wavelengths were determined and plotted in Figure 3. The vertical wavelength can also be predicted from the horizontal wavelength, mean wind, and observed frequency by

$$\lambda_z^2 = \lambda_x^2 \frac{f^2}{N^2 - f^2} \quad (2)$$

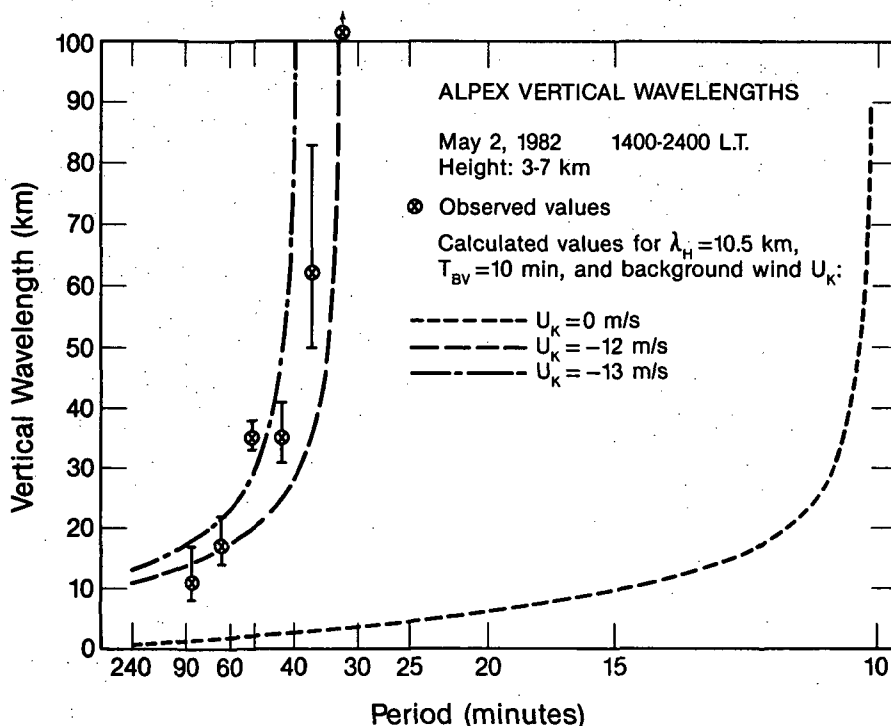


Figure 3. Vertical wavelengths vs. wave period. Circled points represent radar observations on May 2, 1982. Broken lines are calculated vertical wavelengths for a horizontal wavelength of 10.5 km and various wind components in the direction of wave propagation.

where N is the Brunt-Vaisala frequency and the intrinsic frequency, f , is given by (1). Figure 3 shows that the observed vertical wavelengths agree with the values predicted for a background wind component of 12-13 m/s in the direction opposite the wave. The actual wind component, measured at Nimes, averaged about 12 ± 2 m/s between balloon launches at 1400 LT May 2 and 0200 LT May 3.

The reason that the May 2 wave event showed an untrapped, propagating wave with measurable vertical wavelengths can perhaps be explained by the wind profile taken at the very end of this period (0200 LT May 3). As Figure 2 indicates, the mean wind then was such that the intrinsic frequency was never Doppler shifted beyond the Brunt-Vaisala frequency, thus allowing waves to propagate out of the troposphere.

No definite sources have been identified for any of these waves. They occurred under generally fair weather conditions with no fronts or strong jets in the vicinity. On May 10 and May 14, the waves were propagating in the same direction as the surface winds and so their sources may have been located near the ground. During the other times when the waves were propagating into the upper tropospheric winds, it is presumed that these particular waves were observed because they were trapped, propagated longer horizontal distances, and dominated during the rather long averaging periods used in the coherence analysis.

Multi-station radar observations such as those reported here are very valuable in determining gravity wave parameters which cannot be measured easily from a single location. Both horizontal and vertical wavelengths are needed to study waves propagating in an atmosphere with a background wind. A coherence spectral analysis can be used to detect waves that might otherwise go unnoticed. Further observations over longer periods, different horizontal spacings, larger height ranges, and possibly with oblique as well as vertical beams would contribute greatly to the understanding of gravity waves in the atmosphere.

3.17 THE ACOUSTIC GRAVITY WAVE INDUCED BY A POINT SOURCE IN THE MIDDLE ATMOSPHERE

Zhang Xun Jie and Xiong Nian Lu

Department of Space Physics,
Wuhan University, Wuhan, China

In the present paper, acoustic gravity wave (AGW) results computed for a stationary impulsive point source and a moving point source in the middle atmosphere are presented. For a stationary impulsive point source we have extended ROW's (1967) far field formula of the AGW into the near field one, which comprises the Zeroth order Bessel's function and its derivative terms. When $(t-t_0)$ is not very large, the contribution of derivative terms is important. The computed results agree with the experimental ones. For a moving point source with supersonic speed, AGW is calculated using the moving point source theory. We have compared two solar eclipse results that occurred in the lower latitude and over the ocean on Feb. 16, 1980, and June 11, 1983. The results show that the theoretical curve of AGW is fairly consistent with the observed ones. We preliminarily considered that the solar eclipse occurred in the lower latitude because the moon shadow cooling effect in the ozonosphere could excite the AGW.

Up to the present time, most of the investigations have studied the source problem of AGWs due to a stationary impulsive point source using the method of Fourier transform by Row (ROW, 1967). In Row's method, considering the far

field approximation, the formula, $G_0(r, z, t) = \omega_b J_0(\omega_c \sqrt{t^2 - t_0^2}) / 4\pi R$, is ob-

tained. Recently, we got the experimental results of AGWs produced by the stationary impulsive point source in the stratosphere using the Doppler frequency shift technique. When the distance between the observation point and the source is not very large, the far field approximation cannot be used. So, the theory must be modified to agree with the observation.

Using hydrodynamic equations to describe the behavior of atmosphere and the Fourier transform, the transient response of the atmosphere due to a point source excitation can be obtained in the following fashion:

$$G_0(r, z, \omega) = \frac{1}{4\pi R} \frac{\sqrt{\omega^2 - \omega_b^2}}{\omega^2 - \omega_c^2} \frac{1}{\sqrt{\omega^2 - \omega_c^2}} \exp [it_0 \sqrt{\omega^2 - \omega_c^2}] \quad (1)$$

here we assume $\omega_a = \omega_b$, and denote $p' / \sqrt{\rho_0}$, $v_z / \sqrt{\rho_0}$, $V_r / \sqrt{\rho_0}$ as $G_0(r, z, \omega)$

According to the Fourier transformation table

$$\begin{aligned} -iJ_0(\omega_c \sqrt{t^2 - t_0^2}) &\longleftrightarrow \frac{1}{\sqrt{\omega^2 - \omega_c^2}} \exp [it_0 \sqrt{\omega^2 - \omega_c^2}] \\ \sqrt{\omega^2 - \omega_b^2} &= i\omega_b \sqrt{(1 - \omega^2/\omega_b^2)} = i\omega_b [1 - \frac{1}{2} \frac{\omega^2}{\omega_b^2} - \frac{1}{24} \frac{\omega^4}{\omega_b^4} - \dots] \end{aligned}$$

We know

$$\begin{aligned} 1 &\longleftrightarrow \frac{1}{2\pi} \delta(t), \quad \omega^2 \longleftrightarrow -\frac{1}{2\pi} \delta''(t), \quad \omega^4 \longleftrightarrow \frac{1}{2\pi} \delta^{(4)}(t) \\ \sqrt{\omega^2 - \omega_b^2} &\longleftrightarrow i\omega_b [\delta(t) - \frac{1}{2\omega_b} (-\delta''(t)) - \frac{1}{24 \cdot \omega_b} \delta^{(4)}(t) - \dots] \end{aligned}$$

so $G_0(r, z, t)$ can be written as a convolution:

$$\begin{aligned}
 G_0(r, z, t) &= \int_{-\infty}^{+\infty} g_1(t - \tau) g_2(\tau) d\tau \\
 &= \frac{\omega_b}{8\pi R} [J_0(\omega_c \sqrt{t^2 - t_0^2}) + \frac{1}{2\omega_b^2} \frac{\partial^2}{\partial t^2} J_0(\omega_c \sqrt{t^2 - t_0^2}) \\
 &\quad - \frac{1}{24\omega_b^4} \frac{\partial^4}{\partial t^4} J_0(\omega_c \sqrt{t^2 - t_0^2}) + \dots]
 \end{aligned} \quad (2)$$

$G_0(r, z, t)$ is expressed in terms of the function $J_0(\omega_c \sqrt{t^2 - t_0^2})$ and its derivatives, the series converges rather rapidly. If we want to take to the order of z/R , only the term $J_0(\omega_c \sqrt{t^2 - t_0^2})$ needs to be computed, and the error would not be greater than $\frac{1}{2}(\frac{z}{R})^2$. If we want to take to the order of $(z/R)^2$, the 1st and 2nd terms must be used, and the error is not larger than $\frac{1}{24}(z/R)^4$. For example, when $z=220$ km, $r=270$ km, $z/r=0.8$, the error is not greater than $\frac{1}{24}(0.8)^4 \approx 2\%$.

$$G_0(r, z, t) = \frac{\omega_b}{8\pi R} [J_0(\omega_c \sqrt{t^2 - t_0^2}) + \frac{1}{2\omega_b^2} \frac{\partial^2}{\partial t^2} J_0(\omega_c \sqrt{t^2 - t_0^2})] = \frac{\omega_b}{8\pi R} \cdot g(t) \quad (3)$$

$$\begin{aligned}
 g(t) &= (1 - \frac{\omega_c^2}{2\omega_b^2} - \frac{t^2}{t^2 - t_0^2}) J_0(\omega_c \sqrt{t^2 - t_0^2}) \\
 &\quad + \frac{\omega_c^2}{2\omega_b^2} \frac{1}{\omega_c \sqrt{t^2 - t_0^2}} \frac{t^2 + t_0^2}{t^2 - t_0^2} J_0(\omega_c \sqrt{t^2 - t_0^2})
 \end{aligned} \quad (4)$$

From the above result, we know that as $t \rightarrow t_0$, the second term is important.

As $t \rightarrow t_0$, the coefficient of J_1 is $\frac{1}{(t^2 - t_0^2)^{3/2}}$, one of J_0 is $\frac{1}{(t^2 - t_0^2)}$.

As $t \rightarrow \infty$ the coefficient of J_1 becomes zero. One of J_0 is $(1 - \frac{\omega_c^2}{2\omega_b^2})$.

Assume the action coefficient of the velocity due to an impulsive point source is G , then

$$v_x = \frac{\omega_b}{8\pi R} \cdot \frac{G}{\sqrt{\rho_0}} g(t) \quad (5)$$

$$v_z = \frac{\omega_b}{8\pi R} \cdot \frac{G}{\sqrt{\rho_0}} g(t) \quad (6)$$

We have measured the curves of Doppler frequency shift of an impulsive point source using the HF Doppler sounding technique (Figure 1).

First, we can calculate the disturbance of the electron density.

$$\frac{\partial N'}{\partial t} + \nabla \cdot [N_0 (\vec{V} \cdot \hat{B}) \hat{B}] = 0 \quad (7)$$

where \hat{B} is parallel to the magnetic field and is a constant vector.

$$\frac{\partial N'}{\partial t} + N_0 (\hat{B} \cdot \nabla \vec{V} \cdot \hat{B}) + (\hat{z} \cdot \hat{B}) (\vec{V} \cdot \hat{B}) \cdot \frac{\partial N_0}{\partial z} = 0 \quad (8)$$

$$\vec{V} = \sqrt{2} \frac{AG}{\sqrt{\rho_0}} g(t) \frac{\vec{R}}{R^2} \quad (9)$$

here $A_1 = \frac{\omega_b}{8\pi} \cdot \rho_0 = \rho_{00} e^{-z/H}$,

We assume the background ionospheric electron density varies linearly with height in the reflection region, $N = az + b$, and

$$\hat{B} \cdot \hat{r} = \cos \theta_1, \quad \hat{B} \cdot \hat{z} = \cos \theta_2, \quad \hat{B} \cdot \hat{R} = \cos \theta_3$$

where $a, b, \theta_1, \theta_2, \theta_3$ are all constants. Using the perturbation method, we obtain the disturbance expression of the electron density:

$$N' = - \frac{G}{\sqrt{\rho_{00}}} e^{-z_0/2H} \cdot \frac{A_1 \cos \theta_2 \cos \theta_3}{4H^2} (z - z_0) (az + b) \frac{1}{z} Q(t) \quad (10)$$

$$Q(t) = \int_{t_0}^t g(t) dt \quad (11)$$

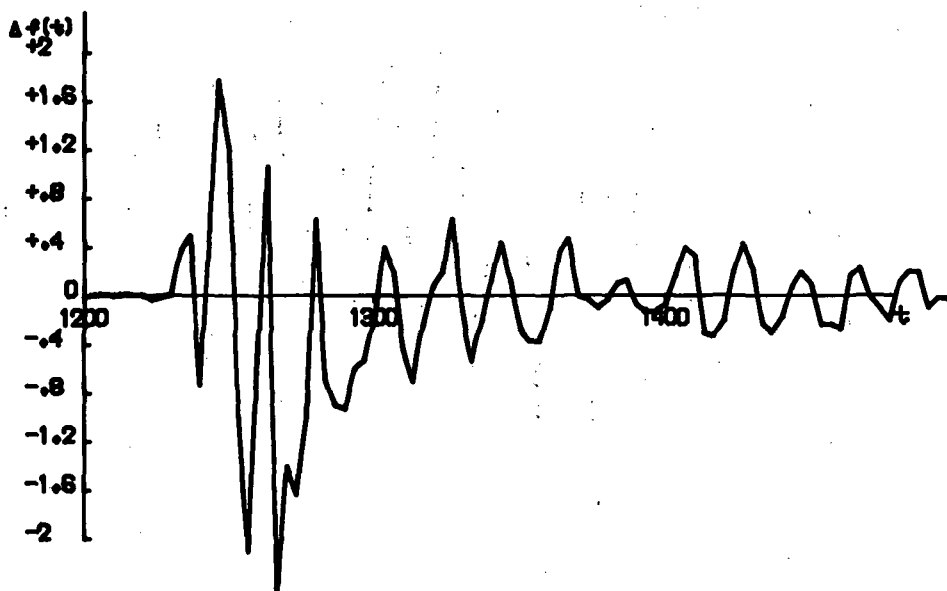


Figure 1. HF Doppler record of a stationary point source.

z_0 is the reflection height of the radio wave under quiet conditions. Neglecting the geomagnetic field and electron collisions, the refractive index of the radio wave is as follows:

$$n^2 = 1 - \frac{Ne^2}{\epsilon_0 m \omega_e^2} = 1 - \frac{(N_0 + N')e^2}{\epsilon_0 m \omega_e^2} \quad (12)$$

When $n[z_R(t)] = 0$, it yields

$$n^2[z_R(t)] = 1 - \frac{\alpha}{\omega_e^2} [az_R(t) + b] - \frac{\alpha}{\omega_e^2} N'[z_R(t)] = 0 \quad (13)$$

Where ω_e is the wave frequency, $\alpha = e^2/\epsilon_0 m$.

Substituting (10) into (13), we obtain

$$z_R(t) = z_0 \left(1 + \frac{1}{D}\right) \quad (14)$$

$$D = \frac{G}{\sqrt{\rho_{00}}} \frac{\omega_b}{8\pi} \cdot \frac{\cos\theta_2 \cos\theta_3}{4H^2} e^{z/2H} \frac{1}{\omega_c} \cdot \int_{\omega_c t_0}^{\omega_c t} g(x) dx \quad (15)$$

Finally, we obtain the normalized Doppler frequency shift:

$$\widetilde{\Delta f(t)} = \frac{g(t)}{\sqrt{Q(t)}} \quad (16)$$

Figure 2 shows the plot of $g(t)/\sqrt{Q(t)}$ as a function of t . It agrees with the measured Doppler frequency shift variation shown in Figure 1.

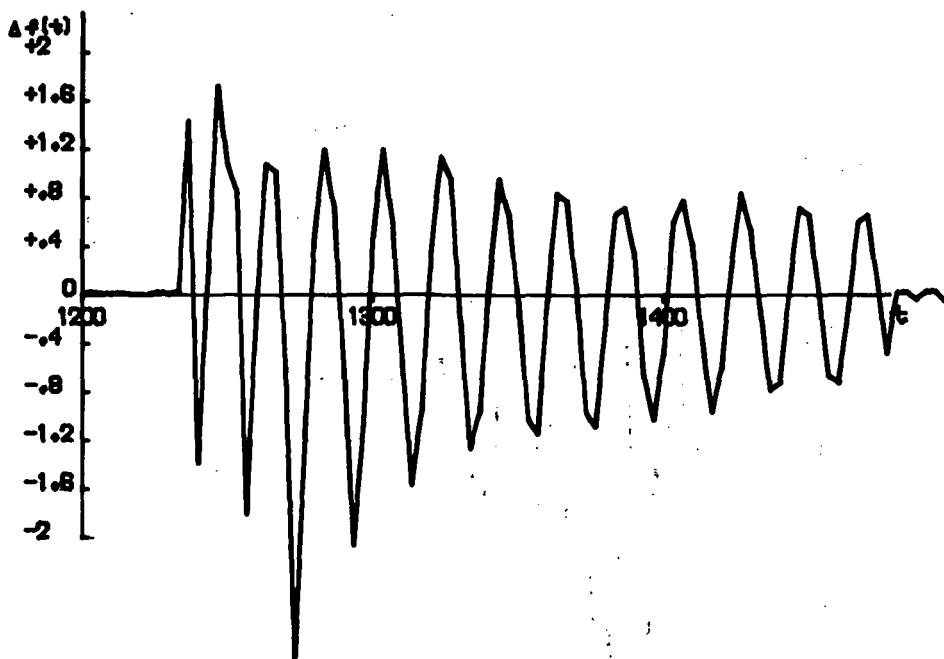


Figure 2. The normalized Doppler frequency shift curve.

In the far field approximation, just $J_0(\omega_c \sqrt{t^2 - t_0^2})$ is important. When considering the near field problem, we cannot neglect the effect of $J_1(\omega_c \sqrt{t^2 - t_0^2})$ and it is important just as $t - t_0$ is not very large. For large time t , the contribution of $J_1(\omega_c \sqrt{t^2 - t_0^2})$ becomes negligibly small and the dominant effect is of $J_0(\omega_c \sqrt{t^2 - t_0^2})$, this becomes the far field response. LIANG

(1936) began the experiment on ionospheric effects during a solar eclipse. Since 1980, we have conducted three solar eclipse observations to study if gravity waves are generated by the moon shadow. In two of them, on Feb. 16, 1980, and June 11, 1983, the totality zone occurred in low latitudes over the ocean, and another one on July 31, 1981, in high latitudes over the land.

Figures 3 and 4 are HF Doppler frequency shift curves on Feb. 16, 1980, and June 11, 1983. These curves could reflect the atmospheric response to the processes of the solar eclipse. From these curves we can see that there are two kinds of perturbations, one of them is of a short period, another one a longer period. The short period one occurred during the interval between the first and second contacts of totality. Some reports consider these perturbations to be the gravity wave induced by the atmospheric cooling, but after comparing these results with other observations of the solar eclipse we conclude that the short period perturbations are generated by the local solar active regions (ROW 1967, YEH 1974).

In these totality experiments, the Chinese scientists performed many kinds of observations, including the optic, solar radio emission, geomagnetic, and ionospheric vertical sounding experiments. Therefore, we can compare the HF Doppler result with other results. Figure 5 is the solar obscuration picture on Feb. 16, 1980. We see that there were three important active regions on the

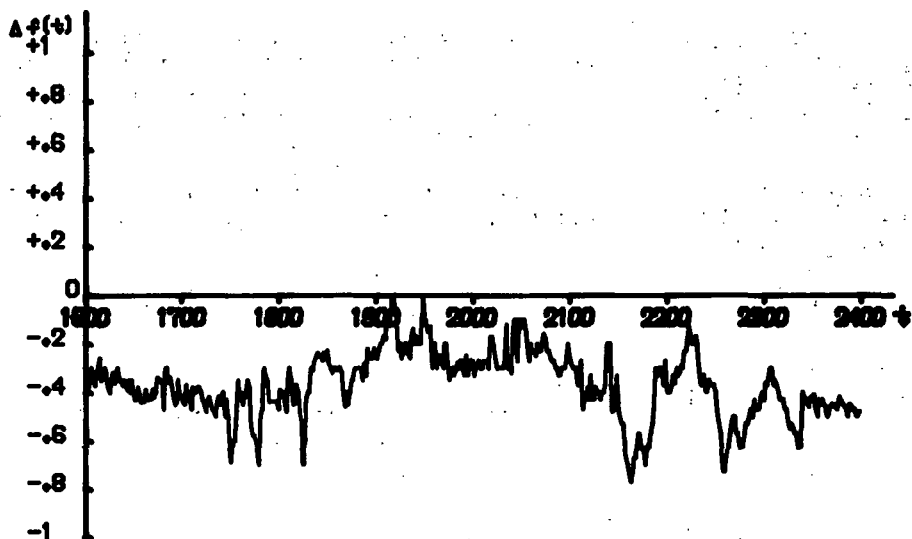


Figure 3. HF Doppler record on Feb. 16, 1980.

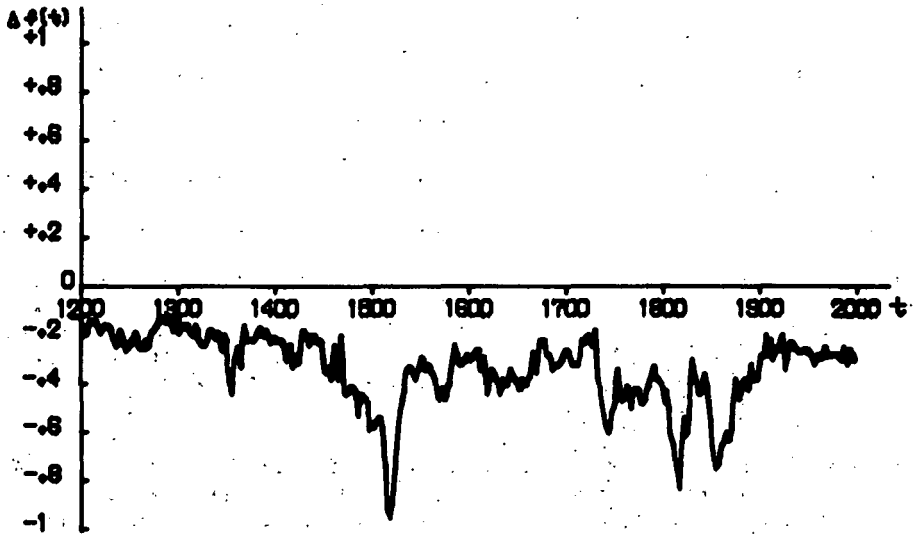


Figure 4. HF Doppler record on June 11, 1983.

solar disc: numbers 70, 77, and 80. When the solar active region was covered, the ionospheric ionization density decreased, so electron density and consequently Doppler frequency shift perturbations occurred at the same time. We compared HF Doppler results with the optic observation, solar radio emission flux, field strength record, and the fading frequency of the received signal etc. We discovered that their perturbations correspond fairly well to the local solar active region obscurations. In past analysis of the solar eclipse data this point was neglected.

On June 11, 1983, there was also a strong active region; it corresponded to the short period perturbation at that day.

The longer period perturbation occurred after the fourth contact. By computation, it shows that they could be produced by the atmospheric cooling when the moon shadow sweeps through the lower middle atmosphere. Yen, Liu and Kato have developed the theory of the moving point source response in the atmosphere.

Consider an impulsive point source moving in a horizontal direction with a supersonic speed U ; the expression of the response in the atmosphere is written as follows:

$$\begin{aligned}
 G(R, t) \sim & \frac{1}{4\pi^2 R} \sqrt{\frac{2\pi}{R|\xi_1''(\omega_{s1})|}} \left| g(\omega_{s1}) \right| \cos[\xi_1(\omega_{s1})R - \omega_{s1}t - \frac{\pi}{4}] \\
 & + \frac{1}{4\pi^2 R} \sqrt{\frac{2\pi}{R|\xi_1''(\omega_{s2})|}} \left| g(\omega_{s2}) \right| \cos[\xi_1(\omega_{s2})R - \omega_{s2}t + \frac{\pi}{2}] \\
 & + \frac{1}{4\pi^2 R} \sqrt{\frac{2\pi}{R|\xi_1''(\omega_{s3})|}} \left| g(\omega_{s3}) \right| \cos[\xi_1(\omega_{s3})R - \omega_{s3}t]
 \end{aligned} \tag{17}$$

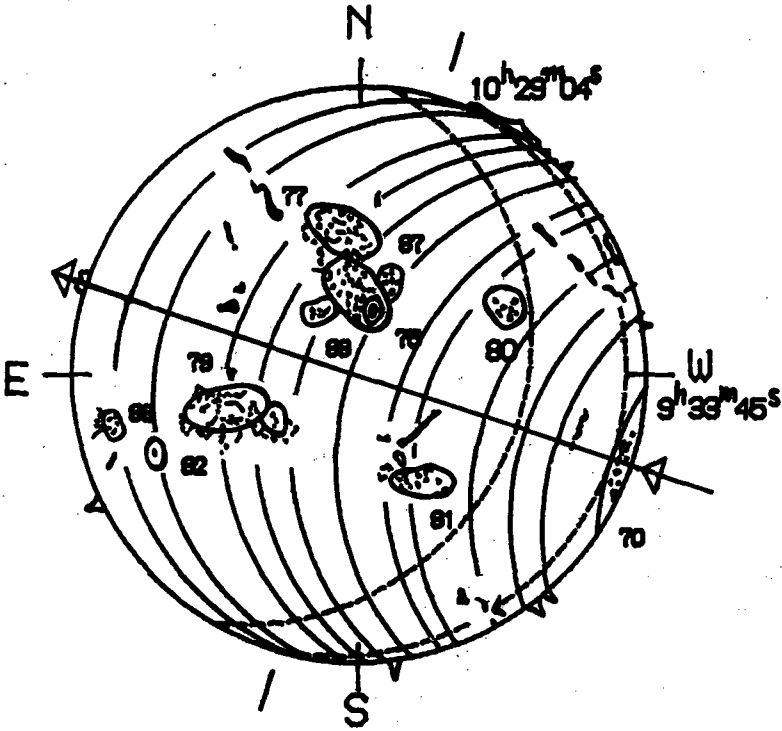


Figure 5. The solar obscuration picture on Feb. 16, 1980.

$$\xi_1(\omega) = \frac{\sqrt{\alpha^2 - 1}}{\alpha C_0} \sqrt{\frac{(\omega^2 - \omega_1^2)(\omega^2 - \omega_c^2)}{\omega^2 - \omega_b^2}} \quad (18)$$

$$g(\omega) = \sqrt{\frac{\omega^2 - \omega_b^2}{\omega^2 - \omega_c^2}}, \quad \alpha = U/C_0$$

It consists of three parts: acoustic model, buoyancy model, and gravity model.

First, we discuss the results on June 11, 1983. From the solar eclipse data we know that the moon shadow velocity is 640 m/s, and the speed of sound is taken as 300 m/s. The reflection height of the radio wave is 230 km. The working frequency of the radio wave is 12 MHz. Under such circumstance we seek three saddle point values.

$$\chi_{s1} = \omega_{s1}/\omega_b = 1.2333$$

$$\chi_{s2} = \omega_{s2}/\omega_b = 0.78$$

$$\chi_{s3} = \omega_{s3}/\omega_b = 0.2145$$

Using the $G(R,t)$, we can calculate the reflection height variation of a radio wave with time. Finally, we obtain the simulated curve of normalized HF Doppler frequency shift.

In Figure 6 the solid line is the simulated curve, the dashed line the experimental curve. We can see they are consistent with each other.

Using the same method, the simulated curve of the solar eclipse on Feb. 16, 1980, has been obtained. We take the following parameters: the velocity of the moon shadow is 870 m/s, the reflection height of the radio wave is 140 km, the working frequency of the radio wave is 5.27 MHz, the speed of sound is 300 m/s. Figure 7 is the curve of normalized Doppler frequency shift.

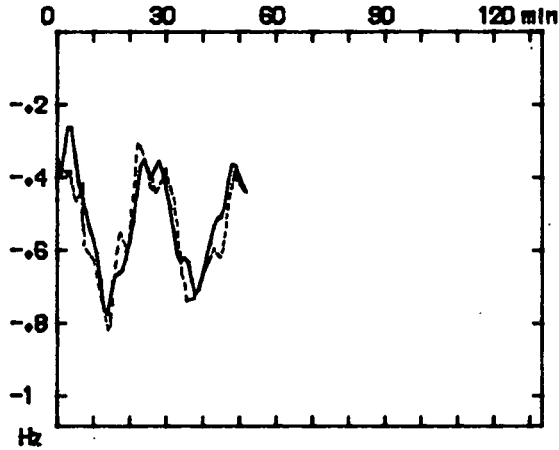


Figure 6. A comparison of the theoretical curve with experimental one.

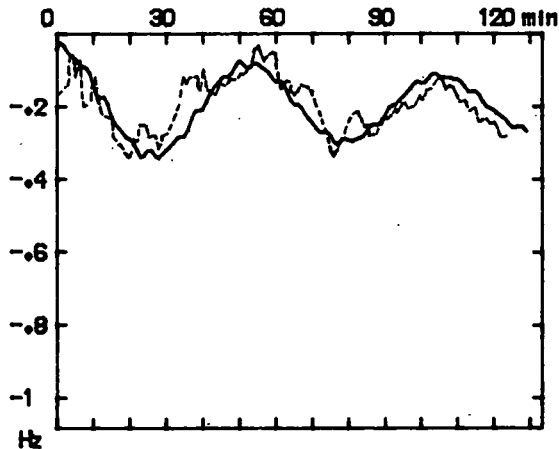


Figure 7. A comparison of the theoretical curve with experimental one.

Because of the geomagnetic disturbance on July 31, 1981, we have not analyzed this record.

From the above results, we preliminarily consider that the solar eclipse occurred in the lower latitude and over the ocean could excite the acoustic gravity wave. Using the HF Doppler technique, it is easy to observe. By virtue of the moving point source theory, the calculated results are seen to be consistent with the experiments. It is important to consider the solar active region effect on the lower ionospheric layer in the analysis record.

REFERENCES

- Kato, S. (1980), Dynamics of the Upper Atmosphere, Center for Academic Publications Japan.
- Liang, P. H. (1936), Chinese J. Physics, 2, 169.
- Row, R. V. (1967), J. Geophys. Res., 72, 1599.
- Yeh, K. C. and C. H. Liu (1974), Rev. Geophys. and Space Phys., 12, 193.
- Zhang, X. J. and N. L. Xiong (1981), Acta Geophys. Sinica, 24, 263.
- Zhang, X. J. and N. L. Xiong (1985), J. Atmos. Terr. Phys., (in press).

3.18 A NUMERICAL STUDY OF NONLINEAR INTERACTIONS BETWEEN MEAN FLOW AND BREAKING INTERNAL GRAVITY WAVES

Hideji Kida

Meteorological Research Institute
Yatabe, Tsukuba,
Ibaraki 305, Japan

INTRODUCTION

During these several years, internal gravity waves have been one of the important phenomena in understanding the general circulation as well as eddy motions in the atmosphere, particularly in the mesosphere and lower thermosphere (HOUGHTON, 1978; LINDZEN, 1981; MATSUNO, 1982; HOLTON, 1982, 1983; MIYAHARA, 1984). Therefore, in order to reproduce the middle atmospheric general circulation, it is necessary to incorporate vertically propagating internal gravity waves into GCMs.

So far, the important role of internal gravity waves in the middle atmosphere has been demonstrated mainly by 2-dimensional models with parameterizations of wave, mean-flow interactions, e.g., LINDZEN (1981) or MATSUNO (1982).

In this paper, some results from numerical simulations (KIDA, 1983) on nonlinear interactions between mean flow and internal gravity waves will be briefly presented. We need such numerical investigations indeed, because in the near future we'll face the subject to simulate the general circulation of the entire atmosphere by use of any fine mesh GCM explicitly including mesoscale internal gravity waves. In fact, such a fine mesh SKYHI model is running in GFDL.

TWO-DIMENSIONAL SIMULATIONS

Before we discuss the results from a 3-dimensional simulation, we'll examine those from 2-dimensional simulations. The primitive equation is used for the model. The Coriolis force is neglected. Namely,

$$\frac{\partial u}{\partial t} + \frac{\partial u^2}{\partial x} + \frac{\partial u\omega}{\partial p} = -\frac{\partial \phi}{\partial x} + F + Dm$$

$$\frac{\partial T}{\partial t} + \frac{\partial uT}{\partial x} + \frac{\partial \omega T}{\partial p} - \frac{RT}{Gp}\omega = Q + Dm$$

$$\frac{\partial u}{\partial x} + \frac{\partial \omega}{\partial p} = 0$$

$$\frac{\partial \phi}{\partial \ln p} = -RT$$

where x , p , and t are independent variables of eastward and upward directions and time, respectively, and u , ω , T and ϕ are eastward velocity, vertical p -velocity, temperature and geopotential height, respectively. R is gas constant. F is an assumed restoring force; $F = -k_L(u - \bar{u}_0)$ where k_L is a coefficient (i.e., reciprocal of time constant), \bar{u}_0 is a horizontal velocity prescribed as a function of height (Figure 1). Q is thermal dissipation given in a form of Newtonian cooling; that is, $Q = -k_L(T - \bar{T}_0)$ where \bar{T}_0 is a prescribed function of height (Figure 1). k_L is given as in Figure 2. Dm is dissipation due to molecular diffusion, this being taken into account above the level of 115 km. Note that the coefficients of molecular diffusion were artificially assumed to be larger than the real ones to avoid false re-

Vertical profiles of \bar{T}_0 & \bar{U}_0 (2-D)

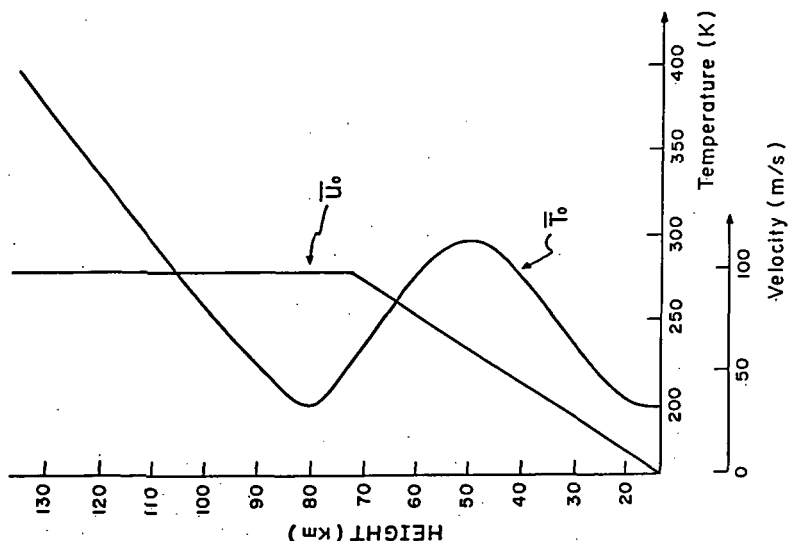


Figure 1. Vertical profiles of reference velocity and temperature.

Vertical profiles of T_L , T_{rad} & T_{mol} (2-D)

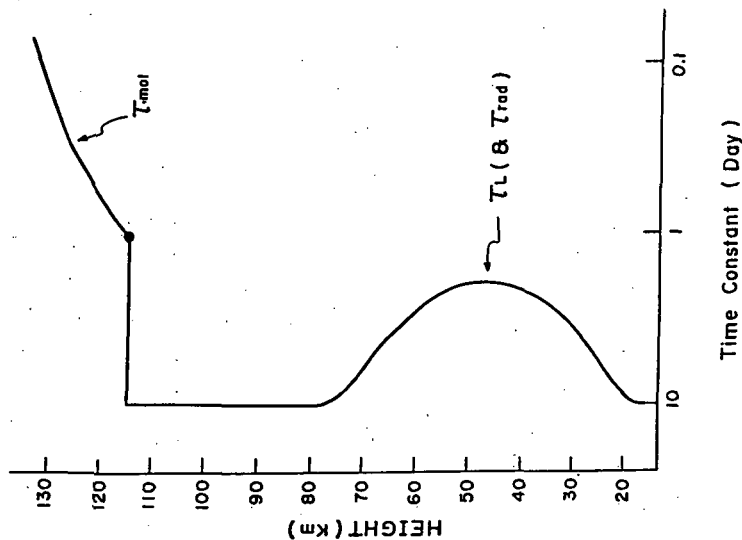


Figure 2. Vertical profiles of coefficients used for molecular dissipation (only over 115 km) and radiative dissipation.

flection at the upper boundary, and that mechanical dissipation around 80 km to 115 km was not specified because the present numerical model was expected to explicitly represent small-scale eddy motions at those levels.

The model domain covers 500 km in horizontal and from 15 km to 135 km in height. Cyclic conditions were imposed at the lateral boundaries.

The initial vertical profiles of horizontal motion and temperature are the same as those described in Figure 1; the velocity is zero at the lowest boundary, increases with increasing height up to 70 km and becomes constant (100 m/s) over the level of 70 km. The temperature profile is near that of U.S. STANDARD ATMOSPHERE (1976).

As a simple experiment, a standing oscillation of velocity divergence was forced at the lowest level of the model as done by PLUMB and MCEWAN (1978) in their laboratory experiment. This excitation produces westward and eastward propagating gravity waves with the same amplitude and period. The period and horizontal wavelength are tentatively taken to be 4 hours and 500 km, respectively.

Figure 3 shows an instantaneous horizontal-height profile of isentropic surfaces at 15 hours after the initial state. The edge of excited internal gravity waves arrived at higher levels and began to break down as if in the surf zone on shore. The phase of the waves moved downward, meaning that they are propagating westward. This also implies that wave selection occurs in the shear layer. We can see remarkable unstable layers with small-scale convective motions and, reversely, highly stable layers.

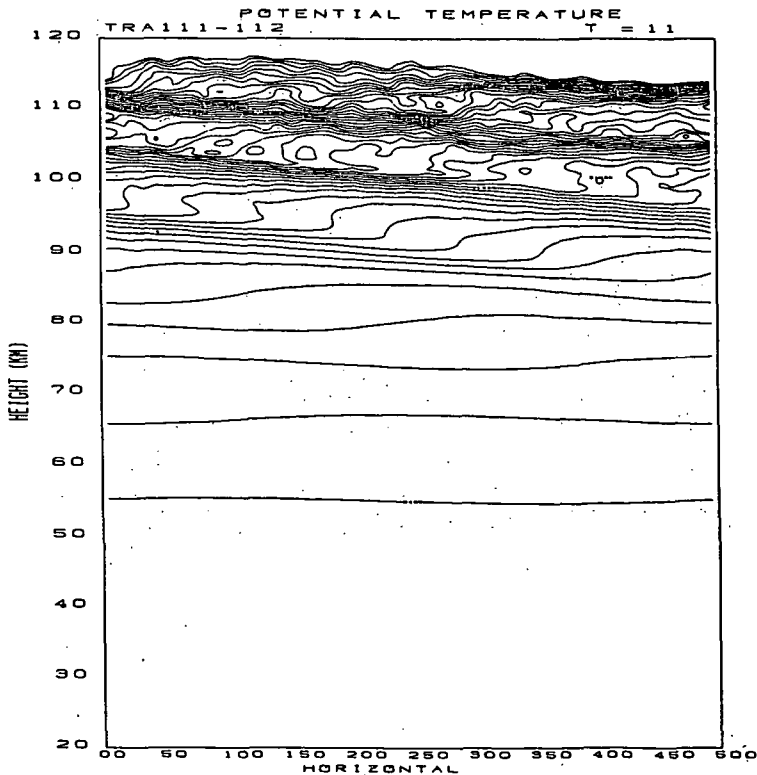


Figure 3. An instantaneous horizontal-height section of upward propagating internal gravity waves with horizontal wavelength of 500 km. Solid lines show isentropic surfaces.

As a result of wave, mean-flow interactions, the vertical profile of mean flow was gradually and systematically changed. Around the mesopause the mean flow is greatly reduced from 100 m/s to nearly zero in this case.

In the real atmosphere, however, origins of internal gravity waves are not always easily identified. Generally speaking, it is impossible to predict the generation of the waves. In this regard, the above experiment was too simple to be compared with those in the real atmosphere. Therefore we have to deal with more realistic situations, at least, more than the previous one. To do so, randomly generated internal gravity waves should be introduced into the model. In the second experiment, such a situation was investigated by randomly excited internal gravity waves with various wavelength and period at the lower boundary of the model. Of course, their amplitudes must be specified within a proper range of magnitude.

Figure 4 shows an instantaneous horizontal-height distribution of eddy velocity (u') at 140 hours after the initial state when the mean flow around the mesopause is almost in an equilibrium state. It must be noted that small-scale motions take place particularly over 70 km, although irregular motions are excited throughout the entire domain.

In spite of such complex and apparent nonsystematic eddies, it is surprising to see that the mean flow was very smoothly changed, as shown in Figure 5. The main characteristics of the time evolution of the mean flow is almost the same as that in the first experiment of simple wave forcing. Figure 5 shows also a systematic 2-3 days oscillation of the mean flow over the level of 90 km. This is mainly due to the assumed restoring force, F , which is somewhat artificially introduced to take into account a possible effect of the Coriolis force to the mean flow, and in part probably due to a wave, mean-flow interaction mechanism of QBO (PLUMB, 1977).

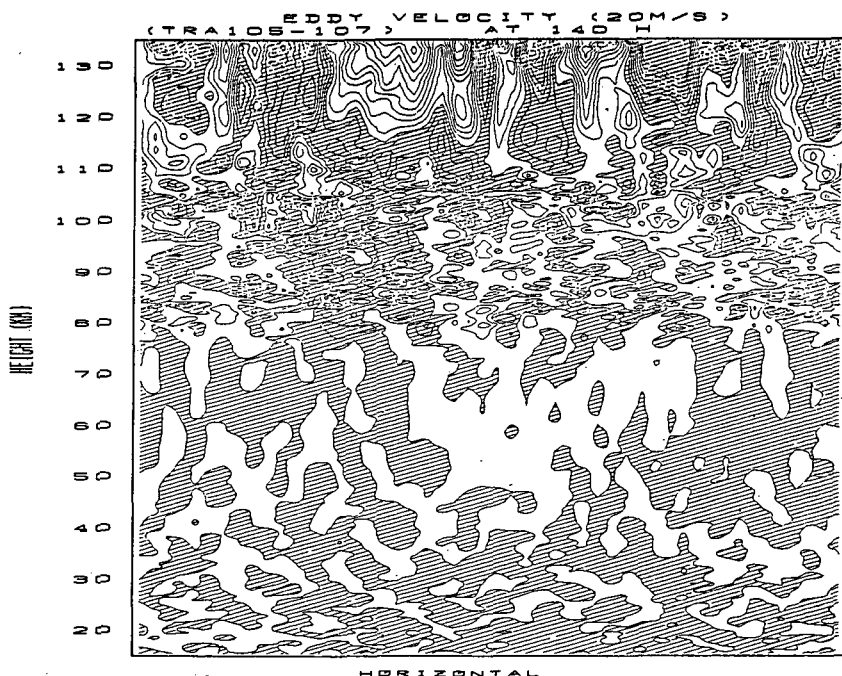


Figure 4. An instantaneous horizontal-height section of eddy component of horizontal velocity. Contour interval is 20 m/s. Shaded areas denote negative deviation from horizontal mean.

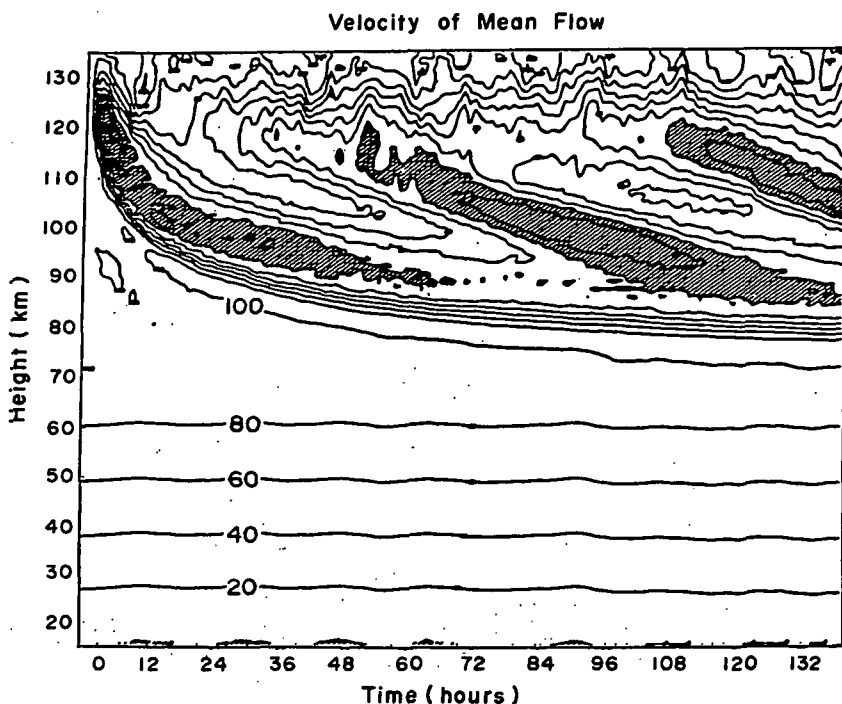


Figure 5. Time evolution of horizontal mean flow from the initial to the end of the sixth day. Contour interval is 20 m/s. Shaded areas denote negative velocity.

A THREE-DIMENSIONAL SIMULATION OF THE MIDDLE ATMOSPHERE

The above 2-D experiments suggested the possibility of reproducing the general circulation of the mesosphere and lower thermosphere. Then, we will proceed to discussions on a simulation of the middle atmosphere with a 3-D model capable of explicitly representing internal gravity waves (KIDA, 1985). The 3-D model used is a usual GCM described by primitive equations in pressure coordinate. Molecular diffusion and ion drag are incorporated, while subgrid-scale eddy diffusion is not taken into account in the model because of representation of small-scale eddies.

External radiative heating by ozone is assumed as that of LEOVY (1964) at solstice conditions. The maxima of heating and cooling are 12 degrees per day at 50 km over the poles. But it should be remembered that the diabatic heating term includes a Newtonian cooling operating to calculated temperature deviation from global horizontal mean. Note that the ozone external heating is assumed to be zero over the mesopause.

The model domain is not perfectly global but zonally limited to ten degrees sector. Cyclic conditions are employed at east and west lateral boundaries. The grid sizes of the model are 1° longitude \times 5° latitude to the horizontal direction and about 1.6 km to the vertical direction.

At the initial state, the model atmosphere was motionless, and its temperature was a function of height as shown in Figure 1. Time integrations were performed for about a month. Zonal means of motions and temperature reached

almost the quasi-equilibrium states at three weeks after the initial state. During the time integrations, grid-scale random noises were imposed at the lower boundary of the model (i.e., around the tropopause level) to excite various modes of internal gravity waves.

Figure 6 describes time- and zonal-mean zonal velocity. Easterlies are shaded. We can see easterlies in the summer hemisphere and westerlies in the winter hemisphere. In particular, the so-called reverse winds are well reproduced in this experiment: easterlies over westerlies and vice versa.

Compared with the CIRA model, the calculated summer easterly jet is too strong by a factor of about 2. This discrepancy can be considered to be due to the oversimplified heating.

Figure 7 describes the meridional velocity. The shaded area shows motions toward the summer pole. It must be noted that systematic meridional flow is formed from the summer pole to the winter pole in levels 80 km to 100 km. The magnitude of the velocity is 10 to 15 m/s in the time mean. HOLTON's (1983) and MIYAHARA's (1984) models have also predicted such strong meridional motions. In addition to these theoretical studies, those motions were reported as an observational evidence by MANSON et al. in this Kyoto MAP Symposium.

Figure 8 describes time- and zonal-mean temperature. The cold and warm cores at the mesopause level are clearly seen in the summer and winter poles, respectively. The simulated cold core is relatively close to the observation, but the winter warm core is about 30 degrees overestimated. This is because the calculation of diabatic heating and cooling is too simplified.

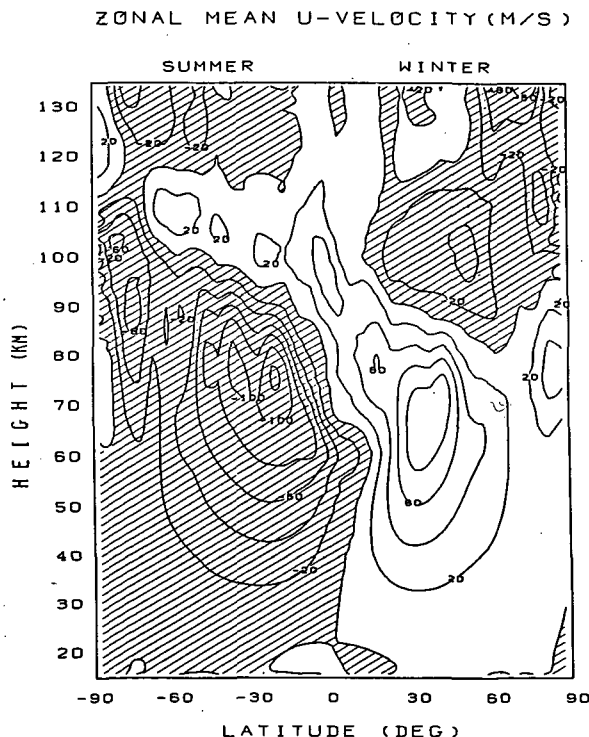


Figure 6. Latitude-height section of time and zonal mean zonal motion. Contour interval is 20 m/s. Negative velocity is shaded.

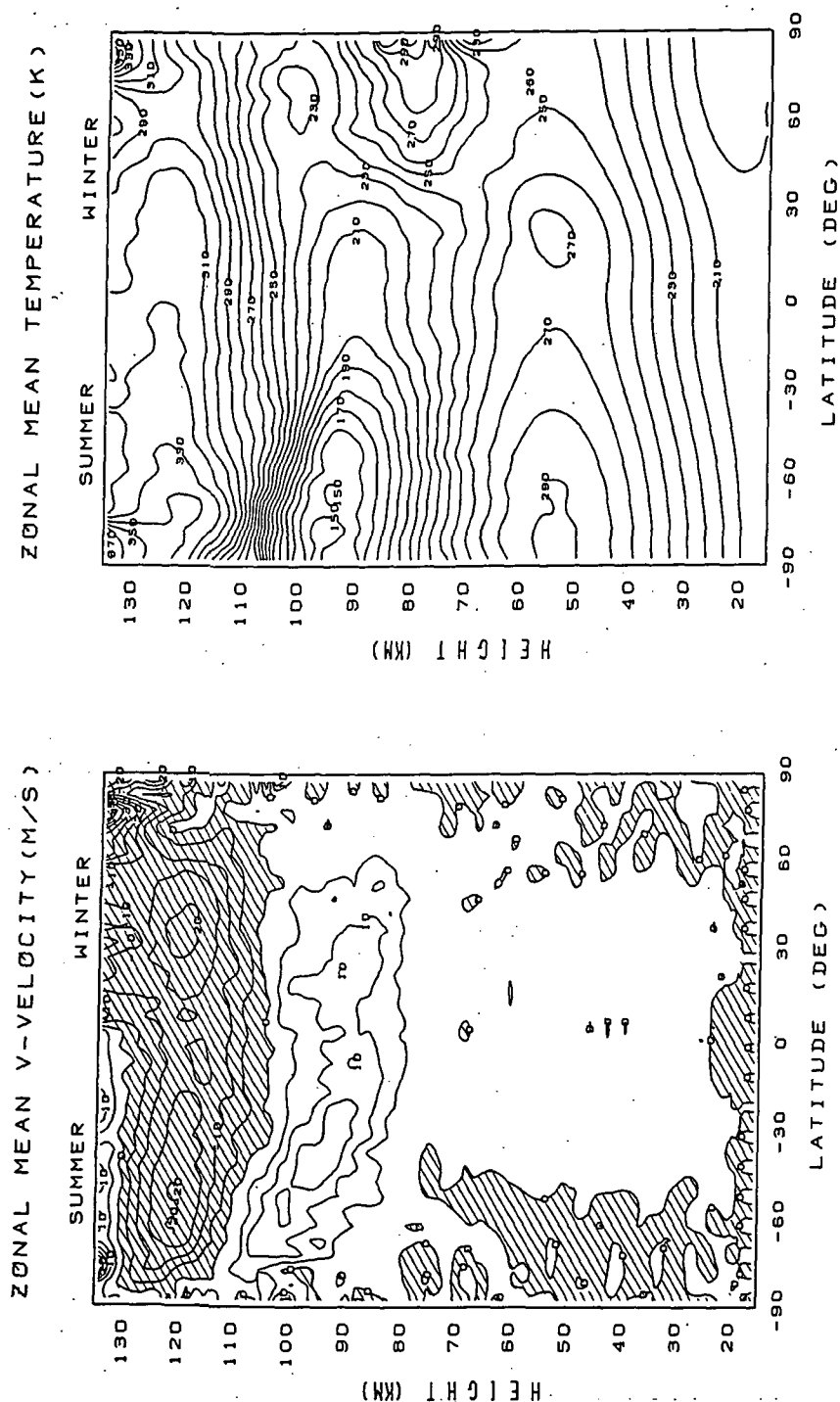


Figure 7. Latitude-height section of time and zonal mean meridional motion. Contour interval is 5 m/s. Negative velocity is shaded.

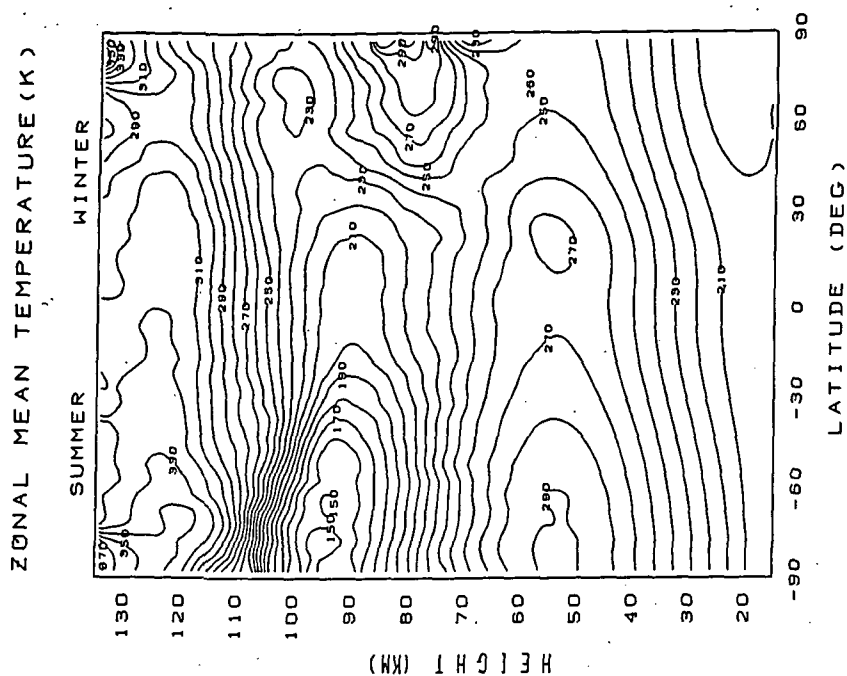


Figure 8. Latitude-height section of time and zonal mean Kelvin temperature. Contour interval is 10 degrees.

In the stratosphere and lower mesosphere, temperature is almost in radiative equilibrium: a balance between the external heating and Newtonian cooling. On the other hand, as the external heating rate is assumed as very small or zero over 70 km, the effect of adiabatic vertical motions to temperature change balances the Newtonian cooling. Note that the latter works as not cooling but heating where the temperature is lower than the global mean. Therefore, we can say that the configuration of temperature around the mesopause is maintained by meridional circulation dynamically forced by internal gravity waves.

These results are not always new but are essentially like those of previous works, e.g., LEOVY (1964), HOLTON (1982, 1983), MATSUNO (1982) and MIYAHARA (1984). A feature of the present simulation is that basic equations of the model includes no parameterization in a dynamical aspect.

REFERENCES

- Holton, J. R. (1982), J. Atmos. Sci., **39**, 791-799.
 Holton, J. R. (1983), J. Atmos. Sci., **40**, 2497-2507.
 Houghton, J. T. (1978), J. Roy. Meteorol. Soc., **104**, 1-4.
 Kida, H. (1983), Presented at Spring and Fall meetings of Meteorol. Soc. Japan, and the Fourth Japanese MAP Symposium (Proc. 135-136).
 Kida, H. (1985), To be published in PAGEOPH, Vol. 122, No.5.
 Leovy, C. B. (1964), J. Atmos. Sci., **25**, 327-341.
 Lindzen, R. S. (1981), J. Geophys. Res., **86**, 9707-9714.
 Matsuno, T. (1982), J. Meteorol. Soc. Japan, **60**, 215-226.
 Miyahara, S. (1984), Dynamics of the Middle Atmosphere, (edited by, Holton and Matsuno), Terra Sci. Pub. Company, Tokyo, Japan, 271-287.

3.19 EFFECTS OF BREAKING GRAVITY WAVES ON THE CHEMICAL COMPOSITION OF THE MESOSPHERE AND LOWER THERMOSPHERE

S. Solomon

Aeronomy Laboratory
National Oceanic and Atmospheric Administration
Boulder, CO

R. Garcia

National Center for Atmospheric Research
Boulder, CO

Recent theoretical studies indicate that the eddy diffusion and momentum forcing in the mesosphere and lower thermosphere arise principally from the effects of breaking gravity waves. The propagation and dissipation of gravity waves depend strongly on season and latitude because of its relationship to the background zonal wind. These processes have significant effects on the transport of chemical species in that region, so that observations of variations in chemical constituents provide useful tracers for dynamical theory.

A parameterization of gravity wave propagation and dissipation has been incorporated in our coupled dynamical-chemical model in order to study these effects. Several easily observable airglow features of the mesosphere-thermosphere region will be shown to provide sensitive indications of gravity wave influences. In particular, theoretical predictions of large seasonal and latitudinal variations in the atomic oxygen green line (near 100 km), the Meinel bands of excited OH (near 90 km), and the O_3 densities inferred from $O_2(^1\Delta_g)$ emission at altitudes from 75-90 km are shown to be in remarkably good agreement with observations. For example, the observed latitude gradients in greenline emission, and the occurrence of a sharp spring maximum, are extremely well reproduced by the present model when the dissipation and propagation of gravity waves are considered. Implications of these sensitive chemical tracers for the dynamics of the mesosphere-lower thermosphere region and its relationship to gravity waves will be discussed.

3.20 LOCAL EFFECTS OF GRAVITY WAVE PROPAGATION AND SATURATION

David C. Fritts

Geophysical Institute

and

Department of Space Physics and Atmospheric Sciences
University of Alaska
Fairbanks, Alaska 99701

INTRODUCTION

In recent years, gravity waves have been recognized to play a major role in the dynamics of the middle atmosphere. Perhaps the major effects of such motions are the reversal of the vertical shear of the mean zonal wind and the occurrence of a large turbulent diffusivity in the mesosphere due to gravity wave saturation. Yet, despite the importance of these gravity wave effects, the processes and the consequences of gravity wave propagation and saturation are only beginning to be understood in detail. The linear saturation theory first introduced by HODGES (1967) and further developed by LINDZEN (1981), for example, predicts drag and turbulent diffusion due to saturating wave motions. This theory, however, fails to address a number of issues that are certain to be important for gravity wave propagation and saturation in the middle atmosphere. These issues, including wave transience, wave superposition, local convective adjustment, and nonlinearity, will be discussed briefly below.

MECHANISMS CONTRIBUTING TO SATURATION

Three distinct mechanisms have been suggested by various researchers to account for gravity wave saturation. These include the convective instability of high-frequency (essentially 2-D) gravity waves (HODGES, 1967; LINDZEN, 1981), the dynamical instability of inertio-gravity waves (BALSLEY et al., 1983), and nonlinear wave-wave interactions (WEINSTOCK, 1976, 1982). There is, I believe, good evidence of the first two in atmospheric and laboratory data (see FRITTS, 1984). Convectively and dynamically unstable layers evolve almost simultaneously for high-frequency motions, permitting convective instabilities to dominate in most cases. But because low-frequency motions have enhanced velocity shears and reduced vertical displacements, these motions favor dynamical instabilities. Nonlinear interactions no doubt contribute to wave amplitude reductions, but they appear unable to prevent the occurrence of convective or dynamical instabilities.

WAVE TRANSIENCE

The effects of wave transience were not addressed in the linear saturation theory advanced by LINDZEN (1981). Yet transience is expected to have a number of important effects for saturating gravity waves in the middle atmosphere. These effects include a modulation of the intensity of saturation and turbulent diffusion, temporally and spatially varying accelerations of the mean flow, and a corresponding potential for the acceleration of the horizontal phase speed of the wave motion itself. Evidence of the first and last of these effects can be seen in Figure 1. Shown are the horizontal velocity perturbations for a gravity wave propagating upward toward an initial critical level at $z/z_0 = 0.6$ ($z_0 = 100$ km) at 4.5, 5.0, and 5.5 wave periods after the forcing began at the lower boundary. Regions of convective instability in the potential temperature field are denoted by vertical bars at the right side of each panel. Two points

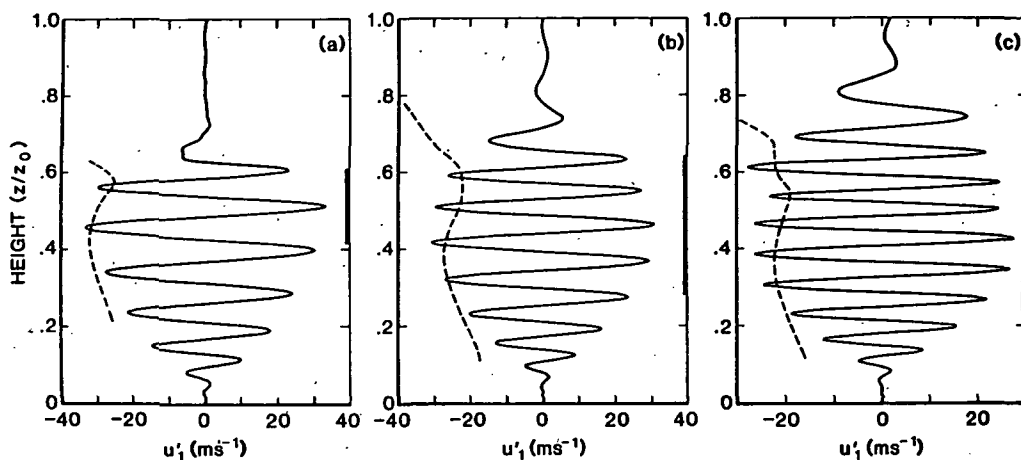


Figure 1. Horizontal perturbation velocity for monochromatic incident wave subject to convective adjustment at 4.5, 5.0, and 5.5 wave periods.

are of interest. First, transience permits the wave motion to saturate initially in the region near the critical level, then in a region of increasing depth both above and below this position. Unlike the linear saturation theory, this results in a gradual time-averaged transition to saturation. Second, we note that because the mean flow accelerations due to transience are large, there is a large "self-acceleration" of the wave phase speed. This is due to the residence of the wave motion in that region undergoing a mean flow acceleration and permits the wave motion to propagate well beyond the initial critical level. The reader is referred to FRITTS and DUNKERTON (1984) for additional details and discussion.

CONVECTIVE ADJUSTMENT

Large-amplitude, high-frequency gravity waves appear to saturate via the turbulent breakdown of convectively unstable layers. This process is represented in our numerical model by a convective adjustment scheme which acts to restore unstable portions of the wave field to neutral stability. As such, convective adjustment provides a local dissipation of incident waves and a local source of other motions.

The principal effect of convective adjustment is the limit it places on saturating wave amplitudes. As seen in Figure 1, a monochromatic wave motion (which is subject to convective adjustment) is seen to have a maximum amplitude given approximately by the intrinsic phase speed of the motion, $u' \sim 1.2 (c - \bar{u})$. The limiting amplitude is slightly larger than that predicted by linear saturation theory, $u' \sim c - \bar{u}$, due to gradual adjustment process. In the absence of convective adjustment, the incident wave is found to attain an amplitude approximately twice as large. It should also be noted that convective adjustment does not appear to seriously disrupt the incident wave structure nor prevent its continued vertical propagation.

The amplitude reduction due to convective adjustment is seen more clearly by comparing the saturated and unsaturated momentum fluxes shown in Figure 2. The initial effect of convective adjustment is a reduction of the wave amplitude (and momentum flux) only in the region of adjustment. At later times, however, a reduction is also observed at upper levels due to the continued vertical propagation of a wave now reduced in amplitude.

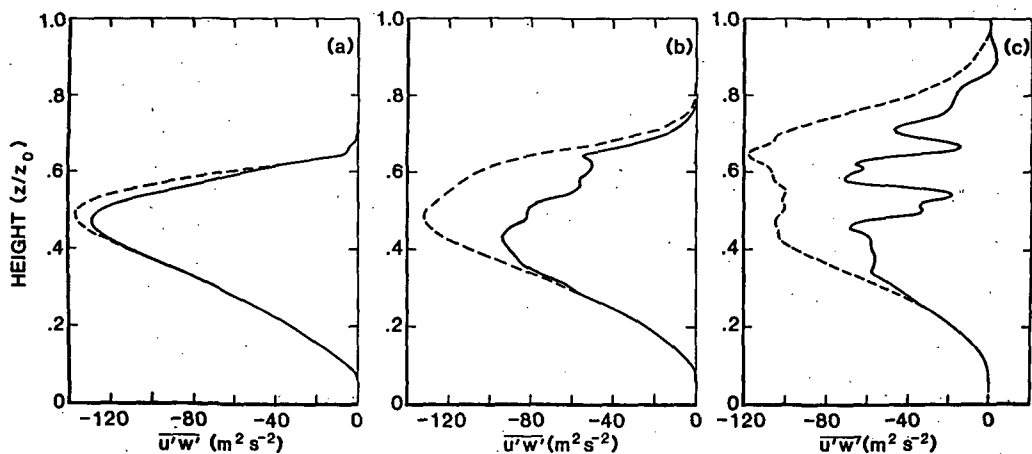


Figure 2. Momentum flux for saturated (—) and unsaturated (---) wave shown in Figure 1.

When several wave motions are contributing to the saturation process, individual wave amplitudes are found to be much smaller. A simulation performed with three incident waves resulted in saturated amplitudes of $u' \sim .2 - .8 (c - \bar{u})$ at levels at which convective instability was observed. The horizontal perturbation velocities and the corresponding intrinsic phase speeds, $\bar{u} - c$, are shown for two of the incident motions in Figure 3. Thus, the saturation of a spectrum of wave motions results in individual wave amplitudes in better agreement with atmospheric observations. Additional discussion of these results can be found in DUNKERTON and FRITTS (1984), FRITTS and DUNKERTON (1984), and FRITTS (1985).

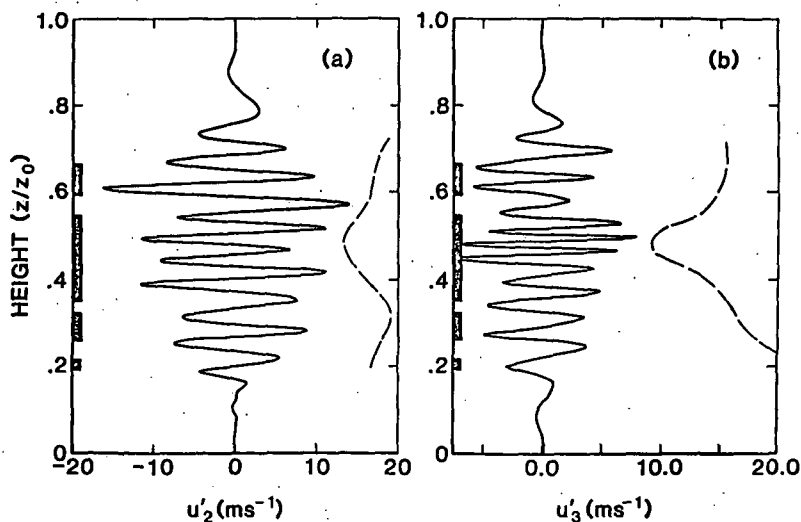


Figure 3. As in Figure 1, but for two of three incident wave motions subject to convective adjustment at 4.5 wave periods.

NONLINEARITY

Several simulations were also performed to examine the effects of nonlinear wave-wave interactions on the propagation and saturation of an incident wave or waves. These showed that nonlinearity, which contributing somewhat to the reduction of incident wave amplitudes, is unable to prevent the occurrence of convectively unstable layers. This suggests that the primary cause of gravity wave saturation in the middle atmosphere is instability within the wave field. However, nonlinearity is seen to be effective at exciting other wave motions, as described in the following section.

EXCITATION OF HARMONICS

Two processes, local convective adjustment and nonlinearity, have been found to result in the efficient excitation of harmonics of large-amplitude gravity wave motions. Those due to convective adjustment are caused by the local modification of the total potential temperature and vorticity fields; those due to nonlinearity result from the lack of quadrature in the nonlinear advective terms in the equations of motion. For the cases considered to date, both processes result in comparable wave motions, which typically have horizontal and vertical wave numbers equal to some multiple of those of the incident wave and a direction of propagation consistent with the incident motion. The motions excited in the second harmonic for a single incident wave due to nonlinearity, convective adjustment, and both processes operating together are shown at two times during the evolution in Figure 4. Note that nonlinear excitation occurs throughout the domain while that due to convective adjustment is confined to unstable regions (shown by vertical bars).

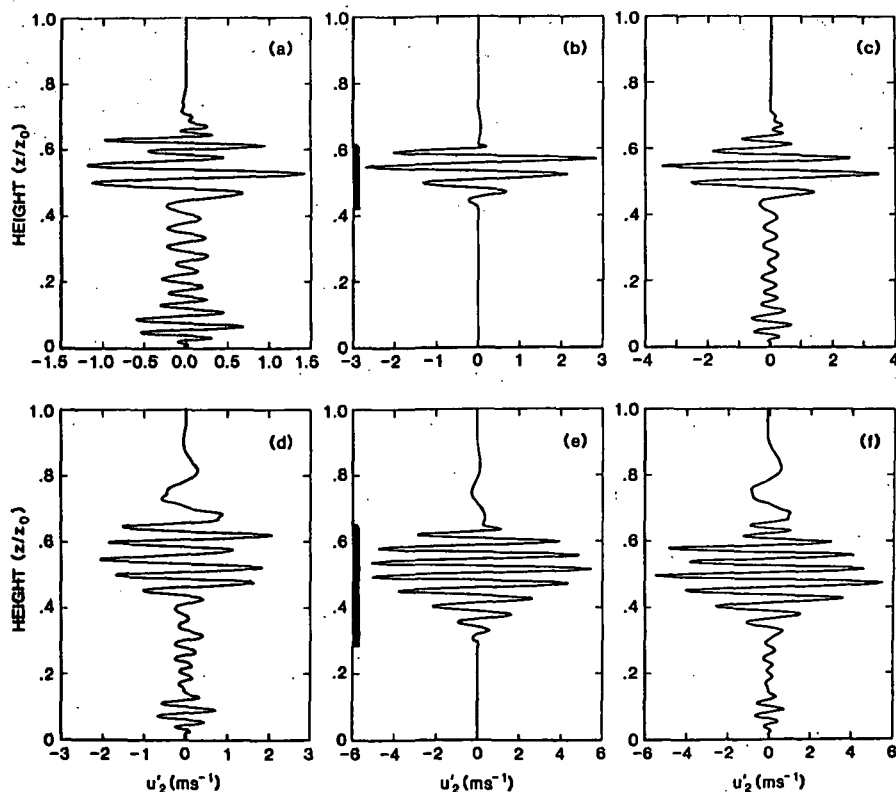


Figure 4. Second harmonic due to nonlinearity (a and d), convective adjustment (b and e), and both processes (c and f) at 4.5 and 5.0 wave periods.

REFERENCE

- Balsley, B. B., W. L. Ecklund and D. C. Fritts (1983), VHF echoes from the high-latitude mesosphere and lower thermosphere: Observations and interpretations, J. Atmos. Sci., **40**, 2451-2466.
- Dunkerton, T. J. and D. C. Fritts (1984), Transient gravity wave-critical layer, Part I: Convective adjustment and the mean zonal acceleration, J. Atmos. Sci., **41**, 992-1007.
- Fritts, D. C. (1984), Gravity wave saturation in the middle atmosphere: A review of theory and observations. Rev. Geophys. Space Phys., **22**, 275-308.
- Fritts, D. C. (1985), A numerical study of gravity wave saturation: Nonlinear and multiple wave effects, submitted to J. Atmos. Sci..
- Fritts, D. C. and T. J. Dunkerton (1984), A quasi-linear study of gravity wave saturation and self-acceleration. J. Atmos. Sci., **41**, in press.
- Hodges, R. R., Jr. (1967), Generation of turbulence in the upper atmosphere by internal gravity waves. J. Geophys. Res., **72**, 3455-3458.
- Lindzen, R. S. (1981), Turbulence and stress due to gravity wave and tidal breakdown. J. Geophys. Res., **86**, 9707-9714.
- Weinstock, J. (1976), Nonlinear theory of acoustic gravity waves. I. Saturation and enhanced diffusion. J. Geophys. Res., **81**, 633-652.
- Weinstock, J. (1982), Nonlinear theory of gravity waves: Momentum deposition, generalized Rayleigh friction, and diffusion. J. Atmos. Sci., **39**, 1698-1710.

3.21 THE SPEED OF WAVE-WAVE INTERACTIONS IN THE ATMOSPHERE

K. C. Yeh and C. H. Liu

Department of Electrical and Computer Engineering
University of Illinois
Urbana-Champaign, IL 61801

INTRODUCTION

In recent years there have been measurements of mesoscale fluctuations of wind and temperatures in the atmosphere ranging in height from the troposphere to the mesosphere by a variety of experimental techniques (VINNICHENKO and DUTTON, 1969; DEWAN, 1979; BALSLEY and CARTER, 1982; LILLY and PETERSEN, 1983; NASTROM and GAGE, 1983; DEWAN et al., 1984). These measured fluctuations reveal a degree of universality in their various spectra (VANZANDT, 1982; DEWAN et al., 1984). In checking the internal consistency of these various spectra a modified GARRETT and MUNK (1972, 1975) spectrum was used by VanZandt. Originally, Garrett and Munk synthesized a universal spectrum based on measured space-time fluctuations in the open ocean. Central in their work is the assumption that these fluctuations arise from gravity waves which satisfy a certain dispersion relation. The success of the universal spectrum in the atmosphere therefore implicitly implies that these atmospheric fluctuations are also caused by gravity waves. This, of course, does not indicate that the waves are the exclusive source of atmospheric perturbations. As a matter of fact, in addition to the wave theory (DEWAN, 1979) there is a proposal in the literature that interprets these mesoscale fluctuations as a two-dimensional turbulence (GAGE, 1979). Both of these physical mechanisms have been put to test by comparing with experimental data recently (GAGE and NASTROM 1984). The results strongly suggest that gravity waves and two-dimensional turbulence are both important in determining the observed velocity spectra.

The purpose of this paper is to investigate processes involving wave-wave interactions and their speed in controlling the spectrum. Presumably whatever processes that may occur in the atmosphere, the fastest process will be controlling. Consequently, the interaction speed will give us an indication whether any particular process will be dominating or not.

WEAK TURBULENCE THEORY

The weak turbulence theory involving wave-wave interactions has been well developed (e.g., TSYTOVICH, 1970; DAVIDSON, 1972). We are applying this theory to gravity waves in the atmosphere whose properties are well known (HINES, 1960; YEH and LIU, 1974). The theory is formulated in terms of wave action, and its equation is obtained after making a number of assumptions. These are:

- (1) The turbulence is a homogenous random field with a zero mean (BATCHELOR, 1956).
- (2) The turbulence is weak (NEWELL, 1968)
- (3) All Fourier components are interacting with a random phase (TSYTOVICH 1970), and
- (4) Only resonant interactions are important

With these four assumptions, a Boltzmann-like equation can be derived for the action density (MCCOMAS and BRETHERTON, 1971). The resulting Boltzmann-like kinetic equation can be used to prove a number of interesting properties (DAVIDSON, 1972). For example, the action density will never be negative if it started out as a positive quantity. It can also be shown that the kinetic equation leads to energy conservation and momentum conservation.

SPECIAL PROCESSES

The kinetic equation is nonlinear and is impossible to solve analytically in general. Studies of interaction speed among a discrete resonant trio (YEA and LIU, 1981) have shown that the process is fast when all three waves have the wave number of the same order of magnitude or when one of the three waves has a wave number many order of magnitudes different from the remaining two. If the former is the case (i.e., all three waves have similar wave number and frequency), the use of the kinetic equation will describe how the action density and hence the energy will evolve with time by resonant interactions in a narrow range of k and ω . The full nonlinear equation must be used in this case and no approximation can be made. If, on the other hand, the latter is the case (i.e. one of the three interacting waves belongs totally to a different part of the spectrum), the kinetic equation can be simplified by an equivalent linearization procedure. The resulting linearized equation describes how the action density will evolve with time by interacting resonantly with waves at a different part of the spectrum. It is this latter type of resonant interactions we wish to examine. Numerical evaluations have shown the importance of this type of interaction for ocean waves (MCCOMAS and BRETHERTON, 1977), of which there are three distinct kinds: elastic scattering, parametric subharmonic instability and induced diffusion (MCCOMAS and MULLER, 1981a, 1981b). These are discussed and investigated in the following.

ELASTIC SCATTERING

In this process, two of the three interacting waves have almost the same horizontal wave number and nearly the opposite vertical wave number. This implies that the frequencies are nearly equal. The remaining member of the three interacting waves must have a wave number that is nearly vertical and its frequency nearly zero. Roughly, this case can be described as scattering of the incident wave by a "zero" frequency vertical wind shear. Earlier studies for this particular process have demonstrated that the vertical shear does not participate in the energy exchange but merely acts as a catalyst in converting the incident energy into the scattered energy (YEH and LIU, 1979), hence the name elastic scattering. As such, this process can be viewed as the process responsible for making the action density (and hence energy spectrum) vertically symmetric. Time-constant contours for this elastic process have been plotted in Figure 1, one for 5 min and the other for 30 min. These contours depict the time constant required to achieve vertical symmetry if not so initially, and the results show that an incident wave with larger k (or smaller wavelength) will be able to achieve it in a shorter time.

PARAMETRIC SUBHARMONIC INSTABILITY

In this process the energetic waves of a moderate or large-scale transfer their energy to small-scale waves at one-half of the frequency. Consequently, this process is known as the parametric subharmonic instabilities. Based on the kinetic equation, it is possible to calculate the time constant with which a small-scale wave can gain energy from the more energetic large-scale waves. The results are shown in Figure 2. As it turns out, only small-scale waves propagating with an elevation angle of 60° or more can gain energy. This is why Figure 2 starts at $\theta=60^\circ$. Three contours are plotted in Figure 2, corresponding to a time constant of 5 min, 30 min and 5 hr.

INDUCED DIFFUSION

Consider the time evolution of small-scale (or large wave number) waves by a resonant three-wave process involving two nearly identical waves of large-wave vectors interacting resonantly with the more energetic wave of a small-wave vector. For this process a diffusion equation can be derived from the kinetic

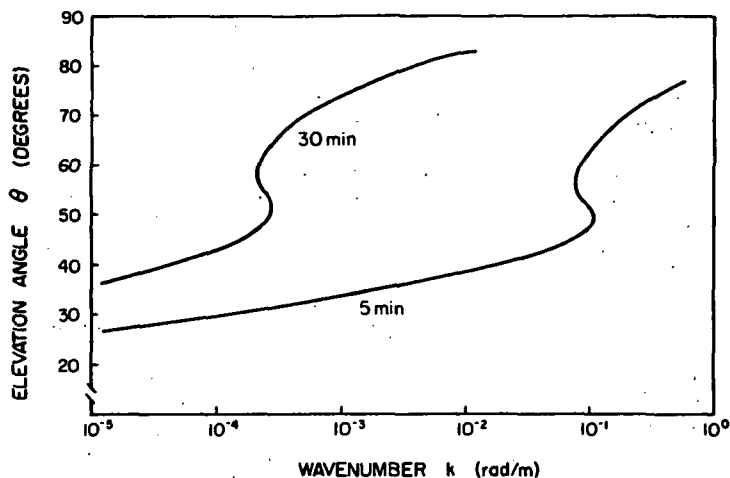


Figure 1. Contours of time constant for the elastic scattering as a function (k, θ) of the incident wave.

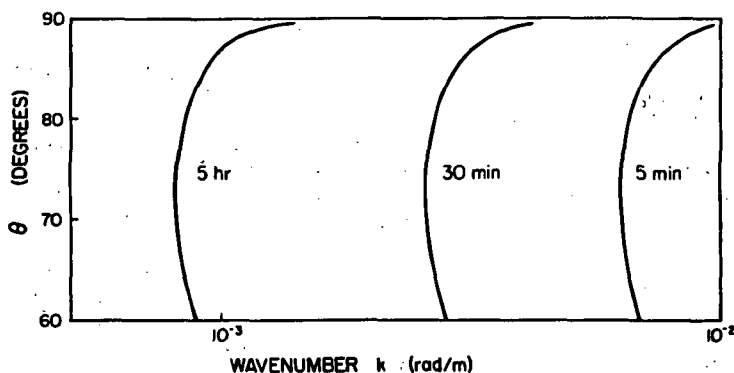


Figure 2. Contours of time constant for the parametric subharmonic instabilities. The wave that gains the energy has wave vector (k, θ) .

equation. The diffusion of action density takes place one dimensionally in k_z -space. Based on the diffusion equation, the diffusion time can be estimated. The resulting diffusion times are plotted in Figure 3 as contours. The representative values go from 10^2 to 10^5 sec in every decade. Near and below the 10^2 sec contour the predicted diffusion time is so fast that the weak turbulence assumption is violated. Outside this region, the theory should be valid and gives the valid diffusion time.

DISCUSSION AND CONCLUSION

In this paper resonant wave-wave interactions are considered. Studies of the interaction coefficient show that rapid transfer of wave action can take place in the disjointed parts of the spectrum for three processes, namely: elastic scattering, parametric subharmonic instability and induced diffusion. Of the three processes, the vertical shear plays a role in two. The vertical

shear of a moderate scale interacts through elastic scattering to make the spectrum vertically symmetric. On the other hand, the vertical shear of a large scale interacts through induced diffusion and is responsible for diffusion in k_z space. When interacting with a vertical shear, it is known that the vertical shear acts as a catalyst and is not involved in energy transfer (YEH and LIU, 1970). Consequently, in both elastic scattering and induced diffusion, the vertical shear does not gain or lose energy.

Through parametric subharmonic instability the more energetic large-scale waves are feeding energy into moderate- and small-scale waves of an elevation angle of 60° or larger. This region is denoted as above the dotted line in Figure 3. This vertically asymmetric energy-feeding has a tendency to enhance the portion of the energy spectrum with a larger k_z for a given k_h . In configuration space this means that the dimensions of the turbulence in the horizontal direction is larger than that in the vertical direction. When the process of induced diffusion becomes important, further diffusion of the action density along k_z takes place. In this way the turbulence is gradually flattened.

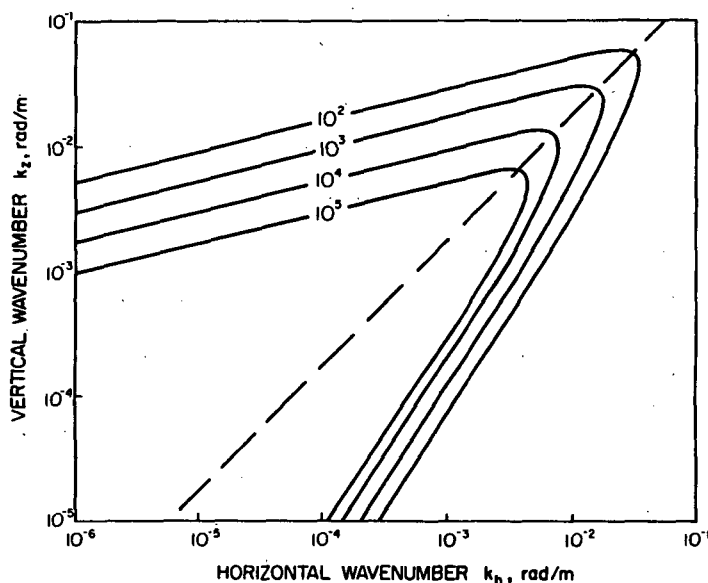


Figure 3. Contours of time constant for the induced diffusion.

ACKNOWLEDGEMENT

This research was supported by the Atmospheric Sciences Division, National Science Foundation through Grant No. ATM-83-12175.

REFERENCES

- Balsley, B. B. and D. A. Carter (1982), The spectrum of atmospheric velocity fluctuations at 8 km and 86 km, Geophys. Res. Lett., 9, 465-468.
- Batchelor, G. K. (1956), Theory of Homogeneous Turbulence, Cambridge Press, London and New York.
- Davidson, R. C. (1972), Methods in Nonlinear Plasma Theory, Academic Press, New York.

- Dewan, E. M. (1979), Stratospheric wave spectra resembling turbulence, Science, 204, 832-835.
- Dewan, E. M., N. Grossbard, A. F. Quesada and R. E. Good (1984), Spectral analysis of 10 M resolution scalar velocity profiles in the stratosphere, Geophys. Res. Lett., 11, 80-83.
- Gage, K. S. (1979), Evidence of $k^{-5/3}$ law inertial range in mesoscale two-dimensional turbulence, J. Atmos. Sci., 36, 1950-1954.
- Gage, K. S. and G. D. Nastrom (1984), On the spectrum of atmospheric velocity fluctuations seen by MST/ST radar and their interpretation, Handbook for MAP Vol. 14., 197-207, SCOSTEP Secretariat, Dep. Elec. Computer Eng., Univ. Il, Urbana.
- Garrett, C. J. R. and W. H. Munk (1972), Space-time scales on internal waves. Geophys. Fluid Dyn., 3, 225-264.
- Garrett, C. J. R. and W. H. Munk (1975), Space-time scales on internal waves: A progress report, J. Geophys. Res., 80, 291-297.
- Hines, C. O. (1960), Internal atmospheric gravity waves at ionospheric heights, Can. J. Phys., 38, 1441-1481.
- Lilly, D. K. and E. Petersen (1983), Aircraft measurements of atmospheric kinetic energy spectra, Tellus, 35A, 379-382.
- McComas, C. H. and F. P. Bretherton (1977), Resonant interaction of oceanic internal waves, J. Geophys. Res., 82, 1397-1412.
- McComas, C. H. and P. Muller (1981a), Time scales of resonant interactions among oceanic internal waves, J. Phys. Oceanogr., 11, 139-147.
- McComas, C. H. and P. Muller (1981b), The dynamic balance of internal waves, J. Phys. Oceanogr., 11, 970-986.
- Nastrom, G. D. and K. S. Gage (1983), A first look at wavenumber spectra from GASP data, Tellus, 35A 383-388.
- Newell, A. C. (1968), The closure problem in a system of random gravity waves, Rev. Geophys. Space Physics, 6, 1-31.
- Tsytovich, V. N. (1970), Nonlinear Effects in Plasma, Plenum, New York.
- VanZandt, T. E. (1982), A universal spectrum of buoyancy waves in the atmosphere, Geophys. Res. Lett., 9, 575-578.
- Vinnichenko, N. K. and J. A. Dutton (1969), Empirical studies of atmospheric structure and spectra in the free atmosphere, Radio Sci., 4, 1115-1126.
- Yeh, K. C. and C. H. Liu (1970), On resonant interactions of acoustic-gravity waves, Radio Sci., 5, 39-48.
- Yeh, K. C. and C. H. Liu (1974), Acoustic-gravity waves in the upper atmosphere, Rev. Geophys. Space Phys., 12, 193-216.
- Yeh, K. C. and C. H. Liu (1981), The instability of atmospheric gravity waves through wave-wave interactions, J. Geophys. Res., 86, 9722-9728.

3.22 A RAY TRACING MODEL OF GRAVITY WAVE PROPAGATION AND BREAKDOWN IN THE MIDDLE ATMOSPHERE

Mark R. Schoeberl

Laboratory for Atmospheres
Goddard Space Flight Center
Greenbelt, MD 20771

Gravity wave ray tracing and wave packet theory is used to parameterize wave breaking in the mesosphere. Rays are tracked by solving the group velocity equations, and the interaction with the basic state is determined by considering the evolution of the packet wave action density. The ray tracing approach has a number of advantages over the steady state parameterization of LINDZEN (1981) as the effects of gravity wave focussing and refraction, local dissipation, and wave response to rapid changes in the mean flow are more realistically considered; however, if steady state conditions prevail, the method gives identical results to LINDZEN (1981).

The ray tracing algorithm is tested using both interactive and noninteractive models of the basic state. In the interactive model, gravity wave interaction with the polar night jet on a β -plane is considered. The algorithm produces realistic polar night jet closure for weak topographic forcing of gravity waves. Planetary scale waves forced by local transfer of wave action into the basic flow in turn transfer their wave action into the zonal mean flow. Highly refracted rays are also found not to contribute greatly to the climatology of the mesosphere, as their wave action is severely reduced by dissipation during their lateral travel.

REFERENCE

Lindzen, R. S. (1981), J. Geophys. Res., 86, 9707-9714.

3.23 A FURTHER STUDY OF GRAVITY WAVE INDUCED DRAG AND DIFFUSION IN THE MESOSPHERE

J. R. Holton and Xun Zhu

Department of Atmospheric Sciences
University of Washington,
Seattle, WA

LINDZEN'S (1981) parameterization for the drag and eddy diffusion produced by breaking internal gravity waves in the mesosphere and lower thermosphere is applied to a modified version of the β -plane channel model of HOLTON (1982), in which an isotropic source spectrum of waves is specified similar to that given by MATSUNO (1982). The transmission for each wave component is influenced by Newtonian cooling and by eddy induced by the breaking of other wave components. In general, the waves with smallest doppler shifted phase speeds break first and produce sufficient eddy diffusion to significantly raise the breaking heights for the higher speed components. Thus, the wave wind profiles for both summer and winter solstice conditions are more realistic than those computed in HOLTON (1982).

REFERENCES

- Holton, J. R. (1982), The role of gravity wave induced drag and diffusion in the momentum budget of the mesosphere, J. Atmos. Sci., **39**, 791-799.
Lindzen, R. S. (1981), Turbulence and stress due to gravity wave and tidal breakdown, J. Geophys. Res., **86**, 9707-9714.
Matsuno, T. (1982), A quasi one-dimensional model of the middle atmosphere circulation interacting with internal gravity waves, J. Meteor. Soc. Japan, **60**, 215-226.

3.24 GRAVITY WAVES AND TURBULENT DIFFUSION COEFFICIENTS FOR CONSTITUENT AND HEAT TRANSPORT IN THE MESOSPHERE AND LOWER THERMOSPHERE

Darrell F. Strobel and John P. Apruzese

Plasma Physics Division
Naval Research Laboratory
Washington, D. C. 20375

Mark R. Schoeberl

Laboratory for Planetary Atmospheres
Goddard Space Flight Center
Greenbelt, MD 20771

Breaking gravity waves maintain a background level of turbulence sufficient to cool the lower thermosphere by 15-100° K, depending on altitude. The corresponding zonal wind deceleration is comparable to the required stress in dynamic models with IR radiative transfer calculated explicitly. The magnitude of required gravity wave cooling provides a stringent upper limit on the globally averaged turbulent diffusion coefficient in the mesopause region of $< 10^6 \text{ cm}^2 \text{ s}^{-1}$. Convergence of the eddy heat flux plus dissipation of gravity waves and conversion of wave energy to heat produces modest heating rates in the middle mesosphere of $\sim 0.5^\circ \text{ K day}^{-1}$. The thermodynamic constraints on the turbulent diffusion coefficient are compared with commonly used eddy diffusion coefficients in photochemical models, and significant differences are found in the lower mesosphere.

3.25 GRAVITY WAVE AND TIDAL MOMENTUM FLUXES AT POKER FLAT, ALASKA

S. K. Avery*, B. B. Balsley and T. Judasz*

Aeronomy Laboratory
National Oceanic and Atmospheric Administration
Boulder, CO 80303

The Poker Flat, Alaska, MST radar has been used to determine the momentum flux due to gravity waves and tides as a function of height and season. The content of $u'w'$ has been investigated using three different signal processing techniques. The results will be discussed in terms of current theories of momentum deposition in the atmosphere. The relationship between the calculated momentum deposition and the radar echo statistics will also be discussed.

* CIRES, University of Colorado, Boulder, CO 80309

3.26 A TEST OF THE VALIDITY OF RADAR AND SCINTILLOMETER MEASUREMENTS AND MODEL ESTIMATES OF C_n^2

T. E. VanZandt, J. L. Green, W. L. Clark, J. M. Warnock

Aeronomy Laboratory
National Oceanic and Atmospheric Administration
Boulder, CO 80303

J. Vernin

Department of d'Astrophysique
Universite' de Nice
06034 Nice Cedex, France

In the lower middle atmosphere extensive measurements of C_n^2 have been made by ST radars and by stellar scintillometers. Profiles of C_n^2 have also been calculated from radiosonde data with a statistical model. However, only a few simultaneous observations have been made in order to establish the validity of the observational techniques.

During 1983 a double-star scintillometer was located at the site of the Sunset radar in Colorado. The light of a star passing through a turbulent layer causes a speckle pattern at the ground. Each component of a double star projects an identical speckle pattern, separated by a distance proportional to the height of the turbulent layer. By suitable processing, the heights of the turbulent layers and the associated C_n^2 can be retrieved from the speckle patterns.

Thus far, simultaneous data have been analyzed on only four nights, two in June and two in October. In October, the radar and scintillometer profiles of C_n^2 agree well above 8 km where humidity was negligible. The model agrees well with the radar profile at all heights. But below 8 km, the model with humidity set equal to zero does not agree well with the scintillometer profile, as it should.

In June, the radar and scintillometer profiles agree well from 16 km up. Below 16 km, however, the optical values of C_n^2 become an order of magnitude or more smaller than the radar values. The model agrees well with the radar profiles above 10-12 km, but it does not agree well with either the radar or optical profiles at lower heights.

Below about 8 km, the discrepancy between the radar and scintillometer profiles can be attributed at least partly to the effect of humidity, but from 8 to 15 km, a different cause must be sought. Several explanations have been considered. The scintillometer C_n^2 may be too small because of the filtering effect of a large inner scale of turbulence in this height. The radar C_n^2 may be too large because of contamination by Fresnel reflection from tilted strata. It may also be noted that the photoelectric detectors were different (and presumably better) in June than in October; that cirrus clouds were often present in June (not in the direction of observation, of course) but not in October, and that in June the scintillometer and radar were looking in somewhat different directions, but in October they were very nearly collinear.

3.27 COMPARISONS OF HORIZONTAL AND VERTICAL VELOCITY SPECTRA IN THE MESOSPHERE, STRATOSPHERE AND TROPOSPHERE: OBSERVATIONS AND THEORY

K. S. Gage, B. B. Balsley and R. Garelo*

Aeronomy Laboratory
National Oceanic and Atmospheric Administration
Boulder, CO 80303

Vertical velocity and horizontal velocity spectra have recently been determined from Poker Flat MST radar data. In this paper we compare the magnitude and shape of the horizontal and vertical velocity spectra with what is predicted from theory under the assumption that both horizontal and vertical spectra are due to a common spectrum of internal waves.

Starting with the vertical velocity spectra for quiet periods, we determine the magnitude and shape of the horizontal velocity internal wave spectra, using relationships from internal wave theory. These calculated horizontal wave spectra are compared with the actual horizontal velocity spectra to help interpret the nature of the observed velocity spectra.

*CIRES Research Associate, University of Colorado, Boulder, CO 80309

3.28 DETERMINATION OF THE ATMOSPHERIC KINETIC ENERGY DENSITY HEIGHT PROFILE OVER POKER FLAT, ALASKA

B. B. Balsley and R. Garelo*

Aeronomy Laboratory
National Oceanic and Atmospheric Administration
Boulder, CO 80303

Continuous measurements of the total wind field in the troposphere (above 3.8 km), stratosphere (below 23 km) and in the mesosphere-lower thermosphere (between roughly 60 km and 95 km) enable a determination of the atmospheric kinetic energy profile and specific wind fluctuation periods. Magnitudes of all three wind components (v , u , w) are first spectrally analyzed, and the resulting spectral energy densities ($\text{m}^2 \text{s}^{-2} \text{Hz}^{-1}$) are then integrated over specific fluctuation periods (e.g., gravity wave periods, tidal periods, longer wave periods). Height profiles of these spectral energy values ($\text{m}^2 \text{s}^{-2}$) are then multiplied by an assumed atmospheric density profile to yield profiles of atmospheric kinetic energy density (Joules-m^{-3}). We present these results and discuss a number of ramifications in terms of energy dissipation processes, vertical energy transport, and seasonal variability.

*CIRES Research Fellow, University of Colorado, Boulder, CO 80309

3.29 GRAVITY WAVE MOTIONS AND MOMENTUM FLUXES IN THE MIDDLE ATMOSPHERE AT ADELAIDE, AUSTRALIA

R. A. Vincent

Physics Department, University of Adelaide
Adelaide, South Australia 5001

D. C. Fritts

Geophysical Institute
and
Department of Space Physics and Atmospheric Sciences
University of Alaska
Fairbanks, Alaska 99701

INTRODUCTION

The momentum flux divergence due to dissipating gravity wave motions is now thought to apply a substantial drag on the mean zonal flow in the middle atmosphere, causing reversals of the vertical shear of the mean zonal wind and of the mean meridional temperature gradient in the mesosphere (LINDZEN, 1981; HOLTON, 1982). Similar processes have been suggested to occur in the stratosphere. Thus, gravity waves appear to play a major role in determining the large-scale circulation and structure of the middle atmosphere. The theoretical and observational evidence in support of this conclusion was reviewed by FRITTS (1984).

Recently, a study was made of gravity wave momentum fluxes in the middle atmosphere using data collected during June 1984 at Adelaide, Australia (35°S). The primary objectives of this study were 1) to identify that portion of the gravity wave spectrum that contributes most of the momentum transport and flux divergence and 2) to examine the temporal variability of wave energies and momentum fluxes.

The data were obtained with an HF (2 MHz) radar operated in a Doppler configuration with two co-planar off-vertical beams. As described by VINCENT and REID (1983), this technique provides a direct measure of the vertical flux of horizontal momentum due to an arbitrary spectrum of gravity wave (and other) motions in the plane of the radar beams.

DATA ANALYSIS AND DISCUSSION

Radial velocity data were collected in 2 km range gates between 60 and 100 km. Because echoes were weak and limited to daylight hours at lower levels, however, our analysis was confined to heights from 70 to 100 km. The data were collected in 2 min segments at staggered heights, and adjacent segments were combined to yield a data set with 4 min resolution at all heights.

The radar beams were nominally directed at 11.6° from zenith, but because specularity enhances the near-vertical contributions to the echo power, the effective beam angle was found to be more nearly vertical. By comparison with the spaced-antenna data, a mean effective pointing angle of $\sim 6.5^{\circ}$ was inferred.

As in VINCENT and REID (1983), the zonal momentum flux due to gravity wave motions was computed from the mean-square velocities in the two Doppler beams. The mean-square velocities were determined for data blocks of length 1, 8, and 24 hr after removing the 12 and 24 hr tidal components and the means and linear

trends. The resulting eight-day average zonal momentum fluxes for each block size are shown in Figure 1. The first point to make is that the average momentum flux is negative and roughly constant with height, suggesting that gravity waves are transporting westward momentum into a region of eastward mean flow. Thus the gravity waves are permitting to a drag to be applied to the zonal flow in this region. This drag has the form

$$\frac{\partial}{\partial t} \bar{u} = - \frac{1}{\rho_0} \frac{\partial}{\partial z} (\rho_0 \overline{u'w'}) \quad (1)$$

which, for $u'w'$ approximately constant, becomes

$$\frac{\partial}{\partial t} \bar{u} \approx \frac{\overline{u'w'}}{H} \quad (2)$$

The second and more significant point is that the dominant fraction of the overall gravity wave momentum flux and divergence is associated with motions with periods less than 1 hr. By comparison, the flux associated with wave periods between 1 and 24 hr is less than 1/3 of the total. The average zonal drag applied between 78 and 96 km by gravity waves with periods of 8 min - 1 hr, 8 min - 8 hr, and 8 min - 24 hr is 50, 61, and 69 $\text{ms}^{-1} \text{day}^{-1}$, respectively. Thus, high-frequency gravity wave motions account for $\sim 70\%$ of the total applied drag in this region.

Another significant feature of the momentum flux and divergence due to gravity waves is the temporal variability. Figure 2 shows the east and west mean-square velocities, and the inferred momentum flux for periods less than 1 hr as a function of time-of-day. These data cover 8 days and 5 heights. The diurnal variability appears to be coupled to the diurnal tidal motions in this region and has significant implications for apparent tidal variability as well. These results will be described in more detail in a forthcoming paper.

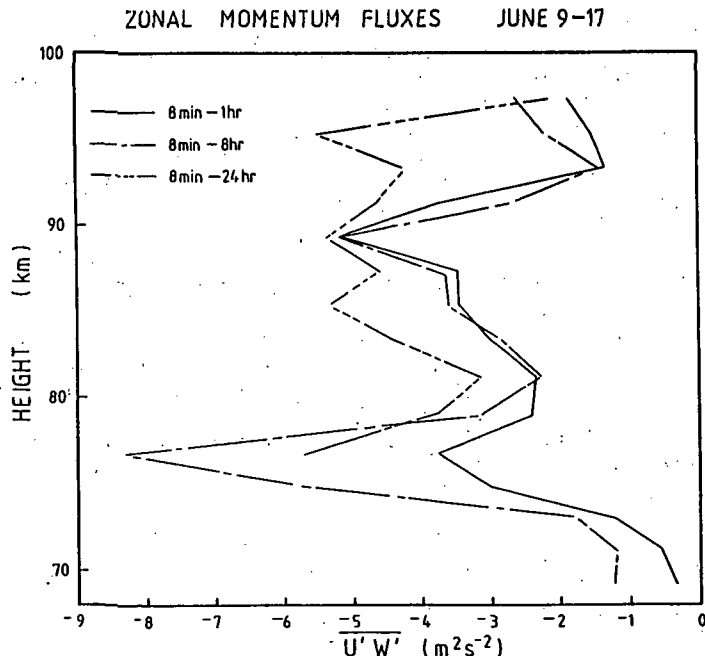


Figure 1. Zonal momentum fluxes due to gravity waves for 8 days during June 1984. Note that high-frequency ($T < 1 \text{ hr}$) motions contribute $\sim 70\%$ of the total.

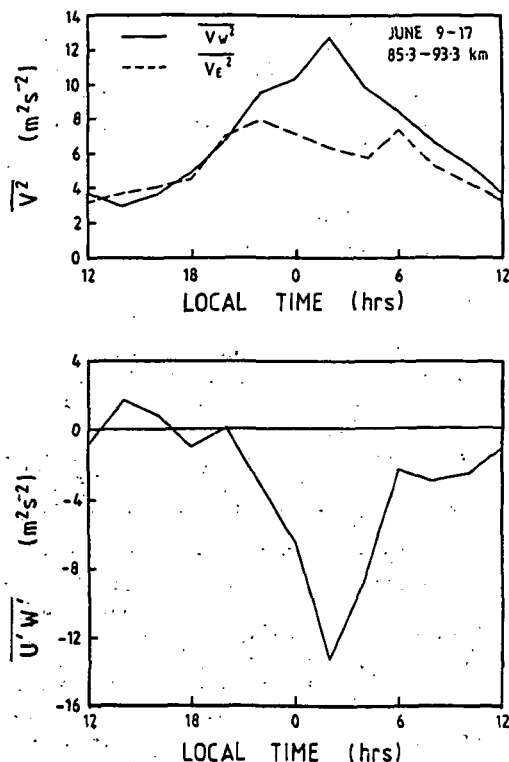


Figure 2. Mean-square velocities and inferred momentum flux for $T < 1$ hr motions versus time-of-day.

REFERENCES

- Fritts, D. C. (1984), Gravity wave saturation in the middle atmosphere: A review of theory and observations, Rev. Geophys. Space Physics., **22**, 275-308.
- Holton, J. R. (1982), The role of gravity wave-induced drag and diffusion in the momentum budget of the mesosphere, J. Atmos. Sci., **39**, 791-799.
- Lindzen, R. S. (1981), Turbulence and stress due to gravity wave and tidal breakdown, J. Geophys. Res., **86**, 9707-9714.
- Vincent, R. A. and I. M. Reid (1983), HF Doppler measurements of mesospheric gravity wave momentum fluxes, J. Atmos. Sci., **40**, 1321-1333.

3.30 BALLOON OBSERVATIONS OF (INERTIO-) GRAVITY WAVES AND TURBULENCE IN THE MIDDLE STRATOSPHERE

H. Tanaka

Water Research Institute, Nagoya University
Chikusa-ku, Nagoya 464, Japan

M. D. Yamanaka*

Institute of Space and Astronautical Science,
Meguro-ku, Tokyo 153, Japan

Balloon observations on (inertio-) gravity waves and turbulence in the middle stratosphere have been carried out totally three times during the MAP period in conjunction with the ISAS balloon group. Many interesting results, which may be divided into three categories, have been obtained.

First, energy spectra of horizontal components of wind fluctuations associated with superposed (inertio-) gravity waves obtained by balloon tracking demonstrate commonly a $-5/3$ power law at about 25 km height.

Second, multiple gust layers with a few tenths of meters in thickness were measured by improved propeller type anemometers, which may be closely related to amplified (inertio-) gravity wave packets propagating upwards.

Third, microstructures of turbulence and various stages of KH billows, each of which is an agency to form a thicker turbulence layer, were measured by newly developed glow-discharge ionic anemometers mounted on the scanning gondola.

These results will be presented and summarized based on the theories of (inertio-) gravity waves which have been rapidly developed within a decade.

*Graduate student of Nagoya University

3.31 MAP-ORIENTED RESEARCH IN THE PEOPLES'S REPUBLIC OF CHINA

Daren Lu

Institute of Atmospheric Physics, Academia Sinica
Beijing, China

In recent years, the interests in the MAP-oriented researches are increasing among the Chinese scientific communities of atmospheric physics, space physics, geophysics, and radio physics. There have been two national Middle Atmosphere Research meetings held in June 1981 and May 1984 in Beijing. These meetings were co-sponsored by the Chinese Geophysical Society and Chinese Meteorological Society. There were about 50 scientists who attended these meetings. They were from various institutes and universities.

The following research fields are being involved or prepared by Chinese scientists:

1. A stratospheric balloon launching facility has been in operation in the Xianghe Observatory, Institute of Atmospheric Physics, Academia Sinica since 1980. At present, the ability of the balloon system is as follows:

Location: Xianghe Observatory, IAP, AS

Latitude 39°46'N, Longitude 117°00'E

Balloon volume: Max 80,000 m³

Gondola loading: Max 350 kg

Sounding altitude: Max 38 km

Observation duration: Max 18.5 h

Observation items: stratospheric aerosols, minor gases, turbulence, cosmic rays, cosmic dust, X-rays astronomy, IR astronomy, remote sensing, etc.

2. Observations of the stratospheric aerosols with a balloon-borne aerosol counter and sampler have been made in IAP, AS. Figure 1 shows an example of the observed vertical distribution of aerosol particle concentration up to 30 km over Northern China. Further observations of stratospheric aerosol and minor gases are being prepared.
3. Long-term monitoring of stratospheric aerosols induced by volcanic eruptions are made with a ruby lidar of IAP, AS. Figure 2 shows an example of the vertical distribution of the stratospheric aerosol backscattering ratio. A new lidar system for the observation of the middle atmosphere has been proposed.
4. An ST radar is being built in the Xianghe Observatory, IAP, AS. The main radar system parameters are:

Frequency: 78 MHz

Transmitter Peak power: 750 kW

Average Power: 3.75-18.75 kW

Pulse length: 2-10 microseconds (variable)

P.R.F.: 2500 Hz

Antenna Type: COCO₂ Pol.Area: 100*100m²

Half beamwidth: 2 deg

Beam scanning: 0-20 deg

88773-88W

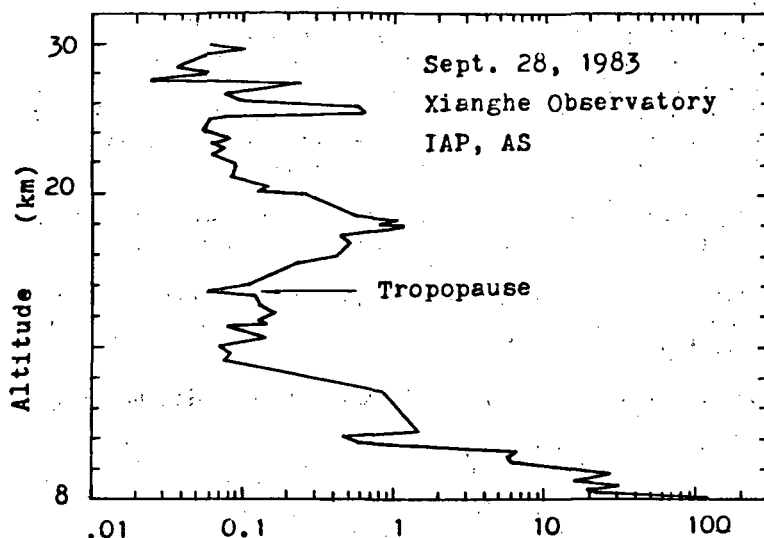


Figure 1. Vertical distribution of atmospheric aerosol concentration.

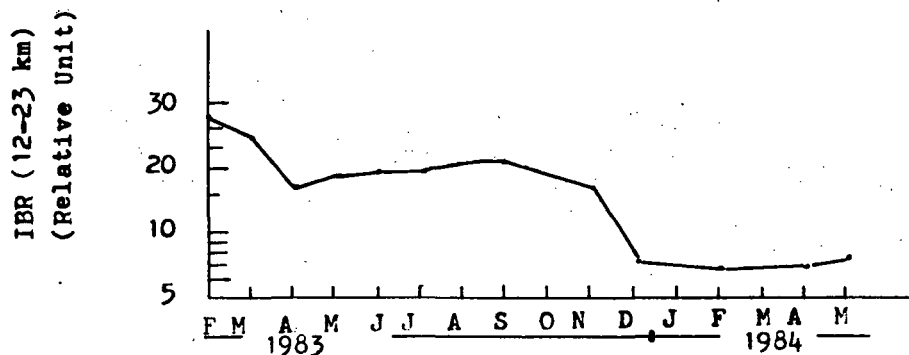


Figure 2. Time variation of integrated backscattering ratio (IBR)

Receiver: Orthogonal coherent receiver

Noise temp. 295 K

Data processing: FFT

It is expected that the radar will be finished in 1987.

4. Ionospheric D-region are investigated with the method of ionospheric absorption on 6-8 MHz in Beijing University, Wuhan University, the Institute of Radio Wave Propagation, and the Ministry of Electronic Industry. During recent two-year observations, two "winter anomalies" have been found at three Chinese stations with geographic latitudes higher than about 30° N. At lower latitude stations no such phenomenon was found at

all. The results also showed that during this period the D-region absorption was totally solar controlled in the summer but apparently related to disturbances in the stratosphere as low as the 30 and 50 mb levels. The data for the two summer periods are also considered in relation to the variation of solar X-ray and Lyman- α radiation. It is shown that under the quiet conditions the $L\alpha$ is the dominant controlling factor.

5. Scientists of IAP are engaged in the photochemistry modeling and radiation parameterization of the middle atmosphere.
6. Scientists of the Institute of Space Physics are engaged in the research of the middle atmosphere electrodynamics and ion chemistry.

The next national Middle Atmosphere Research meeting will be held at the end of 1986.

3.32 QUANTITATIVE STUDY ON DISPERSION RELATIONS OF TIDS OBSERVED BY AN HF DOPPLER ARRAY

M. Tsutsui and T. Ogawa

Radio Atmospheric Science Center
Kyoto University, Uji
Kyoto 611, Japan

A quantitative study on the dispersion relation of traveling ionospheric disturbances (TIDs) has been performed by using data obtained by an HF Doppler array. An average distance from the radio wave transmitter to three receiving stations is about 400 km. As the distances among three stations are 40-50 km, horizontal spacings of the probing point in the ionosphere are 21-26 km. The altitude of the probing point by 8 MHz radio waves ranges from 190 to 210 km. Observed data at these three stations are digitized continuously with a sampling period of 10 sec. Figure 1 shows a schematic illustration of a running analysis method for the present study. The sampling points of the subset data are 1024, and the shifting points in the running are 30. Fourier components ω 's and their wave vectors k 's of the TIDs are calculated from these subset data from the three stations by means of the cross-spectrum analysis. The available range of the analyzed period in the present observation is 1 to 50 min. Then many pairs of ω and k are plotted on $\omega - k$ diagrams. Diagrams of horizontal trace velocity V_{ph} versus wave period T have also been obtained. From these diagrams we can see clear cutoff periods of the internal mode of the atmospheric gravity waves. A morphological classification of the $\omega - k$ and $V_{ph} - T$ obtained through one year has been performed. From the morphological classification, two interesting relations have been found. They are that the dispersion characteristics are changed with the amplitude of Doppler fluctuations and that the cutoff period of the gravity modes, we call it the minimum Brunt-Vaisala period, decrease with the amplitude of the Doppler fluctuations. The result for the latter case is shown in Figure 2. Furthermore, it has also been found that, for very small amplitude fluctuations, a simple dispersion characteristic derived from the linear perturbation theory under an isothermal atmospheric condition (HINES, 1960) has been obtained.

Moreover, we have performed the estimation of the horizontal velocity vectors of the thermospheric wind from their dispersion relations. A key point of the method of obtaining the vectors is to estimate the tilt, in azimuthally different $\omega - k$ diagrams, of a resonant branch ascribed to the Brunt oscillations. In general, the gradient of the resonant branch affected by the thermospheric wind corresponds to $kV\cos\theta$, where k is the wave number in the azimuthal direction taken for the $\omega - k$ diagram, V is the velocity of the thermospheric wind and θ is the angle between the given azimuthal direction and the direction of the thermospheric wind. Therefore, the direction in which the $\omega - k$ diagram represents the steepest branch among $\omega - k$ diagrams taken in all azimuthal directions indicates the direction of the thermospheric wind vector. Figure 3 shows an example of the azimuthally different six $\omega - k$ diagrams in which the dispersion characteristics are modified by the thermospheric wind. From a set of gradients of these linear slopes seen in each diagram, a velocity vector of the thermospheric wind has been estimated by the method of least squares. The result in 1982 (Figure 4) obtained by this method is consistent with those obtained by the incoherent scatter radars (AMAYENC, 1974) and by theoretical approaches (VOLLAND and MAYR, 1974).

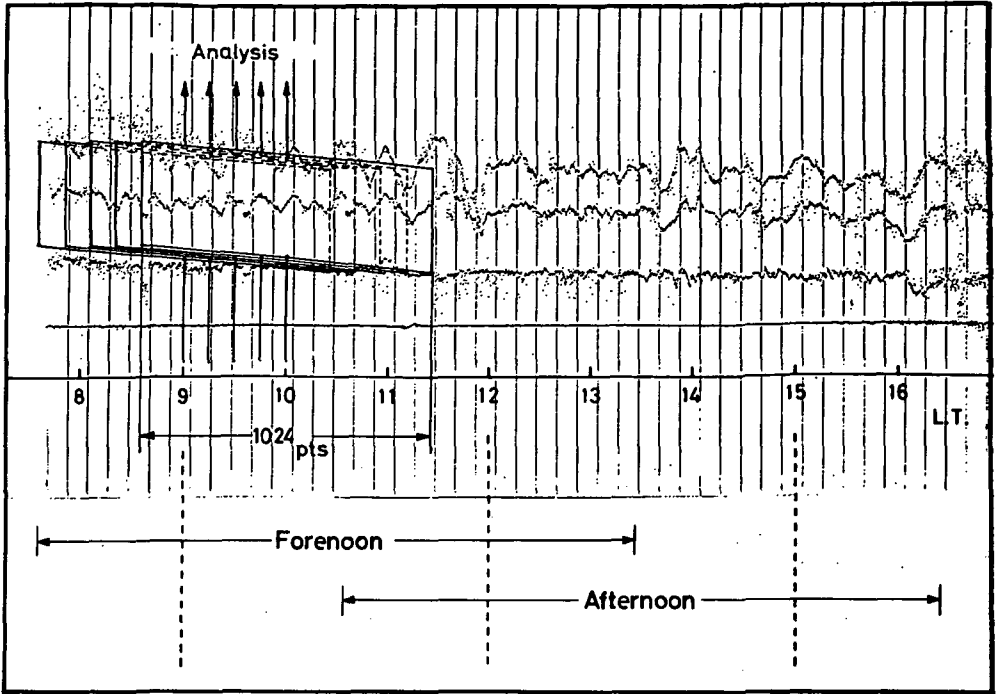


Figure 1. An illustration of "running method" in data samplings. The number of points in a subset data (a time window) is 1024, which corresponds to 170 min, and shifting points in the running method are 30, which correspond to 5 min on a real-time basis, respectively. The samplings are carried out from 07:35 to 13:25 LT (09:00 to 12:00 LT for the median time of the sampling window) for the forenoon period, and from 10:35 to 16:25 LT (12:00 to 15:00 LT) for the afternoon period, respectively.

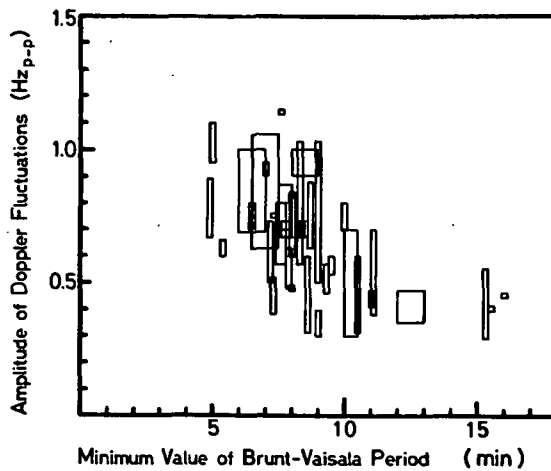


Figure 2. A relation between the cutoff period (the minimum Brunt-period) of the internal gravity waves and the amplitude of the Doppler fluctuations.

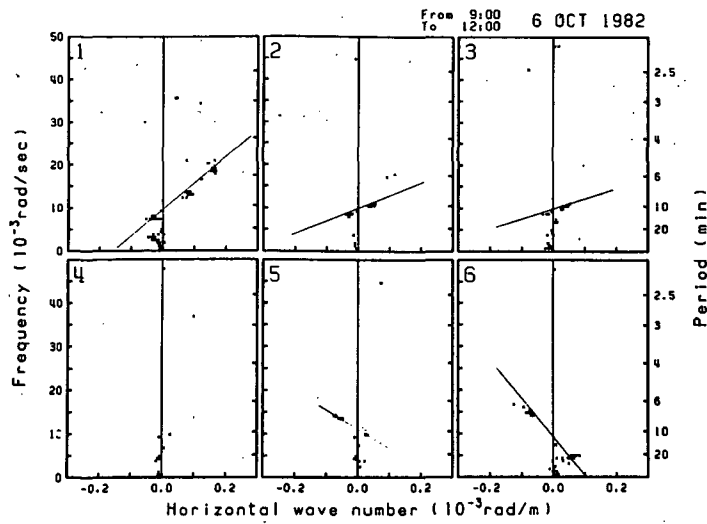


Figure 3. Azimuthally different $\omega - k$ diagrams suggest the presence of the thermospheric wind from the linear slopes seen in each frame. From these branches the horizontal wind velocity $V_o = 60.5$ m/sec and its azimuthal direction $\phi = 343^\circ$ were estimated.

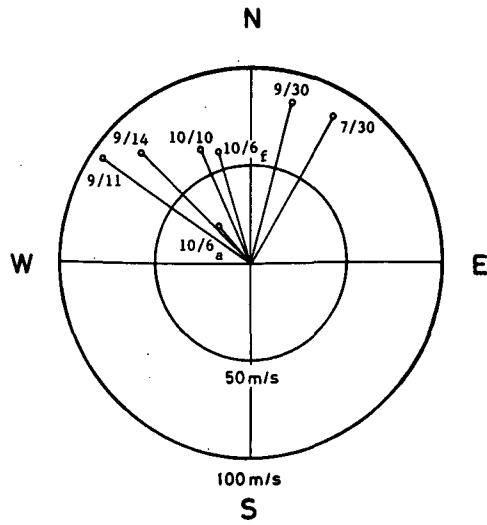


Figure 4. Horizontal velocity vectors of the thermospheric winds obtained by the HF Doppler observations in 1982, where the suffixes f and a mean the forenoon and afternoon periods, respectively. These vectors are consistent with the vector of the neutral wind in the ionosphere obtained by the incoherent scatter radar (AMAYANC, 1974) and by the theoretical calculations of the wind system by VOLLAND and MAYR (1974).

REFERENCES

- Amayanc, P. (1974), Tidal oscillation of the meridional neutral wind at mid-latitude, Radio Sci., 9, 281.
- Hines, C. O. (1960), Internal atmospheric gravity waves at ionospheric heights, Can. J. Phys., 38, 1441.
- Volland, H. and H. G. Mayr (1974), Tidal waves within the thermosphere, Radio Sci., 9, 263.

3.33 HF DOPPLER OBSERVATIONS OF ACOUSTIC WAVES EXCITED BY THE EARTHQUAKE

T. Ichinose*, K. Takagi*, T. Tanaka**, T. Okuzawa***
 T. Shibata***, Y. Sato⁺ C. Nagasawa⁺⁺, and T. Ogawa⁺⁺⁺

*Department of Electronics, Doshisha University, Kyoto 602, Japan

**Toshiba Electric Company, Ltd., Nagoya 415, Japan

***Department of Applied Electronic Engineering,
 University of Electro-Communications,
 Chofu-Shi, Tokyo 182, Japan

⁺Department of Electronics and Communications,
 Tohoku Institute of Technology,
 Sendai 982, Japan

⁺⁺Department of Electrical Engineering, Tokyo Metropolitan University,
 Tokyo 158, Japan

⁺⁺⁺Radio Atmospheric Science Center,
 Kyoto University, Uji 611, Japan

INTRODUCTION

Ionospheric disturbances caused by the earthquake of a relatively small and large epicentral distance have been detected by a network of HF-Doppler sounders in central Japan and Kyoto station, respectively. The HF-Doppler data of a small epicentral distance, together with the seismic data, have been used to formulate a mechanism whereby ionospheric disturbances are produced by the Urakawa-Oki earthquake in Japan. Comparison of the dynamic spectra of these data has revealed experimentally that the atmosphere acts as a low-pass filter for upward-propagating acoustic waves.

By surveying the earthquakes for which the magnitude M is larger than 6.0, referred to the Chronological Science Table (Tokyo Astronomical Observatory), we found the ionospheric effect in 16 cases of 82 seismic events. As almost all these effects have occurred in the daytime, it is considered that it may result from the filtering effect of the upward-propagating acoustic waves.

OBSERVATIONS

The HF-Doppler technique is known to be very sensitive to rapid oscillatory changes in the electron density of the ionosphere (OGAWA, 1958; WATTS and DAVIES, 1960; FENWICK and VILLARD, 1960).

A network of HF-Doppler sounders in central Japan observed atmospheric waves at the time of the Urakawa-Oki earthquake of a magnitude of 7.1, which occurred at 0232:06 UT on March 1982. Figure 1 illustrates the locations of the epicentre, the seismographical observatories, the JJY transmitting station (36.18 N, 139.85 E) and the HF-Doppler stations. Seismograms from four observatories--Urakawa, Akaita, Iida, and Abuyama--are shown in Figure 2.

Figure 3 shows Doppler recordings obtained at Sendai, Tokyo, Sugadaira and Kyoto, respectively. It is evident from the figure that the HF-Doppler traces begin to oscillate suddenly, with a predominant period of around 20s, and that the traces of the 5 MHz wave are more complicated than those for the 8 MHz wave.

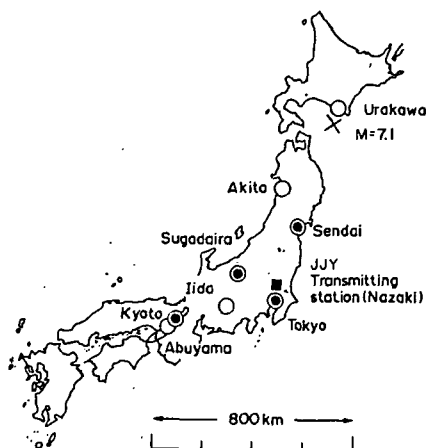


Figure 1. Locations of the epicentre, the seismographical observatories and the JJY HF-Doppler circuit.

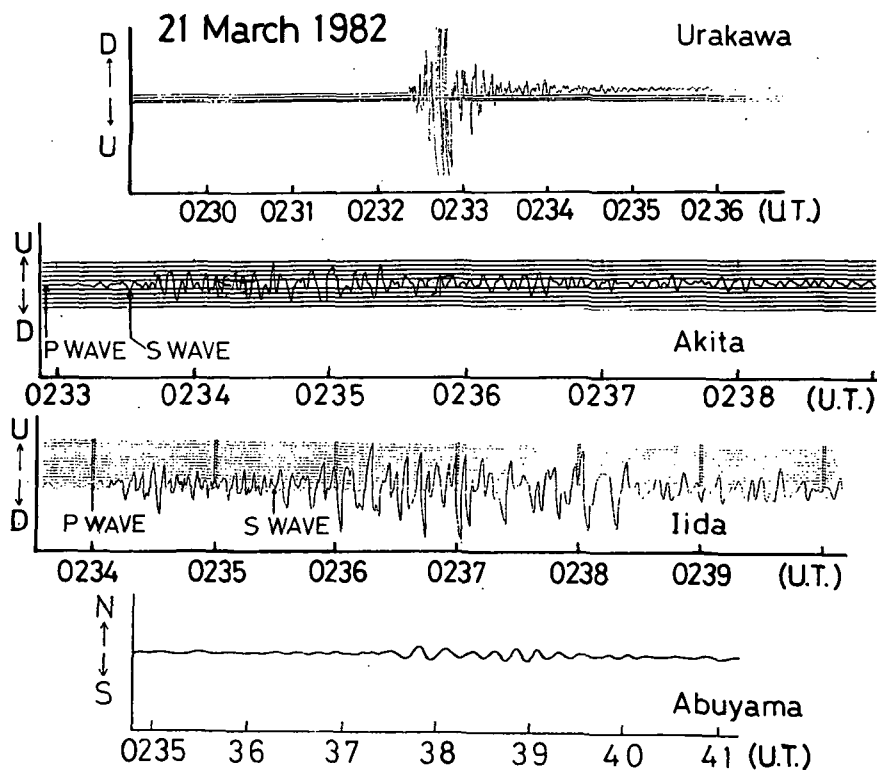


Figure 2. Seismograms taken at Urakawa, Akita, Iida and Abuyama on March 21, 1982.

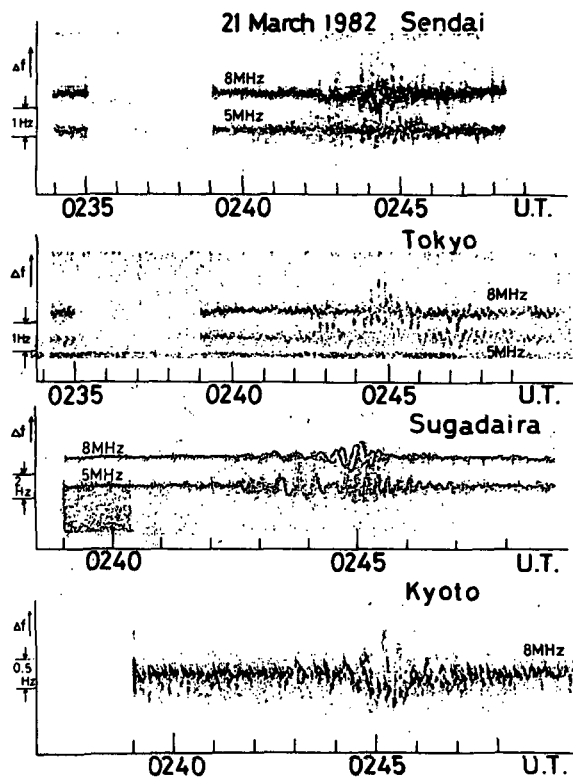


Figure 3. Doppler data taken at Sendai, Tokyo, Sugadaira, and Kyoto on March 21, 1982.

Similarly, Figure 4 shows Doppler recordings obtained at Kyoto at the time of the great earthquakes and large epicentral distance.

DATA ANALYSIS

Ionospheric response

The travel-time curves for both the seismic waves and the HF-Doppler are presented in Figure 5. The line marked 1 in the figure indicates the travel time characteristics for the up-down component of the 20s period in the seismograms taken at Akita and Iida. The method of least squares was used to estimate the gradient of lines 2 and 3 in Figure 5, and a line in Figure 6. In Figure 6, the line indicates the ionospheric response seen in the HF-Doppler data listed in Table 1. The propagation velocities of the disturbances deduced from the HF-Doppler records are found to be nearly coincident with the averaged phase velocity of the seismic waves. This implies that the ionospheric disturbances could be caused by the seismic waves which propagate along the Earth's surface.

If the horizontal wave number k_x of the acoustic waves excited by the up-down motion of the Earth's surface is equal to k_x of the seismic waves at the

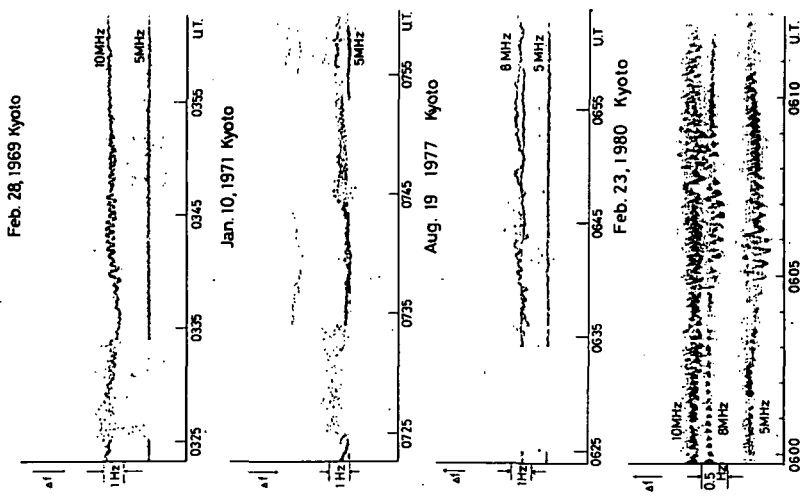


Figure 4. Doppler data taken at Kyoto on February 18, 1969, January 10, 1971, August 19, 1977, February 23, 1980, respectively.

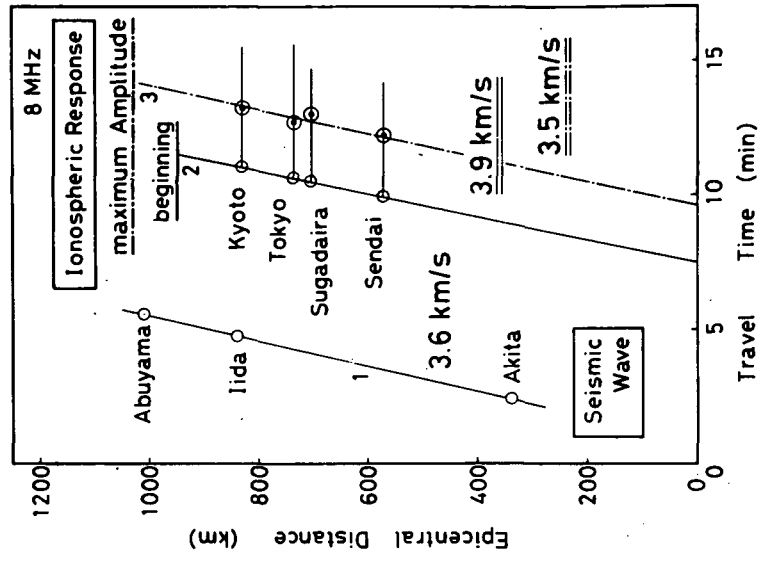


Figure 5. Travel-time curves for the seismicity and the HF-Doppler variations. Line 1 represents the component of 20 s period of the seismic waves and line 2 and line 3 the beginning and the maximum amplitude, respectively, of the HF-Doppler disturbances.

Table 1. Summary of HF-Doppler data at Kyoto on the North Atlantic Ocean, West New Guinea, South of Sumbawa Islands, and Kurile Islands earthquake, respectively.

Epi- central Region	Epi- central Distance (km)	Oceanic Conti- nental (km)	Origin Date	(U.T.) Time	Pre- dominant Period (sec)	Begin- ning of Doppler Shift (U.T.)	Reflec- tion Height (km)	Travel Time (min)	Travel Time of Acoustic Wave (min)	Freq. (MHz)
North Atlantic Ocean (M 8)	11427	$\frac{1142}{10285}$	'69. 2 28.	02:40	60	03:39	278.4	59.0	10.8	10
					34	03:42	278.4	62.0	10.7	
West New Guinea (M 8.1)	4281	$\frac{4238}{43}$	'71. 1 10.	07:17	25	07:44	225.9	27.0	9.5	5
					20	07:45	225.9	28.0	9.5	
South of Sumbawa Island (M 8.0)	5543	$\frac{4545}{998}$	'77. 8 19.	06:08	45	06:41	232.0	33.0	9.7	8
					60	06:42	232.0	34.0	9.8	
					110	06:44	232.0	36.0	10.2	
Kurile Islands Region (M 7.1)	1168	$\frac{561}{607}$	'80. 2 23.	05:51	20	06:05	155.8	14.0	7.8	5
					20	06:06	211.8	15.0	9.2	8

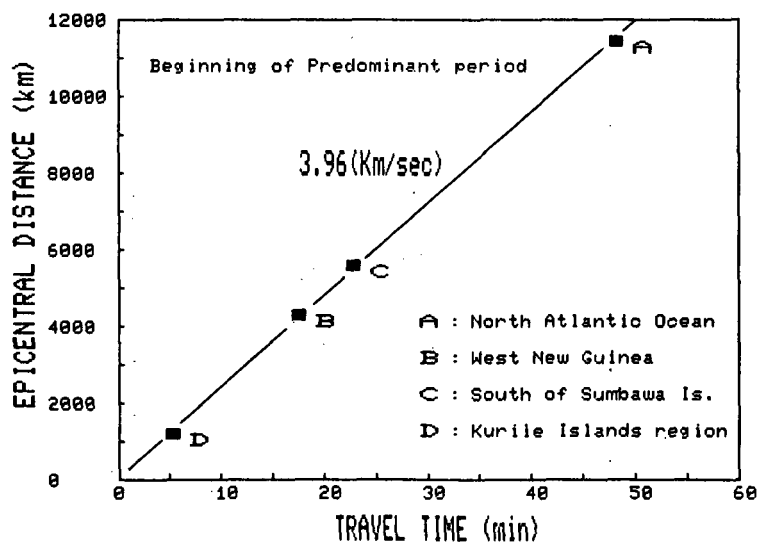


Figure 6. Travel-time curve for the seismicity from the epicentre to the launch point.

C-5

ground-air interface, ray paths for the acoustic waves can be calculated (NAJITA and YUEN, 1979). The travel time of the acoustic wave with the 20s period can be calculated by using the simple form of the dispersion equation (HINES, 1960).

$$\omega^2 - C^2 (k_x^2 + k_z^2) = 0 \quad (1)$$

where ω is the angular frequency, C the velocity of sound and k_x and k_z the horizontal and vertical components of the wave number, respectively. Such calculated travel times (8.8-9.3 min) are found to be very close to those derived from Doppler recordings at the four stations (7.5-9.4 min). This result suggests that seismic waves with a phase velocity of 3.6 km/s and a period of 20s should generate the acoustic waves which propagate upward to cause the ionospheric disturbances.

Spectral features

To examine the propagation characteristics of the atmospheric acoustic waves produced by the earthquake, spectral analyses were carried out on sample records. In the analyses, the MEM (BURG, 1975) was adopted to obtain high resolution power-spectra of the fluctuation records for both HF-Doppler and seismicity.

Figure 7 gives the resultant dynamic spectra for both the HF-Doppler variation (JJY 8 MHz, true-reflection height 195 km) observed at Kyoto and the up-down component of seismic data from Iida, located in the vicinity of the mid-point of the propagation path of JJY waves between Nazaki and Kyoto. In Figure

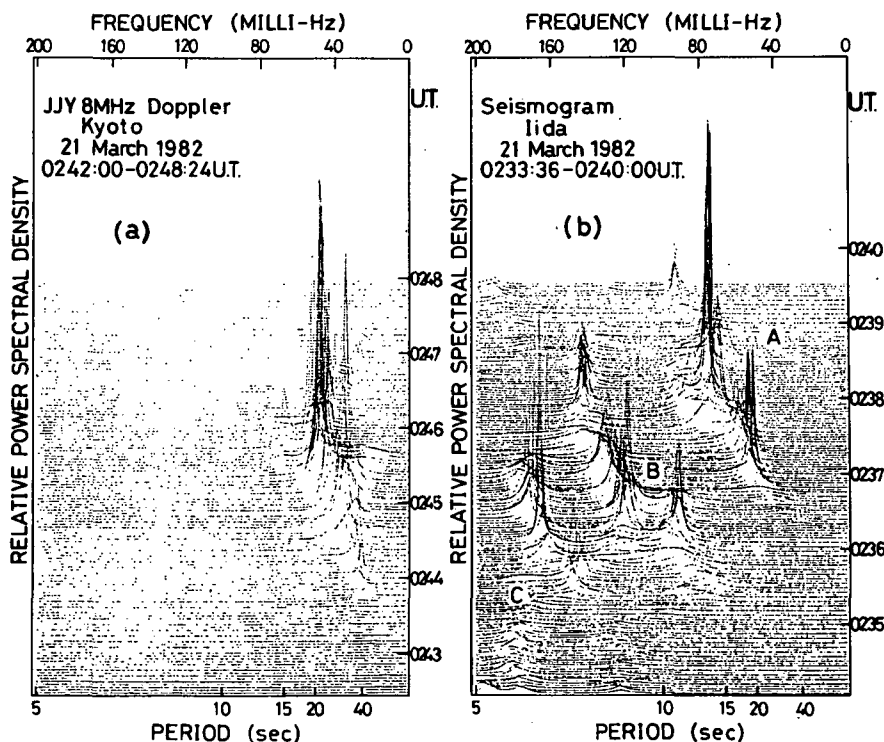


Figure 7. Comparison of the spectra between (a) the JJY 8 MHz Doppler record at Kyoto and (b) the seismogram (up-down component) at Iida.

7(a), the spectral peaks are found only in the period range 50-15s between 0244:00 and 0246:30 UT. These spectral peaks are similar to those of group A in the seismic data. This result suggests that the waves of group A can propagate to reach ionospheric heights.

The dynamic spectra of the 5 MHz and 8 MHz waves at Sugadaira station are shown in Figure 8, where the time-scale on the ordinate differs between the two panels by 47s, corresponding to the travel time of acoustic waves between the true reflection heights (156 km and 214 km) for the 5 MHz and 8 MHz waves, respectively. As can be seen in Figure 8(b), the peak periods shift gradually from 30 to 20s during the interval 0243:30 - 0244:30 UT, and then abruptly move to the peak position around 13s period during the interval 0244:30 - 0246:30 UT. As for the 8 MHz wave in Figure 8(a), the 13s group disappears, and hence only the 20-30s group remains. The above results may be explained in terms of atmospheric filtering, viz. in Figure 7, the longer-period component (A) of the seismic waves can survive to reach an altitude of 195 km to cause the ionospheric disturbance, but the shorter-period components (B, C) are suppressed by an atmospheric filter. In Figure 8, the atmospheric low-pass filter comes into play between 156 km and 214 km height to suppress spectral components in the shorter period of the 5 MHz waves.

Statistical result of HF-Doppler records

By surveying the earthquakes which occurred from January 1968 to December 1981, in Alaska on March 28, 1964 and Urakawa-Oki on March 21, 1982, of magnitude M larger than 6.0, and referring to the Chronological Science Table, we found the ionospheric effect in 16 cases from 82 such seismic events. In these

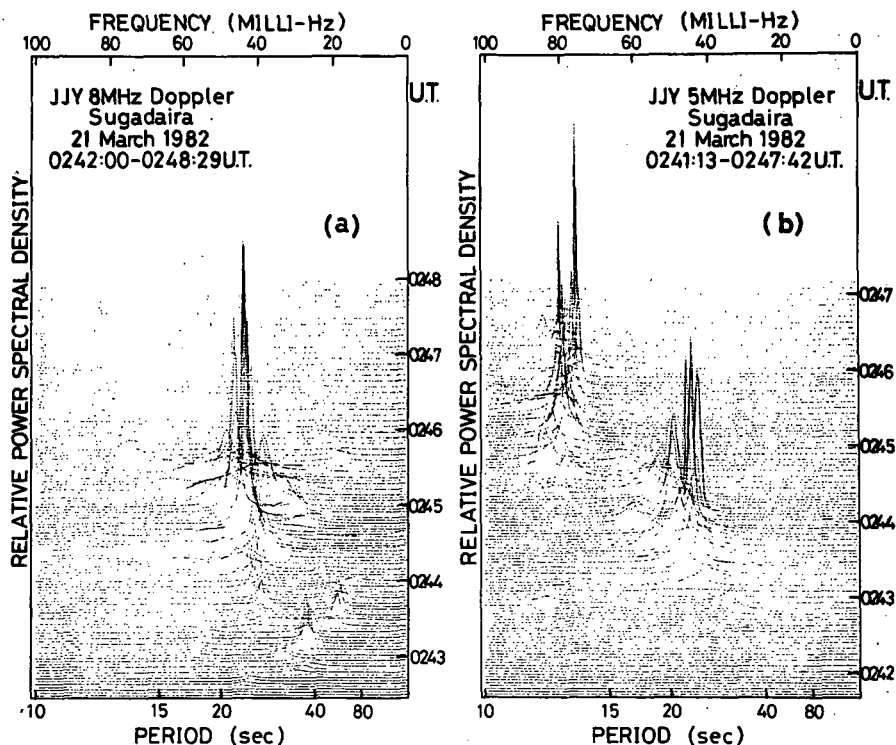


Figure 8. Comparison of the spectra between (a) the JJY 8 MHz and (b) the 5 MHz Doppler record at Sugadaira.

records, HF-Doppler variations of 12 out of 55 examples around the islands of Japan for which the epicentral distance is less than 2300 km are found. Similarly, 4 out of 27 examples around the world for more than 3400 km are found. Figure 9 shows the magnitude dependence in the daytime and the nighttime of HF-Doppler records at Kyoto. As a result, almost all these effects have occurred in the daytime. It may result from the filtering effect of acoustic waves by the difference of the reflection height of JJY waves and the atmospheric temperature between the daytime and the nighttime. Figure 10 shows the frequency characteristics of the atmospheric filter in the daytime and the nighttime calculated by using the theory of viscous damping (PITTEWAY and HINES, 1963) and the CIRA 1972 model. In Table 1, the predominant period observed by the HF-Doppler is from the 20s to 60s. Accordingly, the difference of reflection height in both times may be mainly attributable to the filtering of acoustic waves. The effect by the difference of the atmospheric temperature may not be very notable.

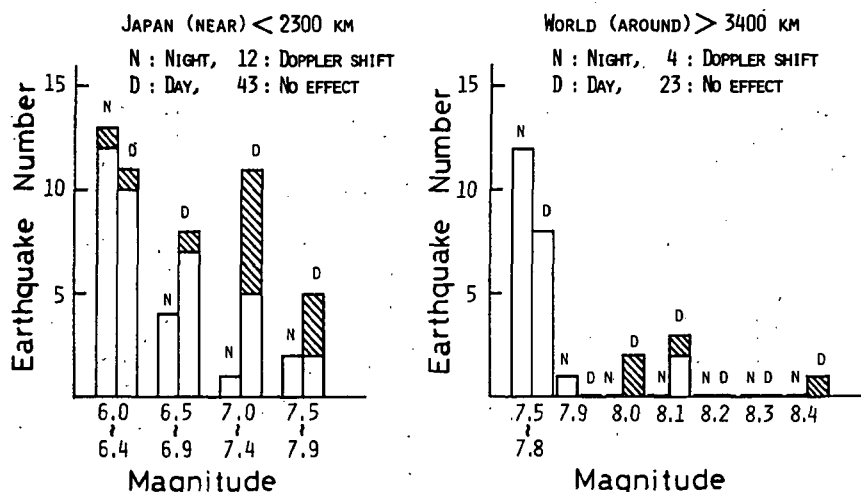


Figure 9. Magnitude dependence in the daytime and the nighttime of HF-Doppler disturbances at Kyoto from 1968 through 1981, Alaskan earthquake of 1964 and Urakawa-Oki of 1982. The hatch denotes HF-Doppler variations.

SUMMARY

From the HF-Doppler observations, the acoustic waves excited by seismic waves near the sub-ionospheric point would propagate upward in almost a vertical direction, with changing wave forms as the cutoff period of the atmospheric filter becomes larger. As almost all the HF-Doppler variations earthquakes have occurred in the daytime, it is considered that it may result from the filtering effect of acoustic waves by the difference of the reflection height of the received wave (for example, 5 MHz) between the daytime and the nighttime.

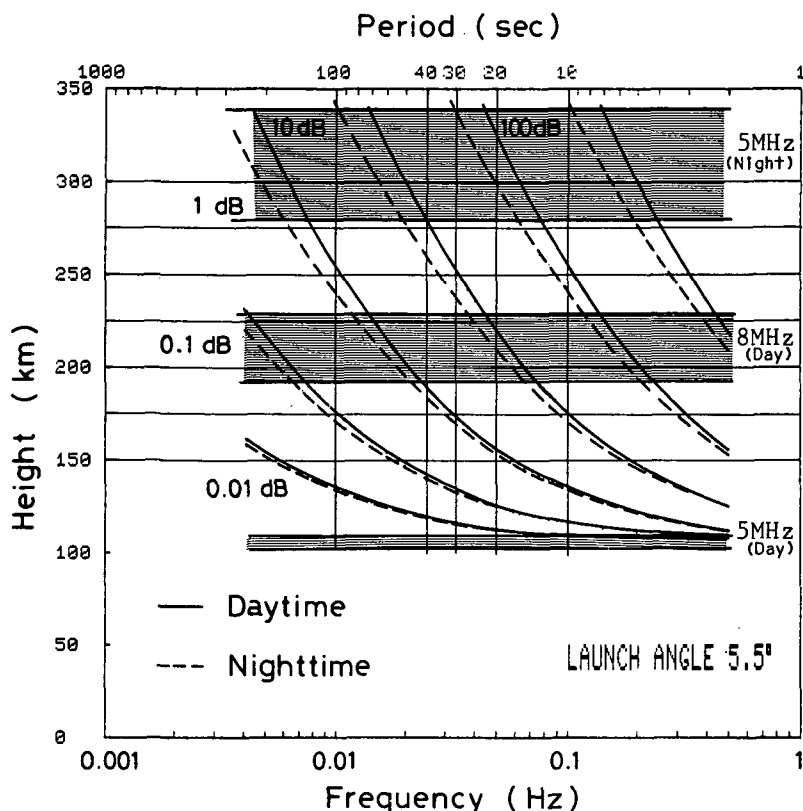


Figure 10. Frequency characteristic of the atmospheric filter in the daytime and the nighttime using the CIRA 1972 model.

ACKNOWLEDGEMENTS

The authors are thankful to H. Mochizuki and the staff of the Japan Meteorological Agency and H. Miki, Abuyama Seismographical Observatory of Kyoto University, for supplying the seismicity data. The ionograms used in this study were provided from the World Data Center C-2 for the Ionosphere.

REFERENCES

- Burg, J. P., Ph. D. thesis (1975), Stanford University, Stanford, CA.
 Fenwick, R. C. and O. G. Villard (1960), Continuous recording of the frequency variation of WWV-20 signal after propagation over 400 km path, *J. Geophys. Res.*, **65**, 3249-1960.
 Hines, C. O. (1960), Internal atmospheric gravity waves at ionospheric heights, *Can. J. Phys.*, **38**, 1441.
 Najita, K. and P. C. Yuen (1979), Long-period oceanic Rayleigh wave group velocity dispersion curve from HF Doppler sounding of the ionosphere, *J. Geophys. Res.*, **84**, 1253.
 Ogawa, T. (1958), Frequency variations in short wave propagation, *Proc. IRE*, **46**, 1934.
 Pitteway, M. L. V. and C. O. Hines (1963), The viscous damping of atmospheric gravity waves, *Can. J. Phys.*, **41**, 1935.
 Watts, J. M. and K. Davies (1960), Rapid frequency analysis of fading radio signals, *J. Geophys. Res.*, **65**, 2295.

3.34 ESTIMATION OF NEUTRAL WIND VELOCITY IN THE IONOSPHERIC HEIGHTS BY HF-DOPPLER TECHNIQUE

T. Kitamura, M. Takefu and N. Hiroshige

Department of Physics,
Kyushu University 33,
Fukuoka 812, Japan

Three net stations located about 100 kilometers apart have been set up around the station of the standard frequency and time signals (JJY) at central Japan (Figure 1), and measurements of atmospheric gravity waves in the ionospheric heights (F-region, 200-400 km) have been made by means of the HF-Doppler technique during the period of February 1983 to December 1983. The frequencies of the signals received are 5.0, 8.0 and 10.0 MHz, but only the 8.0 MHz signals are used for the present study, because no ambiguities due to the interference among other stations such as BPM, BSF, etc. exist by the use of 8.0 MHz.

The technique for recording the frequency fluctuations of the received signals is similar to the one described by TSUTSUI (1983). The output signals from receivers were recorded digitally every 10 seconds on magnetic cassette tapes. The cross-spectrum analyses based on the FFT method have been used to obtain the horizontal phase velocities (and directions) of the atmospheric gravity waves in the F-region. The data window is 5 h 41 m 20 sec, and it has been shifted by every 5 min increment in the whole data set (8 hrs). The spectral peaks of the data at the three stations are compared, and only the events in which the frequency of the gravity wave ranges from 20 to 70 min and the coherence between any two stations greater than 0.5 have been selected for the present analysis.

Two main results concerning the horizontal phase velocity of the atmospheric gravity waves with periods of 40-70 min may be summarized as follows:

1. The value of the phase velocity ranges from 50 m/s to 300 m/s (Figure 2).
2. The direction of the gravity wave propagation shows a definite seasonal variation (Figure 3). The prevailing direction of the gravity waves in winter is from north to south, which is consistent with the results obtained from other investigations. On the other hand, the two directions, from northeast to southwest and from southeast to northeast, dominate in summer (Figure 3).

Furthermore, the horizontal phase velocities of the gravity waves often show somewhat systematical changes, depending on their azimuthal angles of propagation (Figure 4). This may be thought as the manifestation of the effect of the background wind flow, because if the gravity wave propagates in the same direction as that of the wind, the apparent horizontal phase velocity observed will be larger than the actual one, and vice versa. Therefore, it may be concluded that the azimuth with minimum phase velocity corresponds to the direction of the background wind and the average phase velocity represents the approximate value of the wind velocity. Thus, the background wind velocities and directions may be estimated from Figure 4. Although the number of the data available for the present analysis is limited, the gross features obtained are as follows.

3. In winter to spring, the value of the background neutral wind velocity is of the order of 100 m/s, and the wind direction is

mainly from south to north. These are consistent with the theoretical calculation of DICKINSON et al. (1977) (Figure 5).

4. In summer to fall, the value of the background neutral wind velocity is also of the order of 100 m/s, while two directions dominate: one is from north to south and the other is from north-east to southwest.

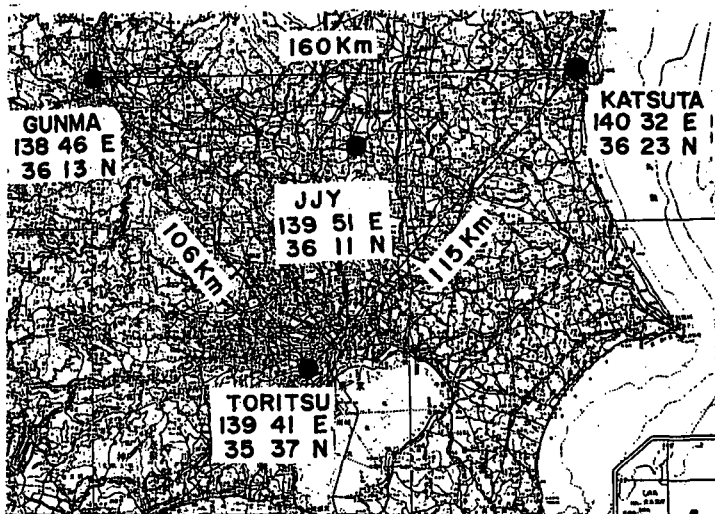
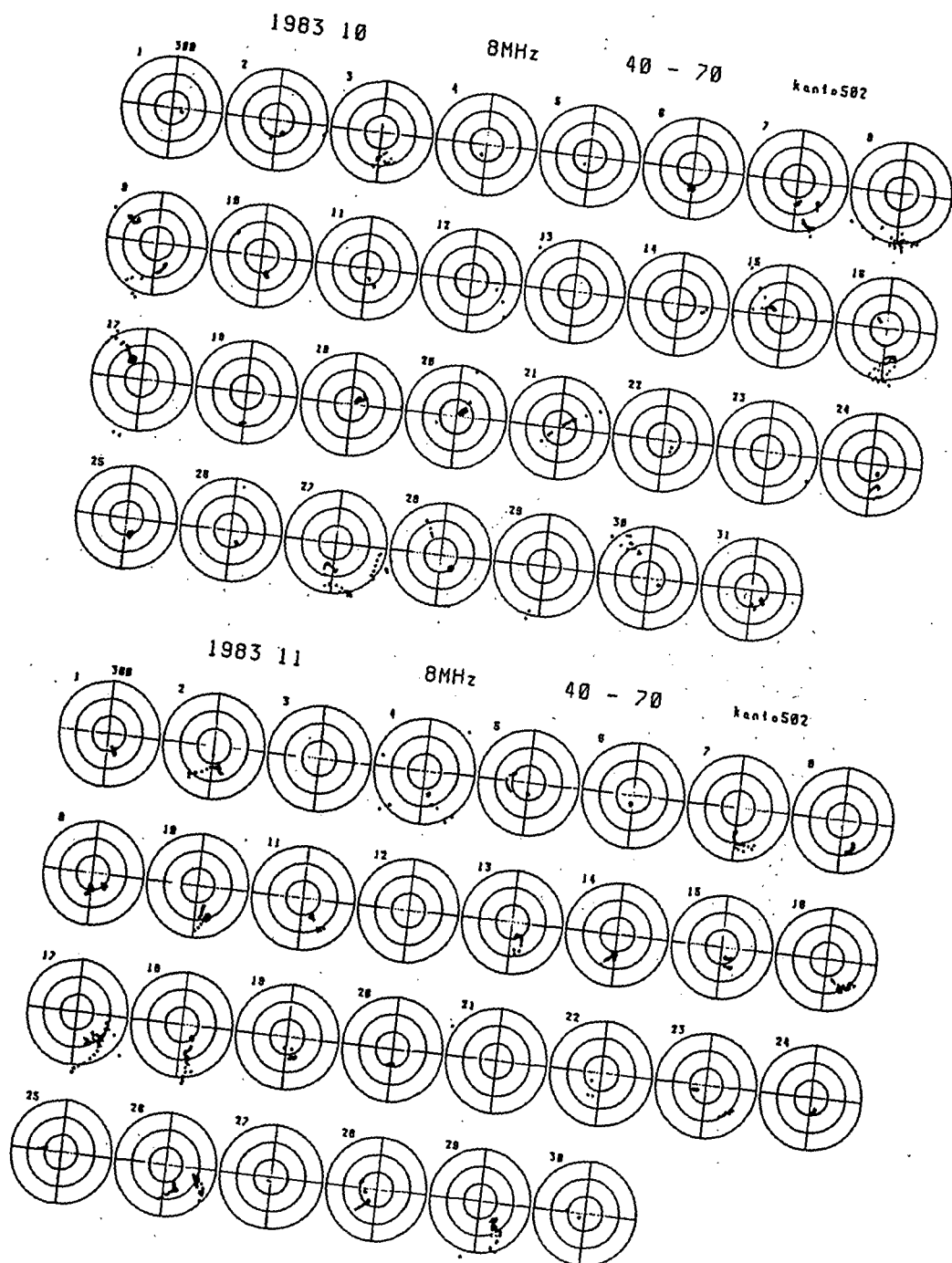


Figure 1.



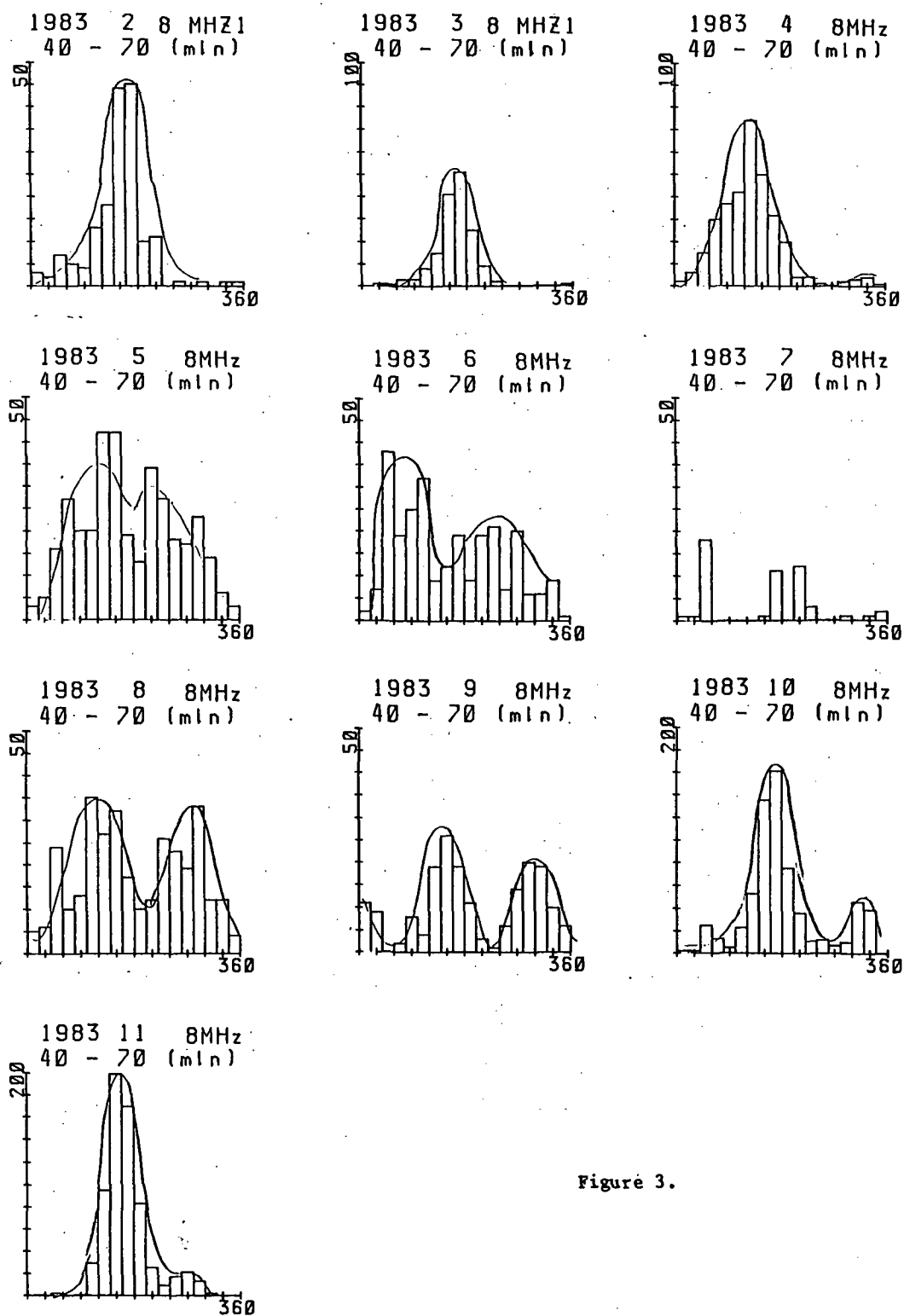


Figure 3.

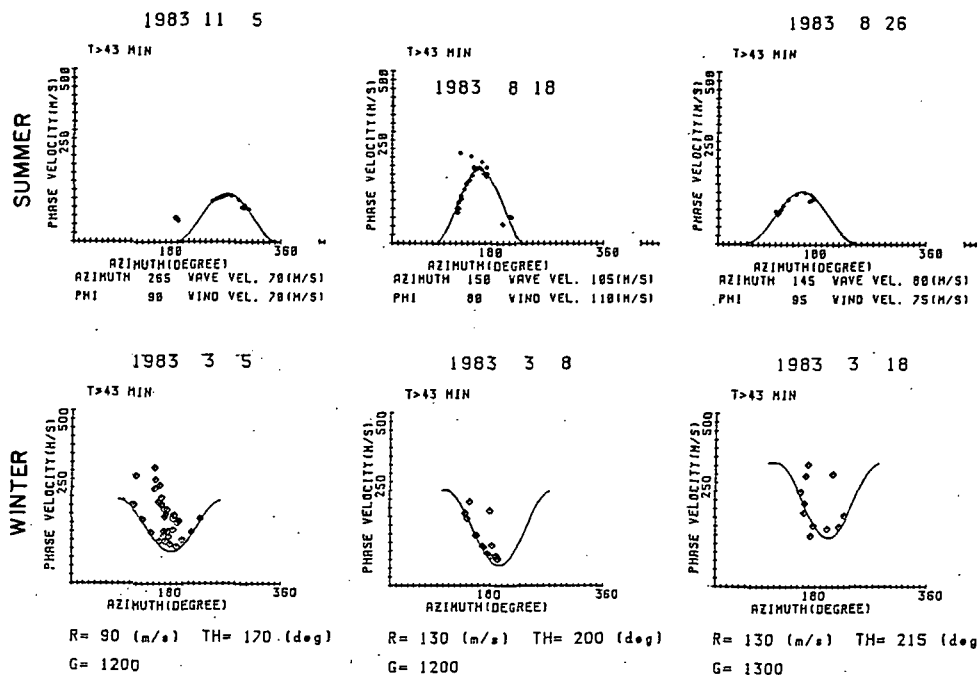


Figure 4.

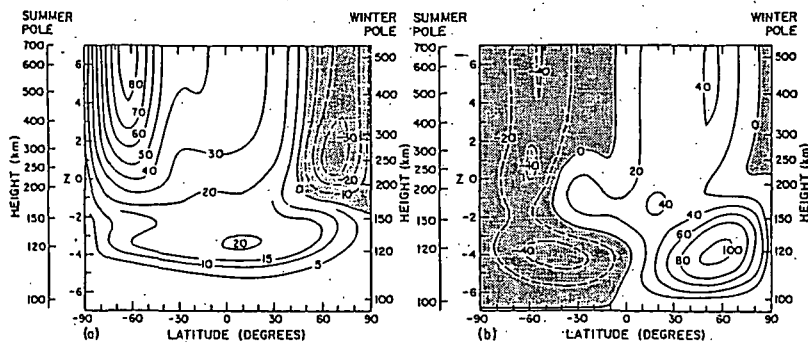


Figure 5.

REFERENCES

- Tsutsui, M. (1983), Ph. D. Thesis, Kyoto University in Japan.
- Dickinson, R. E., E. C. Ridley and R. G. Roble (1977), *J. Atmos. Sci.*, **34**, 178-192.

3.35 OBSERVATION OF THE IONOSPHERIC EFFECT OF TYPHOONS BY A NETWORK OF HF-DOPPLER SOUNDERS IN CENTRAL JAPAN

T. Okuzawa*, T. Shibata*, T. Ichinose**, C. Nagasawa***,
I. Nagano+, M. Mambo+, M. Tsutsui++, and T. Ogawa++

*Department of Applied Electronic Engineering,
University of Electro-Communications,
Chofu-shi, Tokyo 182, Japan

**Department of Electronics,
Doshisha University, Kyoto 602, Japan

***Department of Electrical Engineering,
Tokyo Metropolitan University, Tokyo 158, Japan

+Department of Electrical Engineering
Kanazawa University, Kanazawa 920, Japan

++Radio Atmospheric Science Center,
Kyoto University, Uji 611, Japan

A network of high-frequency CW Doppler sounders detected wave-like ionospheric disturbances during two typhoon periods in September, 1982. The disturbances were observed when severe storm weather occurred within a circle of radius 450 km or so about the radio reflection (mid-path) point in the ionosphere.

Dynamic spectral analyses of the disturbances indicate that there are, in general, one to several peaks of infrasound power which appear in the period range between 2 and 9 min. The spectral content of the wave varies from one typhoon to another, and at times varies from station to station whose radio reflection points are separated at distances from 20 to 200 km. The spectral characteristics of the disturbances varied from hour to hour for a given typhoon.

These variable features may not be explicable only on the basis of the atmospheric filtering action (GEORGES, 1968) and/or the resonant interactions between the infrasonic waves and the atmospheric temperature structure (JONES and GEORGES, 1976). Therefore, we are in favor of the view that characteristics of the infrasound sources in turbulent storm cells, with a certain effect of the irregularities inherent in the ionosphere, are responsible for the observed spectral periods.

Cross-correlation analyses have also been made on sample records to obtain the phase velocity, the wavelength and the azimuth of the propagating disturbances.

REFERENCES

- Georges, T. M. (1968), HF Doppler studies of traveling ionospheric disturbances, J. Atmos. Terr. Phys., **30**, 735-746.
- Jones, R. M. and T. M. Georges (1976), Infrasound from convective storms. III. Propagation to the ionosphere, J. Acoust. Soc. Am., **59**, 765-779.

3.36 A CORRELATION STUDY OF STRUCTURES OF SPORADIC E IONIZATION CLOUDS BASED ON VHF RADIO PROPAGATION MEASUREMENTS

K. Marubashi, S. Kainuma, T. Ishimine, and Y. Shimizu

Radio Research Laboratories
Koganei-shi, Tokyo 184, Japan

Measurements of E_s-reflected VHF radio signals were made for twenty-four propagation paths over Japan in summer seasons of 1982 and 1983. The radio frequencies used were in the range of 80 to 90 MHz, and the propagation path length ranges from 500 km to 2000 km. Electron densities of E_s clouds, or equivalently, f_oE_s values at the path midpoint can be obtained from the signal strength measurements by means of the statistical relation between the f_oE_s and the ionospheric attenuation associated with E_s-reflection. In our measurements, f_oE_s thus obtained ranges from about 10 MHz to 20 MHz, the minimum detectable value of f_oE_s being dependent on the radio frequency used and the propagation path length as well as on the power of transmitted wave and the receiver sensitivity. The cross-correlation analysis of these f_oE_s data allow us to look into structures of E_s clouds of scales as small as 10 km. The result of analysis made so far reveals a very sporadic nature of E_s clouds in both space and time, as the name implies, which is related with atmospheric and/or ionospheric turbulence. However, well-correlated variations are often seen in relatively large scale structures (>50 km). It was found that such structures move typically at a speed of 100 m/s in the east-west direction.

3.37 SATELLITE OBSERVATIONS OF 557.7 NM AIRGLOW AS A
DIAGNOSTIC TECHNIQUE TO STUDY THE DYNAMICS OF THE LOWER THERMOSPHERE

L. L. Cogger, R. Elphinstone and J. S. Murphree

The University of Calgary, Dept. of Physics,
Calgary, Alberta, Canada T2N 1N4

Photometric observations of the airglow limb at 557.7 nm have been made from the ISIS 2 satellite since 1971. From an analysis of 32,000 airglow limb observations obtained during the first two years of operation, the major temporal and spatial characteristics of the night airglow have been identified. Maxima occur in mid-October and mid-April at all latitudes. There is a marked variation with latitude during the equinox periods, with peak intensities near 35 degrees in autumn and near 25 degrees in spring. It is possible to gain considerable insight into the behaviour of the lower thermosphere by combining the airglow observations with a simple model of the photochemical and dynamical processes. In this way a pattern of the latitudinal and temporal variation of atomic oxygen concentration at the peak of the layer as well as the eddy diffusion in this altitude region have been inferred.

The concentration of atomic oxygen shows midlatitude peaks near equinox, and minima about one month after solstice. Average values at midlatitudes are about 1.3 times those at the equator. The amplitude of the semiannual component is about 20% of the mean value at 35 degrees as compared to 10% at the equator, and the amplitude of 12-month component is about 12% at 35° and 5% at the equator. The semiannual component has a minimum that occurs approximately 3 weeks (+1 week) after solstice at all latitudes, while the 12-month component peaks in the summer hemisphere at solstice (+2 months).

Turbulence is largest near the equator. The amplitude of the semiannual variation in turbulence varies from about 60% of the mean value at 35 degrees down to only about 15% at the equator. The corresponding amplitudes of the 12-month components are 40% and 10%. The semiannual component of eddy turbulence peaks approximately 3 weeks (+1 week) after solstice with the 12-month component peaking shortly after spring equinox.

A consistent circulation pattern in the vicinity of 90 to 100 km is for poleward meridional winds of 5-10 m/s at equinox accompanied by upward winds at the equator and downward winds at midlatitudes. Near solstice, there is summer to winter flow at high altitudes (>110 km) accompanied by a return meridional flow below about 105 km.

3.38 LOCAL TIME DISTRIBUTION OF THE SSC-ASSOCIATED HF-DOPPLER FREQUENCY SHIFTS

T. Kikuchi, H. Sugiuchi and T. Ishimine

Radio Research Laboratories
Koganei, Tokyo 184, Japan

The HF-Doppler frequency shift observed at the storm's sudden commencement is composed of a frequency increase (+) and decrease (-), and classified into four types, SCF(+ -), SCF(- +), SCF(+) AND SCF(-). Since the latter two types are special cases of the former two types, two different kinds of electrical field exist in the F region and cause the $E \times B$ drift motion of plasma. HUANG (1976) interpreted the frequency increase of SCF(+ -) as due to the westward induction electric field proportional to $\partial H / \partial t$ and the succeeding frequency decrease due to the eastward conduction electric field which produces ionospheric currents responsible for the magnetic increase on the ground. In spite of his success in interpreting the SCF(+ -), some other interpretations are needed for the explanation of the whole set of SCF's, particularly SCF(- +).

Local time distributions of the SCF's are derived from 41 SCF's which are observed on the HF standard signal (JJY) as received in Okinawa (path length =1600 km) and Kokubunji (60 km). It is shown that the SCF(+ -) appears mainly during the day, whereas the SCF(- +) is observed during the night. The results indicate that the preliminary frequency shift (+) of SCF(+ -) and (-) of SCF(- +) is caused by a westward electric field in the dayside hemisphere, while by an eastward electric field in the nightside hemisphere. The main frequency shift [(-) of SCF(+ -) and (+) of SCF(- +)] is caused by the reversed electric field. Consequently, the preliminary frequency shift is caused by the dusk-to-dawn electric field, while the main frequency shift by the dawn-to-dusk electric field.

It is known that the preliminary reverse impulse of SC^{*} is produced by the ionospheric current of DP-2 type, which is generated by the dusk-to-dawn electric field in the polar region (ARAKI, 1977). The dusk-to-dawn electric field derived from the local time distribution of SCF's at the low latitude may indicate the equatorward transmission of the polar electric field associated with the preliminary reverse impulse of SC^{*}, in agreement with the theoretical study showing the instantaneous transmission of the polar electric field to the equator (KIKUCHI and ARAKI, 1979).

REFERENCES

- Araki, T. (1977), Planet. Space Sci., **25**, 373.
Huang, Y. N. (1976), J. Geophys. Res., **81**, 175.
Kikuchi, T. and T. Araki (1979), J. Atmos. Terr. Phys., **41**, 927.

78473-284

3.39 VERTICAL STOKES DRIFTS PRODUCED BY VERTICALLY PROPAGATING INTERNAL GRAVITY WAVES IN A COMPRESSIBLE ATMOSPHERE

L. Coy and J. Weinstock

NOAA/Aeronomy Laboratory
Boulder, CO 80303

D. Fritts

University of Alaska
Fairbanks, AK 99701

Upward propagating internal gravity waves in a compressible atmosphere are shown to have a non-zero vertical mass flux which is due to an upward Stokes drift. In order to maintain a steady balance in the absence of dissipation and diabatic heating, the upward Stokes drift will be opposed by a downward mean Eulerian velocity such that the Lagrangian vertical velocity is zero.

The magnitude of the Stokes drift is estimated for a single wave and found to depend strongly on the intrinsic phase speed and horizontal wavelength of the wave. For intrinsic phase speeds of 40-50 m/s and horizontal wavelengths of 100-200 km, the magnitude of the Stokes drift for a large amplitude wave (that is, a wave near "breaking" amplitude) is on the order of 1-10 cm/s. The downward mean Eulerian velocity implied by the Stokes drift may be able to explain the mean downward motions observed in the summer mesosphere by the MST radar at Poker Flat, Alaska.

4.1 TRANSPORT PROCESSES AS MANIFESTED IN SATELLITE AND LIDAR AEROSOL MEASUREMENTS

M. P. McCormick

National Aeronautics and Space Administration
Langley Research Center,
Hampton, VA 23665

A large increase in stratospheric aerosol data has become available recently from the SAM II and SAGE satellite sensors and the impetus from increased volcanic perturbations. Six years of SAM II and nearly 3 years of SAGE measurements have been accumulated. The increase in large volcanic eruptions since 1979 has caused an acceleration of new data sets from worldwide lidars and airborne lidar campaigns and from various airborne in situ measurements.

The SAM II and SAGE data sets show the tropical stratosphere as a source for background stratospheric aerosols, and midlatitudes as a possible sink. Analyses of SAM II data show that the aerosol within the northern-wintertime polar vortex becomes isolated from the outside. Subsidence occurs within the vortex, changing the vertical aerosol distribution over the winter period. SAM II and SAGE data show that the aerosol is transported in the stratosphere from low to high latitudes in wintertime. Entry regions of tropospheric air in the Tropics are also evident in the SAGE data as shown by stratospheric cirrus clouds being formed well above the local tropopause.

Nature has provided over the past 5 years a number of large volcanic eruptions which spewed tonnes of new aerosol into the stratosphere. These eruptions have occurred at various latitudes which allow transport differences to be studied. Satellite and lidar aerosol data will be used to describe the stratospheric motions of aerosols produced after these violent volcanic eruptions.

4.2 RUBY LIDAR OBSERVATIONS AND TRAJECTORY ANALYSIS OF STRATOSPHERIC AEROSOLS INJECTED BY THE VOLCANIC ERUPTIONS OF EL CHICHON

O. Uchino, T. Tabata, I. Akita, Y. Okada and K. Naito

Meteorological Research Institute, Yatabe, Tsukuba
Ibaraki 305, Japan

Large amounts of aerosol particles and gases were injected into the lower stratosphere by the violent volcanic eruptions of El Chichon on March 28, and April 3 and 4, 1982. In this report, observational results obtained by a ruby lidar at Tsukuba (36.1°N , 140.1°E) are shown, and some points of latitudinal dispersion processes of aerosols are discussed.

Figure 1 shows the vertical profiles of scattering ratio R observed at Tsukuba where R is defined by a ratio of total backscattering coefficients to atmospheric molecular backscattering coefficients. After the eruptions, a new aerosol layer was detected at an altitude of 15 km on April 25. On May 5, a dominant layer with the maximum scattering ratio R_{max} of about 12 was observed at 23 km with the sub-layer around 15 km. After large fluctuations of R_{max} occurred in the first 5 months, R_{max} began to increase in September. In October, the two layers merged into a layer with a broad vertical width of R . The backscattering coefficient of aerosols integrated vertically; B exhibited enhancements in May and December 1982, and then B decreased gradually at Tsukuba (UCHINO et al., 1984).

Figure 2 shows schematically the global dispersion processes of the El Chichon particles observed by lidars. The leading edge of the particles below 20 km attained to midlatitudes a month faster than that above 20 km, and R_{max} below 20 km was recorded two months faster than that above 20 km.

Figure 3 shows the latitudinal variations of the optical thickness of the stratospheric aerosols. Until October 1982, the El Chichon clouds were confined in low latitudes. Since late November, transport of the aerosols to midlatitudes was largely active. In May 1983, the peak of B was at about 50°N , the minimum at 30°N , and a small maximum near to the equator (McCORMICK et al., 1984).

A theoretical model simulation of very long-term motions of the marked air particles in the troposphere and stratosphere by KIDA (1983) seems to depict some characteristics mentioned above. It is also interesting to compare these characteristics of the dispersion processes of the El Chichon particles with a trajectory analysis on an isobaric surface.

To calculate trajectories of the El Chichon particles every one hour, a method of interpolation was used for the wind data (the Objective Analysis Model of Japan Meteorological Agency) of intervals of 5×5 degrees and 12 hours. On April 4, 49 particles were initially placed in the range of a radius of about 850 km, of which the center was situated at El Chichon. The initial positions are based on the observations of Nimbus 7 satellite (KRUGER, 1983). Their trajectories were calculated during the following three months. Most of the particles on the 100-mb surface moved eastward. Particles initially placed at the extreme northern border of El Chichon circled around the globe during three months, and moved northward to some extent. First increase of R in the lower layer over Japan was simulated in this trajectory analysis. During May and June the particles were dispersed into high latitudes and meandered about north and south (UCHINO, 1985). Figure 4 shows instantaneous positions of the particles on April 30, May 30 and June 29. It is clear that the leading edge of the particles on the 100-mb surface moved to high latitudes within about

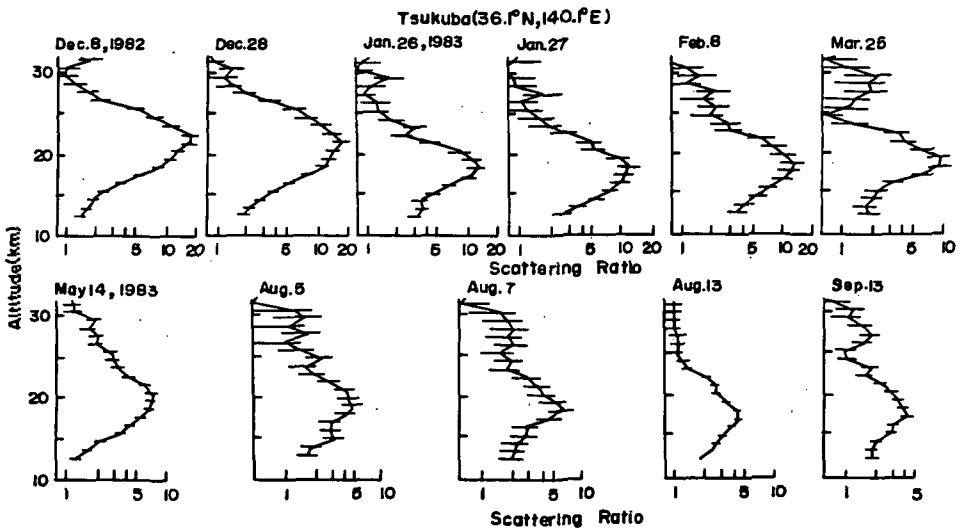
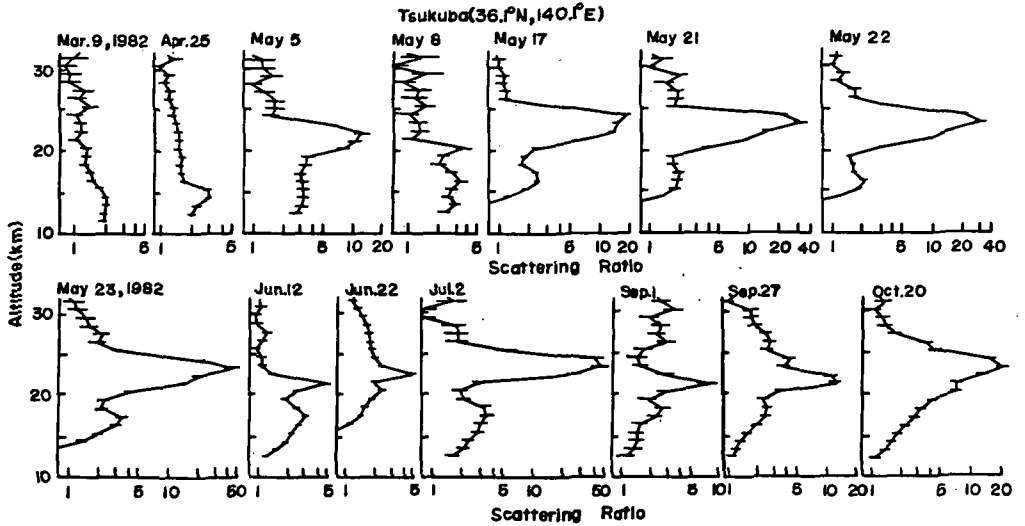


Figure 1. (a) and (b) Vertical profiles of backscattering ratios observed at Tsukuba by the MRI ruby lidar. The bars represent one standard deviation.

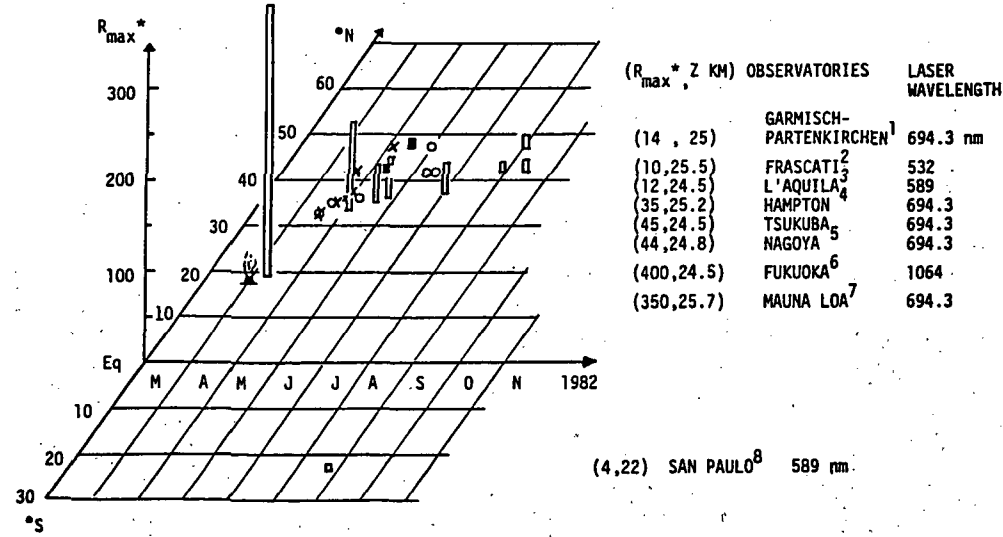


Figure 2. Dispersion of the El Chichon clouds in the lower stratosphere observed by lidars during April through October 1982.
 R_{max}^* = the largest value of the scattering ratio observed in this period, z = the altitude of R_{max}^* ,
 \square, \blacksquare = R_{max}^* observed respectively above $z = 20$ km and below $z = 20$ km
 \circ, \times = the first increase of R observed respectively above 20 km and below km. These data are quoted from: REITER et al., 1983; ADRIANI et al., 1983; D'ALTORINO et al., 1983; SEAN Bulletin, 1983; IWASAKA et al., 1983; HIRONO and SHIBATA, 1983; DELUISI et al., 1983; and CLEMESHA and SIMONICH, 1983.

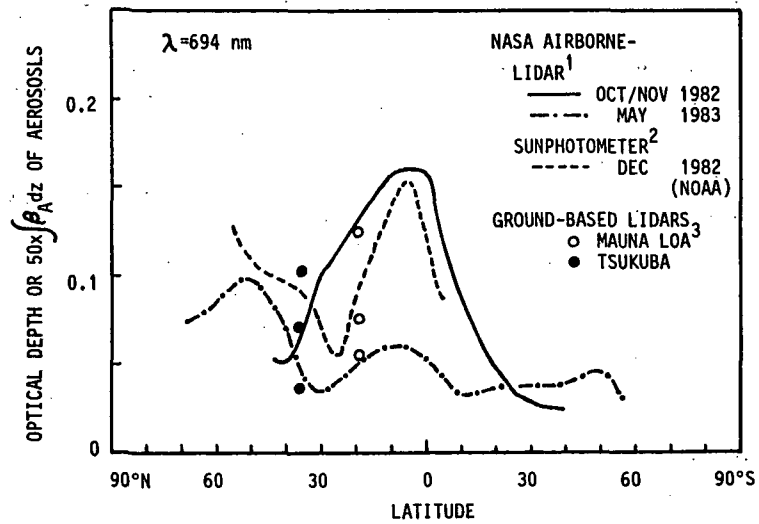


Figure 3. Latitudinal variations of the optical depth or a constant of 50 multiplied by the integrated backscattering coefficient of stratospheric aerosols. Data are quoted from: MCCORMICK and SWISSLER (1983); DUTTON and DELUISI (1983); and SEAN Bulletin 1982 and 1983.

ORIGINAL PAGE IS
OF POOR QUALITY

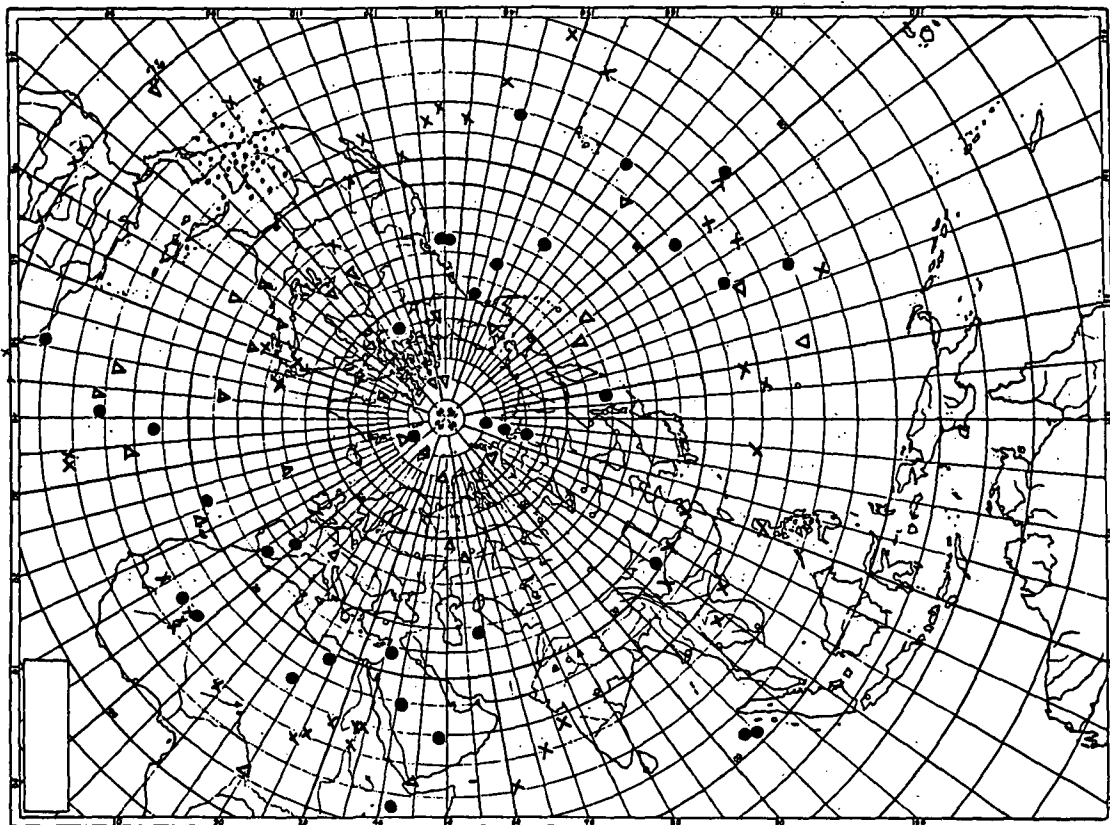


Figure 4. Instantaneous positions of the El Chichon particles on April 4 (•), April 30 (x), May 30 (●), and June 29 (Δ), 1982.

three months. The rate of dispersion of the particles (1 deg/day) is similar to the observational results by lidars.

Trajectories of the El Chichon particles on the 30-mb surface were also calculated with the same initial positions of the particles as those on the 100-mb surface. These particles moved westward, and about ten percent of the particles traveled around a semicircle of the globe during April. This result is not consistent with the observational result by a satellite (ROBOCK and MATSON, 1983). The satellite data show that the particles moved westward and traveled completely around the globe in three weeks and distributed over a latitude band of $20^{\circ}\text{N} \pm 10$ approximately on April 25. The inconsistency would be caused by the defect of wind data of the OAM in latitudes below 20°N . To travel around the globe on a latitude range of 10°N – 20°N in three weeks, the mean zonal wind speed is estimated to be 21.7–20.7 m/s, which is comparable to that obtained from the Monthly Climate Data for the World in April 1982.

Based on this result, a uniform distribution of 45 particles was assumed initially around a latitude circle of 20°N on April 26, 1982. Their trajectories are shown in Figure 5. During the first four months after the eruptions, the particles on the 30-mb surface were dispersed as far as 60°N . From this calculated trajectory analysis, a rate of the dispersion of the particles on the 30-mb surface was also slower than that on the 100-mb surface.

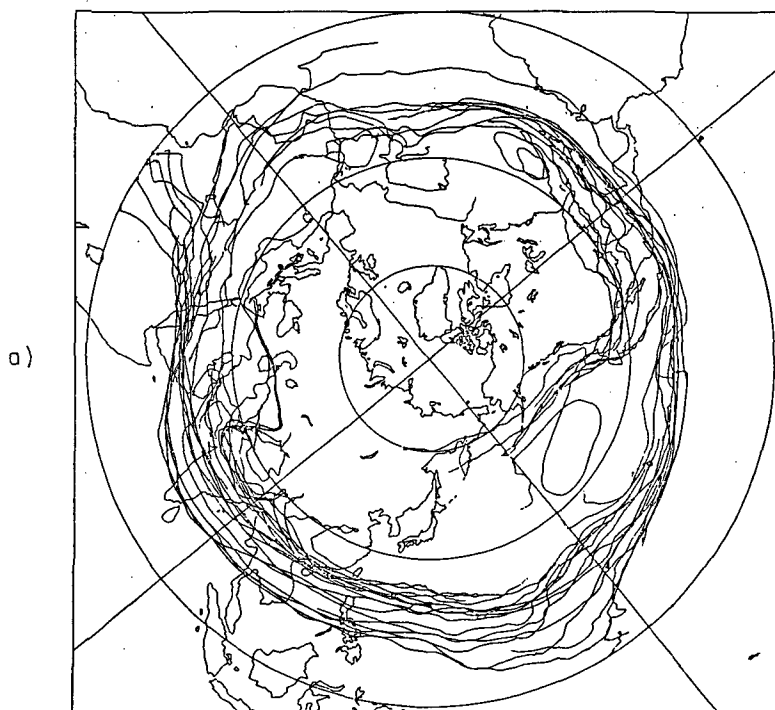
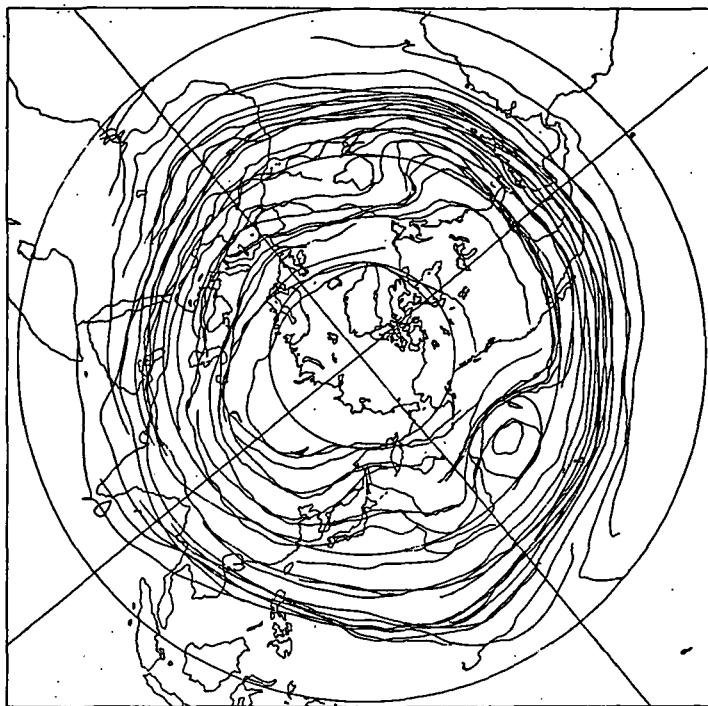


Figure 5. Trajectories of the particles on the 30-mb surface during the period of (a) April 26– May 25, (b) May 26– June 24, (c) June 25– July 24, 1982. Initially a uniform distribution of 45 particles was placed around a latitude circle of 20°N .

b)



c)

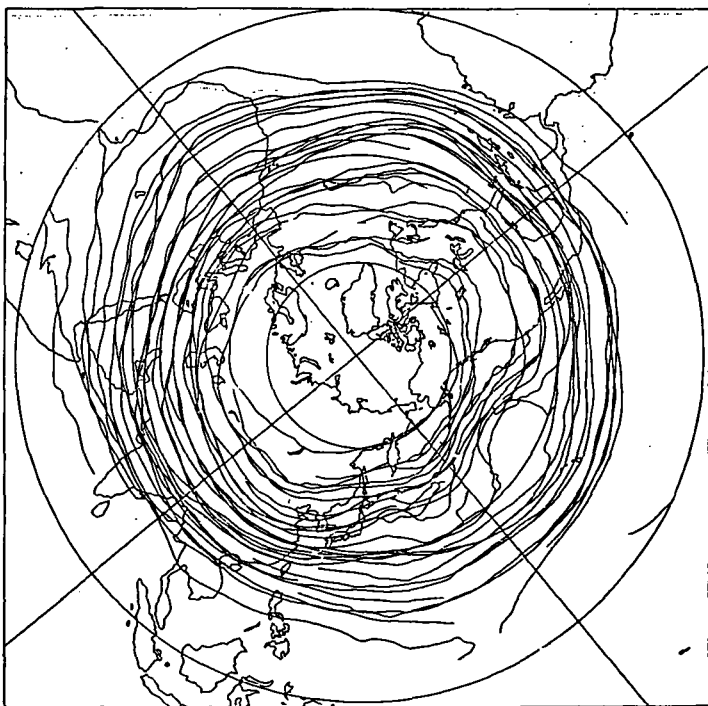


Figure 5 continued.

REFERENCES

- Adriani, A., F. Congeduti, G. Fiocco and G. P. Gobi (1983), Geophys. Res. Lett., 10, 1005.
- Clemesha, B. R. and D. M. Simonich (1983), Geophys. Res. Lett., 10, 321.
- D'Altorio, A. and G. Visconti (1983), Geophys. Res. Lett., 10, 27.
- DeLuisi, J. J., E. G. Dutton, K. L. Coulson, T. E. DeFoor and B. G. Mendonca (1983), J. Geophys. Res., 88, 6769.
- Dutton, E. and J. DeLuisi (1983), Geophys. Res. Lett., 10, 1013.
- Hirono, M. and T. Shibata (1983), Geophys. Res. Lett., 10, 440.
- Kida, H. (1983), J. Meteorol. Soc. Japan, 61, 510.
- Kruger, A. J. (1983), Science, 220, 1337.
- McCormick, M. P. and T. J. Swissler (1983), Geophys. Res. Lett., 10, 877.
- McCormick, M. P., T. J. Swissler, W. H. Fuller, W. H. Hunt and M. T. Osborn, Geof. Int., 23, 187.
- Reiter, R., H. Jager, W. Carnuth and W. Funk (1982), Geophys. Res. Lett., 10, 1001.
- Robock, A. and M. Matson (1983), Science, 221, 195.
- SEAN Bulletin (1982), 7, No. 3-12.
- SEAN Bulletin (1983), 8, No. 1-8.
- Uchino, O., K. Takahashi, I. Tabata, I. Akita, Y. Okada and K. Naito (1984), J. Meteorol. Soc. Japan, 62, 288.
- Uchino, O. (1985), J. Meteorol. Soc. Japan, 63, 288.

4.3 LIDAR OBSERVATIONS OF THE EL CHICHON CLOUD IN THE STRATOSPHERE OVER FUKUOKA

M. Fujiwara, *T. Shibata and M. Hirono

Department of Physics, *Department of Electrical Engineering
Kyushu University, Fukuoka 812, Japan

A volcanic cloud in the stratosphere, originating from the March-April 1982 eruptions of El Chichon, has been observed for about 2.5 years at Fukuoka (33.5°N, 130.4°E) with two wavelengths of Nd-YAG lidar, 1.06 and 0.53 μm . Time and height variabilities of the cloud are described, using the 1.06 μm data, and some results of the two-wavelength measurements are presented.

A sudden enormous increase in the total aerosol backscattering from the stratosphere (backscattering coefficient for 1.06 μm integrated over 13.5-28.5 km range) was followed by a decrease from late spring to summer with large fluctuations. The cloud initially appeared stratified into two layers: the upper one with fine structure and sharp edges in the easterly wind region and the lower dumpy one in the westerly wind region. Most of the aerosols were contained in the upper layer. The two layers merged into a broad, single-peaked layer as the easterly prevailed in the whole region in Fall, when the total aerosol backscattering began to increase. The layer then decreased its peak height as it broadened. The difference in shape of both layers and the increase of total backscattering from Fall can be interpreted by the difference in velocity of material transport in the easterly and the westerly wind region. The behavior of the cloud in the year of eruption is described and discussed more in detail elsewhere (SHIBATA et al., Poster Session).

The increase of the total aerosol backscattering and the change in shape of the layer were accompanied by the variation of wind field in the vicinity of the layer, also, in the subsequent years. As the height of the layer peak was lying around 18 km in these years, easterly winds prevailed at the layer height only in a few months in summer.

Figure 1 shows the time variability of the total backscattering in the two years from December 1982. A line is drawn in the figure by the least-square method, the gradient of which shows the decay of the aerosol content with a time constant of about 9 months in these two years. Being superposed on this decay, a seasonal variation can be seen with a maximum in late Winter or early Spring and a minimum in Summer. The increase from Fall (relative to the line of steady decay) is inferred to reflect the change of the prevailing wind.

In Figure 2 the time variabilities of the peak height and the layer width in 1983 are shown. Tropopause and the wind field are also indicated. A thin stable layer persisted only in a short period from late June to early September, when the easterly prevailed at the layer height. From Fall of 1983 to Spring of 1984 the layer descended down slightly and broadened, as it had done a year before. The increase of the layer height and the decrease of both the layer width and the total backscattering from Spring to Summer seem to be related to the variation of tropopause height to some extent.

Some examples of the ratio of the backscattering coefficient for 0.53 μm to that for 1.06 μm are shown in Figure 3. As the ratio is very sensitive to the normalization process, we chose only the data obtained in the spring of 1983 and 1984, when the height profiles of backscattering have little fluctuations in the region above 30 km. The profiles of both years are very similar, with a few exceptions. The ratio has its minimum value around the height of the layer peak and increases remarkably with height. This indicates that the

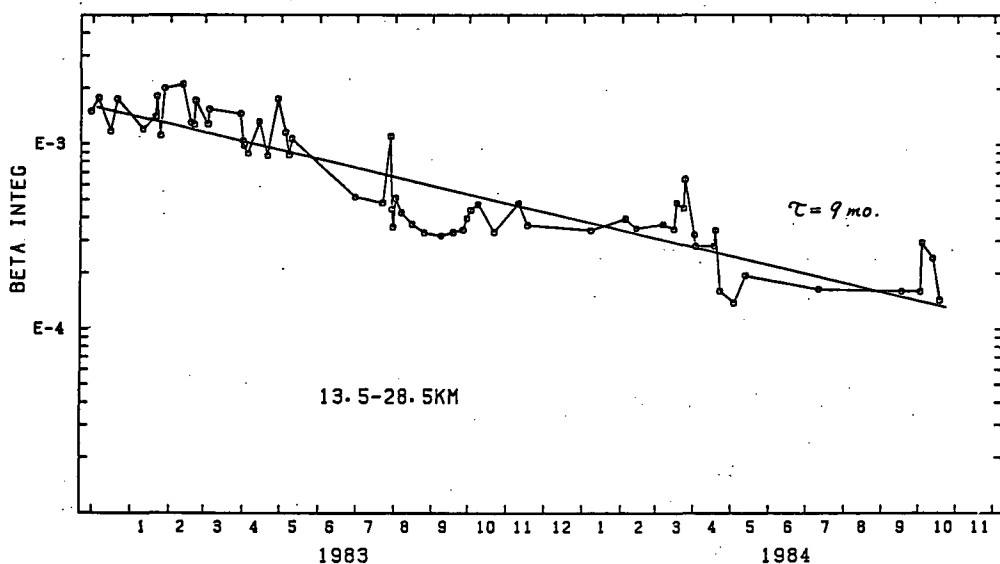


Figure 1. Time variability of aerosol backscattering coefficient for $1.06 \mu\text{m}$ integrated over 13.5-28.5 km in 1983 and 1984.

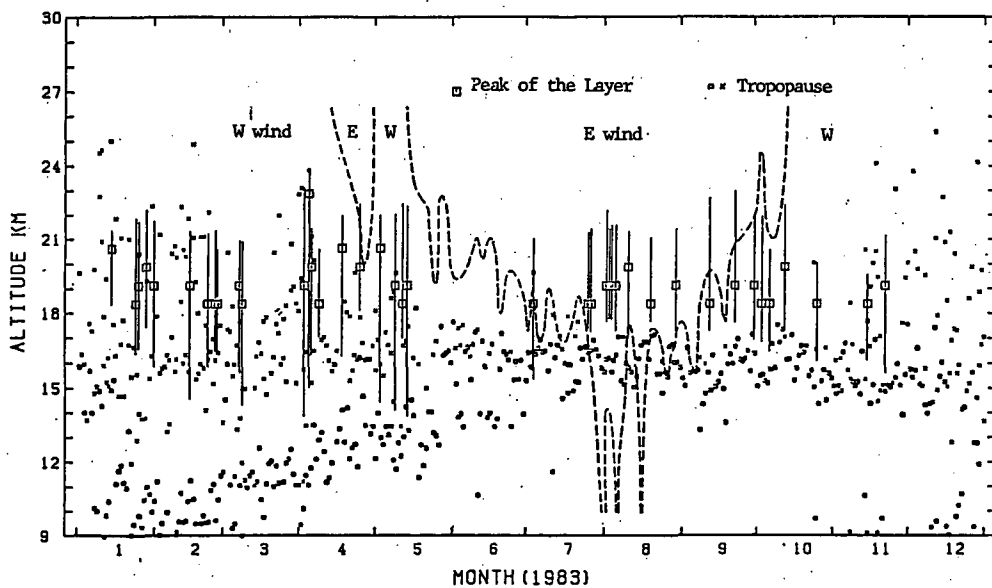


Figure 2. Time variabilities of the peak height and the width of the aerosol layer (scattering ratio minus 1) in 1983. Tropopause and prevailing wind are also indicated.

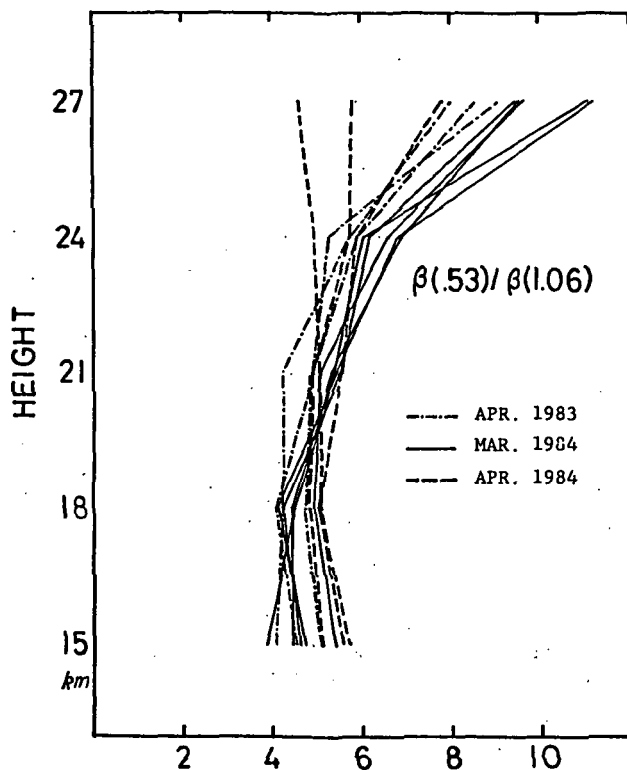


Figure 3. Ratio of the aerosol backscattering coefficient for $0.53 \mu\text{m}$ to that for $1.06 \mu\text{m}$ observed in the spring of 1983 and 1984.

aerosols are larger at the layer peak than the lower or higher regions. Values of the ratio, around 4.5 at 18 km, correspond to values of more than 10 in the channel ratio, $n(r > 1.5 \mu\text{m})/n(r > 2.5 \mu\text{m})$, if the usual types of size distribution function and values of the refractive index are assumed. Values of the ratio need to be examined more carefully.

4.4 ON THE LONG TERM VARIATION OF STRATOSPHERIC AEROSOL CONTENT AFTER THE ERUPTION OF VOLCANO EL CHICHON: LASER RADAR MEASUREMENTS

S. Hayashida and Y. Iwasaka

Water Research Institute, Nagoya University
Furo-cho, Chikusa-ku, Nagoya 464, Japan

We present here the results of measurements of the stratospheric aerosol layer by a ruby lidar ($\lambda=0.6943 \mu\text{m}$) for two years after the eruption of El Chichon (March 29, April 4, 1982, Mexico). The results show the sudden increase in the stratospheric aerosol content after the eruption and its subsequent decline.

THE VARIATION OF THE PROFILES OF THE SCATTERING RATIO AND WIND SYSTEM IN THE LOWER STRATOSPHERE.

The profiles of the scattering ratio observed from April 1982 to January 1983 after the eruption of El Chichon are shown in Figure 1 (IWASAKA and HAYASHIDA, 1983). The increase in the scattering ratio was measured first around 27 km about 20 days after the eruption. Transport processes were connected with the global wind system in the lower stratosphere. From the end of April, the apparent two-layer structure was observed. The upper aerosol layer was observed in the easterly wind region above about 20 km. The upper layer contains most part of aerosols, and it was confined to lower latitude region, possibly due to the absence of the planetary wave (HIRONO et al., 1985).

After September 1982, wind direction changed westerly in the stratosphere. The scattering ratio profiles formed a single broader peak around 24 km (Figure 1). Through this period, the volcanic aerosols dispersed northwards. After the end of November 1982, the peak value of the scattering ratio decreased and the aerosol layer became broader.

MEASUREMENTS OF THE TOTAL BACKSCATTER DEPOLARIZATION RATIO

IWASAKA and HAYASHIDA (1981) describe the detailed procedure in which the total backscatter depolarization ratio (we call it the depolarization ratio for short here) is derived. Depolarization ratio (δ) is given by the ratio of intensity of backscattered light polarized perpendicular (Pr_\perp) to the plane of polarization of the transmitted laser pulse to that polarized in parallel (Pr_\parallel).

The depolarization ratio is usually less than 5%. Figure 2 shows the increase in the depolarization ratio observed in May and its decay in September 1982. The values larger than 10% were observed for about 4 months at around 20 km continuously (Figure 1). When the scattering ratio was large, the perpendicular component of the backscattered light can be regarded as the backscattered light from aerosol particles, as a molecular atmosphere yields a depolarization ratio of only several percent. Figure 1 shows that some non-spherical particles existed at around 20 km for several months after the eruption. Those particles were possibly volcanic ash particles such as silicate particles. GOAD (1982) also found a depolarization ratio of about 18% immediately after the volcanic eruption of Mt. St. Helens.

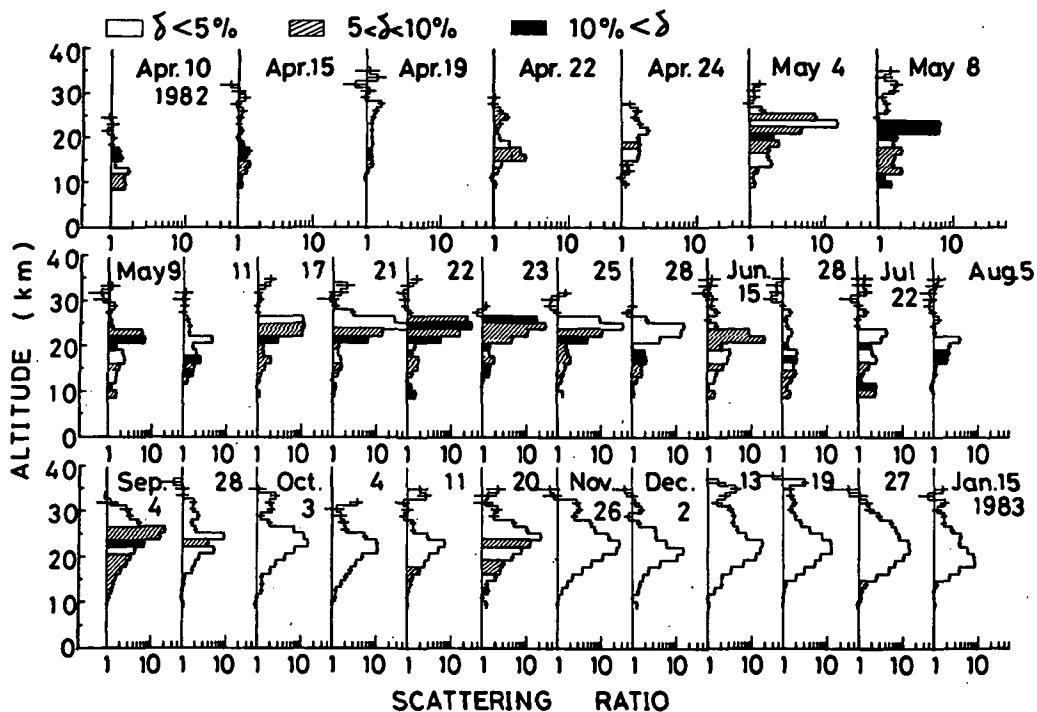


Figure 1. Scattering ratio profiles and depolarization ratio observed from April 10, 1982 to January 15, 1983. Shaded regions show layers of high depolarization ratio.

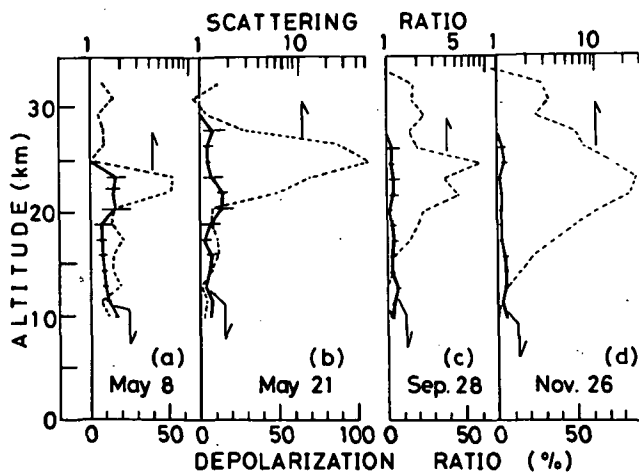


Figure 2. (a) and (b) The increase in depolarization ratio immediately after the eruption of El Chichon.

Figure 2. (c) and (d) The decay of depolarization ratio after September 1982.

ON THE LONG TERM DECAY OF THE STRATOSPHERIC AEROSOL CONTENT (HAYASHIDA, 1985)

Figure 3 shows the time series of the integrated backscattering coefficient (IBC). After the end of November 1982, the IBC value decreased gradually. The pre-injection value was subtracted from the observed values and e-folding decay time of the enhanced amount of stratospheric aerosol content was calculated. The decay times for the indicated periods on the method of least squares are shown in the figure. The decay time depends on the length of the observational period and it becomes longer for longer periods of observation. It seemed that the gravitational settling of large particles caused the fast decay of IBC in the early decay stage.

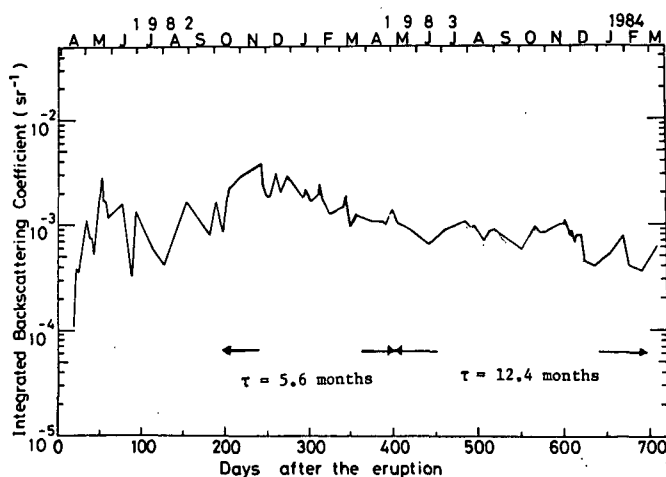


Figure 3. The time series of the backscattering coefficient integrated from 12 km up to 30 km (IBC). The approximate decay times are shown with corresponding observational periods.

REFERENCES

- Goad, J. H. (1982), Atmospheric depolarization ratio decay after the eruption of Mt. St. Helens. Abstracts of papers presented at the Eleventh International Laser Radar Conference, NASA Conference Publication, 2228, 14-16.
- Hayashida, S. and Y. Iwasaka (1983), Lidar observation of stratospheric aerosol increase after the El Chichon eruption: Nagoya April to December 1982, Memoirs of Nat. Inst. Polar Res. Spec. Issue, 29, 191-200.
- Hayashida, S., A. Kobayashi and Y. Iwasaka (1984), Lidar measurements of stratospheric aerosol content and depolarization ratio after the eruption of El Chichon volcano: Measurements at Nagoya, Japan, Geof. Int., **23-2**, 277-288.
- Hayashida, S. and Y. Iwasaka (1985), On the long term variation of stratospheric aerosol content after the eruption of volcano El Chichon, -Lidar measurement at Nagoya, Japan (accepted by J. Meteorol. Soc., Japan).
- Hirono, M., T. Shibata, M. Fujiwara and N. Fujiwara (1984), Enormous increase of volcanic clouds in the stratosphere over Fukuoka after April 1982, Geof. Int., **23-2**, 259-276.
- Iwasaka, Y., S. Hayashida and A. Ono (1983), Increasing backscattered light from the stratospheric aerosol layer after Mt. El Chichon eruption, Laser radar measurement at Nagoya (35 N, 137 E). Geophys. Res. Lett., **10**, 440-442.

4.5 BEHAVIOR OF DECAYING EL CHICHON CLOUD OVER TOYOKAWA, JAPAN (35°N) OBSERVED BY 532-NM LIDAR

M. Takagi, A. Iwata and Y. Kondo

Research Institute of Atmospheric,
Nagoya University,
Toyokawa, Aichi 442, Japan

INTRODUCTION

The stratospheric aerosol state in 1982 and 1983 was in a violent excitation due to the eruption of Mt. El Chichon. A number of direct and indirect soundings of the stratosphere confirmed that the aftereffect of it covered almost the entire Northern Hemisphere by the end of 1982 (e.g., POLLACK et al., 1983). The lidar system constructed by us at Toyokawa (34.8°N, 137.4°E) entered in a routine base observation since December 1982 (IWATA et al., 1983). The start of observation was 8 months after the eruption, and we missed monitoring the drastic variations in the stratosphere just following the event. However, the El Chichon cloud over Japan was reported to have reached the second maximum concentration in November or December 1982 according to the lidar observations at Tsukuba, Nagoya and Fukuoka, so our observations corresponded to the decaying phase of it. Presented are some characteristics of the aerosol profile over Toyokawa during a period of 20 months from December 1982 to July 1984.

OBSERVATIONS AND RESULTS

The data used in this report were obtained at the wavelength of 532 nm, the second harmonic of an Nd:YAG laser. The laser power emitted is 0.5 J/pulse with the repetition of 10 pps. The receiving telescope is a Newtonian type of 50 cm diameter. The lidar system was usually operated in a photon counting mode with a resolution of 300 m in the altitude range 6 to 44 km. An accumulation of received signals for 10 to 30 minutes (6000 to 18000 laser pulse shots) gave an accurate aerosol profile up to 35 km within a 10% measurement error.

The observations were made on almost every fair-weather evening, so the frequency of observations depended on weather conditions in the evening hours. In winter, from December to March, we are favored with good weather and obtain 10 to 16 profiles in a month (and to run after the day-to-day variations in the stratosphere). In other seasons the situation is worse than in winter, but it is still fair enough to see the trend on a long-time scale. Figure 1 shows the variations of the daily aerosol backscattering coefficient integrated in the altitude range from 13.5 to 28.5 km. During this period there were several volcanic activities such as the Una Una eruption in July 1983, but any notable volcanic effects on the stratosphere over Toyokawa were not detected. The values of the integrated backscattering coefficient have descended from $2-4 \times 10^{-3}$ to $6-7 \times 10^{-4} \text{ sr}^{-1}$ during the 20 months. Though there is a slight enhancement in the winter period from November 1983 to February 1984, which may be responsible for the seasonal effect, the trend of the values roughly follows the least square fit decay curve shown in the broken line. The decay time constant is estimated to be 211 days.

As described above, the daily profiles are frequently obtained in winter. Figure 2 is an example of the day-to-day variation of aerosol profiles indicated with contours of the backscattering ratio during 107 days from December 9, 1982 to March 25, 1983 in the beginning part of our observations. The profiles were obtained at evening hours for 55 days. The interruption of daily data, which was interpolated in the figure, was 6 days at the longest during this

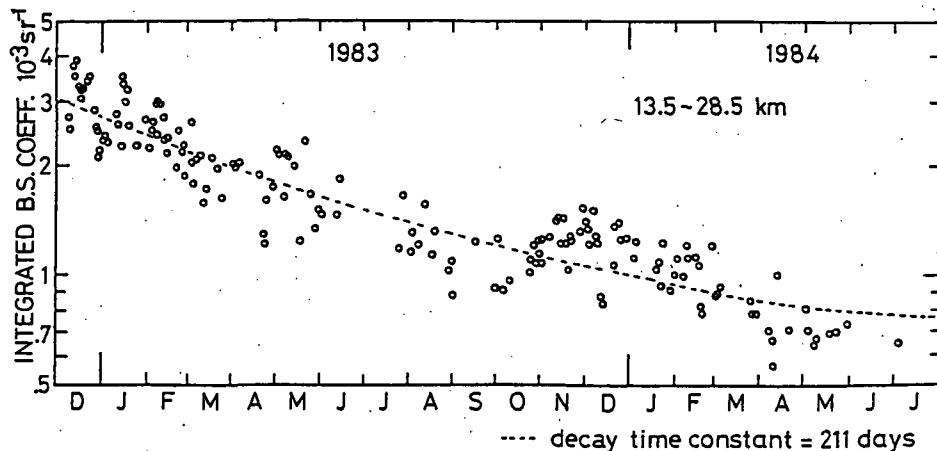


Figure 1. Variation of integrated aerosol backscattering coefficient during the period from December 1982 to July 1984. Broken line shows the least square fit decay curve.

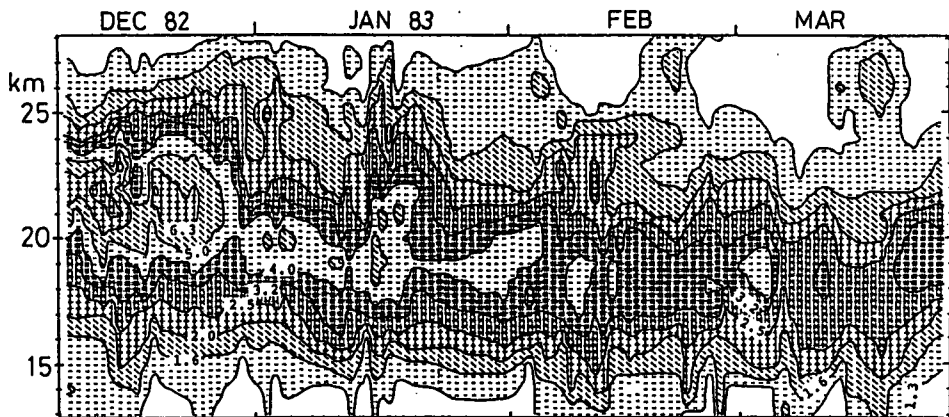


Figure 2. Variation of aerosol profiles indicated by contours of lidar backscattering ratio during the period from December 9, 1982 to March 25, 1983. The daily data interrupted from weather conditions are interpolated.

period. The peak values of the ratio decreased from 8-10 to 3-4 and the altitude of the peak ratio also fell from 22 km down to 17-19 km. Abrupt changes were sometimes found in the course of a gradual decrease of aerosol content. The analysis with reference to the aerological variations is not yet fully made. We present the comparison with the altitude and temperature of the 70 mb level in Figure 3. The aerological data were obtained at Hamamatsu, about 30 km ESE apart from Toyokawa. The level of 70 mb is adopted because the highest backscattering ratio is usually found around this level. The results of the comparison are not always clear, but the high aerosol concentration is likely to accompany the lower temperature and higher altitude of this level. The similar pattern to this is also recognized in other periods of the observation. The correspondence of the aerosol distribution to the aerological variations is thus possible in the time scale of days to months by using the data of lidar observations.

Meanwhile, the satellite "Ohzora" was launched on February 14, 1984 and is sending us information of the global distribution of aerosols. The results of satellite observations will be useful to understand the general features of stratospheric aerosols and at the same time to cooperate with the analysis of lidar data.

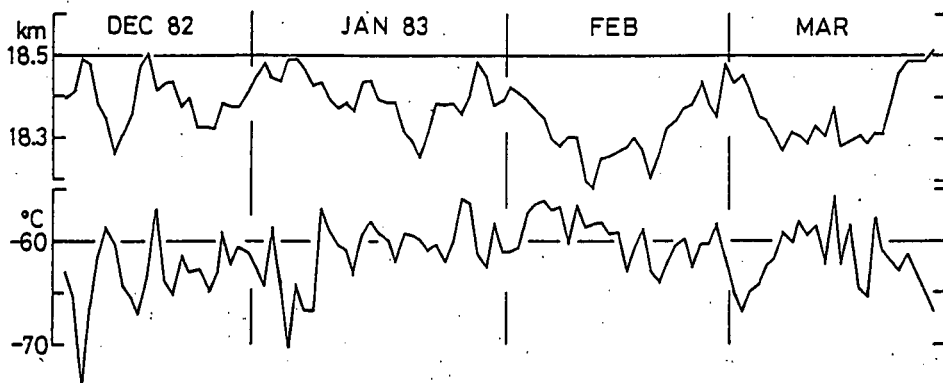


Figure 3. Variation of the altitude and temperature of 70 mb level observed at Hamamatsu, 30 km ESE from Toyokawa, in the same period as in Figure 2.

REFERENCES

- Iwata, A., Y. Kondo and M. Takagi (1983), A laser radar system for the observation of minor atmospheric constituents in the stratosphere, Proc. Res. Inst. Atmos., Nagoya Univ., 30, 25-35.
- Pollack, J. B., O. B. Toon, E. F. Danielsen, D. J. Hofmann and J. M. Rosen (1983), The El Chichon volcanic cloud: An introduction, Geophys. Res. Lett., 10, 989-992.

4.6 COMPARATIVE STUDY OF AEROSOLS OBSERVED BY YAG LIDAR AND AIRBORNE DETECTORS

M. Hirono, M. Fujiwara and T. Shibata*

Department of Physics, *Department of Electrical Engineering
Kyushu University,
Fukuoka 812, Japan

In the present paper, we examine the causal relationship of very large (tropical) volcanic eruptions and El Nino Southern Oscillations (hereafter simply ENSO) based on the unequal atmospheric heating by aerosols observed by lidar and airborne detectors.

The eruption of El Chichon (17°N, 93°W) in April 1982 injected an enormous amount of aerosols into the stratosphere, which immediately formed a sub-tropical zonal flow of the "the volcanic clouds." The densest part of the flow was in the easterly wind region above 20 km at about 20°N until June 1982 (THOMAS et al., 1983) as illustrated in Figure 1. The meridional diffusion of the flow was almost absent until November of the year.

According to HOFMANN and ROSEN (1983), the initial loading of the stratospheric El Chichon cloud in April was about 20 Tg ($T=10^{12}$), probably one half of which settled through the tropopause for nearly several months.

We examined the lidar aerosol scattering profiles at two wavelengths, 1.06 μm and 0.53 μm in Fukuoka and those at the wavelength 0.69 μm in Mauna Loa were kindly supplied by Dr. J. J. DeLusi. These profiles were renormalized, using optical parameters calculated from aerosol size distributions measured S. Texas by detectors on a balloon (HOFMANN et al., 1983), as shown by HIRONO et al. (1984a,b).

We deduced the aerosol distribution in the upper troposphere in the subtropical region shown by the dotted part in Figure 1, and the mixing ratio against altitude at 20°N is shown in Figure 2, averaged for several months after April 1982 from the above-mentioned renormalized aerosol profiles. The distribution of the aerosol mixing ratio $m(\phi)$ against latitude ϕ is estimated as $m(\phi) = m(\phi_0) \Delta^2 / ((\phi - \phi_0)^2 + \Delta^2)$, where $\phi_0 = 20^\circ\text{N}$ and $\Delta = 5^\circ$.

The conventional treatment of the settling aerosols through the troposphere is to neglect their radiative impact upon the atmosphere on the basis of the rapid dispersion and the washout in the troposphere would extinguish the aerosols in about ten days.

According to CZEPLAK and JUNGE (1974) and KIDA (1983), at the tropics from latitudes 0° to 25° in the troposphere, the horizontal diffusion coefficient is smallest on the globe and the washout in altitudes higher than about 6 km will be very small at latitudes 15° to 25°N. Therefore, the residence time of the settling aerosols in the upper troposphere at these latitudes will be much longer than in the other latitudes.

We calculated the atmospheric heating rate Q_A due to aerosols absorbing the solar short-wave and the terrestrial long-wave radiations by using one model of MUGNAI et al. (1978). The refractive index m of the aerosols in the model has an imaginary part -0.005 at a visible wavelength, which is characteristic of impure sulfuric acid aerosols.

The calculated values of Q_A are compared with diabatic heating rate Q_D for March-May by NEWELL et al. (1974) which is thought to be the motivating

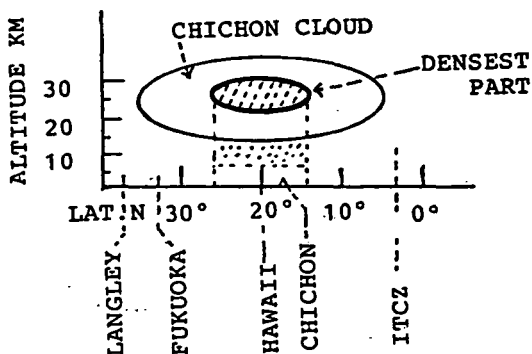


Figure 1. Schematic illustration of zonal El Chichon volcanic cloud. Densest part is shown by shading, and dotted region is discussed on radiative and thermodynamical theory in the text.

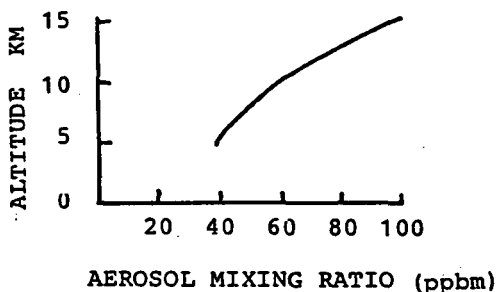


Figure 2. Profile of aerosol mixing ratio in units ppbm at 20°N which estimated to be present for one season after eruption of El Chichon April 1982.

power of the atmospheric general circulation. In Figure 3, Q_D , $Q_D + Q_A$ and $Q_D + 2Q_A$ are shown by dashed lines, solid lines A and B, respectively, at altitudes 12, 10, 8, and 6 km vs. latitudes 0°N - 30°N. It may be seen that Q_A or $2Q_A$ are the same order of magnitude as Q_D near 20°N and have the opposite sign at some altitude range.

Based on diagnostic equation, HOLTON (1972a) shows that tropical Hadley circulation is generated by the meridional gradient of the heating rate in the upper troposphere. The heating Q_A over 15° - 25°N may greatly reduce the meridional gradient due to Q_D alone and hence slow down the Hadley circulation in the northern tropical region or even reverse the sense of the mean air motion, if the value of $m(a)$ is more than the present estimates for the period of our concern.

In reality, however, the Chichon clouds would be inhomogenous zonally as well as latitudinally contrary to the present model, for one season from the eruption, especially near stagnating levels at some longitudes. It would be possible that the settling cloud concentrations at altitudes 8-12 km near Mexico or stagnating levels at other longitudes were about ten times the zonal

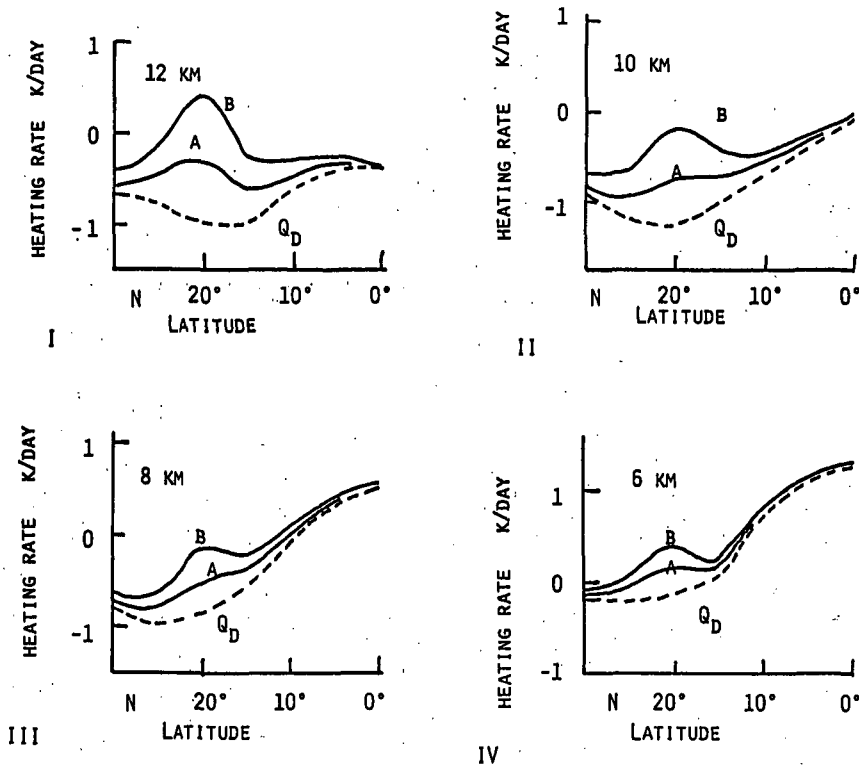


Figure 3. Diabatic heating rate Q_D vs. latitudes at altitudes I:12 km, II: 10 km, III: 8 km, IV: 6 km denoted by dashed lines (NEWELL et al., 1974) and solid lines A: $Q_D + Q_A$, B: $Q_D + 2Q_A$ at every altitude, where Q_A denotes atmospheric heating rate by aerosols.

mean values derived from Figure 2 for at least several weeks. The atmospheric heating by these aerosols will be about 5K/day or more for the period. These heatings may trigger the Kelvin or Rossby gravity waves in the tropical region (HOLTON 1972b), of which the former can significantly modulate the tradewind at the surface. After the initial triggering, the ENSO would start as the coupled atmosphere-ocean oscillation (PHILANDER et al., 1984), if other circumstances were favorable.

The present calculation is valid if the temperature rise in the upper troposphere is negligibly small due to the dissipation of the internal energy by the mechanical work done to modify the Hadley circulation. According to ANGELL et al. (1984), the temperature rise in the northern subtropical region existed but would be about 0.3 K or less by July 1982 in the upper troposphere. Thus, present values of atmospheric heating by aerosols would be approximately valid.

The present scenario of ENSO triggering should be subject to a detailed numerical simulation test to see its validity. Much more work is still necessary to confirm the situation.

REFERENCES

- Angell, J. K. and J. Korshover (1984), Comparison of tropospheric temperatures following Agung and El Chichon volcanic eruptions, Month. Weath. Rev., 112, 1457-63.
- Czeplak, G. and C. Junge (1974), Studies of interhemispheric exchange in the troposphere by a diffusion model, Adv. Geophys., 188, 57-72.
- Hirono, M., N. Fujiwara, M. Fujiwara and T. Shibata (1984a), Comparative study of aerosol properties measured by two-wavelength lidar and detector on balloon, J. Met. Soc. Japan (submitted).
- Hirono, M., T. Shibata and M. Fujiwara (1984b), A possible relationship of volcanic aerosol variations with El Nino Southern Oscillations, J. Met. Soc. Japan (submitted).
- Hofmann, D. J. and J. M. Rosen (1983), Stratospheric sulfuric acid fraction and mass estimate for the 1982 volcanic eruption of El Chichon, Geophys. Res. Lett., 10, 313-6.
- Holton, J. R. (1972a), An Introduction to Dynamic Meteorology, Acad. Press.
- Holton, J. R. (1972b), Waves in the equatorial stratosphere generated by tropospheric heat sources, J. Atmos. Sci., 29, 368-75.
- Kida, H. (1983), General circulation of air parcels and transport characteristics derived from a hemispheric GCM. Part I. Determination of advective mass flow in the lower stratosphere, J. Met. Soc. Japan, 61, 171-87.
- Mugnai, A., G. Fiocco and G. Grams (1978), Effects of aerosol optical properties and size distributions on heating rates induced by stratospheric aerosols, Quart. J. Roy. Met. Soc., 104, 783-96.
- Newell, R. E., J. W. Kidson, D. G. Vincent and G. L. Boer (1974), The general circulation of the tropical atmosphere and interactions with extratropical latitudes Vol. II, M.I.T..
- Philander, S. G. H., T. Yamagata and R. C. Pacanowski (1984), Unstable air sea interactions, J. Atmos. Sci., 41, 606-14.
- Thomas, G. E., B. M. Jakosky, R. A. West and R. W. Sanders (1983), Satellite limb-scanning thermal infrared observations of the El Chichon stratospheric aerosol. First results, Geophys. Res. Lett., 10, 997-1000.

4.7 OPTICAL PROPERTIES OF UPPER-TROPOSPHERIC AND STRATOSPHERIC AEROSOLS AS ESTIMATED FROM SOLAR AUREOLE MEASUREMENTS

M. Tanaka, T. Nakajima and T. Hayasaka

Upper Atmosphere Research Laboratory
Tohoku University, Sendai 980, Japan

An airborne scanning photometer was constructed to measure both direct solar radiation and diffuse sky radiance in the almucanter of the sun at wavelengths of 330, 369, 500, 675, 776, 862, 938 and 1048 nm. Measurements were made by a Merlin IV during flights in February 1983 and February 1984. The data were analyzed using an inversion library method to give a simultaneous estimate of the size distribution of aerosols in the air column above the flight level and their complex index of refraction. Inverted size distribution of aerosols as well as their optical thickness were compared with results obtained by other methods.

4.8 EXICIMER LIDAR MEASUREMENTS OF OZONE

T. Shibata, O. Uchino* and M. Maeda

Department of Electrical Engineering,
Kyushu University*Meteorological Research Institute, Nagamine 1-1,
Yatabe-cho, Tsukuba 305, Japan

Laser radar (lidar) observation of atmospheric ozone was first made with a frequency-doubled dye laser pumped by a flashlamp (GIBSON and THOMAS, 1975; MEGIE et al., 1977). In 1978 we reported a more efficient and simple method by the use of a XeCl excimer laser (308 nm) (UCHINO et al., 1978) and are routinely accumulating data of ozone profiles (UCHINO et al., 1983).

In recent years XeCl excimer lasers have improved rapidly, and now the output power exceeds 100 W. XeCl lasers can generate a higher average power than frequency-doubled dye lasers. Ozone profiles can be observed up to 50 km in altitude with these high power XeCl lasers (PELON and MEGIE, 1984). However, frequency-doubled dye lasers are more easily tuned to the optimum wavelengths than excimer lasers. At wavelengths 280-310 nm by a dye laser pumped by Nd:YAG-laser SHG, ozone profiles below 15 km can be observed (PELON and MEGIE, 1982). In this altitude range it is difficult to observe the ozone concentration at the XeCl laser wavelength (308 nm).

Stimulated Raman scattering (SRS) pumped by excimer lasers can efficiently and simply produce many Stokes and anti-Stokes lines (LOREE et al., 1979), which are useful in lidar observations of ozone. We report the observation of the atmospheric ozone profile in an altitude range of 3-28 km by means of differential absorption lidar in combination with an XeCl laser (308 nm) and SRS pumped by a KrF laser (249 nm) (UCHINO et al., 1983). The wavelengths used for the lidar and the 2nd Stokes line (290 nm) of CH_4 and the 1st (277 nm) and the 2nd (313 nm) Stokes lines of H_2 . In Table 1 performances of our lidar system are shown. The whole laser system was home-made. The maximum output energy per pulse of these SRS and excimer lasers are also shown in this table. Figure 1 shows the simulated relative error of lidar observation of ozone at these wavelengths. The lidar system parameters used are also shown. The U.S. standard ozone model, average aerosol distribution in Fall 1984 for the stratosphere and Elterman's aerosol (ELTERMAN, 1968) model for the troposphere were used. The dashed lines in Figure 1 represent the errors for the natural background condition of the stratospheric aerosols. The measurement errors below 30 km are expected to be lower than 30% except in the range 13-18 km. The large errors in this altitude range are due to the increased aerosols by the eruption of El Chichon in 1982.

Figure 2 shows the observed ozone profile by our lidar system. The wavelengths used to observe each altitude range are also shown. The measurement errors are within 30% except in the range 12-20 km on December 3, and except 13-18 km on December 7. Ozone profiles of the troposphere and the lower stratosphere are obtained by XeCl excimer laser and SRS of CH_4 and H_2 pumped by a KrF laser. It took about 4 hours to obtain these profiles. The observation time would be reduced to a few minutes, if commercial excimer lasers with higher average outputs were used.

As a conclusion, excimer lasers and SRS pumped by excimer lasers are useful and practical in lidar observations of atmospheric ozone because of their simple configuration, a high average power and a high repetition rate, in comparison with the system based on an Nd:YAG laser.

Table 1. Characteristics of lidar system

Transmitter						
Laser	KrF	KrF-pumped H_2 (S_1)	KrF-pumped CH_4 (S_2)	XeCl	KrF-pumped H_2 (S_2)	XeCl-pumped p-Terphenyl
Wavelength (nm)	249	277	290	308	313	340
Absorption cross section (cm^2)	1.1×10^{-17}	4.9×10^{-18}	1.3×10^{-18}	1.2×10^{-19}	5.6×10^{-19}	1.5×10^{-20}
Maximum output energy per pulse (mJ)	508*	50	17	200	44	20
Pulse duration (nsec)	15	10	10	15	10	10

* with stable resonator

Receiver	
Telescope	50 cm diameter (f=5255 cm) coude type
Field of view	1 mrad
Photomultiplier	EMI9558QB (2 ch.)
Filter bandwidth (transmission)	2 nm (10 %)
Separation from laser system	3 m
Photon counter	
vertical resolution	1 μ sec ($\Delta z=150$ m)
channel number	1000
memory	floppy disk

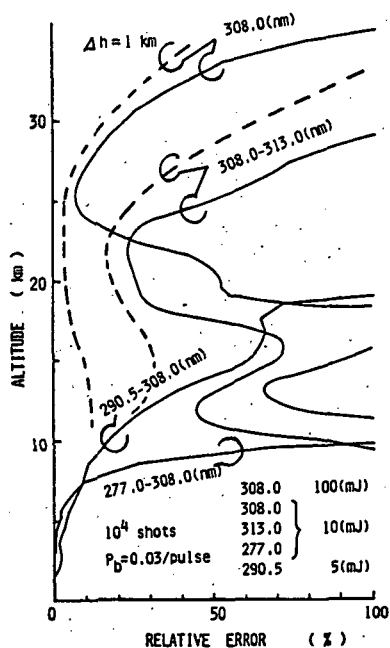


Figure 1. Simulated errors in atmospheric ozone measurement by DIAL. The dashed lines show the errors when the stratospheric aerosols are in nonvolcanic condition.

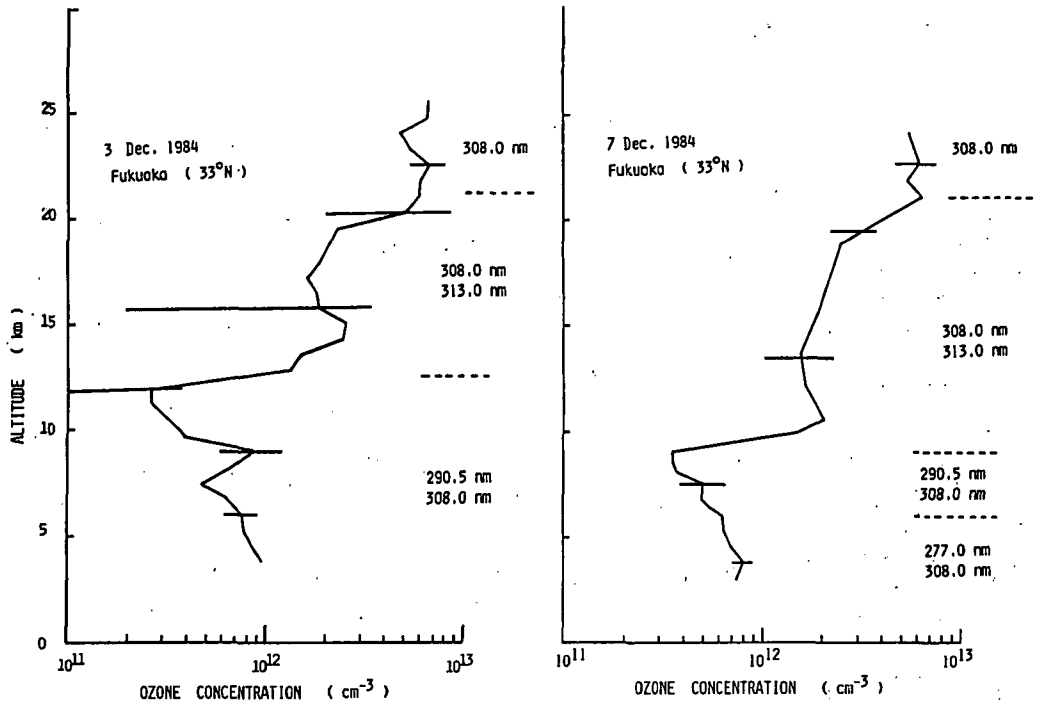


Figure 2. Ozone concentration measured by DIAL on December 3 and 7, 1984.

REFERENCES

- Elterman, L. (1968), UV visible and IR attenuation for altitudes to 50 km, 1968, Environmental Research Paper 285 (Air Force Cambridge Research Laboratory, Bedford, Mass).
- Gibson, A. J. and L. Thomas (1975), *Nature*, **256**, 561.
- Loree T. R., R. C. Sze, D. L. Barker and P. B. Scott (1979), *IEEE J. Quant. Elect.*, **QE-15**, 337.
- Megie, G., J. Y. Allain, M. L. Chanin and J. E. Blamont (1977), *Nature*, **270**, 329.
- Pelon J. and G. Megie (1982), *J. Geophys. Res.*, **87**, 4947.
- Pelon J. and G. Megie (1984), Int. LIDAR conference, abstracts, 247.
- Uchino, O., M. Maeda, J. Kohno, T. Shibata, C. Nagasawa and M. Hirono (1978), *Appl. Phys. Lett.*, **33**, 807.
- Uchino, O., M. Maeda, H. Yamamura and M. Hirono (1983), *J. Geophys. Res.*, **88**, 5273.
- Uchino O., M. Tokunaga, M. Maeda and Y. Miyazoe (1983), *Opt. Lett.*, **8**, 347.

4.9 MEASUREMENT OF NITRIC OXIDE FROM 7 TO 32 KM AND ITS DIURNAL
VARIATION IN THE STRATOSPHERE

Y. Kondo, *W. A. Matthews, A. Iwata and M. Takagi

Research Institute of Atmospherics,
Nagoya University
Toyokawa 442, Japan

*PEL Atmospheric Station,
DSIR, Lauder
Central Otago, New Zealand

This paper appears in the Journal of Geophysical Research, 90, 3813-3819.

REFERENCES

- Kondo, Y., A. Iwata, M. Takagai and W. A. Matthews (1984), Balloon-borne chemiluminescent sonde for the measurement of tropospheric and stratospheric nitric oxide, Rev. Sci. Instrum., 55, 1328-1332.
- Matthews, W. A., Y. Kondo, M. Takagi, and A. Iwata (1984), Nitric oxide profile from 7 to 32 Km, Proceedings of the Int. Ozone Symp., Greece.

4.10 MEASUREMENTS OF CCl_3F , CCl_2F_2 , CCl_4 , N_2O AND SF_6 IN THE NORTHERN HEMISPHERE STRATOSPHERE

Robert Leifer and Russell Juzdan

Environmental Measurements Laboratory
U. S. Department of Energy
New York, NY 10014

ABSTRACT

This paper provides an overview of the Department of Energy's High Altitude Sampling Program and some recent trace gas measurement results.

Analysis of whole air samples, collected in pressurized bottles, provides information on stratospheric inventories and distributions for CCl_3F , CCl_2F_2 , CCl_4 , N_2O and SF_6 in the Northern Hemisphere.

Based on a linear regression analysis of the data the estimated mean Northern Hemisphere stratospheric concentration of each gas increased as follows: CCl_3F changed from 54 to 142 pl/l (4/74-11/83); CCl_2F_2 changed from 133 to 268 pl/l (4/76-11/83); SF_6 changed from 160 to 480 fl/l (4/74-11/83); CCl_4 changed from 58 to 91 pl/l (4/75-11/83); N_2O changed from 246 to 261 nl/l (4/76-11/83)

The calculated mean Northern Hemisphere stratospheric concentrations of N_2O , CCl_3F , CCl_2F_2 , and CCl_4 after 1980 show larger than expected fluctuations with time. Recent volcanic activity may be a partial cause for these fluctuations through induced changes in stratospheric dynamical processes.

INTRODUCTION

This report describes the results of the analysis of trace gases in whole air samples collected in the Northern Hemisphere from 1974 to 1983. Calculations of stratospheric distributions and mean concentrations of CCl_3F (fluorocarbon-11), CCl_2F_2 (fluorocarbon-12), CCl_4 (carbon tetrachloride), N_2O (nitrous oxide) and SF_6 (sulfurhexafluoride) are examined over this 9 year period.

PROJECT AIRSTREAM -- TRACE GAS SAMPLING

Three times a year (spring, summer and fall) stratospheric particulate and gas samples were collected using a WB-57F aircraft flown by the National Aeronautical and Space Administration - Johnson Space Center for the Department of Energy. The samples were analyzed for several radionuclides and several stable chemical compounds. This program, carried out by the Environmental Measurements Laboratory (EML), provided samples from 75°N to the equator and over five latitudes, ranging from 12 to 19 km. From 1974 to 1981, samples were collected using air from the 18th stage of the TF-33 jet engine compressor (bleed air), and they were compressed at pressures up to 200 atmospheres in nickel-plated stainless steel spheres (15 l volume). When installed in the WB-57F, the sampling system (P-system) was capable of pressurizing four spheres, each filled on command from the navigator in the aircraft. After 1981, a new clean air sampling system, CLASS (LEIFER et al., 1980a) was developed for this program to collect sufficient air for the analysis of more than 15 compounds. Outside air enters through a nose probe and is compressed into 3-liter stainless steel bottles to almost 2 atmospheres. The present system allows the collection of up to 9 samples on one flight and it could be expanded to 18 bottles.

CHEMICAL ANALYSIS

During the years 1974 to 1976, P-system spheres were analyzed at EML. Subsequently, Washington State University (1976-1979) and Oregon Graduate Center (1980-1983) were under contract to EML to analyze gas samples. During this period (1974-1983), 980 bottles were analyzed for one or more of the following gases CCl_3F , CCl_2F_2 , CCl_4 , CH_3CCl_3 , SF_6 , N_2O , CO , CO_2 , CH_4 and COS using gas chromatography and either electron capture, flame ionization or mass spectrometry detection depending on the compound. For complete details on the analysis of these gases see VOLCHOK and de PLANQUE (1984), LEIFER et al. (1980b), and RASMUSSEN et al. (1982).

STRATOSPHERIC DISTRIBUTION OF CCl_3F

The CCl_3F data from the analysis of the October 1982 Airstream gas samples are shown in Figure 1. The concentrations of CCl_3F in p1/l are plotted as a function of the sine of the latitude and altitude (pressure). Lines of constant concentration (isopleths) are plotted in the figure and represent a great deal of smoothing. The sampling extends over a 3 week period and the isopleths do not represent an instantaneous period of the stratosphere, but rather a latitude-altitude profile averaged over this time period. Because of space limitations only CCl_3F is shown, but all other compounds analyzed on the same mission have similar patterns. The isopleths follow the general trend of the tropopause, sloping downward at high latitude. See LEIFER et al. (1980c, 1982) for a more detailed discussion of earlier data.

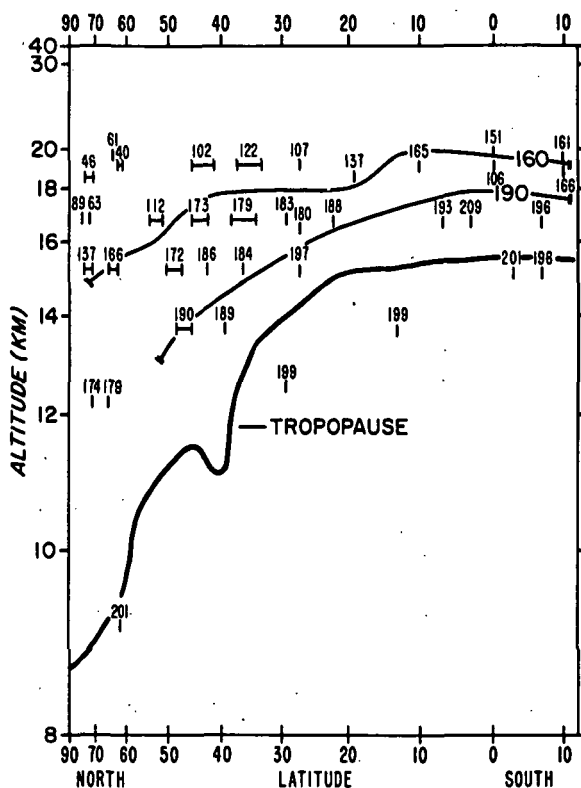


Figure 1. Stratospheric distribution of CCl_3F (p1/l) in the Northern Hemisphere for October 1982.

STRATOSPHERIC MEAN CONCENTRATIONS AND TRENDS

The stratospheric mean concentration derived from measurements of CCl_3F , CCl_2F_2 , CCl_4 , N_2O and SF_6 in the Northern Hemisphere for the years 1974 to 1983, which include our most recent analyses, are plotted in Figure 2. The lines drawn are the best fit to the data determined by linear regression analysis. Most of the compounds show concomitant fluctuations over the measurement period. From 1976 to 1980 N_2O showed no increase (LEIFER et al., 1982) in concentration and the deviations were within the precision of the analyses. Starting in late 1980 and continuing for the next couple of years, larger than expected fluctuations occurred. Similar behavior is seen in CCl_2F_2 and is less evident in the other compounds because of missing data. It was during this period that large volcanic eruptions occurred and it is conceivable that changes in stratospheric dynamical processes due to volcanic injection of gases and aerosols into the stratosphere may have played a role in modifying the mean stratospheric concentrations. The results of the linear regression analysis of the gas data is shown in Table 1. Both CCl_3F and CCl_4 show yearly rates of increase lower than our previously published estimates from 1976 to 1979 (LEIFER et al., 1982) and may reflect continued reductions in surface emission. The 1% rate of stratospheric increase in N_2O is double than that published by KHALIL and RASMUSSEN (1983). Additional analyses will be carried on our data base, especially considering the low correlation coefficient for N_2O . The increasing mean Northern Hemisphere stratospheric concentrations of the halocarbons and N_2O are directly related to anthropogenic activities on the surface of the earth and play an important role in stratospheric ozone reduction. In addition, if stratospheric concentrations of N_2O , halocarbons and other trace gases continue to increase, a global warming could occur comparable to or greater than the projected heating due to CO_2 (KHALIL and RASMUSSEN, 1983).

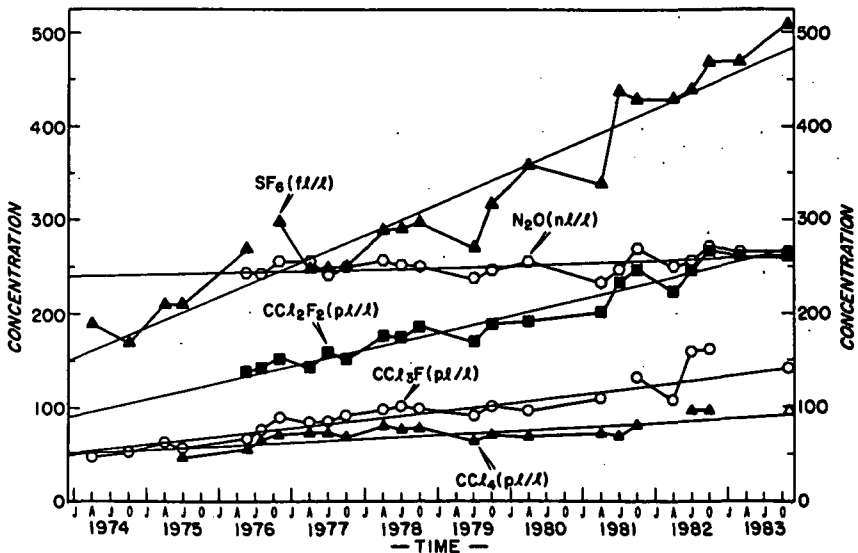


Figure 2. Trends in the mean Northern Hemisphere stratospheric concentrations of N_2O , CCl_2F_2 , CCl_3F , CCl_4 , and SF_6 .

Table 1. Linear regression analysis of stratospheric gas data.

Trace Gases	CCl_3F	CCL_2F_2	CCl_4	N_2O	SF_6
Date	4/74-11/83	4/76-11/83	4/75-11/83	4/76-11/83	4/74-11/83
Predicted Conc.	54-142	133-268	58-91	246-261	160-480
% Change/yr	17	14	7	1	21
Correlation Coeff.	0.95	0.97	0.79	0.45	0.96

ACKNOWLEDGEMENT

The authors would like to thank the flight crew and support staff of NASA/JSC for helping to make the program possible. In addition, we would like to thank Los Alamos National Laboratory for their support in field operations. Finally, we would like to thank Nancy Chieco for her editorial assistance.

REFERENCES

- Krey, P. W., M. Schonberg, and L. Toonkel (1974), Updating stratospheric inventories to January 1973, U.S. Atomic Energy Commission Report HASL-281, I-130 to I-142, New York, NY.
- Khalil, M. A. K. and R. A. Rasmussen (1983), Increase and seasonal cycles of nitrous oxide in the earth's atmosphere, Tellus, **35B**, 161-169.
- Leifer, R., K. G. Sommers, S. F. Guggenheim, and I. Fisenne (1980a), Recent developments in high altitude aircraft sampling: Mount St. Helens and stratospheric trace gases, IEEE Nuclear Science Symposium, Orlando, FL., November 5-7.
- Leifer, R., R. Lagomarsino, and R. Larsen (1980b), Project Airstream: analysis of quality control gas samples, U.S. Department of Energy, Report EML-381, I-129 to I-137, New York, NY.
- Leifer, R., L. Toonkel, R. Larsen, and R. Lagomarsino (1980c), Trace gas concentrations in the stratosphere of the Northern Hemisphere during 1976, J. Geophys. Res., **85**, 1069-1072.
- Leifer, R., R. Larsen and L. Toonkel (1982), Trends in stratospheric concentrations of the trace gases in the Northern Hemisphere during the years 1974-1979, Geophys. Res. Lett., **9**, 755-758.
- Rasmussen, R. A., M. A. K. Khalil, R. W. Dalluge, S. A. Penkett, and B. Jones (1982), Carbonyl sulfide and carbon disulfide from the eruption of Mount St. Helens, Science, **215**, 665-667.
- Volchok, H. L. and G. de Planque (editors) (1984), EML Procedures Manual, U.S. Department of Energy, Report HASL-300, 27th Edition, E-00-07-01 to E-00-07-09, New York, NY.

4.11 A DYNAMICALLY BASED TRANSPORT PARAMETERIZATION FOR ONE-DIMENSIONAL PHOTOCHEMICAL MODELS

J. R. Holton

Department of Atmospheric Sciences
University of Washington
Seattle, Washington

The net vertical tracer flux in the stratosphere is due primarily to advection by the global scale mean meridional circulation. Using a simple model of this circulation, it is shown that the net flux can be approximated by a flux-gradient relationship in which the vertical "eddy diffusion" coefficient is proportional to the square of the diabatic heating rate and inversely proportional to the rate at which meridional tracer gradients are destroyed by horizontal eddy diffusion and chemical damping. Thus, the diffusion coefficient will differ for tracers with differing chemical lifetimes. Profiles computed for various source gases (CH_4 , N_2O , CF_2Cl_2 , and CFCl_3) show that this parameterization provides a modest improvement over conventional formulations utilizing a single diffusion coefficient for all species.

4.12 TRANSPORT OF TRACE SPECIES DEDUCED FROM LIMS OBSERVATIONS

J. C. Gille, L. V. Lyjak, A. K. Smith,
P. L. Bailey, S. T. Massie and C. M. Smythe

National Center for Atmospheric Research
Boulder, CO 80307

INTRODUCTION

One of the critical problems in the middle atmosphere at this time is understanding the interaction between atmospheric motions and photochemistry, and the way in which these two processes maintain the distributions of photochemically active species such as ozone. While a complete understanding will require considering the full 3-dimensional complexity seen in the atmosphere, recent work has shown that a great deal can be learned by considering the zonally averaged distributions and transports, i.e., working in the latitude-altitude plane.

This 2-dimensional approach has been used in the past in Eulerian formulation. Recent work (DUNKERTON, 1978) has shown that formulating the transport problem in terms of the residual mean circulation, which has similarity to the Lagrangian mean motion, results in a more physical picture of the way in which the transport takes place.

In this study, data from the Limb Infrared Monitor of the Stratosphere (LIMS) experiment are used to investigate how well the residual mean formulation works with real data, in the sense of asking how well the predicted ozone changes match those in regions of the lower stratosphere in which chemical changes may be neglected. This allows a test of the approximations that are made, and of the strengths and weaknesses of this approach to transport calculation.

The LIMS is a six channel limb-scanning infrared radiometer which flew on the Nimbus 7 spacecraft (GILLE and RUSSELL, 1984). This study will use the temperature and O_3 data, which are discussed by GILLE et al. (1984) and REMSBERG et al. (1984), respectively.

FORMULATION

The residual mean circulation is derived from the transformed heat equation and the continuity equation. The radiative heating rate was calculated using an updated version of the code described by RAMANATHAN and DICKINSON (1979). This results in a circulation which is poleward during northern winter, having maximum velocities of 2.5 m s^{-1} at 1 mb, with weak upward velocities of several mm s^{-1} poleward of 60°N . The motions thus resemble those of the classical Brewer-Dobson circulation.

The transformed equation for the continuity of ozone mixing ratio may be written (GARCIA and SOLOMON, 1983)

$$\text{ozone tendency} + \text{advection} + \text{chemical eddies} = \text{net chemical source diffusion.}$$

The chemical eddy terms are rather difficult to calculate accurately. They are found to be largest in the upper stratosphere at high latitudes. Since this is not the region of major interest here, and chemical eddies are expected to have a very small effect in the lower stratosphere, they will be neglected hereafter. This is also a region in which the net chemical produc-

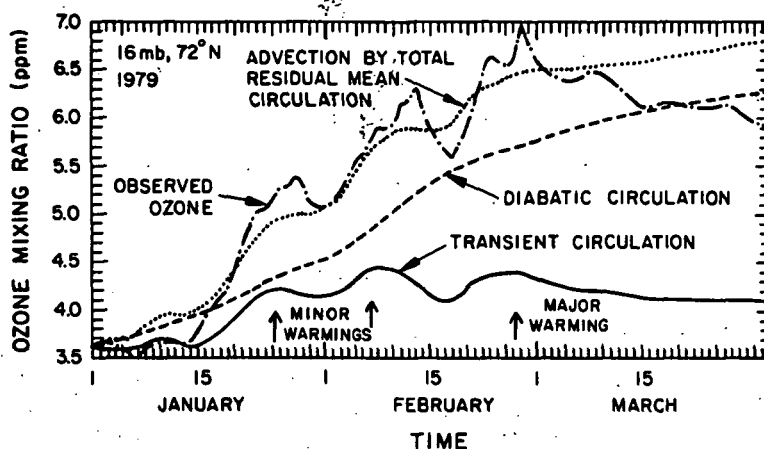


Figure 1. January 1 - April 1, 1979 ozone time series for 10 mb and 68°N comparing observed ozone amounts with those obtained by time integrating the ozone advection due to the diabatic, transient wave, and total transformed Eulerian-mean circulations. Units are ppm.

tion minus loss will be small, so that the balance between the ozone tendency and the motions can be investigated.

RESULTS

The cross sections of the sum of the tendency and advection terms shows that the effect of the motions is to remove ozone from the upper stratosphere and mesosphere, especially at mid- and high latitudes, and to deposit it in the stratosphere below about 40 km. The amount deposited in the lower stratosphere is small in terms of the change in mixing ratio. The loss from the upper stratosphere is presumably made up by photochemical production.

To test how well the advection balances the O_3 changes, the advection has been integrated in two ways, and compared with the observed changes over the winter. In the first method, the ozone cross section for the starting day is advected into the future, using the ozone field resulting from the previous advection and the winds for the day in question. This is what would result for a passive tracer. In the second method, the advection for each day is calculated from the observed ozone field and the winds for that day, and added sequentially to the initial field. This incorporates some of the effects of daily photochemical production, and of small-scale diffusion, and might be termed the active tracer integration.

After integrating out to 30 days from January 27, the two integrations show a number of similarities. The advected fields tend to resemble the initial field more than the observed fields on the later days, indicating that they cannot accurately follow rapid day-to-day changes. However, in the lower stratosphere they show the general changes, even up to 30 days. The "passive tracer" integration gives unrealistic results first, especially in the photochemically active region of the upper stratosphere, where non-physical features appear after 5 days. The "active tracer" also shows unrealistic features after a few days, but they are not as large, and do not grow as quickly.

Another illustrative way to look at the effects of the ozone transports at a given latitude and altitude is to compare the observed ozone values as a

function of time with those predicted due to the transports. At latitudes greater than 60 degrees, and levels below 10 mb, the ozone increases steadily with time from January 1 to early March, after which time it decreases slightly. The time integration by either method shows the same general features, although the "passive tracer" integration breaks down sooner. Neither follows the rapid variations very closely.

A good example is shown in Figure 1, where an "active tracer" integration over the winter period is compared with observations for 16 mb (28 km) at 72°N. The components due to the diabatic circulation and to the transient waves are shown separately. The former shows a steady increase from January to April, but is not as large as observations during mid-winter. The transient changes show increases during the times of the large disturbances, although only the first results in an irreversible change. However, their sum follows the observed ozone changes rather well to the end of February. The drop in March may be due to slow photochemical loss during spring, which is not included in these calculations, or possibly unresolved dynamical effects. The agreement with the more rapid variations during the winter is reasonably good. The impulses occur at the right times, although the calculated values are not as large as the observed ones during the disturbances.

CONCLUSIONS

Ozone values calculated on the basis of advection by the residual mean circulation agree with observations in the lower stratosphere, indicating that on a time average basis the residual mean formulation is an effective way to calculate the transport of trace species. However, use of the diabatic circulation for the total residual mean appears to result in an underestimate of the transports. In the absence of detailed information such as the data used here, to give the additional contribution the use of another approximation, such as eddy diffusion, may be necessary. Otherwise, diffusion by small-scale eddies does not seem to play a major role.

ACKNOWLEDGEMENT

This work was partially supported by the National Aeronautics and Space Administration under Contracts L-9469-B and W-15439. The National Center for Atmospheric Research is sponsored by the National Science Foundation.

REFERENCES

- Dunkerton, T. (1978), On the mean meridional mass motions of the stratosphere and mesosphere, J. Atmos. Sci., **35**, 2325-2333.
- Garcia, R. R. and S. Solomon (1983), A numerical model of the zonally averaged dynamical and chemical structure of the middle atmosphere, J. Geophys. Res., **88**, 1379-1400.
- Gille, J. C. and J. M. Russell III (1984), The Limb Infrared Monitor of the Stratosphere: Experiment description, performance, and results, J. Geophys. Res., **89**, 5125-5140.
- Gille, J. C., J. M. Russell III, P. L. Bailey, L. L. Gordley, E. E. Remsberg, J. H. Lienesch, W. G. Planet, F. B. House, L. V. Lyjak, and S. A. Beck (1984), Validation of temperature retrievals obtained by the Limb Infrared Monitor of the Stratosphere (LIMS) experiment on Nimbus 7, J. Geophys. Res., **89**, 5147-5160.
- Ramanathan, V. and R. E. Dickinson (1979), The role of stratospheric ozone in the zonal and seasonal radiative energy balance of the earth-troposphere system, J. Atmos. Sci., **36**, 1084-1104.
- Remsberg, E. E., J. M. Russell III, J. C. Gille, L. L. Gordley, P. L. Bailey, W. G. Planet, and J. E. Harries (1984), The validation of Nimbus 7 LIMS measurements of ozone, J. Geophys. Res., **89**, 5161-5178.

4.13 LIMB-ATMOSPHERIC INFRARED SPECTRUM OBSERVED ON THE SATELLITE "OHZORA"

A. Matsuzaki, Y. Nakamura, and T. Itoh

The Institute of Space and Astronautical Science,
Komaba 4-6-1, Meguro,
Tokyo 153, Japan

The Institute of Space and Astronautical Science (ISAS) has launched the 9th scientific satellite "OHZORA," meaning "the sky" in English, at 17:00 JST on February 14, 1984. This satellite bears the spectrometer, which measures the infrared spectrum of the solar radiation passing the limb atmosphere in the wavelength region of 2-10 μ m. The spectra observed near the sunrise and sunset for the satellite include the absorption bands of H_2O , CO_2 , CH_4 , O_3 , and N_2O .

The spectrometer is based on multichannel spectroscopy by using image sensors (MATSUZAKI and ITOH, 1983). Since the wavelength is scanned electronically, it can measure the spectrum unaffected by the satellite motion. A definite axis, i.e., the Z-axis of the satellite, which coincides to the optical axis of the spectrometer, is controlled to the direction of the sun, and the finer control to introduce the solar light into the spectrometer is made with a 2-axes-controlled mirror. This solar tracking equipment is derived fast enough to measure the spectra in a moment after sunrise. The solar light introduced into the spectrometer is focused on the slits of the monochromators ($f=100$ mm). For better altitude resolution, the horizontal slit is also used with the vertical slit, which is used for the separation of the dispersion. The dispersion light is detected with the pyroelectric array sensors. To obtain maximum dynamic range and spectral resolution, the three-stage polychromator is used. Thus, the absorption spectrum of H_2O is measured in the 1.6-1.4 μ m range (0.025 μ m/mm), those of CO_2 , CH_4 , and N_2O in the 2.8-4.8 μ m range (0.032 μ m/mm) and those of O_3 in the 8.8-10.2 μ m range (0.0448 μ m/mm). In the 1.6-2.4 μ m and 2.8-4.8 μ m range the Spiricon model IR-32-42 and IR-64-42, slightly modified, are used, respectively. These detectors, however, are not sensitive enough in the 8.8-10.2 μ m range where the solar irradiance is low. In this range, a 16-element pyroelectric array sensor that has no self-scanning system is used. Each element is directly connected to its own pre-amplifier, and the video signal is measured by a lock-in amplifier.

The deconvolution by calculating the theoretical spectra of these constituents gives the distribution of the amounts of constituents in the middle atmosphere. The spectrum of the solar radiation becomes reddish because of the scattering extinction by the atmospheric constituents. This reddish spectrum effect gives the aerosol amount, because the scattering extinction by the stratospheric aerosol is much greater than the molecular scattering extinction in these wavelength regions.

The observation schedule was carried out to get the latitude distribution of H_2O , CO_2 , CH_4 , O_3 , N_2O , and aerosols in the middle atmosphere.

REFERENCE

Matsuzaki, A., Y. Nakamura, and T. Itoh (1983), Spectrometers for rocket, balloon, Multichannel Image Detectors, Vol. 2, (ed. Y. Talmi), 297-321.

4.14 ATMOSPHERIC CONCENTRATIONS AND BEHAVIOR OF HALOCARBONS AND METHANE

Y. Makide, A. Yokohata and T. Tominaga

Department of Chemistry
 Faculty of Science
 University of Tokyo, Hongo
 Tokyo 113, Japan

The atmospheric concentrations of halocarbons and methane in the troposphere and stratosphere were precisely measured by grab-sampling followed by gas-chromatographic analysis in the laboratory.

Chlorofluorocarbons such as CCl_2F_2 and CCl_3F have received a great deal of attention due to their probable impact on the stratospheric ozone: the chlorofluorocarbons accumulated in the troposphere are eventually decomposed by photolysis in the stratosphere releasing Cl radicals which in turn participate in the ClO_x -catalytic chain destroying the ozone, especially in the upper stratosphere. Methane reacts with Cl in the stratosphere reducing the ozone depletion, while its source and future trend of concentration in the troposphere are uncertain. The study of their distribution and behavior in the atmosphere are therefore very important.

After the extensive survey of the locations for collection of atmospheric samples representing the midlatitudes Northern Hemisphere (N.H.) without local contamination, we have measured the concentrations of CCl_2F_2 , CCl_3F , CH_3CCl_3 , CCl_4 , $\text{CHCl}=\text{CCl}_2$ and $\text{CCl}_2=\text{CCl}_2$ with ± 1 pptv precision (pptv = 10^{-12} v/v) in samples collected in Hokkaido and west coast Tohoku area (the northern part of Japan, 40° - 45°N) every summer and winter since 1979. The observed concentrations of CCl_2F_2 and CCl_3F are now above 360 and 200 pptv, respectively, and have been steadily increasing by ~ 15 and ~ 8 pptv/year during the last several years, in accordance with their continuous large-amount emission into the atmosphere and extremely long lifetimes (> 50 years, no decomposition or removal process in the troposphere). The concentration of CH_3CCl_3 has been increasing by ~ 4 pptv/year, which is less than that for CCl_2F_2 or CCl_3F in spite of its larger emission into the atmosphere. Since CH_3CCl_3 is mainly decomposed by the reaction with OH radicals in the troposphere, its lifetime is estimated to be 6-7 years in the troposphere and about one tenth of the released amount reaches the stratosphere, adding to the ClO there. $\text{CHCl}=\text{CCl}_2$ and $\text{CCl}_2=\text{CCl}_2$ with much shorter tropospheric lifetimes (weeks - a few months), showed concentrations below 30 pptv (in contrast to more than 1000 pptv often observed in Tokyo) which, therefore, have no effect on the stratospheric ozone.

The concentrations of CCl_2F_2 , CCl_3F and CH_3CCl_3 observed in Antarctica were about 10, 11 and 30% lower, respectively, than those observed in the N.H. as the result of their predominant emission in the N.H., the presence of ITCZ as the barrier for air exchange between both hemispheres, and the different lifetime of each compound.

Stratospheric and upper tropospheric samples have been collected by means of a balloon-borne grab-sampler developed by Prof. T. Itoh's group at ISAS. Unlike CH_4 , the observed mixing ratios of CCl_2F_2 and CCl_3F remained almost constant throughout the troposphere and decreased sharply in the stratosphere. The mixing ratio of CCl_3F decreased more quickly than that of CCl_2F_2 due to the larger cross section of CCl_3F for UV light absorption. While most CH_4 is decomposed in the troposphere by OH radicals (~ 10 year lifetime), the vertical profile indicated almost no decomposition of CH_4 in the lower stratosphere. The halocarbon distribution near the tropopause was investigated by using an airplane chartered for the MAP measurements.

4.15 TRANSPORT CHARACTERISTICS IN THE MIDDLE ATMOSPHERE AND TWO-DIMENSIONAL MODELING

Hideji Kida

Meteorological Research Institute
Yatabe, Tsukuba
Ibaraki 305, Japan

INTRODUCTION

Transport mechanisms of tracers in the atmosphere were briefly discussed from a viewpoint of Lagrangian motions of air parcels. The viewpoint has a remarkable simplicity to interpret transport processes. It comes from the fact that the tracers are retained by air parcels themselves. In this regard, both momentum and energy are quite different from chemical tracers.

The present problem is what interpretation is best for understanding transport mechanisms of tracers. In this paper, a method is reviewed and proposed, although conceptually.

The numerical model used was a whole hemispheric GCM with the stratosphere. Annual- and zonal-mean diabatic forcing was assumed to drive the general circulation. Time integrations were carried out for about 100 days. The model quasi-equilibrium states were analyzed. See KIDA (1983a,b) for details.

TRAJECTORY SIMULATION

Figure 1 is the time change of positions of air parcels which originated in tropical latitudes at 30 mb. Each figure describes those at 3 months after the initial six months, one year, one and half years and two years, respectively. During the period of the first 3 months, the marked air parcels had been stirred and completely mixed in the zonal direction, and gradually moved poleward. After this stage, they further spread over the whole hemisphere, and eventually converged toward the pole, implying that most of them slowly descended at the extratropical region.

Figure 2 shows the positions of marked air parcels projected on the meridional plane. Note that they are different from those in Figure 1; namely, they were initially distributed in the zonal belt area at tropics in the level of 30 mb (~ 23 km in height). The upper part describes their positions at the sixth month, the lower part at the twelfth month.

Examining these figures, we can point out that there slowly occurs an ascending motion at the tropical region and a descending motion at the extratropical region. Based on these trajectory analyses, a schematical model of Lagrangian motions of air parcels like Figure 3 is deduced; air parcels horizontally and vertically move with herical motions, systematic upward and downward motions at the tropical and extratropical regions, respectively, and besides, random (i.e., unpredictable) quasi-horizontal dispersion (or mixing motions).

DECOMPOSITION OF VELOCITY

The above model permits us to classify the Lagrangian motion of each air parcel in terms of advection, diffusion and wave, although somewhat intuitive at this stage of the discussion.

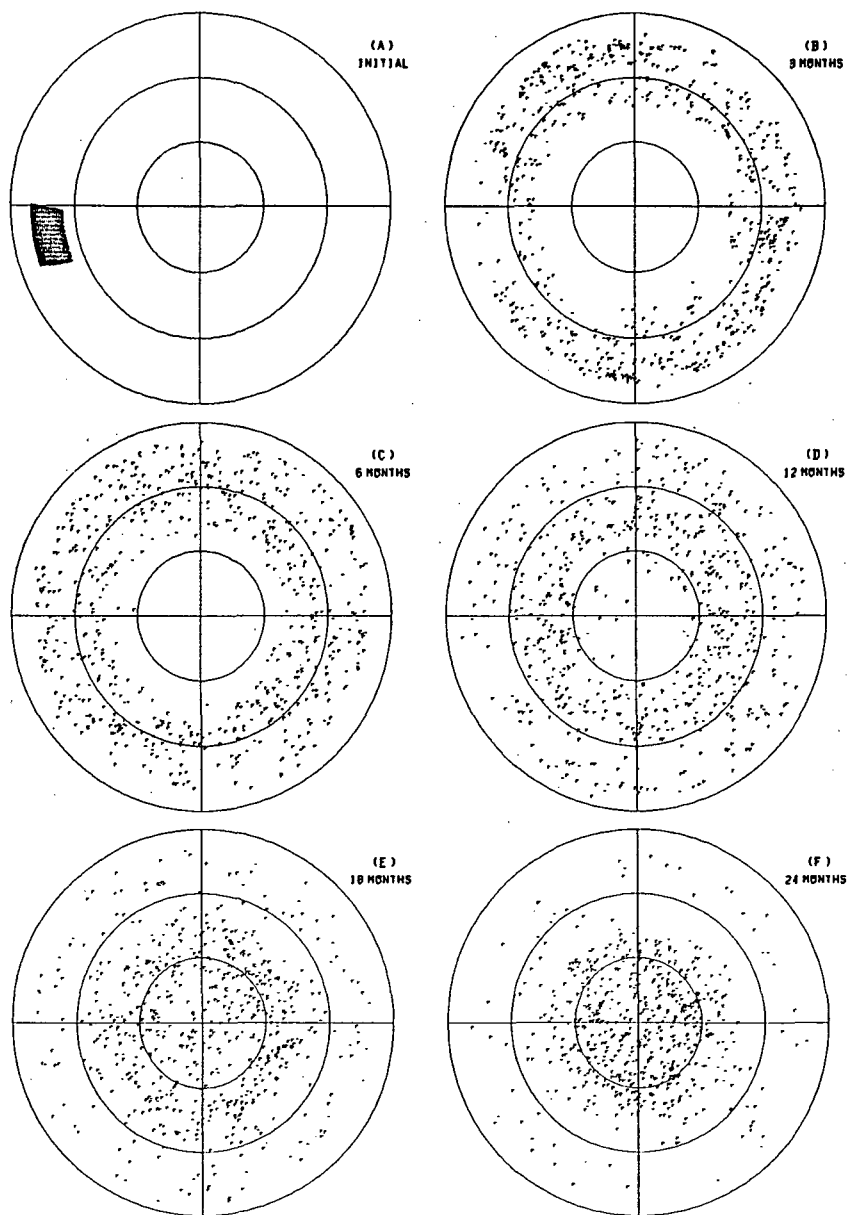


Figure 1. The positions of marked air parcels projected onto the horizontal plane; (A) Initial, (B) The third month, (C) The sixth month, (D) The 12th month, (E) The 18th month, (F) The 24th month,

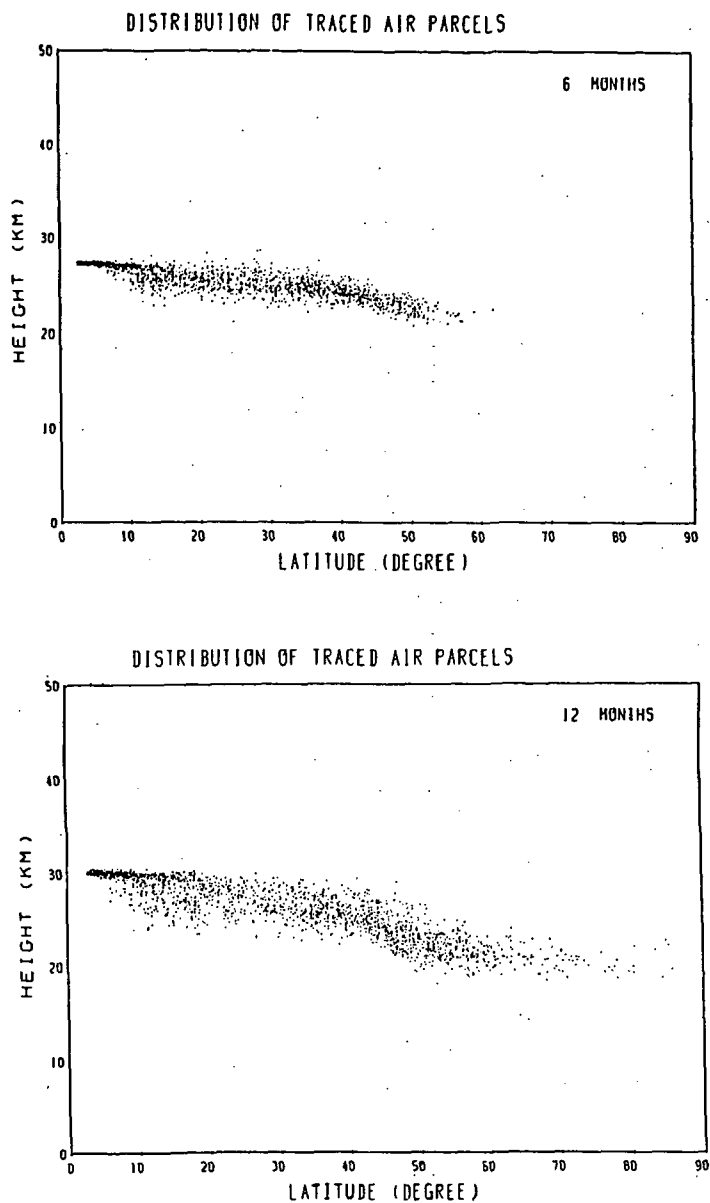


Figure 2. The positions of marked air parcels projected onto the meridional plane; (Upper) At 6 months, (Lower) At 12 months.

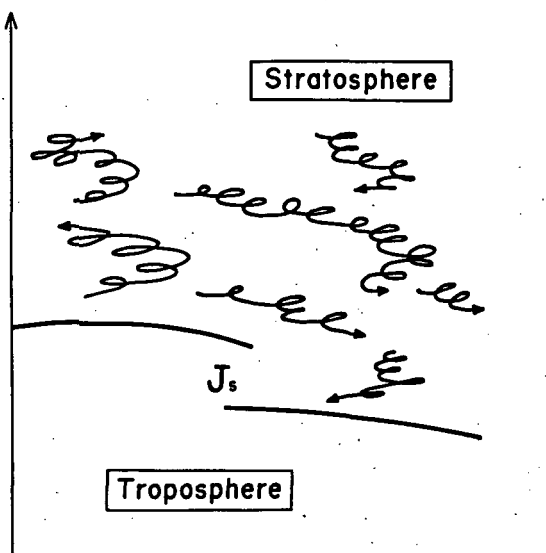


Figure 3. A schematical representation of individual motion of marked air parcels.

The velocity of air at a location usually can be divided into mean and deviation. Now, let us consider this "mean" to be the zonal mean. That is,

$$V = \bar{V} + V'$$

where V is the total velocity, $\bar{(\quad)}$ denotes zonal mean, $(\quad)'$ the deviation from the mean.

On the other hand, when we consider the velocity from a viewpoint of Lagrangian motion in a finite time (Δt) , it may be divided into advection, diffusion and wavy oscillation as mentioned above. Symbolically,

$$V = V_a + V_d + V_w$$

where the first, second and third elements denote advection, diffusion and wavy oscillation, respectively. Among them, the component of wavy motion is defined by the following (integral) condition.

$$\int_t^{t+\Delta t} V_w(n) dt = 0$$

This implies that when we integrate the wavy motion of the air parcel named as n along its trajectory for the characteristic finite period (Δt) , it becomes zero; namely, the Lagrangian mean of the motion of the air parcel must vanish. Therefore, it means no net displacement. In other words, the wavy motion does not change the initial distribution of air parcels on a material surface, i.e., does not stir those air parcels. This is a definition of "wave". In this sense, it is not proper to say that waves (as assumed in the Charney-Drazin theorem) do not change the zonal mean state of any conservation quantity, but we should say that oscillatory motions which do not change the zonal mean state is "wave". Thus, it should be noted that the so-called nontransport theorem is not a property of "wave" but used for a definition of "wave".

Next, diffusive motion can be defined as motion remained when advective and wavy (systematic) motions are subtracted from the instant motion of the air parcel at a location. It is due to any transiency of the velocity field. Note that the diffusive motion results in dispersion, or more correctly speaking, mixing of air parcels. The mixing is the most important and essential property of the newly defined diffusive motion.

Then we will proceed to define the advective motion which we may image as "background current". It will be called a modified Lagrangian mean motion as shown below, and the mean is symbolized by not $(\bar{\quad})$ but childa $(\tilde{\quad})$.

The modified Lagrangian mean motion is defined as average of forward Lagrangian mean motion plus backward Lagrangian mean motion; namely,

$$\tilde{V}^L \equiv \frac{1}{2}(\bar{V}_f^L + \bar{V}_b^L)$$

The forward one, \bar{V}_f^L , corresponds to usual Lagrangian mean motion, but the backward one, \bar{V}_b^L , is newly introduced (KIDA, 1983a). To understand this, let us consider some air parcels specially marked which are scattered around a position. If they converge toward the concerned position and then the center of gravity of them moves there, the motion of the center of gravity of the marked air parcels is called the backward Lagrangian mean motion. Generally speaking, it is unknown which air parcels would converge at the concerned position, because diffusion is always dispersive excepting a unique solution. Fortunately, we can easily get the solution only by tracing trajectories of the air parcels at the concerned position back to the past. Namely,

$$\bar{V}_b^L \equiv \frac{1}{N} \sum_{n=1}^N \left\{ \frac{1}{\Delta t} \int_{t-\Delta t}^t V(n,t) dt \right\}$$

($N \rightarrow \infty$)

Again, using newly defined elements, the velocity can be written as follows:

$$V = \tilde{V}^L + V_d + \bar{V}_w + V_w'$$

where the first term is the advection, the second the diffusion and the third and fourth are the zonal mean and deviation of the wavy motion, respectively. According to this decomposition, the usual zonal mean of velocity consists of the advection and wave-structural zonal mean part, and the usual deviation from the zonal mean consists of the diffusive motion and the deviation part of the wavy motion. Consequently, the zonal mean of the diffusive motion is zero.

The main result from analyses based on the above definitions has been described in KIDA (1983a). It has clearly shown the existence of the Brewer-Dobson circulation in the lower stratosphere. Note that usual Lagrangian mean motion showed a remarkable convergence at the extratropical region. It means that highly diffusive motions of air parcels dominate the so-called Lagrangian mean motion as theoretically discussed. In other words, such diffusive motions, particularly to the horizontal direction, govern individual Lagrangian motion of air parcels there.

For reference, the zonal mean of velocity was almost the same with the wave-structural zonal mean. Therefore, the so-called indirect cell appeared in the model lower stratosphere as in the real atmosphere.

TWO-DIMENSIONAL TRANSPORT MODEL

A modeling of a two-dimensional transport model is discussed, using newly defined velocity elements.

Consider χ as any variable the air parcel retains. The rate of time change of χ is

$$\frac{d\chi}{dt} = -\nabla F$$

where F vector is flux vector of χ .

By inserting the velocity elements into this continuity equation, zonal mean flux can be represented by four terms. Tentatively, the author will call this as a modified Eulerian transport equation. The flux is

$$F = V\chi$$

$$\overline{F} = \overline{V^L} \cdot \overline{\chi} + \overline{V_d \chi'} + \overline{V_w \chi} + \overline{V_w' \chi'}$$

If we invoke the mixing length hypothesis mainly along a line of REED and GERMAN (1965), the fourth term due to waves can be written as

$$\overline{V_w' \chi'} \equiv \overline{V_w' l_w \nabla \chi} = D \overline{\nabla \chi}$$

where the vector l_w denotes the mixing length. As is well known, this may be replaced by a diffusivity tensor, which can be divided into a symmetric part and an antisymmetric part (MATSUNO, 1980). It is noteworthy that the mixing length depends on characteristic life time of tracers, so the tensor is a function of the tracer itself.

On the other hand, diffusive flux $\overline{V_d \chi'}$ can be also described along a line of Reed and German.

$$\overline{V_d \chi'} \equiv \overline{V_d l_d \nabla \chi} = K \overline{\nabla \chi}$$

In this flux, the diffusivity tensor K must be symmetric. Note that this tensor also depends on chemical lifetime of the tracer; namely,

$$|l_d| \sim \exp(-\tau_0/\tau)$$

where τ_0 and τ are characteristic time scales of eddies and chemical time constants of the tracer, respectively.

As stationary waves dominate in the stratosphere, the mixing length $|l_w|$ is larger than $|l_d|$. Figure 4 schematically shows an evolution of dispersion of air parcels which initially located along a latitude circle. The magnitude of dispersion can be evaluated by standard deviation of distance, η , from the center of gravity of marked air parcels.

Typically, the time changes of $(\eta')^2$ tends to oscillate as depicted in the figure, because the marked air parcels repeatedly diverge from and converge into the center of gravity of them by dominant wavy motions with a characteristic period. However, the convergence is not always perfect to cancel the divergence. Consequently, there may occur net dispersion. This is due to true diffusion (as newly defined in the present discussion). In other words, if the wavy motion dominates in the real atmosphere, such true diffusion is relatively smaller.

After all, we can arrive at a modified Eulerian transport equation which consists of four flux divergences; that is,

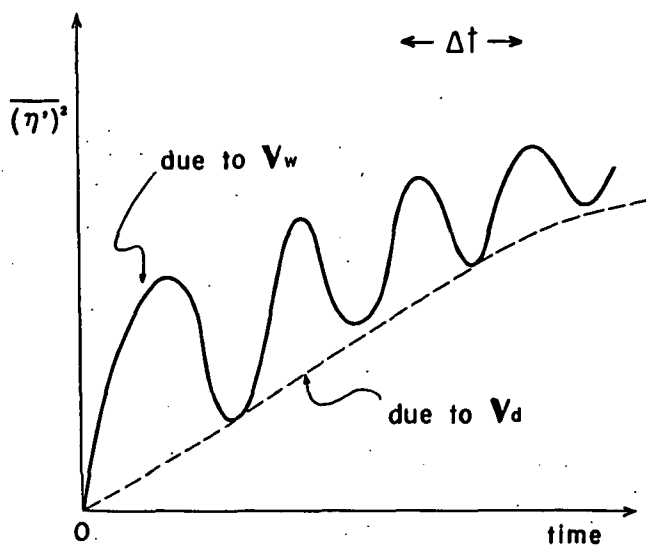


Figure 4. The time change of dispersion of marked air parcels initially concentrated at a position on the meridional plane.

$$\frac{\partial \bar{X}}{\partial t} = -\nabla \bar{V}^L \bar{X} - \nabla \bar{V}_w \bar{X} - \nabla \cdot K \bar{\nabla} \bar{X} - \nabla \cdot D \bar{\nabla} \bar{X}$$

If X is conservative, the two terms in relation with wavy motion are completely cancelled (i.e., nontransport theorem holds) and, therefore, the transport terms reduce to the two, due to advection and diffusion;

$$-\nabla \bar{V}^L \bar{X} - \nabla \cdot K \bar{\nabla} \bar{X}$$

According to an analysis on the model atmosphere, we can approximate this equation only by the vertical advection and horizontal diffusion terms. Thus we have

$$\frac{\partial \bar{X}}{\partial t} \sim -\nabla \cdot \bar{W}^L \bar{X} - \nabla \cdot K_{yy} \bar{\nabla} \bar{X}$$

Further, the vertical advection (i.e., the vertical component of the modified Lagrangian mean motion) may be in practical replaced by "adiabatic vertical motion", \bar{w}^* .

$$\frac{\partial \bar{X}}{\partial t} \sim -\bar{w}^* \bar{\nabla} \bar{X} - \nabla K_{yy} \bar{\nabla} \bar{X}$$

This transport equation is identical with TUNG (1982).

SUMMARY

1. Transport mechanisms can be described in terms of general current, diffusion and wavy oscillation of air parcels.
2. The reality of the Brewer-Dobson circulation can be verified by using the concept of not usual but modified Lagrangian mean motion.
3. A large-scale quasi-horizontal diffusion is important to transport of tracers. This process can be described by a symmetric diffusivity tensor.

4. A wavy-structural diffusivity tensor is also important for short-lived tracers.

REFERENCES

- Kida, H. (1983a), J. Meteorol. Soc. Japan, 61, 171-187.
Kida, H. (1983b), J. Meteorol. Soc. Japan, 61, 510-523.
Matsuno, T. (1980), Pure Appl. Geophys, 118, 189-216.
Reed, R. J. and K. E. German (1965), Month. Wea. Rev., 93, 313-321.
Tung, K. K. (1982), J. Atmos. Sci., 39, 2330-2355.

4.16 THE ZONALLY AVERAGED TRANSPORT CHARACTERISTICS OF THE ATMOSPHERE AS DETERMINED BY A GENERAL CIRCULATION MODEL

R. Alan Plumb

CSIRO Division of Atmospheric Research
Private Bag 1
Mordialloc, Vic. 3195 Australia

Two-dimensional (zonally averaged) modelling has become an established technique for the simulation of the global structure of trace constituents. Such models are simpler to formulate and cheaper to operate than three-dimensional general circulation models, while avoiding some of the gross (and theoretically ill-founded) simplifications of one-dimensional models. Nevertheless, the parameterization of eddy fluxes required in a 2-D model is not a trivial problem. Indeed, this fact has apparently led some to interpret the shortcomings of existing 2-D models as indicating that the parameterization procedure is wrong in principle. There are grounds to believe, however, that these shortcomings result primarily from incorrect implementations of the predictions of eddy transport theory and that a properly based parameterization may provide a good basis for atmospheric constituent modeling.

In most 2-D models, the unresolved eddies are parameterized on the basis of "K-theory", i.e., the eddy flux $\overline{u'q'}$ of a tracer of zonally averaged mixing ratio q is specified via a flux-gradient relationship,

$$\overline{u'q'} = - \underset{\sim}{K} \cdot \underset{\sim}{\nabla} \bar{q}$$

where K is a four-component transport tensor. The symmetric part of this tensor is a representation of diffusive transport, while the antisymmetric part is advective (i.e., it represents a correction that must be applied to the mean wind field in order to obtain the velocity distribution which determines the total advective transport).

While the flux-gradient relation has been in use for some years, it is only relatively recently that it has been formally justified, under the assumption of small-amplitude eddies. Even if it is assumed that this validity extends to realistic flows, the determination of K is not a simple task. Direct application of the results of small-amplitude theory is impracticable, since this would require knowledge of Lagrangian statistics which are not available from observations. Some attempts have been made to estimate K from Eulerian statistics (on the basis of ill-founded assumptions) or from observed tracer distributions (which yield insufficient information to determine K uniquely).

Given these difficulties and uncertainties in the determination of the transport coefficients from atmospheric data, it seems appropriate to calculate them for a general circulation model; the advantages of a truly objective derivation almost certainly outweigh the shortcomings of the models. In collaboration with J. D. Mahlman, the GFDL general circulation/tracer model was used to generate eddy flux statistics in artificial tracer experiments; K was then derived by inversion of the flux-gradient relation.

In the first part of this talk, the transport characteristics of the GCM will be described and related to dynamical processes in the (model and real) atmosphere. The effective transport circulation differs substantially from the Lagrangian mean and residual circulations and is the simplest representation of the model circulation. The diffusive component is coherently structured, comprising the following components:

- 1) Strong quasi-horizontal mixing ($K_{yy} \sim 1 \times 10^6 \text{ m}^2 \text{ s}^{-1}$) in the mid-latitude lower troposphere, apparently associated with fronts and the occlusion of synoptic systems.
- 2) A band of strong quasi-horizontal mixing ($K_{yy} \sim 2 \times 10^6 \text{ m}^2 \text{ s}^{-1}$) stretching across the tropical upper troposphere and into the subtropical winter stratosphere. This band follows the band of weak zonal mean winds and is a manifestation in the model of the "surf zone" recently identified by McIntyre and Palmer as a region of breaking planetary waves.
- 3) Intense vertical mixing ($K_{zz} \sim 30 \text{ m}^2 \text{ s}^{-1}$) through much of the troposphere, associated with subgrid-scale mixing (e.g., model convective processes).
- 4) Vertical mixing ($K_{zz} \sim 5\text{--}10 \text{ m}^2 \text{ s}^{-1}$) through much of the troposphere, associated with subgrid-scale mixing (e.g., model convective processes).

The existence of these GCM-derived coefficients affords an unprecedented opportunity to test the validity of the flux-gradient parameterization. To this end, a zonally averaged (2-D) model was developed, using these coefficients in the transport parameterization. Results from this model for a number of contrived tracer experiments were compared with the zonally averaged results from identical experiments with the parent GCM. The generally very good agreement substantially validates the flux-gradient parameterization, and thus, the basic principle of 2-D modeling.

These results will be reported in full elsewhere (PLUMB and MAHLMAN 1985).

REFERENCE

- Plumb, R. A. and J. D. Mahlman (1985), Zonally-averaged transport characteristics of the GFDL general circulation/transport model. To be submitted to J. Atmos. Sci.

4.17 DYNAMICAL ROLES OF PLANETARY WAVES ON THE WINTER ANOMALY IN THE MIDDLE AND LOWER LATITUDES

Kohji Kawahira

Geophysical Institute,
Kyoto University
Kyoto 606, Japan

The winter anomaly of radio wave absorption in the ionospheric D region (65-90 km), caused by a factor of about ten increase in electron density, has been considered to be due to a factor of about ten increase of the nitric oxide concentration and/or a few tens of degrees Kelvin temperature rise due to a strong temperature dependency of the conversion rate of molecular ions to cluster ions (ARNOLD and KRANKOWSKY, 1977). In order to investigate the mechanism of the winter anomaly, therefore, it is essential to identify what processes could bring about these changes.

It is well known that stratospheric warmings sometimes accompany the winter anomaly in middle latitudes. The present study, thus, concentrates on the winter anomaly which occurred simultaneously during a sudden warming of the 1967/68 winter, from middle December 1967 to middle January 1968. Variations of geophysical and ionospheric parameters are shown in Figure 1 (ROWE et al., 1969). According to ROWE et al., this winter anomaly would have a close relationship to sudden warmings rather than geomagnetic storms from the long-term comparison between the Ap index and the absorption at Pennsylvania (40°N). Furthermore, maximum enhancement of the electron density occurred in the layer between 75-80 km height from late December to early January. From an observational analysis of this winter anomaly, KAWAHIRA (1982) proposed a dominant process to induce this anomaly as shown in the schematic of Figure 2. When large amplitude planetary waves extend to the D region (mesosphere), then geostrophic southward winds could carry abundant NO from a high latitude source region to a middle latitude sink region, resulting in the winter anomaly. NO is most abundant in the polar region during winter (e.g., SOLOMON et al., 1982).

Evidence of this process is given in Figure 3. It is apparent that the geostrophic southward winds are dominant over North America above 70 km height, and here a strong absorption appeared south of 60° geomagnetic latitude indicating the southward transport of NO from higher latitudes. On the other hand, over Eurasia, the weaker absorption could correspond to geostrophic northward winds because the minimum geopotential height is located near 10°W above 70 km. Correspondence between a southward flow and an absorption enhancement can be verified in the time series of the absorption and meridional winds (Figure 4). It is to be noted that southward winds at College from late December to early January are consistent with geostrophic southward winds over North America as shown in Figure 3; thus, planetary wave induced winds could extend to the upper D region at the time of sudden warmings, as has been confirmed in a recent analysis of satellite observations (LABITZKE, 1984). Figure 4 also indicates that southward winds can induce the absorption enhancement even in lower latitudes of 20°N (Mexico City).

On the basis of the evidence and the recent theory of mesospheric circulation (MATSUNO, 1981), a tentative model of the processes of the winter anomaly can be summarized as shown in Figure 5. The downward transport of NO from a lower thermosphere source region by meridional circulation and eddy diffusion induced by breaking gravity waves (LINDZEN, 1981) could contribute to winter NO enhancement in the D region. The winter D region in high and middle latitudes is warmer than in summer, which in turn produces an adequate condition for

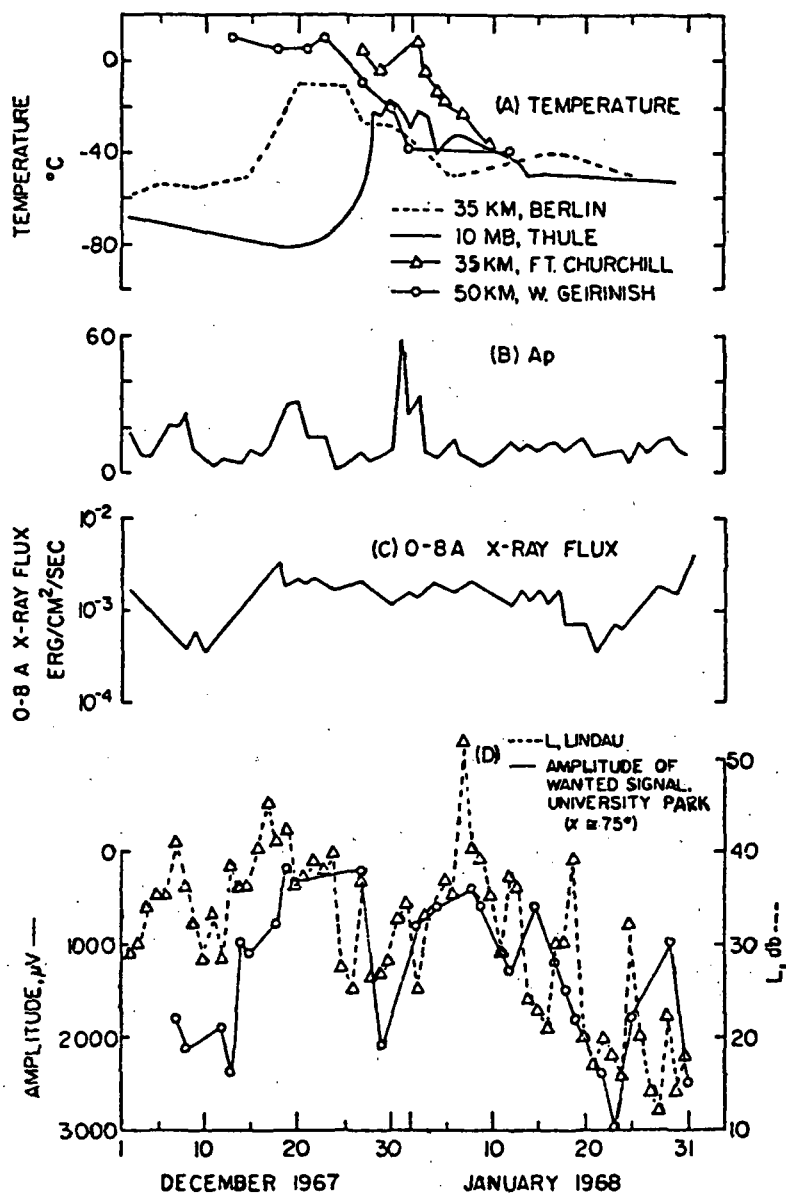


Figure 1. Variations of geophysical and ionospheric parameters during December 1967 and January 1968 (after ROWE et al., 1969).

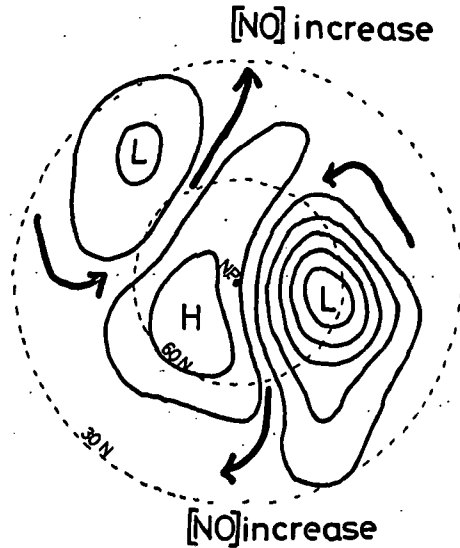


Figure 2. A hemispheric chart of geopotential height in the winter D region at the period of sudden warmings, and a schematic illustration of the mechanism of the winter anomaly (after KAWAHIRA, 1984).

electron enhancement due to a strong temperature dependency of the conversion rate of molecular to cluster ions, R_{NO^+} (ARNOLD and KRANKOWSKY, 1977). Furthermore, planetary waves can extend to the D region only during the winter season. These processes contribute to the winter anomaly. Also, it is noted that the polar night region plays an important role in the NO increase in the winter D region, because NO loss due to the dissociation of solar radiation is nil, and thus NO increases induced by energetic electron precipitation could be important.

Therefore, it is noted that the winter anomaly could be produced by the combined effects of meteorological and geomagnetic disturbances. For example, NO may be transported directly from the source region by atmospheric waves and indirectly by NO enhancement due to energetic electron precipitation associated with geomagnetic storms.

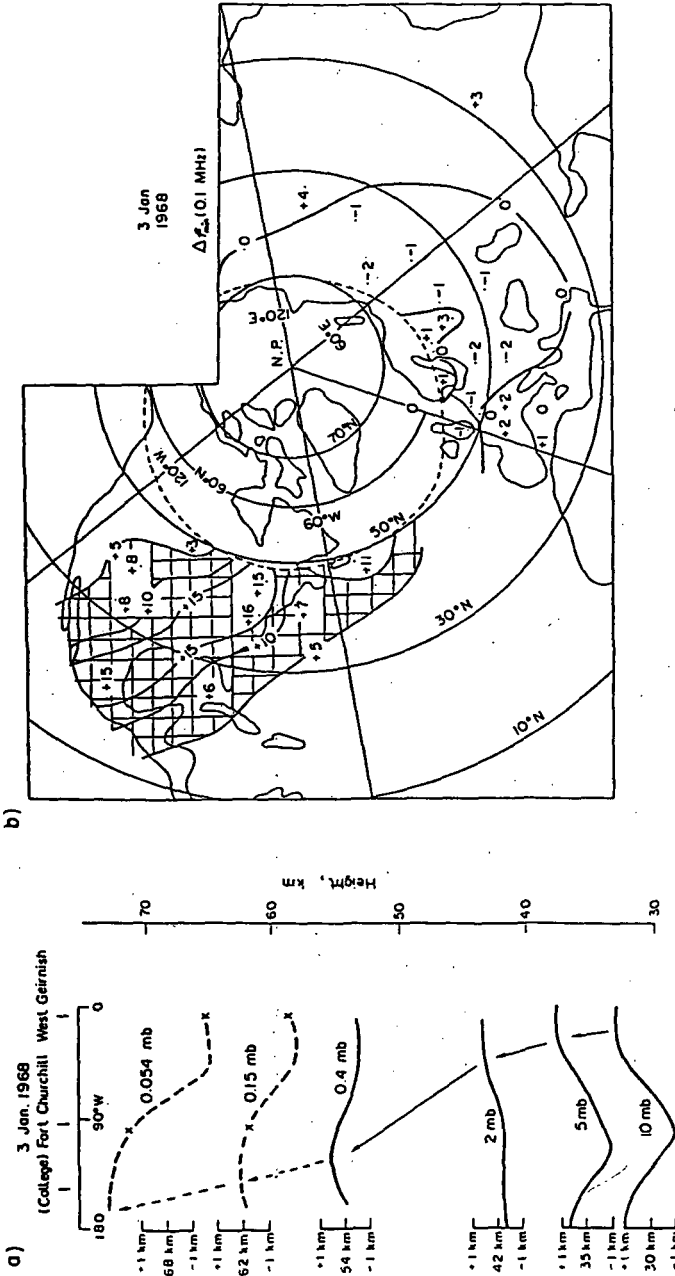


Figure 3. (a) Vertical profile of the geopotential height along 60°N from 0°W to 180°W. The scale of the geopotential height on the left-hand side is twice the real height. The dotted line is estimated from the hydrostatic balance with the use of the observed temperature at Fort Churchill and West Geirinish. (b) Contour of the absorption index, Δf_{min} , a daily deviation from the monthly median value of f_{min} at noon. The positive area is an increase in the absorption, and the negative a decrease. The dotted line indicates 60° geomagnetic latitude (after KAWAHARA, 1982).

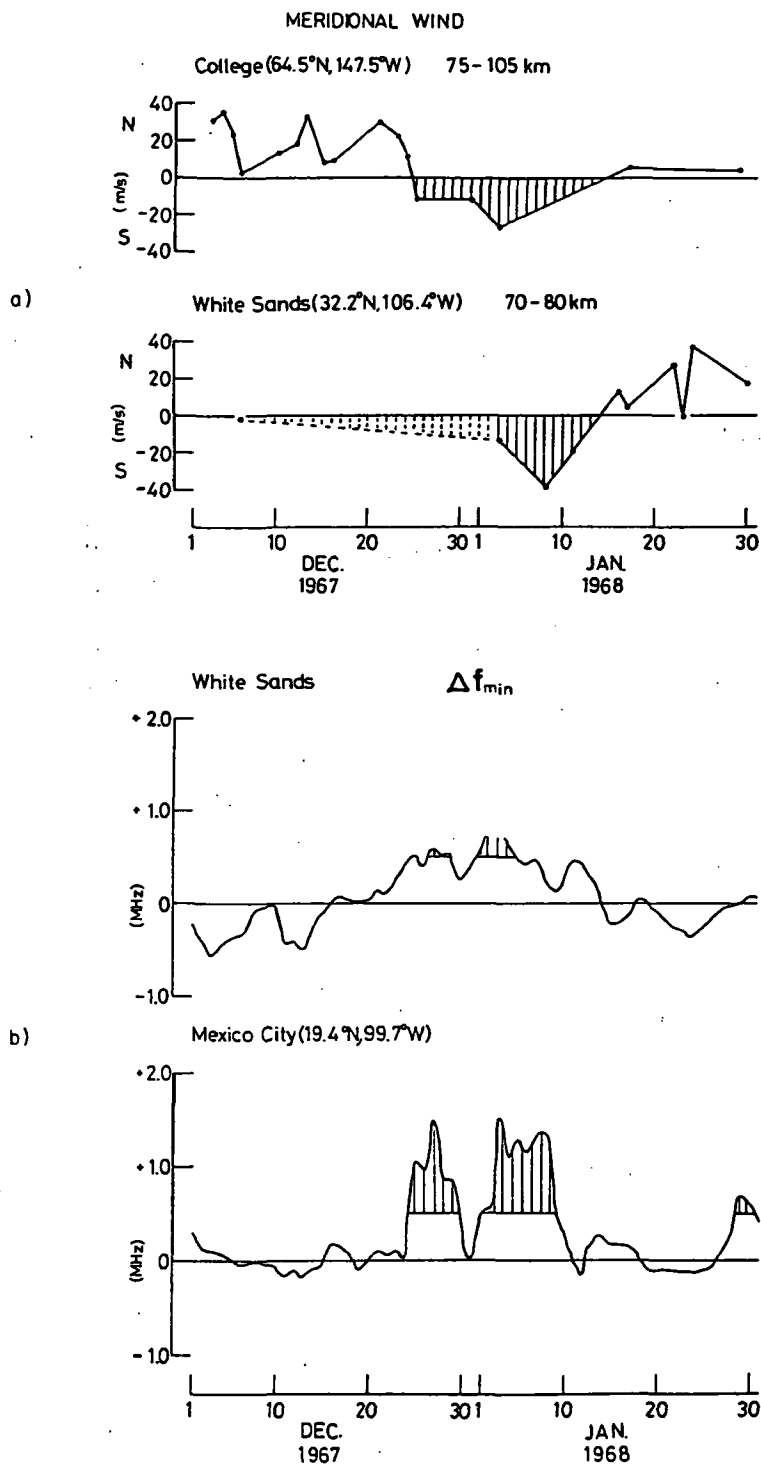


Figure 4. Time series of the absorption at White Sands and Mexico City, and of meridional winds at College observed by meteor radar (after HOOK, 1972) and at White Sands observed by meteorological rocket soundings (after KAWAHIRA, 1984).

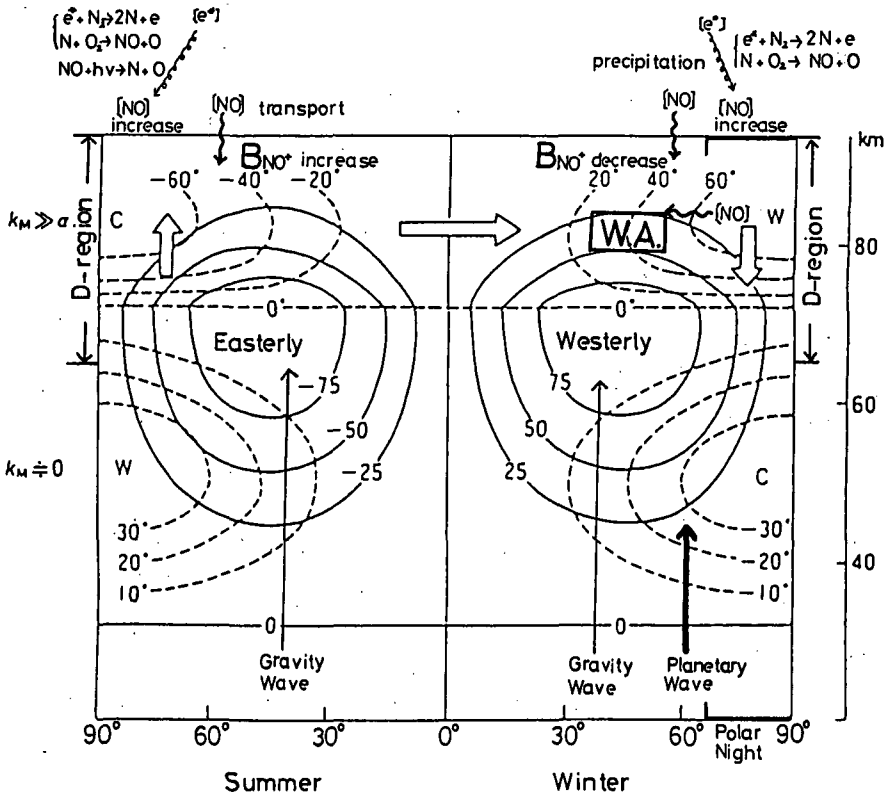


Figure 5. A schematic model of the mechanism of the winter anomaly, W. A.. Thin lines indicate zonal winds (m/s) and dashed lines, zonal mean temperature ($^{\circ}\text{C}$), defined as the deviation from the global mean. K and α are the Rayleigh friction and the Newtonian cooling coefficient, respectively. B_{NO^+} is the conversion rate of $\text{NO} \rightarrow \text{NO}^+ \text{H}_2\text{O}$.

REFERENCES

- Arnold, F. and D. Krankowsky (1977), Dynamical and Chemical Coupling Between the Neutral and Ionized Atmosphere, B. Grandel and J. A. Holtet (eds.), D. Reidel, Dordrecht, Holland, pp. 93.
- Hook, J. L. (1972), J. Geophys. Res., **77**, 3856.
- Kawahira, K. (1982), J. Atmos. Terr. Phys., **44**, 947.
- Kawahira, K. (1984), J. Atmos. Terr. Phys., (in press).
- Lindzen, R. S. (1981), J. Geophys. Res., **86**, 9707.
- Matsumo, T. (1981), Lectures on the Atmospheric Science, 3 (with T. Shimazaki), K. Gambo and T. Asai (eds.), Tokyo Univ. Press (in Japanese).
- Labitzke, K. (1984), Handbook for MAP, Vol. 10.
- Rowe, J. N., A. J. Ferraro, H. S. Lee, and A. P. Mitra (1969), J. Atmos. Terr. Phys., **31**, 1077.
- Solomon, S. P., J. Crutzen, and R. G. Roble (1982), J. Geophys. Res., **87**, 7221.

4.18 TRANSPORT PROCESSES IN THE STRATOSPHERE: MODEL SIMULATIONS AND COMPARISONS WITH SATELLITE OBSERVATIONS

W. L. Grose, R. E. Turner, and J. E. Nealy

NASA Langley Research Center
Hampton, VA

INTRODUCTION

A three-dimensional atmospheric model has been used to study transport processes and to simulate the distribution of chemically active species in the stratosphere. The present results are part of a long-term simulation of the seasonally varying structure of stratospheric trace constituents. The occurrence of a midwinter stratospheric warming and the associated transport of O_3 and HNO_3 during the simulation are described. Comparison of the simulated distributions of O_3 and HNO_3 are made with data from the Limb Infrared Monitor of the Stratosphere (LIMS) experiment (GILLE and RUSSELL, 1984). In addition, distributions of Ertel's potential vorticity on isentropic surfaces (IPV) are evaluated as a diagnostic for interpreting transport processes. Comparisons are made with IPV distributions inferred from LIMS temperature data (GROSE, 1985).

DESCRIPTION OF THE MODEL

The model is formulated in terms of the primitive equations in spherical geometry, using a sigma coordinate system in the vertical dimension with 12 levels extending to approximately 57 km. Dependent variables in the horizontal are represented by triangularly truncated spherical harmonic expansions through zonal wave number 16. A semi-implicit time integration technique with a 30-min time step was adopted. Diabatic heating in the model includes absorption of solar ultraviolet radiation by ozone. Long-wave radiative cooling is incorporated by a Newtonian approximation. A more detailed description of the model can be found in GROSE et al. (1985).

Transport simulations are accomplished in the "off-line" method described by MAHLMAN and MOXIM (1978). Wind and temperature fields generated by the general circulation model (GCM) are stored on tape and later used as input to a tracer model, which consists of a coupled set of species continuity equations for O_3 , NO , Cl , and HNO_3 . Multi-species transport has been incorporated by grouping together those species with relatively rapid chemical inter-conversion rates into "families," whose characteristic chemical time scales are much longer. Although not explicitly transported, HO and CH chemistry is included. Individual rate coefficients and absorption cross-section data conform to the values recommended by DEMORE et al. (1983).

RESULTS

The time history of the zonal mean temperature at 2 mb and $70^\circ N$ from the simulation is shown in Figure 1. This segment of the simulation was selected to illustrate the two warming "pulses" that occurred. The first event, in early January, resulted in a rapid temperature increase over the polar cap. The second event occurred more gradually, but culminated in polar easterlies extending downward to almost 10 mb in early February. A detailed analysis of the warming simulation is presented in BLACKSHEAR et al. (1985). Also depicted in Figure 1 is the amplitude for zonal harmonic height wave 1. Note the high degree of correlation between temperature and wave 1 amplitude.

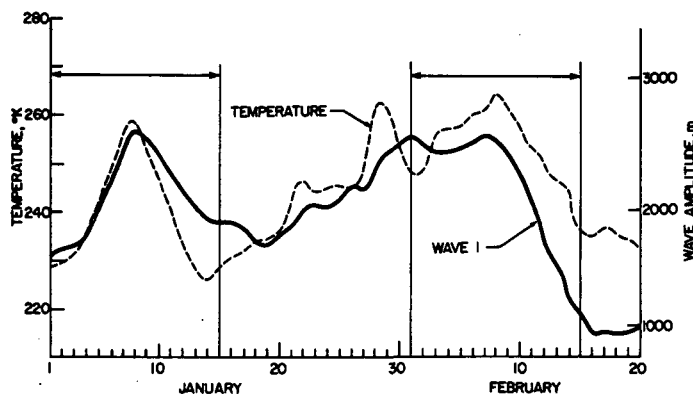


Figure 1. Zonal mean temperature and harmonic wave 1 amplitude from GCM simulation at 2 mb and 70 deg north latitude.

Meridional cross sections of zonally averaged temperatures, T , and zonal winds, U , are presented in Figure 2. for a prewarming situation (model day Jan.1) and for the situation corresponding to reversal of the polar westerlies (model day Feb. 9). Comparison of Figure 2(a) and 2(c) reveals a reversal in the meridional gradient of T poleward of 60°N above 10 mb. Figure 2(d) displays the concomitant reversal of the winds at high latitude.

Simulated ozone distributions at 10 mb are compared with corresponding LIMS data in Figure 3. The LIMS data shown in Figure 3 were chosen because the dynamical situation during the minor warming of January 1979 was similar to that of the model simulation. It is apparent that the model does a credible job of simulating the observed ozone distribution, particularly in high latitudes. The model ozone mixing ratio is about 25 percent larger than the observations at low latitudes. This problem is almost certainly one related to the chemistry and absorption cross sections used in the model. The model ozone distributions in low latitudes exhibit smaller scale structure not present in the LIMS data. If this structure is real, the LIMS resolution (6 zonal waves) is insufficient to resolve its presence. Both simulated and observed ozone distributions exhibit the characteristic signature of "wave breaking" described by McINTYRE and PALMER (1983, 1984) with the use of coarse-grained estimates of Ertel's potential vorticity inferred from Stratospheric Sounding Unit (SSU) data. These signatures were previously noted in the LIMS ozone data by LEOVY et al. (1984). Note also that the "tongues" or incursions of ozone-rich air from lower latitudes into the polar cap noted by LEOVY et al. (1984) also occur in the model.

The simulated distribution of HNO_3 at 10 mb is displayed in Figure 4(a). Peak mixing ratios of HNO_3 occur between 20 and 10 mb in the model simulations. This distribution is in contrast with the LIMS data where peak HNO_3 mixing ratios occur between 40 and 30 mb, and is apparently caused by the N_2O distribution prescribed for the model. The LIMS HNO_3 data for 30 mb is shown in Figure 4(b). Other than the mismatch in altitude, the model data generally shows good agreement with observations.

The distribution of Ertel's potential vorticity, Q , on the 850 K isentropic surface from the simulation is shown in Figure 5(a). The Q maps also depict the characteristics of breaking waves and the presence of a "surf" zone, as described by McINTYRE and PALMER (1983, 1984). Shown for comparison in

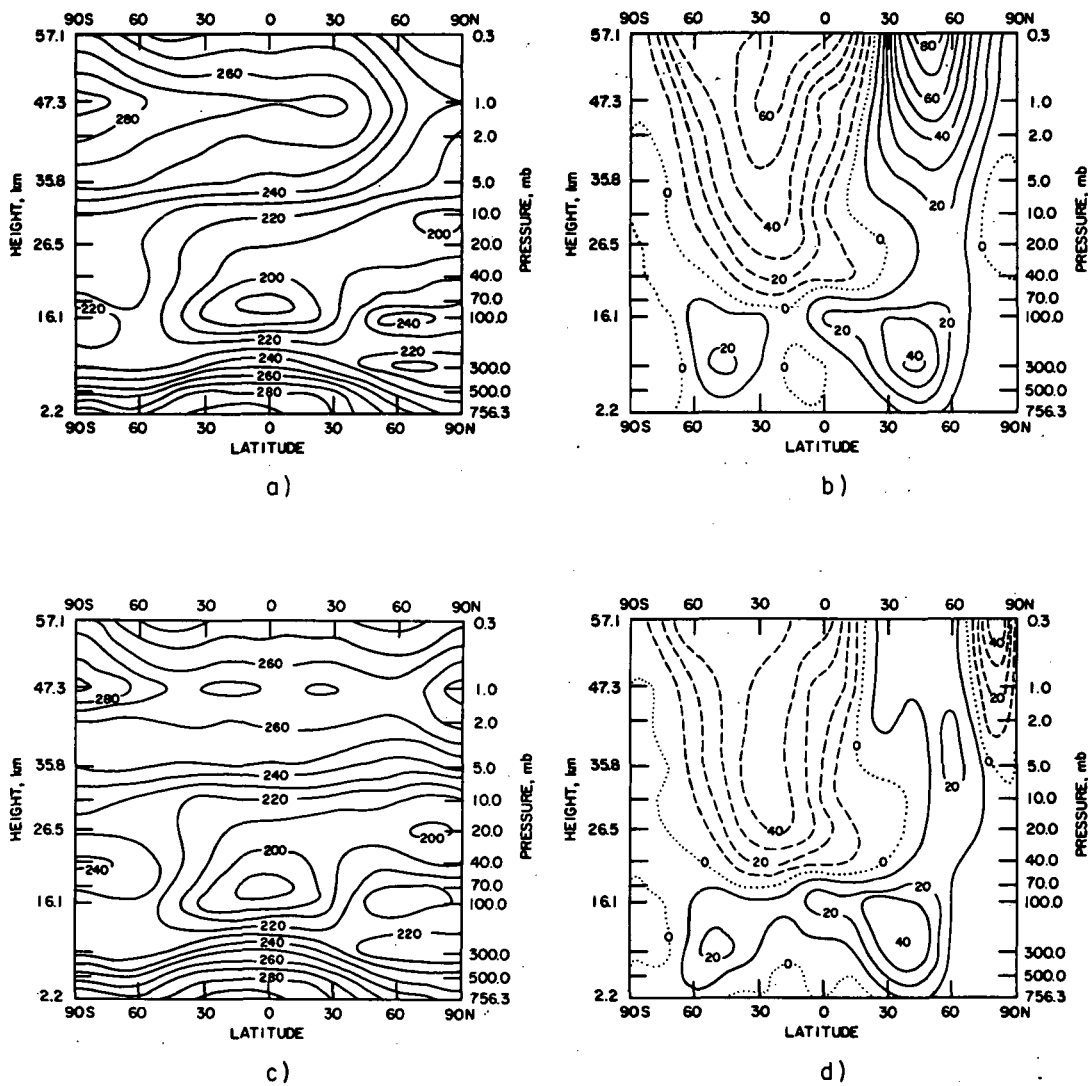


Figure 2. GCM simulation of zonally averaged temperature, K, and zonal wind, m/sec, for: (a) and (b) - Jan. 1, and (c) and (d) - Feb. 9.

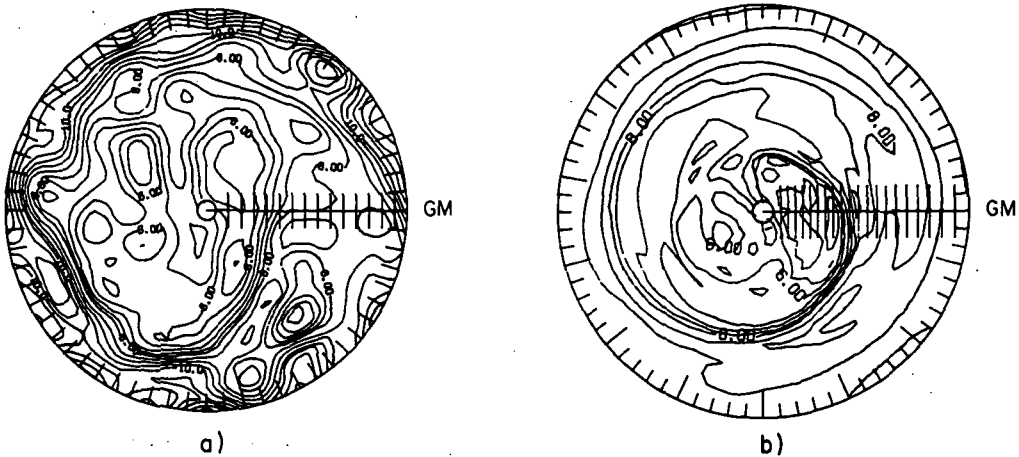


Figure 3. Northern Hemisphere ozone distributions, ppmv, at 10 mb during stratospheric warming for (a) model simulation, and (b) LIMS data of Jan. 27, 1979.

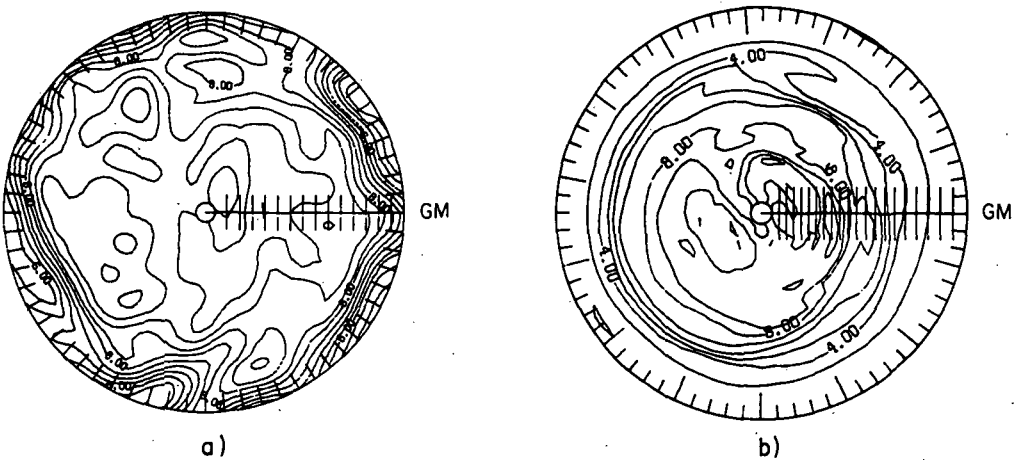


Figure 4. Northern Hemisphere nitric acid distributions, ppbv, during stratospheric warming for (a) model simulation at 10 mb, and (b) LIMS data of Jan. 27, 1979 at 30 mb.

Figure 5(b) is a map of Q derived from the LIMS temperature data (GROSE, 1985). Note the similarity of the distributions with both figures displaying the long tongues of relatively high Q that are drawn out of the central vortex and around the Aleutian high. Also present are the poleward incursions of low Q from low latitudes analogous to the behaviour seen in the ozone maps (Figure 3). Also apparent in the model data are the strong negative (positive) correlations of Q with O_3 (HNO_3). Similar correlations between Q , O_3 , and

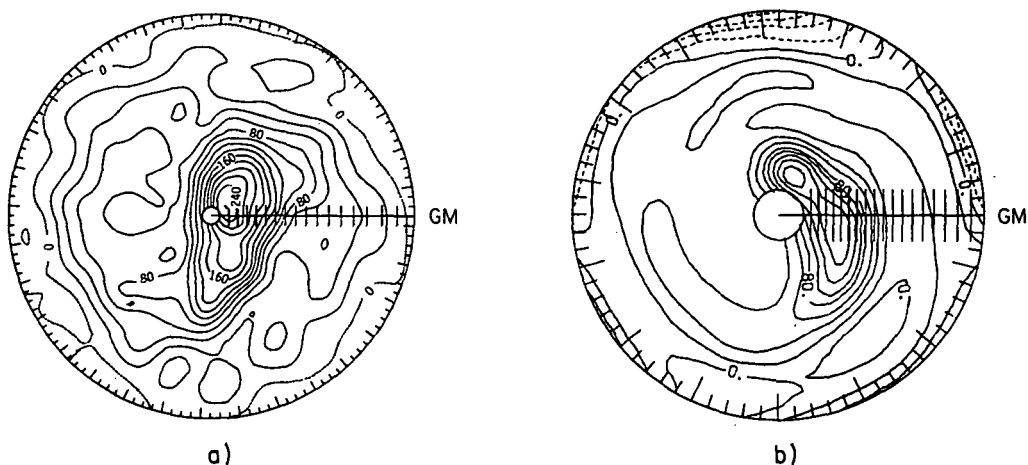


Figure 5. Northern Hemisphere potential vorticity on 850 K isentropic surface during warming for (a) GCM simulation, and (b) values derived from LIMS data of Jan. 27, 1979. (Units are $10^{-5} \text{ K-m}^{-1} \text{ s}^{-1}$).

HNO_3 are apparent from examining the LIMS data and were previously described in GROSE (1985). It is apparent that Q demonstrates strong correlations with quasi-conserved species in the lower stratosphere and provides considerable insight into transport processes.

REFERENCES

- Blackshear, W. T., W. L. Grose, R. E. Turner (1985), Q. J. Roy. Meteorol. Soc.
- Demore, W. B., M. J. Molina, R. T. Watson, D. M. Golden, R. F. Hampson, M. J. Kurylo, C. J. Howard, A. R. Ravishankara (1983), J. P. L. Publication 83-62, Pasadena, CA.
- Gille, J. C. and J. M. Russell III (1984), J. Geophys. Res., **89**.
- Grose, W. L., Advances in Space Research, Pergamon Press, Oxford, England (in press 1985).
- Grose, W. L., W. T. Blackshear, and R. E. Turner, J. Atmos. Sci., (to be submitted).
- Leovy, C. B., C. R. Sun, M. H. Hitchman, E. E. Remsberg, J. M. Russell III, L. L. Gordley, J. C. Gille, L. V. Lyjak, J. Atmos. Sci. (in press 1984).
- Mahlman, J. D. and W. J. Moxim (1978), J. Atmos. Sci., **35**.
- McIntyre, M. E. and T. N. Palmer (1983), Nature, **305**.
- McIntyre, M. E. and T. N. Palmer (1984), J. Atmos. Terr. Phys., **46**.

4.19 OZONE DURING SUDDEN STRATOSPHERIC WARMING: A THREE-DIMENSIONAL SIMULATION

K. Rose

Institut für Meteorologie
Freie Universität Berlin
FRG

G. Brasseur

Institut d'Aéronomie Spatiale
1180 Brussels, Belgium

INTRODUCTION

Sudden warmings which are currently observed in the winter stratosphere are believed to be due to the upward propagation of planetary waves originating in the troposphere. Major warmings are characterized by local increases of the temperature in a deep layer beyond the stratopause, with values of the order of 50 K at 10 mbar appearing over a short period of time (a few days) and leading to significant changes in the rate constant of several chemical reactions. During such events, the dynamical fields in the stratosphere are completely altered, so that dramatic changes in the transport of trace constituents are expected.

The purpose of this short note is to report preliminary results of a 3-D model simulation of the ozone behaviour during winter in connection with the appearance of a stratospheric warming. This paper will concentrate mainly on the middle stratosphere (12 mbar or approximately 32 km) where the chemical lifetime of odd oxygen is quite long, and consequently, transport plays a major role. Further studies will deal with the response of ozone at higher altitude (where the direct relation between ozone chemistry and temperature becomes more important) and extend into a 3-dimensional frame the previous 2-D studies of HARTMANN and GARCIA (1979) and KAWAHIRA (1982).

BRIEF MODEL DESCRIPTION

The 3-D dynamical model which is used in the present study is described by ROSE (1983). It is based on the so-called primitive equations which are solved using a finite difference technique in a space of grid-points with a longitudinal interval of 22.5° , a latitudinal interval of 5° , and a vertical resolution of 3 km. The model is hemispheric and extends from 10 to 80 km altitude. Diabatic processes are parameterized using a Newtonian cooling approximation. In order to simulate the propagation of planetary waves, a wave number 1 and 2 forcing in the geopotential height is imposed at the lower boundary.

The distribution and evolution of ozone is derived by solving for odd oxygen a continuity equation (see, e.g., BRASSEUR and SOLOMON, 1984). The chemical source term takes into account the production of odd oxygen by photodissociation of O_2 and its destruction by direct recombination of O and O_3 as well as the loss due to the presence of odd hydrogen and odd nitrogen. In the present stage of development of the model, the water vapor (H_2O) and odd nitrogen ($NO_x = NO + NO_2$) content is specified by a given mixing ratio (5 ppmv for H_2O and an altitude dependent value for NO_x). Photochemical equilibrium conditions are assumed for O (3P), O (1D), H , OH, and HO_2 . Moreover, NO_2 is assumed to be in immediate equilibrium with NO. The model does not yet consider any diurnal variation in the solar illumination and consequently, in the photodissociation rates, which is a good approximation

for the low levels under consideration, where the photochemical lifetime of odd oxygen is much longer than a day. Further development of the model will include longitudinal variations in the source term instead of a zonally averaged value, as in these preliminary calculations.

RESULTS

In order to perform an initialisation of the odd oxygen distribution (Figure 1), we first ran the chemical model for 25 days with the initial temperature field of the dynamic model. The initial state is zonally symmetric. After the initialisation, a numerical simulation of a sudden stratospheric warming is started and performed as described in detail by ROSE (1983).

At day 16 of the simulation, the cold vortex is removed from the pole (Figure 2a,b). An area of warm air developed in midlatitudes and moves north-eastward (Figure 2b). The O_3 mixing ratio at the 11.6 mbar level is shown in Figure 2c. At this altitude, O_3 nearly behaves like a tracer, i.e., the O_3 distribution is mainly due to transport. To facilitate the discussion of the simulation results, the height field of the 850 K isentropic surface (Figure 2d) is shown. If the motion were adiabatic, an air parcel starting on this isentropic surface would not leave it in the course of the simulation. The arrows in the figures indicate the direction of the motion parallel to the height contours due to geostrophic approximation. Together with the assumption that to a first approximation the motion is adiabatic, Figure 2 indicates that the maximum value of ozone is due to a northeastward transport out of the region where ozone is produced and a downward motion that crosses the 11.6 mbar level. The gross picture shows a counterclockwise advection around the vortex, which leads to an increase of ozone in higher latitudes. In the further course of the simulation, the structure of the height contours (Figure 3a) changes in a way that air of high O_3 mixing ratio is advected more directly to polar latitudes (Figure 3b). Three days later the polar vortex is split (Figure 4a), and still ozone is advected towards high latitudes (Figure 4b) at the easterly edge of the vortex.

During the whole course of the simulation and the northward transport of ozone at this altitude depends strongly on the location and shape of the polar vortex. A displacement from the pole leads to a northward flow at the easterly edge of the vortex and its elongation possibly leads to strong cross polar flow. Those configurations show that the modeling of the ozone distribution during a sudden stratospheric warming is a fully three-dimensional problem.

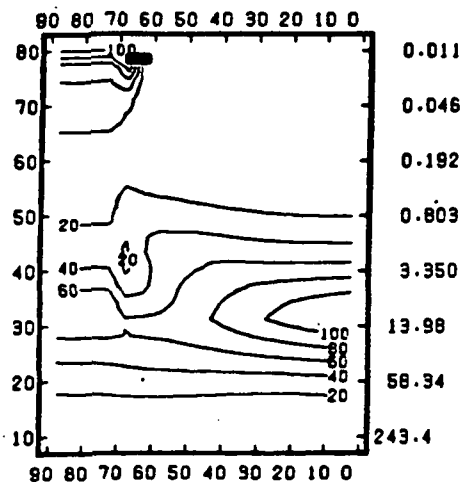
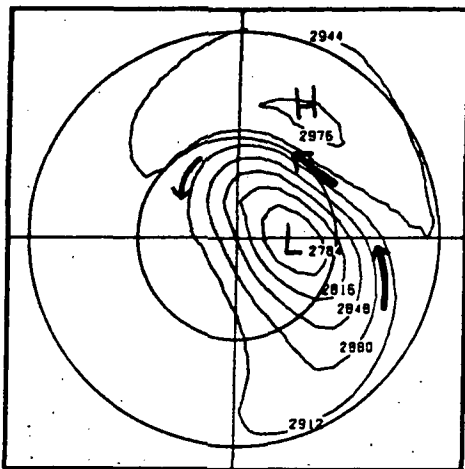
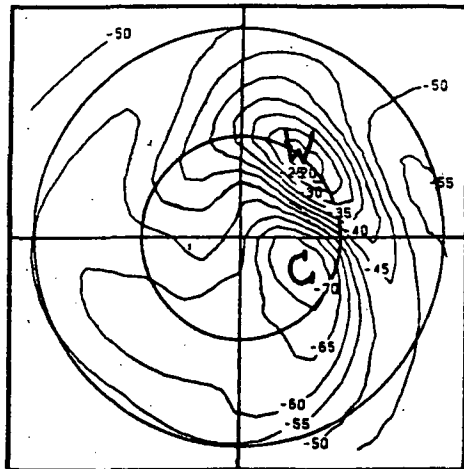


Figure 1. Meridional cross section of the O_3 mixing ratio (10 ppm) at the initial state.



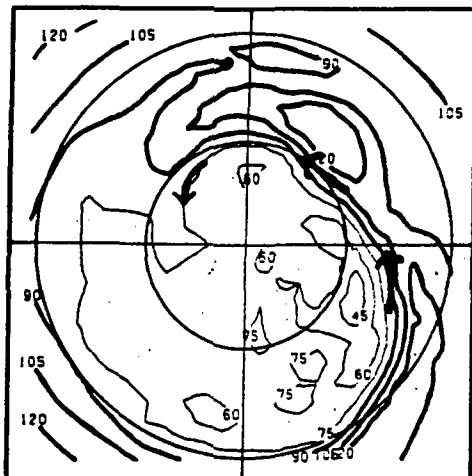
F112 KPRDG=1200NCOM=3073 16.01AGE

a)



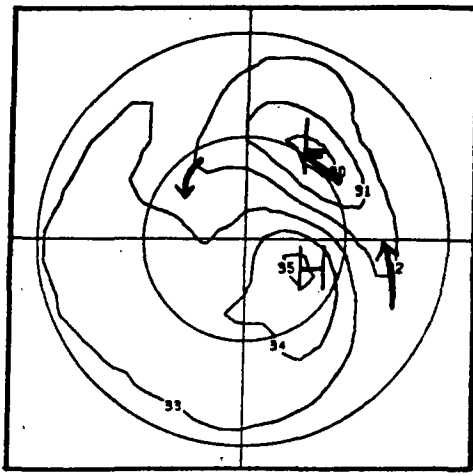
T112 KPRDG=1200NCOM=3073 16.01AGE

b)



G12 23 KPRDG=1200NCOM=3073 16.01AGE

c)



MH85 KPRDG=1200NCOM=3073 16.01AGE

d)

Figure 2 a) Geopotential height (gpdam) of the 11.6 mbar surface,
 b) Temperature (deg C) at the 11.6 mbar surface,
 c) O_3 mixing ratio (10 ppm) at the 11.6 mbar surface,
 d) Height contours (km) of the 850 K isentropic surface, all on day 16 of the simulation.

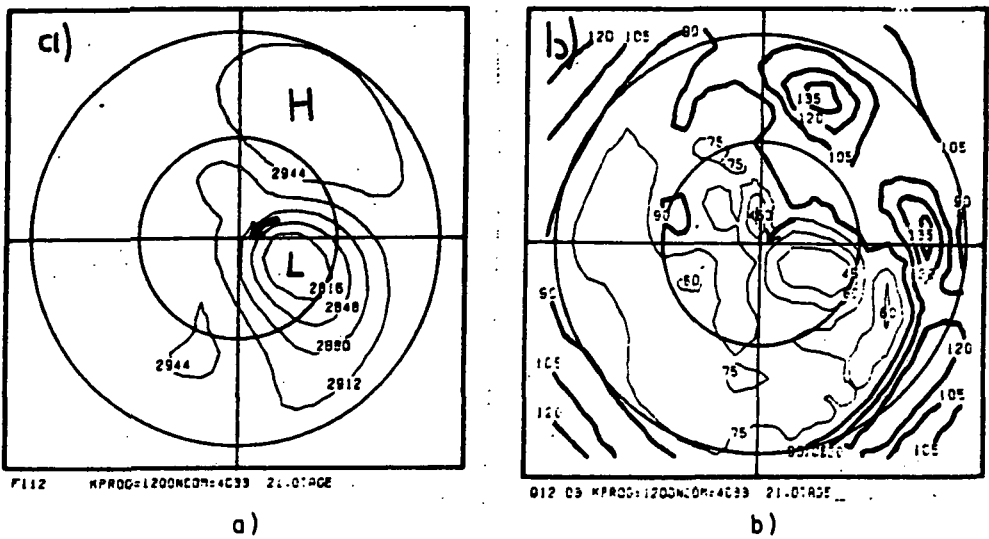


Figure 3 a) Geopotential height (gpdam) of the 11.6 mbar surface,
b) O_3 mixing ratio (10 ppm) at the 11.6 mbar surface,
all on day 21.

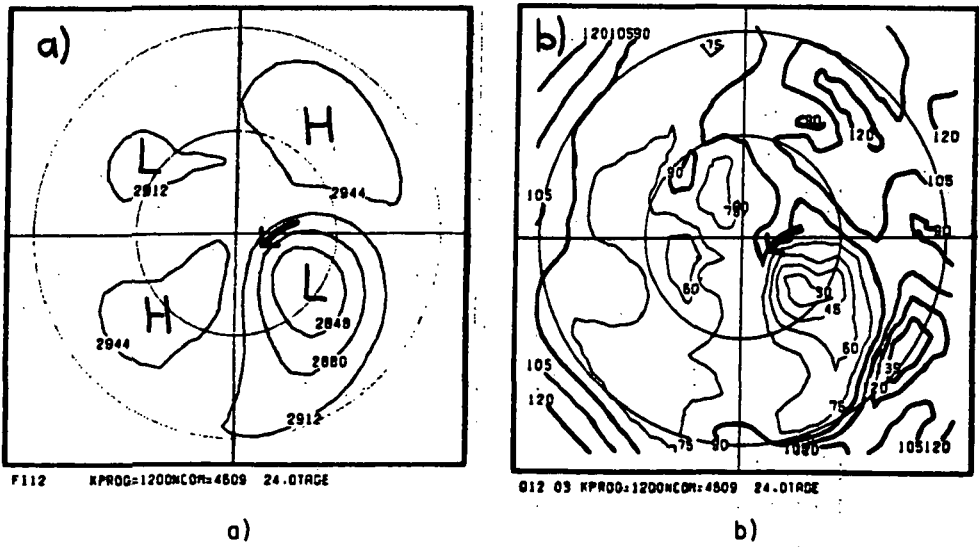


Figure 4. Same as Figure 3 except for day 24.

REFERENCES

- Brasseur, G. and S. Solomon, Aeronomy of the Middle Atmosphere, D. Reidel Publ. Co., Dordrecht, Nederland.
- Hartmann, D. L. and R. R. Garcia (1979), A mechanistic model of ozone transport by planetary waves in the stratosphere, J. Atmos. Sci., **36**, 350-364.
- Kawahira, K. (1982), A two-dimensional model for ozone changes by planetary waves in the stratosphere. I. Formulation and the effect of temperature waves on the zonal mean ozone concentration, J. Met. Soc. Japan, **60**, 1058-1062.
- Rose, K. (1983), On the influence of nonlinear wave-wave interaction in a 3-D primitive equation model for sudden stratospheric warmings, Beitr. Phys. Atmos., **56**, 14-40.

4.20 INTRUSION PROCESS OF STRATOSPHERIC OZONE INTO THE TROPOSPHERE OVER JAPAN

H. Muramatsu, Y. Makino, M. Hirota and T. Sasaki

Meteorological Research Institute
1-1, Nagamine, Yatabe-machi, Tsukuba-gun,
Ibaraki, 305 Japan

The stratospheric-tropospheric exchanges play an important role in determining the distribution and residence time of ozone, aerosol and other substances in the stratosphere and troposphere. In this study we estimate the ozone transport from the stratosphere into the troposphere by so-called "tropopause folding event" associated with the polar front jet stream. We show that in winter ozone transport occurs mainly in the region to the north of Japan in Asia.

We estimate ozone transport rate $M(O_3)$ over any place with area dS by

$$M(O_3) = [O_3] \bar{V}_z P_r dS \quad (1)$$

where $[O_3]$ is the ozone density at 350 mb level (the average level of the polar front jet stream), \bar{V}_z is the mean vertical velocity at 350 mb level, P_r is the probability that the tropopause descends below 350 mb level over any place with area dS . We used the data obtained from aircraft observations for $[O_3]$ and radiosondes for \bar{V}_z and P_r .

Figure 1 shows an example of the aircraft observation on February 14, 1984. The intrusion of the stratospheric air with a high ozone mixing ratio at the 350 mb level is 220 ppb. Intrusion of the stratospheric air during 24 hours is shown in Figure 2. Shading represents the region of the stratospheric air, where the potential vorticity is higher than $10^{-5} K mb^{-1} sec^{-1}$. Filled circles show the region of high ozone mass mixing ratio (100 ppb) shown in Figure 1.

Vertical velocity was estimated by marking the air parcel and tracking it on the isentropic surface. The mean vertical velocity of the air parcel was estimated from the air parcels with potential temperature between 296 K and 300 K. Obtained value is $2.5 cm sec^{-1}$ for this case.

We estimated the probability that the tropopause descends below the 350 mb level, using all the data of radiosondes in February and shown in Figure 3. It is shown that the probability is maximum over northern Japan (Hokkaido) to Sakhalin, where the tropopause folding event can be observed on about 14 days in February.

We assume that ozone density $[O_3]$ and corresponding mean vertical velocity \bar{V}_z obtained by aircraft observations and radiosondes are representative for the Asian area, i.e., for the region where the probability of the folding event was estimated. Then the ozone transport rate is estimated by Equation 1.

Table 1 shows the summary of the result including another case on 20 February 1983. The ozone transport rate for the Northern Hemisphere was obtained from multiplying 3 by the value for Asia, assuming three cyclogenetic regions in the Northern Hemisphere. DANIELSEN and MOHNEN (1977) obtained the average vertical flux of 1.99×10^{29} molecules sec^{-1} for the Northern

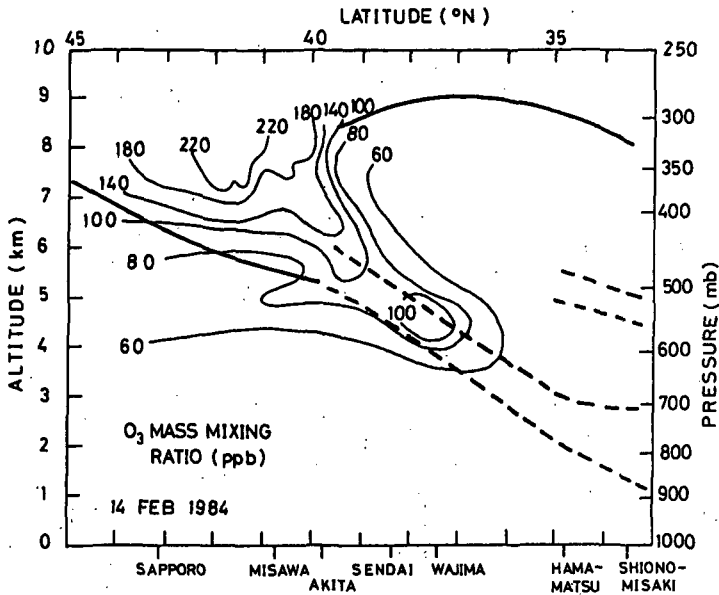


Figure 1. Vertical cross section of ozone.

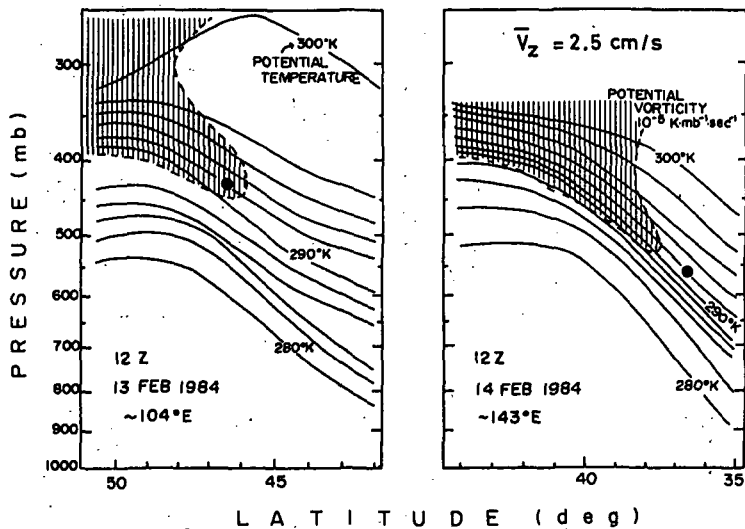


Figure 2. Downward transport of the stratospheric air.

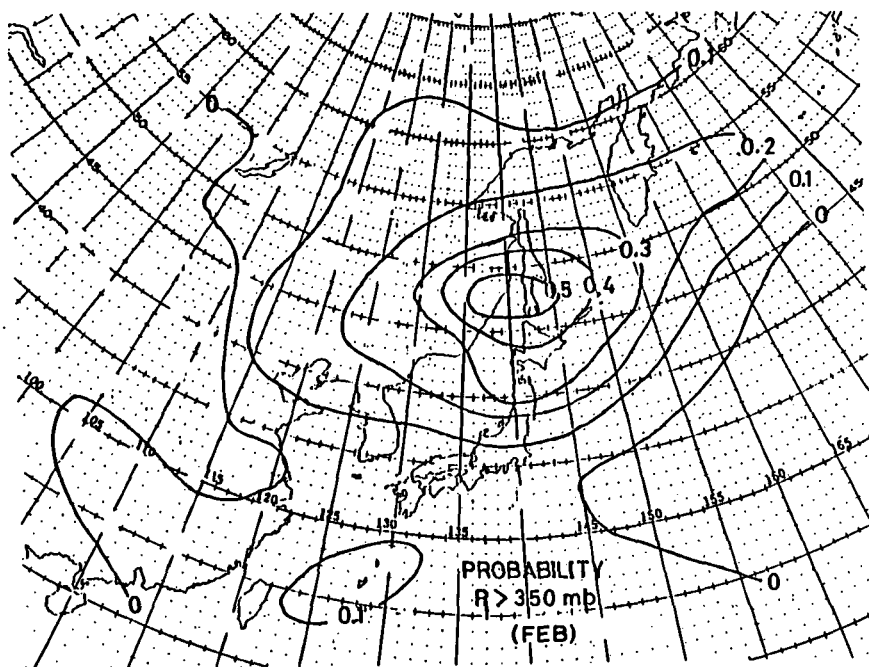


Figure 3. Distribution of the probability of tropopause folding event.

Table 1. Summary of the result.

Dates	[O ₃] (ppbv)	\bar{v}_z (cm/sec)	Ozone transport rate (molecules/sec)	
			Asia	Northern Hemisphere
20 Feb. 1983	184	3.0	1.8×10^{29}	5.3×10^{29}
14 Feb. 1984	135	2.5	1.1×10^{29}	3.2×10^{29}

Hemisphere from the mass outflow rate and representative ozone mixing ratio. Their value is close to the upper limit of 1.95×10^{29} molecules sec⁻¹ estimated by FABIAN and JUNG (1970) from ozone destruction at the surface.

According to the seasonal variation of the ozone transport rate shown by DANIELSEN and MOHNEN (1977), the ozone transport rate in February should be close to the average annual value. Our values obtained in February over northern Japan are 2 to 3 times those of FABIAN and JUNG (1970) and DANIELSEN and MOHNEN (1977). The ozone transport rate estimated from the aircraft observation made in March 1981 (MURAMATSU et al., 1984) shows a higher transport rate of 6.5×10^{29} molecules sec⁻¹ for the Northern Hemisphere.

REFERENCES

- Danielsen, E. F. and V. A. Mohnen (1977), Project Dustorm Report: Ozone transport, in situ measurements, and meteorological analyses of tropopause folding, J. Geophys. Res., 82, 5867-5877.
- Fabian, P. and C. E. Junge (1970), Global rate of ozone destruction at the earth's surface, Arch. Met. Geophys. Biokl., Ser. A, 19, 161-172.
- Muramatsu, H., T. Sasaki, M. Hirota and Y. Makino (1984), An aircraft observation of an intrusion process of stratospheric ozone into the troposphere, Papers in Meteor. and Geophys., 35, 1-10.

4.21 AN INTERPRETATION FOR THE INTERANNUAL VARIATIONS OF THE GLOBAL DISTRIBUTION OF TOTAL OZONE

Fumio Hasebe

Laboratory for Climatic Change Research
Geophysical Institute,
Kyoto University Kyoto 606, Japan

INTRODUCTION

The quasi-biennial oscillation (QBO) and the four-year oscillation (FYO) in total ozone are discussed. In order to understand these oscillations, we try to get a comprehensive view of the ozone and the stratospheric temperature. The standpoint here is to examine if these oscillations could be understood as a reflection of the general circulation changes in the stratosphere. The description of the circulation will be based on the Lagrangian-mean point of view (e.g., HOLTON, 1980), although only a rough estimate could be obtained, of course. For the sake of simplicity, the ozone is assumed to be an inert tracer following the atmospheric motion.

QUASI-BIENNIAL OSCILLATION IN TOTAL OZONE

The characteristic features of the QBO in the zonal mean total ozone could be summarized as follows (HASEBE, 1983, 1984): (1) The positive deviations in the tropical total ozone correspond to the westerly phase of the equatorial zonal wind at 50 mb. (2) There is a phase reversal at 15°S. (3) Between the northern middle and high latitudes, the phase is often opposite. (4) The phase in the southern midlatitudes is delayed about a half year to that in the northern midlatitudes. For these features, the following dynamical processes would be responsible.

In the equatorial region, the observed total ozone QBO could be reproduced from the observed temperature QBO by considering the diabatic mean meridional circulation (HASEBE, 1984). The essence is as follows: The vertical wind shear associated with the downward propagating westerly and easterly wind regimes is accompanied by a horizontal temperature gradient satisfying the thermal wind relation. On the time scale of the QBO, these temperature anomalies suffer from radiative damping. The diabatic heating (cooling) in the cold (warm) region drives the upward (downward) motion (REED, 1964; PLUMB and BELL, 1982). Since the ozone mixing ratio has a strong vertical gradient, the ozone variations are brought about.

As to the extratropical QBO, HOLTON and TAN (1980, 1982) tried to understand the observed seesaw structure between the northern middle and high latitude geopotential height field by the modulation of the tropospheric dynamical forcing. The ozone QBO appears to be consistent with their idea. The scenario is as follows: during the easterly phase of the equatorial zonal wind, tropospheric forcing is concentrated at latitudes higher than the zero wind line in midlatitudes. The stronger forcing brings about earlier and larger amplification of planetary waves in the winter that follows. Such an amplification is accompanied by the poleward transport of ozone and potential temperature in excess of the equatorward transport by the mean meridional circulation. Owing to the excessive transport by the waves, total ozone and temperature in high latitudes exhibit positive deviations while those in midlatitudes show negative ones; the out-of-phase relation between middle and high latitudes (the seesaw pattern) of total ozone and temperature is thus realized.

Then the whole story of the QBO could be summarized as in Figure 1. In the equatorial region, there is a temperature QBO which satisfies the thermal

wind relation and the ozone QBO driven by a diabatic circulation. There is a phase lag of a half year between the two. For the extratropical QBO, there is a dipole like variation in winter; this is a result of the modulation of the tropospheric dynamical forcing. Depending on the seasonal delay, there is an asymmetry between the two hemispheres. And owing to the weaker tropospheric forcing and/or the miss-matching between the tropical QBO and the seasonal march, the influence is weaker for the Southern Hemisphere. These features are the same for the ozone and temperature.

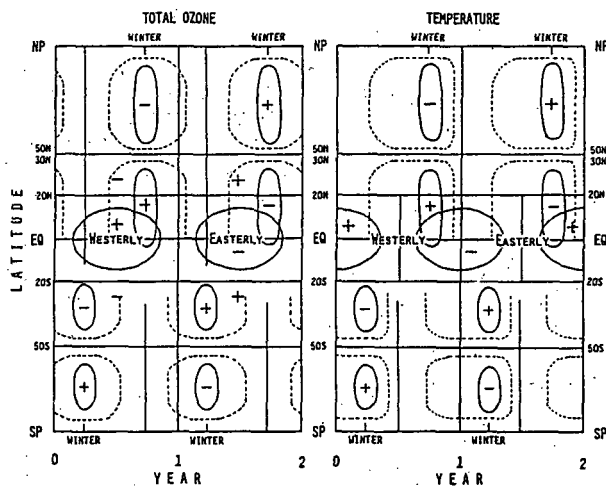


Figure 1. Schematic diagram of the quasi-biennial oscillation in total ozone and temperature, both superpositions of (1) diabatic process in the tropics and (2) extratropical transport by the planetary waves.

FOUR-YEAR OSCILLATION IN TOTAL OZONE

The four-year oscillation (FYO) was noticed in the Northern Hemisphere among the fluctuations of the ground-based network data of fifteen years (HASEBE, 1980). Recently, it is shown that the FYO has a beautifully organized global structure, as in the following (HASEBE, 1983, 1984): (1) The FYO is almost symmetric with respect to the equator. (2) The phase is opposite between the low and high latitudes. (3) There is a tendency that warm sea surface temperatures are followed by the equatorial negative and extratropical positive deviations of total ozone. These features for the FYO are suggestive of the thermally driven circulation changes.

In order to investigate the mechanisms of the FYO, it is helpful to see the long-term variations of the lower stratospheric temperature and the heat flux convergence by eddies for the middle and high latitudes (Figure 2). The important points are as follows: In high latitudes, temperature and ozone are in phase, while the phase of the heat flux convergence precedes $\pi/2$ as expected. In the middle latitudes, the temperature shows scarcely no change, although the heat flux convergence by eddies does. This implies that the heat transport by the waves is cancelled out by that of the mean meridional circulation. These circumstances suggest that the transiency of the waves would play only a minor role, so that the Lagrangian-mean circulation could be approxi-

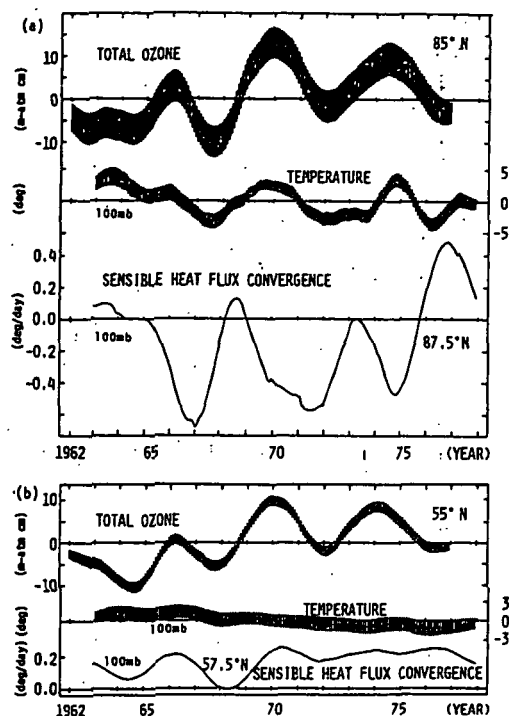


Figure 2. Long-term variations in total ozone, temperature and sensible heat flux convergence by horizontal eddies at 100 mb. (a) high latitude and (b) middle latitude of the Northern Hemisphere.

mated by the residual circulation. In this case, the governing equation for the zonal mean ozone concentration $\bar{\chi}$ would be approximated by

$$\frac{\partial \bar{\chi}}{\partial t} = \frac{\partial \chi_0}{\partial z} \frac{g}{N^2} \left\{ h \left(1 - \frac{\theta^*}{\bar{\theta}} \right) + \frac{\partial \ln \bar{\theta}}{\partial t} \right\} \quad (1)$$

where χ_0 is a basic state ozone mass mixing ratio, h is the Newtonian cooling coefficient, and θ^* is the zonal mean equilibrium potential temperature (HASEBE, 1984, 1985). By using the observed potential temperature for $\bar{\theta}$ in Equation 1, the FYO is qualitatively reproduced in the northern mid- and high latitudes (HASEBE, 1984).

In considering the driving processes of the FYO, it should be noticed that the FYO is in phase with temperature variations in high latitudes. This fact implies that the principal term in Equation 1 is not the first one which represents the local diabatic heating in high latitudes; if this is the case, there must be a phase lag of $\pi/2$. Therefore, it is locally an adiabatic process, primarily. In other words, the ozone and the temperature variations are brought about passively by a circulation which is driven in some other places; that is, low latitudes. This is consistent with the idea that the FYO is a reflection of the general circulation changes induced by the equatorial sea surface temperature anomalies.

CONCLUSION

Characteristic features of the quasi-biennial and four-year oscillations in total ozone (QBO and FYO) are discussed in connection with the lower stratospheric temperature field. It is found that the QBO and the FYO could be understood as a reflection of the general circulation changes in the strato-

sphere. The origin of the phenomenon lies in the stratospheric zonal wind (QBO) and the sea surface temperature (PDO) in the equatorial region. Therefore, the global structure of these oscillations cannot be free from the dynamical interactions between low and high latitudes and between the stratosphere and the troposphere, including the ocean. Then, from the global ozone observations, we are hopeful of getting many interesting characteristics of the earth's atmosphere-ocean systems.

ACKNOWLEDGEMENTS

The author would like to thank Profs. R. Yamamoto and I. Hirota, Kyoto University, J. R. Holton, Univ. Washington, T. Matsuno, Univ. Tokyo, Drs. J. C. Gille, NCAR, and K. K. Tung, MIT, for their helpful comments and discussions. He is also indebted to Mr. M. Shiotani for the treatment of Nimbus 5 SCR data.

REFERENCES

- Hasebe, F. (1980), J. Meteorol. Soc. Japan, **58**, 104-117.
 Hasebe, F. (1983), J. Geophys. Res., **88**, 6819-6834.
 Hasebe, F. (1984), Dynamics of the Middle Atmosphere, J. R. Holton and T. Matsuno, eds., Terra Sci. Publ. Co., Tokyo, 445-464.
 Hasebe, F. (1985), In Proceedings of the International Ozone Symposium, Greece, September 1984.
 Holton, J. R. (1980), Phil. Trans. Roy. Soc. London, **A296**, 73-85.
 Holton, J. R. and H.-C. Tan (1980), J. Atmos. Sci., **37**, 2200-2208.
 Holton, J. R. and H.-C. Tan (1982), J. Meteorol. Soc. Japan, **60**, 140-148.
 Plumb, R. A. and R. C. Bell (1982), Quart. J. Roy. Meteorol. Soc., **108**, 335-352.
 Reed, R. J. (1964), Quart. J. Roy. Meteorol. Soc., **90**, 441-466.

4.22 EMISSION, ABSORPTION AND GROUP DELAY OF MICROWAVES IN THE ATMOSPHERE IN RELATION TO WATER VAPOUR CONTENT OVER THE INDIAN SUBCONTINENT

A. K. Sen¹, A. K. Dev Gupta², P. K. Karmakar³, S. Dev Barman⁴,
A. B. Bhattacharya⁵, N. Purkait¹, M. K. Das Gupta¹, and J. S. Sehra⁶

¹ Institute of Radiophysics & Electronics, University of Calcutta, India

² Scottish Church College, Calcutta, India

³ St. Andrew's High School, Calcutta, India

⁴ Bajkul Milani College, Midnapore, West Bengal

⁵ Serampore College, Howrah, West Bengal, India

⁶ Department of Electronics Govt. of India, New Delhi, India

INTRODUCTION

The advent of satellite communication for global coverage has apparently indicated a renewed interest in the studies of radio wave propagation through the atmosphere, in the VHF, UHF and microwave bands. The extensive measurements of atmospheric constituents, dynamics and radio meteorological parameters during the Middle Atmosphere Programme (MAP) have opened up further the possibilities of studying tropospheric radio wave propagation parameters, relevant to earth/space link design. The three basic parameters of significance to radio propagation are thermal emission, absorption and group delay of the atmosphere, all of which are controlled largely by the water vapour content in the atmosphere, particularly at microwave bands. As good emitters are also good absorbers, the atmospheric emission as well as the absorption attains a maximum at the same frequency of 22.235 GHz, which is the peak of the water vapour line. The group delay, on the other hand, is practically independent of frequency in the VHF, UHF and microwave bands. However, all three parameters exhibit a similar seasonal dependence originating presumably from the seasonal dependence of the water vapour content. Some of the interesting results obtained from analyses of radiosonde data over the Indian subcontinent collected by the India Meteorological Department (IMD) is presented in this paper.

EQUATIONS

Absorption

The attenuation rate in dB/km due to absorption in the atmosphere is given by (BARRETT and CHUNG, 1962)

$$\alpha = \frac{1.05}{10^{28}} \cdot \frac{Nv^2}{T^{5/2}} \cdot \frac{644}{T} \cdot \frac{\Delta v_p}{(v-v_0)^2 + \Delta v_p^2} + \frac{\Delta v_p}{(v+v_0)^2 + \Delta v_p^2} \quad (1)$$

$$+ \frac{1.52}{10^{52}} \cdot \frac{Nv^2 \Delta v_p}{T^{3/2}} \text{ cm}^{-1}$$

where N = no. of molecules per cm^3

v = frequency, Hz

T = kinetic temperature, °K

and Δv_p = pressure broadened line halfwidth parameter given by

$$\Delta v_p = 2.62 \times 10^9 \frac{(P/760)}{(T/380)^{0.625}} (1 + 0.0046\rho) \text{sec}^{-1} \quad (2)$$

P being the total atmospheric pressure, mmHg and ρ , the density of water vapour in gm m^{-3} .

Emission

The antenna temperature T_a due to thermal emission from the atmosphere can be deduced from the attenuation rate, α by the relation (MEEKS and LILLEY, 1963)

$$T_a = T_s e^{-\int_h^\infty \alpha(x) \sec \theta dx} + \int_h^\infty \alpha(x) T_e e^{-\int_h^\infty \alpha(x) \sec \theta dx}, \sec \theta dx \quad (3)$$

where T_s = the brightness temperature of a source above the atmosphere, such as the Sun
 h = height above the earth's surface
 θ = the zenith angle of the ray path
 $\alpha(x)$ = atmospheric attenuation rate at a slant range x in nepers per unit distance
 and T = kinetic temperature of the atmosphere.

The first term of Equation (3) describes the absorption process while the second term describes the emission process.

From Equations (1), (2) and (3) RAINA et al. (1981) deduced the relation between the emission noise temperature T_a and the integrated water vapour content for vertical propagation at 22.235 GHz.

$$T_a = 1.34 \times 10^{-3} W + 3.5 \quad (4)$$

This relation can be utilised to estimate T_a directly from the integrated water vapour content calculated from the radiosonde data. The estimate of T_a can, in turn, be employed to deduce α from the relation (ALLNUTT, 1976).

$$\alpha = \log 10 \frac{T_m}{T_m - T_a} \text{ dB/km} \quad (5)$$

where T_m = mean temperature of the atmosphere assumed to be 275 K.

Group Delay

The polarisation P of water vapour in the atmosphere due to a radio wave of frequency $\omega = 2\pi f$ is given by (DEBYE 1957).

$$P(\omega) = \frac{\epsilon - 1}{\epsilon + 2} \frac{M}{\rho} = \frac{4\pi N}{3} \left[\alpha_o + \frac{\mu^2}{3kT} \frac{1}{1 + i\omega\tau} \right] \quad (6)$$

where ϵ = dielectric constant

M = molecular weight

ρ = density

N = Avogadro's number

μ = permanent dipole moment

k = Boltzman's constant

T = absolute temperature

and τ = relaxation time for external field-induced orientation of the molecules to return to random distribution after the field is removed.

For frequencies less than 100 GHz, $\omega\tau \ll 1$ and

$$P(\omega) = \frac{4\pi N}{3} \left[\alpha_o + \frac{\mu^2}{3kT} \right] \quad (7)$$

In fact, the dispersive effect of water vapour is insignificant at microwaves below 30 GHz (BEAN and DUTTON 1968) as indicated in Equation (7). The refractive index, n , of air may, therefore, be assumed to be independent of frequency. The additional phase path due to troposphere is given by

$$\phi = \int_0^h \frac{2\pi}{\lambda} n \, dh \quad (8)$$

where h is the length of the tropospheric path.

Expressing n in terms of a more convenient refractivity unit $N = (n-1)10^6$ we have the group delay given by

$$\begin{aligned} \tau &= \frac{d\phi}{d\omega} \\ &= \frac{d}{d\omega} \left[\int_0^h \frac{2\pi}{\lambda} \left(\frac{N}{10^6} + 1 \right) dh \right] \\ &= \frac{10^{-6}}{c} \int_0^h N dh + \frac{1}{c} \int_0^h dh \end{aligned} \quad (9)$$

where c = velocity of light.

The first term in Equation (9) represents the tropospheric delay while the second term indicates the free space delay. Accordingly, the excess delay due to the troposphere is given by

$$\tau_T = \frac{10^{-6}}{c} \int_0^h N \, dh \quad (10)$$

The refractivity, N , of the atmosphere depends on the water vapour content in the atmosphere as well as on other meteorological parameters as given by (SMITH and WEINTRAUB, 1953).

$$N = 77.6(1 - 0.077e/P)P/T + 3.735 \cdot 10^5 e/T^2 \quad (11)$$

where e = water vapour pressure, mb.

For practical work in radio-meteorological studies, Equation (11) may be reduced further as (BEAN and DUTTON 1968)

$$N = 77.6 \frac{P}{T} + 3.73 \cdot 10^5 \frac{e}{T^2} \quad (12)$$

The water vapour pressure may be determined by radiosonde measurements of the dew point temperature, T_D , and employing the relation (SWINGLE, 1953)

$$e = 6.1078e^{5369\left(\frac{1}{273} - \frac{1}{T_D}\right)} \quad (13)$$

The other atmospheric parameters, P and T , are also obtained by the radiosonde measurements, and all these enable N to be estimated from Equation (12). Substituting N as a function of height h in Equation (10), the excess group delay $\Delta\tau$ is estimated.

ESTIMATES

The height profiles of water vapour density, $W(h)$ and refractivity $N(h)$ over the Indian subcontinent obtained from radiosonde data of the India Meteorological Department, collected during a 4-year period from 1968-1971, have been employed to estimate the radio propagation parameters T_a , α and $\Delta\tau$ from the Equations (4), (5) and (10), respectively. The estimates for two extreme regions of India where the values of a parameter attain a maximum and minimum are shown in Figure 1. The figure clearly shows that the seasonal trend of each of the parameters is similar to the maximum occurring in a monsoon over the Assam valley and the minimum in winter over the desert area of Rajasthan.

DISCUSSION

The fact that the estimates indicate a minimum value of each of the radio propagational parameters T_a , α and $\Delta\tau$ over the desert area of Rajasthan suggest that this would be an ideal location for an earth station in space communication, the situation being worse over the Assam valley. Also, in estimating the National coverage by a satellite over the Indian Subcontinent, the radio propagation parameters over the Assam Valley will be a determining factor. As each of the parameters are largely controlled by the integrated water vapour content as indicated by the present estimates, a continuous monitoring of the integrated water vapour content is desirable for an assessment and prediction of the effect of the troposphere on the propagation of microwaves in earth/space links. Such a continuous monitoring of the integrated water vapour content can be made effectively, with a higher precision than that of radiosonde measurements, by employing a microwave radiometer at the peak of the water vapour line at 22.235 GHz, with its antenna beam pointed vertically upwards. It may be mentioned here that the radiometric monitoring of the integrated water vapour content has recently been started on a round-the-clock basis at the Institute of Radio Physics and Electronics, University of Calcutta, in collaboration with the Space Application Center (SAC), Indian Space Research Organization, Ahmedabad. The SAC is also organizing similar radiometer monitoring from a number of locations in India, while the National Physical Laboratory is reviving its radiometric monitoring, shortly.

ACKNOWLEDGEMENTS

This work is a part of the Indian Middle Atmosphere Programme (IMAP) entitled (1) Studies on water vapour content in the atmosphere from radiometric

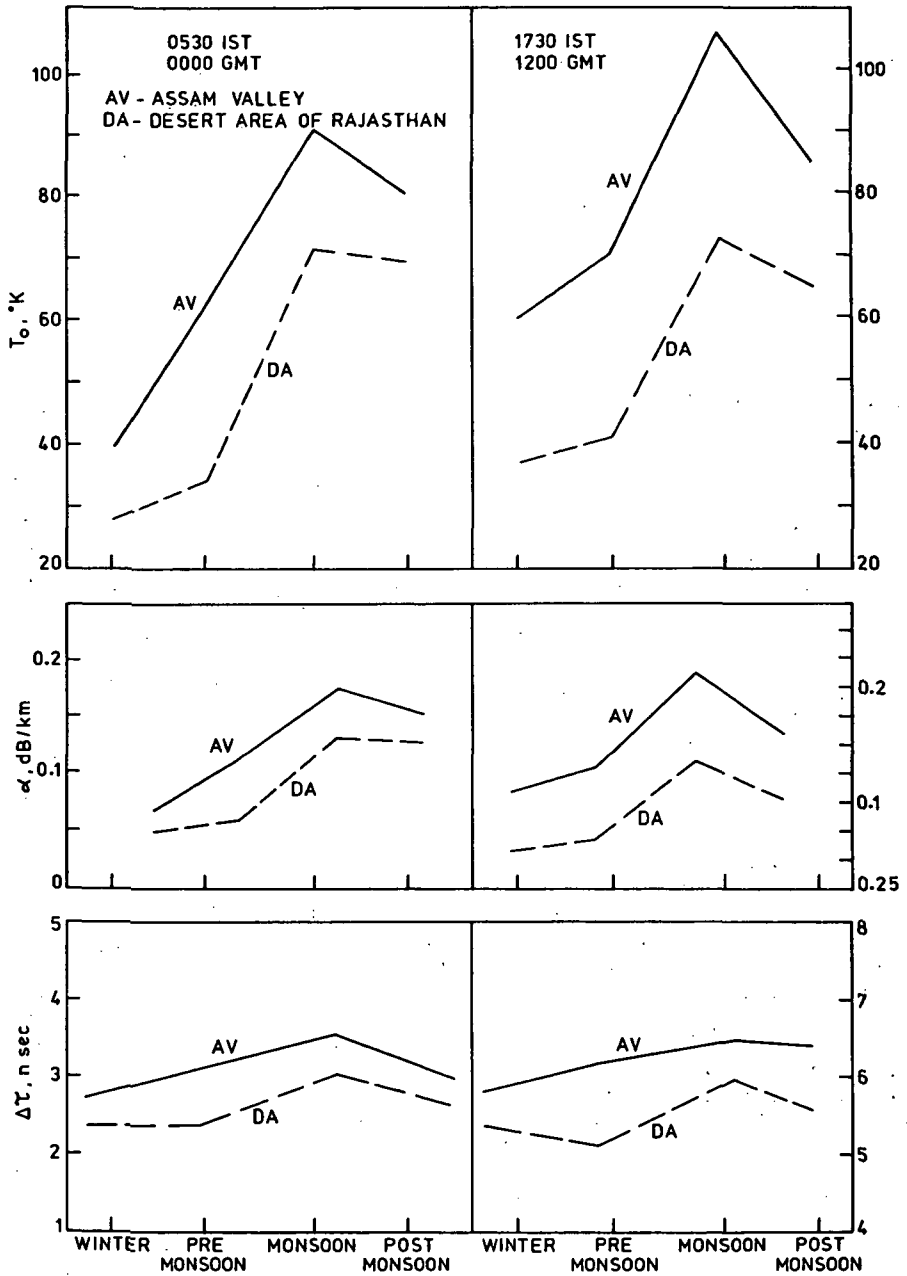


Figure 1. Seasonal variation of radio propagation parameters: seasonal variation of antenna temperature, T_a , that of attenuation rate, α , and that of excess group delay, $\Delta\tau$.

measurements at 22.235 GHz, and (2) Modeling of the troposphere from radio propagation and radio refractive index data. It is also supported by a project entitled "Studies of microwave attenuation from radiometric measurements at 12 and 22 GHz", financed by the University Grants Commission, Government of India. The authors are grateful to the Director, India Meteorological Department, Government of India, and Dr. A. P. Mitra, Director, National Physical Laboratory, for providing the relevant data and helpful discussions.

REFERENCES

- Allnutt, J. E. (1976), Proc IEE, 123, 1197.
 Barrett, A. H. and V. K. Chung (1962), J. Geophys. Res., 67, 4259.
 Bean, B. R. and Dutton, E. J. (1968), Radio Meteorology, Dover Publications, N.Y., Chap. 1, p.1.
 Debye, P. (1957), Polar Molecules, Dover Publications, N.Y., 89.
 Meeks, M. L. and A. E. Lilley (1963), J. Geophys. Res., 68, 1683.
 Raina, M. K., D. Vandana, G. S. Uppal and R. Chadha (1981), Ind. J. Radio Space Phys., 10, 41.
 Smith, E. K. and S. Weintraub (1953), Proc. IEE, 41, 1035.
 Swingle, D. M. (1953), Proc IRE, 41, 385.

4.23 AIRCRAFT OBSERVATION OF NO_x IN THE TROPOSPHERE AT MIDLATITUDE

Y. Kondo, W. A. Matthews*, A. Iwata, Y. Morita and M. Takagi

Research Institute of Atmospheric
Nagoya University
Toyokawa 442, Japan

*PEL Atmospheric Station, DSIR, Lauder
Central Otago, New Zealand

Aircraft observations of NO (NO and NO_2) over the sea surrounding the Japanese islands ($30-43^\circ$, $131-141^\circ\text{E}$) were carried out in the winter of 1983 and 1984 at latitudes between 3 and 8 km. The main NO_x features observed were as follows:

- 1) Over the Pacific Ocean between the latitudes of $30-35^\circ\text{N}$, the observed NO_x mixing ratio at 3-8 km was a fairly constant 0.2 ppbv. The NO mixing ratio increased with altitude from 20 pptv at 3 km and reached 40 pptv at 7 km.
- 2) The NO_x mixing ratio measured in the air mass transported from the stratosphere was also about 0.2 ppbv.
- 3) Over the Sea of Japan tropospheric NO_x started increasing with latitude north of 35°N and reached about 1 ppbv at 40°N .

REFERENCES

- Kondo, Y., A. Iwata and M. Takagi (1983), A chemiluminescent NO - detector for the aircraft measurement, J. Meteorol. Soc. Japan, **61**, 756-762.
- Kondo, Y., A. Iwata, W. A. Matthews, Y. Morita and M. Takagi (1984), Measurement of oxides of nitrogen in the free troposphere over Japan, Proc. Int. Ozone Symp., Greece.

4.24 NUMERICAL SIMULATION OF EL CHICHON VOLCANIC CLOUD

T. Shibata, M. Fujiwara* and M. Hirono*

Department of Electrical Engineering, *Department of Physics
 Kyushu University, Hakozaki, Higashiku
 Fukuoka 812, Japan

The stratospheric volcanic cloud from the eruption of El Chichon, Mexico, on April 4, 1982 was observed routinely by a Nd:YAG lidar system from April 18, 1982 at Kyushu University. There were two notable phenomena detected by lidar observation of the El Chichon volcanic cloud: (1) The main enhanced layer was formed in the summer easterly wind region over Fukuoka (33.5°N, 130.4°E). The layer had two high gradient top and bottom boundaries. The layer width slowly broadened until September 1982, when the easterly wind changed to the westerly wind. A similar phenomenon was observed after the eruption of Mt. St. Helens in May 1980 (HIRONO et al., 1984). (2) The stratospheric integrated backscattering coefficient (IBC) reached a peak value on May 3, 1982. It then gradually decreased until August, but re-increased significantly from September to December 1982. After January 1983, IBC decreased slowly. This remarkable re-increase had not been seen in past increases which had been observed by lidar at Kyushu University.

If it is assumed that the vertical diffusion coefficient D is constant around the layer, and that the initial distribution of the layer is a Gaussian distribution, then the half-width of the layer σ at t is given by

$$\sigma^2 = \sigma_0^2 + 11.1 Dt$$

where σ_0 is the initial value of the half width. Then σ^2 is the linear function of t . Figure 1 shows σ^2 for each observed layer. After October it rapidly increased in value. The regression lines are also shown in the figure. The derived D value before September is $3.1 \times 10^2 \text{ cm}^2 \text{ s}^{-1}$ and after October is $2.3 \times 10^3 \text{ cm}^2 \text{ s}^{-1}$. This value of $3.1 \times 10^2 \text{ cm}^2 \text{ s}^{-1}$ between altitudes of approximately 20 km and 30 km before September is nearly one or two orders of magnitude smaller than the vertical eddy diffusion values which are derived to explain the observed distribution of chemical components or radioactive debris in the stratosphere in this height range.

Figure 2 shows the IBC variation. IBC reached its maximum value in the beginning of May 1982, and although fluctuating largely, gradually decreased, until in August 1982 the IBC reached its minimum value. It then increased, until December 1982 and January 1983 were of the same magnitude as those in May 1982. Since February 1983, the IBC has been slowly decreasing. Two explanations are possible to account for the re-increase of the IBC; (a) The changes in horizontal transport caused the variation IBC. (b) The delayed oxidation of SO_2 caused the re-increase of IBC.

Using the fully interactive one-dimensional stratospheric sulfate aerosol model simulation (the details are in SHIBATA et al., 1984) the following conclusions are drawn: the stratospheric vertical eddy diffusion coefficient in the summer easterly region is of the order of $10^2 \text{ cm}^2 \text{ s}^{-1}$ or smaller. The observed re-increase of the IBC from September to December 1982 was caused not only by the delayed oxidation of injected SO_2 but also by seasonal variation of the meridional advective and diffusive transport from lower to higher latitudes in these periods. The nucleation in the cloud makes the simulated results more plausibly fit the observed results. It is predicted that the stratospheric materials of tropospheric origin would be in smaller concentrations in the summer easterly wind region. As estimated by ARNOLD and BUHRKE (1983), HSO_3 would also condense on $\text{H}_2\text{SO}_4\text{-H}_2\text{O}$ liquid aerosol particles.

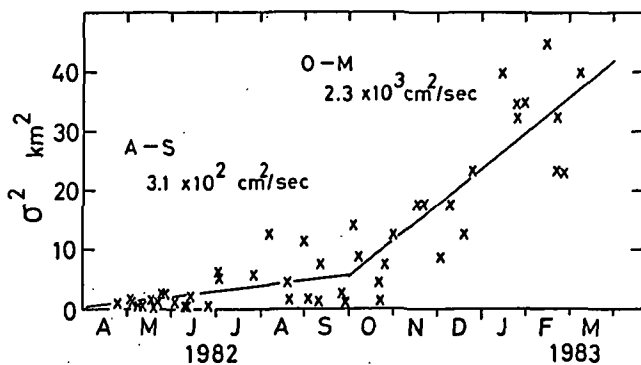


Figure 1. The observed variation of σ^2 from April 1982 to March 1983 and the regression lines.

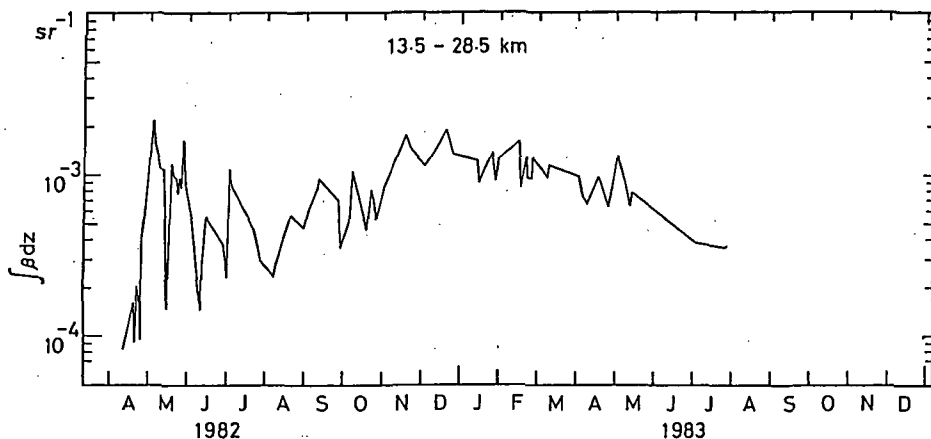


Figure 2. The observed IBC between 13.5 and 28.5 km altitude from April 1982 to July 1983.

REFERENCES

- Arnold F. and Th. Buhrke (1983), Nature, **301**, 293.
 Hirono M., M. Fujiwara, T. Shibata and N. Kugumiya (1984), J. Atmos. Terr. Phys..
 Shibata, T., M. Fujiwara and M. Hirono (1984), J. Atmos. Terr. Phys..

4.25 A NEGATIVE ION MODEL IN THE LOWER STRATOSPHERE

Hiroto Kawamoto and Toshio Ogawa

Geophysical Institute, Kyoto University
Kyoto 606, Japan

INTRODUCTION

There are a number of problems in the electricity of the stratosphere at middle latitudes; e.g., the positive relation between the seasonal variation of negative polar conductivity and that of ozone density (OGAWA, 1983), the observed dependence of the daytime variation of conductivity on the solar zenith angle (OGAWA, 1983), and the interaction between the ions and aerosols (TAKAGI and MORITA, 1980; HAMILL et al., 1982), particularly the processes of the conversion from negative ions to the sulfate aerosols; e.g., ion-nucleation (ARNOLD, 1982) and the growth through multi-ion complexes (ARNOLD, 1980). As a basic tool for investigating these problems, we have constructed a negative ion chemical model in the altitude region of 15-30 km.

Recently, the success of *in situ* mass analysis of stratospheric ions has revealed the nature of the most abundant ions in the stratosphere (ARIJS, 1983). Further, the height variations of negative ion composition between 15 and 34 km were obtained with the balloon-borne mass spectrometer by VIGGIANO et al. (1983). Therefore, a comparison of the calculated result with the observed result will be given.

MODEL CALCULATION

Ionization by galactic cosmic rays and mutual ion recombination and ion attachment to aerosols have been taken into consideration for the ion production and loss processes, respectively. To calculate the individual concentration of negative ions, we have simulated the chemical processes which start from electrons and reach the ion clusters having NO_3^- and HSO_4^- cores. This simulation was carried out by means of the signal flow graph technique introduced into atmospheric ion chemistry by WISEMBERG and KOCKARTS (1980). The schematic diagrams of the used negative ion chemical system are shown in Figure 1, which consists of two parts. The scheme shown in Figure 1(a) is considered for the negative ion core processes which start from electrons and reach the NO_3^- and HSO_4^- cores. The scheme shown in Figure 1(b) is considered for the evolution of ion clusters having NO_3^- and HSO_4^- cores. The reaction rate constants used in this study are tabulated in the paper by KAWAMOTO and OGAWA (1984). The four reactions indicated by the broken lines in Figure 1(b) were not included in the calculations because the reaction rate for them have not been published. The eight kinds of cluster ions in Figure 1(b) where their atomic mass numbers are indicated are the main negative ions observed in the lower stratosphere, and the calculated fractional abundances of the eight ions will be compared with the measured fractional abundances later.

The neutral gaseous constituents used in the calculations are mainly adopted from the U.S. Standard Atmosphere (1976), the papers by ACKERMAN (1979), TURCO et al. (1979), and TURCO et al. (1981). Refer to KAWAMOTO and OGAWA (1984) for the detailed explanation.

RESULTS AND DISCUSSIONS

Under the steady-state condition at each height from 15 km to 30 km, the concentration of the individual negatively charged species were calculated by simulating the chemical processes, which consist of 96 reactions, including

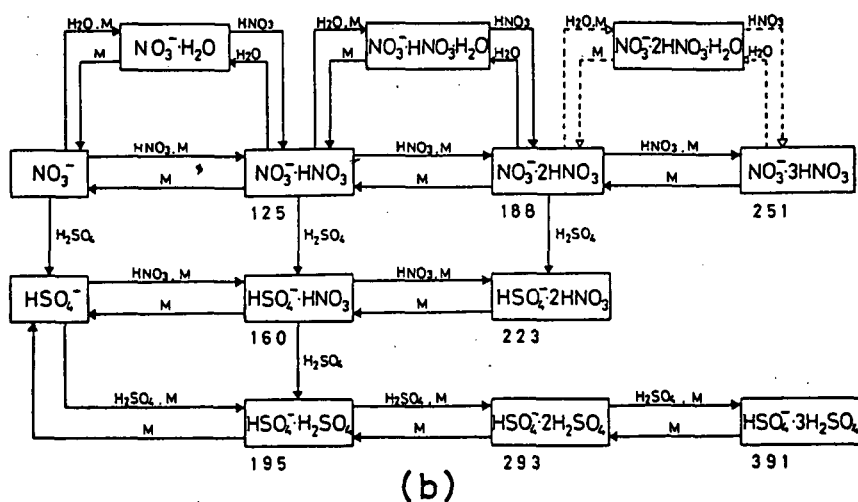
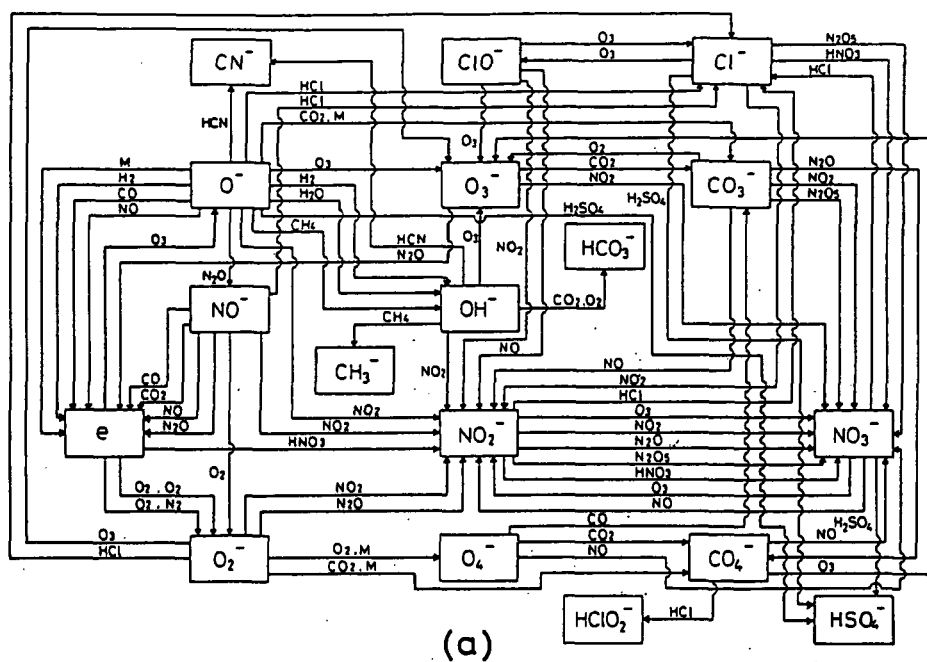


Figure 1. Reaction schemes from electrons to the stratospheric negative ions.
(a) Negative ion core processes. (b) Cluster ion processes (see text).

28 negatively charged species and 16 neutral gaseous constituents. The fractional abundances calculated for the negative ions were compared with the observed results by using a balloon by VIGGIANO et al. (1983) in Figure 2. The main negative ions in the lower stratosphere are divided into the following three categories:

(1) $\text{NO}_3^-(\text{HNO}_3)_1$ ($l=1,2,3$). Among these species, the $l=2$ (188 AMU) type of ions are predominant at all altitudes where the calculations were made. The fractional abundances of this type of ions are about 90% below the 26 km altitude, which generally agreed with the observed values. The fractional abundances of the $l=3$ (251 AMU) type of ions are about 10 times smaller than the observed values (10^{-2} — 10^{-1}), but the shape of height variation has a similar feature to the observed one. In contrast to these two species, the fractional abundances of the $l=1$ (125 AMU) type of ions are much smaller (10^{-3} — 10^{-1}) than the observed ones (10^{-2} — 10^{-1}). An explanation was made for this difference that the dissociation from the ions of larger l values than 1 to the ions of $l=1$ occurs during the ion sampling in the mass spectrometer more frequently in the lower altitudes. This effect was called the "cluster breakup" by ARIJS (1983), and a further investigation on this phenomenon is needed.

(2) $\text{HSO}_4^-(\text{HNO}_3)_m$ ($m=1,2$). Among these species, the $m=2$ (223 AMU) type of ions, which have the HSO_4^- core replacing the NO_3^- core of the dominant $\text{NO}_3^-(\text{HNO}_3)_2$ ions, are more abundant than the ions of $m=1$ (160 AMU) at all altitudes where the calculations were made. The fractional abun-

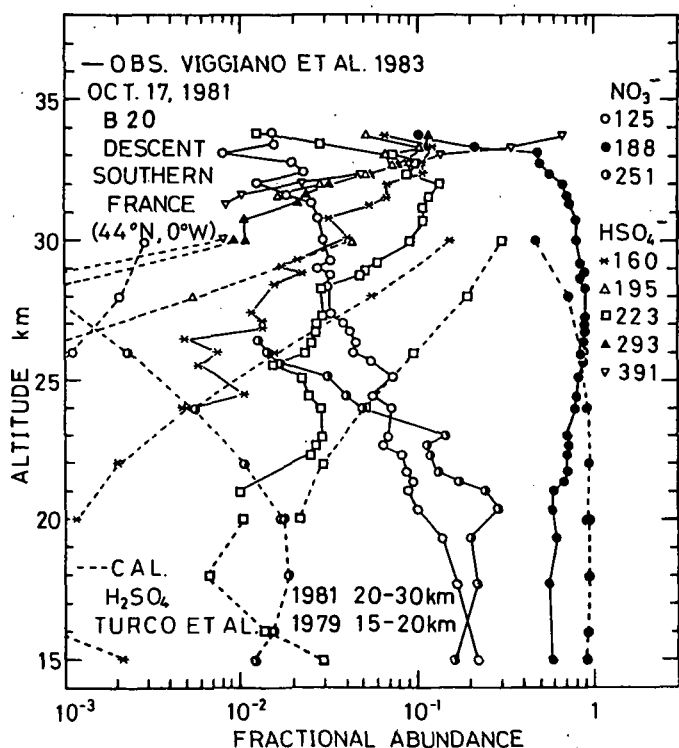


Figure 2. Comparison between the calculated (broken lines) and observed (solid lines) negative ions in fractional abundance for the main eight species.

dances of these two ions ($m=1$ and 2) increase slowly with height above about 20 km altitude, and have generally the same tendencies in height variation as those of the observed ones, but the ion quantities are different. This difference is ascribed to the difference between the theoretical $H_2SO_4 + HSO_4^-$ height distribution (TURCO et al., 1981) used in the calculations and the actual $H_2SO_4 + HSO_4^-$ height distribution during the observation (VIGGIANO and ARNOLD, 1983).

(3) $HSO_4^- (H_2SO_4)_n$ ($n=1,2,3$). The fractional abundances of these species (195, 293, and 391 AMU, respectively) show the rapid increases with height above about 20 km. These calculated height distributions have a common feature to the observed height distributions of these species, and support the conversion from these negative ions to the sulfate aerosols in the higher altitudes.

REFERENCES

- Ackerman, M. (1979), J. Atmos. Terr. Phys., **41**, 723.
 Arijis, E. (1983), Ann. Geophys., **1**, 149.
 Arnold, F. (1980), Nature, **284**, 610.
 Arnold, F. (1982), Nature, **299**, 134.
 Hamill, P., R. P. Turco, C. S. Kiang, O. B. Toon, and R. C. Whitten (1982), J. Aerosol Sci., **13**, 561.
 Kawamoto, H. and T. Ogawa (1984), Planet. Space Sci., **32**, 1223.
 Ogawa, T. (1983), Proceedings in Atmospheric Electricity, L. H. Ruhnke and J. Latham, editors, A. Deepak Publishing, 88.
 Takagi, M. and Y. Morita (1980), J. Geomag. Geoelectr., **32**, 671.
 Turco, R. P., P. Hamill, O. B. Toon, R. C. Whitten and C. S. Kiang (1979), J. Atmos. Sci., **36**, 699.
 Turco, R. P., O. B. Toon, P. Hamill and R. C. Whitten (1981), J. Geophys. Res., **86**, 1113.
 U. S. Standard Atmosphere (1979), U.S. Govt. Printing Office, Washington, D. C.
 Viggiano, A. and F. Arnold (1983), J. Geophys. Res., **88**, 1457.
 Viggiano, A. A., H. Schlager, H., and F. Arnold (1983), Planet Space Sci., **31**, 813.
 Wisenberg, J. and G. Kockarts (1980), J. Geophys. Res., **85**, 4642.

4.26 AIRCRAFT MEASUREMENTS OF AEROSOLS IN THE UPPER TROPOSPHERE AT MIDLATITUDES

Y. Morita, M. Takagi and Y. Kondo

Research Institute of Atmospheric
Nagoya University, Toyokawa
Aichi 442, Japan

ABSTRACT

Aircraft measurements of aerosols were made during the years 1982 to 1984 in the upper troposphere. In some cases, the influence of the local atmospheric pollution originating from the land surface was observed. The background concentration of the Mie particle was about 0.1 cm^{-3} at an altitude of 6-8 km. An air mass of stratospheric origin was observed over the Japan Sea in the winters of 1983 and 1984. The Mie particle concentration increased and the CN concentration decreased in the stratospheric air mass. Though the aerosol count ratio of two size ranges was found to be a large value in 1983, the value decreased to that of a background level in the stratosphere in 1984. The volcanic eruption of Mt. El Chichon seems to be responsible for the large aerosol count ratio of the measurements of 1983.

INTRODUCTION

The recent growth of the industrial potential of the world has resulted in a sort of global pollution, and today there is hardly any place in the world which can boast of a perfectly clean atmosphere. The possibility that pollution may even extend to the upper troposphere and lower stratosphere is now real. For example, the background stratospheric aerosol concentration may have been increasing during the past 20 years (HOFMANN and ROSEN, 1981). Big volcanic eruptions, such as Mt. St. Helens in 1980 and Mt. El Chichon in 1982, enhanced strongly the number density of the stratospheric aerosol layer (e.g., HOFMANN and ROSEN, 1982; 1984), and the enhanced aerosol extended over the global stratosphere. The influence of volcanic eruptions is also visible in the upper troposphere. Aerosol in the upper troposphere also plays an important role of the formation of the stratospheric aerosol layer. Investigations on the temporal and spatial variations of the aerosol in the upper troposphere and lower stratosphere are one of the important subjects to monitor the present and future atmospheric environment. For this purpose, aircraft measurements of aerosol were made during the years 1982 to 1984 in the upper troposphere.

MEASUREMENTS

Number concentration and size distribution of the Mie particle (aerosol particles with diameter greater than $0.3 \mu\text{m}$) were measured by using a light scattering aerosol particle counter. The particle counter was made to be suitable for the aircraft measurements in the upper troposphere. The particle counter has two pulse height discriminators to differentiate the size of the particles having the diameter $\geq 0.3 \mu\text{m}$ and $\geq 0.5 \mu\text{m}$, respectively, for the refractive index of 1.40. A rough indication of the size distribution is obtained from the count ratio of two size ranges. The construction and calibration of the counter are described in detail (MORITA and TAKAGI, 1983). The thermal growth chamber was used for the measurements of aerosol particles with a diameter less than $0.1 \mu\text{m}$ (condensation nuclei). The chamber grows the small particle to an optically active size and following the growth, the particle is counted individually by the light scattering aerosol particle counter. The measurements covered the latitude range of about 30°N and 40°N , and sixteen vertical profiles and seven horizontal distributions of aerosols

were obtained up to about 8 km over the northern and southern coastal areas of the Japanese islands. Merlin IV-A aircraft was used in the present measurements.

RESULTS AND DISCUSSION

Figure 1 shows the aircraft flight paths carried out in 1983 and 1984. Though the measurements have been made over the northern and southern coastal areas of the Japanese islands, the present discussion concerns mainly the results obtained from the measurements over the Japan Sea. The stratospheric air intruded down into the troposphere and the air mass of stratospheric origin was observed in the measurements on February 20, 1983, and on February 14, 1984.

Figure 2 shows the vertical profiles of Mie particle concentration of February 20, 1983. The concentration decreases exponentially with altitude up to about 6 km. Above about 6 km, the concentration attains a nearly constant value of around 0.1 cm^{-3} (profile 1). This concentration is thought to be a background level in this region. High aerosol concentration was observed in the stratospheric air mass (profile 2). Vertical profiles of aerosol count ratio on February 20, 1983, are shown in Figure 3. Though the fluctuations of the profiles are observed throughout the altitude range, the average value is nearly constant with altitude except for profile 2, which was obtained in the stratosphere air mass. The large count ratio of profile 2 indicates the presence of particles which are abundant in a smaller size range than those which usually appear in the lower stratosphere. The volcanic eruption of Mt. El Chichon seems to be responsible for the large aerosol count ratio.

Figure 4 shows the vertical profiles of the Mie particle and CN concentration on February 14, 1984. The small increase in the Mie particle concentration around 7 km was obtained in the stratospheric air mass. In the stratospheric air mass, CN concentration decreases and attains a nearly constant value of about 50 cm^{-3} . In contrast with the measurements of 1983, the aerosol count ratio was found to be large in the troposphere and small in the

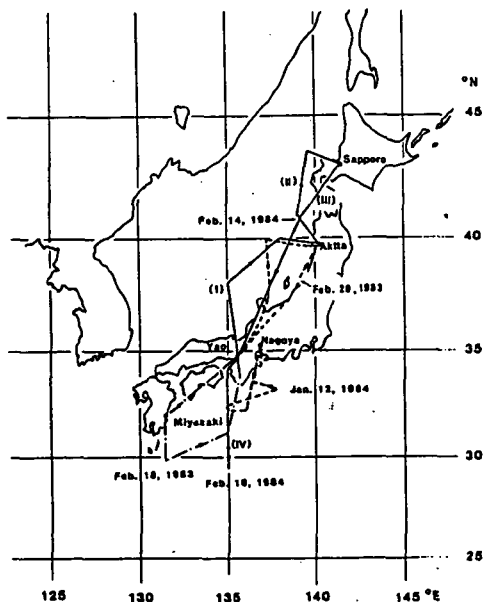


Figure 1. Aircraft flight paths carried out in 1983 and 1984.

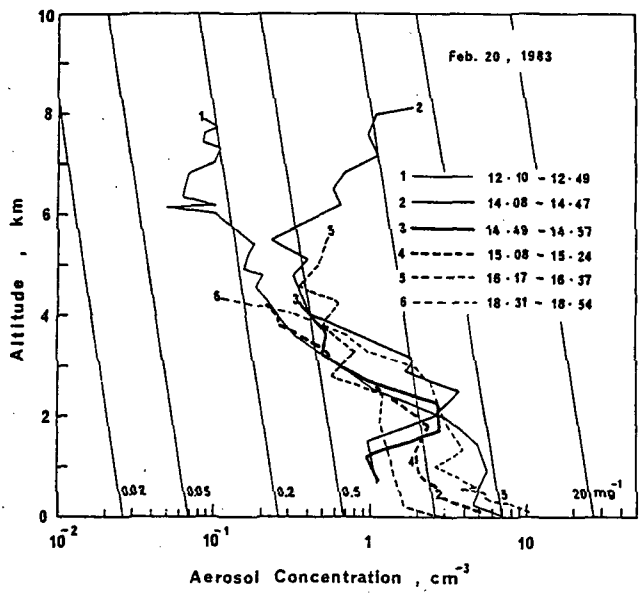


Figure 2. Vertical profiles of Mie particle concentration on February 20, 1983.

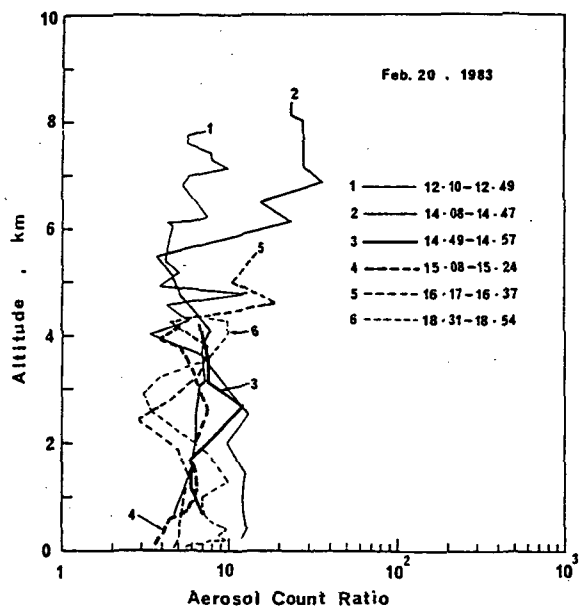


Figure 3. Vertical profiles of aerosol count ratio on February 20, 1983.

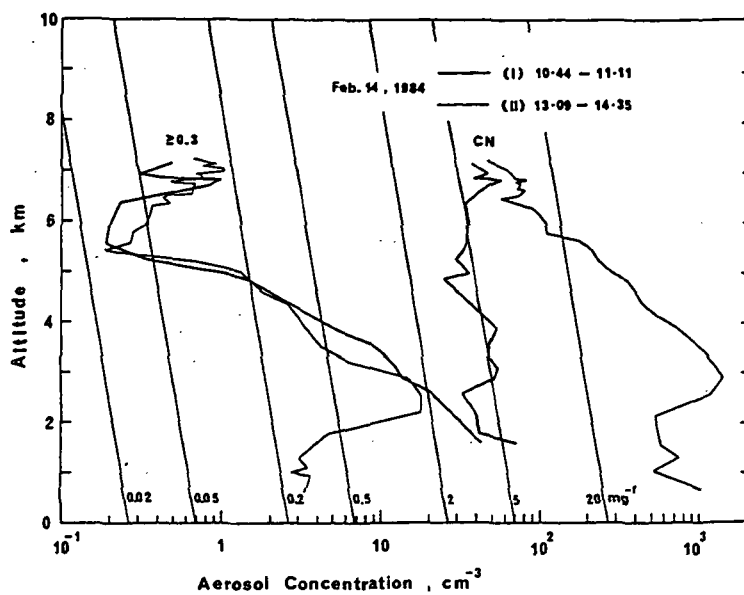


Figure 4. Vertical profiles of Mie particle and CN concentration on February 14, 1984.

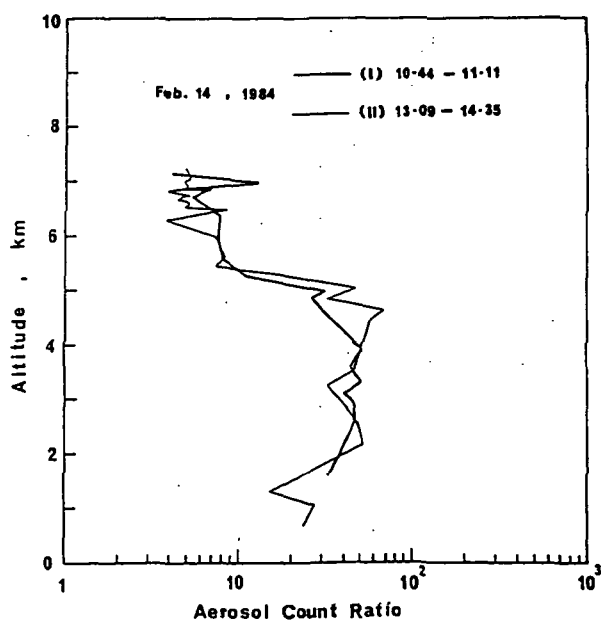


Figure 5. Vertical profiles of aerosol count ratio on February 14, 1984.

stratospheric air mass (Figure 5). The small size ratio is similar to that of the background level at midlatitudes (HOFMANN and ROSEN, 1981). This suggests that the effect of the Mt. El Chichon eruption has disappeared by the time of the measurements of 1984.

In some cases, rapid changes in aerosol concentration were observed in the vertical and horizontal measurements at altitudes of 5-6 km. The changes were attributed to the influence of the local atmospheric pollution originating from land.

ACKNOWLEDGEMENTS

We thank Prof. A. Ono of the Water Research Institute, Nagoya University, for his discussion and organization of the aircraft measurements. This work was financially supported by the Scientific Research Grant of MAP of the Ministry of Education.

REFERENCES

- Hofmann, D. J. and J. M. Rosen (1981), On the background stratospheric aerosol layer, J. Atmos. Sci., **38**, 168-181.
- Hofmann, D. J. and J. M. Rosen (1982), Balloon-borne observations of stratospheric aerosol and condensation nuclei during the year following the Mt. St. Helens eruption, J. Geophys. Res., **87**, 11039-11061.
- Hofmann, D. J. and J. M. Rosen (1984), On the temporal variation of stratospheric aerosol size and mass during the first 18 months following the 1982 eruptions of El Chichon, J. Geophys. Res., **89**, 4883-4890.
- Morita, Y. and M. Takagi (1983), Balloon measurements of stratospheric aerosol by light-scattering aerosol particle counters, Bull. Inst. Space Astro. Sci., **8**, 87-99 (in Japanese).

4.27 LIDAR OBSERVATIONS OF THE NIGHTTIME SODIUM LAYER AT 33°N

Michihiro Uchiumi, Motokazu Hirono and Motowo Fujiwara

Department of Physics, Faculty of Science
Kyushu University,
Fukuoka 812, Japan

Measurements of the nighttime atmospheric sodium layer have been performed intermittently since 1977, using a dye lidar at Fukuoka (33.4°N, 130.2°E). The Kyushu lidar uses a flashlamp pumped dye laser tuned to the sodium D₂ line (589.0 nm) as a transmitter. The dye laser used in the Kyushu lidar system has been described (NAGASAWA et al., 1980; NAGASAWA, 1983). Sporadic enhancements of the total column abundance of the layer during the Perseids meteor shower were observed on the nights of August 12-13, 1978, 1979, 1981, and 1983. Degrading weather conditions prevented observation on the nights during 1980 and 1983. Figure 1 shows a contour plot of the sodium layer for the period of 8 hours from 21:00 to 5:00 JST on the night of August 12-13, 1983. The predominant feature visible in the figure is the increase in the height of peak density from 21:00 to 2:00 JST, and the slight decrease in the height of the peak density from 2:00 to 5:00 JST. The average abundance had a maximum of about $7 \times 10^{13}/\text{m}^2$ on August 13. Figure 2 presents a plot of the nightly average abundance for available data. The sodium layer abundance increased on the night of August 12-13, 1983, during the peak of the Perseids meteor shower, and the following night, August 13-14, almost went back to the monthly mean.

The annual average in abundance observed at Fukuoka ($4 \times 10^{13}/\text{m}^2$) is in good agreement with the twilight observation made at Kitt Peak (32°N) and the lidar measurements at Sao Jose dos Campos (23°S). Figure 3 shows the seasonal variation of the sodium layer at Fukuoka. It shows the mean column abundance of the sodium for each night on which observations were made. The abundance shows interannual variation in abundance to some extent in fall and winter. The layer has less abundance in spring and more abundance in fall and winter. In the meantime, Hunten reviewed the twilight observation of the layer 1967, although the lidar observations had not been performed yet. He concluded that there is a striking winter maximum at latitudes above 50°; it is still noticeable at 40°, but has almost disappeared at 32°, according to Kitt Peak data, and that phase reverses in the Southern Hemisphere. At Fukuoka (33°N), however, the abundance has the significant maximum from fall to winter.

Figure 4 shows four sodium layer profiles averaged over the different periods of time from 1981 to 1983. A night is divided into four periods: A, B, C and D. "A" represents a period of three hours from 18:00 to 20:59 JST. "B", "C" and "D" also represent the period of three hours indicated in the figure caption. Here, each vertical profile shown in Figure 2 is derived from the photon counts integrated over the individual period of A, B, C and D, provided that the laser line width does not vary from 1981 to 1983. It should be noticed that these profiles also contained the nights during the Perseids meteor shower, on which the abundance of the layer tends to increase as the night progresses. On individual nights, the abundance does not always increase monotonously as the night progresses, but varies with time in various manners. It is found, however, that on the average, the abundance of the layer increases as the night progresses.

Aug.12, 1983

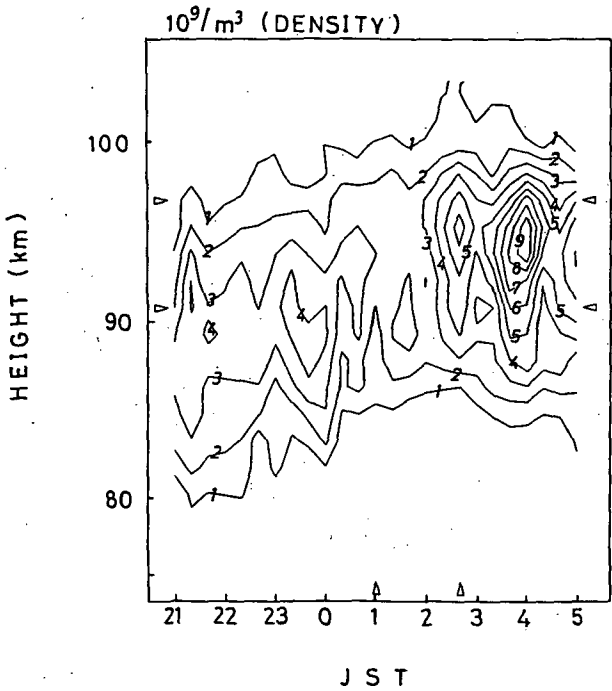


Figure 1. Contour plot of the sodium density on August 12-13, 1983.

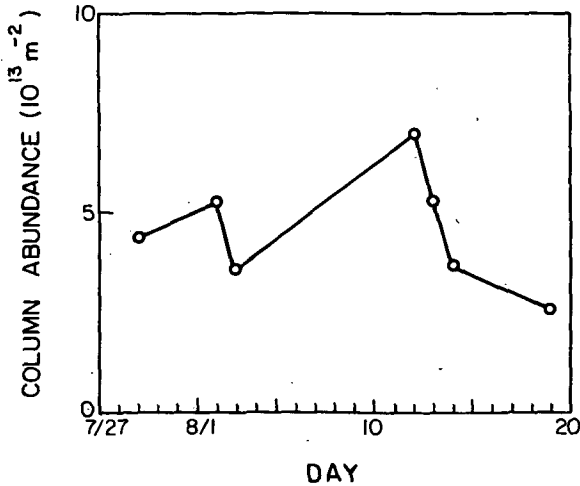


Figure 2. Day-to-day variation of the nocturnal average of the column abundance on August 1983.

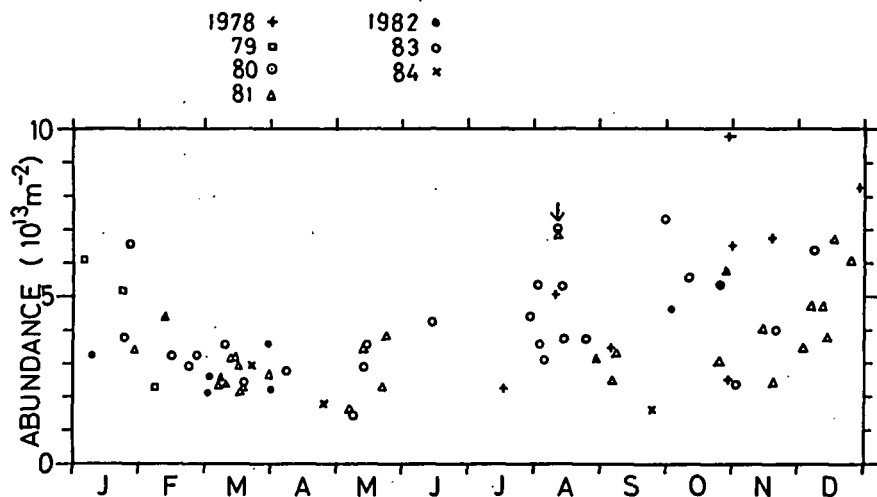


Figure 3. Seasonal variation of Na total column abundance. The arrows correspond to anomalous values correlated with the Perseids meteor shower.

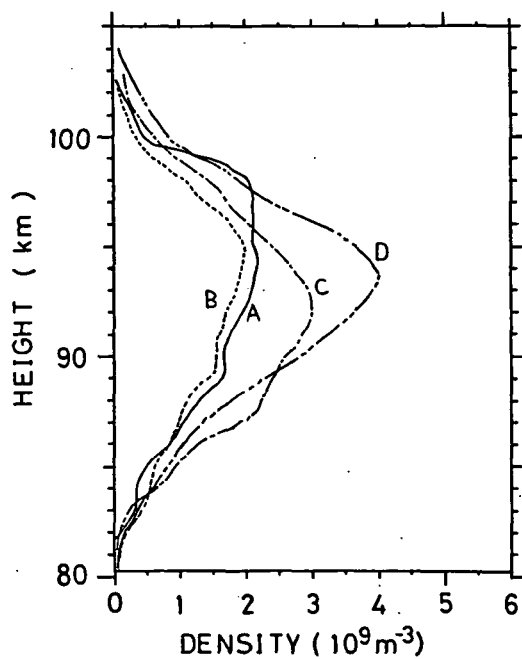


Figure 4. Nocturnal variation of sodium profiles averaged for three years from 1981 to 1983. A = 18:00-20:59 JST, B = 21:00-23:59 JST, C = 0:00-2:59 JST, D = 3:00-6:00 JST.

REFERENCES

- Hunten, D. M. (1967), Spectro studies of the twilight airglow, Space Sci. Rev., 6, 493-308.
- Nagasawa, C., M. Hirono and M. Fujiwara (1980), A reliable efficient forced oscillator dye laser to measure the upper atmospheric sodium layer, J. Appl. Phys., 19, 143-147.
- Nagasawa, C. (1983), Development of dye laser radar and observation of the atmospheric sodium layer, Ph.D. thesis of Kyushu University.

4.28 ION LOSS PROCESSES IN THE STRATOSPHERE

B.S.N. Prasad and S. Chandramma

Department of Physics,
University of Mysore,
Mysore-570 006, India

GENERAL

Small ions consisting of aggregates of a few molecules determine the stratospheric electrical parameters such as conductivity, mobility, etc. The small ion density is controlled by the ionizing mechanisms for the production of ions and electrons and the loss processes for these charged particles. Ion production in stratosphere is chiefly due to galactic cosmic rays, and the loss processes are due to recombination and attachment. Free electrons do not exist at stratospheric heights. The primary positive ion O_2^+ and the electrons are converted into complex clusters of positive and negative ions.

The equilibrium ion density (positive or negative) is governed by the equation of continuity for the production and loss of these ions. In the generalized equation of continuity, the gain or loss of ions due to transport is neglected. When aerosols or particulates are not present in the atmosphere, ions are lost due to ion-ion recombination. In the presence of aerosols, small ions can also be lost by attachment to the aerosols, and thus aerosols are likely to cause perturbations in the stratosphere electrification. A simplified model approach is adopted to study the effect of aerosols on the equilibrium ion density. The results of our analysis for the equatorial station Thumba (8.5°N) are presented in this paper.

METHOD OF ANALYSIS

Figure 1 shows the simplified model of this study. Cosmic ray ion production rate q and ion-ion recombination rate coefficient α_i are calculated from the parameterization formula (ARIJS et al., 1983). The neutral density $[M]$ for these formulas are taken from the equatorial model atmosphere (SASI and SENGUPTA, 1979).

The equation of continuity for the stratosphere ions is written as

$$\frac{dn^\pm}{dt} = q - \alpha_i n^{\pm 2} - \beta Z n^\pm \quad (1)$$

Where n^\pm = positive or negative ion density

β = attachment co-efficient of ions to aerosols

Z = aerosol number density

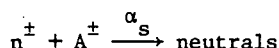
Let n and n_0 be the equilibrium ion number density with and without aerosols. Then from equation (1), under steady-state conditions, we have

$$n_0 = \sqrt{\frac{q}{\alpha_i}} \quad (2)$$

$$n = \sqrt{\left(\frac{\beta Z}{2\alpha_i}\right)^2 + \frac{q}{\alpha_i}} - \left(\frac{\beta Z}{2\alpha_i}\right) \quad (3)$$

We can thus compute n and n_0 from a knowledge of β and Z , since q and α_i are known from the parametrization formulae. Height profiles of Z are taken for aerosol radii 0.1, 0.01 and 0.001 μm from TURCO et al. (1981) and the corresponding value of β are taken from GRINGEL et al. (1978).

The quantity $(n_0 - n) = \Delta n$ gives the decrease in equilibrium ion density due to the presence of aerosols, and this we designate as the charged aerosol density A^\pm . Since $\Delta n \ll n$ it is assumed that the loss of n due to recombination with A^\pm is negligible compared to ion-ion recombination loss. The loss of charged aerosols due to recombination with oppositely charged ions is of the form



From the equation of continuity for the production and loss of charged aerosols we write

$$\alpha_s = \frac{\beta Z n}{n \cdot \Delta n} \quad \text{or} \quad \alpha_s = \frac{\beta Z}{n_0 - n} \quad (4)$$

Using Equation (2), (3) and (4) we can determine α_s for the assumed values of q , α_i , Z and β .

Equations (2) and (3) are rearranged to express the depletion of stratospheric ions as $(\Delta n/n_0)$ and the quantity βZ is computed in terms of n/n_0 . These relations are

$$\frac{\Delta n}{n_0} = \frac{n_0 - n}{\Delta n} = \left(1 - \frac{n}{n_0}\right)$$

$$\beta Z = 2x \sqrt{q\alpha_i}$$

$$\text{where } x = \frac{1 - (n/n_0)^2}{2(n/n_0)}$$

Since the relation between β and r is known, we compute and plot the percentage depletion of stratospheric ions for a given aerosol number density Z and radius r . A set of such plots are useful in predicting the ion depletion under conditions of aerosol enhancement.

RESULTS

Ion production rate q and recombination coefficient α_i are shown in Figure 2. In Figure 3 we have shown the ion densities n_0 and n , and it is seen that n has a marked dependence on aerosol number density and size. The effect of large aerosols is negligible at higher altitudes, and the effect of small aerosols is negligible at lower altitudes. The experimental measurement of ion density at Thumba (SAMPATH et al., 1983) is available for 50 km and above, and this is also shown in Figure 3. The importance of small aerosols in modifying stratospheric ion density is clearly seen.

Figure 4 shows α_s from our calculations. This is of the same order of magnitude as α_i and has a similar height dependence. We find α_s is independent of aerosol size and number density. The Δn values in Figure 4 show the effectiveness of large and small aerosols at low and high altitudes, respectively.

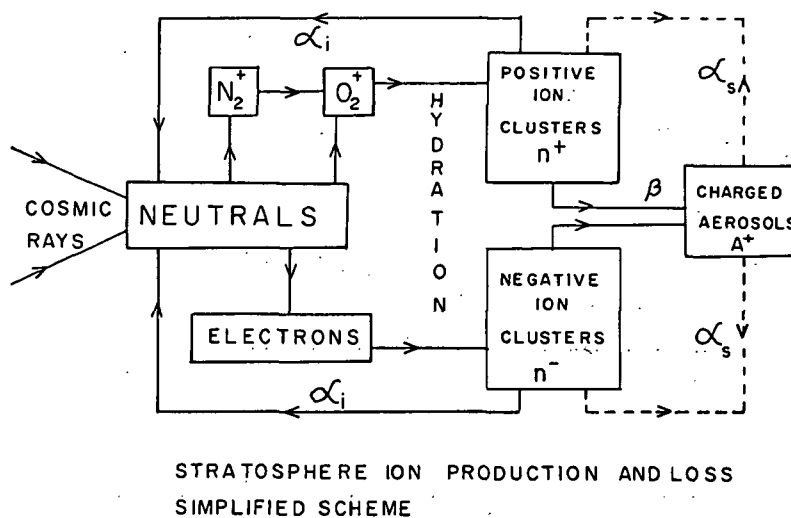


Figure 1. Simplified model used in this study.

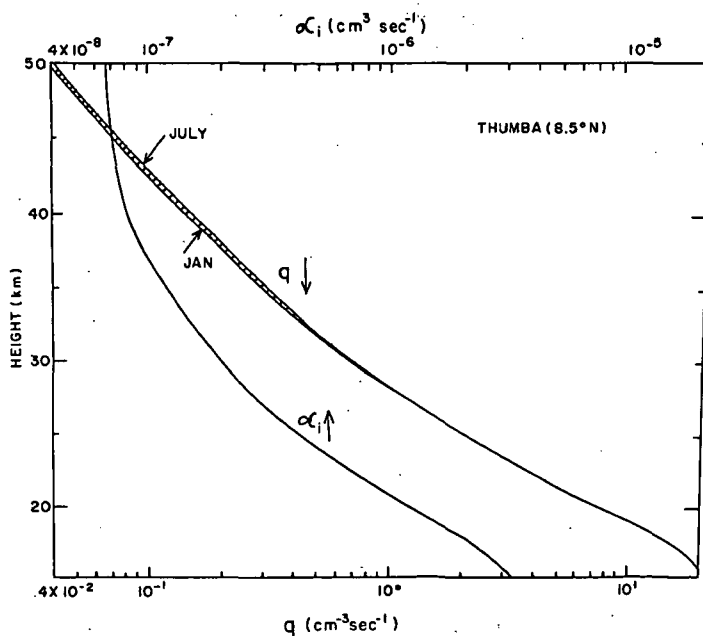


Figure 2. Ion production rate q and ion-ion recombination coefficient Thumba (8.5°N).

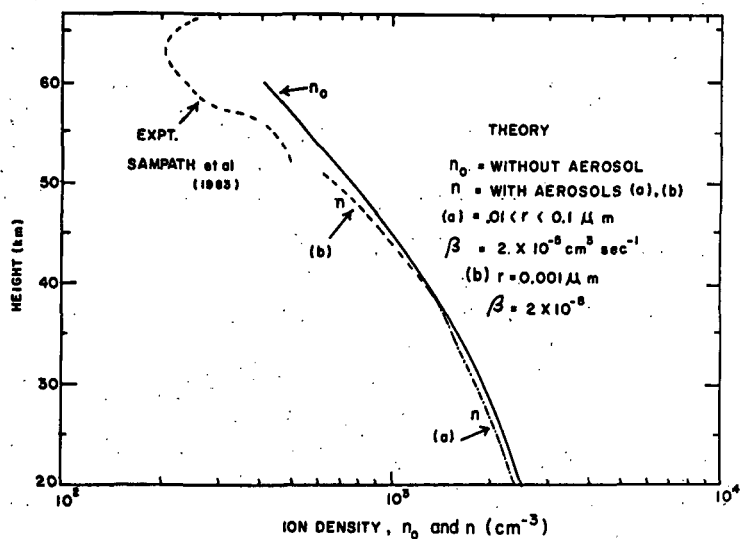


Figure 3. Experimental and calculated ion densities at stratospheric heights.

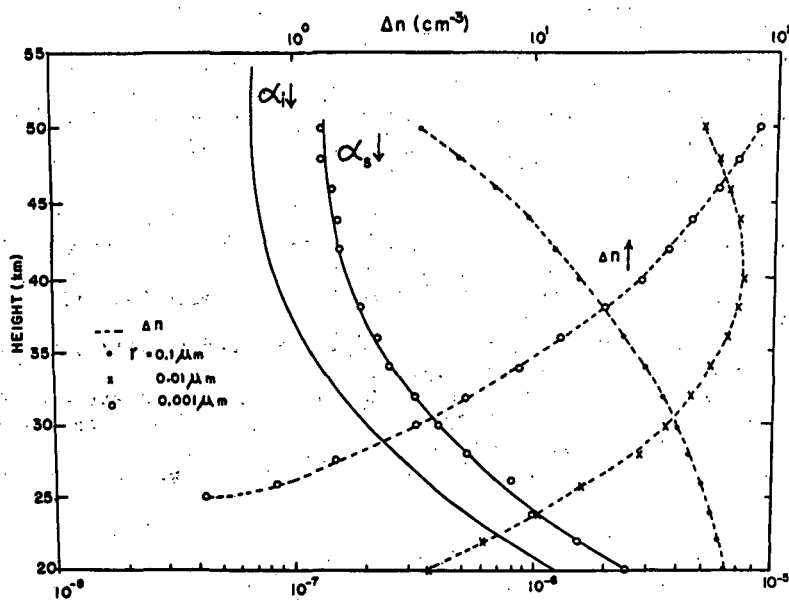


Figure 4. Height variation of α_i , α_s and Δn (see text).

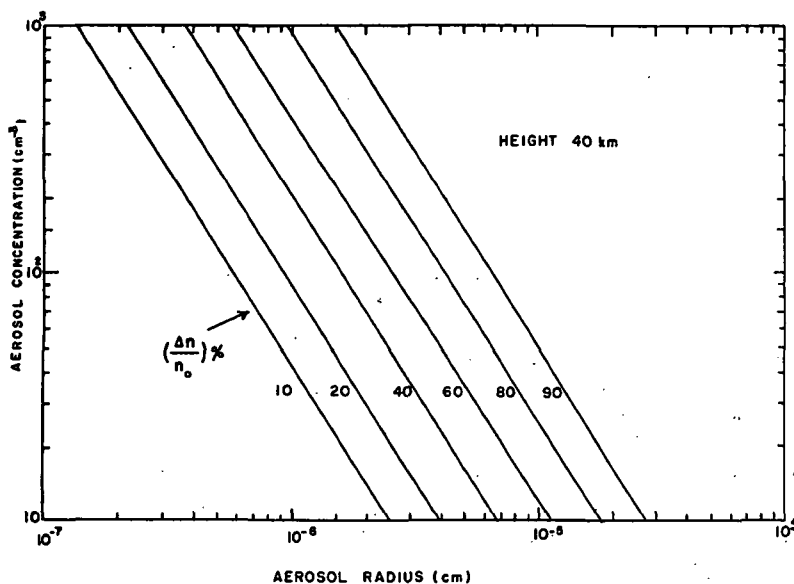


Figure 5. Percentage depletion of stratospheric ions at 40 km (see text).

Plots of percentage depletion at 40 km are shown in Figure 5. Similar plots are obtained for other heights. These straight line graphs satisfy the relation $(Zr^{-1.6}) = \text{constant}$.

ACKNOWLEDGEMENT

This work is financed by the University Grants Commission, New Delhi, through a grant under Indian Middle Atmospheric Programme.

REFERENCES

- Arijs, E., D. Nevejans, J. Ingles, and P. Frederick (1983), Annales. Geophys., **1**, 161-166.
- Gringel, W., K. H. Kaselau, and R. Muhleisen, (1978), Pageoph., **116**, 1101-1113.
- Sampath, S., V. Sasikumar and S. Murali Das (1983), IMAP Bulletin, 83/2, 7. IMAP Programme Office, Bangalore, India.
- Sasi, M. N. and K. Sengupta (1979), A model equatorial atmosphere over the Indian zone from 0 to 80 km. VSSC: TR: 46:157:79, Vikram Sarabhai Space Centre, Trivandrum, India.
- Turco, R. P., O. B. Toon, P. Hamlin and R. C Whitten (1981), J. Geophys Res., **86**, 1113-1128.

4.29 VERTICAL DISTRIBUTION OF ACETONITRILE IN THE ATMOSPHERE

J. Ingels, D. Nevejans and E. Arijs

Belgian Institute for Space Aeronomy
 Ringlaan 3,
 B-1180 Brussels, Belgium

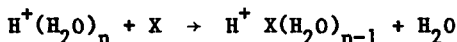
Mass spectrometric measurements of the stratospheric ion composition with rocket-borne and balloon-borne instruments showed the presence of so-called non-proton hydrates (NPH), i.e., $H^+ X_n(H_2O)$ (ARNOLD et al., 1977; ARIJS et al., 1978; ARNOLD et al., 1978). ARNOLD et al. (1978) suggested acetonitrile as a possibility for the molecule X. This hypothesis has been the subject of controversial discussions (FERGUSON, 1978; MURAD and SWIDER, 1979), but high resolution mass spectra (ARIJS et al., 1980) and laboratory investigations (BOHRINGER and ARNOLD, 1981; SMITH et al., 1981) seem to support this hypothesis.

Since 1978, positive ion composition measurements between 20 and 45 km have been performed with balloon-borne instruments (ARNOLD, 1980, 1982; HENSCHEN and ARNOLD, 1981; ARIJS, 1983; ARIJS et al., 1983a,b), to determine fractional ion abundances of proton hydrates (PH) and NPH.

As pointed out by ARNOLD et al. (1978), the number density of CH_3CN can be calculated from the observed fractional ion abundances through the continuity equation for NPH

$$k_1 [PH] [CH_3CN] = \alpha [n_-] [NPH]$$

where α is the ion-ion recombination coefficient, $[n_-]$ the total negative ion density and k_1 the rate coefficient for reactions of the type



The total fractional abundances of NPH and PH ions, $[NPH]$ and $[PH]$, can be deduced from ion mass spectra, assuming that ion count rates reflect ion abundances.

For k_1 , a value of $3 \times 10^{-9} \text{ cm}^3 \text{ s}^{-1}$ was chosen, according to laboratory measurements of SMITH et al. (1981). The $[n_-]$ was calculated with the parameterization formula of HEAPS (1978). For α a parameterization of the form

$$\alpha = 6 \times 10^{-8} \left(\frac{300}{T}\right)^{1/2} + 1.25 \times 10^{-25} [M] \left(\frac{300}{T}\right)^4 \text{ cm}^3 \text{ s}^{-1}$$

was adopted where T is the temperature in Kelvin and $[M]$ the total neutral number density in cm^{-3} . This parameterization is a compromise for the different values of α as obtained by recent *in situ* measurements (ROSEN and HOFMAN, 1981), laboratory experiments (SMITH and ADAMS, 1982) and theoretical studies (BATES, 1982).

The volume mixing ratios of acetonitrile, obtained with our most recent mass spectra are shown in Figure 1. These results are compared with data of the MPIH group (Max Planck Institute, Heidelberg), which have been recalculated with the values of α and $[n_-]$ explained here.

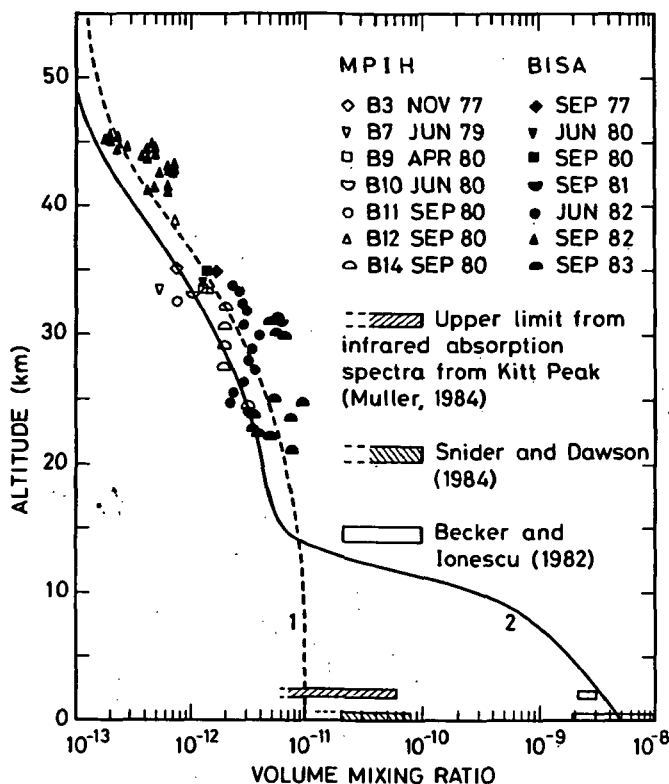
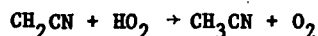
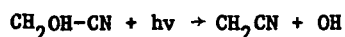
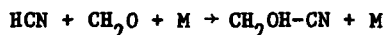
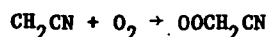


Figure 1. Vertical distribution of acetonitrile (CH_3CN) in the atmosphere.

Two different hypotheses have been advanced to explain the presence of acetonitrile in the stratosphere. MURAD et al. (1984) propose an in situ formation mechanism based on the following reactions:



Probably, the first reaction may be much slower than supposed by MURAD et al. (1984). However, if fast enough to explain the data of Figure 1, it should represent a major sink for HCN, and the HCN values measured by CICERONE and ZELINER (1983) should be very difficult to explain. Furthermore, the reaction



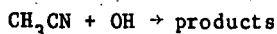
may be fast enough to destroy all CH_2CN , before any acetonitrile is formed (BRASSEUR et al., 1984).

Therefore, it appears more likely to accept the proposal suggested by BRASSEUR et al. (1983), which assumes that acetonitrile is released at the

earth's surface and that it diffuses into the atmosphere, where it is destroyed by reaction with OH radicals mainly.

Recently, measurements of CH_3CN near the earth's surface have supported this hypothesis. The two measurements reported in literature (BECKER and IONESCU, 1982); SNIDER and DAWSON, 1984) are also shown in Figure 1. As can be seen, both data sets differ by about a factor of 100.

Also given in Figure 1 are two curves obtained through model calculations by BRASSEUR et al. (1983), obtained by taking a fixed surface concentration and a zero flux at 100 km altitude as boundary conditions. The only chemical loss reaction introduced was



for which a reaction rate coefficient as measured by HARRIS et al. (1981) was adopted. Curve 1 assumes a mixing ratio at ground level of 10 pptv and no washout. Curve 2 was obtained with a surface mixing ratio of 5 ppbv and a washout coefficient of $2 \times 10^{-6} \text{ s}^{-1}$. As can be seen, both curves can reproduce the data obtained by ion mass spectrometry. However, the main problem remains a determination of the loss due to washout. If the data of BECKER and IONESCU (1982) are representative for a background atmosphere, a large loss due to rainout has to be introduced.

According to HEICKLEN (1981), the lifetime due to washout can be calculated with

$$\tau_s = (1 + \frac{k}{f}) \times \tau_0$$

where f is the fractional volume of air occupied by liquid water, τ_0 the average lifetime with which droplet removal occurs in the troposphere (about 10 s) and k Henry's law constant (ratio of the molecule number density in the vapour phase and the molecule number density in the liquid phase). From a compilation of available data on the acetonitrile - water liquid-vapor equilibrium, a value of $k = 9 \times 10^{-3}$ can be found for an average tropospheric temperature of 245 K (ARIJS and BRASSEUR, 1984). Taking for $f = 10^{-6}$ (about 1 g.m⁻³ liquid water in the air), a τ_s of 9×10^3 s is found. This value is in good agreement with the residence time for rain out recently found by HAMM et al. (1984).

It is therefore concluded that curve 1 is a better approximation of reality and that the measurements of SNIDER and DAWSON (1984) seem more realistic than those of BECKER and IONESCU (1982), which apparently are more representative for polluted areas.

Recent investigations of infrared spectra indicating that upper limit for CH_3CN at 2000 m altitude is about 20 pptv (Muller, private communication) seem to support this supposition.

Curve 1 corresponds to a global emission of 0.023 MT/yr. This emission can be explained easily by sources such as biomass burning, car exhaust gases and direct release of CH_3CN from industrial processes. It is expected that the actual emission calculated with a small washout loss will be somewhat larger, although we do not expect changes larger than a factor of 3.

In fact, new model calculations, taking into account loss terms such as reaction with atomic oxygen and chlorine atoms (which seem to be very low; OLBREGTS et al., 1984) and photodissociation are needed, as well as a systematic investigation of possible emission sources.

And although the vertical distribution of acetonitrile as known and presented here, is likely to be consistent with our general knowledge of its atmospheric chemistry, more in situ measurements (especially below 20 km) are needed to clarify the remaining problems.

REFERENCES

- Arijs, E. (1983), Positive and negative ions in the stratosphere, Annales Geophysicae, **1**, 149.
- Arijs, E. and G. Brasseur, Acetonitrile in the stratosphere and implications for positive ion composition, in preparation.
- Arijs, E., J. Ingels and D. Nevejans (1978), Mass spectrometric measurement of the positive ion composition in the stratosphere, Nature, **271**, 642.
- Arijs, E., D. Nevejans and J. Ingels (1980), Unambiguous determination of major stratospheric positive ions, Nature, **288**, 684.
- Arijs, E., D. Nevejans, J. Ingels and P. Frederick (1983a), Positive ion composition measurements between 33 and 20 km altitude, Annales Geophysicae, **1**, 161.
- Arijs, E., D. Nevejans, and J. Ingels (1983b), Positive ion composition measurements and acetonitrile in the upper stratosphere, Nature, **303**, 314.
- Arnold, F. (1980), Multi-ion complexes in the stratosphere, implications for trace gases and aerosols, Nature, **284**, 610.
- Arnold, F. (1982), Ion nucleation, a potential source for stratospheric aerosols, Nature, **299**, 134.
- Arnold, F., H. Bohringer and H. Henschen (1978), Composition measurements of stratospheric positive ions, Geophys. Res. Lett., **5**, 653.
- Arnold, F., D. Krankowsky and K. H. Marien (1977), First mass spectrometric measurements of positive ions in the stratosphere, Nature, **267**, 30.
- Bates, D. R. (1982), Recombination of small ions in the troposphere and lower stratosphere, Planet. Space Sci., **30**, 1275.
- Becker, K. H. and A. Ionescu (1982), Acetonitrile in the lower troposphere, Geophys. Res. Lett., **9**, 1349.
- Bohringer, H. and F. Arnold (1981), Acetonitrile in the stratosphere - implications from laboratory studies, Nature, **290**, 321.
- Brasseur, G., E. Arijs, A. De Rudder, D. Nevejans and J. Ingels (1983), Acetonitrile in the atmosphere, Geophys. Res. Lett., **10**, 725.
- Brasseur, G., R. Zellner, A. De Rudder and E. Arijs (1985), Is hydrogencyanide (HCN) a progenitor of acetonitrile (CH_3CN) in the stratosphere? Geophys. Res. Lett. (in press).
- Cicerone, R. J. and R. Zellner (1983), The atmospheric chemistry of hydrogen cyanide (HCN), J. Geophys. Res., **88**, 10689.
- Ferguson, E. E. (1978), Sodium hydroxide ions in the stratosphere, Geophys. Res. Lett., **5**, 1035.
- Hamm, S., J. Hahn, G. Helas and P. Warneck (1984), Acetonitrile in the troposphere: residence time due to and uptake by the oceans, Geophys. Res. Lett., **11**, 1207.
- Harris, G. W., T. E. Kleindienst and J. N. Pitts Jr. (1981), Rate constants of OH radicals with CH_3CN , $\text{C}_2\text{H}_5\text{CN}$ and $\text{CH}_2=\text{CH-CN}$ in the temperature range 298-424 K, Chem. Phys. Lett., **80**, 479.
- Heaps, M. G. (1978), Parametrization of the cosmic ray ion-pair production rate above 18 km, Planet. Space Sci., **26**, 513.
- Heicklen, J. (1981), The removal of atmospheric gases by particulate matter, Atmosph. Environment, **15**, 781.
- Henschen, G. and F. Arnold (1981), Extended positive ion composition measurements in the stratosphere. Implication for neutral trace gases, Geophys. Res. Lett., **8**, 999.
- Murad, E. and W. Swider (1979), Chemistry of meteor metals in the stratosphere, Geophys. Res. Lett., **6**, 929.
- Murad, E., W. Swider, R. A. Moss and S. Toby (1984), Stratospheric sources of CH_3CN and CH_3OH , Geophys. Res. Lett., **11**, 147.

- Olbregts, J., G. Brasseur and E. Arijs (1984), Reaction of acetonitrile and chlorine atom, J. Photochem., 24, 315.
- Rosen, J. M. and D. J. Hofman (1981), Balloon-borne measurements of electrical conductivity, mobility and the recombination coefficient, J. Geophys. Res., 86, 7406.
- Smith, D., N. G. Adams and E. Alge (1981), Ion-ion mutual neutralization and ion-neutral switching reactions of some stratospheric ions, Planet. Space Sci., 29, 449.
- Smith, D. and N. G. Adams (1982), Ion recombination in the stratosphere, Geophys. Res. Lett., 9, 1085.
- Snider, J. R. and G. A. Dawson (1984), Surface acetonitrile near Tucson, Arizona, Geophys. Res. Lett., 11, 241.

4.30 MEASUREMENTS OF CONCENTRATIONS OF CHLOROFLUOROMETHANES (CFMs)
CARBON DIOXIDE AND CARBON ISOTOPE RATIO IN STRATOSPHERIC
AND TROPOSPHERIC AIR BY GRAB-SAMPLING SYSTEMS

T. Itoh, H. Kubo, and H. Honda

The Institute of Space and Astronautical Science
Tokyo 153, Japan

T. Tominaga, Y. Makide, and A. Yokohata

Department of Chemistry, Faculty of Science
University of Tokyo
Tokyo 113, Japan

H. Sakai

Ocean Research Institute
University of Tokyo,
Tokyo 164, Japan

EXPERIMENTAL PROCEDURE

The balloon-borne grab-sampling system has been launched from Sanriku Balloon Center three times since 1981. It consists of four blocks as shown in Figure 1: (1) six sampling cylinders, (2) eight motor driven valves, (3) control and monitor circuits, and (4) pressurized housing.

Particular consideration is paid to the problem of contamination. Strict requirements are placed on the choice of materials and components, construction methods, cleaning techniques, vacuum integrity, and sampling procedures. The material, which sample air passes through or is stored in, is stainless steel. The sampling cylinders are electropolished inside, passivated by exposing them to HMDS (hexamethyldisilazane) and vacuum baked at 150°C for several hours. The valves used in the system are an all-stainless bellows-sealed type. Vacuum components are connected by welding or mini-conflat flanges. An aluminium pressurized housing and a 4-m long inlet line are employed to prevent the sampling air from contamination by outgassing of sampling and control devices (See Figure 2). A winch with a 100-m long stainless steel wire is employed to separate the grab-sampler from the balloon and the parachute (Figure 3). The sampling is performed during the descent of the system (Figure 4).

A command from the station initiates each sampling procedure at the specified altitude. Opening the appropriate valve, waiting for some time, and closing it are executed automatically by an on-board microprocessor-based controller. The sampling during the parachute descent is also performed under the procedure programmed beforehand (see 5 and 6 in Figure 4).

Another grab-sampling system aboard the airplane Merlin-IVA collected air samples of troposphere and lower stratosphere above the sea near the northern part of Japan in 1983 and 1984.

These air samples were brought back to the laboratory, and the concentrations of CFMs and methane were measured by gas-chromatography equipped with an electron capture detector and a flame ionization detector, respectively, and those of carbon dioxide were measured by the condensation-evaporation method. A part of carbon dioxide was introduced into a mass-spectrometer, and the carbon isotope ratio ($^{13}\text{C}/^{12}\text{C}$) was decided.

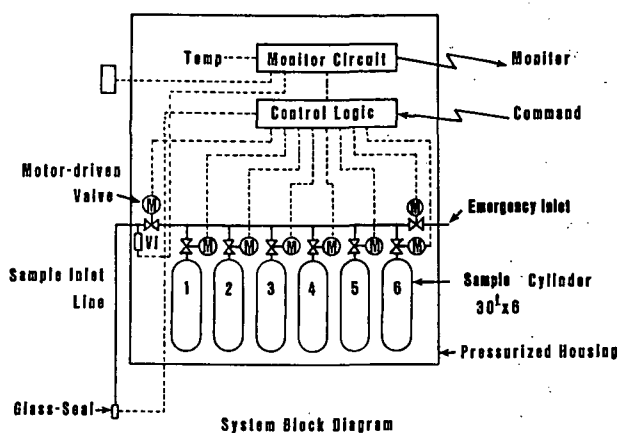


Figure 1. Block diagram of a balloon-borne grab-sampling system.

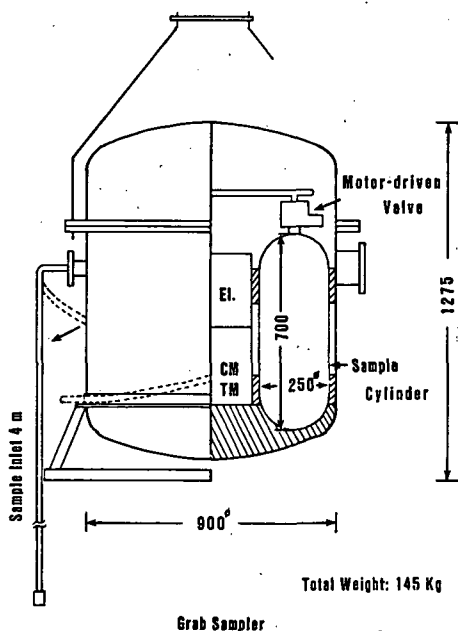


Figure 2. Scientific gondola in an aluminum pressurized housing.

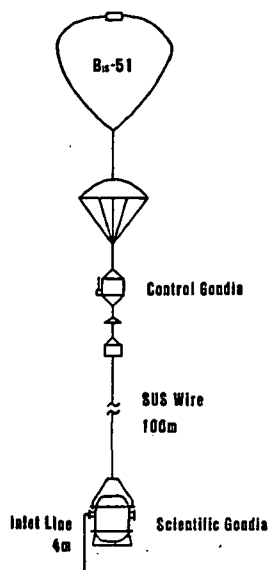


Figure 3. Balloon flight train.

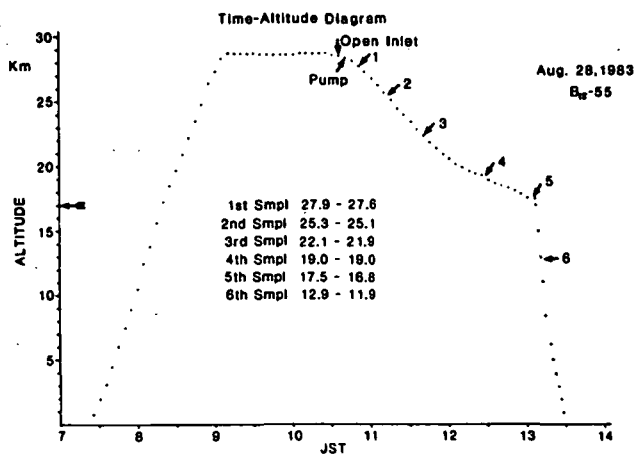


Figure 4. Time-altitude diagram. Numbers show the sampling points, and the arrow shows the tropopause height.

RESULTS AND DISCUSSIONS

Vertical profiles of mixing ratios of CF_2Cl_2 , CFCl_3 and CH_4 are shown in Figure 5. Mixing ratios of CF_2Cl_2 and CFCl_3 in the stratosphere do not show the discernible effect of the increase of those in the ground level background, and decrease with altitude. Decreasing rate of CFCl_3 is larger than that of CF_2Cl_2 . CH_4 mixing ratio, on the other hand, shows diffusive equilibrium, as the photodissociation cross section of CH_4 is small and concentrations of OH radical and $\text{O}(^1\text{D})$ are low.

Vertical profiles of CO_2 mixing ratio are shown in Figure 6. Mixing ratio in 1981 is about the same value obtained at Mauna Loa, Hawaii. Vertical profile in 1983 shows the tendency that mixing ratio in the stratosphere decreases with altitude from 350 ppm at the tropopause to 341 ppm at 22 km. Mixing ratio in the troposphere decreases as the altitude becomes lower, because it was measured in summer when the earth's surface is the sink of CO_2 .

Figure 7 shows the relation between CO_2 mixing ratio and $\delta^{13}\text{C}$ value for the same samples shown in Figure 6. $\delta^{13}\text{C}$ value in 1983 decreases with the increase of CO_2 mixing ratio. This tendency is the same as reported by KEELING et al. (1979) and MOOK et al. (1983). This is explained as follows: Fossil fuel burning and deforestation produce CO_2 whose $\delta^{13}\text{C}$ value is about -23‰ . High mixing ratio CO_2 contains these lighter anthropogenic CO_2 more and shows lower $\delta^{13}\text{C}$ value. Here,

$$\delta^{13}\text{C}(\text{‰}) = \left\{ \frac{(^{13}\text{C}/^{12}\text{C})_{\text{sample}}}{(^{13}\text{C}/^{12}\text{C})_{\text{PDB}}} - 1 \right\} \times 1000$$

The vertical profile of CO_2 mixing ratio obtained by airplane sampling is shown in Figure 8. Mixing ratio increases as the altitude becomes lower, because it was measured in winter when the earth's surface is the source of CO_2 due to respiration of vegetation and oxidation of soil organism. Mixing ratio decreases about 13 ppm between the altitudes of 0.7 km and 8 km. Mixing ratio in the stratosphere (s.s.) is a little lower than that in the troposphere of the same altitude.

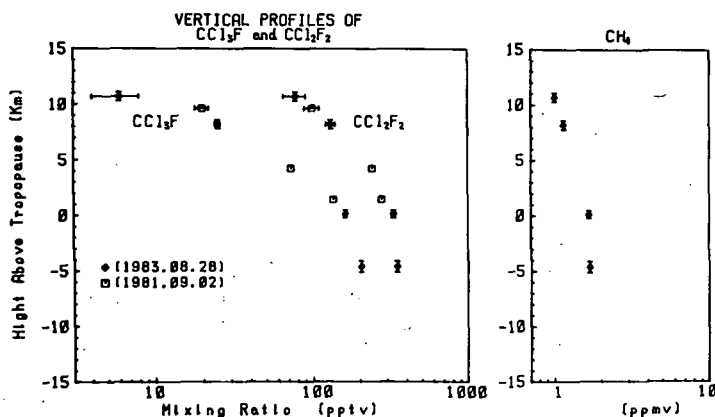


Figure 5. Vertical profiles of mixing ratios of CCl_3F , CCl_2F_2 , and CH_4 .

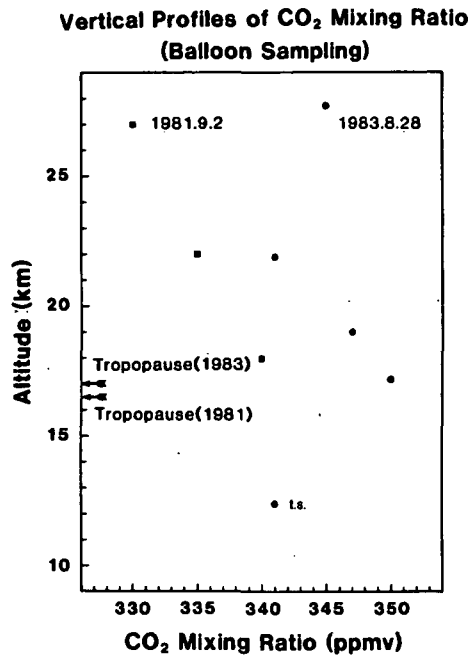


Figure 6. Vertical profiles of CO₂ mixing ratio. t.s. denotes the troposphere.

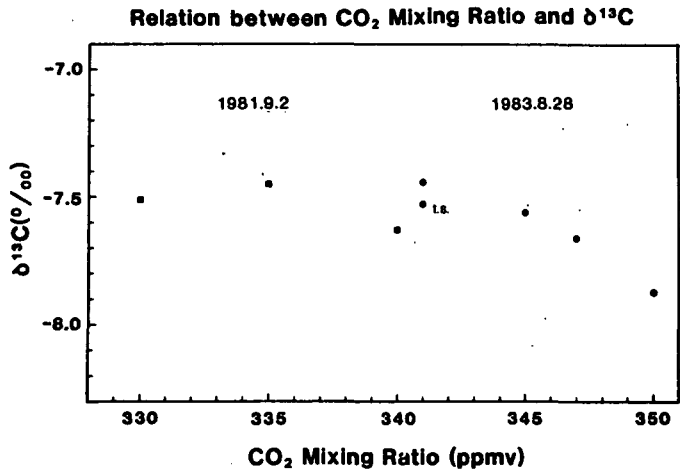


Figure 7. Relation between CO₂ mixing ratio and $\delta^{13}\text{C}$ value. t.s. denotes the troposphere.

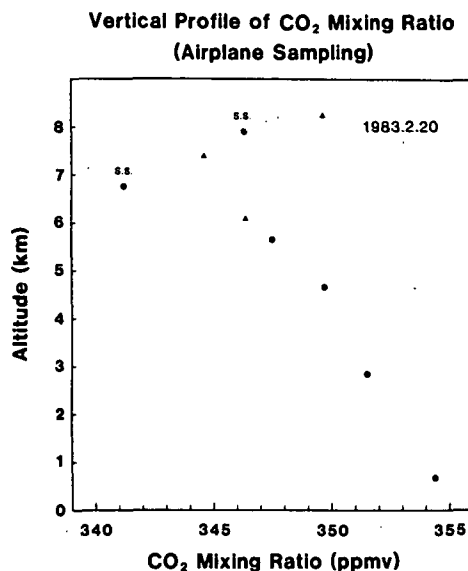


Figure 8. Vertical profile of CO₂ mixing ratio. s.s. denotes the stratosphere and triangles indicate data of far apart location.

Figure 9 shows the relation between CO₂ mixing ratio and $\delta^{13}\text{C}$ for the same samples shown in Figure 8. $\delta^{13}\text{C}$ value of higher mixing ratio CO₂ is lower. $\delta^{13}\text{C}$ value of CO₂ in the stratosphere is a little higher than that in the troposphere, probably due to the time delay when the lighter CO₂ passes through the tropopause.

The results of an airplane sampling experiment performed above the Pacific Ocean in summer, 1984, in the south of Japan will soon be reported, and balloon-borne cryo-sampling experiment will also be carried out in summer, 1985.

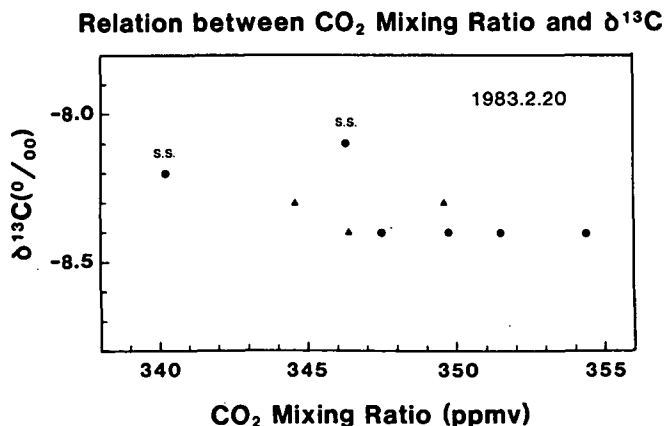


Figure 9. Relation between CO₂ mixing ratio and $\delta^{13}\text{C}$ value. s.s. denotes the stratosphere and triangles indicate data of far apart location.

REFERENCES

- Keeling, C. D., W. G. Mook and P. P. Trans (1979), Recent trends in the $^{13}\text{C}/^{12}\text{C}$ ratio of atmospheric carbon dioxide, Nature, 277, 121.
- Mook, W. G., M. Koopmans, A. F. Carter and C. D. Keeling (1983), Seasonal, latitudinal, and secular variations in the abundance and isotopic ratios of atmospheric carbon dioxide I; Results from land stations, J. Geophys. Res., 88, 10915.

4.31 UV LIDAR MEASUREMENTS OF THE STRATOSPHERIC AEROSOL LAYER AND COMPARISON WITH OTHER OPTICAL DATA

O. Uchino

Meteorological Research Institute
Yatabe, Tsukuba
Ibaraki 305, Japan

INTRODUCTION

After the violent volcanic eruptions of El Chichon in Mexico (17.33°N, 93.20°W) in late March and early April 1982, enhanced stratospheric aerosols have been monitored by ruby (lasing wavelength $\lambda=694.3$ nm) or Nd:YAG lidars ($\lambda=1064$ or 532 nm). By these lidars, visible or near-infrared optical informations of stratospheric aerosols and their space-time variations can be obtained. It is usually difficult to measure the background level of stratospheric aerosols by an ultraviolet (UV) lidar, since Rayleigh scattering prevails over Mie scattering in the stratosphere.

However, after the large volcanic eruptions, UV lidar measurements of stratospheric aerosols are possible. In order to obtain UV optical properties of stratospheric aerosols, measurements have been made at Fukuoka (33.65°N, 130.35°E) by a p-terphenyl dye laser at a wavelength of 340.5 nm. Observational results during October 1982, through May 1983, are shown and will be compared with the results obtained by a ruby lidar at Tsukuba (36.05°N, 140.13°E).

UV LIDAR OBSERVATION

The scattering ratio $R(z)$ at an altitude of z km is defined by

$$R(z) = (\beta_A(z) + \beta_M(z)) / \beta_M(z)$$

where β_M is molecular backscattering coefficient and β_A aerosol backscattering coefficient. The scattering ratio was determined by taking aerosol extinction coefficient $\tau_A(z)$ into account using a parameter of $A = \tau_A / \beta_A$. Assuming both 75% H_2SO_4 -25% H_2O sulfuric acid particles and two size distribution functions of aerosol particles, the values of A were calculated using Mie scattering theory. The assumed size distribution functions correspond to a power law and a bimodal (HOFMANN and ROSEN, 1983) and channel ratio $N_{0.15} / N_{0.25}$ are respectively 7.72 and 1.59 where N_s denotes number of aerosol particles per cm^3 greater than s μm in radius, and the values of A are 38.4 and 22.7, respectively. For three values of $A=0$, 22.7 and 38.4 sr, the vertical profiles of $R(z)$ on November 2, 1982 are shown in Figure 1. For these values of A the maximum scattering ratio R_{max} differs from about 18% at an altitude of 25 km. Except for the data of November 2, and 17, January 24, and February 28, the differences of R_{max} from other data were within 10% for these A values. For the above four data, it changed from 18% to 28%. Although A is dependent on time and space, the following figures are shown for $A=22.7$ sr.

Figure 2 shows vertical profiles of $R(z)$ during October 1982 through May 1983. The bars in the figure represent one standard deviation of $R(z)$. Sharp structures of aerosol layers were observed in October 1982. The maximum scattering ratio was 3.70 at an altitude of 24.4 km on October 21. The altitude of R_{max} , that is, z_{max} decreased with time. z_{max} was 24 km in October 1982 and it decreased downwards to 20 km at the end of January 1983. The maximum value of the optical mixing ratio of aerosols $\gamma_{340} = R_{max} - 1$ changed by a

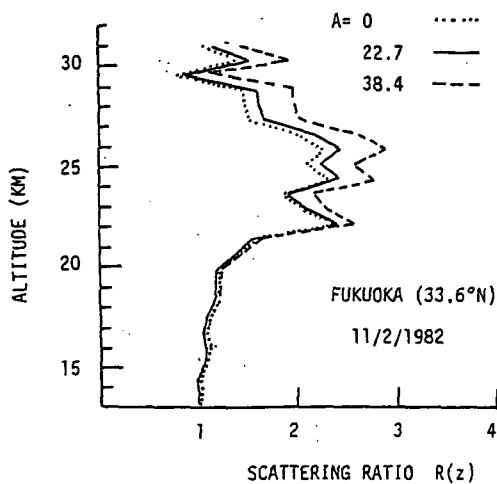


Figure 1. Vertical profiles of scattering ratio $R(z)$ at a wavelength of 340.5 nm for three values of A .

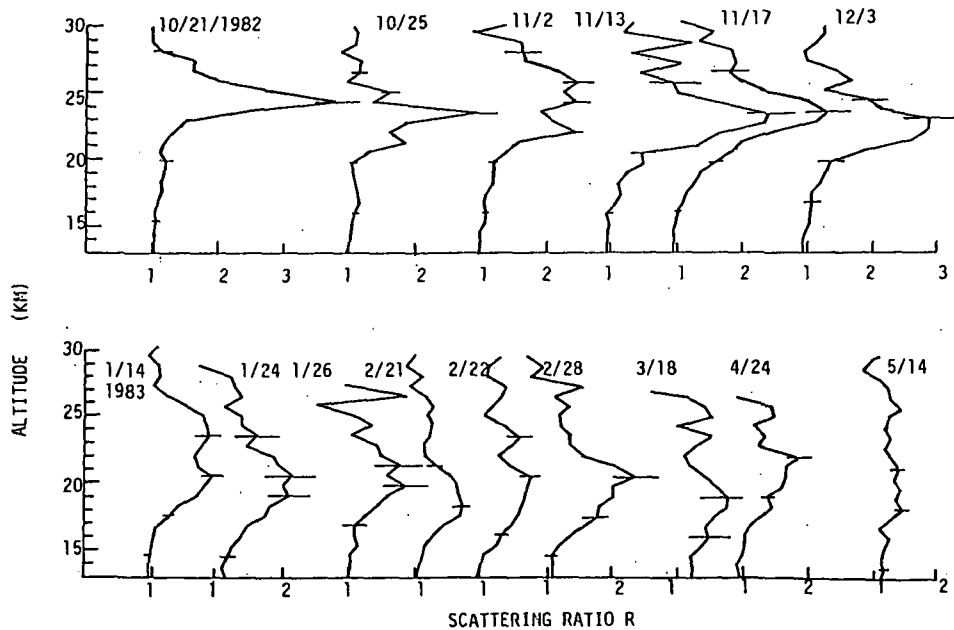


Figure 2. Profiles of scattering ratio $R(z)$ observed by a UV lidar at Fukuoka (33.6°N).

factor 2.4 from 2.2 to 0.93 during the period from October 1982, to February 1983, (UCHINO et al., 1984).

A RELATION BETWEEN γ_{694} AND γ_{340}

In this section the constant K_{RU} defined by $\gamma_{694} = K_{RU} \gamma_{340}$ will be estimated by using γ_{340} observed by a UV lidar at Fukuoka and γ_{694} observed by a ruby lidar at Tsukuba (UCHINO et al., 1984). Even if β_A is constant, γ is not the same value for different altitudes since β_M is a function of altitude. As shown in Figure 3, Z_{max} observed at Fukuoka was on the average about 0.7 km higher than those at Tsukuba. This difference is within the vertical resolutions of the ruby lidar and the UV lidar of 1 km and 0.75 km, respectively. The observational results of γ_{694} and γ_{340} , or $R_{max}-1$, are shown in Figure 4, from which the ratio of γ_{694} to γ_{340} is found to be about 10. Comparing γ_{340} at Fukuoka with γ_{694} at Hampton (37.1°N, 76.3°W), K_{RU} was about 8 during December 1982, through February 1983, when the difference of Z_{max} at both places was within about ± 1 km. On the other hand, K_{RU} was about 9 between Fukuoka and Mauna Loa (19.5°N, 155.6°W) during October through December 1982, when the difference of Z_{max} was within ± 1 km. The data of γ_{694} at Hampton and Mauna Loa are quoted from SEAN Bulletin (1982, 1983).

These estimates infer $K_{RU} = 8-10$ during October 1982, through February 1983. This value of K_{RU} is comparable to that calculated from an optical model of stratospheric aerosols. Based on the above-mentioned bi-modal distribution function of aerosol sizes measured by balloon-borne particle counter on October 23, 1982, (HOFMANN and ROSEN, 1983) and assuming refractive indices of 1.46-0.005i for $\lambda=694.3$ nm and 1.48-0.005i for $\lambda=340$ nm, K_{RU} is calculated to be 8.8 according to the Mie scattering theory (N. Fujiwara, private communication, 1983).

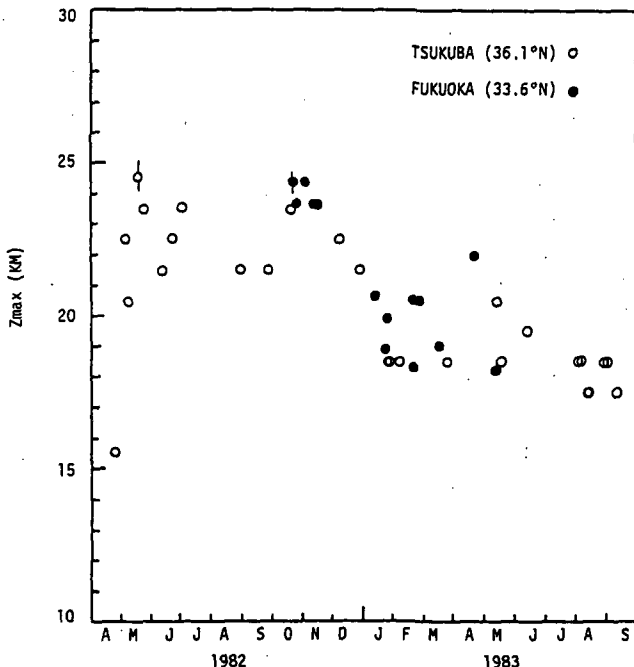


Figure 3. Time variations of the altitudes of R_{max} observed at both Tsukuba and Fukuoka.

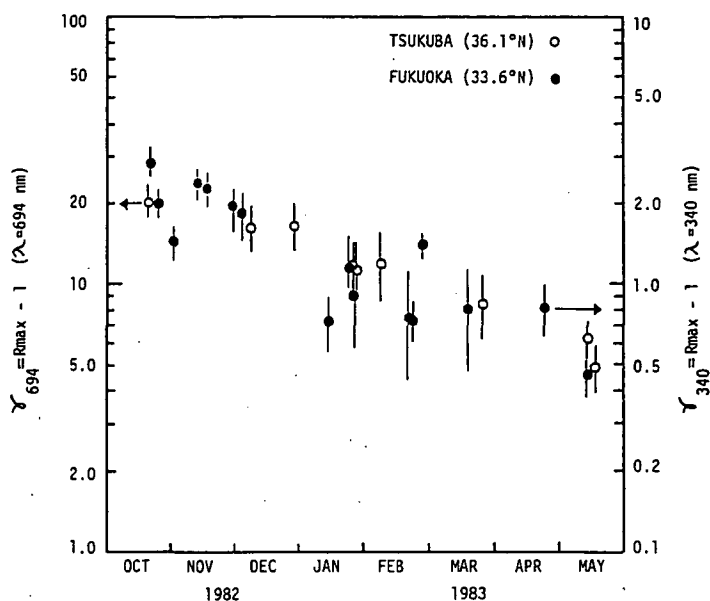


Figure 4. Comparison between γ_{694} observed at Tsukuba and γ_{340} observed at Fukuoka.

The ratio of $\beta_A(340)/\beta_A(694)$ are $1.72 \sim 2.17$ for $K_{RU} = 8 \sim 10$, and are smaller than those (~ 3.5) calculated from the distribution functions of the aerosol sizes in the background level of the stratospheric aerosols. This observational result of K_{RU} after the volcanic eruptions of El Chichon means an abundance of the particles with the radii greater than $r = 0.1 \mu\text{m}$.

REFERENCES

- Hofmann, D. J. and M. Rosen (1983), Science, **222**, 325.
 SEAN Bulletin, **7**, No. 3-12, **8**, No. 1-8.
 Uchino, O., M. Maeda, M. Tokunaga, K. Seki and T. Hayami (1984), J. Meteorol. Soc. Japan, **61**, 171.
 Uchino, O., K. Takahashi, I. Tabata, I. Akita, Y. Okada and K. Naito (1984), J. Meteorol. Soc. Japan, **62**, 679.

4.32 THE RECENT IMPROVED ROCOZ (ROCOZ-A) OZONE MEASUREMENTS

H. S. Lee
Washington Analytical Service Corporation
5000 Philadelphia Way
Lanham, MD 20706

Measurements of the daytime vertical cumulative ozone profile in the stratosphere and high troposphere have been made at NASA Wallops Flight Facility during the period between August 1983 and October 1984 by an improved filter photometer rocket ozonesonde (ROCOZ-A). A measurement precision of 2 to 3 % between 20 and 55 km altitudes has been established by three series of four nearly simultaneous measurements. The cumulative ozone profiles show an exponential behavior at high altitude stratosphere which continues down to 37 km in August and to 44 km in February. The ratio of the cumulative ozone scale height and the pressure scale height in this altitude range shows a small variation between 0.5 and 0.57.

Intercomparisons of 1984 data with 1983 data show annual repeatability of the ozone profile within the instrument's precision.

5.1 BALLOON-BORNE OBSERVATIONS OF STRATOSPHERIC AEROSOL IN ANTARCTICA FROM 1972 TO 1984

D. J. Hofmann

Department of Physics and Astronomy
University of Wyoming
Laramie, WY 82071

Stratospheric levels of particles with $r \geq 0.15 \mu\text{m}$ have been monitored with optical particle counters in approximately monthly balloon soundings at Laramie, Wyoming (41°N) since 1971. These measurements have been used to characterize the background stratospheric aerosol layer (HOFMANN et al., 1975; ROSEN et al., 1975; HOFMANN and ROSEN, 1981a) and the disturbed layer following major volcanic eruptions (HOFMANN and ROSEN, 1977, 1981b, 1982a, 1983a, 1984).

Levels of particles with $r \geq 0.01 \mu\text{m}$ have also been measured with balloon-borne counters since 1973 (ROSEN and HOFMANN, 1977; ROSEN et al., 1978; ROSEN and HOFMANN, 1983; HOFMANN et al., 1985). The latter are collectively called condensation nuclei (CN) as they are characteristic of aerosol in the early stages of growth. While they dominate the size distribution in the troposphere, they are a trace species in the undisturbed stratosphere.

The instrumentation used for balloon-borne aerosol measurements has been described in the literature (HOFMANN et al., 1975; ROSEN and HOFMANN, 1977; HOFMANN and ROSEN, 1982a). Basically, the ambient air sample is passed through a light beam, and the scattered light is analyzed to discriminate particles having $r \geq 0.15 \mu\text{m}$ and $0.25 \mu\text{m}$. For detection of particles with sizes below the light scattering detection limit ($r = 0.05 \mu\text{m}$), a thermal growth chamber is employed which causes aerosol having radii greater than about $0.01 \mu\text{m}$ to grow optically active sizes.

From 1972 until 1980, annual balloon soundings from McMurdo Station (78°S) and/or Amundsen-Scott Station (90°S), in Antarctica, have also been conducted to crudely monitor Southern Hemisphere aerosol levels. These measurements were continued in 1983 and 1984. Brief reports of the results have appeared in the Antarctic Journal of the U.S. (HOFMANN et al., 1972-1980), and some of these data have been used in analyses (HOFMANN et al., 1973; ROSEN et al., 1975; ROSEN et al., 1978; HOFMANN and ROSEN, 1985).

Figure 1 shows profiles of $r \geq 0.15 \mu\text{m}$ aerosol concentrations as measured during January at the south pole from 1972 to 1975 and in 1980. The former are typical of undisturbed conditions and indicate the small degree of variability under these conditions. The latter indicates the effect of minor volcanic activity, visible in the 10-15 km region.

Figure 2 shows similar data at McMurdo in January from 1973 to 1979 and a highly disturbed profile measured in October 1983. The enhanced aerosol in the 12-18 km region are believed to be due to the eruption of El Chichon, which occurred in Mexico in April 1982. The absence of aerosol above 18 km is unusual, and apparently related to the extremely high temperatures encountered at this level in the Antarctic spring. Measurements in November 1984 gave similar results, although the 15 km El Chichon aerosol concentration had decayed by a factor of two.

Figure 3 summarizes observations of this aerosol since 1971, showing peak stratospheric aerosol mixing ratios from monthly soundings at Laramie and from the Antarctic soundings. We see that the data sets are in agreement under undisturbed periods (nonvolcanic). Unfortunately, soundings were not conducted

01872-004

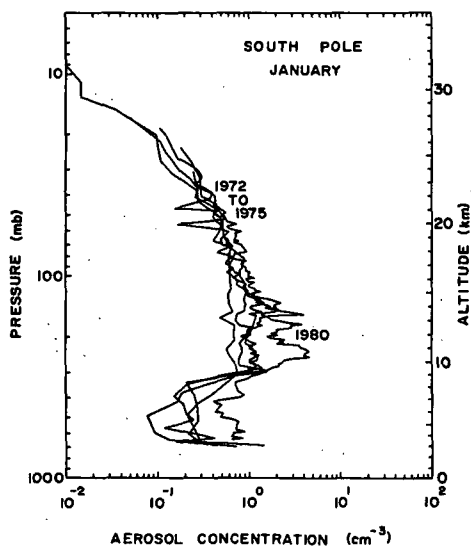


Figure 1. Aerosol ($r \geq 0.15 \mu\text{m}$) concentration profiles measured in January with balloon-borne particle counters at the south pole annually from 1972 to 1975 and in 1980.

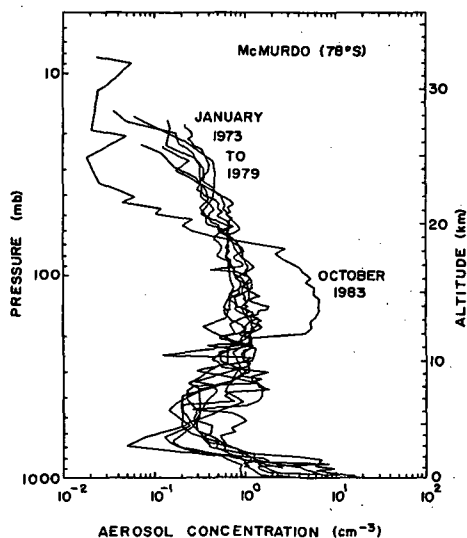


Figure 2. Aerosol ($r \geq 0.15 \mu\text{m}$) concentration profiles measured in January with balloon-borne particle counters at McMurdo Station annually from 1973 to 1979 and in October of 1983.

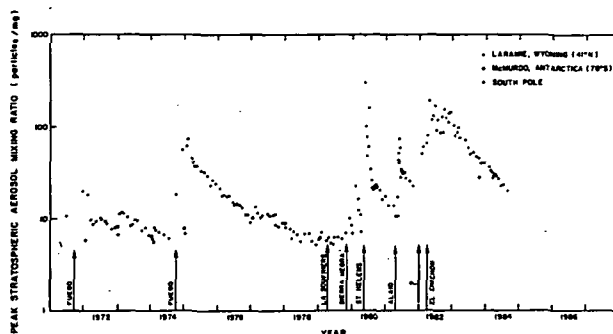


Figure 3. Aerosol ($r \geq 0.15 \mu\text{m}$) mixing ratio at the stratospheric maximum versus time from individual balloon soundings at Laramie and in Antarctica. Arrows indicate the times of major volcanic eruptions which disturbed stratospheric aerosol levels. The eruption in early 1982 was not conclusively identified.

in Antarctica during the volcanically active period between mid 1980 and 1983.

Figure 4 shows CN ($r \geq 0.01 \mu\text{m}$) profiles at the south pole in January from 1977 to 1980. Again, during undisturbed periods and during the summer season, CN profiles exhibit considerable similarity with high tropospheric and low stratospheric concentrations.

Figure 5 compares the springtime CN sounding conducted on October 27, 1983 at McMurdo with one conducted in the summer of 1976. We see an unusual enhancement above about 18 km in 1983, in the region where the larger aerosols appear to be absent (see Figure 2). The temperature profiles in Figure 5 indicate high temperatures at high altitude in 1983. This can be seen in Figure 6, where temperatures at 10 and 30 mbar, as measured at the south pole, are shown. The warming began about two weeks before the 1983 sounding.

Enhanced levels of CN have also been detected at altitudes of about 30 km at Laramie (HOFMANN and ROSEN, 1982a, 1983b; ROSEN and HOFMANN, 1983; HOFMANN et al., 1985). These CN "events" are not directly connected with volcanic eruptions but are apparently related to such events. The latter have been detected during the late winter - early spring (January-April) period in the Northern Hemisphere annually since 1979. They are believed to be associated with stratospheric warming episodes which are capable of evaporating resident sulfuric acid droplets at 30 km, the vapor from which serves as a source of numerous very small aerosols when it is cooled in a sufficiently rapid manner (ROSEN and HOFMANN, 1983; HOFMANN et al., 1985).

In April 1982, the volcanic El Chichon (17.3°N) underwent a massive eruption, which resulted in at least 10^7 metric tons of sulfuric acid aerosol forming in the stratosphere (HOFMANN and ROSEN, 1983a, 1984; MCCORMICK and SWISLER, 1983). This sulfur-rich eruption is believed to be the largest in terms of the resulting stratospheric aerosol optical depth since at least the Katmai eruption in the Northern Hemisphere 1912 and the eruption of Agung in the Southern Hemisphere in 1963 (POLLACK et al., 1983), and possibly the largest since that of Krakatau in 1883 (RAMPINO and SELF, 1984). This event created the motivation for continuing soundings in Antarctica in 1983.

The $r \geq 0.15 \mu\text{m}$ aerosol observations in October 1983 at McMurdo indicate maximum mixing ratios in the stratosphere almost as large as those measured at

ORIGINAL PAGE IS
OF POOR QUALITY

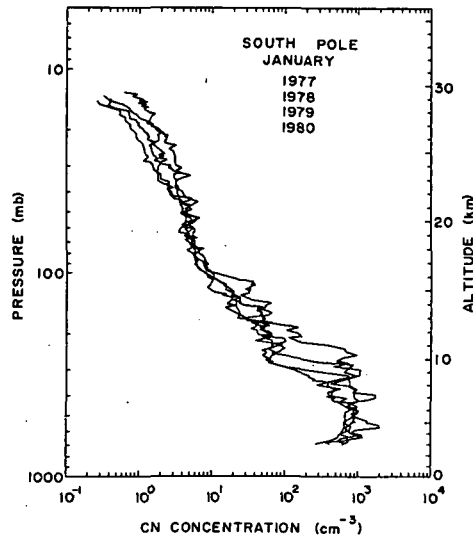


Figure 4. Condensation nuclei ($r \geq 0.01 \mu\text{m}$) concentration profiles measured in January with balloon-borne counters at the south pole annually from 1977 to 1980.

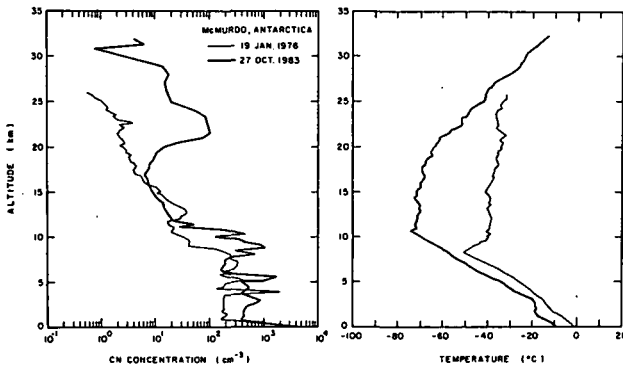


Figure 5. Condensation nuclei ($r \geq 0.01 \mu\text{m}$) concentration and temperature profiles measured with balloon-borne sensors at McMurdo during 1976 and 1983.

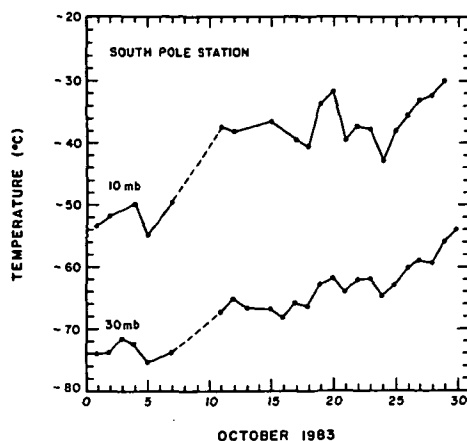


Figure 6. Radiosonde temperatures at the 10 and 30 mbar pressure levels measured at South Pole Station in October 1983.

Laramie during the same period with a value of ~ 30 as compared to ~ 40 particles per milligram ambient air (normal background value is about 6). The unusually large size of the aerosol attributed to the El Chichon eruption (HOFMANN and ROSEN, 1984) can be used as an aerosol tracer. The ratio of the $r \geq 0.15 \mu\text{m}$ to $r \geq 0.25 \mu\text{m}$ concentrations, observed in Antarctica in 1983, indicates that the aerosol was most likely due to the El Chichon eruption about 18 months earlier. Thus, the transport of aerosol from the Northern Hemisphere to the Antarctic region, in the stratosphere, appears to have been relatively efficient.

The CN enhancement observed during the October 1983 Antarctic sounding between 20 and 30 km is possibly related to the CN nucleation mechanism discussed earlier. In relation to this, it is important to again point out that the enhanced CN layer begins at precisely the point where an unusual absence of larger ($r \geq 0.15 \mu\text{m}$) aerosol begins, as if one were being lost to form the other. This is highly suggestive of an evaporation - condensation mechanism in operation.

A large CN event observed at Laramie in January 1983 occurred coincident with a stratospheric warming between 17 and 31 January in the north polar region (-15°C at 31 km, -30°C at 24 km) and subsequent cooling of about 30°C during transport to the latitude of Laramie in a time interval of about 24 hours. Although the CN increase appeared at lower altitudes in Antarctica, the events are strikingly similar. While the saturation vapor pressure of the approximately 75% sulfuric acid, 25% water aerosol (HOFMANN and ROSEN, 1983a) at stratospheric temperatures is not well known, depending also on the water vapor concentration, aerosol evaporation is expected to occur at temperatures in excess of -30°C in the 25-30 km region, i.e., the aerosol should not exist in condensed form even in a standard atmosphere above about 35-40 km (TURCO et al., 1979; HOFMANN et al., 1985).

In the Southern Hemisphere, the warming events associated with our observations appear quite complicated. Remotely sensed temperatures over the Southern Hemisphere, from a NOAA satellite (provided by M. Gelman, NOAA Climate Analysis Center), indicates warm regions of limited extent forming, moving around the pole in an easterly direction and dissipating only to be replaced by a new warm region, often at a position on the opposite side of the pole.

In regard to aerosol measurements in the winter polar vortex, soundings from the Ice Island T-3 (now abandoned) at about 85°N in December of 1971 and 1972 and in late November of 1973, under normal, cold stratospheric conditions, did not reveal a sharp upper boundary in the aerosol concentration (HOFMANN et al., 1973), suggesting that an absence of aerosol above 18 km is not an ordinary vortex feature. Nevertheless, with no other stratospheric measurements near the winter south polar vortex, one cannot rule out the possibility that the aerosol layer is naturally depressed due to descending motions in the vortex. However, it is clear that the CN are not depressed, so that such an explanation meets with considerable difficulty. Possibly related to this are the aerosol optical extinction measurements in the north polar region reported by MCCORMICK et al. (1983). They similarly found an absence of aerosol above about 18 km in the general region of the north polar vortex. Since their observations occurred shortly after the stratospheric warming event of January 1983, the larger, detectable aerosol may have evaporated.

While the aerosols which may have evaporated above 18 km in Figure 2 are probably not substantial in number, they may be sufficient in terms of providing condensable vapors. In the absence of the warm temperatures, the aerosol profile above 18 km would probably have decreased more gradually with a concentration of about 1 cm^{-3} at 20 km. This apparent deficit of 1 cm^{-3} for an average radius of about $0.2 \mu\text{m}$, a typical size of the El Chichon aerosol for this period (HOFMANN et al., 1985). These would have been diluted through dispersion and coagulation to a concentration on the order of 100 cm^{-3} , as observed, during this period. Thus, the total mass budget appears to balance, all things considered. Preliminary analysis of soundings at both McMurdo and the south pole in November 1984, under similar stratospheric warming conditions, suggest similar results.

In summary, while very few measurements of the Antarctic middle atmosphere aerosol distribution exist, a relatively clear picture of a high degree of stability emerges for summer measurements under nonvolcanic conditions. Following major volcanic eruptions, transport of excess aerosol to the Antarctic stratosphere appears to be a rather efficient process. During seasons when the middle atmosphere undergoes large temperature fluctuations as in the springtime, the situation becomes very complicated with possible changes in state of the predominant sulfuric acid aerosol present. This can result in day-to-day variations and may serve to prolong the decay of the aerosol by effectively converting large droplets to small ones. It is thus important, for climatic studies, to continue measurements in the Antarctic middle atmosphere. Only here, free of political implications associated with overflight of sovereign territory, can the many important middle atmosphere phenomena related to the polar vortex be adequately studied with *in situ* measurements.

ACKNOWLEDGEMENTS

The author is indebted to his colleagues at the University of Wyoming, in particular J. M. Rosen, whose ideas led to much of the foregoing interpretation, and to the Atmospheric Physics staff for aid in the field measurements. This research was supported by the Division of Polar Programs and the Atmospheric Sciences Section of the U.S. National Science Foundation.

REFERENCES

- Hofmann, D. J. et al. (1972-1980), Reports in Ant. J. of the U.S., 7, 122, 8, 183, 9, 121, 10, 189, 11, 99, 12, 162, 13, 185, 14, 200, 15, 183.
- Hofmann, D. J., J. M. Rosen, T. J. Pepin and R. G. Pinnick (1973), Particles in the polar stratospheres, Nature, 245, 369-371.

- Hofmann, D. J., J. M. Rosen, T. J. Pepin and R. G. Pinnick (1975), Stratospheric aerosol measurements I: Time variations at northern midlatitudes, J. Atmos. Sci., **32**, 1446-1456.
- Hofmann, D. J. and J. M. Rosen (1977), Balloon observations of the time development of the stratospheric aerosol event of 1974-1975, J. Geophys. Res., **82**, 1435-1440.
- Hofmann, D. J. and J. M. Rosen (1981a), On the background stratospheric aerosol layer, J. Atmos. Sci., **38**, 168-181.
- Hofmann, D. J. and J. M. Rosen (1981b), Stratospheric aerosol and condensation nuclei enhancements following the eruption of Alaid in April 1981, Geophys. Res. Lett., **8**, 1231-1234.
- Hofmann, D. J. and J. M. Rosen (1982a), Balloon-borne observations of stratospheric aerosol and condensation nuclei during the year following the Mt. St. Helens eruption, J. Geophys. Res., **87**, 11,039-11,061.
- Hofmann, D. J. and J. M. Rosen (1982b), Stratospheric condensation nuclei variations may relate to solar activity, Nature, **297**, 120-124.
- Hofmann, D. J. and J. M. Rosen (1983a), Stratospheric sulfuric acid fraction and mass estimate for the 1982 volcanic eruption of El Chichon, Geophys. Res. Lett., **10**, 313-316.
- Hofmann, D. J. and J. M. Rosen (1983b), Condensation nuclei events at 30 km and possible influences of solar cosmic rays, Nature, **302**, 511-514.
- Hofmann, D. J. and J. M. Rosen (1984), On the temporal variation of stratospheric aerosol size and mass during the first 18 months following the 1982 eruption of El Chichon, J. Geophys. Res., **89**, 4883-4890.
- Hofmann, D. J., J. M. Rosen and W. Gringel (1985), Delayed production of sulfuric acid condensation nuclei in the polar stratosphere from El Chichon volcanic vapors, J. Geophys. Res., in press.
- McCormick, M. P. and T. J. Swissler (1983), Stratospheric aerosol mass and latitudinal distribution of the El Chichon eruption cloud for October 1982, Geophys. Res. Lett., **10**, 877-880.
- McCormick, M. P., C. R. Trepte and G. S. Kent (1983), Spatial changes in the stratospheric aerosol associated with the north polar vortex, Geophys. Res. Lett., **10**, 941-944.
- Pollack, J. B., O. B. Toon, E. F. Danielsen, D. J. Hofmann and J. M. Rosen (1983), The El Chichon volcanic cloud: An introduction, Geophys. Res. Lett., **10**, 989-992.
- Rampino, M. R. and S. Self (1984), The atmospheric effects of El Chichon, Scientific American, January, pp 48-57.
- Rosen, J. M., D. J. Hofmann and J. Laby (1975), Stratospheric aerosol measurements II: The worldwide distribution, J. Atmos. Sci., **32**, 1457-1462.
- Rosen, J. M. and D. J. Hofmann (1977), Balloon-borne measurements of condensation nuclei, J. Appl. Meteorol., **16**, 56-62.
- Rosen, J. M., D. J. Hofmann and K. H. Kaselau (1978), Vertical profiles of condensation nuclei, J. Appl. Meteorol., **17**, 1737-1740.
- Rosen, J. M. and D. J. Hofmann (1983), Unusual behavior in the condensation nuclei concentration at 30 km, J. Geophys. Res., **88**, 3725-3731.
- Turco, R. P., P. Hamill, O. B. Toon, R. C. Whitten and C. S. Kiang (1979), A one-dimensional model describing aerosol formation and evolution in the stratosphere: I. Physical processes and mathematical analogs, J. Atmos. Sci., **36**, 699-717.

5.2 LASER RADAR OBSERVATION OF THE POLAR STRATOSPHERIC AEROSOL LAYER

Y. Iwasaka¹, T. Hirasawa², H. Fukunishi²,
M. Fujiwara³, R. Fujii², and H. Miyaoka²

¹Water Research Institute, Nagoya University, Chikusa-ku, Nagoya 464 Japan

²National Institute of Polar Research, Itabashi-ku, Tokyo 173, Japan

³Faculty of Science, Kyushu University, Fukuoka 812, Japan

The polar stratosphere has been speculated to be an active sink region of various stratospheric materials; ozone, water vapor, NO_x , aerosol particles and so on, but this process is not theoretically and/or observationally made clear. The observation of the polar stratospheric aerosol layer using laser radar certainly contributes to the study of the global transport of these stratospheric minor constituents. In addition to this, from the viewpoint of aerosol science, there may be many interesting phenomena which cannot be found in the stratosphere at mid and low latitudes; the effect of precipitation of high energy molecules and atoms, of very cold winter stratosphere, of very cold mesopause in summer (IWASAKA, 1981, 1982).

We have made laser radar observation as one of the main activities of the Antarctic Middle Atmosphere (AMA) project at Syowa Station (69.00°S, 39.35°E), Antarctica since May 1983. Here we should like to describe the outline of laser radar measurement at Syowa Station and some other topics, even if it is brief.

The scattering ratio is defined by

$$R = [B_1(z) + B_2(z)]/B_1(z) \quad (1)$$

where $B_1(z)$ and $B_2(z)$ are the backscatter coefficient of air molecules and of aerosol particles, respectively. The mixing ratio of aerosol particles is optically given by $[R - 1]$. In Figure 1, the vertically integrated backscatter coefficient of aerosols in the height range of the stratosphere given by

$$\int_{z_2}^{z_1} B_2(z) dz, \quad z_1 \sim z_2 = \text{the integrated height range}$$

is indicated. The annual average of this value is about 10^{-3} sr^{-1} and apparently in a rather high level in comparison with the measurements in mid and low latitudes. This may be due to the global transport of aerosol particles into the polar region, or due to the volcanic effect of eruptions of Mt. El Chichon and some others. In the winter season, a noticeably enhanced aerosol layer was measured frequently. This enhancement was certainly associated with the decrease of stratospheric temperature, as pointed out by McCORMICK et al., (1982) (see the temperature distributions shown in Figure 2).

In Figure 3 we show the vertical profiles of scattering ratios measured at the pre-enhancement stage (profiles in Figure 3a) and the fully enhanced stage of an Antarctic aerosol layer (profiles in Figure 3b). During periods of pre-enhancement of the stratospheric aerosol layer, the maximum value of the scattering ratio is about 3, but values of more than 5 were observed very frequently during the fully enhanced periods. The layer thickness became larger gradually during the developed time of the aerosol layer. However, after the fully enhanced stage (October and November) the layer thickness became smaller and the peak height of the layer was measured at a very low altitude, frequently about 10 km or lower. All of these are not found in low and mid latitudes and suggest that there are many peculiar factors of the polar stratospheric aerosol layer. Thus more intensive studies on these events are desired.

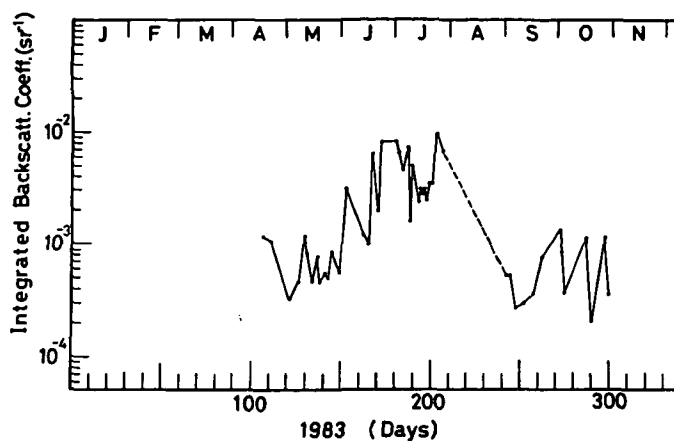


Figure 1. Change of the vertically integrated backscatter coefficient in the height range of the stratosphere measured at Syowa Station (69.00 S, 39.35 E).

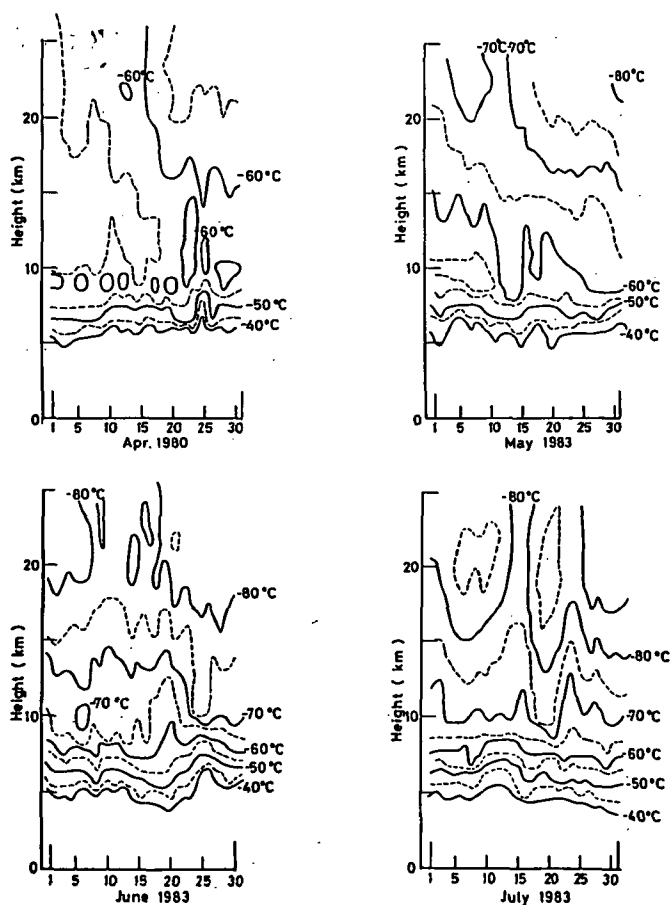


Figure 2. Temperature distribution of the stratosphere measured at Syowa Station (69.00 S, 39.35 E).

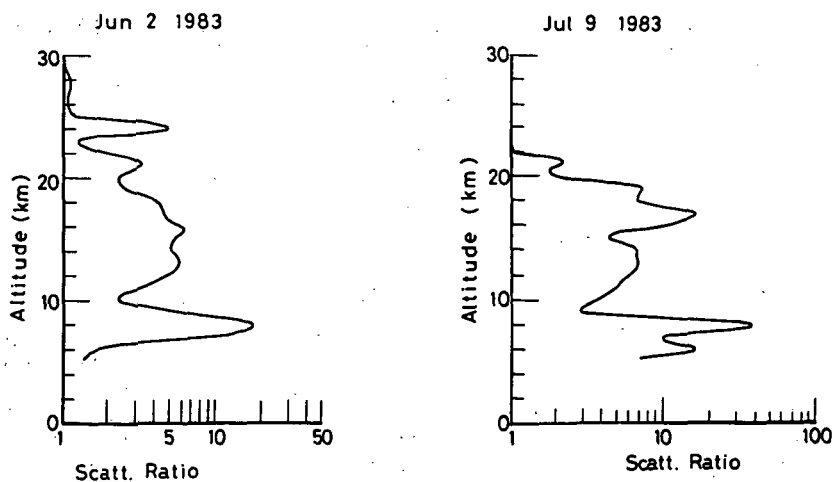


Figure 3a. The vertical profiles of scattering ratio measured during the period of pre-enhancement of the stratospheric aerosol layer.

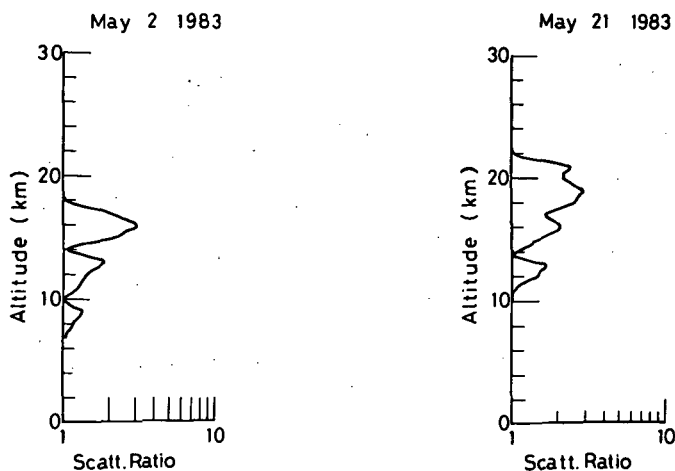


Figure 3b. The vertical profiles of the scattering ratio measured during the period of enhancement of the stratospheric aerosol layer.

REFERENCES

- Iwasaka, Y. (1981), Stratospheric "Cist" and water vapor budget in the stratosphere, Mem. Nat'l. Institute of Polar Res., 19, 188-194.
- Iwasaka, Y. (1982), Formation of noctilucent cloud particles and the temperature distribution at the polar mesopause, Mem. Nat'l. Institute Polar Res., 22, 247-253.
- McCormick, M. P., H. M. Steel, P. Hamill, W. P. Chu, T. J. Swissler (1982), Polar stratospheric cloud sightings by SAM II, J. Atmos. Sci., 39, 1387-1397.

5.3 A SPECIAL OZONE OBSERVATION AT SYOWA STATION, ANTARCTICA FROM FEBRUARY 1982 TO JANUARY 1983

Shigeru Chubachi

Meteorological Research Institute
1-1 Nagamine, Yatabe, Tsukuba-gun
Ibaraki 305, Japan

INTRODUCTION

The behavior of stratospheric ozone at high latitudes is especially interesting, since the stratospheric ozone at high latitudes is thought to be transported from low latitudes through dynamical processes. However, only limited information has so far been obtained, because ozone observations at high latitudes are sparse. There are only two ozone observation stations operating in Antarctica: Syowa Station and Amundsen-Scott, where the total ozone has been observed in sunlit months only. To make up for this deficiency, extensive observations were carried out at Syowa Station as part of MAP. Some preliminary results of these observations are shown here.

OBSERVATIONS AND RESULTS

Total Ozone

Figure 1 shows the result of total ozone observations at Syowa Station. Total ozone was observed with a Dobson spectrophotometer. Open circles and open boxes show the total ozone with sunlight in the summer season, and solid circles show the ones with moonlight in the winter season. Two hundred-twenty observations were made on 41 nights from April 13 to October 4. Among them, 9 night observations with moonlight from September 4 to October 4 were compared with those with sunlight. No systematic difference was found between the sunlight and moonlight observations. Combining these types of observations, we can depict the annual variations of total ozone at Syowa Station. This figure shows interesting features. One is a sudden increase on October 28. The total ozone increased 140 DU within 34 hours. Another interesting feature is the winter maximum. However, such an increase in winter was not found in observations made by Ishida in winter 1969. It is not clear whether such an increase in winter is common or peculiar to 1982. Further observations in winter at Syowa Station are necessary.

Ozonesonde

Figure 2 shows a time-height cross section of ozone partial pressure with the type KC-79 ozonesonde. The ozonesonde soundings were carried out two or three times per month. The total number of flights was 49. However, at present, only 22 ozone profiles are available and used in our present analysis. This figure shows that the increases in total ozone are mainly due to the increase of ozone partial pressure in the peak ozone of the ozone profile. The maximum partial pressure appeared at about a 90 mb level in winter, and in the 60-40 mb region in summer. This figure shows that the sudden increase of total ozone on October 28 was a result of the rapid increase of ozone partial pressure in the 100-20 mb region. A significant variation of ozone partial pressure was found at 10 mb in early October, preceding the sudden increase of total ozone on October 28.

DISCUSSIONS

Figure 3 shows a time-height cross section of air temperature. This fig-

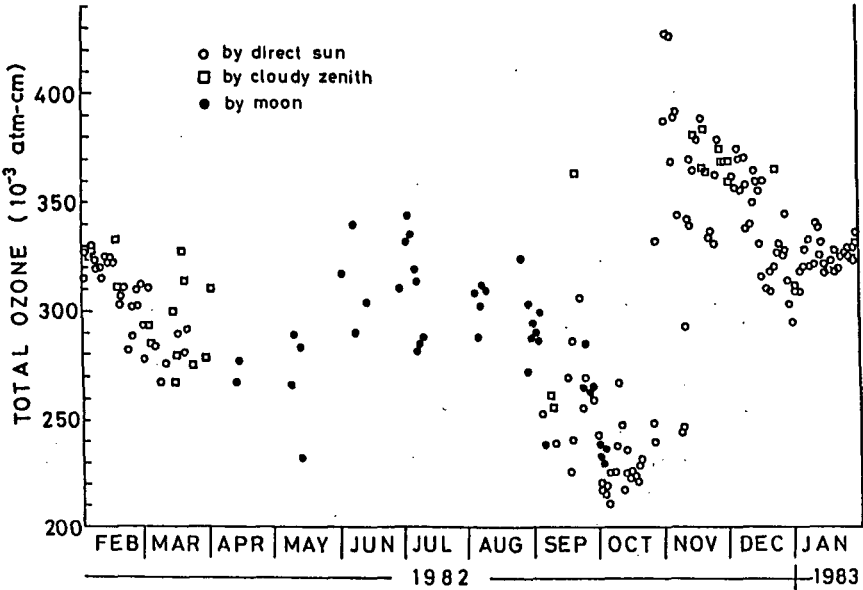


Figure 1. Total ozone at Syowa Station. Open circles: direct sun measurement, squares: cloudy zenith measurement, filled circles: moon measurement.

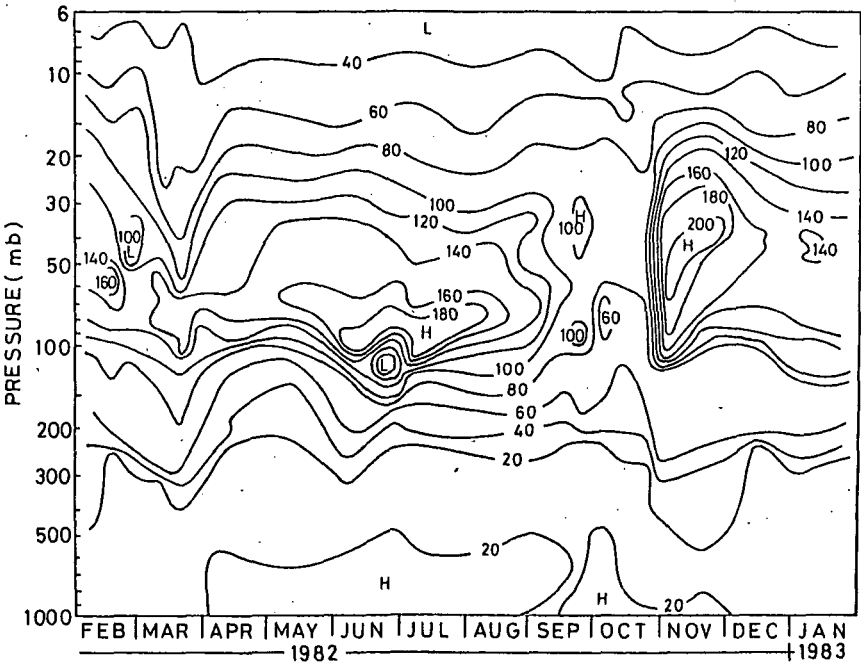


Figure 2. Time-height cross section of partial pressure of ozone at Syowa Station constructed from 22 ozonesonde observations. (unit: mb).

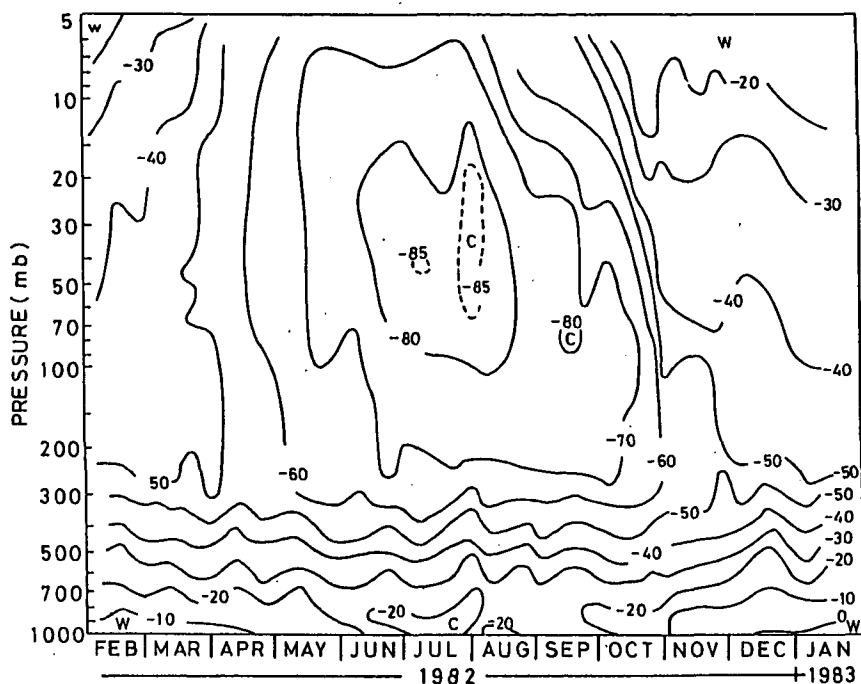


Figure 3. Time-height cross section of air temperature at Syowa Station constructed from 33 ozonesonde soundings (unit: $^{\circ}\text{C}$).

ure suggests that the sudden increase of total ozone on October 28 is related to the warming at 100–30 mb. At 10 mb, a rapid warming was observed in early October preceding the sudden warming. In Figure 4, small points show the total ozone observed at Syowa Station from 1966 to 1980, and open circles show these observed from February 1982 to January 1983. This figure shows that the annual cycle of total ozone observed from February 1982 to January 1983 is essentially similar to those in 1966–1980 at Syowa Station. In September and early October 1982, the total ozone was as small as 220 DU. Similar low values were observed at Amundsen-Scott on October and November in 1982. Figure 5 shows a comparison of total ozone measured at Amundsen-Scott and at Syowa Station. Open circles show our results at Syowa Station, and closed circles show the total ozone at Amundsen-Scott. This figure shows that the sudden increase of total ozone on October 28 at Syowa Station occurred at Amundsen-Scott about one month later. Figure 6 shows a vertical profile of the ozone partial pressure and air temperature obtained by ozone sonde soundings on the day of the sudden increase (October 28; heavy curve) and the one day before (October 27; thin curve) of the sudden increase of the total ozone. Here it is seen that the increase of ozone partial pressure and warming occurred in the stratosphere.

SUMMARY

- 1) Extensive ozone observation was carried out at Syowa Station from February 1982 to January 1983.
- 2) The annual cycle of total ozone has two maxima. One is in winter, and the other is in early November.

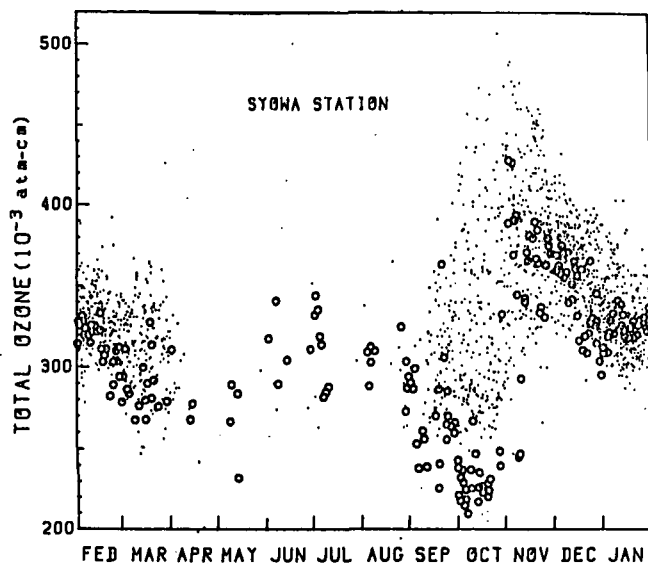


Figure 4. Total ozone observed at Syowa Station from 1966 to 1980 (•) and from February 1982 to January 1983 (o).

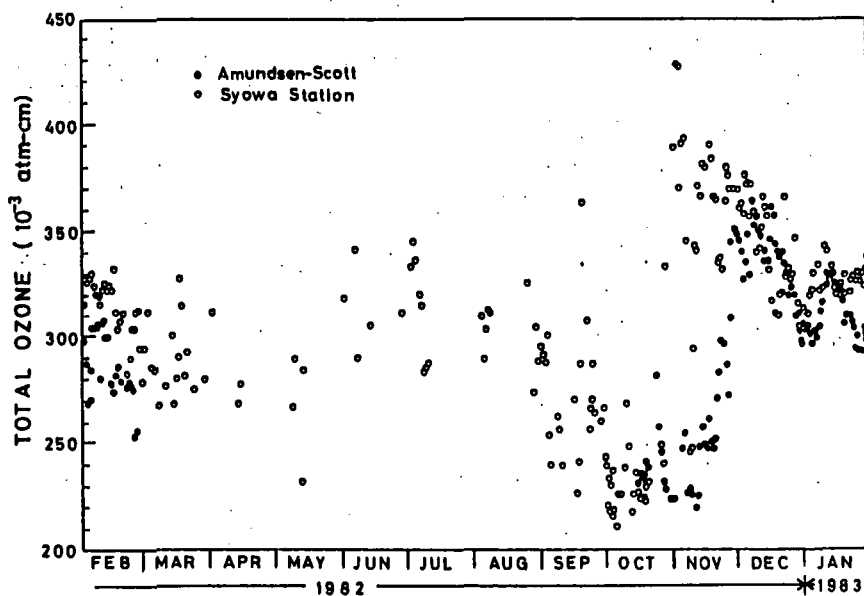


Figure 5. Comparison of total ozone at Amundsen-Scott with that at Syowa Station observed from February 1982 to January 1983.

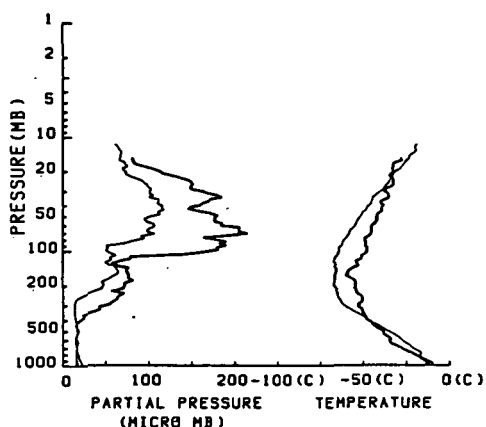


Figure 6. Vertical profiles of partial pressure of ozone and air temperature obtained with ozonesonde soundings on the day of (October 28; heavy curve) and one day before (October 27; thin curve) the sudden increase.

- 3) The smaller value of total ozone since 1966 was observed in the present observation from September to October. A similarly small value was also observed at Amundsen-Scott at the same time.
- 4) On October 28, the sudden increase of total ozone was observed at Syowa Station. About one month later, it appeared at Amundsen-Scott.
- 5) The peak height of ozone partial pressure is at 90 mb level in winter, and 60-40 mb in summer.
- 6) The warming and increase of ozone partial pressure was observed in the lower stratosphere with the sudden increase of total ozone on October 28.

To verify these results, further extensive observations are necessary at Syowa Station.

REFERENCE.

Ishida, K., T. Suzuki and S. Sakai (1971), Total ozone observation at Syowa Station, Antarctica in 1969, Nankyoku Shiryo (Antarctic. Rec.), 39, 32-38.

5.4 OBSERVATION OF ATMOSPHERIC MINOR CONSTITUENTS BY FTIR AT SYOWA STATION, ANTARCTICA

Y. Makino¹, H. Muramatsu¹, S. Kawaguchi², T. Yamanouchi²,
M. Tanaka³, and T. Ogawa⁴

¹Meteorological Research Institute, 1-1, Nagamine, Yatabe-machi,
Tsukuba-gun, Ibaraki, 305 Japan

²National Institute of Polar Research, 9-10, Kaga 1-chome,
Itabashi-ku, Tokyo, 173 Japan

³Tohoku University, Aoba, Aramaki, Sendai, 980 Japan

⁴University of Tokyo, 3-1, Hongo 7-chome, Bunkyo-ku, Tokyo, 113 Japan

As a part of the Antarctic MAP activity, a ground-based spectroscopic observation of atmospheric infrared transmission was started at Syowa station (69°00'S, 39°35'E) in March 24, 1983.

Observations of sunlight as a radiation source were made with a Fourier transform infrared spectrometer having a maximum path difference of 80 mm and an apodized FWHM resolution of $\sim 0.12 \text{ cm}^{-1}$. In routine operation through the year, the resolution of $\sim 0.8 \text{ cm}^{-1}$ was applied for economy of data-processing time. The 408 spectra for 72 days were obtained in about 10 months until January 23, 1984. From the absorption features revealed in the spectra over the wave number range of $500\text{--}7500 \text{ cm}^{-1}$, a preliminary estimate of $\text{N}_2\text{O } 2\nu_1$ band absorption was attempted.

An apparent transmittance was defined at the wave number 2576 cm^{-1} , where the absorption by N_2O molecules affected the observed intensity strongly. A ray-tracing technique and a line-by-line calculation with a model atmosphere and the AFGL atmospheric absorption line parameters compilation (MCCLATCHEY et al., 1973), were applied to the calculation of the synthetic spectra.

In Figures 1 and 2, observed transmittances at the solar zenith angles between $72^\circ\text{--}88^\circ$ are shown together with the curves of transmittance calculated from the mixing ratio profile of N_2O , which is uniform in the troposphere (324, 270 and 216 ppbv, respectively) but decreases above the tropopause (10 km). The best fit value is 270 ppbv in the troposphere throughout the year (for example, see Figure 1) except Antarctic springtime (September and October) and polar nights (May-July), when we cannot see any sun. We find the higher values to agree with the observed transmittances in September (Figure 2) and rather higher and scattered values in October 1983.

Table 1 shows observed N_2O mixing ratios by other methods or sites. GOLDMAN et al. (1983) made the spectroscopic observation with a higher resolution (0.02 cm^{-1}) of N_2O absorption at $1220\text{--}1260 \text{ cm}^{-1}$ region on December 5, 1980. WEISS (1981) and HIROTA et al. (1985) measured N_2O from sampled air with the gas-chromatographic method. They all obtained a value close to 302 ppbv. To elucidate the cause of the differences, it is necessary to take more precise spectroscopic and meteorological data, as well as to consider the different methods.

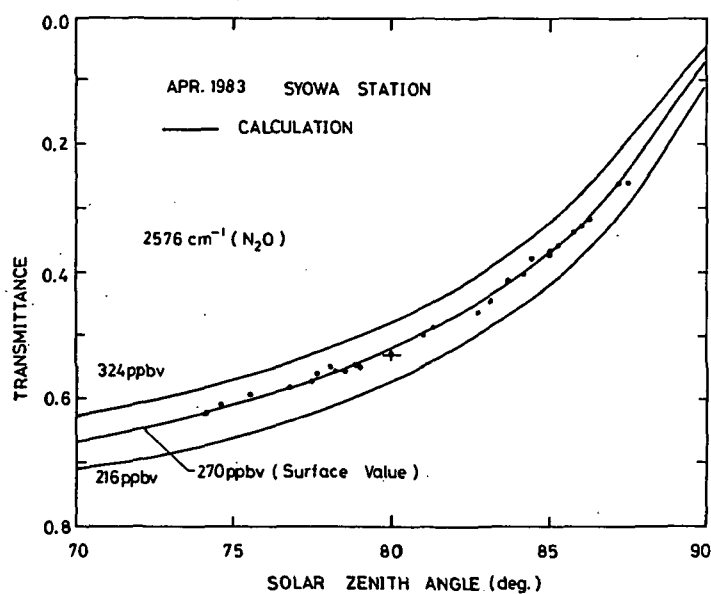


Figure 1. Observed change of atmospheric transmittance with solar zenith angle in April 1983. Solid curves represent the results of line-by-line calculation.

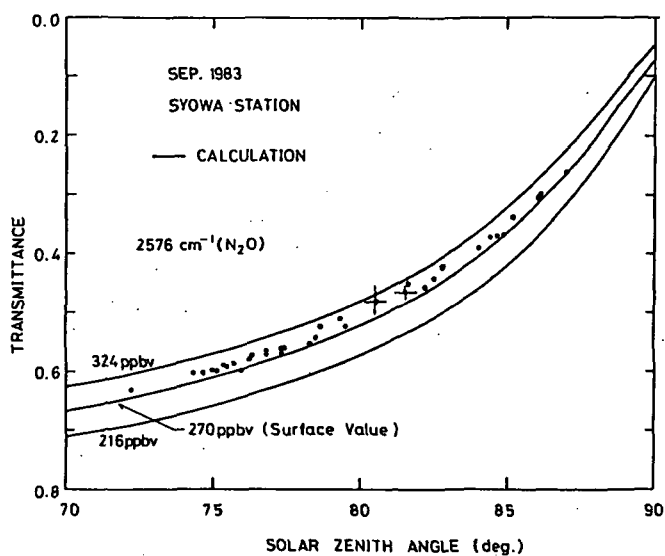


Figure 2. Same as in Figure 1 but in September 1983.

Table 1. Comparison of observed N_2O volume mixing ratios at surface in Antarctica.

Authors	GOLDMAN et al. (1983)	HIROTA et al. (1985)	WEISS (1981)
N_2O mixing ratio	283-310 ppbv 302 ppbv (best fit)	302 ppbv	299.2 ± 0.2 ppbv 0.52 ± 0.13 ppbv/yr
Period	on 5 Dec. 1980	av. Feb. 1982 - Jan. 1984	in 1978
Site	South Pole	Syowa St.	South Pole

REFERENCES

- Goldman, A., F. G. Fernald, F. J. Murcray, F. H. Murcray and D. G. Murcray (1983), Spectral least squares quantification of several atmospheric gases from high resolution infrared solar spectra obtained at the South Pole, J. Quant. Spectrosc. Radia. Transfer, **29**, 189-204.
- Hirota, M., S. Chubachi, Y. Makino and H. Muramatsu (1985), Gas-chromatographic measurements of atmospheric CF_2Cl_2 , $CFC1_3$ and N_2O in the Antarctica, MAP Handbook, 1984, this volume.
- McClatchey, R. A., W. S. Benedict, S. A. Clough, D. E. Burch, R. F. Calfee, K. Fox, L. S. Rothman, and J. S. Garing (1973), AFCRL atmospheric absorption line parameters compilation, AFCRL-TR-73-0096.
- Weiss, R. F. (1981), The temporal and spatial distribution of tropospheric nitrous oxide, J. Geophys. Res., **86**, 7185-7195.

5.5 MEASUREMENT OF POLAR STRATOSPHERIC NO₂ FROM THE 23RD AND 24TH JAPANESE ANTARCTIC RESEARCH EXPEDITION (JARE) BALLOON EXPERIMENTS

K. Shibasaki, N. Iwagami, and T. Ogawa

Geophysics Research Laboratory,
University of Tokyo
Tokyo 113, Japan

As a part of the Japanese activities of MAP in the Antarctica, balloon-borne measurements of the stratospheric NO₂ profile were planned and carried out by the JARE 23rd and 24th wintering parties. Few results have been reported so far as the stratospheric NO₂ profile at high latitude (KERR and McELROY, 1976; EVANS et al., 1981). There were no reported balloon measurements carried out in the Southern Hemisphere. In this abstract we will present the first balloon-borne measurement of the stratospheric NO₂ in the Antarctica.

Three balloons named JA21, JA25 and JA26 were launched from Syowa Station (69°S, 35.6°E) using 5000 m³ plastic balloons. JA21 balloon was launched on November 24, 1982, and JA25 and JA26 balloons on November 12 and 20, 1983, respectively. On board the balloon was a compact spectrometer newly designed for a balloon observation. Its optical system was based upon the Jobin-Yvon H20 spectrometer, and some modifications were added to it; i.e., scanning wavelength region was restricted between 4280 Å and 4515 Å, scanning rate of 200 Å per minute was adopted, and so on. A detailed description of the basic system and the data analysis were given in a paper by OGAWA et al. (1981).

Figure 1 shows a variation of NO₂ column density versus time measured from the JA21 balloon. Because a maximum solar zenith angle was 92.1° at a balloon altitude, sunset and sunrise data were taken during the same flight. A vertical profile of the stratospheric NO₂ was derived from an apparent variation of the NO₂ column density as seen in Figure 1. Figure 2 shows a derived profile of the polar stratospheric NO₂. The principle of the inversion method was described in the paper by OGAWA et al. (1981), and the estimation of errors was given by IWAGAMI et al. (1985).

The sunset and the sunrise profile are similar. This fact is reasonable, because there occurred no night condition above 20 km and the conversion of NO₂ to N₂O₅ might not be remarkable. A prominent feature seen in Figure 2 is a double-peak structure. To our knowledge, this is the first paper that reports a vertical profile with the double-peak structure. We suggest that the cause of this double peak is dynamical conditions. According to the results of daily sonde measurements, the center of the northward flow was located at around 15 km, while the southward flow had prevailed above 20 km since a couple of days before the balloon observation. This implies that an upper peak was maintained by NO₂ rich air mass from the lower latitude stratosphere and a lower peak was due to airflow from the high latitude stratosphere. The above considerations may be supported by model calculations (e.g., SOLOMON and GARCIA, 1983), in which the altitude of the maximum in NO₂ becomes higher at low latitudes.

As for the JA25 balloon, Figures 3, 4, and 5 show preliminary results. To be brief, the result seems to be similar with that of JA21. However, the detailed data analysis is now being advanced, and a final conclusion is not presented. The data taken with the JA26 balloon are also being analyzed. Figure 6 gives some profiles obtained by our group at different latitudes. The peak altitude seems to become lower, in general, toward high latitudes as predicted by model calculations. Detailed analyses must be made further, and we cannot present a definitive conclusion now.

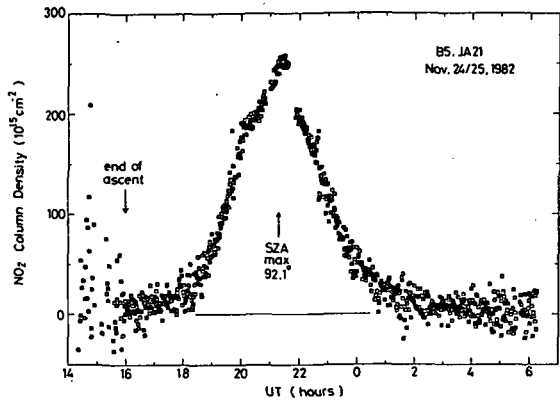


Figure 1. Variation of NO_2 column density as a function of universal time measured from the JA21 Balloon. Local time at Syowa Station is 3 hours in advance of universal time. An increase and a decrease of the NO_2 column density corresponding to those of the solar zenith angle are seen in the figure (after IWAGAMI et al., 1985).

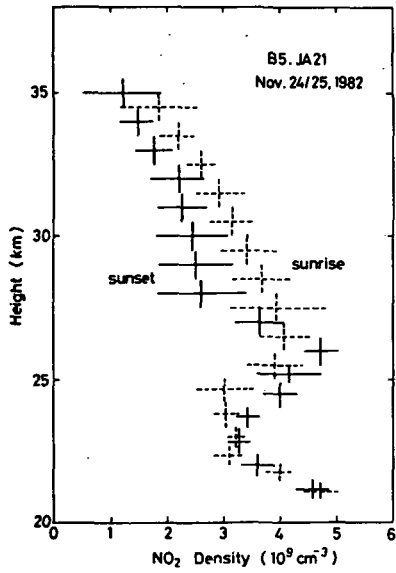


Figure 2. Vertical profile of the stratospheric NO_2 determined from the data given in Figure 1. Solid and dashed crosses correspond to sunset and sunrise profiles, respectively (after IWAGAMI et al., 1985).

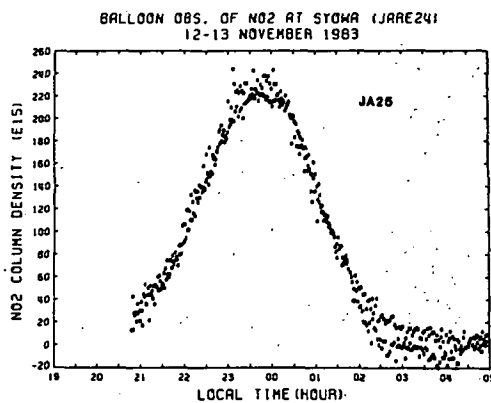


Figure 3. Same as Figure 1 except for the JA25 balloon measurement.

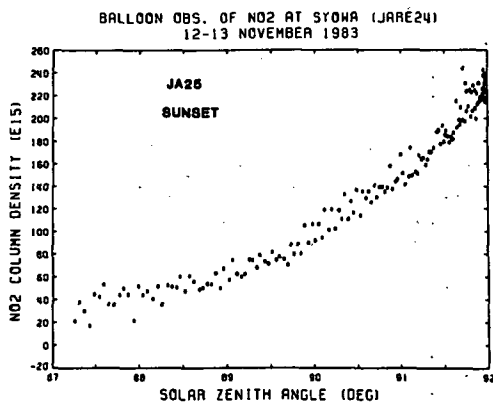


Figure 4. Same as Figure 3 except for data obtained at sunset as a function of the solar zenith angle.

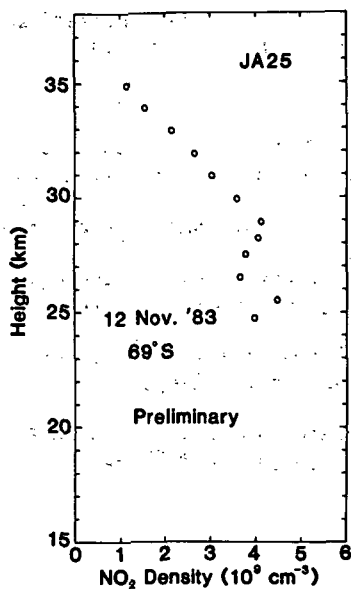


Figure 5. Same as Figure 2 except for the JA25 balloon measurement. The profile is a preliminary one corresponding to data shown in Figure 4.

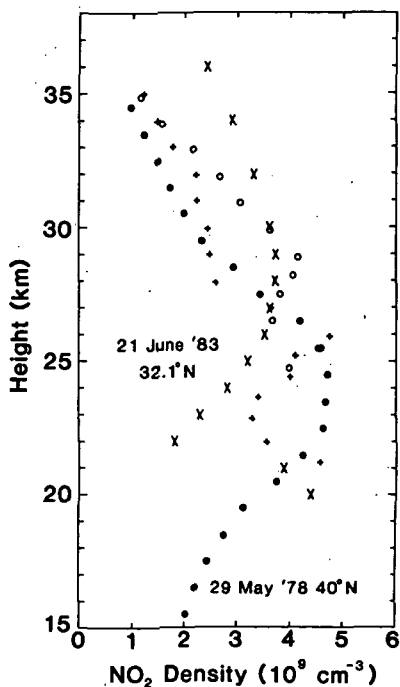


Figure 6. NO₂ number density profiles taken at different latitudes. Solid circles indicate a profile taken during May 29, 1978 at 40°N; crosses indicate a profile taken during June 21, 1983 at 32.1°N; pulses and open circles indicate profiles taken during JA21 and JA25 balloon measurements at Syowa, respectively.

ACKNOWLEDGEMENT

The authors wish to thank all members of JARE 23rd and 24th wintering party for their encouragement and help with the balloon measurements.

REFERENCES

- Evans, W. F. J., C. T. McElroy, J. B. Kerr and J. C. McConnell (1981), Simulation of nitrogen constituent measurements from the August 1976 stratoprobe III flight, J. Geophys. Res., **86**, 12066-12070.
- Iwagami, N., T. Ogawa and K. Shibasaki (1985), Balloon measurements of stratospheric NO₂, J. Meteorol. Soc. Japan, in press.
- Kerr, J. B. and C.T. McElroy (1976), Measurement of stratospheric nitrogen dioxide from the AES stratospheric balloon program, Atmosphere, **14**, 166-171.
- Ogawa, T., K. Shibasaki and K. Suzuki (1981), Balloon observation of the stratospheric NO₂ profile by visible absorption spectroscopy, J. Meteorol. Soc. Japan, **59**, 410-416.
- Solomon, S. and R. R. Garcia (1983), On the distribution of nitrogen dioxide in the high-latitude stratosphere, J. Geophys. Res., **88**, 5229-5239.

5.6 DECOMPOSITION OF CO₂ MOLECULES DUE TO AURORAL X-RAYS

K. Sekihara

Tokyo Science University

Tokyo, Japan

INTRODUCTION

It has been reported by SEKIHARA (1981), that the circumpolar measurement from a commercial airliner reported by PRATT and FALCONER (1979) was subjected to a strong influence of a geomagnetic storm, specifically at the beginning stage through the North Pole.

The main point of interest was the increase of CO concentration by the order of 10 ppb that took place simultaneously with a temperature decrease of several degrees, which was regarded as a result of enhanced cooling to space due to CO₂ decomposition.

Later inspection of the original magnetogram of eleven auroral zone stations revealed that the observation started 13 hours after the main phase of a geomagnetic storm, which lasted for 22 hours.

The purpose of this paper is to make a quantitative estimation of CO₂ decomposition due to auroral X-rays that should take place during the degradation of photoelectrons injected into the lower stratospheres.

THE AMOUNT OF ENERGY DEPOSITION OF AURORAL X-RAYS IN THE LOWER STRATOSPHERE

The author uses the results of BERGER et al. (1974), which at the level of 20 km (50 mb) gives the value of 8×10^{-6} eV/cc per one precipitated electron at the top of the atmosphere with the energy distribution $1/\alpha \exp(-T_0/\alpha)$ where T_0 is the electron energy and the parameter α is taken as 200 keV.

Moreover, the total precipitated energy flux is assumed to be $10^3 \times 22 \times 60 \times 60 = 7.92 \times 10^7$ ergs/cm², thus giving the energy deposition $6.242 \times 10^{11} \times 8 \times 10^{-6} \times 7.92 \times 10^7 = 3.95 \times 10^{14}$ eV/cc at that level.

Photoelectric effect of the air molecule produces electrons of 10-50 keV. This means that the above-mentioned energy deposition corresponds to the injection of 3.95×10^{10} photoelectrons/cc of 10 keV or 7.91×10^9 photoelectrons/cc of 50 keV. These two cases will be assumed in the following calculation.

THE PHOTOELECTRON DEGRADATION PROCESSES

A.E.S. Green and his coworkers (GREEN and DUTTA, 1967; STRICKLAND and GREEN, 1969; SAWADA et al., 1972; GREEN and SAWADA, 1972; PORTER et al., 1976; JACKMAN et al., 1977; GREEN et al., 1977) have elaborated to deduce analytical expressions regarding the main processes of electron collision including cross sections and yield spectra of secondary electrons with respect to major atmospheric molecules. This enabled them to calculate the population of any excited state of the atmospheric molecules of interest.

Thus, the population of CO₂ molecules leading to dissociation via electron degradation processes in the atmosphere can be expressed as follows:

$$J_j(E_o) = \int_{W_j}^{E_o} U_{\text{air}}(E, E_o) p_{\text{CO}_2, \text{diss}}(E) dE \quad (1)$$

where J_j denotes the population of CO_2 excited states leading to dissociation,

E_o and W_j denote incident and threshold energies, respectively,
 $U_{\text{air}}(E, E_o)$ is the yield spectrum of secondary electrons of the air,
 $p_{\text{CO}_2, \text{diss}}$ is the dissociation probability of CO_2 molecules,
 W_j is 5.45 eV, and
 E_o is 10 keV or 50 keV as mentioned above.

$p_{\text{CO}_2, \text{diss}}(E)$ is expressed by the ratio of the mass weighted average cross section of CO_2 dissociation to total inelastic cross section of air molecules. Both the yield spectrum and total inelastic cross section are expressed by the mass weighted average values. Thus,

$$U_{\text{air}}(E, E_o) = 0.7551 U_{\text{N}_2}(E, E_o) + 0.2301 U_{\text{O}_2}(E, E_o) \\ + 0.0129 U_{\text{Ar}}(E, E_o) + 0.0004 U_{\text{CO}_2}(E, E_o) \quad (2)$$

$$\sigma_{\text{air}}(E) = 0.7551 \sigma_{\text{N}_2}(E) + 0.2301 \sigma_{\text{O}_2}(E) \\ + 0.0129 \sigma_{\text{Ar}}(E) + 0.0004 \sigma_{\text{CO}_2}(E) \quad (3)$$

$$p_{\text{CO}_2, \text{diss}}(E) = 0.0004 \sigma_{\text{CO}_2, \text{diss}}(E) / \sigma_{\text{air}}(E) \quad (4)$$

CROSS SECTION OF CO_2 DISSOCIATION

This point is not fully discussed by the papers of Green's group. However, we have the paper of FOX and DALGARNO (1979) and the experiment of CORVIN and CORRIGAN (1969), and discussions will be given on the basis of these papers. As will become clear later, the cross section below 10 eV plays a very important role. Based on theoretical studies and spectroscopical experiments Fox and Dalgarno, assumed two cross sections, namely, the non-resonant one slowly increasing from the threshold and the resonant one equal to total inelastic cross sections of CO_2 from threshold to 7 eV. Corvin and Corrigan deduced a resonant dissociation cross section of $3.5 \times 10^{-17} \text{ cm}^2$ at 7eV on the basis of their glow discharge experiment. The author made the calculation on the basis of three assumptions, that is, a resonant and non-resonant cross section of Fox and Dalgarno (Case I), a resonant one of Corvin and Corrigan with a non-resonant one of Fox and Dalgarno (Case II), and the only non-resonant one of Fox and Dalgarno (Case III). These are shown in Figure 1.

RESULTS AND DISCUSSIONS

Figure 2 shows the total inelastic cross sections of the air and its major

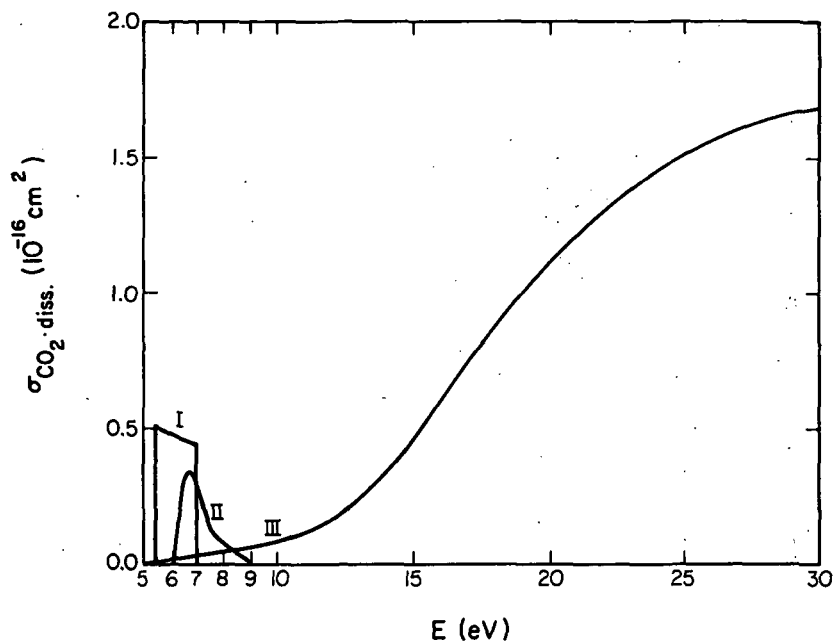


Figure 1. Dissociation cross section of CO_2 for electron impact.

constituents. It should be noticed that there is a deep minimum between 5-9 eV which comes from primarily the behavior of N_2 and then O_2 .

Figure 3 shows the curves of $U_{\text{air}}(E, E_0)$ and $\text{PCO}_2 \cdot \text{diss.}(E)$. Here the steep increasing tendency of U_{air} towards smaller E is shown in both two cases, which means the production of an overwhelming amount of secondary electrons. In the curves of $\text{PCO}_2 \cdot \text{diss.}(E)$ we can notice the vital importance of assumed cross sections at the region of very slow energy near the threshold.

Table 1 shows the calculated values of dissociation population for one incident photoelectron and those of storm-time simulated numbers, respectively. The energy difference in the incident photoelectrons seems to give a trivial effect in this calculated range. However, the assumption with respect to the dissociation cross section gives an effect of vital importance, as can be seen by the figures of the ratio and the concentration in Table 1. One of the reasons comes from the fact that there is a steep increasing tendency of secondary electrons towards lower energies, and another, and more important reason, is that the total inelastic cross section of the air molecules drastically decreases in this energy region, which raises the probability by almost one order of magnitude. The storm-time simulated concentration of dissociation of Case I in Table 1 are 13.8 ppb and 11.2 ppb, respectively. This harmonizes with the observation which was mentioned earlier. It may be mentioned, however, that the observation was done at about 150 mb, which is appreciably lower than the assumed height of the calculation. According to McCORMICK (1984), there is a persistent subsidence within the polar vortex area. Then it can be a good remedy for solving the discrepancy. A full paper will appear in the Memoirs of National Institute of Polar Research, Japan.

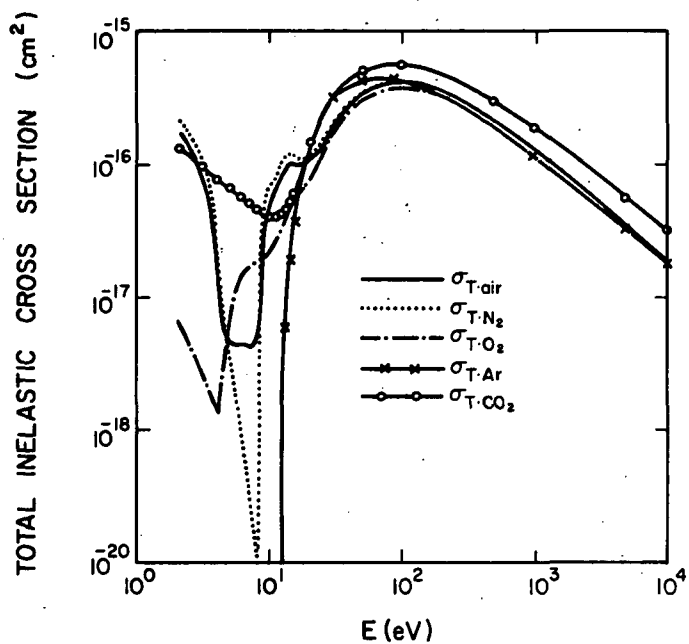


Figure 2. Total inelastic collision cross sections of main atmospheric constituents.

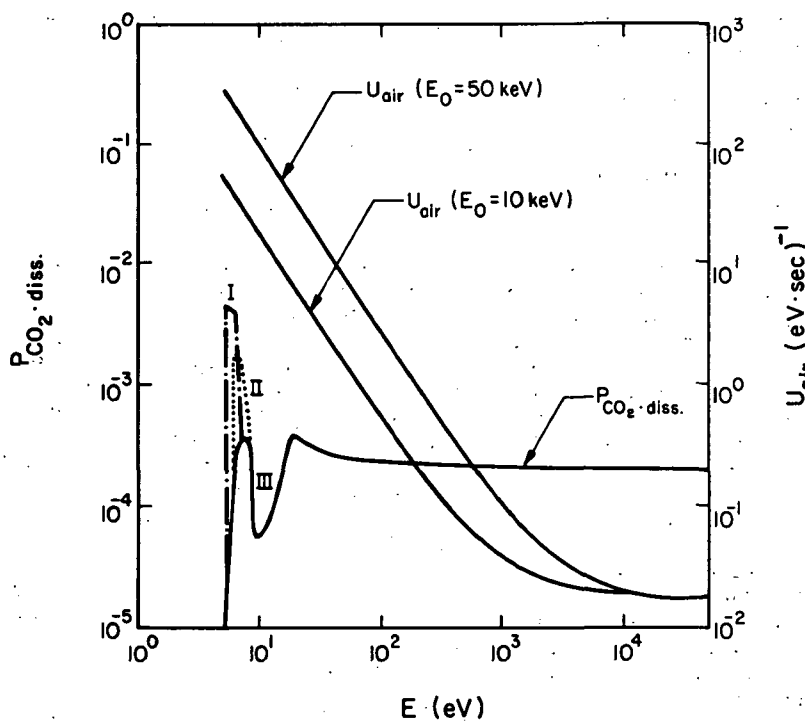


Figure 3. Yield spectrum and dissociation probability.

Table 1.

CO₂ dissociation population for the degradation of one incident photoelectron and the corresponding concentration at 20 km for storm time simulation.

Photoelectron Energy	10 keV			50 keV		
	I	II	III	I	II	III
Assumed Cross Section of Dissociation						
Population	0.41	0.25	0.15	1.87	1.12	0.67
Ratio	2.7	1.6	1.0	2.8	1.7	1.0
Concentration (ppb)	13.8	7.3	4.6	11.2	6.7	4.0

See text about the assumption of Case I, Case II and Case III. As to the storm time simulation energy deposition of 3.95×10^{14} ev/cc at 20 km or 50 mb was assumed.

REFERENCES

- Berger, M. J., Seltzer and K. Maeda (1974), J. Atmos. Terr. Phys., **36**, 591-616.
- Corvin, K. K. and S. J. B. Corrigan (1969), J. Chem. Phys., **50**, 2570-2574.
- Fox, J. L. and A. Dalgarno (1979), Planet. Space Sci., **27**, 491-502.
- Green, A. E. S. and S. K. Dutta (1967), J. Geophys. Res., **72**, 3933-3941.
- Green, A. E. S. and T. Sawada (1972), J. Atmos. Terr. Phys., **34**, 1719-1728.
- Green, A. E. S., C. H. Jackman and R. H. Garvey (1977), J. Geophys. Res., **82**, 5104-5111.
- Jackman, C. H., R. H. Garvey and A. E. S. Green (1977), J. Geophys. Res., **82**, 5081-5090.
- McCormick, M. P. (1984), International MAP symposium, Kyoto, Program and Abstract, No. 4.1, 59.
- Porter, H. S., C. H. Jackman and A. E. S. Green (1976), J. Chem. Phys., **65**, 154-167.
- Pratt, R. and P. Falconer, (1979), J. Geophys. Res., **84**, 7876-7882.
- Sawada, T., D. J. Strickland and A. E. S. Green (1972), J. Geophys. Res., **77**, 4812-4818.
- Sekihara, K. (1981), NASA, Marshall Space Flight Center, Space Sciences Laboratory Preprint Series No. 81-123.
- Strickland, D. J. and A. E. S. Green (1969), J. Geophys. Res., **74**,

5.7 VHF RADAR OBSERVATION OF THE MIDDLE ATMOSPHERE AT SYOWA STATION, ANTARCTICA

K. Igarashi, T. Ogawa, T. Tanaka and Y. Kuratani

Radio Research Laboratories
Koganei, Tokyo 184, Japan

R. Fujii and T. Hirasawa

National Institute of Polar Research
1-9-10 Kaga, Itabashi-ku
Tokyo 173, Japan

ABSTRACT

The newly developed pulsed Doppler radars with 50 and 112 MHz were installed at Syowa Station (69°00'S, 39°35'E geographic; 70.0°S, 80.2°E geomagnetic) in 1982 and 1983, respectively. They have the nominal peak power of 15 kW; the narrow antenna beams (4° in the horizontal plane) in two different directions (approximately geomagnetic south and geographic south with a crossing angle of about 33°), the three operation modes (spectrum, double-pulse and meteor mode) (IGARASHI et al., 1982). The radars were designed to measure the intensity and Doppler velocity of auroral radar echoes due to the 3- and 1.34-m irregularities appearing often in the disturbed E region and also to detect the meteor echoes in the 80-100 km altitudes, thereby to clarify how the middle atmosphere in the polar region behaves in response to the energy input from the magnetosphere, especially during a substorm. In this paper we present some initial results obtained through the radar operation during 1982-1983 to show that our system is useful for continuous monitoring of the lower auroral ionosphere (OGAWA et al., 1983).

POWER SPECTRA OF RADAR ECHOES

As a result of the spectrum mode, we present that the Doppler velocities measured by the radar are consistent with the magnetic D-component measured below the radar echo region. Figure 1 shows the magnetic H-component at Syowa Station, the peak echo intensity profile, the half-power width of the Doppler power spectra, the magnetic D-component at Mizuho Station (70°42'S, 44°20'E geographic; 72.3°S, 81.5°E geomagnetic) and Syowa Station from bottom to top panel. From this Doppler spectra we can obtain the drift velocities of plasma irregularities in the altitude of the E region (IGARASHI et al., 1985a). The variation of the magnetic D-component is equivalent to the north-south component of the electrojet current intensity in the ionosphere. As compared with the magnetic D-component, variations are almost the same as the Doppler velocity spectra. It is suggested that little difference between the amplitude of the magnetic D-component and the Doppler velocities indicate the relation between the conductivities and electric fields in the E region.

COMPARISONS WITH BALLOON OBSERVATIONS

As a result of the double-pulse mode, we present the comparison of the electric field measurements with the VHF Doppler radar and the balloon. Figure 2 shows the summary plots of the double-pulse mode. From bottom to top, the figure shows the CNA, the magnetic H-component at Syowa Station, the peak echo intensity and the range time intensity for the GMS beam. In the upper three panels the drift velocities at the slant range of the peak echo intensity are shown. V is the drift velocity along the GGS beam. V_y is the drift velocity along the GMS beam. V_x shows the east-west component of the drift velocities

C-7

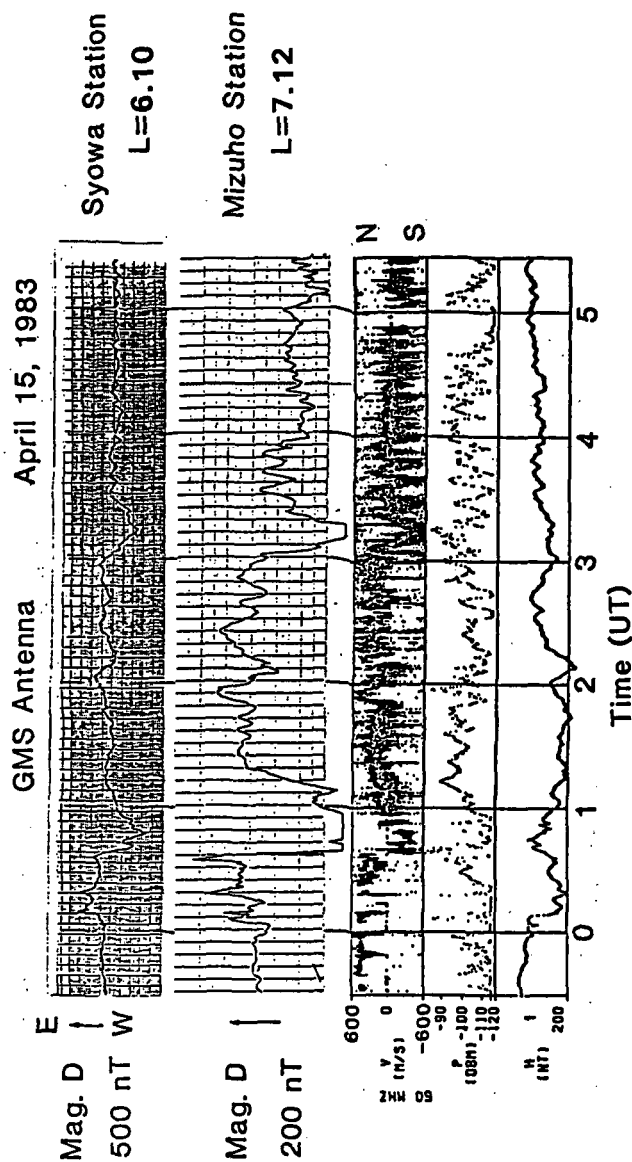


Figure 1. Comparison with the variations of the Doppler power spectra and that of magnetic D-component.

ORIGINAL PAGE IS
OF POOR QUALITY

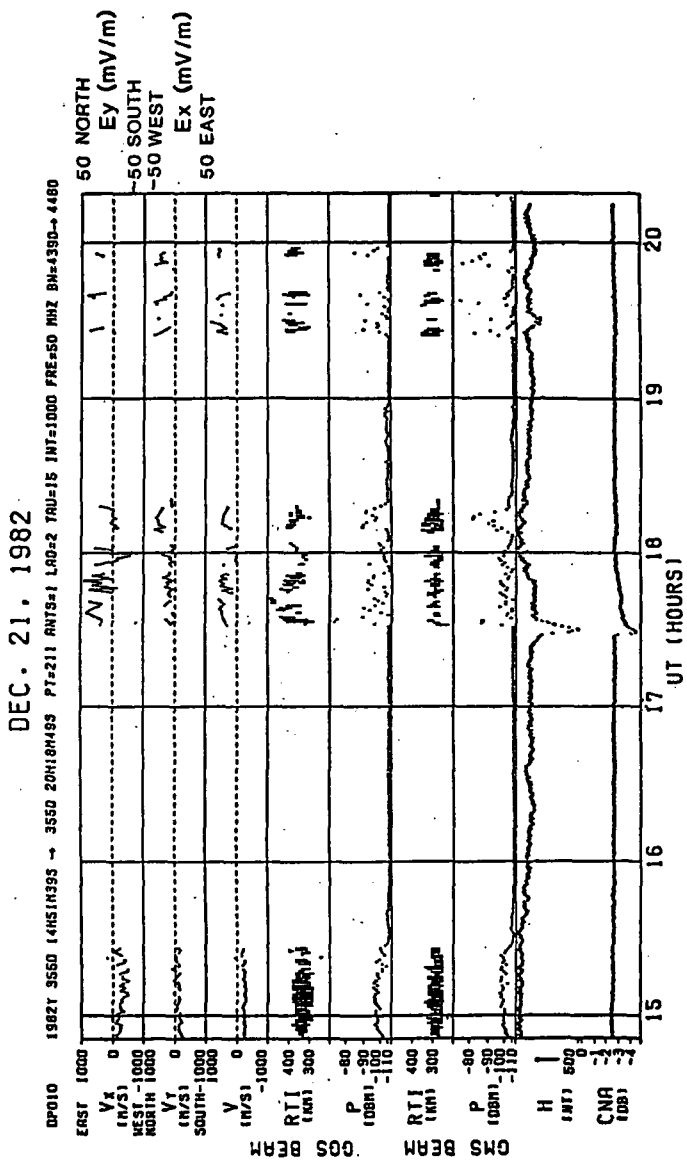


Figure 2. Summary plots of the mean Doppler velocities of the ionospheric irregularities deduced from the radio auroral echoes.

which were derived by combining the Doppler velocity at the maximum echo intensity along the GGS beam with that along the GMS beam (IGARASHI et al., 1985b).

Figure 3 shows the trajectory of the balloon. The balloon flew to the geographical west direction. The altitude of the balloon is about 25 km high. The balloon flying direction is different from the observation region of the radar. It is the geomagnetic south direction. But it is meaningful in comparing the large-scale electric fields. The upper panel of Figure 4 shows that the electric fields estimated from the two drift velocity components point nearly to the northwest direction after the severe substorm about 17:30 UT. On the other hand, the lower panel of the figure shows the *in situ* electric fields measured with the balloon. Just at the breakup, the direction of the electric fields changed from the southwest to the northwest. Therefore, the electric field directions measured with the radar are consistent with the results of the balloon.

ALTITUDE PROFILES OF MEAN WIND VELOCITY

As an initial result of the meteor mode, we present the comparative results of the mean wind profile. In Figure 5, the altitude profile of the mean wind measured by the Syowa Station radar is compared with other profiles obtained at northern high latitudes and also with theoretical results (CARTER and BALSLEY, 1982). The Syowa Station zonal wind profile seems to be similar to the CIRA 1982 model and to the Kiruna meteor radar results. The data at 87 km are peculiar. On the other hand, the meridional winds, except at 85 km, are between the profile from Saskatoon and Poker Flat. It is confirmed that the mean meridional flow in the summer upper mesosphere is equatorwards. The altitude profiles of mean meridional and zonal components are nearly consistent with the results in the summer northern high latitudes in the opposite hemisphere (OGAWA et al., 1985). Figure 6 shows the result of the altitude profiles of mean wind in the summer period compared with that in the winter period. Both the zonal and meridional wind velocities in the winter period are weaker than the mean wind velocities in the summer period. In the summer period the north-south components direct equatorwards, and their magnitudes are between 10 and 20 m/s in the 85-95 km altitudes.

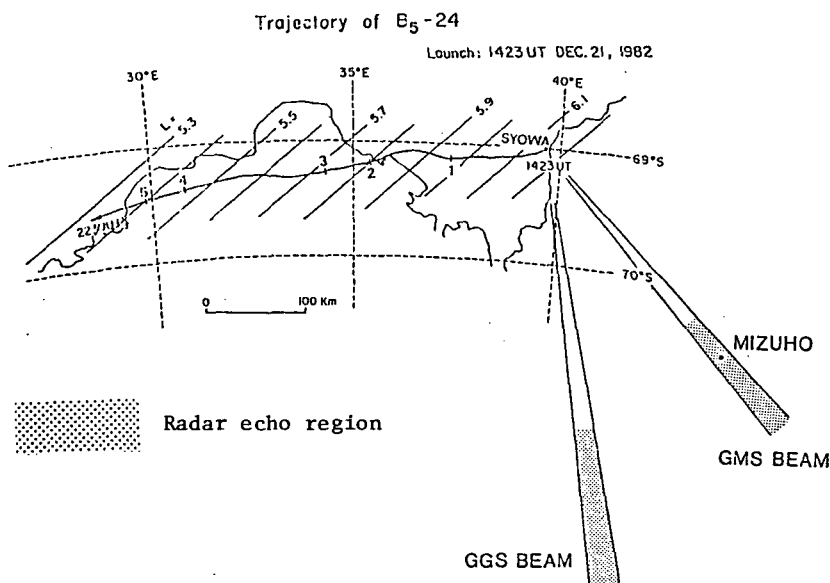


Figure 3. Trajectory of the balloon and radar echo regions.

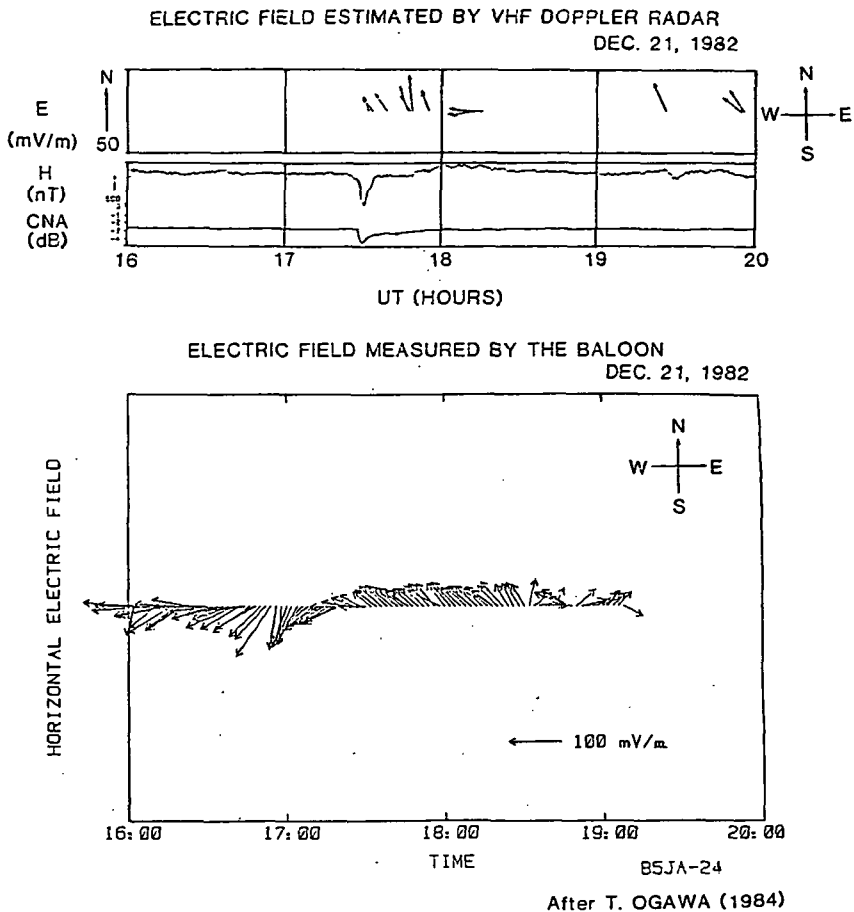


Figure 4. Comparison of electric fields measured by the balloon and the radar.

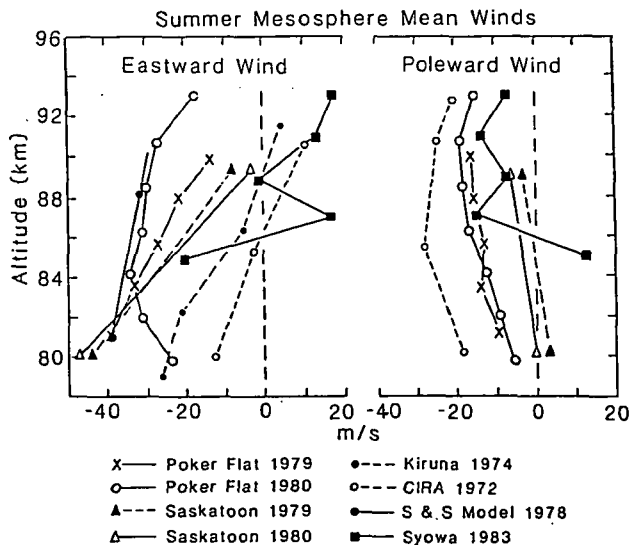


Figure 5. Comparison of altitude profiles of summer mesospheric mean wind.

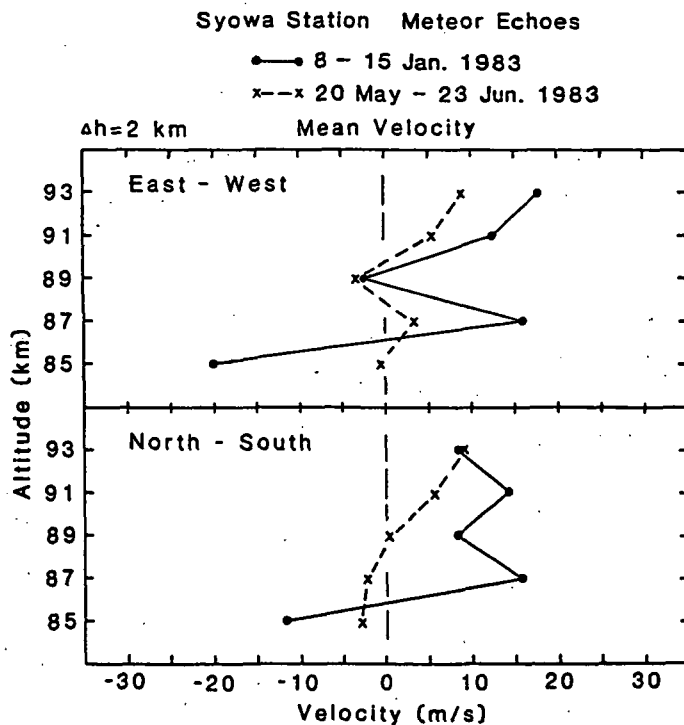


Figure 6. Comparison of altitude profiles of mesospheric mean wind in the periods of summer and winter.

REFERENCES

- Carter, D. A. and B. B. Balsley (1982), The summer wind field between 80 and 93 km observed by the MST radar at Poker Flat, Alaska (65 N), J. Atmos. Sci., **39**, 2905.
- Igarashi, K., T. Ogawa, M. Ose, R. Fujii and T. Hirasawa (1982), A new VHF Doppler radar experiment at Syowa Station, Antarctica, Mem. Nat'l. Inst. Polar Res., special issue, **22**, 258.
- Igarashi, K., T. Ogawa, Y. Kuratani, R. Fujii and T. Hirasawa (1985a), Aurora observations using the Syowa Station 50-MHz Doppler radar, submitted to J. Radio Res. Lab..
- Igarashi, K., T. Ogawa, Y. Kuratani, R. Fujii and N. Sato (1985b), 50MHz auroral Doppler radar observations associated with Pc 5 geomagnetic pulsations, submitted to Mem. Nat'l. Inst. Polar Res., special issue.
- Ogawa, T., K. Igarashi, M. Ose, Y. Kuratani, R. Fujii and T. Hirasawa (1983), Preliminary results of new 50 MHz Doppler radar experiment at Syowa Station, Mem. Nat'l. Inst. Polar Res., special issue, **26**, 193.
- Ogawa, T., K. Igarashi, Y. Kuratani, R. Fujii and T. Hirasawa (1985), Some initial results of 50 MHz meteor radar observation at Syowa Station, submitted to Mem. Nat'l. Inst. Polar Res., special issue.

5.8 WINDS IN THE LOWER THERMOSPHERE OVER MAWSON, ANTARCTICA

N. P. Jones and F. Jacka

Mawson Institute for Antarctic Research
University of Adelaide
G.P.O. Box 498, Adelaide
South Australia 5001

INTRODUCTION

This paper presents measurements of the neutral wind field in the lower thermosphere over Mawson, Antarctica, made during the austral Spring of 1981. The Mawson Institute's Fabry-Perot spectrometer was used to study the [OI] $\lambda 588$ nm emission in the night airglow and aurora. Wind velocities were inferred from Doppler shifts of this emission.

INSTRUMENT

The instrument used in this work is that described by JACKA (1984) except that at the time of these measurements, the low resolution Fabry-Perot etalon was not commissioned. Consequently, the measurements are confined to nighttime only. The Mawson partial reflection drifts (PRD) was also not commissioned at the time.

EMISSION INTENSITY ALTITUDE DISTRIBUTION

The altitude distribution of the nighttime O(1S) $\lambda 558$ emission is reviewed by JACKA (1984) but briefly, in the night airglow most of the emission comes from a region about 7 km thick at about 97 km altitude, and a lesser amount, about 20%, from F-region heights (about 250 km). The height distribution of the auroral emission depends on the energy spectrum of the primary auroral particles. Computation by VALLANCE-JONES (1974) yields half intensity levels at about 105 km and 140 km.

The instrument records the total emission along its line of sight, and the uncertainty about the emission intensity altitude distribution during the acquisition of a line profile translates to a lack of height resolution in the resultant wind measurement.

OBSERVING CYCLE

An observing cycle consists of measurements in geographic north, east, south and west, all at sixty degrees from the zenith, followed by a measurement in the zenith. The acquisition of each airglow/aurora profile was followed by an instrument calibration, performed by recording the profile of the 546 nm emission from a single isotope Hg-198 lamp. This frequent calibration is necessary to enable correction for the effect of instrument drift. It should be noted that to achieve a 5 m/s wind precision one requires a 10 fm (10^{-14} m) wavelength precision.

A typical profile acquisition requires about 20 min and a typical cycle about 100 min. Some improvement in time resolution could be achieved without loss of precision by reducing the wavelength scanning range from the present 12.5 pm to say 8 pm.

DATA REDUCTION

Firstly, the instrument response at 558 nm, synthesised from the recorded $\lambda 546$ nm profiles, is removed from the airglow/aurora profile by numerical deconvolution. The recovered source spectrum is then fitted with a Gaussian. The width of the Gaussian relates to the temperature in the emitting region. The centre position relates to the Doppler shift, and the integrated area divided by the acquisition time is proportional to the emission intensity. The centre positions are corrected for instrument drift, then the rest of the wavelength is subtracted. The residual Doppler shifts are converted first to line-of-sight velocities then to horizontal velocities positive northward and eastward. Typical standard errors in these velocities are ± 5 m/s. In order to produce vector winds, half hourly samples of the horizontal velocity measured in each direction are generated by interpolation. East-looking and west-looking velocity samples are then averaged to produce a station zonal velocity, and similarly for meridional samples. The zonal and meridional samples are then combined to produce half-hourly station wind vectors.

REST WAVELENGTH

The question of rest wavelength deserves further comment. Since the 558 emission is forbidden line, it is difficult to build a laboratory source to give a direct reference. Such lamps have been built, and one is under development in Adelaide (Torop, private communication) for use at Mawson, but it is not yet in routine service.

A less direct method is to assume that vertical velocities are small and use individual zenith measurements by the author, and others (WARDILL et al., 1985) at $\lambda 630$ nm (emission intensity peak around 250 km altitude) have found vertical velocities of many tens of m/s.

It should be noted that errors in the rest wavelength will result in errors in horizontal winds, velocity gradients, and divergence.

The method adopted here is to use the nightly average of the drift corrected zenith peak positions, i.e., it is assumed that the average vertical velocity over the observing period is zero. Evidence for the validity of this will be presented later.

DATA SET

The data were obtained at Mawson, an Australian National Antarctic Research Expedition station on the Antarctic coast, Lat 68°S , Long 63°E geographic. Useful data were obtained on 9 nights during September and October 1981. The record lengths vary from about 10 hours in September down to about 4 hours later in the (austral) Spring.

RESULTS

Firstly, the vertical velocities. Individual zenith measurements indicate occasional significant nonzero vertical velocities, with departures from the nightly mean of ± 15 m/s not being uncommon. It is suggested that these could be vertical perturbation velocities associated with gravity waves, but the time resolution of these is not adequate to make positive identifications. It is planned that during 1985 the Mawson FPS will be used to make high time resolution zenith only studies of the $\lambda 588$ nm emission, hopefully on a 24-hour basis.

The average overall nights of the vertical velocity samples is zero within experimental error, i.e., there is no evidence for a significant diurnal trend

in the vertical velocity which would put the zero calibration in error.

HORIZONTAL VELOCITIES

Figure 1. shows the horizontal velocity vector samples for the whole of the observing period. Note that the days are ordered by increasing EKp, an index of planetary magnetic activity. Note that velocities are of the order of 100 m/s.

The zonal flow tends to be typically eastward before local midnight, and westward after midnight. Meridional flow was typically southward (poleward) all night, with a tendency to decrease in magnitude during the night.

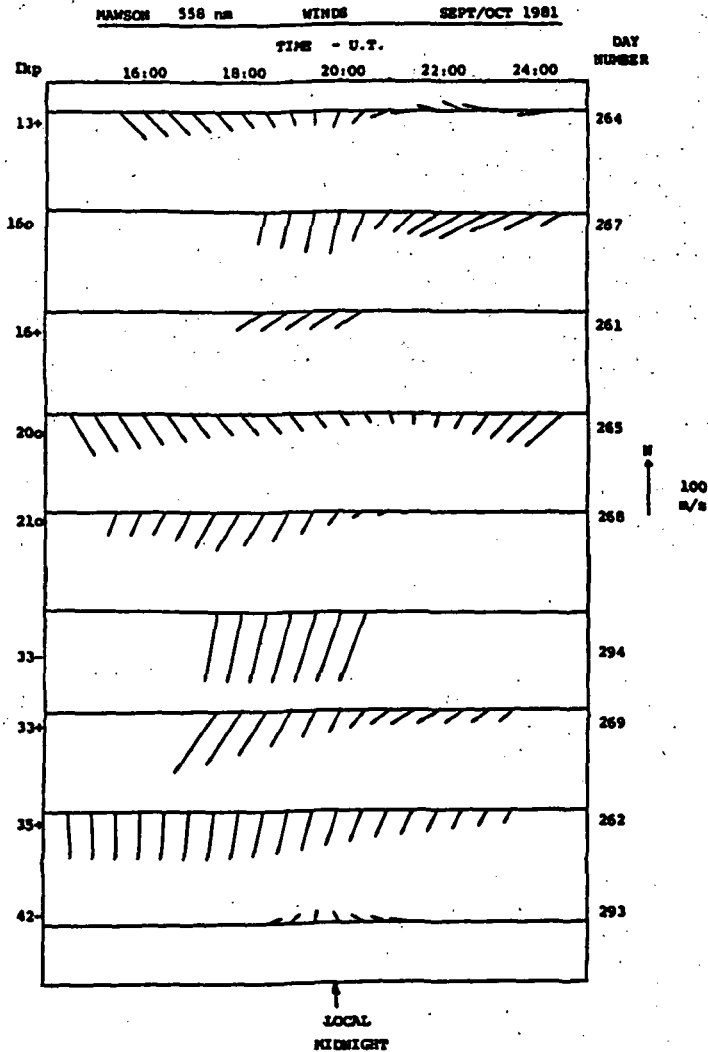


Figure 1.

Kp DEPENDENCE

Figure 2 shows the same data as Figure 1 except that the data have been averaged into 3 "bins" of increasing ΣKp . There is a clear trend for velocities to be greater on more disturbed days.

GRADIENTS AND DIVERGENCE

Since this technique measures the meridional velocity at two different latitudes, and the zonal velocity at two longitudes, one can get estimates of the meridional gradient of the meridional flow, and zonal gradient of the zonal flow. It was found that meridional velocities measured to the south were typically 50 m/s more southward than those measured to the north. Zonal velocities measured looking east were typically 50 m/s more eastward than those measured to the west. If one assumes that the velocity gradients are linear, and that the velocities are measured at the same altitude, then the above implies persistent (all night) positive divergence of the horizontal flow.

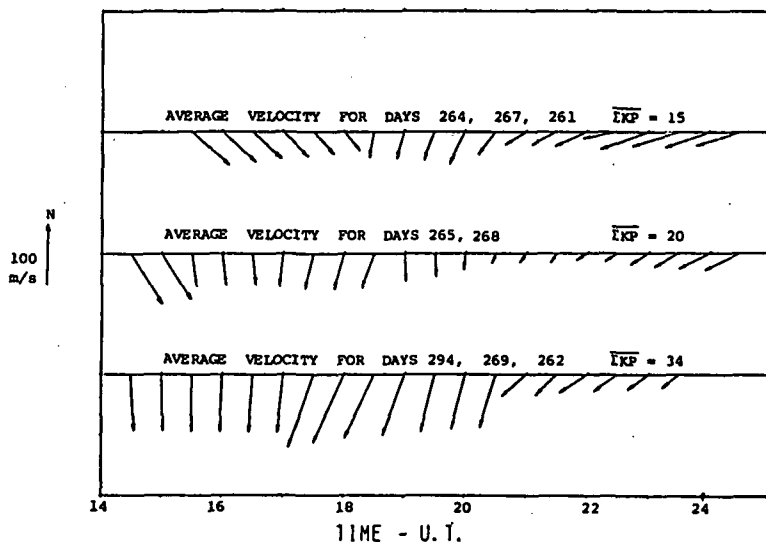


Figure 2.

CONCLUSIONS

Perhaps the most important feature of the results of this work is the very poor agreement with radar observations and model predictions. For example, MACLEOD and VINCENT (1984), using the Mawson PRD radar in the 1981/82 summer, obtained a value for the mean meridional flow at 95 km of less than 5 m/s, and a diurnal component of about 12 m/s. Their results are in good agreement with current models. The biggest uncertainty about the FPS data is the emission height.

It is hoped that the 1984 data from Mawson will provide an opportunity for side-by-side, hour-by-hour comparisons of the FPS and PRD results to help explain the differences.

REFERENCES

- Jacka, F. (1984), Application of Fabry-Perot spectrometers for measurement of upper atmosphere temperature and winds, Vol. 13, 19-40, SCOSTEP Secretariat, University of Illinois, Urbana-Champaign.
- MacLeod, R. I. (1984), Spaced antenna wind measurements in the Antarctic summer mesosphere, submitted to J. Atmos. Terr. Phys.
- Vallance-Jones, A. (1974), Aurora, D. Reidel Publ. Co.
- Wardill, P. and F. Jacka (1985), Vertical motions in the thermosphere over Mawson, Antarctica, in preparation.

5.9 BALLOON MEASUREMENTS OF AEROSOL IN THE ANTARCTIC STRATOSPHERE

Y. Morita and M. Takagi

Research Institute of Atmospheric
Nagoya University
Toyokawa, Aichi 442, Japan

Y. Iwasaka and A. Ono

Water Research Institute
Nagoya University, Furo-cho
Chikusa-ku, Nagoya 464, Japan

ABSTRACT

Three balloon soundings of aerosol were conducted from Syowa Station, Antarctica in April, June and October 1983. Number concentration and the size distribution of aerosol particles with diameter greater than $0.3 \mu\text{m}$ were measured by using a light scattering aerosol particle counter. The influence of the eruption of Mt. El Chichon on the aerosol concentration in the stratosphere was observed on October 16. Very high aerosol concentration at stratospheric heights was obtained from the first successful aerosol balloon sounding in winter Antarctic stratosphere. The result gives direct evidence of winter enhancement in the Antarctic stratosphere.

INTRODUCTION

The stratospheric aerosol states are remarkably perturbed by big volcanic eruptions, such as Mt. St. Helens in 1980, and Mt. El Chichon in 1982. The volcanic eruptions inject into the stratosphere a great amount of aerosols and gaseous substances. These increase strongly the number density of stratospheric aerosol layers (e.g., HOFMANN and ROSEN, 1982; 1984a), and the enhanced aerosol layer extends over the global stratosphere. The influence of volcanic eruptions is visible even in the Antarctic stratosphere. A few measurements of aerosols have been made in the Antarctic stratosphere (HOFMANN et al., 1973; 1977). Their measurements concern an austral summer and the behavior of aerosols, such as seasonal variations in the Antarctic stratosphere, has not yet been clarified. Recent optical measurements by satellites indicate the enhancement of the Antarctic stratospheric aerosol layer every austral winter (McCORMICK et al., 1982). Though possible formation mechanism of the enhanced aerosol layer has been examined (STEELE et al., 1983), the overall picture is far from complete. Our present knowledge of the aerosol in the Antarctic stratosphere is very meager. To understand the complex behavior of the Antarctic aerosols, measurements of number density and the size distribution of aerosol have to be made in the various seasons. For this purpose, three balloon soundings of aerosol were conducted from Syowa Station, Antarctica in 1983.

MEASUREMENTS

The balloon flights were conducted on April 1, June 3 and October 16, 1983. Number concentration and the size distribution of aerosol particles with diameter greater than $0.3 \mu\text{m}$ were measured by using a light scattering aerosol particle counter. The counter is made to be suitable for the balloon measurements in the Antarctic stratosphere. The counter has two pulse height discriminators to differentiate the size of the particles having the diameter $\geq 0.3 \mu\text{m}$ and $\geq 0.5 \mu\text{m}$, respectively, for the refractive index of 1.40. Thus a rough indication of the size distribution is obtained. The construction and

calibration of the counter are described in detail (MORITA and TAKAGI, 1983). The weight of the entire assembly of the equipment was about 12 kg. The time taken to complete one set of measurements of all parameters (temperatures of the air and pump, pressure, particle concentration having the diameter $\geq 0.3 \mu\text{m}$ and $\geq 0.5 \mu\text{m}$) was 75 seconds. In order to calibrate the rate of air flow and the light source intensity, the lobe pump rotation rate and the light intensity were checked at an interval of about 10 minutes during the flights. The aerosol particle counters were carried aloft by 3 kg rubber sounding balloons. The telemetering frequency used was 1680 MHz.

RESULTS AND DISCUSSION

Though three aerosol soundings were carried out, the present discussion concerns the last two flights (June 3 and October 16), because the result of the flight on April 1 is limited in the troposphere. Figure 1 shows the vertical profiles of aerosol concentration having the diameter greater than $0.3 \mu\text{m}$ and aerosol count ratio of two size ranges ($D \geq 0.3 \mu\text{m}$ and $\geq 0.5 \mu\text{m}$) obtained on October 16, 1983. The concentration profile shows that high aerosol concentration layers exist at altitudes between 4 and 8 km. Compared with the number density obtained from the measurements during a period of low volcanic activity (HOFMANN et al., 1977), the present measurement shows higher aerosol concentration in the stratosphere. The higher concentration could be attributed to the effect of the eruption of the Mexican volcano El Chichon in April 1982. These aerosols may have been transported to the south pole region following the eruption. The lidar observation at Syowa Station suggested that the effect of the volcanic eruption of Mt. El Chichon was visible in the Antarctic stratosphere by May 1983 (IWASAKA et al., 1985). Similar results showing the influence of the eruption of Mt. El Chichon on the aerosol concentration in the Antarctic stratosphere are observed at the U.S. Station on McMurdo, Antarctica in October 1983 (HOFMANN and ROSEN, 1984b). The profile of aerosol count ratio shows that the size distribution with small particles dominates in the high aerosol concentration region in the troposphere. The size ratio of the stratospheric aerosol layer is similar to that of the background level observed at midlatitudes in the Northern Hemisphere (HOFMANN and ROSEN, 1981).

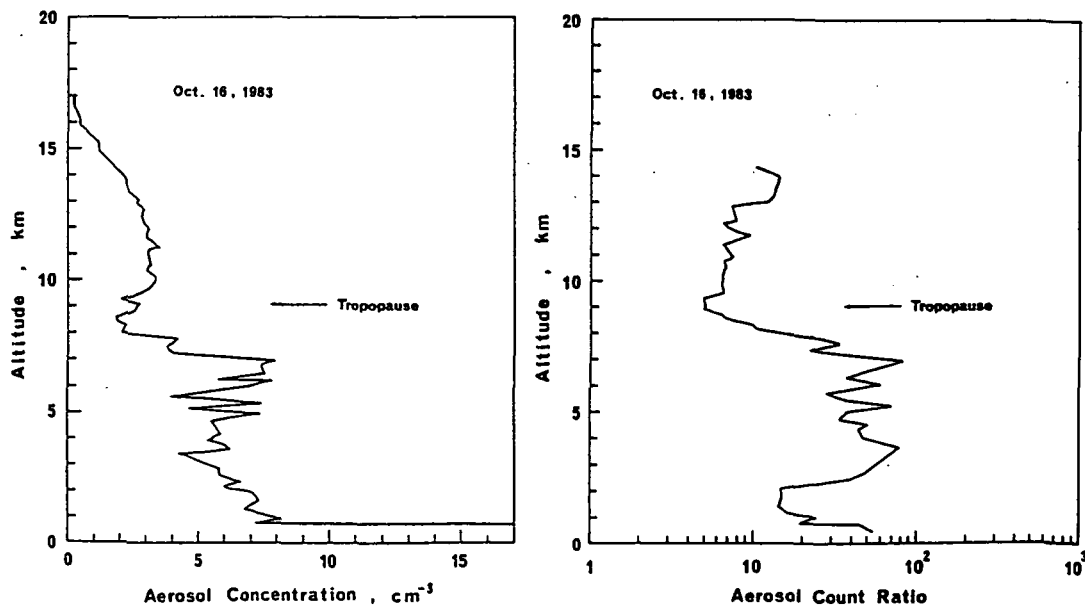


Figure 1. Vertical profiles of aerosol concentration ($D \geq 0.3 \mu\text{m}$) and aerosol count ratio of two size ranges ($D \geq 0.3 \mu\text{m}$ and $\geq 0.5 \mu\text{m}$) on October 16, 1983.

Figure 2 shows the vertical profiles of the aerosol concentration and the aerosol count ratio of the two size ranges obtained on June 3, 1983. This is the first successful aerosol balloon sounding in the winter Antarctic stratosphere. Very high aerosol concentration was obtained during both the ascent and descent measurements in the stratosphere. Though the effect of Mt. El Chichon eruption in Mexico may be partly responsible for the enhanced aerosol, this result gives a direct evidence of "winter increase of the aerosol concentration in the Antarctic stratosphere". The profiles of aerosol count ratio indicate that the high aerosol concentration at stratospheric heights differs from that at altitudes around the tropopause. The large aerosol count ratio suggests the presence of small particles around the tropopause. The particle size in the enhanced aerosol concentration region is similar to that normally appearing in the midlatitude stratosphere. SAM II satellite system shows a pronounced increase in extinction on occasions when the temperature falls to a low value. The present enhancement is also observed during the cold stratospheric temperatures.

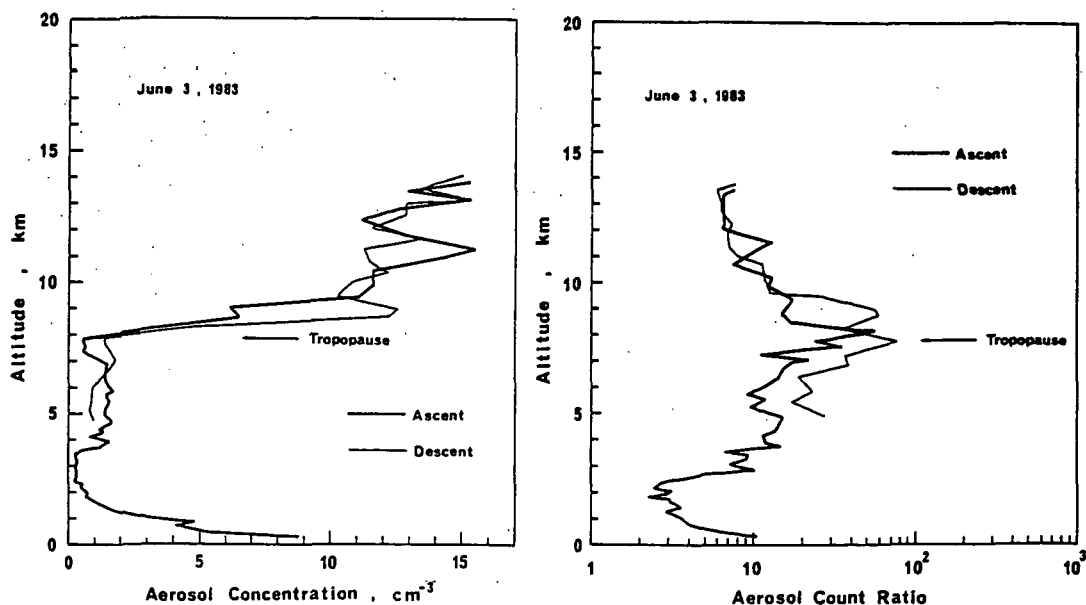


Figure 2. Vertical profiles of aerosol concentration ($D \geq 0.3 \mu\text{m}$) and aerosol count ratio of two size ranges ($D \geq 0.3 \mu\text{m}$ and $\geq 0.5 \mu\text{m}$) on June 3, 1983.

It may be mentioned here that all the aerosol profiles in the present measurements have a good correlation to the results from the simultaneous lidar measurements made by IWASAKA et al. (1985).

Though the present measurements provide the direct evidence of a pronounced increase in the stratospheric aerosol concentration in austral winter, our present knowledge in this regard is limited. Further and more detailed aerosol measurements in the Antarctic stratosphere are warranted.

ACKNOWLEDGEMENTS

We thank the members of JARE-24th who made an enormous effort to launch the balloons. We also thank Dr. T. Ito of the Meteorological Research Institute for his valuable discussion. This work was financially supported by the Scientific Research Grant of the Antarctic MAP of Ministry of Education.

REFERENCES

- Hofmann, D. J., J. M. Rosen, T. J. Pepin and R. G. Pinnick (1973), Particles in the polar stratosphere, Nature, **245**, 369-371.
- Hofmann, D. J., J. M. Rosen, G. L. Olson, N. T. Kjome, A. L. Schmeltekopf and P. D. Goldman (1977), Measurements of trace gases and aerosols in the antarctic stratosphere, Antarctic Journal of the U.S., October issue.
- Hofmann, D. J. and J. M. Rosen (1981), On the background stratospheric aerosol layer, J. Atmos. Sci., **38**.
- Hofmann, D. J. and J. M. Rosen (1982), Balloon-borne observations of stratospheric aerosol and condensation nuclei during the years following the Mt. St. Helens eruption, J. Geophys. Res., **87**, 11039-11061.
- Hofmann, D. J. and J. M. Rosen (1984a), On the temporal variation of stratospheric aerosol size and mass during the first 18 months following the 1982 eruptions of El Chichon, J. Geophys. Res., **89**, 4883-4890.
- Hofmann, D. J. and J. M. Rosen (1984b), Antarctic observations of stratospheric aerosol and high altitude condensation nuclei following the El Chichon eruption, Geophys. Res. Lett., (in press).
- Iwasaka, Y., T. Hirasawa, H. Fukunishi, M. Fujiwara, R. Fujii and H. Miyaoka (1985), Laser radar observation of the polar stratospheric aerosol layer, Proc. Int. MAP Symp..
- McCormick, M. P., H. M. Steele, P. Hamill, W. P. Chu and T. J. Swissler, Polar stratospheric cloud sightings by SAM II, J. Atmos. Sci., **39**, 1387-1397.
- Morita, Y. and M. Takagi (1983), Balloon measurements of stratospheric aerosol by light scattering aerosol particle counters, Bull. Inst. Space Astro. Sci., **8**, 87-99 (in Japanese).
- Steel, H. M., P. Hamill, M. P. McCormick and T. J. Swissler (1983), The formation of polar stratospheric clouds, J. Atmos. Sci., **40**, 2055-2067.

5.10 BALLOON-BORNE OBSERVATION OF AITKEN NUCLEI IN THE ANTARCTIC STRATOSPHERE AND TROPOSPHERE

Tomoyuki Ito, Miwako Ikegami, Izuo Kanazawa

Meteorological Research Institute
Yatabe, Tsukuba Ibaraki 305, Japan

Yasunobu Iwasaka

Water Research Institute, Nagoya University
Chikusa, Nagoya 464, Japan

INTRODUCTION

Aitken nuclei ($0.002 \leq r \leq 0.1 \mu\text{m}$) in the atmosphere are produced through gas-to-particle conversion processes, and they grow in size by heterogeneous nucleation processes and others to produce larger aerosol particles. In the study of global background aerosol pollution, full knowledge on such aerosol processes in the clean atmosphere is essentially required. In this sense, it is important to examine the behavior of aerosols in a "clean" atmosphere which is not contaminated directly by aerosols and gases emitted from the earth's surface. The Antarctic atmosphere is thought to be such a clean atmosphere. From an extensive surface observation of aerosols carried out at Syowa Station ($69^{\circ}00'S$, $39^{\circ}35'E$) Antarctica, it has been revealed that various phenomena relating to long-range transport of trace constituents and/or photochemical processes resulting in production or growth of aerosol particles are clearly observed in Antarctica (ITO and IWAI, 1981; IWAI et al., 1981; ONO et al., 1981; KOIDE et al., 1981; ITO et al., 1982; ITO, 1983; ITO, 1985). Furthermore, the importance of polar stratosphere in aerosol study has been recognized through recent works by HOFMANN and ROSEN (1983) and MCCORMICK (1985). However, the observation of aerosols over Antarctica using an airplane or a balloon was quite scarce (HOFMANN et al., 1973; 1976; 1977; HOGAN, 1979).

As a part of the Middle Atmosphere Program in Japan, the through-year observation of gases and aerosols over Antarctica was started in 1983, at Syowa Station, using lidar, FTIR, instrumented airplane, and aerosol sonde. This paper gives a preliminary report of observations made by balloon-borne Aitken nuclei sonde in 1983, at Syowa Station.

INSTRUMENT

For the balloon-borne observation of stratospheric Aitken nuclei, various types of sonde have been used. JUNGE et al. (1961) developed the sonde having an expansion fog chamber with photographic recording. The working fluid is water and the expansion ratio is about 1.25, so supersaturation of more than 300% is attained. A similar sonde was used by KASELAU et al. (1974). In these sonde, data were obtained after recovering the sonde. LANGER (1969) and ROSEN (1974) developed the sonde with the telemetering system which does not require recovering the sonde and tedious data processing as the photographic recording type does. The Langer's sonde comprises a mixing cloud chamber and an acoustic particle detector. The working fluid is water and the supersaturation is about 1%. The Rosen's sonde comprises a thermal gradient diffusional growth chamber and an optical particle detector. The working fluid is glycol. The supersaturation was about 10% in early works, but recently increased up to 100-200% (ROSEN and HOFMANN, 1981).

Another type of Aitken nuclei sonde was reported by ITO et al. (1983). The sonde comprises an expansion fog chamber with a photoelectric detection and

a telemetering system. The working fluid is water and the expansion ratio is 1.20, which produces supersaturation of about 230%. The sonde is much smaller in weight as compared with Rosen's, which seems to be a great advantage in operation under severe conditions such as in Antarctica.

The concentration of nuclei is measured in terms of the maximum intensity of the light scattered laterally from a light pencil traversing fog, which is produced by adiabatic expansion in the chamber. In such a method, the calibration of nuclei counting is valid only for the measurement made under the constant expansion ratio and the constant temperature of air sample just before the expansion.

To fix the expansion ratio irrespective of ambient pressure is an essential requirement for the measurement of Aitken nuclei concentration at different heights by balloon or airplane. In the present sonde, an air sample is expanded by changing the volume of a fog chamber itself. Volume change is performed by moving a flexible ceiling of the chamber which is made of rubber film. Thus, the expansion ratio is kept at constant value determined by a ratio of a chamber volume after expansion to that before expansion. Expansion with sufficient speed is also required to attain the super-saturation theoretically expected from the given expansion ratio. The present expansion method has an advantage in attaining sufficient expansion speed as compared with the method used by JUNGE et al. (1961) where the expansion is achieved by sliding a cylindrical piston.

The temperatures of the fog chamber are conditioned by the waste heat from the water activated battery which is used as a power source for the electronic circuit of the sonde. After a 30 sec flashing of the chamber with a fresh air sample, the sample is delayed expanding for the pre-conditioning in humidity (100%) and temperature (about 20°C). Since the working fluid, water, boils at 20°C in atmospheric pressure lower than 25 mb, the present sonde is applicable for altitudes lower than about 25 km.

The signal of measured concentration is inserted into a rawinsonde signal and transmitted to a ground station every minute for 10 sec. The total weight of a sonde is 8 kg, comprising a 4 kg fog chamber, a 3.5 kg battery and a 0.5 kg rawinsonde.

OBSERVATION

The sonde was flown with two 3 kg rubber balloons at 16:00 LST on October 17, 1983. During the sounding, no cloud appeared over the Syowa Station. The sounding was made for about 70 min until the battery of the sonde died. Since the resultant ascending velocity of the balloon was about 200 m/min, although 300 m/min was preferred, the concentration was obtained every 200 m or so from the surface to about 15 km.

RESULT AND DISCUSSION

Figure 1 shows the vertical profile of the mixing ratio of Aitken nuclei obtained by the sounding in 1983. The vertical profile of air temperature measured by the same sonde is also shown in Figure 1. According to the temperature profile, the tropopause heights are placed at 200 mb (about 10 km).

In the figure, it can be seen that the vertical variation of concentration is quite systematic and random fluctuations of individual measurements are rather infrequent. This fact seems to indicate that the whole system of the sonde, including the automatic Aitken counter, worked properly.

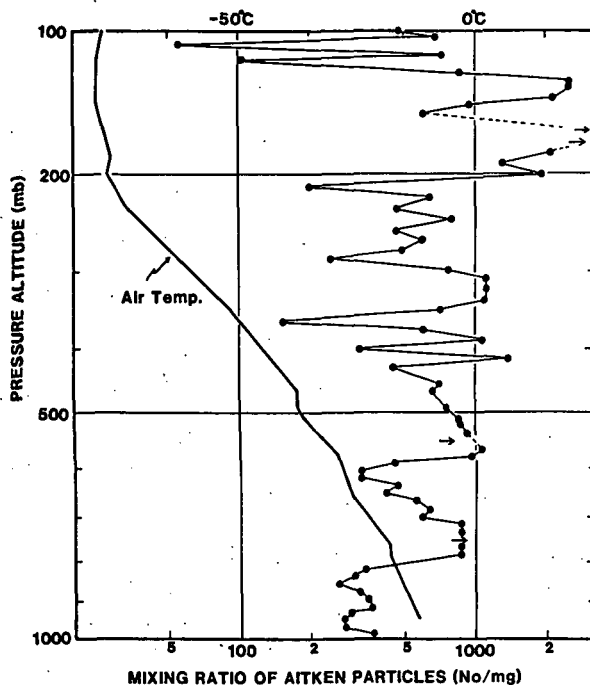


Figure 1.

Main results can be summarized as follows: The mixing ratio of Aitken nuclei higher than 1000/mg is seen around 750 mb, 600 mb, 300 mb and above 200 mb, whereas the surface value is a few hundred/mg. The maximum mixing ratio is seen in the stratosphere just above the tropopause.

In Figure 2, the previous results obtained at McMurdo in January 1976, and at the South Pole in January 1977, by HOFMANN et al. (1976, 1977) are reproduced as well as the present result.

It can be seen that the results at McMurdo, South Pole, and Syowa give quite a similar vertical profile of nuclei concentration in the troposphere. The tropospheric average concentration in the present result is comparable with those in the previous results. The high concentration layers in the troposphere are also seen in the previous results. The high concentration layer over Antarctica has been found also in the aircraft observation by HOGAN (1979). The high concentration aloft has been predicted also by ITO and IWAI (1980) during the course of examination of the event of sudden increase of Aitken nuclei in the surface air in Antarctica. Thus, the tropospheric high concentration layer seen in the present result seems to give a representative figure in the Antarctic troposphere.

The most important finding in the present results is that the high concentration layer with nearly 1000/cc is seen in the lower stratosphere. This finding gives quite a different figure as compared with the previous results. It has been reported by many researchers that the world stratosphere has been contaminated since 1979, by the large volcanic eruptions. The stratospheric high concentration in the present results may also be attributed by contamination due to volcanic eruptions which increased since 1979. It is worthy to

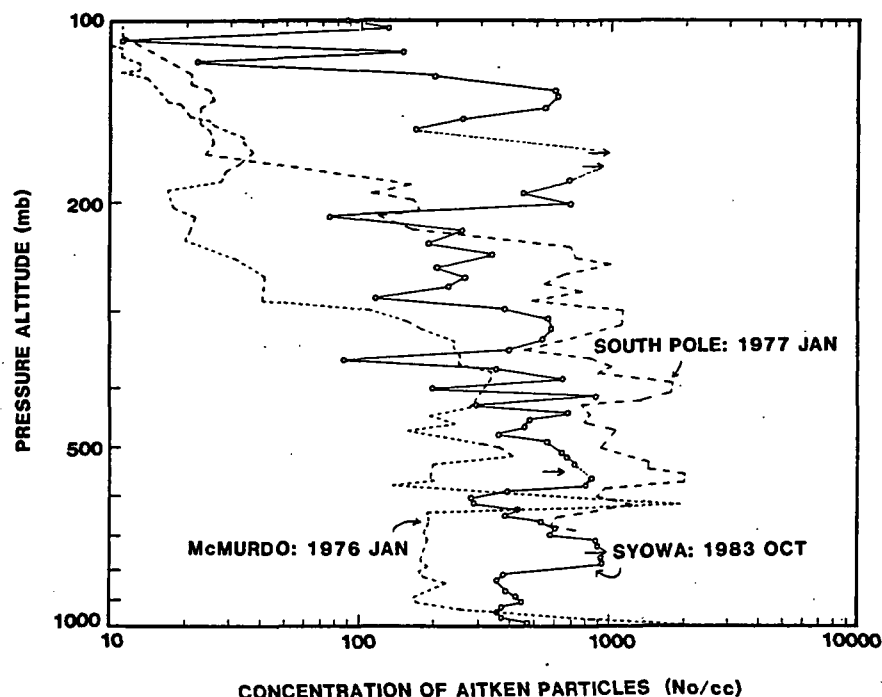


Figure 2.

note that the present findings of the stratospheric high concentration give evidence of a formation of Aitken nuclei in the stratosphere. The quite sophisticated numerical model of stratospheric aerosols has been developed by TURCO et al. (1979). The model, however, cannot predict the production of Aitken nuclei in the stratosphere. In order to assess the volcanic effect on stratospheric aerosols, the numerical model including the process of the Aitken nuclei formation in the stratosphere is required.

REFERENCES

- Hofmann, D. J., J. M. Rosen, T. J. Pepin and R. G. Pinnick (1973), Nature, **245**, 369-371.
- Hofmann, D. J., J. M. Rosen, N. T. Kjome, G. L. Olson and A. L. Schmeltekopf (1976), Antarct. J. U. S., **11**, 99-101.
- Hofmann, D. J., J. M. Rosen, G. L. Olson, N. T. Kjome, A. L. Schmeltekopf and P. D. Goldan (1977), Antarct. J. U. S., **12**, 162.
- Hogan, A. W. (1979), J. Appl. Meteorol., **18**, 741-749.
- Ito, T. (1983), Pap. Meteorol. Geophys., **34**, 151-219.
- Ito, T. (1985), J. Atmos. Chem., **3**, 69-91.
- Ito, T. and K. Iwai (1981), J. Meteorol. Soc. Japan, **59**, 262-271.
- Ito, T., A. Ono and K. Iwai (1982), Mem. Nat'l. Inst. Polar Res., special issue, **24**, 289-296.
- Ito, T., M. Ikegami and I. Kanazawa (1983), Mem. Nat'l. Inst. Polar Res., special issue, **29**, 185-190.
- Iwai, K., A. Ono and T. Ito (1981), Mem. Nat'l. Inst. Polar Res., special issue, **19**, 131-140.
- Junge, C. E., C. W. Chagnon and J. E. Manson (1961), J. Meteorol., **18**, 81-108.

- Kasela, K. H., P. Fabian and H. Rohrs (1974), Pageoph, 112, 877-885.
- Koide, T., T. Ito, N. Yano and T. Kobayashi (1981), Mem. Nat'l. Inst. Polar Res., special issue, 19, 152-159.
- Langer, G. (1972), Powder Technol., 6, 5-8.
- McCormick, M. P. (1985), Advances in Space Res., to be published.
- Ono, A., T. Ito and K. Iwai (1981), Mem. Nat'l. Inst. Polar Res., special issue, 19, 141-151.
- Rosen, J. M. (1974), contact N0001-70-A-0266-0011, Univ. of Wy., Laramie.
- Rosen, J. M. and D. J. Hofmann (1981), Rep. AP-68, Dept. of Phys. and Astron., Univ. of Wy., Laramie.
- Rosen, J. M. and D. J. Hofmann (1983), J. Geophys. Res., 88, 3725-3731.
- Turco, R. P., P. Hamil, O. B. Toon, R. C. Whitten and C. S. Kiang (1979), NASA Tech. Rep., 1362.

5.11 GAS-CHROMATOGRAPHIC MEASUREMENTS OF ATMOSPHERIC CF₂Cl₂, CFC1₃ AND N₂O IN ANTARCTICA

M. Hirota, Y. Makino, S. Chubachi, and H. Muramatsu

Meteorological Research Institute
1-1, Nagamine, Yatabe-machi
Tsukuba-gun, Ibaraki 305, Japan

M. Shiobara

Upper Atmosphere Research Laboratory
Faculty of Science, Tohoku University
Sendai 980, Japan

Stratospheric ozone is produced photochemically and destroyed by reactions with such minor constituents as O, NO_x, HO_x, and ClO_x. Chlorofluoromethanes (CF₂Cl₂ and CFC1₃) and dinitrogen oxide (N₂O) are considered as major sources of the stratospheric ClO_x and NO_x, respectively. It is well known that CF₂Cl₂ and CFC1₃ are released only by man's activities, and are being accumulated in the troposphere (WMO, 1981; NRC, 1982).

In order to assess the influence of these compounds on the natural ozone balance, we have measured these gases over Japan since 1978 (HIROTA et al., 1984). Measurements of Antarctic air samples are also indispensable to understanding the global distributions of these gases, because most CF₂Cl₂ and CFC1₃ have been released in the Northern Hemisphere.

Antarctic air samples were obtained by the 23rd, 24th and 25th Japanese Antarctic Research Expeditions, and analyzed by a gas-chromatographic method using an electron capture detector. Three experimental results were obtained: 1) latitudinal distribution of these gases from Tokyo to Syowa Station (69.0°S, 39.6°E), 2) time trends at Syowa Station, and 3) vertical distributions over Syowa Station. In this abstract, results of 2) will be reported.

EXPERIMENTAL

Details of our air sampling and gas-chromatographic measurements are described elsewhere (HIROTA et al., 1985). Only some changes in sampling of air and reference gas will be given here.

From February 1983 to January 1984, air samples at Syowa Station were collected 4 m above the ground surface at the northeast side of a hut of the Upper Atmosphere Physics Laboratory.

The preparation method of a reference gas for N₂O was changed. A mixed gas of 970 ppm(=10⁻⁶ v/v) N₂O in air (Takachiho) was used as a primary reference gas for N₂O. In order to make a reference gas for practical use, this gas was diluted to 0.3 ppm with ultra pure nitrogen gas (99.9995 %) using a Standard Gas Generator SGGU-72AC3 (Standard Technology). Uncertainties in the measurements are summarized in Table 1. Measurement results are all shown by volume mixing ratios, where ppb=10⁻⁹ and ppt=10⁻¹².

RESULTS AND DISCUSSION

Time trends of CF₂Cl₂, CFC1₃ and N₂O at Syowa Station are shown in Figure 1. Air samples were collected more frequently in the latter half of 1983. The value of CF₂Cl₂ in August 1982 was too high. Except for this,

Table 1.

Uncertainties in the gas-chromatographic measurements.

species	CF ₂ Cl ₂	CFC1 ₃	N ₂ O
Detection limit	15 ppt	4 ppt	10 ppb
mixing ratio in ref. gas	434 ppt	414 ppt	303 ppb
error in repeated measurements of a ref. gas	1.9%	0.6%	2.1%
error in measurements of several ref. gases	2.3%	3.2%	2.9%
error in repeated measurements for samples	+1.0%	+0.9%	+2.0%

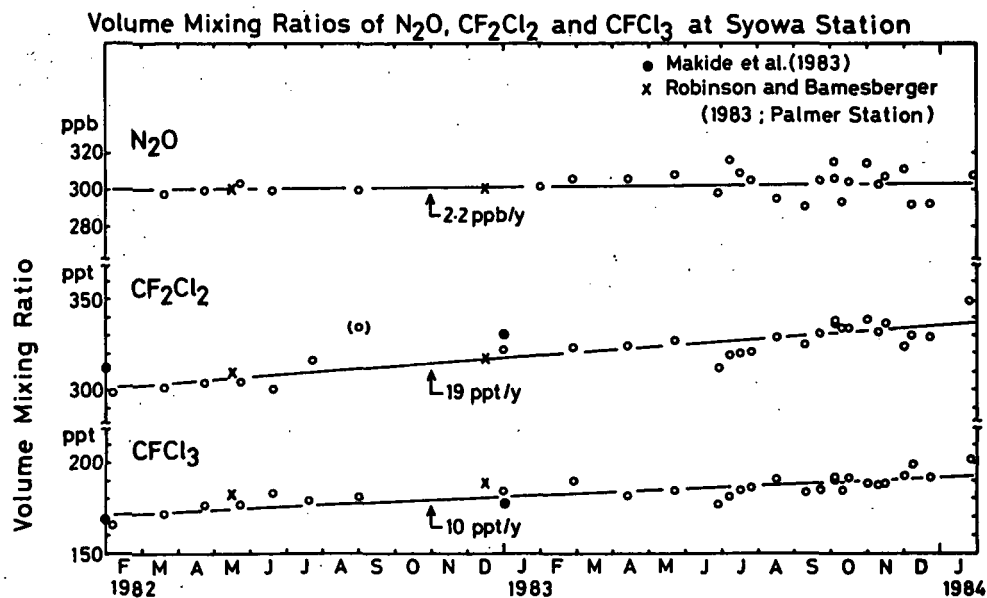


Figure 1. Atmospheric volume mixing ratios of CF₂Cl₂, CFC1₃ and N₂O at Syowa Station from February 1982 to January 1984. —; linear trend calculated by the method of least squares.

CF_2Cl_2 and CFCl_3 showed steady increase, and a change in the air sampling method in February 1983 (HIROTA et al., 1985) would have no effect on the results.

Solid lines in Figure 1 show linear trends of these compounds calculated by the method of least squares. From February 1982, to January 1984, annual increases of 19.2 ppt/year for CF_2Cl_2 and 10.2 ppt/year for CFCl_3 (6.1 and 5.6 %/year at January 1983, respectively) were obtained. Correlation coefficients were 0.87 for CF_2Cl_2 and 0.82 for CFCl_3 . Clear seasonal variations, however, were not observed. Correlation coefficient between CF_2Cl_2 and CFCl_3 was 0.83.

Annual increase of N_2O was 2.2 ppb/year in the same period (0.7 %/year at January 1983). In other words, N_2O was almost constant in this period within the range of experimental uncertainty.

In Figure 1, solid circles indicate the results of MAKIDE et al. (1983, 1985) and cross marks indicate those at Palmer Station (65.5°S, 64.1°W) (ROBINSON and BAMESBERGER, 1983) which are weekly average values. In the measurements of MAKIDE et al., annual increases for CF_2Cl_2 and CFCl_3 during 1982, were 21.1 and 8.1 ppt/year, respectively, which were in good agreement with ours. Similar trends (~15 ppt/year for CF_2Cl_2 and ~8 ppt/year for CFCl_3) were observed in the Northern Hemisphere in recent years (MAKIDE et al., 1985). Although observations at Palmer Station did not cover a whole year, annual increase for CFCl_3 (12.8 ppt/year) was also in agreement with ours. That for CF_2Cl_2 (13.2 ppt/year), however, was a little lower than ours. Values of N_2O at Palmer Station were in good agreement with ours.

In Table 2, values of January 1, 1983, at Syowa Station are compared with mean values observed over Japan (38-34°N) from October 1982, to February 1983, (HIROTA et al., 1984). With an improvement in the calibration method, the mean value of N_2O was revised.

Mean values of CF_2Cl_2 and CFCl_3 at Syowa Station were lower than those observed over Japan by 6%. This is because most CF_2Cl_2 and CFCl_3 have been released in the Northern Hemisphere. On the other hand, there was no difference in values of N_2O . This would be due to the more uniform distribution of the sources of N_2O than those of CF_2Cl_2 and CFCl_3 .

Table 2.

Mean volume mixing ratios of CF_2Cl_2 , CFCl_3 and N_2O .

species	CF_2Cl_2 (ppt)	CFCl_3 (ppt)	N_2O (ppb)
Over Japan (Oct. 1982-Feb. 1983)	335(7)*	194(7)*	301(7)*
At Syowa Station (Jan. 1, 1983)	316	182	302

* = Standard deviations are shown in ().

REFERENCES

- Hirota, M., H. Muramatsu, Y. Makino, T. Sasaki, and Y. Toyama (1984), The vertical distributions of atmospheric CF_2Cl_2 , CFCI_3 and N_2O over Japan, J. Meteorol. Soc. Japan, **62**, 158-164.
- Hirota, M., S. Chubachi, Y. Makino and H. Muramatsu (1985), Gas-chromatographic measurements of atmospheric CF_2Cl_2 , CFCI_3 and N_2O in Antarctica, Mem. Nat'l. Inst. Polar Res. special issue, **34**, 20-27.
- Makide, Y., A. Yokohata and K. Tominaga (1983), Atmospheric concentrations of halocarbons in Antarctica (abstract), Mem. Nat'l. Inst. Polar Res., special issue, **29**, 225.
- Makide, Y., A. Yokohata and K. Tominaga (1985), Atmospheric concentrations and behavior of halocarbons and methane, this volume.
- NRC (1982), Causes and effects of stratospheric ozone reduction: An update, National Academy Press, Washington, D.C.
- Robinson, E. and W. L. Barnesberger (1983), Air chemistry monitoring at Palmer Station, Antarctic J. U. S., **18**, 253-254.
- WMO (1981), The stratosphere 1981, theory and measurements, WMO Global Ozone Research and Monitoring Project Report, No. 11.

5.12 50-MHz METEOR RADAR OBSERVATION AT
SYOWA STATION, ANTARCTICA

T. Tanaka, T. Ogawa and K. Igarashi

Radio Research Laboratories
Koganei, Tokyo 184, Japan

R. Fujii

National Institute of Polar Research
1-9-10 Kaga, Itabashi
Tokyo 173, Japan

The 50-MHz Doppler radar installed at Syowa Station (69°00'S, 39°35'E), Antarctica, in 1982 can detect continuously a meteor echo if an operator assigns the meteor mode operation to the radar. The radar has two narrow antenna beams (4° in the horizontal plane), one toward geomagnetic south and the other toward approximately geographic south, with a crossing angle of about 33°. This enables us to determine a two-dimensional neutral wind pattern. The minicomputer annexed to the radar controls the transmission and reception of a 50-MHz wave. If the receiver detects a meteor echo, the "flag" signal is sent to the computer. Then the computer begins to determine the echo range with a time resolution of 1 μ s and to sample every 200 μ s for 1 s the Doppler signal and echo intensity at the particular range (R). The line-of-sight velocity (V_d) of the echo trail is calculated from the output from the Doppler signal detection circuit having an offset frequency by using the so-called zero-crossing method. The echo amplitude decay time calculated by a least-mean square method is used to obtain the ambipolar diffusion coefficient (D) and then to calculate the echo height (H). The digitized Doppler signals and echo intensities at 500 sampling points are stored on magnetic tapes together with V_d , D, H and R for later analysis in Japan. The computer cannot discriminate between meteor and radio aurora echoes, so that it is necessary for the neutral wind analysis to select only meteor echo not contaminated by radio aurora echo.

About 120 day observations were made during 1982-1983. Some early results are as follows:

- 1) The occurrence probability of meteor echoes is highest around 06h LT and lowest around 21h LT, being almost consistent with results at other latitudes.
- 2) The echo altitudes range from 70 to 110 km. Most of the echoes come from the 80-100 km altitudes, and the number of occurrences has a Gaussian-type distribution with the maximum occurrence around 90 km.
- 3) The echo slant ranges are between 110 and 600 km.
- 4) Results for diurnal variation of zonal and meridional winds at the altitude range 85-95 km are shown in Figures 1 and 2 for summer and winter cases, respectively. In both seasons, variations of meridional (N-S) winds include both diurnal and semidiurnal components, showing the influence of atmospheric tides at these altitudes. Zonal winds seem to direct westward in the evening and eastward in the morning, suggesting the effects of plasma convections at higher altitudes.
- 5) Altitude profiles of summer and winter mean winds are shown in Figure 3. In summer, the north-south components direct equatorward in the 87-95 km altitude, with their magnitudes between 10 and 20 m/s. However, poleward winds appear below the altitude 89 km in winter. These observations are almost consistent with those at northern high latitudes.

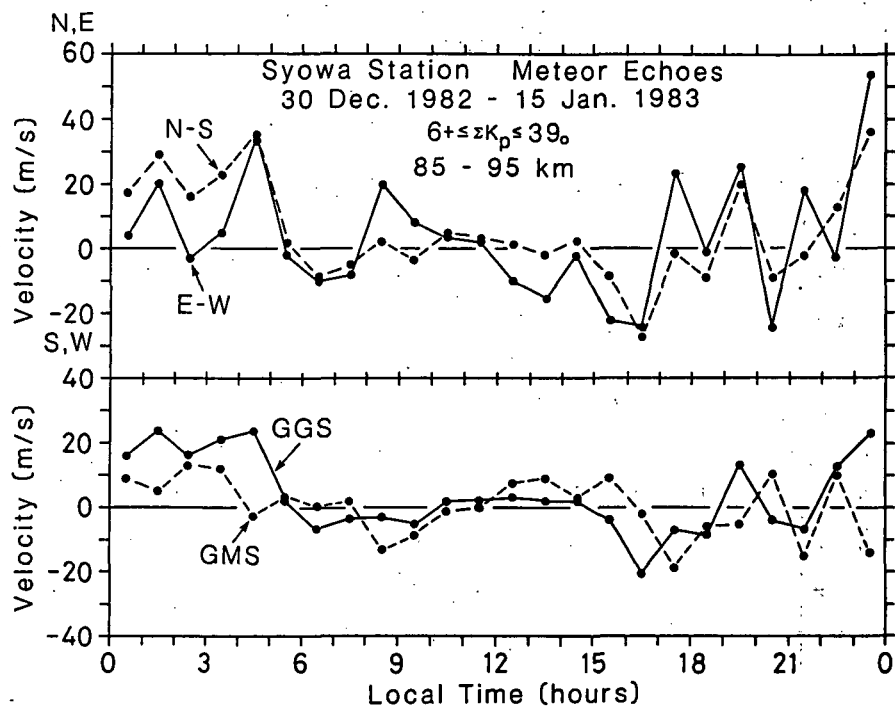


Figure 1.

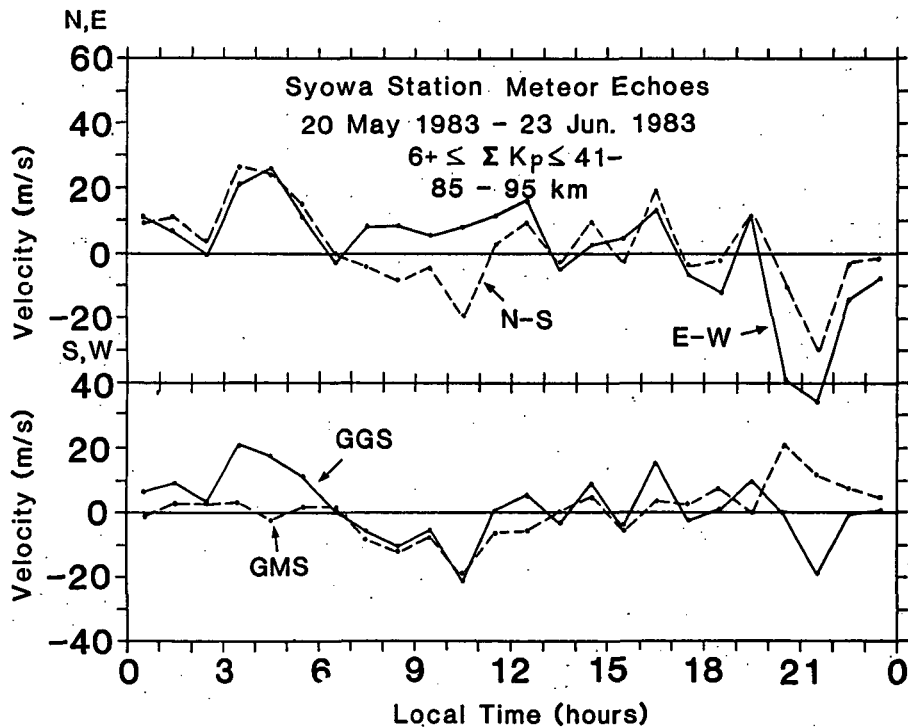


Figure 2.

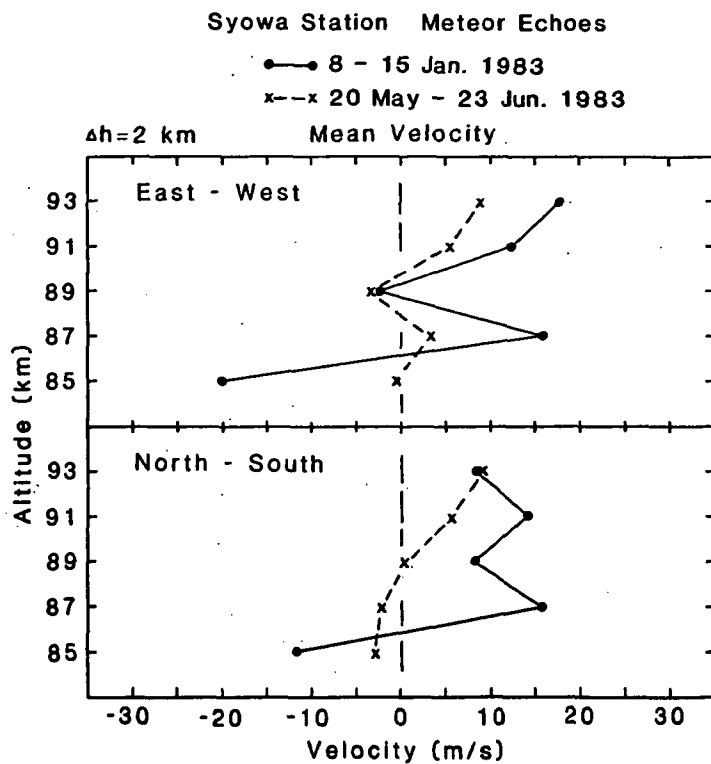


Figure 3.

5.13 RESEARCH ACTIVITIES ON "ANTARCTIC MIDDLE ATMOSPHERE"

by JARE 25th Team

T. Hirasawa, H. Fukunishi, M. Ayukawa, M. Ejiri, R. Fujii

National Institute of Polar Research
Itabashi, Tokyo 173, Japan

Y. Iwasaka

Water Research Institute, Nagoya University
Chikusa-ku, Nagoya 464, Japan

M. Tanaka

Geophysical Institute
Tohoku University, Sendai 980, Japan

The Antarctic Middle Atmosphere (AMA)-Japan research project was set about by the JARE (Japan Antarctic Research Expedition) 23rd team in 1982, and since then the JARE-24th and JARE-25th teams have been continuing research on the Antarctic Middle Atmosphere.

Here we should like to show some results gained by JARE-25th team members who are now working at Syowa Station (69.99°S, 39.35°E), Antarctica. In their activities satellite measurements (Exos-C) and rocket soundings are used.

Three rockets of the S310 type were launched at Syowa Station (Geomagnetic Latitude = 69.9°S) for the purpose of directly observing the electron density, ionospheric temperature, auroral patterns and luminosity in situ. In Figures 1 and 2, samples of rocket measurements are shown. A CCD TV camera mounted on rocket S-310JA-8 caught beautiful auroral images during the breakup phase of the substorm. The JARE-25th team made timely rocket observations during the pre-breakup and post-breakup phases of the substorm, in addition to measurements shown in Figures 1 and 2. Vertical profiles of electron density and auroral emission 4278A measured by three rockets are compared in Figures 3 and 4, respectively.

To gather information on the distribution of minor constituents and their temporal change in the Antarctic middle atmosphere, satellite trackings have been made since February 1984, at Syowa Station. These observations should contribute to the study of global transportation of minor gases and aerosol particles. In Figure 5, a block diagram of the Exos-C satellite tracking system used at Syowa Station is shown. Laser radar measurements and IR spectroscopic measurements, which have been continued, coordinated with satellite measurements, and thus these measurements should give us high quality information for a comprehensive understanding about the polar middle atmosphere.

In Figure 6, a measurement system of the solar aureole and direct radiation is shown. This is used to monitor the density and size distribution of particulate matter in the polar atmosphere (Detailed description is given by SHIOBARA et al.). This measurement also coordinates with a laser radar measurement.

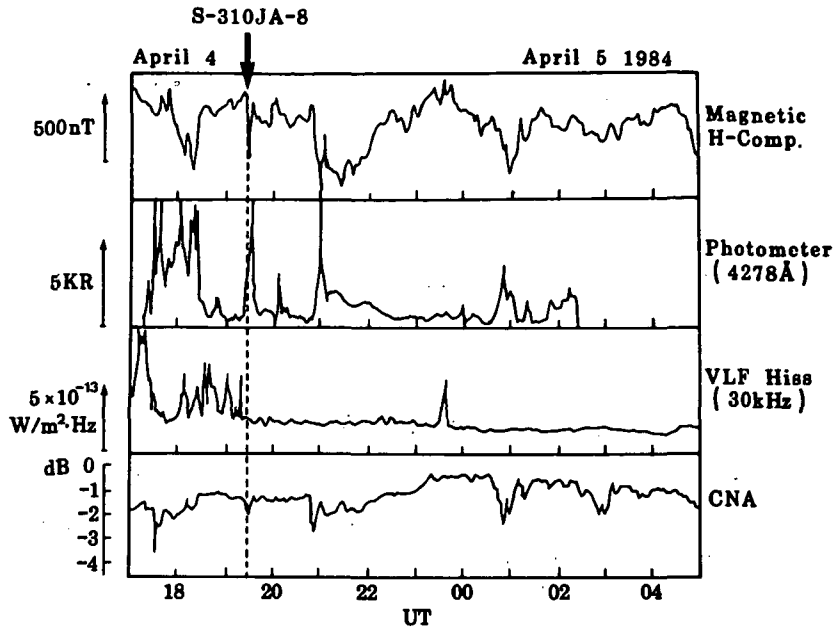


Figure 1.

Auroral Image Observed by CCD TV Camera

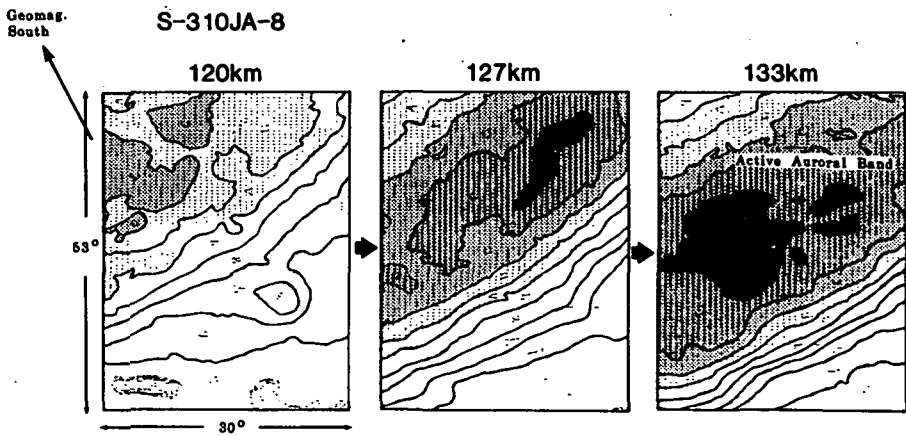


Figure 2.

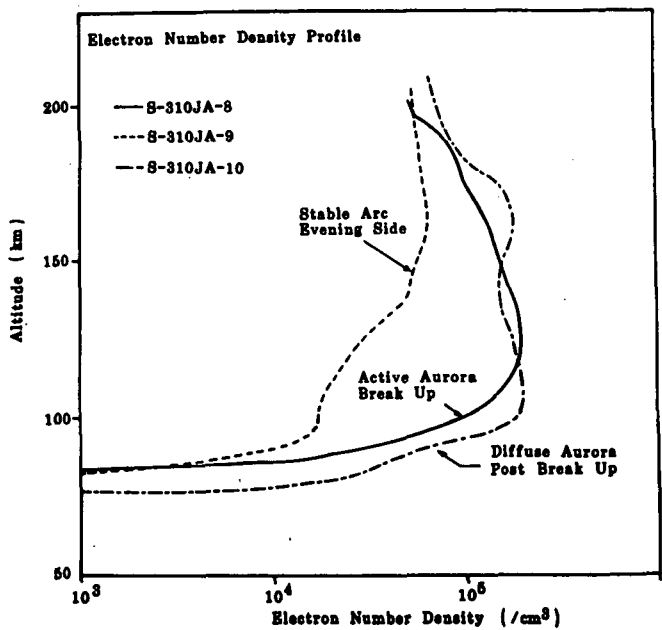


Figure 3.

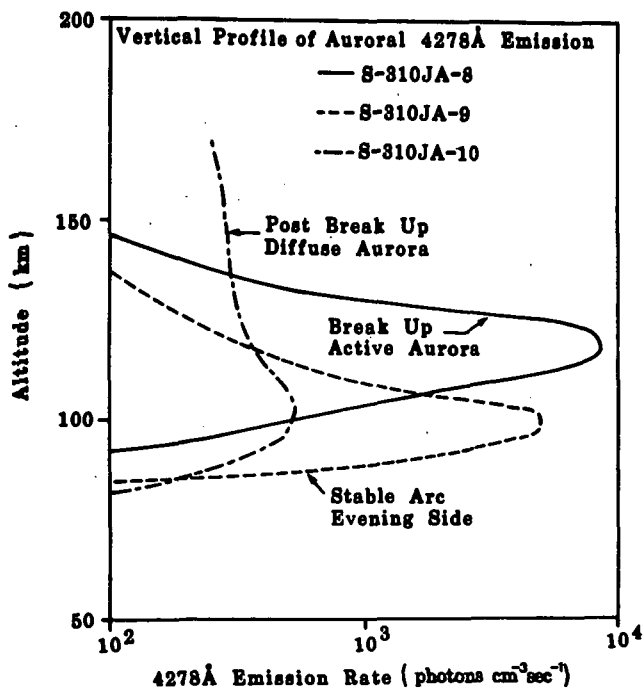


Figure 4.

Diagram of EXOS-C Satellite Tracking System

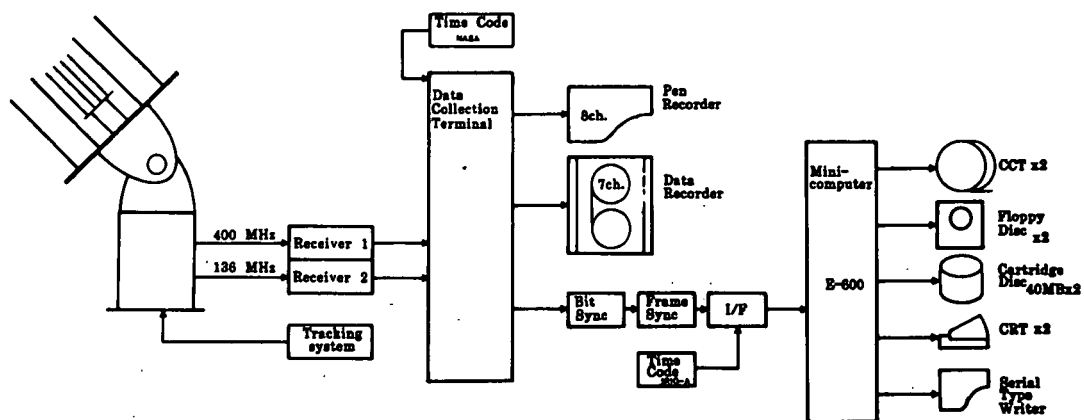


Figure 5.

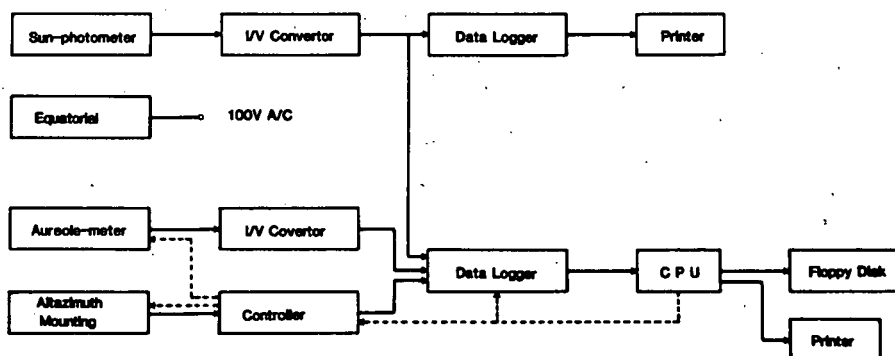
Measurement system of solar aureole and
direct radiation in Antarctica

Figure 6.

5.14 OBSERVATION OF TOTAL OZONE FIELDS IN THE ANTARCTIC ATMOSPHERE FROM TOVS OF TIROS-N/NOAA

T. Yamanouchi and Sadao Kawaguchi

National Institute of Polar Research
1-9-10, Kaga, Itabashi-ku
Tokyo 173, Japan

I. Iwashina and K. Suzuki

University of Electro-Communications
1-5-1, Chofugaoka, Chofu-shi
Tokyo 182, Japan

Total ozone amounts in the Antarctic atmosphere are derived from infrared nadir scanning data of TIROS Operational Vertical Sounder (TOVS) of NOAA-6 and 7. HRPT data of the TIROS-N/NOAA series of meteorological satellites have been received at Syowa Station (69°00'S, 39°35'E), Antarctica, about once a day since February 1980, by the Japanese Antarctic Research Expedition. HIRS/2 data of TOVS were extracted from HRPT data after being converted into CCT at the home institute. Total ozone amounts were derived for the northeastern part of the Antarctic, for about 100 orbits in 1981 and 1982.

FIRST METHOD

Total ozone amounts are derived by a single statistical regression method proposed by CROSBY et al. (1981). HIRS/2 has only one channel (channel 9) in ozone 9.6 μm band. Channel 9 radiance in the ozone 9.6 μm band is written as

$$I = B(T_s) \tau(p_s) - \int_0^{p_s} B(T(p)) \frac{\partial \tau(p)}{\partial p} dp \quad (1)$$

where $\tau(p)$ is transmittance, $B(T)$ is Planck function, T , p , T_s and P_s are temperature, pressure, temperature and pressure at the ground surface, respectively. Besides channel 9 radiance, we use radiances of channels 1, 2 and 3 which have information on the temperature around the ozone layer and channel 8 in the window region. Total ozone amount U is obtained by the linear regression method from brightness temperatures T_i of five channels as

$$U = \bar{U} + \sum_{i=1}^5 C_i (T_i - \bar{T}_i) \quad (2)$$

where \bar{U} is the average total ozone amount and C_i are regression coefficients for five channels. Regression coefficients are determined for each season using the ground-based Dobson spectrophotometer measurements at Syowa Station.

Total ozone amounts thus derived are compared to those from Dobson measurements in Figure 1. At Syowa Station where the regression is made, the rms deviation is about 3 DU (10^{-3} atm cm) in the season of a small variation of the ozone amount, and about 13 DU in the season of a large variation. Another comparison is made for the independent data set at the South Pole (Amundsen-Scott Station). The rms deviation is about 32 DU and the mean difference is about 5 DU (YAMANOUCHI et al., 1984).

SECOND METHOD

Another method similar to that by PRABHAKARA et al. (1976) is also used to derive total ozone amounts. This method is based on the assumption that the height of the ozone layer is proportional to the total ozone amount. The

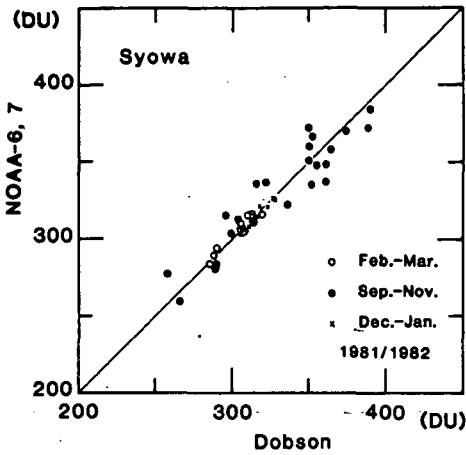


Figure 1. Scatter diagram of total ozone amounts at Syowa Station obtained from satellites by the regression method (NOAA-6 and -7) and Dobson measurements.

radiative transfer equation for the channel 9 of HIRS/2 is solved approximately with the surface temperature from the channel 8, and with the temperature around the ozone layer obtained from channels 1, 2 and 3. Channel 9 radiance in the ozone $9.6 \mu\text{m}$ band is approximated as

$$\begin{aligned}
 I &= B(T)_s \cdot \tau(p_s) - \int_0^{p_s} B(T(p)) \frac{\partial \tau(p)}{\partial p} dp \\
 &\approx B(T_s) \cdot \tau(p_s) + B(T_e) \cdot (1 - \tau(p_s)) \\
 &= B(T_s) \cdot (1 - A) + B(T_e) \cdot A
 \end{aligned} \quad (3)$$

where A is the total band absorptance. Then

$$\frac{B(T_s) - 1}{B(T_s) - B(T_e)} = A \quad (4)$$

The absorptance is approximated with the constant k as

$$A = f(U) \approx k U \quad (5)$$

The height of the ozone layer (\bar{p}) is assumed to be proportional to the total ozone amount U as

$$U = \bar{U} + C (\bar{p} - \bar{p}_m) \quad (6)$$

$$T_e = T(\bar{p}) \quad (7)$$

Equation 4 is solved with equations 5, 6 and 7.

A good agreement is found for total ozone amounts thus derived and those of Dobson measurements at Syowa Station in the season of the so-called stratospheric sudden warming (rms ≈ 12 DU) as shown in Figure 2; however, only vague agreements are seen in other seasons (rms ≈ 36 DU).

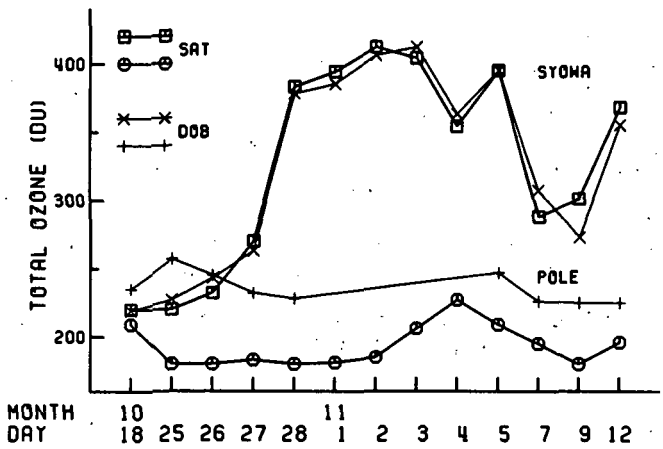


Figure 2. Total ozone amounts obtained from satellite by the second method are compared to those from Dobson measurements in the season of "stratospheric sudden warming", 1982.

VARIATION OF OZONE HORIZONTAL DISTRIBUTION

Seasonal variations of the horizontal distribution of the total ozone are given. The maximum region of ozone is found to traverse from the lower latitude ($\leq 60^{\circ}$ S) to the higher latitude, sometimes to the inland of the Antarctic, from winter to summer, before and after the so-called sudden warming. The increase of the total ozone at Syowa Station occurs when the maximum region reaches.

A good correlation is seen between the ozone amount and the atmospheric temperature in the 50-100 mb level (Figure 3). The maximum region of ozone corresponds to the high temperature region of channels 2 and 3. Dynamical advections of ozone are suggested as shown by SCHOEBERL and KRUEGER (1983).

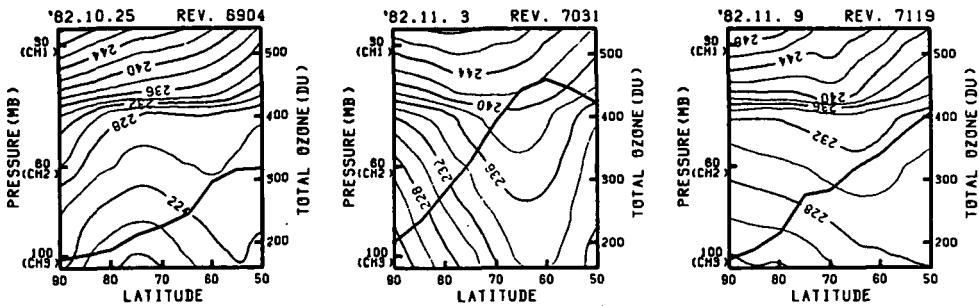


Figure 3. Latitudinal variations of vertical temperature distribution (channel brightness temperature) and total ozone amount obtained by NOAA-7 (thick line) in October and November 1982.

REFERENCES

- Crosby, D. S., W. G. Planet, A. J. Miller and R. M. Nagatani (1981), Evaluation and comparison of total ozone fields derived from TOVS and SBUV, Proc. Quadrennial Int. Ozone Symp., 1980, Boulder, 161-167.
- Prabhakara, C., E. B. Rodgers, B. J. Conrath, R. A. Hanel and V. G. Kunde (1976), The Nimbus 4 infrared spectroscopy experiments. 3. Observations of the lower stratospheric thermal structure and total ozone, J. Geophys. Res., 81, 6391-6399.
- Schoeberl, M. R. and A. J. Krueger (1983), Medium scale disturbances in total ozone during southern hemisphere summer, Bull. Am. Meteorol. Soc., 64, 1358-1365.
- Yamanouchi, T., I. Iwashina and Y. Seo (1984), Derivation of total ozone amount in the Antarctic atmosphere from TOVS of TIROS-N/NOAA satellites, Antarct. Res., 81, 9-15.

5.15 SEASONAL AND DIURNAL VARIATION OF THE ATMOSPHERIC NO₂ AT SYOWA STATION, ANTARCTICA

K. Shibasaki

Geophysics Research Laboratory
University of Tokyo
Tokyo 113, Japan

Extensive attention has been directed to nitrogen dioxide (NO₂) since its important role in the atmospheric chemistry relating to the stratospheric ozone (e.g., WMO, 1982) has been pointed out. However, the behavior of NO₂ in the atmosphere has still not been fully confirmed; although ground-based, balloon and satellite measurements of NO₂ have been reported by many scientists. Especially, only a few measurements made at high latitude in the Southern Hemisphere have been reported (NOXON, 1978; MCKENZIE and JOHNSTON, 1982, 1984).

I measured the total atmospheric NO₂ by ground-based visible absorption spectroscopy at Syowa Station (69°S, 39.6°E), Antarctica. The observation continued from March 1983, to January 1984. Since the principles of measurement, instrumentation and the method of data analysis are described in detail in the paper by OGAWA et al. (1981), I will describe them briefly here. Our measurement system consists of a sun and moon tracker, a monochromator with photo-metric detector, and a digital data recorder. Some modifications were added to the early system. A condenser lens of 50 mm was settled before the entrance slit of a NIKON G500 II monochromator in order to make nighttime observation, using the moon as a light source. High data acquisition rate of one solar spectrum per minute was adopted in place of one solar spectrum per 4 minutes. In January 1984, spectral data were taken with a compact spectrophotometer designed for a balloon observation.

An example of ratio spectra is given in Figure 1. A spectrum obtained from the balloon-borne measurement at Palestine (IWAGAMI, personal communication, 1984) was used as a reference, NO₂ free, one. Absorption bands by NO₂ are clearly seen. A least-squares method is adopted to deduce NO₂ column density from the whole spectral data. Figure 2 shows an apparent variation of deduced NO₂ column densities with solar zenith angle.

The vertical column density of the stratospheric NO₂ was derived statistically from such a result as illustrated in Figure 2. I assumed that NO₂ in the stratosphere was distributed between 10 km and 35 km, that the tropospheric NO₂ abundance was negligible, and that there occurs no change in NO₂ distribution during the measurement. Under the above assumptions, each of the derived NO₂ column densities can be expressed as follows:

$$N(x_i) = A + F(x_i) \cdot N_0$$

where $N(x_i)$ is NO₂ column density derived at a solar zenith angle of x_i , A is an offset constant attributed to the instrument, $F(x_i)$ is the geometrical factor, and N_0 is the vertical column density of NO₂.

In the above formula, A should be zero, if a solar spectrum and a reference one were acquired with the same spectrometer. In this study, A was not zero but nearly constant, because the reference spectrum was obtained with a Jobin-Yvon H20 monochromator while observed ones with a NIKON G500 II monochromator. $F(x_i)$ was calculated using the model atmosphere and normalized to $F(0) = 1$. Using a least-squares technique, that is,

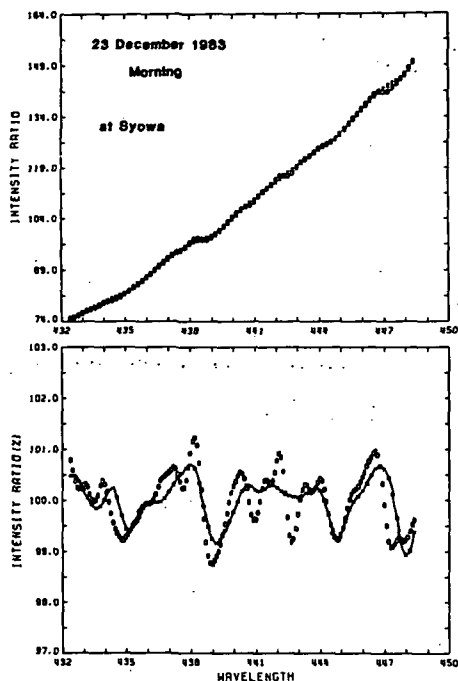


Figure 1. A ratio spectrum obtained during the morning observation of December 23, 1983. Circles indicate observed data, and a solid line with asterisks indicates a calculated one. The upper panel shows an actual ratio spectrum between an observed and a reference solar spectrum, and the lower panel shows the upper with the tilt removed.

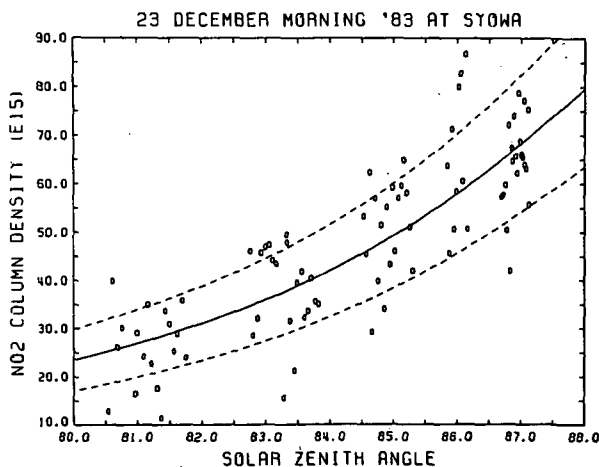


Figure 2. Column densities of atmospheric NO_2 as a function of solar zenith angle measured on the morning of December 23, 1983. The solid curve shows an estimated variation of stratospheric NO_2 abundance as deduced using a technique described in the text. Dashed curves show one standard deviation of data.

$$\frac{\partial R}{\partial N_0} = 0, \frac{\partial R}{\partial A} = 0$$

where R , a residual function, is $\{N(x_i) - A - F(x_i) \cdot N_0\}^2$, N_0 was derived.

Before making a comparison between this value and those reported by other experimenters, the correctness of the second assumption must be evaluated. Contribution of the tropospheric NO_2 to the derived N_0 becomes bigger with increasing solar zenith angle in comparison with that of the stratospheric NO_2 . The discrepancy may occur between the observed NO_2 column densities and those calculated taking the stratospheric NO_2 only into account. But such a discrepancy was not clearly recognized, even if a solar zenith angle became nearly 90 degrees. This fact means that the second assumption is reasonable. N_0 can be considered to represent the stratospheric NO_2 abundance. Further, taking the detection limit of our system into consideration, it is concluded that a mixing ratio of NO_2 in the Antarctic troposphere is <0.01 ppbv.

Figure 3 shows all data obtained through a year at Syowa Station. A summer maximum and a winter minimum can be clearly seen. This seasonal trend agrees well with that measured at Barrow (71°N) by NOXON et al. (1983) and with the theoretical result given by SOLOMON and GARCIA (1983). As for the difference between morning and evening NO_2 column densities, however, it seems to be smaller than that reported by NOXON et al. (1983) and by SOLOMON and GARCIA (1983). Whether an interhemispheric difference in seasonal behavior of the stratospheric NO_2 exists or not, further studies will be needed.

The difference between the vertical NO_2 abundance measured on the morning and that on the evening is discernible. But I could not draw a confirmative conclusion about a detail time dependence behavior of the atmospheric NO_2 abundance during a day (Figure 4). Also, I cannot state a definitive conclusion about the nighttime abundance of the stratospheric NO_2 , because only few data were acquired and the data quality was poor.

In conclusion, seasonal behavior of the stratospheric NO_2 measured at Syowa, Antarctica shows good agreement with that obtained at high latitude in

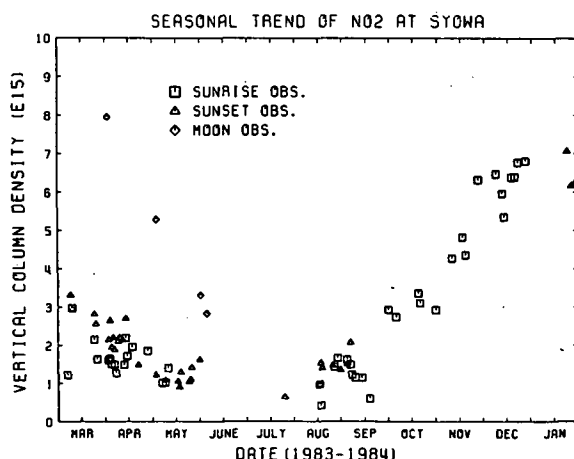


Figure 3. Seasonal variation of stratospheric NO_2 abundance at Syowa Station, Antarctica. All data including morning, evening, and night measurements are shown.

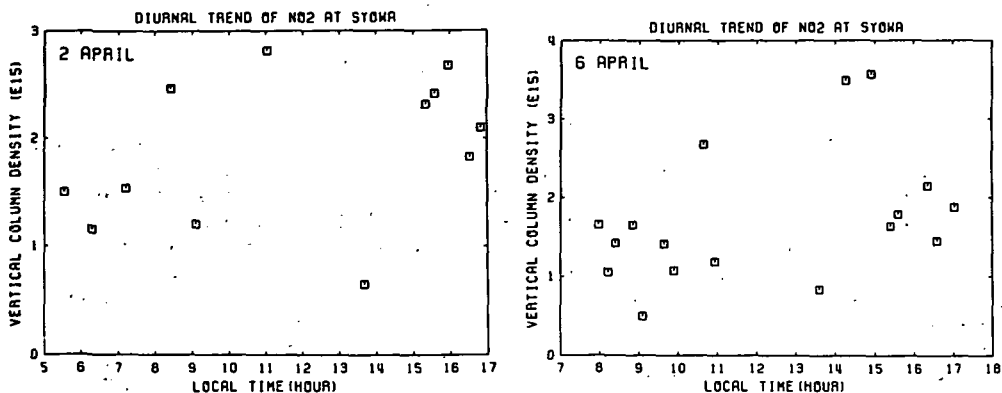


Figure 4. Illustration of the diurnal behavior of stratospheric NO_2 abundance. Each square gives the four- or five-minute average.

the Northern Hemisphere. However, day-to-day variations are large and complicated. Further studies will be needed in relation to nighttime decay, nighttime abundance and stratospheric meteorological conditions. Some of them will be presented in the near future.

REFERENCES

- McKenzie, R. L. and P. V. Johnston (1982), Seasonal variations in stratospheric NO_2 at 45°S , J. Geophys. Res. Lett., **9**, 1255-1258.
- McKenzie, R. L. and P. V. Johnston (1984), Spring time stratospheric NO_2 in Antarctica, Geophys. Res. Lett., **11**, 73-75.
- Mount, G. H., D. W. Rusch, J. F. Noxon, J. M. Zawondny and C. A. Barth (1984), Measurements of stratospheric NO_2 from the Solar Mesosphere Explorer satellite 1. An overview of the results, J. Geophys. Res., **89**, 1327-1340.
- Noxon, J. F. (1978), Stratospheric NO_2 in the Antarctic winter, Geophys. Res. Lett., **5**, 1021-1022.
- Noxon, J. F., W. R. Henderson and R. B. Norton (1983), Stratospheric NO_2 : 3, The effects of large-scale horizontal transport, J. Geophys. Res., **88**, 5240-5248.
- Ogawa, T., K. Shibasaki and K. Suzuki (1981), Balloon observation of the stratospheric NO_2 profile by visible absorption spectroscopy, J. Meteor. Soc. Japan, **59**, 410-416.
- Solomon, S. and R. R. Garcia (1983), On the distribution of nitrogen dioxide in the high-latitude stratosphere, J. Geophys. Res., **88**, 5229-5239.
- WMO (1982), The stratosphere 1981: theory and measurement, Report No. 11, WMO Global Ozone Research and Monitoring Project.

5.16 THE CHANGE OF DEPOLARIZATION OF BACKSCATTERING LIGHT FROM THE POLAR STRATOSPHERIC AEROSOL LAYER

Y. Iwasaka

Water Research Institute
Nagoya University
Nagoya 464, Japan

The change of polarization properties of scattered light strongly depends on the non-sphericity of target particles. It should be helpful information for the study of stratospheric aerosols to know the non-sphericity of stratospheric aerosol particles (IWASAKA and HAYASHIDA, 1981).

Here we should like to describe the change of the total backscatter depolarization ratio of the stratospheric aerosol layer measured at Syowa Station (69.00°S, 39.35°E), Antarctica.

The total backscatter depolarization ratio is defined by,

$$D = B_a(z) / B_p(z)$$

where $B(z)$ and $B_p(z)$ are the backscatter coefficients measured at a perpendicular polarized plane to the polarization plane of emitted laser pulse and at a parallel plane, respectively.

In Figure 1 the temperature distributions measured by radio sondes which were launched near the lidar station are shown. The cold atmosphere with the temperature below -80°C was frequently observed in mid-winter. The backscatter coefficient of stratospheric particulate matter was deduced from the measurements of backscatter light intensity (lidar), temperature (radio sonde), and pressure (radio sonde). The vertically integrated backscatter coefficient in the height range of the stratosphere given by

$$\int_z B(z) dz$$

where z = range of integration and shows a large value in the winter season as indicated in Figure 2.

We show two typical results of the total backscatter depolarization ratio measured on June 2, 1983, and June 30, 1983, in Figure 3. Both are obtained during the period of winter enhancement stage of the Antarctic aerosol layer, but there is a noticeable difference between these two. The results measured on June 2 when the aerosol layer just started to enhance shows a low depolarization ratio, and the measurement on June 30 when the enhancement was fully developed shows a very large depolarization ratio. This observational fact certainly suggests that there were many non-spherical particles in the stratosphere during the period when the stratospheric aerosol layer fully enhanced, and supports the idea that many ice crystal particles formed in the cold winter stratosphere is an essential factor, which causes a noticeable enhancement of the Antarctic stratospheric aerosol layer. However, the measurement on June 2, 1983, suggests that there are possibly other different processes which control the winter enhancement of the polar stratospheric aerosol layer, especially at an early stage of the enhancement.

This enhancement can play an important role in the global budget of stratospheric water vapor and sulfur compounds, and thus it should be necessary to make more detailed and intensive studies.

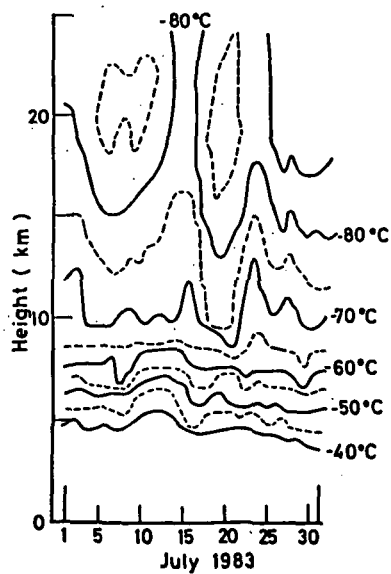
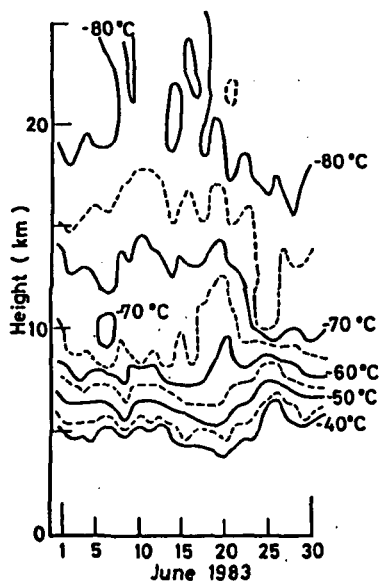
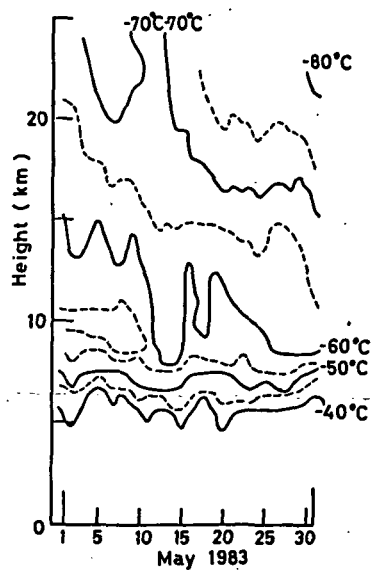
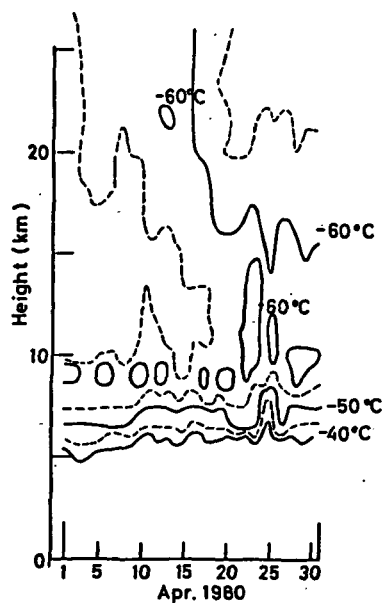


Figure 1. Temperature distribution of the stratosphere measured at Syowa Station (69.00°S, 39.35°E).

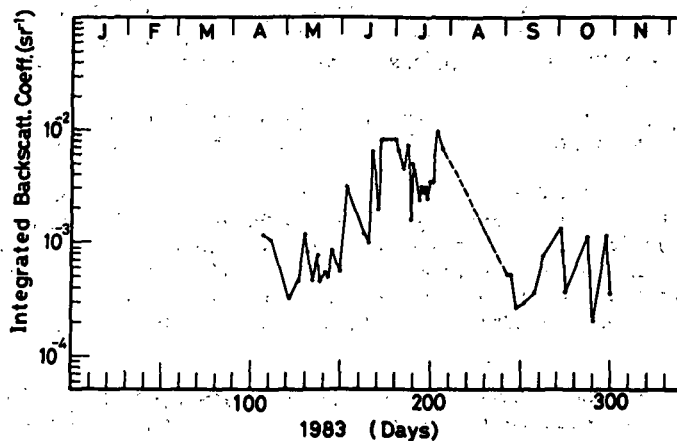


Figure 2. Temporal change of the vertically integrated backscatter coefficient in the height range of the stratosphere.

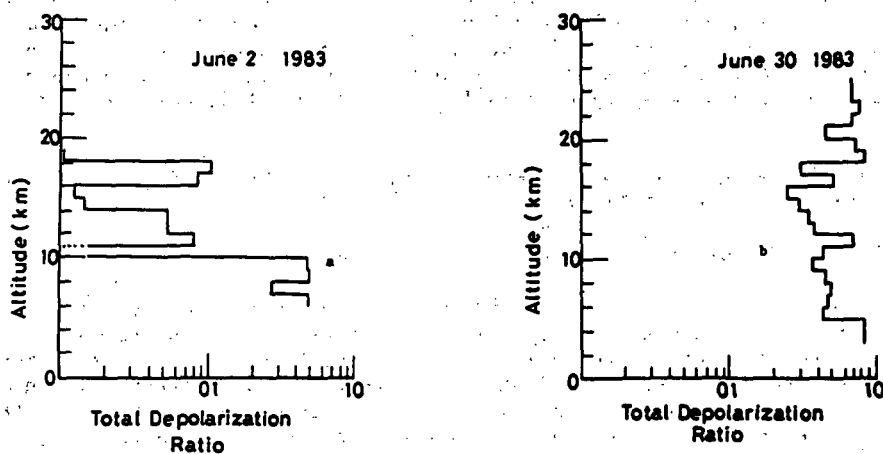


Figure 3. The depolarization change measured during the period of the early stage of enhancement of the stratospheric aerosol layer (a) and measured during the period of a fully developed stage (b).

REFERENCES

- Iwasaka, Y. and S. Hayashida (1981), *J. Meteorol. Soc. Japan*, **59**, 611-614.
 Steele, H. M., P. Hamill, M. P. McCormick and T. J. Swisler (1983), *J. Atmos. Sci.*, **40**, 2055-2067.

5.17 THE STRATOSPHERIC AEROSOL PARTICLE MEASUREMENT
 BY BALLOON AT SYOWA STATION (69.00°S, 39.35°E):
 OUTLINE OF SPECIAL SONDE (RUBBER) CAMPAIGN JARE 24

Y. Iwasaka¹, T. Morita², T. Itoh³, K. Shibasaki⁴, Y. Makino³
 T. Tanaka⁵, K. Tsukamura⁶, T. Yano⁶, K. Kondoh⁶, G. Iwashita⁶

¹Water Research Institute, Nagoya University, Chikusa-ku, Nagoya 464, Japan

²Research Institute of Atmospherics, Nagoya University, Toyokawa 442, Japan

³Meteorological Institute, Tsukuba-gun, Ibaraki 305, Japan

⁴Geophysical Research Laboratory, University of Tokyo, Tokyo 113, Japan

⁵Radio Research Laboratories, Koganei-shi, Tokyo 184, Japan

⁶Japan Meteorological Agency, Tokyo 100, Japan

During the period of AMA (Antarctic Middle Atmosphere), various style balloons were used to measure atmospheric parameters at Syowa Station (69.00°S, 39.35°E), Antarctica. Here we should like to describe the measurements which were made using balloons specially designed to monitor stratospheric aerosol particles. This type balloon was first used by JARE (Japan Antarctic Research Expedition) 24th Team (Leader Prof. S. Mae, National Institute of Polar Research) in 1983. Until that time, the Japan Antarctic Research Expedition Team had been using only a large plastic balloon to monitor various minor constituents in the stratosphere. The plastic balloon was very useful, but it took a long time to arrange a balloon launching. Additionally, launching time strongly depended on weather conditions, so we frequently had let good launching chances slip, owing to bad weather conditions, especially winds with speeds greater than 2 m/sec. Usage of a specially designed sonde enabled us to make a timely launching of the balloon and to save manpower, since a launch of this type of sonde was so easy that we could lift it even if it was very bad weather.

The following should be pointed out concerning the campaign of the specially designed rubber balloon:

1) We made our first success of a winter season launching.

2) We could have good cooperative measurements with laser radar measurements. In Figure 1, a typical sonde arrangement is shown. A sample of measurements is shown in Figure 2. Figure 2a and 2b show the stratospheric aerosol content measured by balloon and by laser radar, respectively, in early June, when the stratospheric aerosol layer began to enhance. These results suggest that aerosol particle number density rapidly increased in the early stage of enhancement of the polar stratospheric aerosol layer. In Table 1, launching dates and items are summarized.

Table 1.

Specially designed rubber sondes at Syowa Station (69.00°S, 39.35°E)

1983 April 1	Large particle, density and size distribution
June 3	Large particle, density and size distribution Aitken particle, density
October 16	Large particle, density and size distribution
October 17	Aitken particle, density

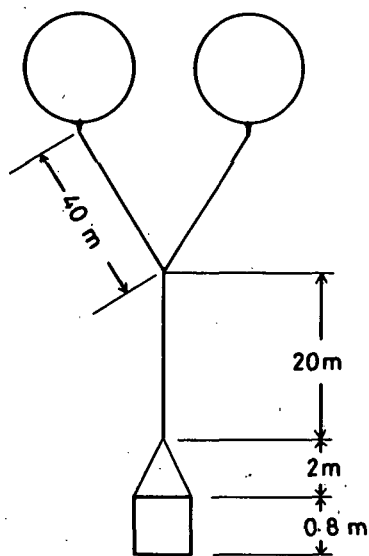


Figure 1.

Figure 2 (a).

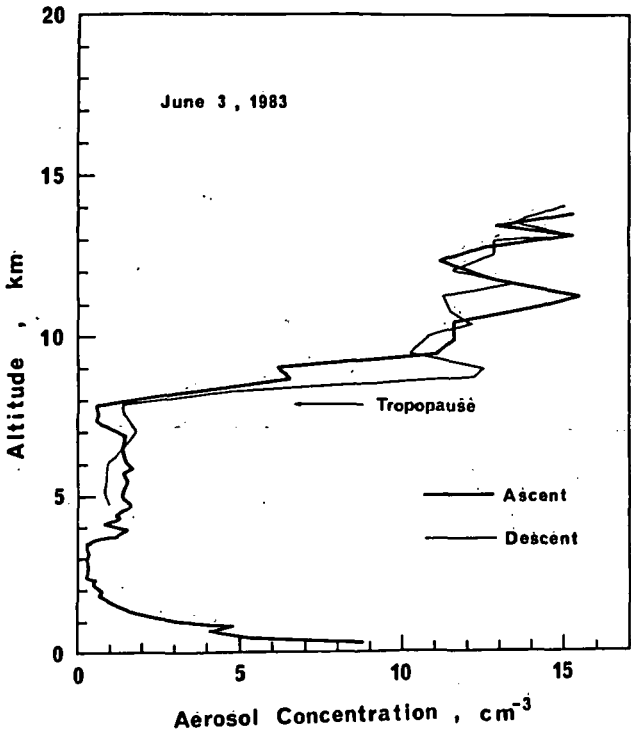
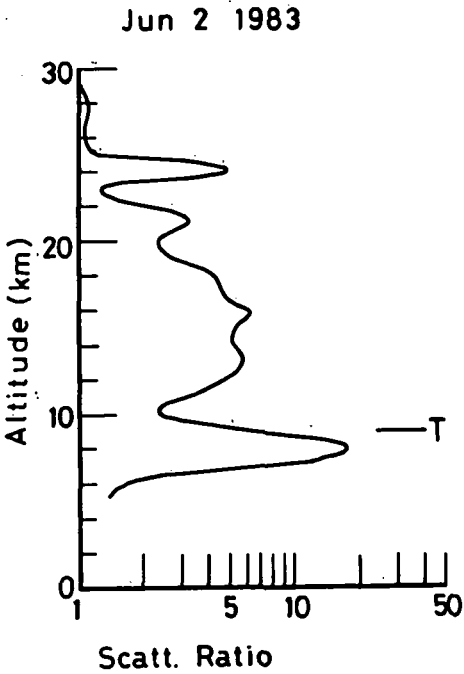


Figure 2 (b).



5.18 WATER VAPOR CONTENT IN THE POLAR ATMOSPHERE
MEASURED BY LYMAN- α /OH FLUORESCENCE METHOD

Y. Iwasaka, S. Saitoh and A. Ono

Water Research Institute,
Nagoya University, Nagoya 464, Japan

The water vapor of the polar stratosphere possibly plays an important role in various aeronomical processes; for example, OH radical formation through photodissociation of H_2O , formation of water cluster ions, radiative energy transfer in the lower stratosphere, condensation onto particulate matter, and so on. In addition to these, it has been speculated, from the viewpoint of global transport and/or budget of water vapor, that the polar stratosphere functions as an active sink. STANFORD (1973) emphasized the existence of the stratospheric Cist cloud in the polar stratosphere which brought a large loss rate of stratospheric water vapor through a so-called freeze-out of cloud particles from the stratosphere into the troposphere. However, these geophysically interesting problems unfortunately remain to be solved, owing to the lack of measurements on water vapor distribution and its temporal variation in the polar stratosphere.

Here we should like to describe the water vapor content measured at Syowa Station (69.00°S, 39.35°E), Antarctica using a balloon-borne hygrometer (Lyman - α /OH fluorescence type), even if it is preliminary. The instrument and its test have been described in other papers (e.g., IWASAKA et al., 1981; MURABAYASHI et al., 1982).

Figure 1 shows the balloon train used here. To make the operation of the balloon launching speedy and easy, we chose twin rubber balloons (each rubber weighed 3 kg). To prevent contamination, the length between the balloon and the physical instrument was set to be 70 m. Total weight of the instrument, including weight of the battery, was 9.0 kg.

A block diagram of the instrument is shown in Figure 2.

Water vapor measurement by the balloon was made on October 27, 1983, at Syowa Station (69.00°S, 39.35°E), Antarctica. Unfortunately, the balloon burst at about 15 km height, and we could not take a vertical profile of the water vapor content of the lower stratosphere.

The result is compared with the observation due to a carbon plate hygrometer which was mounted in a routine radiosonde. The comparison shows good agreement, even though it is limited in the lower atmosphere. Above the troposphere, a very dry region was found. We cannot conclude definitely that such a dry region is always observed in the polar region, since it is speculated that water vapor changes in various time and space scales. Here we should like to present the speculation that water vapor content in this season can be influenced by the winter enhancement of the polar stratospheric aerosol layer (IWASAKA et al., 1985, this volume).

To clarify water vapor distribution of the polar stratosphere, it is necessary to gain more observational facts which cover all seasons of the year.

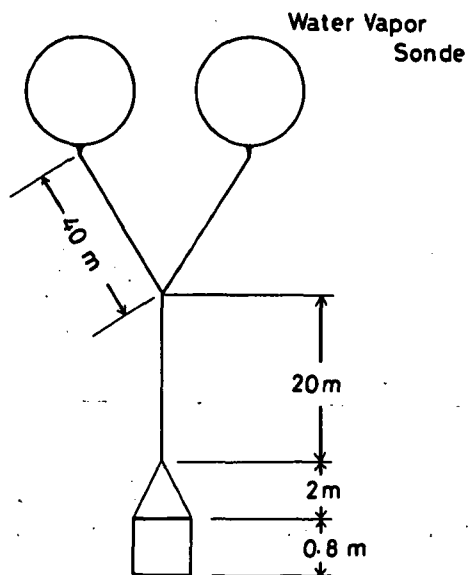


Figure 1. Balloon train used at Syowa Station (69.00°S , 39.35°E).

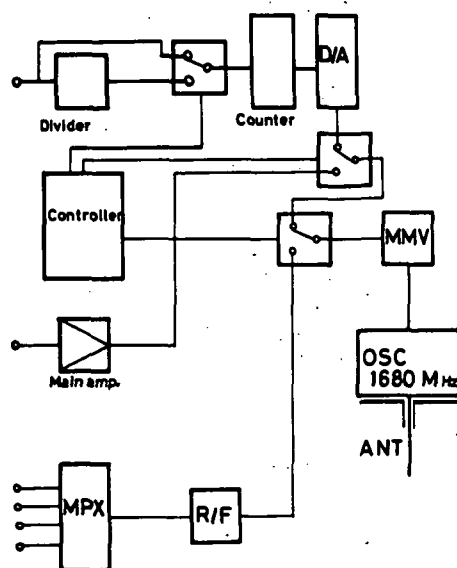
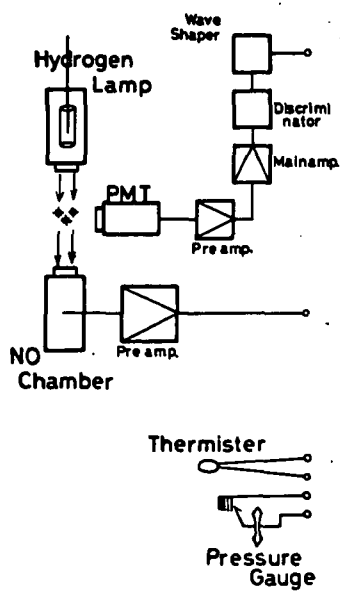


Figure 2. Block diagram of water vapor sonde.

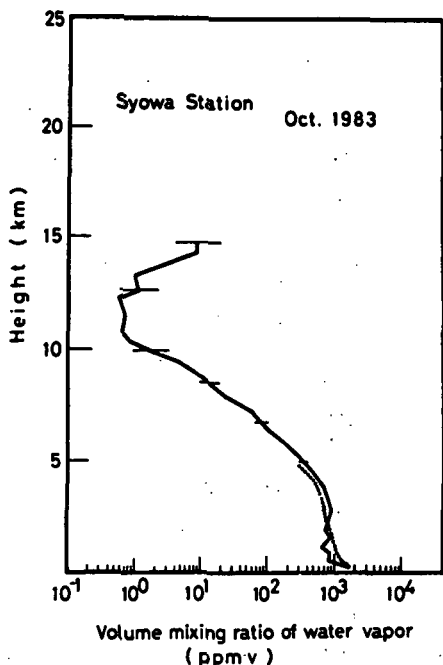


Figure 3. Water vapor content measured at Syowa Station (69.00°S , 39.35°E), Antarctica. Carbon plate hygrometer was also used to compare (dotted line). Error range is indicated by "—".

REFERENCES

- Iwasaka, Y., S. Murabayashi and Y. Yamashita (1981), A new method to measure water vapor content of the polar middle atmosphere using photochemical reaction " $\text{H}_2\text{O} + h\nu$ (121.6 nm) \rightarrow OH + H," Mem. Nat'l. Inst. Polar Res., **19**, 195-209.
- Murabayashi, S., Y. Iwasaka and Y. Yamashita (1982), A note on the new type hygrometer using the photochemical reaction: $\text{H}_2\text{O} + h\nu$ (Ly- α line) \rightarrow OH + H, and OH + $h\nu$ ($\lambda = 309$ nm), Mem. Nat'l. Inst. Polar Res., **22**, 239-246.
- Stanford, J. L. (1973), Possible sink for stratospheric water vapor at the winter Antarctic pole, J. Atmos. Sci., **30**, 1431-1436.

AUTHOR INDEX

AUTHORS	PAGE NUMBERS
Ahmed, M. I.	190
Akita, I.	330
Apruzese, J. P.	294
Araki, T.	182
Arijs, E.	426
Avery, S.	19; 295
Ayukawa, M.	498
Bailey, P. I.	360
Balsley, B. B.	19; 23; 206; 260; 295; 297; 298
Bhattacharya, A. B.	399
Brasseur, G.	386
Boville, B. A.	161; 165
Carter, D. A.	206; 260
Chandramma, S.	421
Chandrasekhar, G.	190
Chanin, M. L.	247
Chubachi, S.	453; 491
Clark, R. R.	19
Clark, W. L., Jr.	220; 296
Cogger, L. L.	326
Coy, L.	328
Craig, R. L.	19; 76
Crochet, M.	260
Czechowsky, P.	207
Das Gupta, M. K.	399
Devara, P. C. S.	190
Dev Barman, S.	399
Dev Gupta, A. K.	399
Echizenya, Y.	15
Ecklund, W. L.	206; 260
Ejiri, M.	498
Elford, W. G.	19
Elphinstone, R.	326
Fairlie, T. D. A.	99
Fellous, J. L.	19
Forbes, J. M.	50
Fraser, G. J.	19
Fritts, D. C.	212; 282; 299; 328
Fujii, R.	450; 471; 495; 498
Fujiwara, M.	337; 346; 406; 417; 450
Fukao, S.	201
Fukunishi, H.	450; 498
Gage, K. S.	297
Garcia, R. R.	132; 169; 281
Garello, R.	260; 297; 298
Gartner, V.	35
Geller, M. A.	10
Gelman, M. E.	24; 89
Gille, J. C.	360
Green, J. L.	296
Grose, W. L.	381
Hasebe, F.	395
Hauchecorne, A.	80; 247

Hayasaka, T.	350
Hayashi, Y.	179
Hayashida, S.	340
Haynes, P. H.	126
Hirasawa, T.	450; 471; 498
Hirono, M.	337; 346; 406; 417
Hirooka, T.	72
Hiroshige, M.	319
Hirota, I.	11; 72; 117
Hirota, M.	391; 491
Hofmann, D. J.	443
Holton, J. R.	293; 359
Honda, H.	431
Ichinose, T.	310; 324
Igarashi, K.	471; 495
Ikegami, M.	486
Indira, K.	32; 96
Ingels, J.	426
Ishii, T.	15
Ishimine, T.	15; 325; 327
Ito, T.	486
Itoh, T.	363; 431; 513
Iwagami, N.	461
Iwasaka, Y.	340; 450; 482; 486; 498; 510; 513; 516
Iwashina, I.	502
Iwashita, G.	513
Iwata, A.	343; 354; 405
Jacka, F.	248; 477
Jacob, P. G.	248
Johnson, K. W.	24; 89
Jones, N. P.	477
Judasz T.	295
Juzdan, R.	355
Kainuma, S.	325
Kamiyama, H.	253
Kanazawa, I.	486
Kantor, A.	28
Karmakar, P. K.	399
Kato, S.	19; 57; 66; 201
Kawaguchi, S.	458; 502
Kawahira, K.	375
Kawamoto, H.	408
Kida, H.	273; 365
Kikuchi, T.	327
Kitamura, T.	319
Klostermeyer, J.	216
Kodera, K.	186
Kondo, Y.	343; 354; 405; 412
Kondoh, K.	513
Kubo, H.	431
Kumar, S.	42
Kummel, U.	109
Kuratani, Y.	471
Labitzke, K.	1; 109
Lee, H. S.	442
Leifer, R.	355
Lindzen, R. S.	259
Liu, C. H.	287
Lu, D.	220; 303

Lyjak, L. V.	360
Maeda, M.	351
Makide, Y.	364; 431
Makino, Y.	391; 458; 491; 513
Mambo, M.	324
Manson, A. H.	19; 61; 226
Marcos, F. A.	28
Marks, C. J.	140
Marubashi, K.	325
Massebeuf, M.	19
Massie, S. T.	360
Matsuzaki, A.	363
Matthews, W. A.	354; 405
McCormick, M. P.	329
Meek, C. E.	19; 61; 226
Memmesheimer, M.	35
Michaelis, V.	14
Miyahara, S.	154
Miyaoka, H.	450
Morita, Y.	405; 412; 482; 513
Mukherjee, B. K.	32; 96
Muramatsu, H.	391; 458; 491
Murphree, J. S.	326
Murthy, B. V. K.	46
Murty, Bh. V. R.	32; 96
Nagano, I.	324
Nagasawa, C.	310; 324
Nagpal, O. P.	42
Naito, K.	330
Nakajima, T.	350
Nakamura, Y.	363
Nealy, J. E.	381
Nevejans, D.	426
Ogawa, T.	306; 310; 324; 408; 458; 461; 471; 495
Okada, Y.	330
Okuzawa, T.	237; 310; 324
O'Neill, A.	14; 99; 105; 140
Ono, A.	482; 516
Parameswaran, K.	46
Plumb, R. A.	76; 373
Pope, V. D.	105; 140
Prasad, B. S. N.	421
Purkait, N. N.	69; 399
Quiroz, R. S.	89
Reddy, R. S.	96
Reid, I. M.	226
Riddle, A. C.	23; 260
Roper, R. G.	19
Rose, K. O.	46; 109; 386
Rosenthal, A. J.	145
Ruster, R.	207; 216
Saitoh, T.	516
Sakai, H.	431
Salby, M. L.	132; 169
Sasaki, T.	391
Sato, T.	201
Sato, Y.	310
Schoeberl, M. R.	116; 292; 294
Sehra, J. S.	399

Sekihara, K.	466
Sen, A. K.	399
Shibasaki, K.	461; 506
Shibata, T.	237; 310; 324; 337; 346; 351; 406
Shibazaki, K.	513
Shimizu, Y.	325
Shiobara, M.	491
Shiotani, M.	11; 117
Smith, A. K.	116; 360
Smith, M. J.	19
Smith, S. A.	212
Smythe, C. M.	360
Solomon, S.	281
Strobel, D. F.	294
Sugiuchi, H.	327
Suzuki, K.	502
Tabata, T.	330
Takagi, K.	310
Takagi, M.	343; 354; 405; 412; 482
Takahashi, M.	157
Takano, K.	174
Takeda, M.	182
Takefu, M.	319
Tanaka, H.	232; 302
Tanaka, M.	350; 458; 498
Tanaka, T.	471; 495; 513; 310
Tattelman, P.	28
Tominaga, T.	364; 431
Tomita, F.	253
Tsuda, T.	19; 57; 66; 201
Tsukamura, K.	513
Tsutsui, M.	306; 324
Tung, K. K.	145
Turner, R. E.	381
Uchino, O.	330; 351; 438
Uchiuni, M.	417
Uryu, M.	157; 174
VanZandt, T. B.	212; 220; 296
Vernin, J.	296
Vincent, R. A.	19; 76; 196; 299
Warnock, J. M.	296
Weinstock, J.	242; 328
Xiong, N. L.	264
Yamanaka, M. D.	232; 302
Yamanouchi, T.	458; 502
Yamazaki, K.	121
Yano, T.	513
Yeh, K. C.	287
Yokohata, A.	364; 431
Zhang, X. J.	264
Zhu, X.	293

CUMULATIVE LISTING FOR THE MAP HANDBOOK

Volume	Contents	Date of Publication
1	National Plans, PMP-1 Report, PMP-2 Report, PMP-3 Report, Approved MAP Projects	June 1981
2	Symposium on Middle Atmosphere Dynamics and Transport (Extended Abstracts)	June 1981
3	PMP-5 Report, MSG-1 Report, MSG-2 Report, MSG-3 Report, Antarctic Middle Atmosphere Project (AMA), EXOS-C Scientific Observations, WMO Report No. 5, Updated Chapter 2 of MAP Planning Document, Condensed Minutes of MAPSC Meetings	November 1981
4	Proceedings of MAP Assembly held in Edinburgh, 14-15 August 1981, Condensed Minutes of MAP Steering Committee Meetings held in Edinburgh, Proceedings of MAP Open Meeting held in Hamburg, 19 August 1981	April 1982
5	A Catalogue of Dynamic Parameters Describing the Variability of the Middle Stratosphere during the Northern Winters	May 1982
6	MAP Directory	November 1982
7	Acronyms, Condensed Minutes of MAP Steering Committee Meetings, Ottawa, May 1982, MAP Project Reports, National Reports, Committee Reports, PMP and MSG Reports, Workshop Reports, Announcements and Corrigendum	December 1982
8	MAP Project Reports: DYNAMICS, GLOBUS, and SSIM, MSG-7 Report, National Reports: Czechoslovakia, USA	July 1983
9	Papers presented at the URSI/SCOSTEP Workshop on Technical Aspects of MST Radar, May 23-27, 1983, Urbana	December 1983
10	Papers presented at the International Symposium on Ground-Based Studies of the Middle Atmosphere, May 9-13, 1983, Schwerin, German Democratic Republic	May 1984
11	Condensed Minutes of the MAP Steering Committee Meetings held in Hamburg 13-14 August 1983, Research Recommendations for Increased US Participation in the Middle Atmosphere Program, GRATMAP Project Report, MAP Study Group MSG-7 Report	June 1984
12	Coordinated Study of the Behavior of the Middle Atmosphere in Winter (PMP-1) Workshops	July 1984
13	Ground-Based Techniques	November 1984
14	Papers presented at the URSI/SCOSTEP Workshop on Technical Aspects of MST Radar, May 22-25, 1984, Urbana	December 1984
15	Balloon Techniques	June 1985
16	Atmospheric Structure and its Variation in the Region 20 to 120 km: Draft of a New Reference Middle Atmosphere	July 1985
17	Condensed Minutes of MAP Steering Committee Meeting, Condensed Minutes of MAP Assembly, MAP Projects and Study Group Reports, National Reports	August 1985
18	Papers presented at MAP Symposium, November 26-30, 1984, Kyoto (Extended Abstracts)	December 1985

MAP SYMPOSIUM

Kyoto, Japan
November 26-30, 1984

CONTENTS

I:	CLIMATOLOGY OF THE MIDDLE ATMOSPHERE.	1
II:	LARGE-SCALE WAVE DYNAMICS	50
III:	GRAVITY WAVES AND TURBULENCE.	196
IV:	TRANSPORT PROCESSES OF TRACE SPECIES AND AEROSOLS	329
V:	MAP IN THE ANTARCTICA	443